DISCLAIMER

Final Project Report 10/2019 - 9/2024 – Award No. DE-FE0031773

Final Project Report:

Pressure Gain, Stability, and Operability of Methane/Syngas Based RDEs Under Steady and Transient Conditions

Principal Investigator:

Mirko Gamba and Venkat Raman

Department of Aerospace Engineering
University of Michigan

Contents

Chapter 1

Objectives of This Study

RDE research has gained prominence in the US, in part due to the sustained investment from DOE through the UTSR and related programs. The principal advantage of detonation-based combustion is the pressure gain within the combustor, which may be utilized in multiple ways. The increase in pressure can reduce the number of stages for the compressor, or compensate for the pressure drop in conventional deflagration-based devices, as well as increase the compactness of the power generation process. This last advantage allows modular units that can augment existing capacity. Further, RDEs are particularly robust with high-hydrogen content fuels including in syngas-based plants and other gasification based cycles. This versatility of use has been a primary source of interest in RDEs. US and international research in the last few years have also provided detailed insight into the key technological hurdles that need to be overcome before RDE-based power generation becomes a reality.

The scope of the proposed work addresses key issues associated with losses associated with the detonation wave and other processes internal to the RDE operation, as well as it develops modeling tools for the evaluation of these losses and exhaust emissions in RDEs. The main challenge in studying RDEs is that RDE performance is highly reliant on the specifics of the design so much so that simple/canonical systems alone cannot provide useful engineering information, but practical RDE designs are sufficiently complex and involve extreme operational environments that detailed access either experimentally (laser diagnostics, for instance) or computationally (direct numerical simulations) are as yet to become practical. To overcome this challenge, we have conducted a combined experimental/simulation/analytical study investigating key phenomena that control the characteristics of operation of RDEs. As a result, the study has developed tools and methods that can be used to evaluate performance and design approaches using reduced-physics models, with the assumptions validated using detailed simulations, and the model prediction tested using experimental observations.

The specific objectives of the research were:

- **Objective 1:** Develop and demonstrate a low-loss fully axial injection concept, taking advantage of stratification effects to alter the detonation structure and position the wave favorably within the combustor.

- **Objective 2:** Obtain stability and operability characteristics of an RDE across operating conditions to aid in the development of operability and performance rules for the operations of other systems.

- **Objective 3:** Develop quantitative metrics for performance gain as well as quantitative description of the loss mechanisms through a combination of diagnostics development, reduced-order modeling, and detailed simulations.

The work proposed has made contribution on design of low-loss inlets that has broad application within the power generation industry for use with pressure gain combustion. The operability and stability of different designs, while focusing on axial air inlet designs, has been analyzed. The effect of nozzle and injection conditions was studied. This work has built on our previous DOE UTSR funded programs, with the goal of further understanding operation of RDEs and elevate the readiness of design consideration. In addition, a suite of diagnostic and modeling tools have been developed to obtain quantitative metrics on performance based on measurements, which can be readily transferred to other experimental configurations.

In the following sections, the advancement completed in this study are reported.

Chapter 2

Experimental Testing Infrastructure and Methods

2.1 Description of RDE Testing Facility

The University of Michigan has tested a range of air-breathing RDE configurations and characterized their operation through a variety of methods [1, 2, 3, 4, 5]. A simplified fluidic and instrumentation schematic of the RDE test facility is shown in Figure 2.1. This figure highlights the key features of the overall test setup that was used for all tests conducted throughout the course of this research.

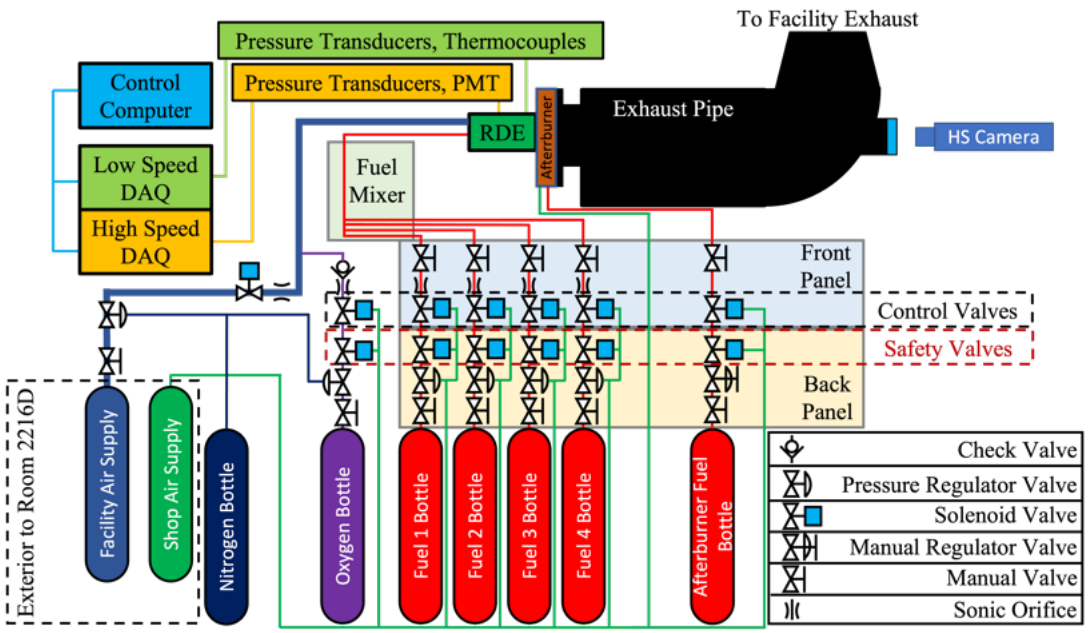

Figure 2.1: Schematic showing the basic layout of the RDE testing facility at the University of Michigan.

As can be seen in Figure 2.1, the facility air and shop air supplies are generated and provided from outside of the RDE test facility. Within the test facility, a total of

four fuel lines are installed. Each line can be used independently or in concert with each other for very high flow rates and/or if a multi-component fuel blend is desired. An additional fuel line for feeding the downstream afterburner is also installed. An additional line is installed that is capable of providing supplemental oxygen to the air stream. A high-pressure nitrogen bottle is used to set the pressure on the air and oxygen pressure regulators, while shop air is used to set the pressure on the fuel pressure regulators. The system comprises manual, pressure regulating, and solenoid valves, as well as a check valve on the oxygen line to prevent backflow. Flow rates are metered through sonic orifices: an air orifice of 13.97 mm diameter and fuel orifices adjustable between 1.32-4.78 mm. Manual valves control reactant bottle flows, pressure regulating valves set upstream pressures and flow rates, while solenoid valves are computer-controlled for test-specific flows.

The laboratory control computer runs a custom control software written in the National Instruments LabView programming environment. This software was pre-existing from prior research efforts [6] and consists of two main components, the master control and low-speed data acquisition program and the high-speed data acquisition program. These programs run in parallel for individual test sequences. Desired flow-rates for each specific test are defined within the control program. The software is flexible in that mass flow rates can be ramped from the starting value to a second desired value mid-test. Dynamic or real-time ramping cannot be performed with the existing software suite, as current test times are limited to 2-5 seconds of "fuel on" a single ramp is all that can be accomplished. The ability to ramp was leveraged for two specific cases that will later be further outlined. These included cases which were incapable of directly initiating at a given inlet condition, and high-flow cases in which thrust measurements were taken.

The sample rate of the low-speed data acquisition system was 200 Hz, while the sample rate of the high-speed data acquisition system was 500 kHz. Data was collected using National Instruments (NI) PCI-6133, PCI-6259 (2X), and PCIe-6353 data acquisition cards, with sensor-to-DAQ connections made through NI BNC-2090 (4X) and BNC-2090A (3X) breakout accessories. One BNC-2090A was used for the high-speed sensors, while all others were dedicated to the low-speed sensors. A total of 8 high-speed channels and 48 low-speed channels were available for each test.

A variety of high-speed sensors were utilized throughout the course of this work. These sensors included various high-speed pressure transducers, a microphone installed within the facility, and a Photo-Multiplier Tube (PMT). The pressure transducers that were utilized included water-cooled Kulite EWCTV-13-312-500A, Kulite

XTEL-190L-250A, and Kulite XTL-123G-190M-17BARA sensors. The water-cooled Kulites were used when installed along the outer wall of the detonation channel, while the others were used when installed within the air and fuel plenums.

The low-speed sensors installed throughout the course of this work are numerous. A variety of pressure transducers, thermocouples, and load cells were used. This included conventionally installed pressure transducers and those installed in a Capillary Tube Averaged Pressure (CTAP) configuration. Thermocouples included bare wire and probe type configurations of Types B, C, J, and K.

As mentioned, a typical test sequence consisted of 2-5 seconds of "fuel on" test time. These typical sequences also included several seconds of air-only flow prior to fuel flow initiation, and several seconds of air-only flow following fuel flow cessation. These air only periods allowed for air flow to establish and settle to a steady value and for the downstream afterburner to light off, and for hot combustion byproducts to be exhausted following each test sequence. Additional test sequences were conducted with zero commanded fuel flow, these cold-flow tests were used to determine the basic flow characteristics of each RDE configuration.

The one constant across all tests and configurations is the facility exhaust system with coupled afterburner. This afterburner is operated at all times when positive fuel flow is commanded. The afterburner thus serves as a safety measure to ensure that all fuel introduced to the RDE is burned prior to exiting the facility. Depending on the RDE configuration and reactant flow rates being tested, the afterburner also serves as a primary or secondary initiation mechanism by leveraging flashback into the detonation channel. When this occurs, rotational operation can result. A predetonator firing directly into the detonation channel was also used a direct initiation mechanism.

As the RDE is directly coupled to the afterburner and facility exhaust system, RDE combustion byproducts are vented into a large exhaust vessel of 52 cm diameter and approximately 2 meters in length, which then converges down to a 10 cm pipe. The exhaust gases are then vented to the atmosphere through an approximately 20 meter long, 10 cm pipe. The large duct that is coupled to the RDE is of an elbow shape with a quartz window installed downstream of the RDE for optical access normal to the exit plane of the RDE. These features can all be noted in Figure 2.1 above.

A fused quartz window was installed within the exhaust stream directly downstream of the RDE normal to the exhaust plane. This window was utilized to capture high-speed videos looking up into the channel for all test cases. These images were

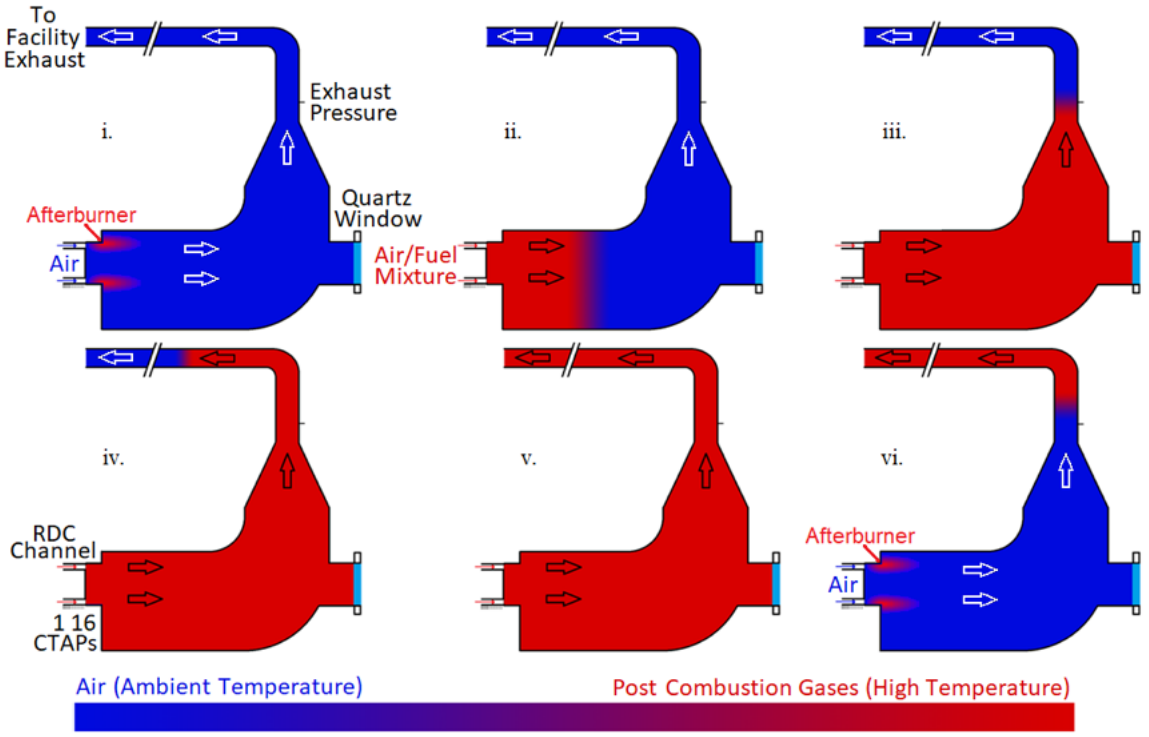

Figure 2.2: Diagrams showing the various phases of operation during a typical RDE test. (i) Cold-flow of air; (ii) ignition; (iii) and (iv) transients; (v) RDE/exhaust steady state operation, and (vi) shutdown.

then post-processed to determine characteristics of the wave system(s) within the RDE for each individual test through the circuit wave analysis (CWA) methodology we have developed in earlier phases of this program [7]. High-speed imagery in this location was captured through either a Phantom v711 or Phantom TMX camera. These videos were typically captured at frame-rates of 50,000 frames per second (fps) or higher. These videos were then post-processed to generate $x - t$ diagrams and perform additional analysis. The cameras were triggered via TTL pulses provided by the main RDE control program. The Phantom v711 was limited in that it is only capable of saving approximately 1.4 seconds of video at the nominal settings of 55,000 fps at a resolution of 288 x 280 pixels . The Phantom TMX was used when available, and enable to record the entirety of each test due to the larger onboard memory.

An electrically heated pebble bed was designed and fabricated in order to en-

able testing with elevated temperature air. This pebble bed was designed for "single run" operation in which the total thermal mass contained within the device was sufficient to enable 10 s of continuous flow at 1 kg/s at 700 K. Although not tested to these extreme conditions, a test sequence was conducted in which air inlet temperatures exceeding 500 K were achieved. Additionally, two high-temperature flow control valves were designed and fabricated to allow for the diversion of flow during heating/operation cycles. The calculations used in the sizing and design of the pebble bed are summarized by Abdulmohsin in his PhD dissertation [8]. The equations included within were discretized on a per-layer basis to enable an accurate determination of the overall size required. Although the focus of Abdulmohsin's effort was related to nuclear reactors, the fundamental equations are applicable for a variety of applications.

The resultant basic design of the pebble bed is that of a 0.5 m section of pipe filled with approximately 5,000 15 mm diameter steel balls. Through the heating methodology outlined in Figure 2.3, the balls within the pebble bed were heated with a 4.5 kW electric heater. Heating was performed in the reverse direction, with a low-pressure facility vacuum applied at the upstream end of the pebble bed. This ensured the bulk of the heating flow passed through the pebble bed, while allowing a small amount of leakage through the RDE to provide pre-heating to the supply lines. Axially dispersed Type-K thermocouples were used to determine the temperature distribution within the pebble bed itself. Once the desired temperature distribution was achieved, the heater inlet and facility exit were capped, and RDE air flow was passed through the pebble bed. As noted previously, peak temperatures of greater than 500 K at the RDE inlet were tested.

The pebble bed was designed to be modular and adaptable to all RDE configurations. Due to its compact size, it is able to moved in and out of the laboratory on an as-needed basis. Additionally, the connections on either end are matched to the existing air feed system such that it can be installed in-line without modification to existing hardware.

The pebble bed is shown in the as-installed configuration in Figure 2.4. The pebble bed was installed in-line with the nominal air supply system, and the array of heated pebbles can be seen in the cutaway of the pebble bed. This installation methodology shows a direct hard-line connection to the RDE inlet, though this connection is capable of being modified to a flexible connection in the future if thrust measurements are desired.

An oxygen supply system was designed and fabricated to enable testing with

oxygen-enriched air for a subset of tests. This system is shown on the fluidic schematic of Figure 2.1. Oxygen is introduced into the air feed line downstream of the sonic orifice, and the system itself was sized to be capable of providing up to 150 g/s of pure oxygen. The sonic orifice used for this system is 3.63 mm in diameter.

The existing air supply system was modified with a swirling mixing element to prevent direct oxygen impingement upon the surfaces of the air feed system. This arrangement can be seen in Figure 2.5. The incoming air is split into four streams that recombine radially at the point at which the oxygen is introduced. This recombination occurs with the four lines offset from each other such that a swirl is introduced, ensuring rapid mixing.

The use of pure oxygen required additional safety precautions to be taken during assembly and operation. All feed lines from the oxygen supply bottle to the mixing element were fabricated using 316 stainless steel hardware that were cleaned to oxygen-safe standards. The air feed lines downstream of the oxygen introduction point were also switched from carbon steel to 316 stainless steel.

A hydrogen/oxygen pre-detonator was added to the facility and was used for all test sequences since installation. This was added to enable direct initiation of a reaction within the detonation channel, as the afterburner is incapable of flashing back into the channel for all test conditions. This pre-detonator is controlled through the main control program, within which the firing time can be set. The pre-detonator is programmed to fire at 7 Hz and was typically fired for approximately 1 second following the fuel on command.

The pre-detonator is of a custom design, with two control boxes which dictate operation based upon TTL pulses received from the control program. Hydrogen and oxygen are provided directly into the pre-detonator through automotive fuel injectors controlled by the first control box. A spark plug is then commanded to fire by the second control box. A Schelkin spiral is installed near the spark plug within the pre-detonator which causes a DDT. This detonation wave then continues from the 1/2 inch tube of the pre-detonator into a 1/4 inch tube which is coupled directly the detonation channel of the RDE.

2.2 Thrust Measurements

A custom, purpose-built thrust stand was used throughout the course of this research to generate thrust measurements for a subset of the tests conducted. This thrust stand

was developed in earlier phases of this program [9] and was adapted and improved upon in this program. The basic arrangement of the final configuration of this system is shown in Figure 2.6. The combustor is mounted directly to a trolley that translates freely on a linear rail system. A load cell secured to the fixed thrust stand on which the carriage system translates is coupled to the RDE along the axial centerline and provides a measure of gross thrust. This load cell is a TE Connectivity FN3050-A2 with a full-scale range of +/-1000 N. The load cell output was recorded at 200 Hz by the previously outlined low-speed data acquisition system.

While most RDEs for which thrust measurements have been reported exhaust to ambient atmosphere, this facility requires the combustor to be directly connected to the previously summarized exhaust system. This presents a difficult problem if accurate thrust measurements are desired, as a suitable RDE-exhaust interface requires flexibility to allow for load cell deflection, zero net force to avoid tainting load cell measurements, and the ability to maintain a constant seal. Due to the ignition effects shown in Figure 2.2, the original axial face seal arrangement was found to disengage upon ignition and lead to thrust measurements which could not be accurately corrected.

Various iterations of the RDE-exhaust interface and pressure correction methodology were tested throughout the course of this research before arriving at the final configuration shown in Figure 2.6. Initial testing with the thrust stand utilized an axial face seal directly installed on the RDE exit flange with a limited amount of pressure correction. This was subsequently iteratively improved by first adding additional pressure measurement locations on the exhaust of the RDE and by incorporating a flange adapter that reduced the effective area on which facility-induced effects could act, and allowed for a radial seal which ensured consistent seal engagement.

As shown in Figure 2.6, the RDE is coupled to the exhaust mating flange with a non-rigid connection while maintaining proper sealing. In the final (shown) configuration this was accomplished by having a graphite radial slip seal between the combustor exit flange and the exhaust mating flange. This is shown as the inset of Figure 2.6 and differs from a prior work in which the aforementioned axial face seal arrangement was used (see [10]).

Direct loading of the thrust stand arrangement for calibration and pre-load was enabled through a mechanism coupled directly to the load cell on the reverse side of the RDE to load cell interface. Calibration of the load-cell was conducted approximately every fifth test by applying known forces up to full-scale of the load cell through the pre-load system. A 45 N pre-load was applied for all tests, with the

contribution of the pre-loading on the resultant thrust measurements accounted for through calibration and tare runs. The overall calibration of the load cell was found to deviate by less than 0.5% throughout the course of testing.

As alluded to previously, due to the coupling of RDE with the facility exhaust system and the use of a bluff-body exhaust nozzle, base pressure forces acting on the RDE exit flange and bluff-body RDE exhaust cap at the exit were accounted for by instrumenting the aft-facing surfaces with CTAPs. The pressure force acting on the center body cap was measured through 17 CTAPs dispersed radially and azimuthally, while the pressure force acting on the outer flange was measure through 6 CTAPs installed at various azimuthal locations. The CTAP locations used for pressure correction are indicated in Figure 2.7. A visualization of the radial location of the CTAPs in the center body cap and a breakdown of areas assigned to each CTAP is shown. Using these measurements projected on the corresponding areas and assuming an axi-symmetric pressure distribution, the resulting pressure forces are found by summing the individual contributions. As all reactants are introduced normal to the thrust vector and do not introduce an axial momentum component to the control volume, the force measured by the load cell (F_{meas}) is used with the pressure corrections to determine the resultant corrected thrust for each test case according to the following final form:

$$F_{\text{g}} = F_{\text{meas}} + \Delta P_{\text{fl}} A_{\text{fl}} + \Delta P_{\text{cap}} A_{\text{cap}} \tag{2.1}$$

Due to exhaust pressurization effects during ignition, testing with the thrust stand necessitated initiating at low-flow conditions and ramping to the desired test condition. As the RDE is directly coupled to the exhaust, the pressure rise within the exhaust that manifests upon initiation (Phases ii.-iv. of Figure 2.2) results in a measured thrust spike as seen by the load cell. This necessitated longer run times to enable the system to reach a quasi-steady state. Tests for which thrust measurements were taken were thus typically 5 seconds of fuel-on, with thrust measurements taken as mean values across the second to last half second of fuel on (4-4.5 seconds after the fuel-on command).

2.3 RDE Injection Configurations

A total of four distinct RDE configurations were tested throughout the course of this research, with additional sub-configurations. An azimuthal schematic for each

configuration is shown in Figure 7.8. These configurations and the acronyms to which they will be referred to as going forward are the following:

- Fixed Axial Inlet (FAI),
- AFRL Radial Inlet (AFRL),
- Variable Axial Inlet (VAI), and
- Variable Axial Inlet with Wide Channel (VAI-W).

The optional exhaust restriction is indicated on those configurations for which variable area hardware could be installed. The VAI-W configuration has only been tested with the contour shown below, and further details will later be provided.

Several overall characteristics are common across all four configurations. The available sensor locations for CTAP and High Speed Pressure (HSP) sensors are shown for each configuration, with the use of spacers these can be offset relative to the center body. This remains largely unchanged configuration-to-configuration due to the use of the same instrumented outer body for all. The outer diameter of the detonation channel is thus 152 mm for all configurations. The center core dimensions are constant for the FAI, AFRL, and VAI configurations, with a constant channel width of 7.6 mm from station 3.2 to station 7. The VAI-W channel details will be later outlined.

All configurations are assembled in a similar manner. The outer body is held in place by upstream and downstream flanges which are secured through 3/4"-16 threaded rods secured in tension. The central core of all configurations are secured internally to the upstream flange/plenum hardware. As such, upon assembly on the bench each configuration becomes a self-contained unit that can be lifted on and off of the RDE mount point on the afterburner/exhaust or the thrust trolley.

2.3.1 Fixed Axial Inlet

The FAI RDE configuration has been utilized for a variety of studies [11, 4, 10]. As the name suggests, this configuration has a fixed area axial air inlet. The continuous slot along the outer wall through which air is introduced has width of 1.6 mm. The nominal Area Ratio defined as

$$\mathrm{AR} = \frac{A_{3.2}}{A_{3.1}} \tag{2.2}$$

is 4.6 for this configuration. $A_{3.2}$ is the detonation channel area and $A_{3.1}$ is the air injection are. The AR ratio is defined in the same way for all following configurations as well, with the exception of the VAI-W configuration as will be discussed next. Fuel is introduced through 120 evenly spaced jets of 0.89 mm in diameter. These jets are aft-facing and angled at a 30 degree offset relative to the RDE center-line. This configuration has been tested with a constant area channel with no exhaust restriction ($A_8 = A_{3.2}$) and with a 50% exhaust restriction ($A_8 = 0.5 \times A_{3.2}$).

The FAI configuration is nominally of a 104 mm channel length. This is defined as the axial distance from the fuel injectors to the RDE exhaust plane formed at the end of the center body. With the use of additional shorter length center bodies and various spacers, channel lengths of 71, 119, and 137 mm were also tested throughout this research. As results later presented with deviations from the nominal channel length will be identified as appropriate.

2.3.2 AFRL Radial Inlet

The AFRL RDE configuration has also been extensively studied by a variety of research groups [12, 13] in the same basic configuration. This configuration was developed as a direct copy of the heritage AFRL geometry. This configuration possesses a radial axial air inlet. The continuous slot through which air is introduced has a height of 0.89 mm, which is consistent with configurations tested by Rankin *et al.* [14]. The nominal area ratio of channel ($A_{3.2}$) to air injection area ($A_{3.1}$) is thus 10 for this configuration. Fuel is introduced axially through 120 evenly spaced jets of 0.89 mm in diameter in a jet-in-crossflow configuration. These jets are directly aft-facing immediately following the point of minimum area of the air inlet and are of the same number (120) and size (0.89 mm) as that of the FAI configuration.

This configuration was tested with a constant area channel with no exhaust restriction ($A_8 = A_{3.2}$) and with a 50% exhaust restriction ($A_8 = 0.5 \times A_{3.2}$). However, results from this configuration are sparse. This configuration was predominantly tested with the addition of supplemental oxygen seeking to demonstrate operation with hydrocarbon fuels. As this was nearly entirely unsuccessful, this configuration has a limited amount of data with hydrogen-air mixtures, which is the focus of this research effort.

2.3.3 Variable Axial Inlet

The VAI RDE configuration was outlined and characterized in [3], but has largely been un-presented thus far. As is suggested by the name, this configuration possesses a variable area axial air inlet. This inlet is continuously variable across a wide range of resultant inlet areas, as the continuous slot along the outer wall through which air is introduced is capable of being varied through a range of values. The nominal area ratio of channel ($A_{3.2}$) to air injection area ($A_{3.1}$) can be varied from 2 to infinity for this configuration. Fuel is introduced through 120 evenly spaced jets of 0.89 mm in diameter. These jets are aft-facing and angled at a 30 degree offset relative to the RDE centerline. This configuration has been tested with a constant area channel with no exhaust restriction ($A_8 = A_{3.2}$) and with a 50% exhaust restriction ($A_8 = {}^1\!/_2 A_{3.2}$). Nominal area ratios for which tests have been conducted in this configuration are 2.5, 3, 4, 5, and 8, with the preponderance of data obtained at the AR = 3, 4, and 5 inlet set-points. The nominal channel length of the VAI configuration is 115 mm as measured from the fuel injectors to the RDE exhaust plane.

This configuration was designed with the goal of maintaining aerodynamic similarity across different inlet area ratio configurations without modifying the downstream detonation channel configuration. This axial inlet also allows for a continuous and direct connection between the channel and plenum to permit analysis of their coupling during operation. This differs from other designs that possess multiple discrete air injectors and/or a radial inlet in this way.

2.3.4 Variable Area Inlet - Wide Channel

The VAI-W RDE configuration possesses the same inlet design and characteristics as the VAI configuration. However, instead of the constant area channel of the FAI/AFRL/VAI configurations, the channel configuration is such that the inner wall is smoothly contoured from the minimum area throat of the inlet to the largest area portion of the channel. At this widest point the channel inner diameter is 121.4 mm and outer diameter is 152 mm, with a resultant 15.2 mm channel width. A convergent nozzle was installed at the channel exhaust with an approximately 47% area restriction relative to the maximum cross-sectional channel area. The resultant A_8 of the VAI-W configuration thus matches the channel area of the other configurations, and matches the exhaust areas of those configurations when no exhaust restriction is installed. The nominal channel length of the VAI-W configuration is 127.5 mm as

measured from the fuel injectors to the RDE exhaust plane to allow for the smoothly contoured exhaust restriction.

In order to maintain commonality between configurations, the AR calculation of Equation 2.2 is modified when calculated for the VAI-W configuration. Station 3.2 for this configuration is chosen to be the point at which the detonation channel area is equal to that of the constant-area FAI, AFRL, and VAI configurations. This is shown by the placement of the station marker in Figure 7.8. Due to the variable channel area within this configuration, this distinction is made to ensure that an equivalent AR between configurations represents a constant geometric area at station 3.1.

2.4 Luminescent Particle Tracking Measurements

2.4.1 Summary of Approach

All of the RDE configurations previously outlined in Figure 7.8 were tested with the same outer body. It is through this outer body that the various sensors shown in this figure are installed. This includes the aforementioned PMT sensor, which is installed external to the RDE looking directly inward into the channel through a 19.2 mm diameter sapphire window. This window has historically only been used for this purpose, as this port was blocked off with a stainless steel blank when not in use. By removing the PMT sensor, this port-hole provides direct optical access within the RDE channel. For initial testing of optical analysis methodologies, optical chemiluminescence of the operating RDE was imaged directly through this port-hole. Through the use of this port-hole and the design and fabrication of a 360 degree quartz outer body, this optical access to the RDE channel presented opportunities not previously explored.

During the installation of the oxygen supply system outlined in a prior section, the previous air supply system was removed. This supply system consisted of carbon steel pipe sections and was of the same material as the air supply system throughout the entire facility. Upon removal, a significant coating of iron oxide was noted throughout, and it was theorized that particles scavenged from this old hardware would present the opportunity for flow visualization without the possibility of contamination that may result from more conventional Particle Image Velocity (PIV) seeding materials.

The methodology that was devised using this seeding material was termed Luminescent Particle Tracking (LPT). This method results in similar outputs as a conventional PIV approach, though due to the small aperture window of the majority of

testing and the lack of artificial illumination over short time scales the particles were too sparse for conventional PIV analysis or particle tracking methods. All videos captured using this methodology were captured with the previously summarized Phantom TMX viewing the detonation channel directly through the PMT port-hole or the optically accessible outer body at a distance of 0.5 m. Videos were obtained at 70k fps at resolutions of 256x256 pixels when viewing through the port-hole, and 768x256 pixels when viewing through the optically accessible outer body. The port-hole videos were obtained with the camera looking directly orthogonal to the center-line of the RDE, while videos taken with the optically accessible outer body were taken with the camera offset 15 degrees (as shown in Figure 2.13) to allow for direct viewing of the inlet and to mitigate potential damage to the camera if the quartz window were to fail.

The harvested iron oxide particles were introduced upstream of the RDE directly into the air supply system. All particles were directly placed within the air stream with no attempt at metering, as such the distribution of particles for individual test cases is assumed to be random. Each time particles were introduced a consistent amount of approximately 0.5 grams was inserted. Due to the particles being manually harvested iron oxide, the true size and morphology distributions are unknown. However, a representative sample was directly imaged to verify basic characteristics. This representative sample is shown in Figure 2.9, with a human hair of approximately 90 micron diameter included for relative scaling. For reference, several individual particles are circled in yellow and multiple large groupings of particles in which individual particles are difficult to discern are outlined are in blue. Although the true distribution of sizes and morphology for all particles used in this methodology remains unknown, this example shows that the preponderance of particles are of 90 micron diameter or smaller.

Due to the modular nature of the FAI RDE configuration, the outer body is capable of being offset with various spacers. As such, videos were obtained looking directly into the forward base of the channel, the aft end of the channel immediately before the channel exhaust, and at the exhaust plane through the port-hole. Videos were obtained at the three axial locations in the FAI configuration with 71 mm length channel, and at the forward base of the channel in the FAI configuration with 119 mm channel. These locations will be identified as the Forward, Aft, and Exhaust locations. With the optically accessible outer body, videos were obtained in the FAI configuration at one axial location near the air/fuel inlets in the 119 mm length channel. A modified inner wall contour was used for a subset of these tests. Each of

these viewing locations with the associated RDE channel configurations are shown in Figure 2.10.

2.4.2 Viewing Through Optical Port-Hole

A representative sequence of frames taken through the optical port-hole is shown in Figure 2.11. This sequence was taken at 70,000 fps and an exposure time of 14 μs at the forward location in the 71 mm channel length FAI configuration. Run conditions for this example were an inlet air mass flow of 150 g/s and equivalence ratio of 0.6. Flow reversal of a persistently luminescent particle can be observed from frames 1-12. The visible area of each individual frame is 19.2 mm x 19.2 mm through the circular aperture. Similar sequences of frames were analyzed for all tests conducted in this manner, with results presented in later sections.

For the videos obtained looking through the PMT window, particles were tracked manually in a manner similar to that illustrated by the yellow arrows in Figure 2.11. This manual tracking was performed in a multi-step process. The videos were cropped and shortened such that only the visible area of the PMT window was retained and that only periods of steady operation were considered for manual tracking. A custom script was generated to present all frames of interest to the user in increments of 120 sequential frames simultaneously. This script was then used to capture and log user identified locations within each of these frames. Individual particles were tracked by manually identifying the leading edge of discrete particles in individual frames and then calculating the associated velocities based upon the known dimensions of the PMT window (1.9 cm diameter). As the velocities are calculated based upon frame-to-frame particle displacement, only particles visible for two or more frames are considered.

2.4.3 Optically Accessible Outer Body

In order to enable enhanced optical access into the channel of the four previously summarized RDE configurations tested throughout the course of this study, an Optically Accessible Outer Body (OAOB) was designed and fabricated. This outer body was designed such that it can serve as a drop-in replacement for the instrumented outer body used with all four configurations shown in Figure 7.8, or that it can be used as an extension of said instrumented outer body. The design is of the form of a stainless steel clam shell in which a round fused quartz window was installed. The

quartz window was sized to be capable of withstanding the internal stress associated with internal over-pressures of up to 35 bar.

The fully assembled and installed optically accessible quartz outer body is shown in Figure 2.13. The quartz window is of a total height of 51.2 mm, with a total viewable aperture of 25.6 mm around the entire circumference less the 8 supports which support the tensile load associated with securing the window within. Two of these supports can be viewed in the image showing the installed outer body. These supports allow the window to float on the internal O-rings and avoid placing excess axial stress on the fragile window. This outer body was tested with the FAI RDE configuration, with results from this test campaign to be summarized in the following chapter.

All testing to date with this outer body used a similar methodology to that outlined for those videos obtained looking through the port-hole. Although particles were introduced for testing conducted with the OAOB, automated tracking of these particles was not successful. Attempts were made to leverage the particle detection step of Sbalzarini and Koumoutsakos [15] used within the MOSAICsuite plug-in for the NIH ImageJ software package [16] for particle tracking and identification with limited success, but due to the presence of many false positives and insufficient recognition of visible particles the analysis to follow will focus on observed chemiluminescence within the RDE inlet. The approximate region of interest is shown in red in Figure 2.12.

An image showing the RDE in operation obtained from a webcam within the test facility is shown in Figure 2.14. This webcam was used for all test cases with the optically accessible outer body installed to enable remote viewing such that the operator would have indication to initiate the emergency procedures of the SOP in the event of a failure of the fused quartz window.

A representative sequence of frames taken through the optically accessible outer body is shown in Figure 2.12. This sequence was also taken at 70,000 fps with an exposure of 14 μs in the 119 mm channel length FAI configuration at an inlet air mass flow of 150 g/s and equivalence ratio of 0.6. The chemiluminescence associated with the passing detonation wave can be seen moving from left to right, with a luminescent particle following behind. The visible area of each individual frame is approximately 25 mm x 60 mm through a rectangular aperture partially blocked in a hemispherical fashion by the hardware containing the fused quartz window.

2.5 Uncertainty Analysis

An uncertainty analysis was conducted to quantify the uncertainties associated with a variety of experimental measures. A summary of the approaches that will be used for this analysis is provided by Farrance and Frenkel [17]. Per rules 4 and 6 of Table 6 in the referenced article, the standard uncertainty (u) associated with output quantity y can be found based upon the standard uncertainty of input variables x. This methodology is appropriate for evaluation of the standard uncertainty through multiplicative relationships with uncorrelated variables. The basic equation to determine standard uncertainty is given below in Equation 2.3. Note that additional variations of this basic equation exist for non-multiplicative relationships, these formulations can be found in the previously referenced article [17].

$$u(y) = y\sqrt{\sum_{i=1}^{n}\left(\frac{u(x_\mathrm{i})}{x_\mathrm{i}}\right)^2} \tag{2.3}$$

The first experimental quantities of interest that will be analyzed are the reactant flow rates and associated equivalence ratio. These quantities are determined through the use of the choked flow equation, with a generalized form given below by Equation 2.4. For the analysis to follow the gas properties (γ, R) and discharge coefficient (C_d as provided by supplier) are assumed known, while the pressure, temperature, and flow areas have associated uncertainties. The uncertainties in the pressure and temperature measurements are based upon the corresponding sensor accuracy, and the uncertainty in the flow area of the various sonic orifices is assumed based upon the last significant digit of the nominal diameter. For an example, a nominal 0.188 inch orifice is assumed to have a true geometric diameter that falls between 0.1875 inch and 0.1885 inch, and as such $u(\sqrt{(A)}) = 0.0005$ inch.

$$\dot{m} = C_\mathrm{d} A\sqrt{\frac{\gamma {P_\mathrm{t}}^2}{R T_\mathrm{t}}\left(\frac{2}{\gamma+1}\right)^{\left(\frac{\gamma+1}{\gamma-1}\right)}} \tag{2.4}$$

Using Equations 2.3 and 2.4, the resulting reactant flow uncertainties for all test cases were found. These are presented as a function of the nominally calculated flow rates in Figure 2.15. These results are presented independent of the RDE configuration as these values are all calculated based upon measurements not dependent upon the RDE geometry.Relative uncertainties range from approximately 0.5-5% for air

mass flow rates and approximately 0.25-2.5% for fuel mass flow rates. It can be seen that the nominal mass flow-rate and uncertainty relationship is singular for the air stream, with multiple curves present in this relation for the fuel stream. This is an artifact of the facility configuration. All tests were conducted with air metered through a single orifice that was unchanged throughout, while dependent upon the desired run conditions the fuel stream was metered through multiple orifices and combinations of orifices as shown in the multiple fuel lines of Figure 2.1.

The corresponding variability of each of these measures is also shown in Figure 2.16. This measure is defined as the 95% confidence interval for all experimental observations during the steady portion of each individual test. Variability ranges from approximately 0.5-10% for air mass flow rates and approximately 0.25-5% for fuel air mass flow rates. By comparing Figures 2.15 and 2.16, the variability of the flow rates is largely of the same order as the uncertainty, with the largest values of relative variability for each calculated parameter generally occurring at lower mass flow rates.

An example operating map illustrating the range of conditions tested in the VAI-W configuration is shown in Figure 2.17. This configuration was chosen as it is a relatively regimented data set that allows for viewing of the relative trends in associated uncertainties (black bars) and variabilities (red bars). Plot marker size is reduced to ensure these bounds can be observed. The experimental variabilities are largely of greater magnitude than the corresponding uncertainties. As this presentation is representative of conditions tested in other configurations and of approximately the same magnitude as a nominally sized plot marker, later figures will not include bars on these parameters for ease of presentation.

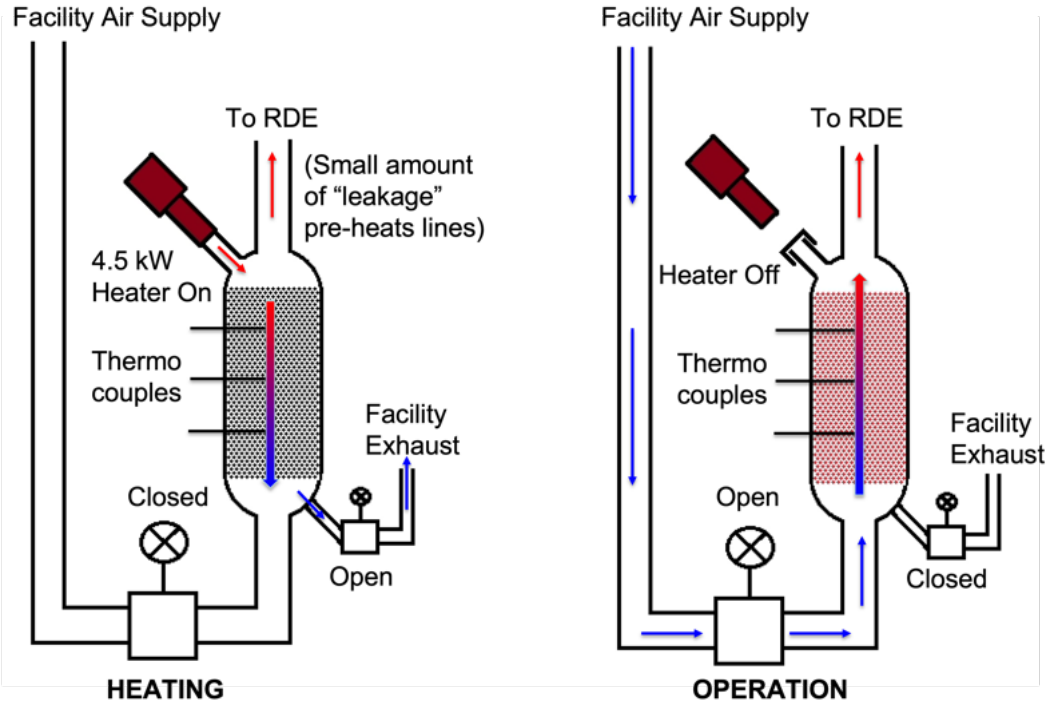

Figure 2.3: Schematic illustrating the characteristics of the heated pebble bed during a heating cycle (left) and during RDE operation (right).

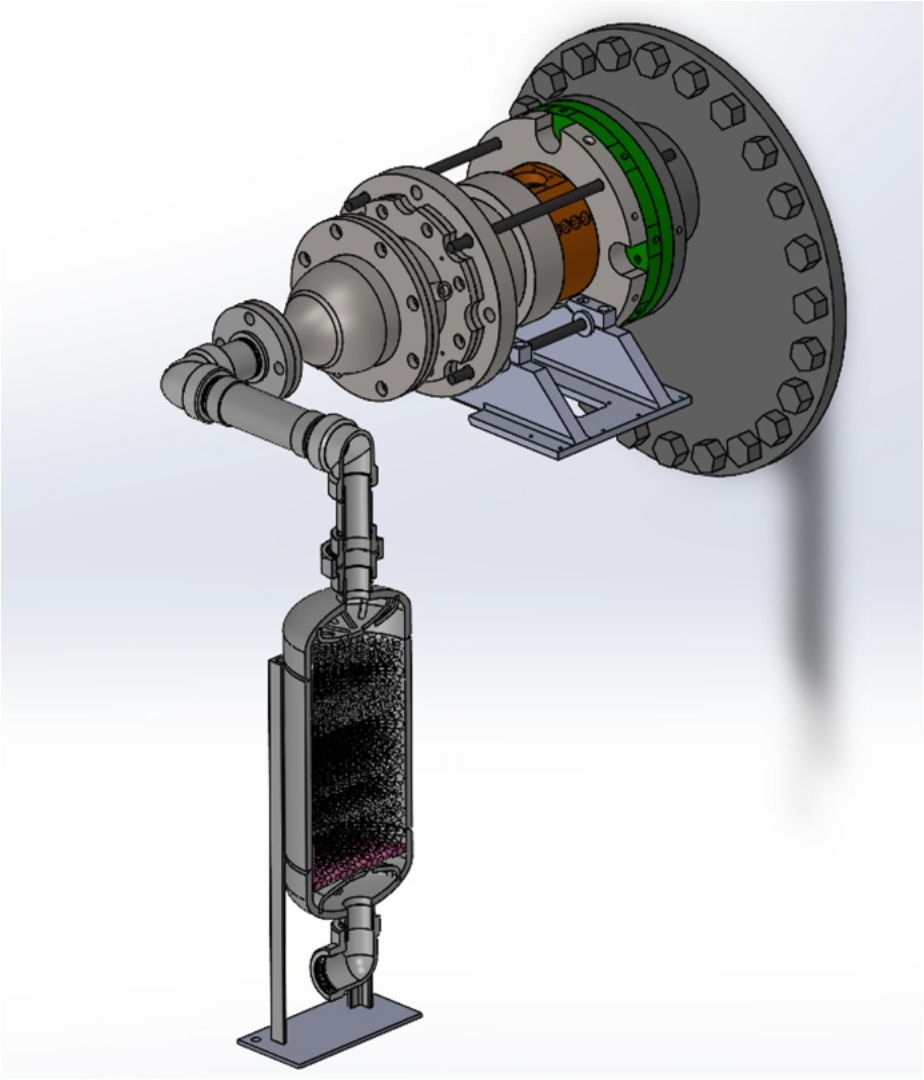

Figure 2.4: Schematic illustrating the characteristics of the heated pebble bed during a heating cycle (left) and during RDE operation (right).

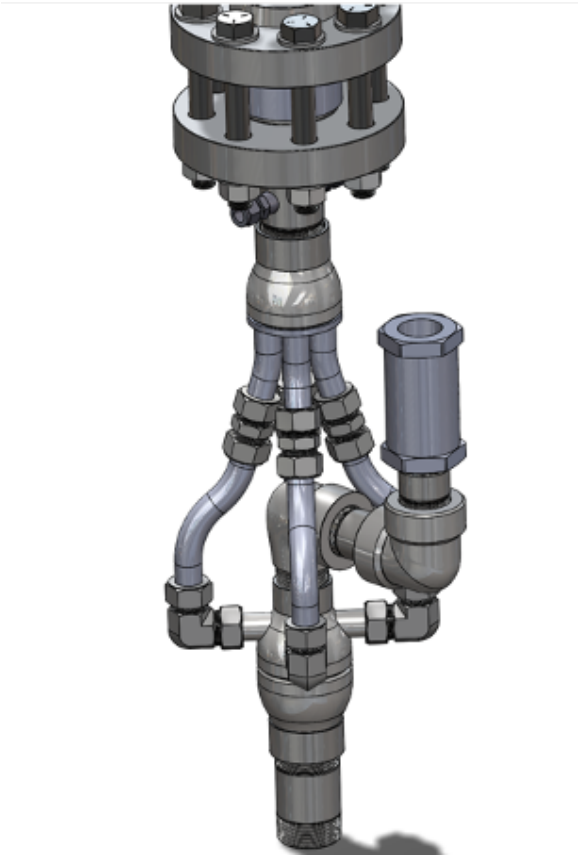

Figure 2.5: Oxygen/air mixing element.

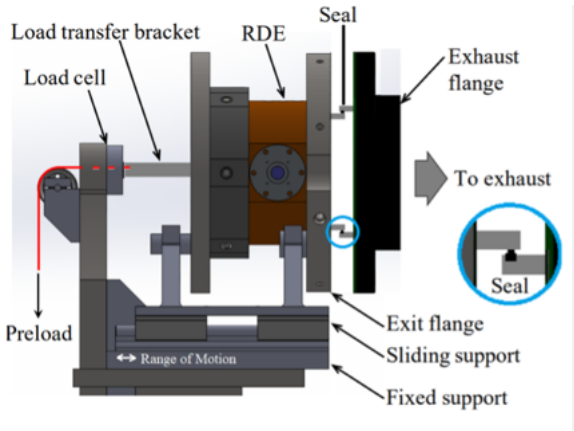

Figure 2.6: Diagram of final thrust stand configuration used for thrust measurements.

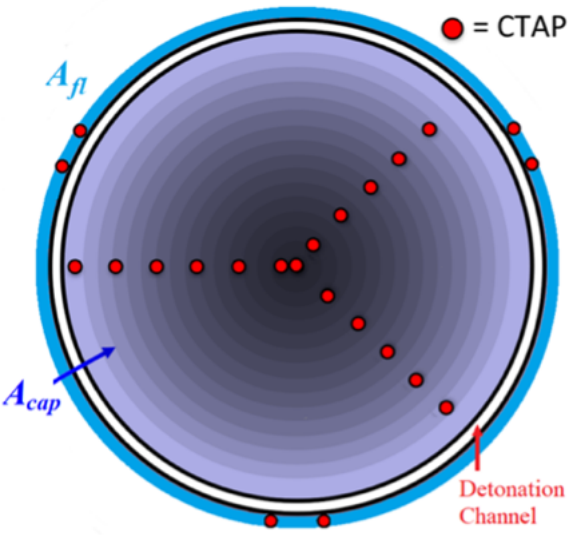

Figure 2.7: Diagram of of CTAP locations on exhaust cap used for thrust calculations.

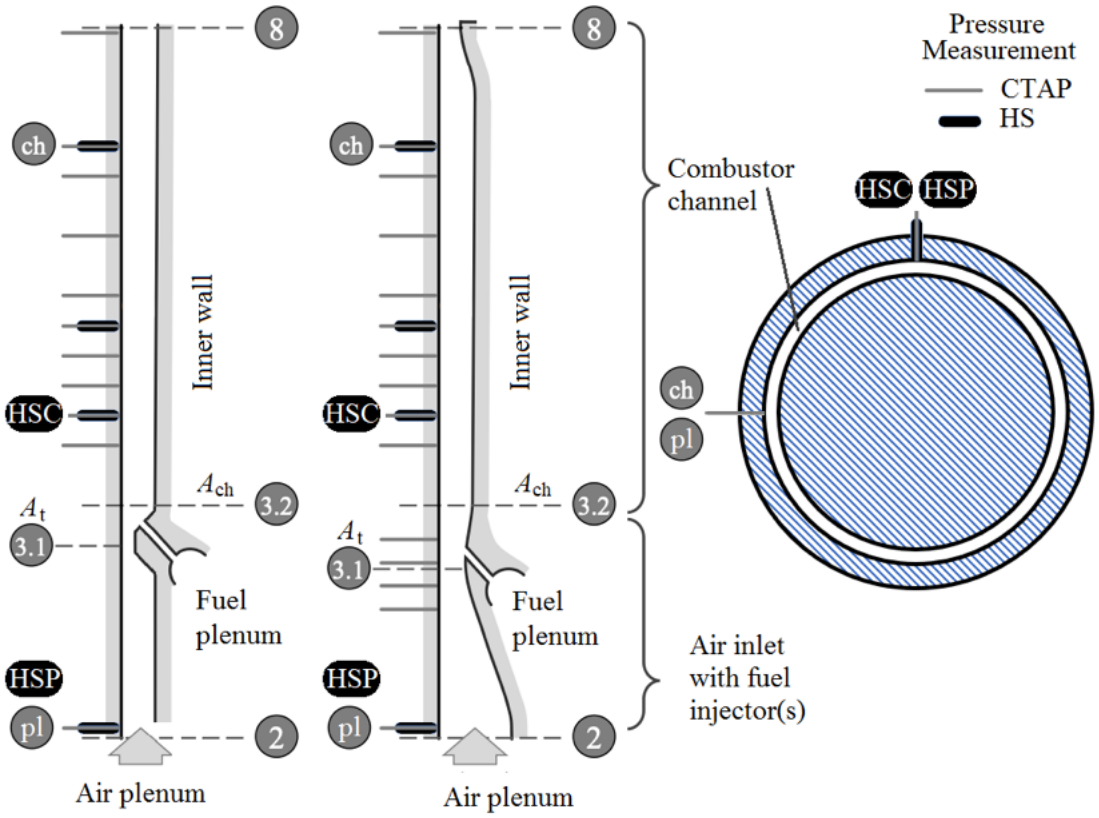

Figure 2.8: Schematic diagram of the four RDE configurations tested. From left to right these are the Fixed Axial Inlet, AFRL Radial Inlet, Variable Axial Inlet, and Variable Axial Inlet with Wide Channel configurations. Axial locations of CTAP and High-Speed Pressure measurement locations indicated.

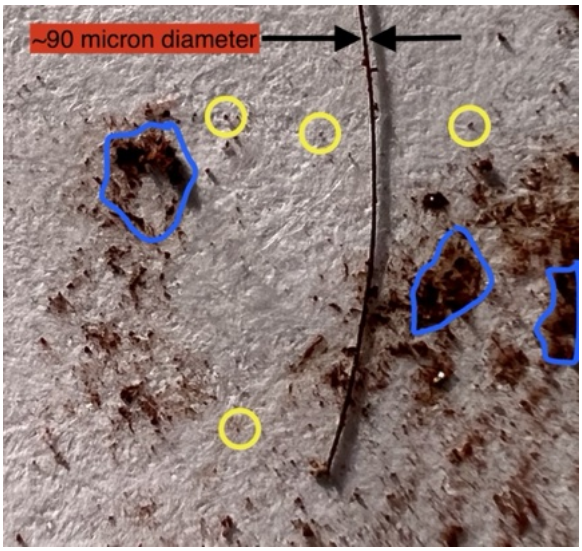

Figure 2.9: Representative sample of LPT particles with human hair for scale. Several individual particles (yellow) and groupings of multiple particles (blue) are highlighted.

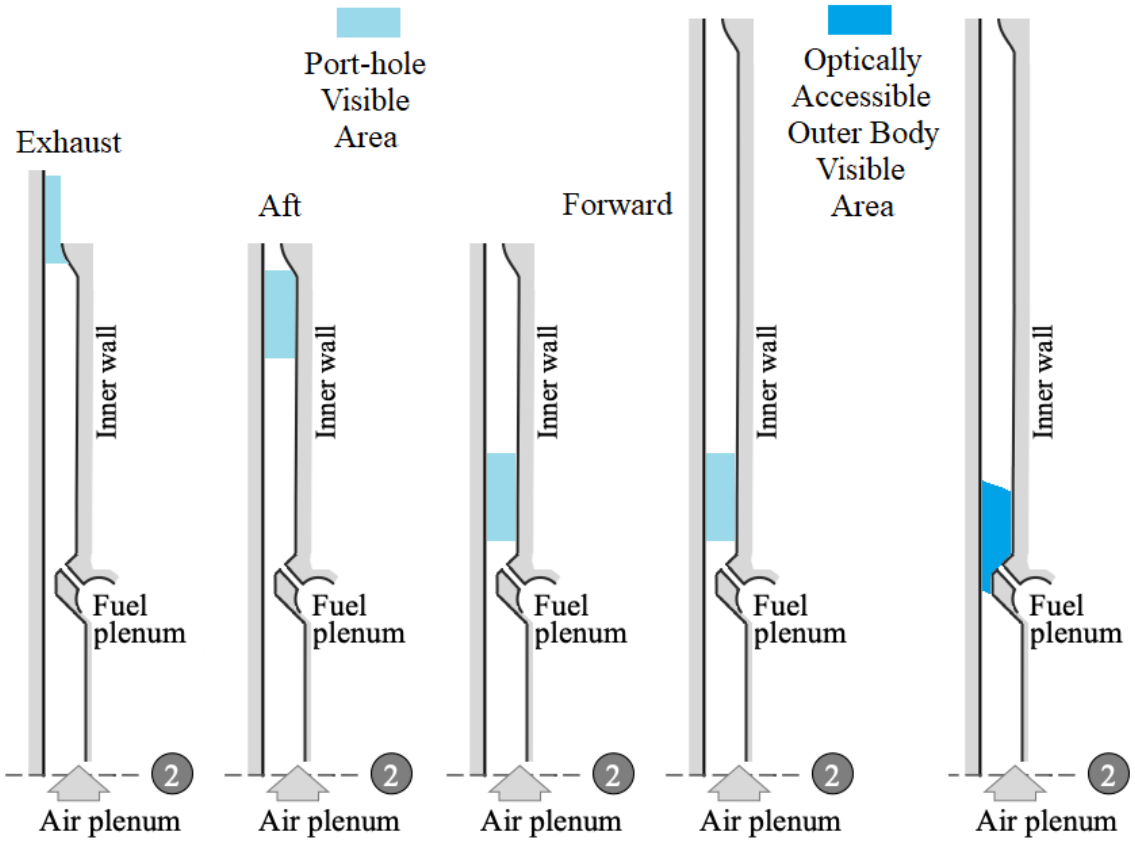

Figure 2.10: Luminescent Particle Tracking (LPT) visible areas for all configurations tested with this methodology. From Left to Right: Exhaust, Aft, and Forward port-hole viewing locations shown for 71 mm channel length configuration, Forward viewing location shown for 119 mm channel length configuration, and Optically Accessible Outer Body viewing location shown for 119 mm channel length configuration.

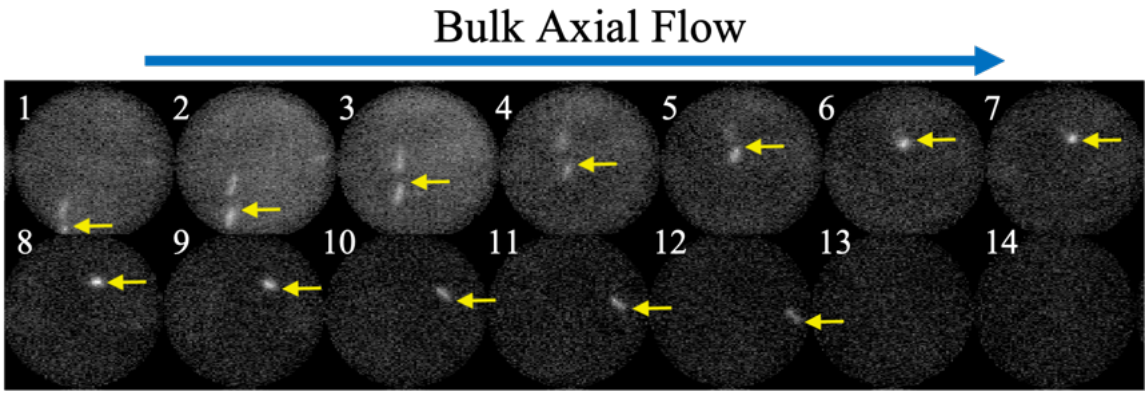

Figure 2.11: Representative Luminescent Particle Tracking (LPT) sequence of frames taken through the optical port-hole at the forward viewing location, with bulk axial flow from left to right and visible flow reversal. Yellow arrows in frames 1-12 indicate leading edge of particle of interest.

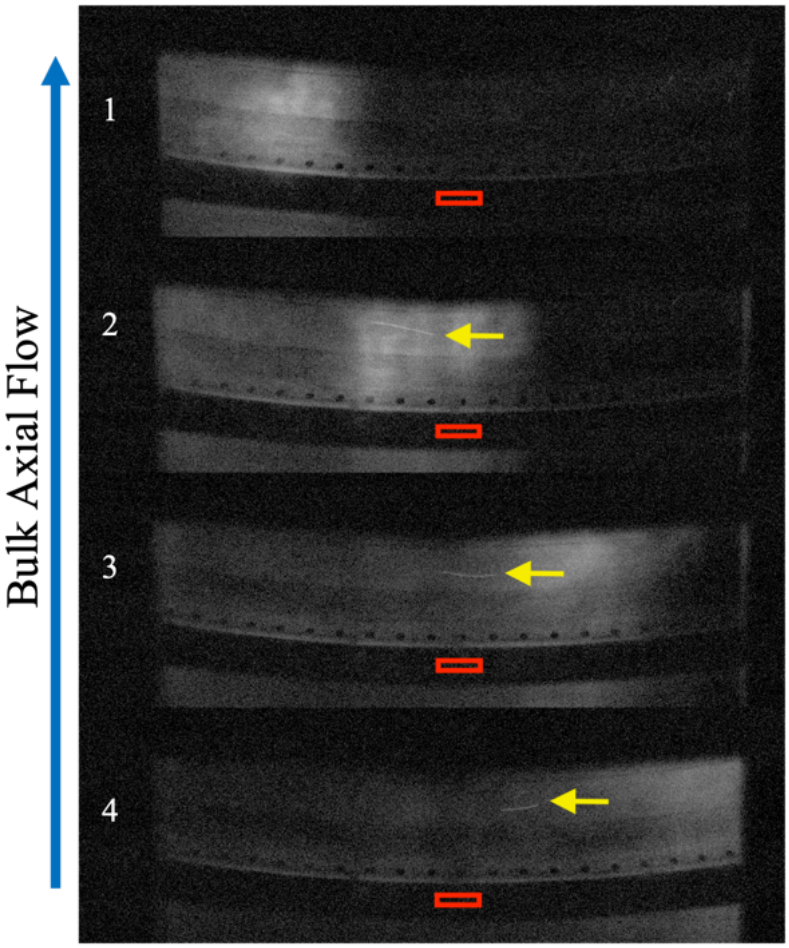

Figure 2.12: Representative Luminescent Particle Tracking (LPT) sequence of frames taken through the optically accessible outer body. Bulk axial flow from bottom to top. Chemiluminescence associated with detonation wave can be seen moving left to right. Leading edge of individual particle streak highlighted with yellow arrows in frames 2-4. Region of interest used for optical chemiluminescence analysis shown in red.

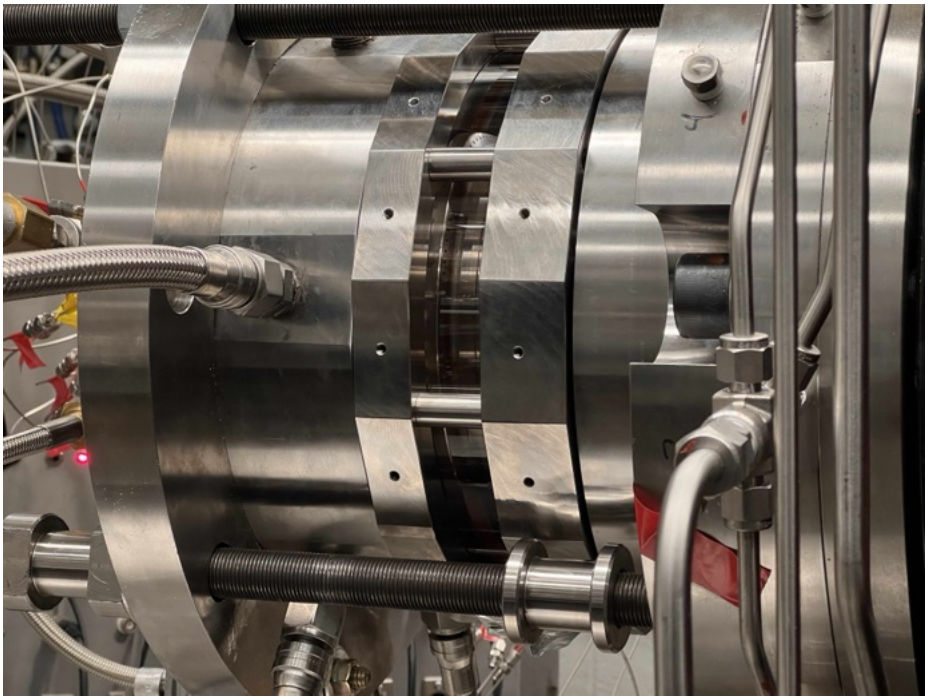

Figure 2.13: Optically accessible outer body as installed on FAI RDE configuration. Image taken from same location as Phantom TMX camera used to collect high-speed videos. The base of the detonation channel is observed directly.

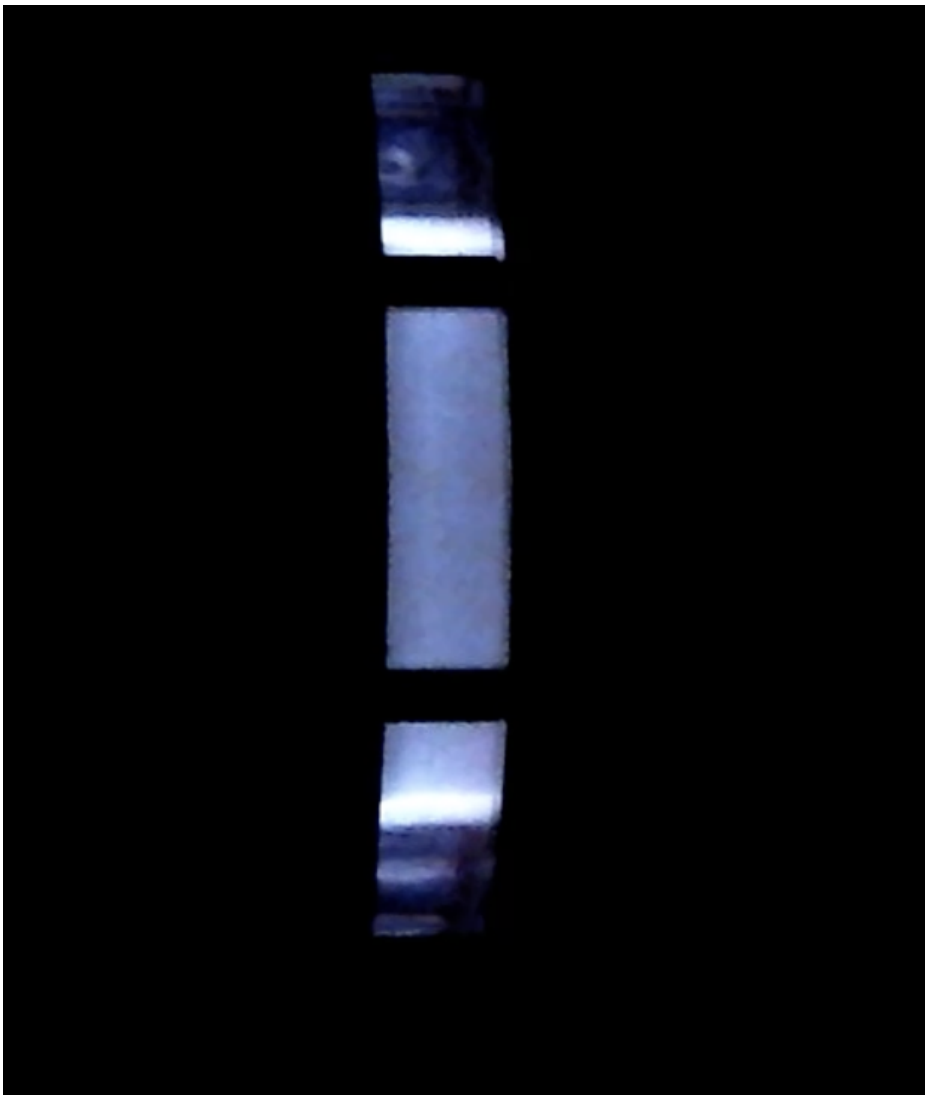

Figure 2.14: Image showing FAI RDE configuration in operation with optically accessible outer body installed.

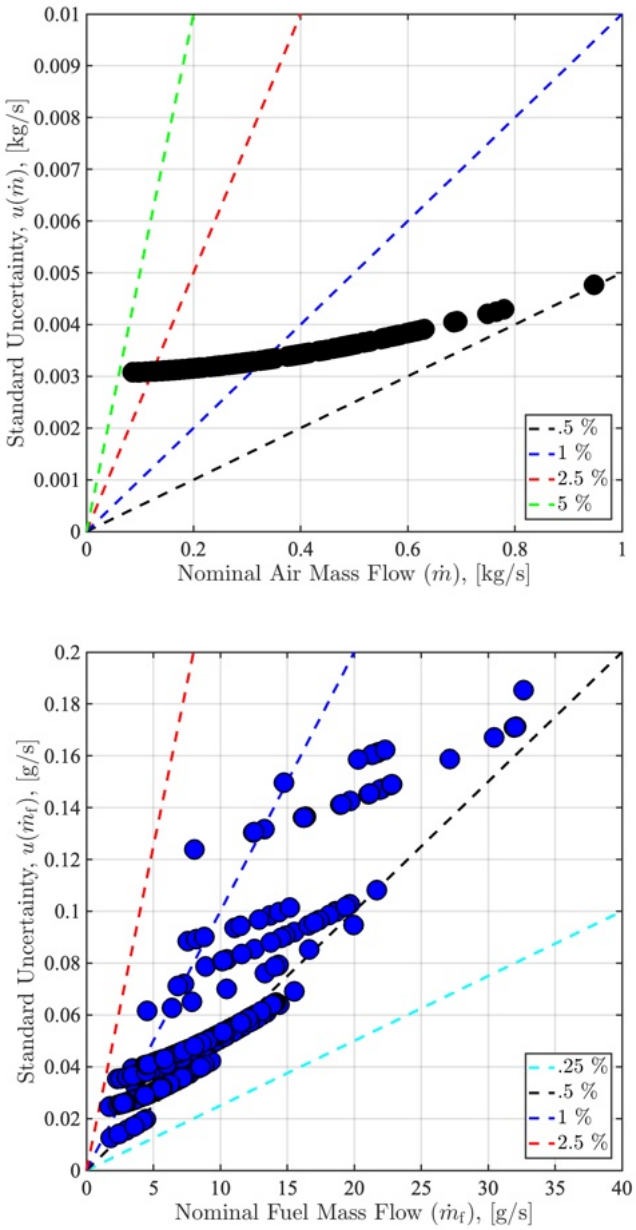

Figure 2.15: Uncertainty analysis for reactant flow rate for air (top) and fuel (bottom).

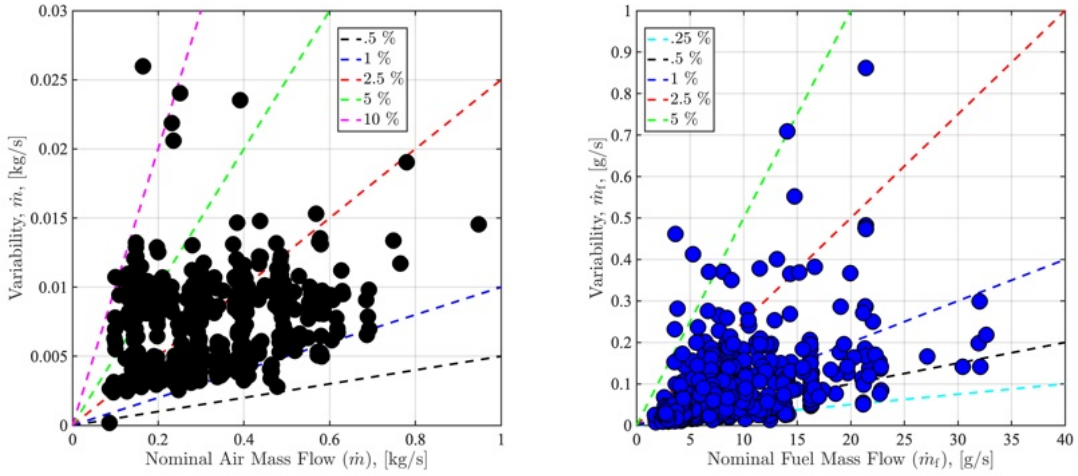

Figure 2.16: Experimental variability (95% confidence interval) for reactant flow rates, air (top) and fuel (bottom).

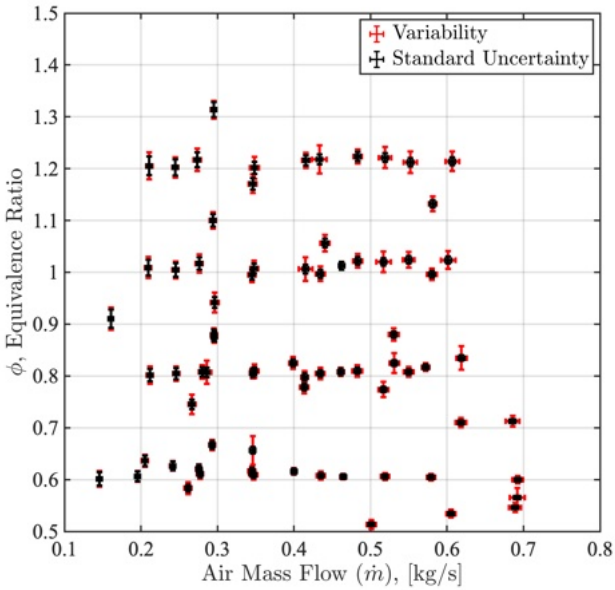

Figure 2.17: Summary of all conditions tested with VAI-W configuration illustrating representative uncertainties and variabilities of air mass flow rates and equivalence ratios. Uncertainties and variabilities are of similar relative extent as nominally sized plot markers, as such flow-rates and equivalence ratio markers will be presented without variability/uncertainty bars.

Chapter 3

Operation Verification and Analysis

3.1 Introduction

This chapter provides a description of results from testing the combustor configurations highlighted earlier. This includes a quantification of basic characteristics of the RDE configurations under analysis, a summary of many conventional analysis techniques that are used to quantify and evaluate operation of an RDE in various operating modes, a description of conditions tested throughout this research, and the presentation of additional techniques that were developed throughout this effort that were leveraged in pursuit of the research objectives.

In order to quantify the basic characteristics of various RDE configurations, results generated during cold-flow testing are presented. Cold-flow testing is defined as non-reacting testing during which air is flown without fuel. Results from these tests are later used in the quantification of inherent pressure losses and for comparison with data obtained during subsequent hot-flow testing for a determination of induced pressure losses.

A description of the relevant measurements and methodologies used to verify and characterize RDE operation follows, within which specific operating modes are identified and analyzed. For the purposes of later analysis, only rotational operating modes are considered. Multiple rotational sub-modes are identified, and their pseudo-steady nature is demonstrated. An analysis of the coupling between the detonation channel and supply plenum is also conducted.

With the basic operating modes and characteristics identified, a summary of some of the operating conditions tested is included. These operating maps are shown to demonstrate the wide variety of inlet conditions tested from which specific data will later be used for analysis related to the research objectives. This will also include new techniques developed that quantify various aspects of RDE performance and an analysis of geometry changes on individual performance metrics.

3.2 RDE Flow Path Characterization

The ability to generate an accurate understanding of the performance or behavior of any RDE configuration first requires an accurate characterization of the flowpath. This initial characterization is accomplished by conducting non-reacting flow tests in which air is flowed in the absence of fuel. These tests enable the determination of several characteristics of the RDE that will be relevant for later analysis. These non-reacting flows will subsequently be referred to as "cold flows", while reacting flow tests in which fuel was supplied to the RDE will be referred to as "hot flows".

3.2.1 Determination of Key Parameters

Although our very early test campaigns did not always include dedicated cold flow testing, it is now a standard procedure to collect a sweep of cold flow data any time the RDE configuration is modified in any way. This ensures that any physical differences that may have manifested during assembly are accurately captured in the specific data collected. Dedicated cold flow testing was typically conducted across a sweep of inlet air mass flows ranging from 150-500 g/s in increments of 50 g/s. The upper bound of flow rates tested was increased as needed if hot flow testing above this flow rate was projected. With that exception, these flow-rates represented typical upper and lower bounds for later hot flow testing. For data from those early test campaigns without dedicated cold flow testing, the cold flow characteristics of the RDE were determined from the data collected during the pre-fuel portion of hot flow tests in which only air was flowing.

The data collected from cold flow testing was first used to determine the inlet discharge coefficient ($C_{d,3.1}$) for each test sequence of each RDE configuration. Cold flow testing was performed up to and beyond flow-rates at which the inlet throat (station 3.1) choked and the relationship between total pressure within the plenum ($P_{t,3}$) and

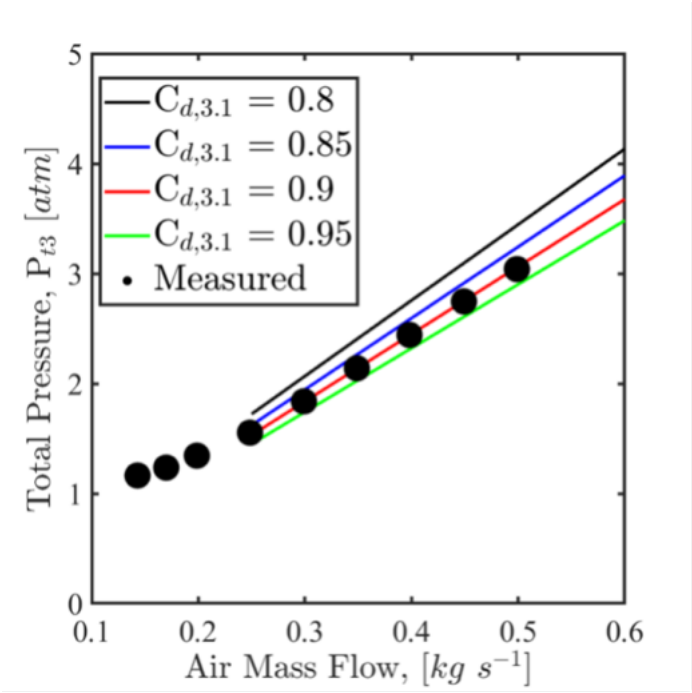

Figure 3.1: Evaluation of $C_{\mathrm{d},3.1}$ for FAI configuration.

air mass flow-rate ($\dot{m}$) became linear. The choked flow equation is given below in Equation 3.1. This equation can be re-arranged as shown to directly determine the equivalent discharge coefficient based upon the known geometric area of the inlet and measured temperatures and pressures within the plenum.

$$\dot{m} = C_{\mathrm{d},3.1} A_{3.1} \sqrt{\frac{\gamma {P_{\mathrm{t},3}}^2}{R T_{\mathrm{t},3}} \left(\frac{2}{\gamma+1}\right)^{\left(\frac{\gamma+1}{\gamma-1}\right)}} \Rightarrow C_{\mathrm{d},3.1} = \frac{\dot{m}}{A_{3.1}} \left[\frac{\gamma {P_{\mathrm{t},3}}^2}{R T_{\mathrm{t},3}} \left(\frac{2}{\gamma+1}\right)^{\left(\frac{\gamma+1}{\gamma-1}\right)}\right]^{-1/2} \tag{3.1}$$

Example results from the determination of $C_{\mathrm{d},3.1}$ for one cold flow sweep in the FAI configuration is shown in Figure 3.1. This figure shows the measured air mass flow rate versus the measured pressure within the plenum and a variety of curves corresponding to differing values of $C_{\mathrm{d},3.1}$. As can be seen, this discharge coefficient of this configuration is approximately 0.9. This is consistent with expected values for a configuration such as this. The inlet configuration used in this configuration is

a hybrid of the cylindrical and conical converging nozzle shapes studied by Alam *et al.* [18], in which the experimentally determined discharge coefficient falls within the predicted range of 0.95 (pure cylindrical) and 0.87 (pure conical).

The FAI and AFRL configurations outlined in the prior chapter are fixed by their nature and as such the nominal geometric area remains known and invariant at all times. However, the inlet of the VAI and VAI-W configurations is continuously variable. Although the internal set-point that dictated the inlet position was set to specific known/desired values that correspond to particular inlet areas, the variations in pressure profiles observed in different test sequences with the same nominal inlet configuration indicate that assembly differences resulted in small changes in the geometric inlet area. This was accounted for by determining the effective inlet area for all cases, regardless of whether fixed as with the FAI and AFRL configurations, or variable as with the VAI and VAI-W configurations. This quantity is formed by combining the inlet discharge coefficient ($C_{\mathrm{d},3.1}$) and air inlet area ($A_{3.1}$) into one term that will be referred to as the effective air inlet area ($A_{3.1,\mathrm{eff}}$), as shown below in Equation 3.2. This quantity will be used going forward to define the inlet mass flux outlined in Equation 3.3.

$$A_{3.1,\mathrm{eff}} = C_{\mathrm{d},3.1} A_{3.1} \tag{3.2}$$

$$\dot{m}'' = \frac{\dot{m}}{A_{3.1,\mathrm{eff}}} \tag{3.3}$$

A slightly modified version of the same approach utilized to independently determine the discharge coefficient for the air inlet was repeated for the optional 50% restriction exhaust nozzle that was used with the FAI, AFRL, and VAI configurations. The relationship of Equation 3.1 was again used with several modifications. The stations used in this calculation were stations 7 (conditions upstream of the nozzle) and 8 (A_8). As the CTAP installed in the station 7 position provided a measure of static pressure, isentropic relations (where $A/A^* = 2$) were used to determine the equivalent stagnation conditions. Results from this determination are shown in Figure 3.2. The exhaust configuration is analogous to a 16° pure conical nozzle, for which a prediction from the data of Alam *et al.* directly matches the experimental value of 0.97 [18]. This implies that these parameters can be estimated from correlations found in literature based upon specific geometric characteristics if cold flow data were not available as here.

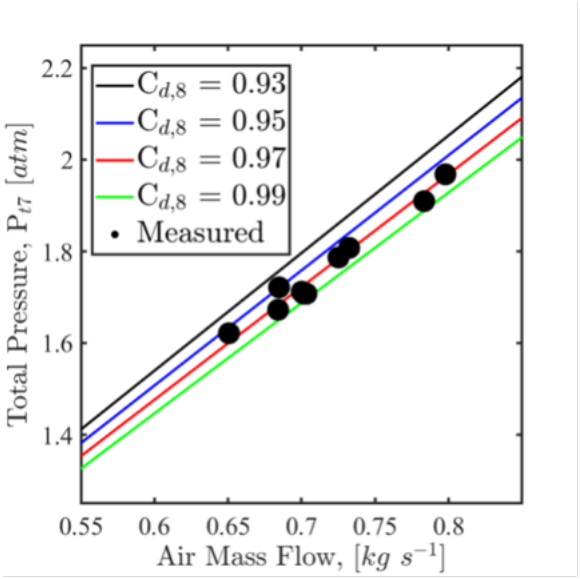

Figure 3.2: Evaluation of $C_{d,8}$ for FAI configuration.

Having been validated for both the inlet and exhaust in the forward direction, the discharge coefficient correlations given by Alam *et al.* were thus used to determine the corresponding value in the reverse direction. The nominal FAI configuration profile at the air inlet is mirrored in the forward and reverse direction (as shown in Figure 7.8), and as such the forward C_d is assumed to be equivalent to that in the reverse direction. However, the modified inner wall contour (as shown in Figure 7.8) differs in that it is analogous to the pure conical nozzle as with the exhaust restriction summarized in the prior paragraph. The reverse flow discharge coefficient is thus assumed to be 0.97 as predicted by Alam *et al.* [18] and as was experimentally verified for the similar profile at the exhaust.

3.2.2 Static Pressure Profile

One of the original design goals of the VAI configuration was to demonstrate aerodynamic similarity within the flow path at various inlet area set-points. In seeking to demonstrate this feature, results from the aforementioned cold flow test sequences were used to evaluate the static pressure profile throughout the RDE. This analysis was extended to the other configurations for comparison. Figure 3.3 shows the static

pressure profile measured along the outer wall of the RDE at varying inlet air mass fluxes for the variety of configurations. The two plots represent those tests conducted with $A_8/A_{3.2} = 1$ (upper) and with a 50% nozzle restriction installed ($A_8/A_{3.2} = 0.5$, lower). Recall that for the purposes of the VAI-W configuration, the area at station 3.2 is defined to be the same as that of the VAI configuration, so the geometric area at station 8 for all configurations is constant in the upper figure. Thus, although the VAI-W configuration possesses a 47% exhaust restriction relative to the largest portion of the channel, this is compared to the constant area channel when installed with other configurations due to the consistent geometric area at station 8.

The specific values of air mass flux chosen for presentation represent values for which all configurations have at least one data point $\pm 10 \mathrm{kgm^{-2}s^{-1}}$, while intermediate values of air mass flux have profiles that lay between the ones indicated in Figure 3.3. In general, the pressure decreases along the inlet and across the region of minimum inlet area, and then pressure recovers downstream in the detonation channel. At low air mass flux cases, the profiles for the three ARs within the VAI and VAI-W configurations are very similar, while the FAI and AFRL configurations indicate a greater static pressure loss within the channel for all conditions. Within the VAI and VAI-W datasets, differences between the inlet configurations (AR) becomes more apparent as the air mass flux is increased. This is particularly apparent around the location of the fuel injector where the curves diverge, especially at the high mass flux case. This is hypothesized to be due to the formation of shock waves within the channel at these high mass flux conditions. However, the downstream pressure recovery as shown toward the channel exit remains unchanged despite this upstream variation. This pressure recovery is partially enforced by the approximately ambient pressure boundary condition at the RDE exit.

A measure of the overall static pressure drop (from plenum to channel) is defined based on the results of Figure 3.3 and similar profiles. This measure is based on the difference between the plenum (P_3) and local channel pressure nearest the RDE exhaust (P_7) relative to the plenum pressure, which are derived from the profiles similar to those shown in Figure 3.3. Results are shown in Figure 3.4 as a function of air mass flux in all RDE configurations. This metric is related to the inverse of the static pressure drop across the device, as it represents the fraction of available plenum static pressure remaining within the channel. Thus, it is related to the stagnation pressure loss the system experiences. This quantity will be further analyzed in the following section. The static pressure drop increases with air mass flux with a nearly self-similar behavior that is largely independent of inlet area ratio configuration.

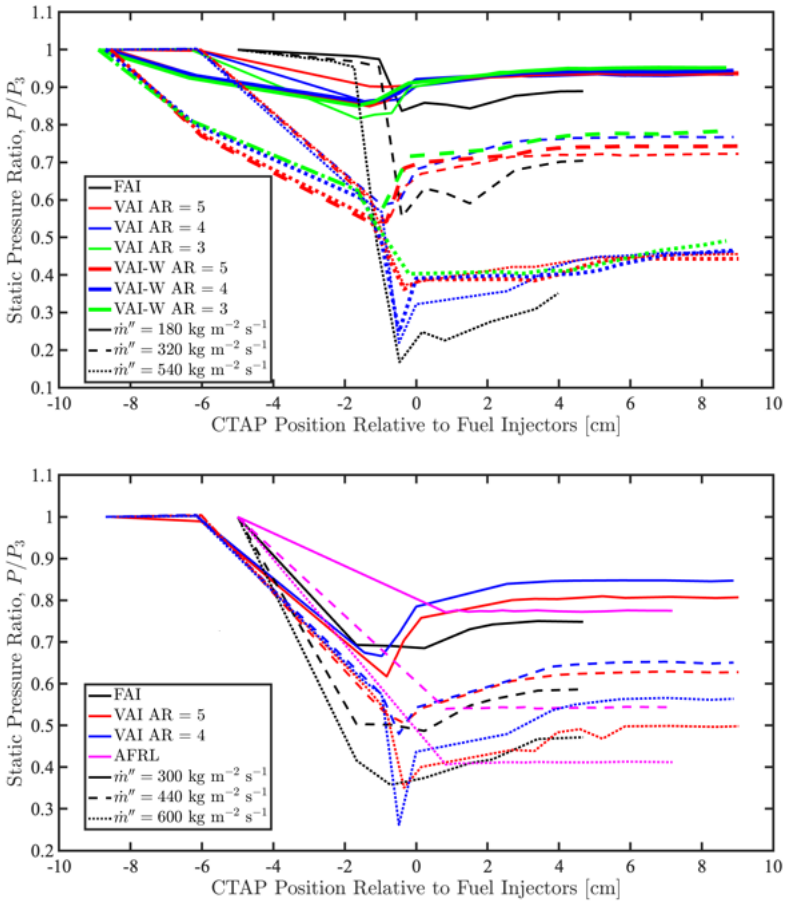

Figure 3.3: Non-reacting axial static pressure profile normalized by plenum pressure for and air mass fluxes for all configurations for which data is available. Data collected where $A_8/A_{3.2} = 1$ (upper), and where $A_8/A_{3.2} = 0.5$ (lower). Note that not all configurations have been tested with both exhaust conditions.

The similarity of the relationship between plenum and channel exit pressures across all inlet area ratios is apparent in the overlap of the pressure profiles shown in Figure 3.4. This characteristic indicates that aerodynamic similarity between the various configurations largely holds. The radial air injection AFRL configuration indicates a variant level of static pressure retention. This is due to the non-axial flow path. These self-similar trends also hold true at the channel midpoint (not shown),

but there is variation at the base of the channel at elevated air mass fluxes as the profiles of Figure 3.3 previously indicated.

An additional metric that was calculated from the data collected during cold flow testing was that of the Mach number at the throat. The flow through the inlet was assumed to be isentropic. This assumption results in a preservation of the stagnation state and for the resultant Mach number at the inlet to be calculated using Mach number-area relations, which were used to derive Equation 3.4. The discharge coefficient was again combined into the effective inlet area $A_{3.1,\text{eff}}$ term outlined previously in Equation 3.2.

$$\dot{m} = A_{3.1,\text{eff}} \sqrt{\frac{\gamma}{RT_{\text{t},3}}} P_{\text{t},3} M_{3.1} \left(1 + \frac{\gamma - 1}{2} M_{3.1}^2\right)^{-\frac{\gamma+1}{2(\gamma-1)}} \tag{3.4}$$

Given a measure of the plenum stagnation pressure $P_{\text{t},3}$ the total temperature temperature $T_{\text{t},3}$, and mass flow rate $\dot{m}$, the resultant flow Mach number at the inlet throat was found for the VAI configuration with no exhaust restriction. The results are summarized in Figure 3.5. The plenum pressure ($P_{t,3}$) is assumed to be equal to the stagnation pressure because of the large flow area and low Mach number ($M < 0.05$) in this location for all RDE configurations. The air mass flow rate at which the inlet chokes was found to be approximately 200 g/s at the most restrictive AR = 5 set-point and approximately 300 g/s at the least restrictive AR = 3 set-point. This corresponds to an effective air mass flux at the throat ($\dot{m}''_{\text{eff}}$) of approximately 290 kg m^{-2} s^{-1}, and the curves for each inlet configuration again overlap when compared on an effective air mass flux basis as was also found for the static pressure loss values of Figure 3.4. This again illustrates aerodynamic similarity and will enable comparison between hot flow and cold flows in later sections across the different RDE configurations.

3.3 Verification and Characterization of RDE Operation

Nearly all hot flow tests conducted throughout the course of this research that will be further analyzed were accomplished with hydrogen-air mixtures. Although additional targeted testing with hydrocarbon fuels such as ethane and ethylene were attempted at various points, successful operation of any of the four RDE configura-

tions on these reactant mixtures was not achieved. Additional tests were conducted in which supplemental oxygen and/or carbon dioxide were introduced, these tests will be presented for one configuration under consideration but will not be further analyzed. Further modifications to the existing configurations are believed to be needed to enable operation on additional fuels, and as such all later analysis will focus on RDE operation and behavior with only hydrogen-air mixtures. However, all of the analysis to follow is generally applicable to RDEs independent of reactant mixtures if operation is achievable.

Successful operation of the RDE during hot flow testing was verified and characterized through the data obtained from the high-speed pressure sensors installed within the detonation channel and air plenum and through optical chemiluminescence of the wave(s) within the channel. Optical chemiluminescence will be examined in later sections. The high-speed pressure sensors were used to characterize the dynamic characteristics of the wave(s) within the channel using several performance metrics. The time axis indicated in the time-history plots of quantities presented in subsequent figures refer to time with the origin ($t = 0$ s) centered on the time the fuel was commanded open within the control software.

To demonstrate some of the characteristics of these data that will be further examined, a selection of the high-speed pressure data for three similar test cases at three discrete air inlet set-points in the VAI configuration is shown in Figure 3.6. The conditions for each case (from left to right) were air mass flow rates of 430 g/s, 405 g/s, and 380 g/s and equivalence ratios of 0.61, 0.73, and 0.62, with increasing value of AR (3, 4, 5). These three cases are presented due to their similar test conditions (mass flow rate and equivalence ratio) and are representative of detonative operation in all configurations. Further analysis of the key features present in traces such as this will follow. Figure 3.6 shows the pressure time history measured in the plenum and at the base of the detonation channel (refer to Figure 7.8 for sensor location).

Each of the pressure traces presented in Figure 3.6 have the characteristic rapid and periodic pressure rise associated with a continually propagating detonation wave confined to the detonation channel. Several features of note that will be used in the later calculation of performance metrics include the frequency of operation (f), the magnitude of the pressure rise for the cycle ($\triangle P = P_2$ - P_1), and the pressure ratio (P_2/P_1) of the cycle. Pressure P_1 and P_2 are defined as the minimum and maximum value of pressure across each cycle. For reference, for each of the examples presented in Figure 3.6 these values are approximately 1 atm and 3 atm respectively. Thus each of these cases indicate a pressure rise of approximately 2 atm and a pressure ratio of

approximately 3. The frequency of operation is used to calculate the associated wave speed based upon the circumference of the RDE channel, and the pressure rise and pressure ratio are two metrics used to quantify the relative strength of the wave(s) throughout the steady portion of each test.

The cases of Figure 3.6 show similar test cases with similar operating characteristics at the three nominal AR set-points of the VAI configuration, though there are also several differences that can be observed. Although the air mass flow rates are not identical, the mean plenum pressure of the most restrictive inlet (right) is notably higher than that of the more open inlet configurations. This is consistent with the pressure variation of Figure 3.4. Additionally, the response of the plenum to perturbations at this most restrictive case is the most attenuated. The plenum is still receiving feedback (pressure variation) from the rotating detonation wave developing downstream but it is at a reduced magnitude relative to that of the AR = 3 and AR = 4 configurations. The implications of this feedback, which manifests in the form of inlet blockage and/or backflow, will be later analyzed. In spite of having a larger plenum pressure, the minimum pressure reached in the channel prior to wave arrival is also at its lowest in the AR = 5 configuration due to the more restrictive and thus hypothesized to be more lossy inlet relative to the other more open configurations.

The sample data presented in Figure 3.6 illustrate successful operation for a small duration of time, a larger subset of the data from the AR = 3 test case from Figure 3.6 is presented in Figure 3.7 to demonstrate the sustained and steady nature of operation at these test conditions. The top row represents the frequency content of the data from the water-cooled Kulite high-speed pressure sensors installed within the channel (left) and non-water cooled sensors installed within plenum (right) for this test case. Both illustrate the characteristic frequency of a rotating detonation wave within the channel at approximately 0.7 times that of the associated frequency of an ideal Chapman-Jouguet detonation for the mean pre-wave arrival conditions associated with this test case. This ideal wave speed was calculated using the NASA Chemical Equilibrium with Applications (CEA) code [19]. The direct use of the frequency as an analog for wave speed assumes that the wave is propagating into a quiescent environment, this assumption will later be analyzed. The low-speed pressures (bottom left) and a time trace of the cycle-minimum and average pressure measured by the high-speed pressure transducers (bottom right) are also shown to represent the relative steadiness observed during successful operation. This presentation shows the presence of system-wide pressure spikes during the ignition transient that will later be analyzed.

The spectral content shown in Figure 3.7 illustrates the coupling of the air plenum

and channel and that the air plenum environment (right column) is responding the effect of the dynamic events occurring within the downstream channel (left column). As the inlet becomes more restrictive the response within the plenum becomes more attenuated. This phenomena is directly related to research objective #2 and will be further analyzed in later sections.

3.4 Observed Operating Modes

Based upon the characteristics of the measurements obtained from the high-speed pressure transducers identified in Figure 7.8, along with the high-speed chemiluminescence video of the annulus, four primary modes of operation of the various RDE configurations were identified; they are:

1. Purely deflagrative;
2. Longitudinal pulsing;
3. Rotating detonation wave(s) and/or wave system(s); and
4. Simultaneously co-existing longitudinal pulsing and rotating detonation wave(s) and/or wave system(s).

The four modes of operation were predominantly identified through the spectral content and magnitude of pressure variations as measured by the high-speed pressure transducers identified in Figure 7.8 and the Circuit Wave Analysis (CWA) methodology [2]. The purely deflagrating mode shows no periodic component within any of the pressure traces, and was also observed to illustrate no visible periodic behavior in the high-speed videos obtained from the camera looking up the exhaust. Cases which illustrated operation in this mode will not be further analyzed.

The longitudinal pulsing mode shows periodic pressure pulsations at low frequency (f), corresponding to 600-800 Hz or approximately 20% of the rotational frequency of an ideal Chapman-Jouguet detonation wave (f_{CJ}) as predicted by the NASA Chemical Equilibrium with Applications code [19]. This mode was also found to be capable of generating intermittent pressure pulsations of significant magnitude that were found to saturate the installed pressure transducers. This resulted in the destruction of several of these transducers and as such testing was not performed in regions where this operating mode was expected, and analysis of tests which operated in this off-nominal and destructive mode will not be pursued.

The next observed mode was that of a rotating wave or wave system, and is the operating mode from which the term RDE is derived. This is identified through the periodic rapid pressure rise associated with the passing wave(s) and a frequency of operation that is typically 60-70% that of f_{CJ}. This rotational operation is also confirmed through visual analysis of the high-speed videos taken with the downstream camera through the CWA methodology. An example sequence of frames showing a representative video obtained in this mode of operation is shown in Figure 3.8. In this example the leading edge of the continuously propagating single wave is highlighted for each frame. This video was taken during Run 2830. Further analysis will be focused on cases which operated in this mode.

The final mode of operation that was observed is that of both longitudinal pulsing and rotational operation. For this mode the characteristics of both modes were observed during the course of an individual test, during which the reactant flow rate settings remained unchanged. Behaviors during the rotational portions of these tests will be included in later analysis, while the longitudinal pulsing portions will be excluded for the reasons outlined above.

3.4.1 Rotational Sub-Modes of Operation

The rotational mode of operation includes many sub-modes, with this section focused on intra-modal changes that occur within individual test cases conducted at constant inlet conditions. Because changes between pulsing and rotational modes were observed to occur on timescales significantly longer than that of a typical rotational cycle, presently it is difficult to determine if these hybrid modes are induced by dynamics of small-scale process associated with the detonation or if they are due to large-scale ones, such as detonation quenching/re-initiation supported by the continuously operated afterburner, or perhaps macroscopic disruptions of the inlet or exhaust flow as a consequence of the detonation wave dynamics. As such, the focus of this section is on mode changing that occurs on sufficiently short timescales (on the order of one cycle/rotation) that are assumed to be due to local dynamics associated with small-scale processes of the detonation.

Data from a subset of tests encompassing sweeps in inlet air mass flux and equivalence ratio for the VAI-W configuration will be further analyzed, with the conditions summarized in Figure 3.9. This configuration was chosen for this in-depth analysis as various distinct phenomena were observed in a relatively confined region of inlet conditions. These sweeps include tests that exhibit the previously outlined longi-

tudinal pulsing mode (2) and multiple sub-modes of rotational operation (3). The four distinct sub-modes of rotational operation observed are defined as follows: (A) uni-directional single-wave operation (USW) in which a single wave or multitude of waves propagate only in one direction, (B) steady operation with a uni-directional dominant wave or multitude of waves and a weak counter-rotating wave or multitude of waves (UDW), (C) bi-directional operation in which the dominant wave(s) and weak counter-rotating wave(s) alternate directionality for significant and distinct time periods (BDW), and (D) chaotic operation in which the dominant wave direction is constantly alternating and does not persist in one direction for significant or clearly discernible periods of time (CDW).

3.4.2 Analysis of Rotational Operating Sub-Modes

Utilizing the optical chemiluminescence observed in the high-speed videos taken for all test cases such as that shown in Figure 3.8, $x-t$ diagrams are generated. These $x-t$ diagrams were used to characterize the wave(s) within the channel and determine their position and relative strength based upon local signal intensity. These diagrams are generated by segmenting the viewable area of the RDE exhaust into $N_{\mathrm{B}} = 101$ azimuthal bins and determining the average signal intensity within these bins for each frame. An example diagram is shown in Figure 3.10 in which steady single wave operation can be observed, this case was conducted at an inlet air mass flux of 400 $\mathrm{kg\,m^{-2}\,s^{-1}}$ and equivalence ratio of $\phi = 0.6$. The CWA methodology uses these $x-t$ diagrams to determine the characteristics of the wave(s) within the RDE. For further details outlining the specific approaches used in this method see Chacon and Gamba [2].

CWA results from four cases exhibiting the previously outlined sub-modes of operation are shown in Figure 3.11, with key features identified. In these plots the markers represent observed waves, with $\log(S)$ representing the relative strength of the wave(s) defined by the observed emission intensity, and v/D_{CJ} representing the wave speed relative to an ideal Chapman-Jouguet detonation evaluated at the global equivalence ratio. The sign of v/D_{CJ} indicates the directionality of the detected wave(s). The USW case shows a single wave with limited indications of any counter-rotating waves. The UDW case clearly shows a continually present weak counter-rotating wave, with the dominant wave continuing in the same direction throughout the course of the test. The BDW case again shows the presence of a (weaker) counter-rotating wave, but the direction of the dominant wave is seen to change multiple times for discrete

periods throughout the course of the test. The CDW case is characterized by a pair of counter-rotating waves of relatively similar intensity that do not indicate discrete time periods in which the wave propagating in either of the directions is significantly and consistently identified as stronger. It is also worth noting that as suggested by the spreading of the measured rotational speed v/D_{CJ}, change in operation from USW to UDW, BDW and CDW can result in an increase in cycle-to-cycle variation of the wave speed.

The BDW and CDW cases are unique in that there are clear deviations in the mode of operation with no identifiable causes or leading indicators that would explain the observed mode changes. Run conditions were held constant throughout each of these tests, and no changes in system level behavior were observed that would explain the cause of or result from the switch in dominant wave directionality. This can be observed in Figure 3.12. These represent phase averages of the pressure and PMT data (top) and the probability density functions (PDFs) of measurable quantities (bottom) obtained during various identified analysis intervals throughout each test case of Figures 3.9 and 3.11. The measurable quantities were referenced to ideal CJ conditions for wave speed and channel pressure rise, and to a constant 2 atm for observed pressure rise within the plenum. This constant does not have a physical meaning but was chosen to place all distributions on the same scale.

For the USW and UDW cases operation was segmented into three discrete 0.5 second periods to generate the curves and statistics shown, with little variation observed throughout the course of each test. For the BDW case the time periods of (+/-) dominant wave directionality correspond to the discrete periods identified in Figure 3.11. For the CDW case the $x-t$ diagrams and CWA results were used to identify four short-duration windows (in each direction) in which greater than five consecutive cycles of constant dominant wave directionality could be identified which were then used to generate the phase average profiles and statistics. As these periods only result in a total of 51 (+) and 266 (-) cycles for analysis the probability densities are considerably less smooth than the other operating modes in which statistics were based on sample sizes on the order of 1000 cycles for each analysis interval.

All examples indicate minimal deviations in the average pressure and PMT profiles and in the wave speed and pressure rise observed in both the channel and plenum throughout the course of each individual test, and the BDW and CDW modes similarly indicate minimal deviations in these quantities when the dominant wave changes direction. The BDW example shows minimal differences despite the multiple directional changes, while the CDW case also shows minimal differences in the brief peri-

ods in the dominant wave maintains constant directionality for 5 cycles. Based upon these findings, in which the sub-modes of rotational operation indicate self-similar behaviors throughout steady test periods, the sub-modes of rotational operation are all treated equally as rotational.

3.4.3 VAI Channel and Plenum Dynamics

The coupling of the channel and plenum was notionally illustrated and identified in the data presented in Figures 3.6 and 3.7 but not further analyzed. Related research indicating this coupling and the feasibility of using sensors installed within the plenum to characterize the reactions occurring within the channel was previously performed by Anand *et al.* [20], while here the main characteristics and properties from further reducing data presented so far is performed. This analysis will focus on a subset of data obtained in the VAI configuration with no exhaust restriction under similar operating conditions where rotational operation was observed for all inlet configurations. Those test conditions fall within an air mass flow band of 380-430 g/s and an equivalence ratio of 0.61-0.73.

The data from test cases within these ranges was used to generate phase-averaged pressure profiles as-measured in the channel and plenum, which are shown in Figure 3.13. The phase-averaged profiles were generated over a total of 100 cycles that occurred at the midpoint of rotational operation, with the shaded areas representing a one standard deviation interval at each radial position relative to the wave peak. A negative azimuthal position indicates a measurement taken prior to wave arrival, while a positive azimuthal position indicates after the wave has passed. The phase-averaged pressure profiles show similarities across all inlet configurations in that the rate of pressure onset is similar in magnitude and duration for all, with the peak pressure being observed at the most open AR = 3 inlet. The minimum static pressure immediately prior to wave arrival was found to be lowest at the AR = 4 configuration, which is hypothesized to be an artifact of this test case having a higher flow rate than that of the more restrictive AR = 5 inlet. The AR = 4 configuration also shows the most pronounced response within the plenum which is also believed to be due to the slightly higher equivalence ratio present in this case as compared to the others. The mean plenum pressure for this case is still larger than that of the more open AR = 3 configuration and less than that of the more restrictive AR = 5 configuration as would be expected.

The methodology used in the development of Figure 3.13 was also used to char-

acterize the effect of changes in equivalence ratio and air mass flow at set inlet areas. These sets of 100-cycle phase-averaged pressure profiles are shown in Figure 3.14. Each column represents data from each of the three inlet area setpoints, from the least restrictive AR = 3 setpoint in the left column to the most restrictive AR = 5 in the right. The figures within the first row represent sweeps through equivalence ratio at a relatively constant mass flow rate, with all of the tests shown for AR = 3 falling between 500-600 g/s and all tests for the other two setpoints falling between 250-350 g/s. The figures within the second row represent sweeps through mass flow rate at relatively constant equivalence ratio, with all of the tests shown for AR = 3 and AR = 5 having an equivalence ratio from 0.6-0.7 and the tests shown for AR = 4 having an equivalence ratio between 0.7-0.8.

Multiple trends can be observed in the profiles shown in Figure 3.14. There is general consistency across equivalence ratio holding air mass flow constant and across mass flow while holding equivalence ratio constant. The most significant deviation from this trend is in the AR = 4 configuration, where with increasing mass flow the discrete and pronounced spike appears at higher mass flows (as seen in Figure 3.13) that is not present in lower flow cases. The plenum shows the greatest response in the most open AR = 3 configuration, with a dampened response present in the more restrictive configurations. At high mass flows there is a pronounced plenum response, but at lower mass flows this dampens to a relatively flat profile throughout the cycle. The AR = 5 configuration shows very little variation throughout the cycle with varying mass flow, though the broadband plenum response to the increased mass flow is significant despite the profile within the channel showing little variation as mass flow doubles. The frequency content of the plenum sensor corresponds to that of the channel sensor but at a significantly attenuated magnitude.

The previous figure indicated the phase-averaged characteristics of the plenum to channel interaction. This cycle-phase-level analysis is particularly relevant to the researcher, but the run-averaged quantities are of more relevance to any future designers and end-users of an RDE in a real-world application. The mean ΔP within the plenum and within the channel during steady operation are the performance metrics of merit chosen for this comparison and are shown in Figure 3.15. These are key metrics that will need to be fully understood and mapped when an RDE is to be coupled to turbomachinery. The left figure illustrates the relationship between the plenum and channel ΔPs, and the right figure compares plenum ΔP with that of the observed wave speed W. Although the dataset is sparse for the AR = 4 and AR = 5 configurations the general trends in the relationship between the pressure

rise in the channel and plenum are evident. The more open AR = 3 and AR = 4 configurations show a similar trend across the run conditions thus far tested, with the trendline for the AR = 5 configuration showing a reduced plenum pressure rise at higher corresponding channel pressure rises. The relationship between plenum ΔP and observed wave speed W in this configuration is not well defined, but linear fits to guide the eye are provided for all other conditions.

The demonstrated coupling between the pressure rise within the channel and the plenum form a dynamic representation of the induced pressure losses that will be analyzed in the following chapter. As shown in this and the prior section, this coupling is consistent and repeatable from cycle-to-cycle as can be observed in the cycle-averaged profiles. This consistent behavior, as demonstrated within the rotational mode of operation throughout this section, will later allow for the use of bulk quantities in the generation of a pseudo-static representation of these dynamic behaviors.

3.5 Operating Maps of Various Configurations

Prior sections demonstrated several basic characteristics of successful operation and how basic performance metrics for a given test condition were verified and quantified using high and low-speed pressure measurements and data collected from high-speed optical analysis. Before proceeding into further analysis of these results, a summary of the conditions tested in the various configuration throughout this research will be presented. These summaries of successful conditions are conventionally termed operating maps, as they represent the regions of known operability for a given RDE configuration.

3.5.1 VAI Configuration

An operating map for the VAI configuration was generated for the three nominal air inlet areas (AR = 3, 4, 5) as outlined in prior sections. This operating map is shown in Figure 3.16, where W/D_{CJ} is used as a performance metric for the relative quality of the detonation. This is the ratio of the observed wave speed (W) to the ideal Chapman-Jouguet wave speed (D_{CJ}) for the inlet conditions for each particular case, which was again calculated using the NASA CEA code [19]. For this presentation, only those cases which illustrated operation in a rotational mode are included and wave speeds are calculated based upon the dominant frequency observed during said

operation. The wave is assumed to propagate at the channel midpoint, which can results in a variation of ±10% if the wave were actually propagating along the channel outer or inner walls. Additional test points illustrated deflagrative and/or longitudinal pulsing modes of operation, but as mentioned previously further analysis of these cases was not performed.

When using the wave speed ratio as the figure of merit, the cases which indicated steady operation in a rotating mode shown below nearly universally become more ideal with increasing mass flow and decreasing equivalence ratio. There is little apparent variation in wave speed ratio for similar test conditions at varying ARs. A maximum wave speed of approximately 80% that of an ideal Chapman-Jouguet detonation was found at lean test conditions in the AR = 5 configuration with a 50% exhaust restriction installed, with minimums approaching 60%. The presence of the exhaust restriction largely led to a decrease in observed wave speed.

The two additional performance metrics of pressure rise and pressure ratio were also found for all test cases outlined above and are shown in Figure 3.17. NASA's CEA code was again used to calculate the ideal values. For the pressure ratio metric, P_2 represents the peak pressure of the passing wave and P_1 represents the minimum pressure immediately prior to the arrival of the wave. For the pressure ratio metric, $\triangle P$ represents the difference between P_2 and P_1. Of the three performance metrics thus far presented, wave speed is most commonly provided in literature but the pressure ratio and pressure rise metrics are also important parameters for the designer of a practical device. Each of these parameters is pertinent to the relative gain that could be realized in an RDE, as the pressure ratio/rise are related to the increase in static pressure behind the wave while the wave speed is related to the increase in dynamic pressure behind the wave through induced flow. This induced flow will be further analyzed in later sections.

The performance metrics associated with pressure rise and pressure ratio do not have the clear trends that are present in the wave speed metric, and both reach significantly lower values relative to their predicted ideal value. Peak pressure ratios of no higher than 29% that of the ideal Chapman-Jouguet pressure ratio were found, with peak values being observed in the AR = 3 and AR = 4 configurations with no exhaust restriction. Peak pressure rise relative to the predicted ideal value was also found at these conditions and reached a maximum value of only approximately 12% that of the ideal predictions. Unlike with the wave speed metric, the sparseness of the individual datasets for each inlet area configuration makes it difficult to determine the complete trends for these parameters.

On a qualitative basis, the highest equivalence ratio conditions that were tested generally resulted in the lowest performance by these metrics for their configuration. However, the lower equivalence ratio test points show a wide spread relative to their ideal predictions, indicating further testing would be necessary to determine the true trends for this configuration. From a practical standpoint the relative degradation of performance when compared to ideal detonations for these metrics is of similar importance as demonstrating a high wave speed.

3.5.2 FAI Configuration

The majority of tests conducted throughout this research were conducted in the FAI configuration. This configuration is the most highly tested due to its ability to be highly instrumented, unlike the VAI and VAI-W configurations. Due to the internal mechanism that allows for the continuously variable inlet present on these configurations, there is limited access to the center body for additional instrumentation and limited ability to modify the center body configuration. The FAI configuration is more adaptable in that sensors can be installed within the center body and directly within the fuel plenum. This includes the required pressure correction CTAPs shown in Figure 2.7 that are unable to be installed on the VAI/VAI-W configurations. Additionally, the FAI configuration is more adaptable in that a variety of channel lengths (71-137 mm) and contours (constant area and smoothly contoured) are able to be tested with no further modifications.

A summary of the conditions which exhibited rotational operation in this configuration is shown in Figure 3.18. As with the VAI configuration, the discrete air mass flow and equivalence ratio test points are shown at left, with the observed wave speed ratio (relative to an ideal CJ detonation) shown at right. Wave speeds ranging from 52-88% that of a corresponding CJ detonation were found in this configuration. In contrast with the VAI configuration, the highest wave speed ratios were observed both with and without the exhaust restriction at a wide range of air mass flow rates. As will be further outlined in later analysis, it is possible that the cases which exhibit wave speeds exceeding approximately 85% are actually approaching the corresponding CJ speed due to the presence of wave inflow. This phenomena will be later examined.

Although wave speeds ratios were observed to peak at higher values than that observed in the VAI configuration, the pressure ratios and pressure rise ratios do not exhibit then same increase. This is shown in Figure 3.19. The peak pressure ratio found was 27% that of a CJ detonation, while the peak pressure rise ratios do not

exceed 10%. This finding indicates that these parameters are not directly coupled to the detonation wave speed, as despite showing improvement in wave speed a similar improvement is not observed in these pressure metrics.

3.5.3 AFRL Configuration

A very limited subset of tests were conducted in the heritage AFRL configuration. As discussed in prior sections, this configuration possessed a radial air inlet with axial fuel injection and is directly modeled on the geometry developed at the Air Force Research Laboratory. This configuration has only been sporadically tested in the U-M facility, and tests conducted in this configuration were largely undertaken with the goal of demonstrating operation with hydrocarbon fuels. This effort was entirely unsuccessful with mixtures utilizing a pure air oxidizer, but a very limited number of successful tests were performed with the addition of supplemental oxygen through the oxygen-enrichment supply system outlined earlier.

3.5.4 VAI-W Configuration

A regimented set of tests with the 15.2 mm (wide) channel of the VAI-W configuration at various inlet set-points was conducted at the inlet conditions shown in Figure 3.20, with the mean values for each discrete test point shown with individual markers and the regions in which the various operating modes were observed highlighted for each inlet configuration. The error bars represent 90% of observations/samples during the steady portion of each individual test, which is of the same order as the experimental uncertainty. The regions of operability generally follow similar trends independent of the inlet configuration in that purely rotational operation is predominantly observed at high air mass fluxes, which transitions to rotational/longitudinal operation and purely longitudinal operation as inlet air mass flux is reduced. Purely deflagrative operation was only observed at very low inlet air mass fluxes in the AR = 4 and 5 inlet configurations.

As with prior sections, for the purposes of analysis and performance comparison the focus will be on the quasi-steady state portions of those cases that illustrated a rotating detonation mode of operation, including those cases which also exhibited discrete periods of longitudinal pulsing behavior. All analysis is based solely upon the periods of time in which rotational operation was observed. The region of operability was generally consistent for both the VAI and VAI-W channel configurations in

that nearly all test cases conducted at inlet air mass fluxes exceeding 300 kg m^{-2} s^{-1} demonstrated a rotating mode of operation, though it was found that the longitudinal pulsing that arose from the wider channel was significantly stronger than those observed in the narrow channel. The root cause of this behavior is currently unknown, and as this mode of operation was found to be destructive due to the presence of periodic pressure spikes exceeding 35 atm, further exploration actively seeking operation in this mode has not been conducted.

Based upon the previously summarized results from the VAI configuration and earlier efforts utilizing the FAI configuration conducted prior to this research, it has been found that operability characteristics are largely determined by the mass flux through the air inlet ($\dot{m}''$) [11, 3]. Therefore, the VAI-W geometry was systematically tested over a range of nominal inlet air mass fluxes and equivalence ratio conditions. A complete test matrix was completed for the AR = 4 and 5 configurations across inlet air mass fluxes from 150-600 kg m^{-2} s^{-1} and equivalence ratios of 0.6, 0.8. 1.0, and 1.2. Due to the high-intensity longitudinal pulsing exhibited by the AR = 3 configuration when testing at high air mass fluxes which saturated the installed sensors, five of the prescribed test points from the complete test matrix were not tested. This region is shown in white on the upper left plot of Figure 3.20.

A sample of the data collected from a selection of the low-speed (200 Hz) sensors that are used in later analysis is given in Figure 3.21 for a single test condition. The data presented were collected when $\dot{m}'' = 500$ kg m^{-2} s^{-1}, with $\phi = 1.0$ and AR = 5. The data presented is representative of the data collected for all test cases and is shown to illustrate the quasi-steady state conditions that are achieved after the first approximately 0.5 seconds of fuel-on (the facility induced ignition transient [21]). This is similar to prior figures but differs in that this VAI-W configuration represented the first use of the extreme temperature Type B thermocouple installed at the RDE exit plane (station 8). All of the measured CTAP pressures show little variation as before, and although there is a distinct delay in the response of the Type B thermocouple (T_8), it also settles to a relatively constant value after approximately 1 second relative to the fuel-on command. The delay in equivalence ratio onset is due to the finite response time of the fuel control valves.

This configuration was found to exhibit the most consistent performance characteristics as can be seen in Figures 3.22 and 3.23. The wave speed ratios were generally found to be lower than the previously analyzed configurations, with peak values of approximately 70% that of a corresponding CJ detonation. These ratios were largely observed to increase with decreasing equivalence ratio, and the highest values were

found at the AR = 4 inlet set point. The pressure ratios and pressure rise ratios were found to be very consistent across all tests points with little variation with air mass flow. The pressure ratios were predominantly found to improve with decreasing equivalence ratio but not universally so.

3.5.5 Relative Wave Quality from Circuit Wave Analysis

Additional characterization of the observed operating modes was also completed through the use of the previously developed Circuit Wave Analysis (CWA) method [2] for the VAI configuration. Specific details of the methodology can be found in the referenced work. The method allows for automatic identification and classification of the wave system within the channel from the high-speed video taken for each test case. The analysis was conducted for all of the test cases conducted in the VAI configuration with no exhaust restriction for which high-speed video was available. This methodology allows for individual waves to be isolated and analyzed more thoroughly than through the use of the pressure sensor data alone. Two examples of the output from this analysis method are shown in Figure 3.24, where the temporal evolution of any wave that CWA was able to detect is shown. For each data point, the speed, direction (sign) and strength (S, as the amount of energy in the chemiluminescence signal associated with the wave) are shown as discrete means taken over 7 wave cycles for each data point.

The cases presented in Figure 3.24 correspond to AR = 5 test cases conducted in the VAI configuration. The left example is of a test case at an air mass flow 380 g/s and the right is at an air mass flow of 160 g/s. Clear one-wave operation at approximately 0.65 times the ideal Chapman-Jouguet wave speed is found through this method (left) as was also apparent from the waterfall spectra of Figure 3.7. The right example at a lower air mass flow of 160 g/s shows that CWA is detecting a secondary wave system (label B) at lower velocity ($W/D_{\mathrm{CJ}} \approx 0.5$) and significantly lower intensities than that of the primary wave system (label A).

As can be seen from Figure 3.24, although certain test cases show clear single wave operation with little or no secondary wave system(s) (left), other cases do show that secondary waves are present (right), although their strength appears low. To summarize the result provided by CWA for further assessment in a convenient way, an approximate measure of the quality of the wave system within the channel was defined through the quantity α, which is simply referred to as the "relative wave

quality":

$$\alpha = \underbrace{\left(\frac{K_{\frac{1}{2}\mathrm{CJ}}}{K_{\mathrm{total}}}\right)}_{\alpha_1} \underbrace{\left(1 - \frac{K_{\mathrm{sec}}}{K_{\mathrm{total}}}\frac{\overline{S}_{\mathrm{sec}}}{\overline{S}_{\mathrm{prim}}}\right)}_{\alpha_2} \underbrace{\left(1 - \frac{K_{\mathrm{cr}}}{K_{\mathrm{total}}}\frac{\overline{S}_{\mathrm{cr}}}{\overline{S}_{\mathrm{prim}}}\right)}_{\alpha_3} \tag{3.5}$$

The quantity α is the products of individual terms α_1, α_2 and α_3 that are defined to capture different aspects of the wave system extracted through CWA. Each term is essentially defined as the fraction of the total occurrences from CWA (i.e., average wave property over seven cycles) that satisfy a particular condition or exhibit a specific characteristic as further defined below. The quantity α is defined to operate on a scale of 0 to 1 using the data generated from the CWA algorithm. An α value of 1 corresponds to a wave system that contains only a primary wave or wave system moving at a speed greater than 50% of the ideal Chapman-Jouguet wave speed for that test case with no secondary waves. A value of $\alpha = 0$ is achieved when any of the following criteria is met, with each case corresponding to each of the three terms of Equation 3.5:

1. No wave moving greater than 50% that of the ideal Chapman-Jouguet wave speed is detected (this condition defines α_1);

2. A secondary co-rotating wave system at a similar mean intensity to that of the primary wave system is detected throughout the entirety of the camera capture time (this condition defines α_2); and

3. A counter-rotating wave system at a similar mean intensity to that of the primary wave system is detected throughout the entirety of the camera capture time (this condition defines α_3).

This classification and weighting follows what prior efforts using CWA on related geometries have highlighted about the characteristics of wave systems observed during operation [2].

Several consistent trends can be found from this metric of relative wave quality as is shown in Figure 3.25. The peak values of α approach unity and generally do so at low equivalence ratios and high air mass flow conditions (left), though these trends are not universal. The quantity α is found to approach zero during several tests at low mass flows and high equivalence ratios. It was also found that high α values generally correspond to high values of the wave speed ratio (W/D_{CJ}) performance metric (right), though there are again outliers from the overall trend.

Although this metric of relative wave quality was developed during the analysis of this dataset, the calculation of this parameter was also performed for all historical test cases for which CWA was performed on all geometries that have been considered. Inclusive of the data from this test series this includes a total of 871 tests across a variety of RDE geometries and configurations. The results for this work are overlaid over historical results in Figure 3.26, including both the overall relative wave quality metric (α) and the three terms (α_1,α_2,α_3) as compared to the observed wave speed ratio. Several trends can be seen across these quantities relative to the historical family of data. With several exceptions, the axial VAI configuration generally clusters in the high α region relative to historical results, with the associated wave speeds falling at or just below the mean wave speed ratio of historical data in this α range. This is indicative of this configurations ability to maintain a strong primary wave system despite doing so at a slightly reduced wave speed ratio.

The results specific to each individual component also allow for observations to be made about the operating characteristics of this design relative to historical designs. The α_1 metric (top right) illustrates that several test cases indicated abbreviated or intermittent operation during the camera capture time, but that this design generally agrees with historical data in that most results fall within a range of 0.8-1.0 for this metric. As outlined by Shepard *et al.* when presenting the first results from this configuration, seeking to minimize secondary combustion was one of the objectives associated with the VAI design [3], the α_2 and α_3 metrics are of particular interest. Both of these parameters were found in the high range relative to historical data, indicating that secondary and counter-rotating wave systems were found to be very weak or non-existent for the majority of tests conducted with this design. This was found to be true across all inlet configurations, with only one isolated example of α_2 falling below 0.9.

3.5.6 Secondary Combustion

An additional goal of the initial studies focused on the VAI configuration was to determine the presence and relative strength of any secondary combustion. Previous sections utilizing CWA provided some insight into the presence of periodic secondary combustion, but CWA is limited in that it does not capture any secondary combustion that does not coalesce into a detectable wave system that operates with a consistent periodicity. Prior work has been conducted that outlined the basic methodology of using OH* chemiluminescence measured through PMTs looking radially into the

channel from the outer wall as a relative indicator of the heat release associated with parasitic (Q_P), detonation (Q_D), and commensal (Q_C) combustion mechanisms [22, 4]. Parasitic combustion is defined as the component of deflagration that precedes the arrival of the detonation wave, witch commensal combustion being that which follows behind the wave. This methodology defines the total heat release (Q_T) as a summation of the contributions of the three mechanisms and was used to perform a characterization of the presence and relative magnitude of heat release associated secondary combustion in the VAI configuration with no exhaust restriction:

$$Q_T = Q_P + Q_D + Q_C \tag{3.6}$$

Using the methodology of Figures 3.13 and 3.14, 100-cycle phase-averaged profiles of the PMT measurements were generated for each test conducted in the VAI configuration with no exhaust restriction in which the PMT was installed. Example profiles are shown in Figure 3.27 for one test condition at each area ratio set point to illustrate the general profile shape and outline the methodology. The PMT signal has been offset azimuthally to align with the pressure profile, in actuality the PMT is azimuthally and axially offset with respect to the channel pressure sensor. The azimuthal offset between the two is $\pi/2$ radians. This causes the raw PMT signal to be offset relative to the pressure peak by approximately $\pi/2$ or $3\pi/2$ radians dependent upon wave direction. The profiles shown in Figure 3.27 are thus offset to place the PMT peaks in-line with the associated peaks from the high-speed pressure transducers.

The regions of heat release associated with parasitic (green), primary detonation (red), and commensal (blue) combustion mechanisms are shaded and the sum of the shaded areas represent the cycle-averaged total heat release. The scale of the PMT signal is an arbitrary unit based upon the magnitude of the signal but the scale is the same for each test case. The ratio of heat release associated with primary combustion and the total (Q_D/Q_T) represents the primary combustion fraction in detonation mode presented in later figures. The AR = 5 example shown in Figure 3.27 represents the same test case as presented previously in Figure 3.6. As PMT data was not collected for all test cases the other inlet configurations do not correspond to the same test conditions of the example high-speed data in the prior figure.

For this characterization of the presence of secondary combustion, the focus was not to fully describe the characteristics of each mode of secondary combustion events nor focus on their effects, as this was one of the key research areas of prior efforts [6, 23, 24]. This first-order analysis was solely to determine the magnitude of their heat

release relative to that of the primary wave system. As such, this method provides a broader measure of the presence and relative magnitude of secondary combustion when compared to CWA, as CWA only specifically quantifies observable and discrete wave systems and does not account for any secondary burning that is not consistently propagating azimuthally. The results utilizing this method are shown in Figure 3.28.

Figure 3.28 shows that the relative strength of secondary combustion events is generally lower at lower equivalence ratios, and that the relative magnitude of secondary combustion is minimized at high mass flows and low equivalence ratios (left). As shown in the right subplot, there is also a good grouping at high α and low secondary combustion fraction, with relatively good agreement between these two metrics in the AR = 3 and AR = 5 configurations. There are several outliers that indicate that these two metrics alone do not capture all characteristics of secondary combustion mechanisms, but these relationships indicate that both fairly simplistic metrics are capturing difference aspects of the relative strength of the primary wave system and demonstrate that secondary combustion is minimized in the VAI configuration, particularly at the open AR = 3 setpoint. Although it is difficult to draw firm conclusions from this sparse dataset, it appears that the secondary combustion fraction trends downward for similar equivalence ratio conditions with a more open inlet, though further targeted testing with the full sensor suite would be required to determine the validity of this hypothesis.

3.5.7 Impact of Channel Width on Wave Speed

One of the main dynamic parameters of interest for characterization of the operation and performance of an RDE are related to the strength of the wave system within the device. This is characterized through multiple metrics, one of which is the observed wave speed. This metric allows for a relative comparison between all cases and can include condition-specific comparisons to an ideal Chapman-Jouguet detonation for individual test cases. The test conditions presented in Figure 3.20 illustrate the regions of operability, but a more direct comparison of observed wave speeds for behavior in those cases that demonstrated rotational operation is presented in Figure 3.29. The observed wave speed W for each test case was determined through the high-speed pressure data collected with the wave path for each cycle assumed to be of a length corresponding to the channel circumference at the midpoint between the inner and outer walls. The error bars represent 90% of the observations/samples during the steady portion of each test conducted during this study. The equivalence ratios are

binned to the nominal value ±0.1 for presentation in this and future figures. Detailed data is presented for nominal equivalence ratios of 0.6 and 0.8 because data sets in these two conditions are sufficiently robust to allow for a more direct comparison to be made. From Figure 3.29 several observations can be made. Observed wave speeds were generally found to increase with equivalence ratio and with inlet air mass flux up to 600 kg m^{-2} s^{-1}. For similar test conditions within the same inlet configuration the observed wave speed was generally higher in the narrow channel configuration, but not universally so.

3.6 Inherent Pressure Losses Across Inlet

The inherent pressure loss across the inlet is defined to be the decrease of (total) pressure that results specifically due to the RDE inlet flowpath geometry in relation to the mean point of operation (i.e., mass flow rate). This pressure loss is associated with the flow across the inlet in the forward direction, and it cannot be completely avoided. However, it can be mitigated by the design of the inlet flowpath shape. The inherent pressure drop can serve as an initial mechanism used to isolate the plenum or inlet flow from the effects of the detonation wave (e.g., pressure rise). For example, flow blockage or backflow can be avoided or limited if the inlet has a sufficiently large pressure drop. This strategy has been used in early studies to achieve stably operating RDEs [25]. Quantification of the inherent pressure loss is accomplished through the use of pressure measurements across the RDE in cold flows (i.e., no fuel injection or combustion). Cold flow data also used to determine discharge coefficients and to establish the pressure profile throughout the device. In this section, this data will be used to determine inherent losses.

One of the key parameters that is used to characterize overall RDE performance is that of Pressure Gain (PG). Although a positive value of this parameter has yet to be demonstrated for any known RDE configuration, the negative values provided in literature give an indication of the level of loss present in various RDE designs during operation. This parameter can also be utilized to characterize the level of total pressure loss that results during cold flow and is thus inherent to individual RDE configurations.

The Equivalent Available Pressure (EAP) and NPS methods for determination of PG were previously outlined, both of which provide a method through which the total pressure at the RDE exit can be calculated. However, these methods are limited

in that they require thrust measurements (EAP) or in that they are invalid when an exhaust restriction is not installed and $A_8 = A_{3.2}$ (NPS). As all cold flow tests conducted had the necessary instrumentation for an analog of the NPS method that is not reliant upon the A/A^* relations, this will be used in lieu of the EAP or direct NPS method for this characterization. The NPS approach has been modified to perform a similar calculation using measurements obtained at the RDE exhaust plane. By combining conservation of mass and isentropic equations, a relationship can be found to determine the exhaust Mach number. The isentropic relationship between static and total temperature is included in place of a direct measurement of T_8, with the total temperature assumed to be conserved from plenum to exhaust. This relationship is shown below in Equation 3.7.

$$M_8 = \frac{\dot{m}\sqrt{R_8}}{\sqrt{\gamma_8} P_8 A_8} \sqrt{\frac{T_{t,8}}{1 + \frac{\gamma_8 - 1}{2} M_8^2}} \tag{3.7}$$

Equation 3.7 was solved directly for the subsonic solution for all tested cold flow conditions. The resultant Mach number was then used with the PG calculation of Equation 3.8 to determine the cold flow equivalent Pressure Gain (PG_c):

$$PG = \frac{P_{t,8}}{P_{t,2}} - 1 \tag{3.8}$$

The results of this analysis are shown in Figure 3.30. This method of casting the pressure loss as a decrement of total pressure was developed such that it is consistent with the evaluation methodologies used to determine the end-to-end pressure gain of an operating RDE. As such, although these values are similar to the static pressure ratios presented previously, they result in a more analogous representation from the standpoint of pressure gain.

Several features of note are apparent in this analysis. First, the overall trends in PG_c are consistent across all configurations, asymptoting to 0 for the zero air mass flux condition and asymptoting towards a singular configuration-dependent value at high air mass flux conditions. Next, for those cases in which a 50% nozzle was installed (outlined markers), the overall equivalent cold flow pressure gain is higher than those without the nozzle restriction. Additionally, the pressure gain profiles of the VAI configuration without an exhaust restriction and the VAI-W configuration (red marker) are nearly identical for similar inlet air mass fluxes. Recall that the geometric area of the VAI configuration without exhaust restriction and the VAI-W

configuration are the same. This finding implies that smoothly contoured changes in channel geometry do not have a net effect on the pressure losses inherent to the device, and the overall pressure "gain" is based upon the shape of the inlet and the geometric area at station 8. This finding will later be further scrutinized when analyzed under hot flow conditions. Lastly, the most restrictive inlet of the AFRL configuration shows the greatest loss in stagnation pressure, while the less restrictive inlets in other configurations illustrate a greater stagnation pressure retention. The VAI configuration at the AR = 4 setpoint with 50% exhaust restriction was found to be the least inherently lossy from end-to-end. Based upon the observed trends it is believed that the VAI AR = 3 configuration with 50% exhaust restriction would further improve on this metric but this combination has not yet been tested.

3.7 Inlet Blockage Fraction

3.7.1 Initial considerations

The response or dynamics of the inlet of an RDE in operation can be described from multiple perspectives. One point of view is a cycle-resolved description of the response, while an alternative view is a cycle-average description. One example is the quantification of the time-varying, cycle-resolved variation of the mass flux through the propellant inlet [26]. Most commonly the cycle-resolved view is generated through detailed simulations [27], while in experiments only proxies of the time-varying response can be determined. As an example, Matsuoka *et al.* demonstrated the presence of inlet back-flow associated with the passing wave(s) through optical chemiluminescence [28], but these observations were not of sufficient fidelity to determine the cycle-resolved variation of mass flux. Another example is the definition of an inlet or injector response time, which is defined as the time elapsed from the passage of the detonation wave to re-establish a steady flow through the propellant inlet or injectors [11, 29, 28]

In the following analysis, the view of describing the dynamics of the inlet from a cycle-average view is taken. Two aspects are considered in particular. The first aspect is the pressure drop across the air inlet and fuel injection during non-reacting steady flow. This was initially described at Section 3.2.1, but we now use those data to define what we here define as inherent pressure loss and define an equivalent cold flow pressure gain. This cold flow pressure gain is a new parameter developed from similar methodologies used to characterize end-to-end pressure gain during operation.

This parameter is equivalent to the total pressure loss that is realized across the device under cold flow conditions. This quantity allows us to establish the degree of loss that is associated with the design itself, isolated from those losses that may appear only during operation.

Unlike conventional deflagrative combustors which operate at comparatively low Mach numbers throughout the flow path, an RDE typically has an inlet through which reactants flow at or near a Mach number of unity. As shown in the prior chapter, successful operation of an RDE requires high inlet air mass fluxes which correspond to high Mach number flows. This characteristic can induce pressure losses in and of itself, before any reaction is initiated. These unavoidable losses that are associated with the basic concept and specific to individual configurations are thus termed inherent losses.

The second aspect that will be considered and analyzed is the degree of blockage that the passage of the detonation wave imposes on the air inlet and fuel injector(s). In this study, the primary focus will be placed upon the blockage of the air inlet, although similar considerations and calculations relevant to the fuel injection system are also included. An accurate characterization of this phenomena is theorized to be a critical aspect for describing the response of the inlet. Inlet blockage can be described both in terms of a cycle-resolved or cycle-averaged views. The analysis to follow will focus primarily on a cycle-resolved point of view.

A basic representation of the inlet state can be derived by relating the cold flow and hot flow characteristics of the system. Based upon these relationships, the relative portion of the inlet that is blocked by the moving region of high-pressure associated with the detonation wave(s) can be inferred. A newly developed methodology which characterizes this effect is introduced, validated through targeted cold flow testing, and the implications analyzed.

Although the concept of blockage itself does not directly manifest as an overall loss, the implications of this phenomena do result in a variable degree of loss at the system level. Once pseudo-steady operation is achieved, the continually propagating wave(s) within an operating RDE consist of a localized region of high-pressure, and this high-pressure region necessitates that the inlet conditions modulate accordingly. As all RDE configurations under consideration in this study are of the pressure-fed, air-breathing type, positive flow from the plenum to RDE channel can only occur in regions in which the static pressure along a given streamline is decreasing. Thus, for an RDE tested within the laboratory in which mass flow is controlled, the associated plenum pressure for a given flow-rate necessarily adjusts to account for this characteristic.

However, this presents a conundrum in which the very pressure gain occurring within the channel, which is sought to be harnessed, is also actively feeding back directly to the supply pressure within the plenum, which for the pressure gain metric (per Equation 3.8) is the reference state to which the exit static pressure is compared. This characteristic is not unique to the RDE configurations considered in this study, as all known configurations in literature also possess this direct coupling between the RDE channel/exhaust and plenum. This increase in plenum pressure as compared to the reference cold-flow condition thus ultimately results in a system-level loss induced by operation itself, which will be quantified for later analysis of overall pressure gain. These losses are therefore termed induced losses.

3.7.2 Definition and Evaluation of Inlet Blockage

As general characteristics of operating conditions and operating modes of the various RDE configurations under analysis have now been established, further analysis will now be conducted. The inlet blockage fraction metric (B) was first proposed by Shepard *et al.* [3]. Originally the quantity was proposed only as a time-averaged quantity, but in a follow-on effort it was extended to operate on a per-sample basis [21]. This metric relates the inlet plenum pressure observed during reacting flows to that during non-reacting flows to determine an effective inlet air mass flux that would result from the measured plenum pressure. This parameter will later be used to characterize to help isolate and characterize local gains and losses within an operating RDE.

In order to generate the relationships necessary to determine the inlet blockage fraction that will be defined in the next section, non-reacting flow data was used to generate inlet air mass flux versus plenum pressure curves for each configuration. As previously summarized, the inlets of the VAI and VAI-W configurations are continuously variable and confined within the RDE such that the actual area could not be directly measured once installed. The inlet mass flux is thus calculated based upon the effective inlet air mass flux relationship presented in Equation 3.3 for all configurations. The experimental data showing the observed plenum pressure ($P_{t,3}$) as a function of equivalent inlet air mass flux (as defined by Eq. 3.3) for all cold flow cases in the various inlet configurations are shown in Figure 3.31. The methodology that will later be outlined is based upon actual data obtained during these cold flow tests (blue markers and black line curve fits), though a similar version of these curves can also be calculated based upon fully and partially choked flow calculations for

pre-existing datasets if non-reacting flow data is unavailable (red lines). As can be observed in the data presented, these actual and theoretical curves do not always directly overlap, so the use of actual experimental results is preferred. For the purposes of this work all comparisons are made to fits made to experimental values (black lines) obtained through the purposely tested cold flow cases. The use of raw experimental data in this manner ensures that any variability that may be present in the discharge coefficient is captured.

The cold flow curves shown in the previous subsection are used as the basis for determining the blockage fraction based upon experimental data. Based upon these curves, the effective air mass flux in a fully unblocked (cold flow) condition are compared to the known inlet conditions for discrete tests to determine the fraction of the total inlet area required to be unblocked to match the known mass flow-rate if assumed to be fluxing at the effective air mass flux rate in this theorized unblocked region. The remaining area of the inlet is considered the blocked region, in which the net flow must thus be zero to conserve mass.

A graphical representation showing the blocked (red) and unblocked (black) regions of a generic annular RDE configuration is shown in Figure 3.32. Also included are representative (unwrapped) inlet air mass flux profiles for the uniformly unblocked case, the idealized semi-uniform case with blockage, and several notional profiles that satisfy the net-zero flow condition within the blocked region. In this initial development of the parameter no assumption is made as to the shape of the flow or flux profile in the blocked region, it is solely necessary to have a net flow of zero to match the known flow rate from the metering orifice. The ratio of this blocked area to the total inlet area is the blockage fraction B. As noted, this formulation does not account for any partial blockage that may be present, as it casts the inlet as the two discrete regions previously described: (1) the blocked or net-zero flow/flux region, and (2) the fully un-blocked region which is fluxing at the effective air mass flux rate. Thus, B is defined according to:

$$B = 1 - \frac{\dot{m}''_{\text{Hot}}}{\dot{m}''_{\text{Cold}|P_{t,3}}}. \tag{3.9}$$

In its simplest form, the concept of inlet blockage as defined by Equation 3.9 corresponds to a binary representation of the inlet. This simplification allows for a steady representation of an unsteady problem. It does so by equating the "unblocked" fraction of the total inlet area $(1-B)$ required to drive the full mass flow rate through the device to the total area, while assuming the blocked area is completely blocked. The blocked fraction B is assumed to have a net-zero flow through this portion of

the inlet. This simplified representation of the inlet flow field does not account for azimuthal variation or any inlet flow reversal but does reduce the unsteadiness of the flow field at the inlet to a steady representation. However, this simplistic view allows for the definition of an effective inlet mass flux, which is the equivalent air mass flux through the unblocked portion of the inlet. If we postulate and accept that the blocked region of the inlet has zero net flow, then the effective flow through the unblocked portion $(1 - B)$ of the inlet must correspondingly increase to account for the region of zero effective flow. The resulting effective inlet mass flux is thus defined as the mass flux through this unblocked portion according to:

$$\dot{m}''_{\text{eff}} = \frac{\dot{m}''}{1 - B}. \tag{3.10}$$

The definition in Equation 3.10 holds for non-reacting flow cases as well. When the blockage fraction goes to zero as is the case during non-reacting/cold flow conditions, the effective inlet mass flux becomes equivalent to the global inlet mass flux.

As in Figure 3.30, in figures to follow the markers refers to results for the various inlet configurations for which data is presented. Markers without border represent test cases performed with the constant area channel and no exhaust restriction, while markers with black borders represent test cases performed with the 50% converging nozzle installed at the channel exit. The color of the marker indicates the equivalence ratio band for individual test cases (nominal value ± 0.1). The observed plenum pressures for all test cases which exhibited rotational/detonative operation are shown in Figure 3.33. This illustrates the global rise in plenum pressure for a given inlet air mass flux that results from the feedback from the reaction(s) occurring within the RDE channel. This data is then later used in the derivation of the blockage (B) fraction.

Based upon the data presented in Figure 3.33, the blockage fraction B for each case can be computed from Eq. 3.9. Results are shown in Figure 3.34 for the four inlet configurations tested with the nominal 7.6 mm channel width, with notional exponential fits included for visual reference. Several trends can be observed. For a given inlet configuration and equivalence ratio, B is generally found to decrease with increasing inlet air mass flux and approach an asymptotic value. Blockage fraction is also observed to generally increase for similar test conditions as the inlet is opened. The addition of the 50% converging nozzle (markers with black outline) generally results in an increase in blockage fraction relative to similar tests conducted with the constant area channel with no exhaust restriction.

The results of Figure 3.34 present results obtained in the nominal channel width (7.6 mm) FAI and VAI configurations. An additional evaluation of the effects of changes in channel geometry while holding the inlet and exhaust areas constant was also performed. As noted earlier, the VAI-W configuration only differs from the VAI configuration in this respect.

The blockage fraction (of the air inlet) was evaluated for both configurations. Figure 3.35 summarizes the computed blockage fraction of the air inlet as a function of mass flux at the inlet across all geometric configurations for two different equivalence ratios ($\phi = 0.6$ and $\phi = 0.8$). The error bars represent 90% of observations/samples during the steady portion of each test. The results show that the blockage increases as the air inlet throat grows larger (lower AR) for both the VAI-W and VAI configurations. Additionally, both configurations demonstrate a decrease in blockage fraction as the mass flux increased. However, the blockage does not change significantly between the wide-channel VAI-W (filled icons, denoted "W") and the narrow-channel VAI (empty icons, denoted "N") configurations under similar operating conditions. This suggests that channel geometry changes while maintaining the same inlet/exhaust areas do not result in significant differences in the blockage fraction of the air inlet.

3.7.3 Inlet Blockage Fraction based Upon Plenum Pressure

Deng *et al.* developed a metric similar to that outlined in Eq. (3.9) using the observed plenum pressure for a given inlet air mass flux [30]. Instead of comparing the inlet air mass fluxes at a given plenum pressure, this metric compares the plenum pressures at a given air mass flux, and this metric will be defined as (B_{P}) and is given below per Eq. (3.11):

$$B_{\mathrm{P}} = 1 - \frac{P_{3,\mathrm{Cold}|\dot{m}''}}{P_{3,\mathrm{Hot}}}. \tag{3.11}$$

This methodology is similar to the formulation presented in the prior section in that it utilizes a comparison of non-reacting flow characteristics to that of reacting flow in the formulation of a measure of inlet blockage. This leads to identical results for B and B_{P} for individual test cases that are conducted at inlet air mass fluxes that are known to be choked under non-reacting flow conditions. However, at low inlet mass fluxes that fall outside of the linear relationship between pressure and air mass flux there is significant deviation. This will later be seen in several cases where

the calculated value of B for a given test case is significantly larger than that of the corresponding B_P value.

The laboratory test environment presents a unique divergence from real-world devices in that air mass flow rates (and thus, fluxes) are generally the driving parameter for individual test cases. In order to accurately quantify performance based upon known inlet conditions, upstream flow metering devices are typically used to be able to quantify flow rates. As such, the plenum pressure reacts to the defined air/fuel mass flow rates. In an application outside of the laboratory the reverse will be true. The inlet pressure will be dictated and the flow rates (and thus, fluxes) will modulate based upon these pressures. Establishing the blockage fraction based upon the air mass flux is therefore hypothesized to be the appropriate methodology for determining the effective blockage. Thus, the lower predicted effective blockage by the B_P metric is believed to be invalid and a misrepresentation of the actual state of the inlet for a given test condition for those conditions that result in an underprediction relative to the B metric. This hypothesis will be tested and validated in a later section.

However, although the B parameter is posited to be a better representation of the flow field at the inlet, the B_P parameter is also useful from a pressure gain analysis perspective. As this parameter captures the relative plenum pressure rise during operation, this parameter can also be used to determine the relative change of the denominator of the PG equation 3.8. When considering pressure losses from the standpoint of overall pressure gain, this parameter is thus useful for quantifying the induced pressure losses under analysis in this research, despite this parameter originally being posed as a measure of hydrodynamic blockage at the RDE inlet. Although this parameter by itself does not immediately translate to what one might conventionally consider a loss, the resultant increase in supply pressure that this parameter quantifies and its impact upon the end-to-end gain of an operating RDE manifests as a net loss when considered from this standpoint.

3.7.4 Inlet Blockage Fraction Defined based Upon High-Speed Channel Pressure Measurements

An additional metric that was presented by Deng *et al.* utilized a comparison of the relative fraction of each cycle in which the observed channel pressure exceeded that of the plenum pressure [30]. This metric is based upon the assumption that a static pressure within the channel higher than that of the plenum is capable of

locally arresting positive flow, though again this methodology does not account for any reverse flow or local partial blockage, but it does allow for a similar characterization of the overall effective blockage as with the previously defined B metric. Additional works focused on observing chemiluminescence have indicated the presence of burned gas back-flowing up into the air plenum [28, 22].

This metric will thus be defined as B_{HSC} and is calculated as shown below in Eq. (3.12). In this calculation $\overline{t_1}$ represents the mean cycle time, and $\overline{t_3}$ represents the mean time within each cycle in which the pressure measured within the channel exceeds that of the air plenum. An example showing these parameters is shown in Figure 3.37, with a comparison of the calculated values of B_{HSC} to the corresponding values of B shown in Figure 3.38.

$$B_{\mathrm{HSC}} = \frac{\overline{t_3}}{\overline{t_1}} \tag{3.12}$$

The results of Figure 3.38 show that B_{HSC} correlates fairly closely with the calculated values of B for those cases in which the HSC measurements are available, though there are cases in which there is significant variation. This illustrates that a blockage fraction can be deduced for certain test conditions without non-reacting flows for comparison. It must be noted that all test cases included in this study did not include the High-Speed Channel (HSC) pressure measurements taken closest to the air inlet, and as such the datapoints presented in Figure 3.38 do not represent all of the test cases that were analyzed as part of this study.

This correlation between values calculated from the low-speed CTAP plenum pressures within the air plenum and those found from the B_{HSC} metric illustrates that this metric may be able to be applied post-test to datasets for which non-reacting or cold flow data was not obtained. This lends credence to the validity of the B metric as a standalone measure of RDE performance for a given configuration.

3.7.5 Inlet Blockage Fraction Defined based Upon High-Speed Plenum Pressure Measurements

As outlined in previous sections, the original formulation of B utilized mean values for air mass flux and plenum pressures to generate a mean value of blockage fraction for each test case [3]. Due to the low sample rate of the sensors used for these calculations these parameters represent values that are averaged in both time and space. In a follow-on work this metric was expanded to generate this metric on a per-sample

basis for the low-speed (200 Hz sample rate) data collected for each test [21]. This has since been improved to include measurements taken from the HSP transducer installed in the plenum, which allows for a more dynamic representation of changes in effective blockage. The blockage representation utilizing the HSP measurements within the air plenum will thus be referred to as B_{HSP}. The HSP measurements are taken at similar locations as the low-speed measurements used in the evaluation of B. These measurement locations were shown for the various configurations in Figure 7.8.

This methodology uses the same formulation of B as given in Eq. (3.9) but calculates this parameter on a per-sample basis for the data obtained from the HSP transducer installed within the plenum (500 kHz sample rate). These calculations are applied during steady test periods during which air mass flow-rates are invariant, so as such the mean air mass flow-rates are used for determination of the corresponding flux. This methodology uses the same representation of the relationship between $\dot{m}''$ and $P_{\mathrm{t},3}$ for non-reacting flows as was shown in Figure 3.31. Thus, this methodology attempts to capture time-resolved variations in the local blockage as a function of the high-speed plenum pressure measurements without the averaging inherent to the use of a CTAP-type pressure measurement. As the methodology is largely unchanged, the resultant mean values show strong correlation with that generated using low-speed mean values as can be observed in Figure 3.40. This would be expected as the low-speed pressure transducer installed in a CTAP configuration performs this averaging fluidically.

The expansion of this metric to include data from the HSP transducer within the plenum allows for a first attempt to generate a characterization of the dynamic behavior of the effective blockage on sub-cycle timescales. Although this method does not allow for a true characterization of inlet flowfield, it is hypothesized that increased variation of this parameter across each cycle may provide insight into the flow variations that are occurring due to the upstream propagation of the pressure disturbances occurring within the channel. As the concept of inlet blockage is uni-directional (in the forward direction) in nature, the use of this parameter by itself cannot directly generate a cycle-resolved characterization of the local flux across a representative cycle.

However, variation in this parameter on sub-cycle timescales is believed to be representative of the degree of back-flow that is present. In the case of a perfectly diodic inlet through which no feedback to the plenum, and thus no reverse flow is allowed, one would expect the values of B and B_{HSP} to be identical. This would

manifest in an approximately constant value of HSP, as the pressure spikes associated with the passing of the wave(s) within the channel would be arrested by such an ideal inlet. The relative variation between these two parameters is thus hypothesized to be an indicator of the relative variation in the local flow-field at the air inlet. An example of the dynamic variation in this parameter is shown in Figure 3.39.

The example shown in Figure 3.39 illustrates the significant variation in the calculated effective blockage during operation. As the plenum reaches its peak pressure values the maximum values of B_{HSP} approach 0.4, while reaching minimum values of 0.1 during the pressure minimum during the refill portion of the cycle. This variation was captured through the standard deviation of all calculated values during the period of steady rotational operation for each test case, and a ratio of the calculated mean values of B_{HSP} and their associated standard deviations σ_{HSP} is shown in Figure 3.41.

As can be observed in Figure 3.41, higher levels of overall blockage appear to suppress variation within that blockage as calculated based upon the B_{HSP} methodology. This manifests as an increase in the ratio of the mean blockage to its standard deviation. The highest values for this quantity are present when the 50% exhaust restriction is installed, which in fact appears to form a separate family of data for this parameter. It appears that the exhaust nozzle has the effect of suppressing variation in inlet blockage.

3.7.6 Validation of Inlet Blockage Concept Through Physical Blockage Study

All results presented thus far consist of data obtained during RDE operation. As an evaluation of the concept of the blockage fraction, an additional test sequence utilizing non-reacting test conditions to confirm the validity of the concept was devised. The VAI and VAI-W RDE configurations allow for upstream access to the annular throat from within the air plenum, and as such it was hypothesized that including a physical blockage in this region would serve to confirm the blockage fractions calculated through experimental measures during nominal operation.

A test sequence was conducted at each of the three discrete inlet ARs in the VAI-W configuration in which variable amounts of physical blockage were introduced near the inlet throat. All tests for this sequence were with the exit area held constant to that of the constant area channel/non-nozzled configuration. These physical blockages were formed by three pieces of silicon rubber cut to lengths representing

approximately 12.5%, 25%, and 50% blockages of the inlet. In order to represent the azimuthally dissimilar flow-field present within an operating RDE, these physical blockages were placed at two different azimuthal locations. These locations were with the blocked area centered on the plenum CTAP (as the examples in Figure 3.42 show) and diametrically opposed. The mean values for observed plenum pressure between the two conditions were used to form a representative value for an operating RDE at set global inlet air mass flow rates.

The results from this test sequence are shown in Figure 3.43. In this example the effective blockages were calculated through the various metrics previously presented, including the B methodology of Eq. 3.9, the B_{P} methodology of Eq. 3.11, and the B_{HSP} methodology that extends Eq. 3.9 to a per-sample basis (that is then averaged) using the pressure measurements obtained with the plenum high-speed pressure transducer. As these tests were conducted with non-reacting flows the B_{HSC} methodology is invalid due to the lack of reaction-induced pressure rises within the channel.

The results shown in Figure 3.43 indicate that the B and B_{HSP} methodologies provide an accurate representation of the known physical blockages across the range of global inlet air mass fluxes that were tested. Note that the AR = 5 configuration is consistently under-predicted when compared to that of the other ARs, this is due to access limitations within the air plenum that resulted in the physical blockage sitting slightly upstream of the minimum area of the inlet throat. The predicted blockage (as calculated through the B methodology) closely matches the known physical blockages, while the pressure-based methodology of Deng *et al.* is shown to significantly under-predict the inlet blockage at low inlet fluxes. This test sequence illustrates that the B methodology forms a more accurate representation of the blockage fraction at the inlet when compared to this methodology based upon the plenum pressure change at these low inlet fluxes. As previously highlighted, the two methodologies result in the same values at high inlet mass fluxes.

3.7.7 Correlation of Blockage Fraction with Observed Pressure Rise

In addition to propagation wave speed (W) and its ratio relative to that of an ideal Chapman-Jouguet detonation (W/D_{CJ}), an additional measure of RDE performance that is widely used to characterize operation is that of the observed pressure rise across the detonation wave. This is generated based upon the magnitude of the

abrupt pressure increase that accompanies the rotating reaction front. This measure represents the difference between the peaks and troughs that can be observed in the pressure traces of the prior example presented in Figure 3.37. For this example the peak pressures can be seen to reach a value of approximately 3.4 atm, with the minimum observed pressures prior to wave arrival being approximately 1.4 atm. Thus, for this particular example the pressure rise is 2 atm.

Based upon the formulation of B of Eq. 3.9 and if it is assumed that the mass flux through the unblocked portion is zero, an effective mass flux within the unblocked region can be determined. This corresponds to a correction to the global inlet air mass flux based upon the ratio of the unblocked region to the total effective inlet area. The resulting effective air mass flux is thus:

$$\dot{m}''_{\text{eff}} = \frac{\dot{m}''}{1 - B} \tag{3.13}$$

A comparison illustrating the relationship between the effective inlet air mass flux and mean pressure rise observed within the channel (ΔP_{HSC}) is shown in Figure 3.44. For the FAI and VAI (with AR = 5) configurations, it can be seen that there is a strong linear correlation between effective inlet air mass flux and observed pressure rise for similar equivalence ratios. This correlation is less pronounced in the VAI AR = 4 and AR = 3 configurations, though the sparseness of the data in these configurations does not allow final conclusions to be drawn. Further testing is required to determine if these larger inlet configurations exhibit dissimilar trends as compared to the smaller inlet configurations in which the linear relationships are pronounced.

As the observed pressure rise is one of the key parameters that is typically compared to ideal Chapman-Jouguet detonations in performance analysis, this finding is of note. This near linearity implies that in order to achieve a certain pressure rise across the cycle a particular blockage fraction at the inlet must be achieved. Further work characterizing this effect for additional configurations is necessary to determine if this a feature of this specific inlet design or if similar relationships exist for other RDE inlet configurations.

3.7.8 Evaluation of Inlet State Through Corrected Air Mass Flux

Corrected air mass flow (and thus, flux) is an important parameter that is used in conventional jet engine and jet engine sub-component analysis. This correction allows

for reference to a particular state (typically sea level) and the determination of the equivalent flow (flux) at these conditions. This allows for direct comparison between dissimilar inlet conditions.

Corrected air mass flow $\dot{m}_{corr}$ is found according to:

$$\dot{m}_{\text{corr}} = \dot{m}\sqrt{\frac{T_{\text{t},3}}{T_{\text{SL}}}}\frac{P_{\text{SL}}}{P_{\text{t},3}} \tag{3.14}$$

Similarly, the corrected air mass flux is thus given by:

$$\dot{m}''_{\text{corr}} = \frac{\dot{m}}{A_{3.1}}\sqrt{\frac{T_{\text{t},3}}{T_{\text{SL}}}}\frac{P_{\text{SL}}}{P_{\text{t},3}} \tag{3.15}$$

Figure 3.45 shows the measured blockage fraction as a function of the corrected mass flux for all data taken in the study (symbols). The results of the measurement indicates that the blockage fraction is nearly perfectly negatively correlated with the corrected air mass flux for nearly all test cases. As the change in blockage fraction represents an effective change in the $A_{3.1}$ term of the $\dot{m}''_{\text{corr}}$ equation when accounting for flow through the unblocked region, this result would be expected if a fully choked unblocked region was present for all test cases. However, several low air mass flux cases do not lie on the linear flux versus B line. Multiple explanations for this deviation are possible. The first such explanation that will be examined is that the unblocked region is fluxing at a rate corresponding to a subsonic condition.

The formulations of Equations 3.15 and 3.16 are shown without the direct inclusion of the Mach number, this is instead included indirectly in the pressure and temperature corrections. However, these formulations are correlated with the axial Mach number and as such can be leveraged to determine the equivalent inlet Mach number within the unblocked region at the RDE inlet with the assumption of purely axial flow in the forward direction. A formulation that includes Mach number is given by Kurzke [31] according to:

$$\dot{m}''_{\text{corr}} = \frac{P_{\text{SL}}}{\sqrt{T_{\text{SL}}}}\frac{M_{3.1}\sqrt{\gamma/R}}{\left(1+\frac{\gamma-1}{2}M_{3.1}^2\right)^{\frac{\gamma+1}{2(\gamma-1)}}}. \tag{3.16}$$

The dashed lines shown within Figure 3.45 represent the solution of Equation 3.16 for Mach number at the inlet ranging from 0.5 to 1.0 in increments of 0.1. Thus,

the assumption of fully axial flow only in the forward direction would lead to the determination that select low-flux cases do not indicate localized choking within the unblocked region and RDE operation is possible at inlet Mach numbers (within the unblocked region) as low as approximately 0.7.

However, this conclusion requires the assumption of zero reverse flow across the entire cycle and an invariant inlet temperature. The definition of blockage fraction assumes zero net flow across the "blocked" portion of the cycle but does not preclude the possibility of reverse flow within this portion. Accordingly, any amount of reverse flow that is present within the blocked region must be offset with a commensurate amount of forward flow. The simplified flow profiles shown in Figure 3.32 all satisfy this requirement. Note that if reverse flow is present, any requisite equivalent forward flow within the blocked region is not mandated to be the same slug of burned gas. The results shown in Figure 3.46 make this assumption, in that any burned gas which flows back into the plenum also flows out during the blocked portion of each cycle.

However, if this assumption is not made, and burned gases are allowed to either A) persist in whole or in part within the plenum until injected in the unblocked region or B) transfer thermal energy to the incoming flow which is later injected in the unblocked region, a different conclusion can be drawn. This is the second explanation for deviations from the linear relationship between blockage and corrected mass flux which will be considered. As found in previous research efforts in which optical chemiluminescence indicative of burned gas was observed upstream of the inlet [28, 22], Equations 3.14 and 3.15 above can also be leveraged to determine the requisite mean inlet temperature (within the unblocked region) that would be required to maintain $M_{3.1} = 1$. Results from analysis based upon this postulation are shown in Figure 3.46. In this figure the dashed lines represent varying $T_{t,3}$ from 290-390 K in increments of 20 K. This analysis does not account for potential changes in γ or R that could potentially result from burned gas backflow but allows for an order of magnitude determination for required reverse flow to achieve the sonic condition within the unblocked portion of the inlet.

The results of Figure 3.46 indicate that mean inlet temperatures of 350 K are sufficient to enforce the sonic condition within the unblocked portion of the RDE inlet. In other sections it will be shown that observed channel temperatures in the VAI-W configuration varied from approximately 1000 - 1500 K. Although similar data is not available for all configurations, this establishes a reasonable range for estimation. Thus, with an assumed lower bound for back-flow temperatures at 1000 K, only approximately 5% of the total forward flow is required to flow in the reverse

direction to achieve these mean inlet temperatures.

Based upon the aforementioned research efforts in which burned gas back-flow was observed directly through optical chemiluminescence [22, 28], these (relatively) low magnitude back-flows are hypothesized to occur at a level such that they enforce a local sonic condition at the inlet for all RDE test cases within all or a portion of the unblocked region when successful rotational/detonative operation is observed. These back-flows are potentially overcome or reduced in relative magnitude at high inlet mass fluxes, but are believed to be the cause for deviation from the linear relationship between corrected air mass flux and blockage fraction at low air mass fluxes that fall below the universally choked regime. The results of Matsuoka *et al.* clearly show the presence of burned gas within the air inlet for greater than 5% of a representative cycle [28], which serves to support the conclusion of a local sonic condition due to the presence of this backflow as demonstrated in Figure 3.46.

Similar observations and determinations can also be made when analyzing behaviors in the fuel supply system. Although direct cold flow measurements are not available for the fuel system, the discharge coefficient of the fuel injection system was determined with similar cold flows with helium as a hydrogen analog. From this, similar theoretical curves as shown with the red lines of Figure 3.31 were generated for the fuel system, and the blockage fraction at the fuel inlet (B_{fuel}) was calculated per Equation 3.9. From this, a similar analysis using Equations 3.15 and 3.16 with the "f" state replacing station 3 was conducted. The results from these analyses are shown in Figures 3.47 and 3.48.

The results of Figures 3.47 and 3.48 for the fuel supply system are consistent with those of the air supply system shown in Figures 3.15 and 3.16, respectively. One key difference that can be noted is that the blockage observed at the fuel inlet reaches values approaching 0.7, which is significantly higher than the peak values of approximately 0.5 observed at the air inlet. This variance is due to the relative scaling between the two supply systems, and will be briefly analyzed for these and other RDE configurations from literature in a later section.

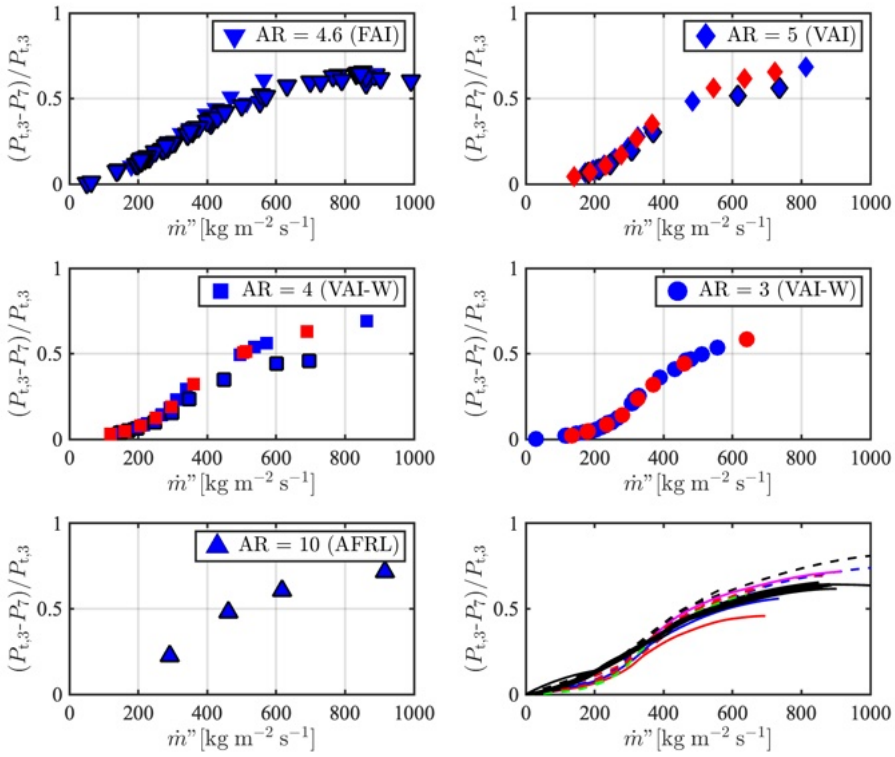

Figure 3.4: Static channel exit to plenum pressure as function of air mass flux for all RDE configurations under analysis. Spline curve fits for all configurations overlaid in bottom right.

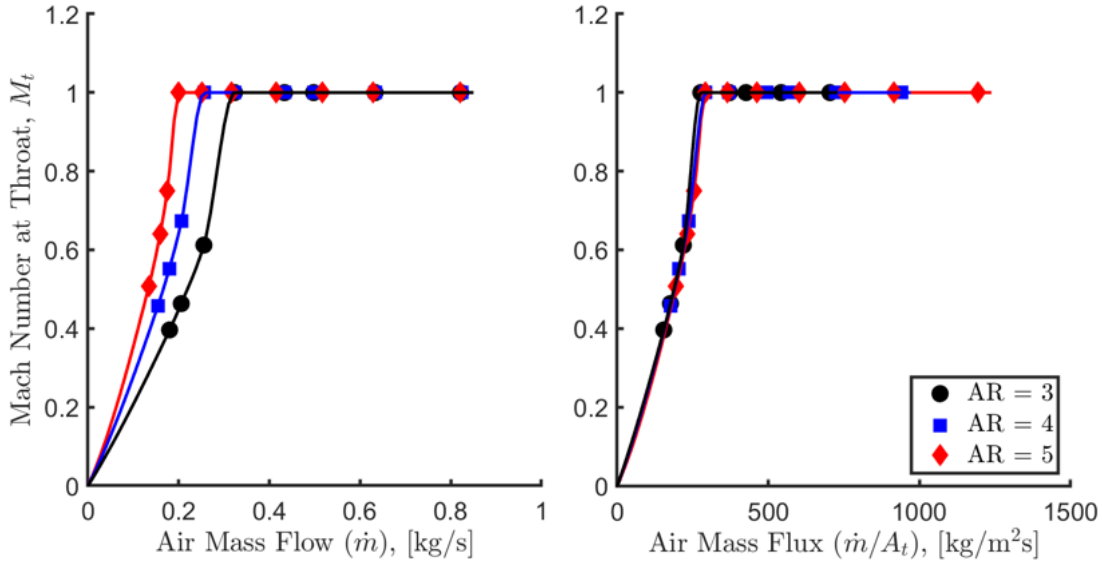

Figure 3.5: Mach Number at the air inlet throat as function of air mass flow (left) and air mass flux (right) for VAI configuration.

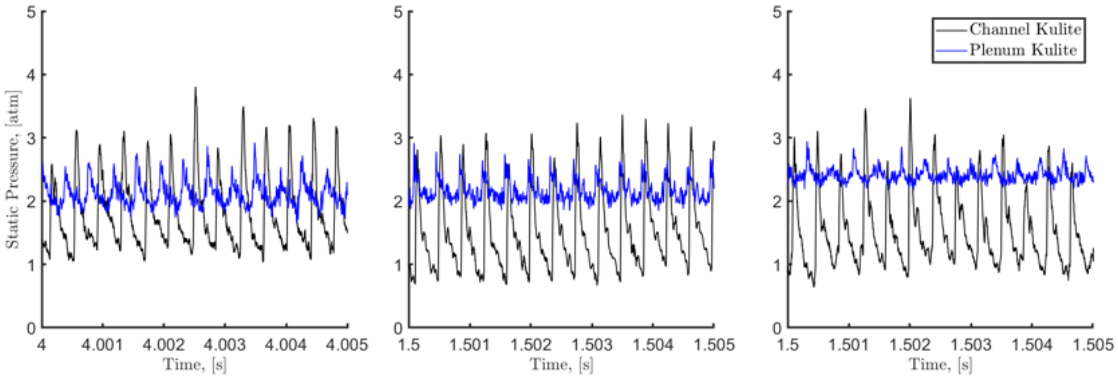

Figure 3.6: Sample high-speed pressure data time traces for AR = 3 (left), AR = 4 (middle), AR = 5 (right). Air mass flows in the range 380-430 g/s, and equivalence ratios in the range 0.61-0.73.

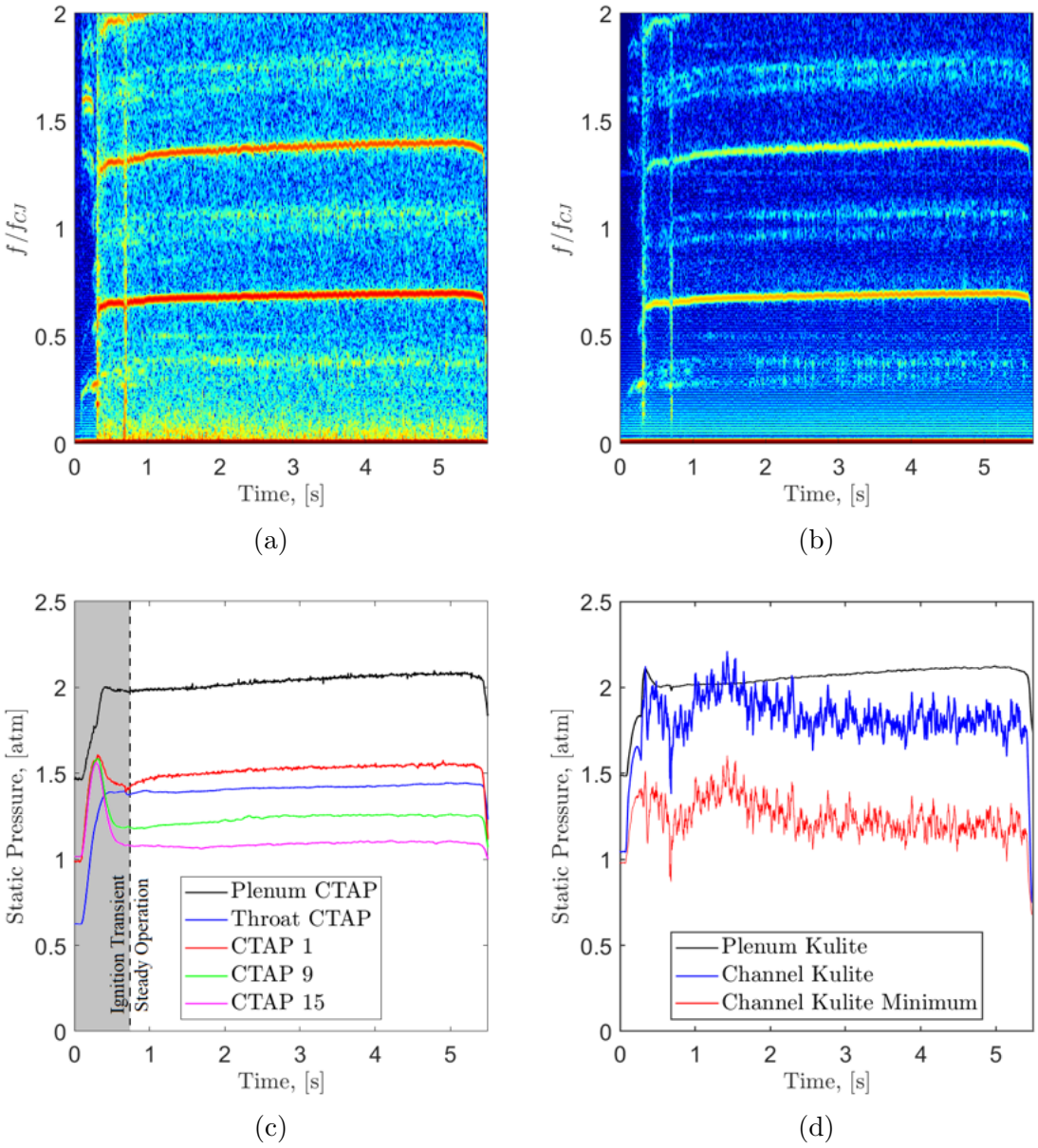

Figure 3.7: Waterfall spectra computed from channel (top left) and plenum (top right) pressure sensors, subset of raw low-speed (bottom left) and moving average high-speed (bottom right) pressure data. AR = 3, air mass flow = 430 g/s, $\phi = 0.61$.

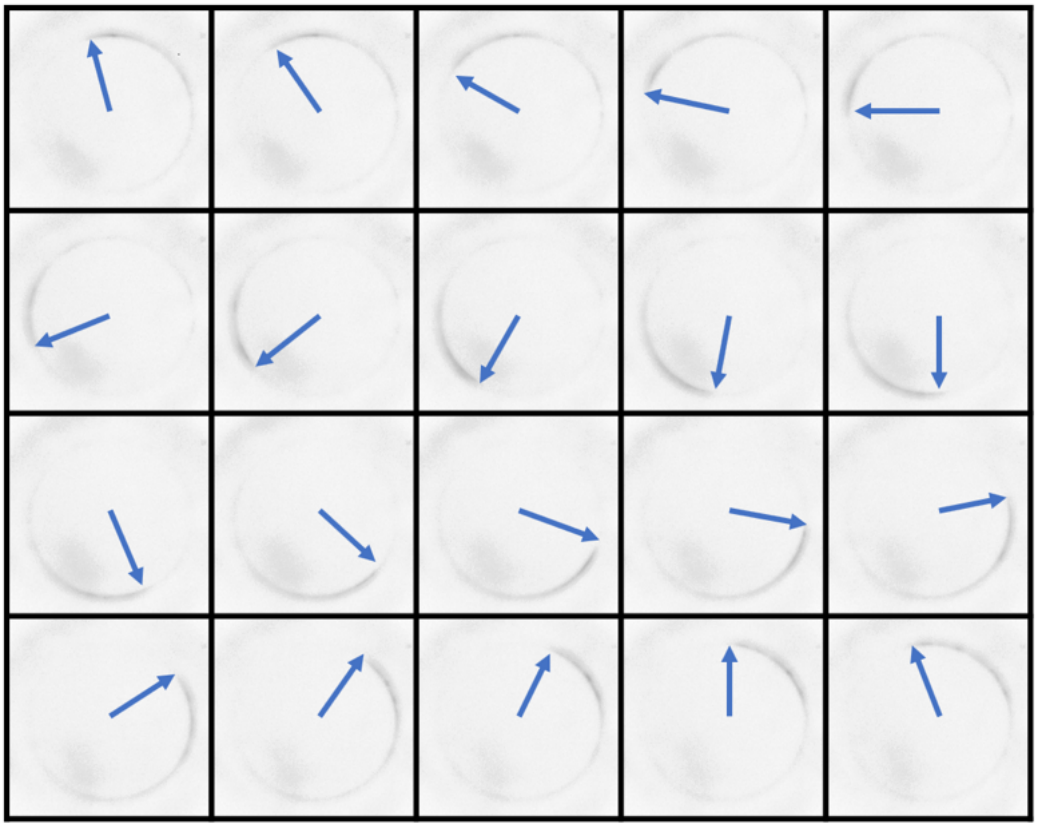

Figure 3.8: Sequence of twenty sequential frames showing observed chemiluminescence during rotational operating mode with leading edge of continuously propagating wave identified with arrows. This case represents Run 2830. Video obtained with Phantom v711 camera at 55k fps with an exposure time of 17.8 μs.

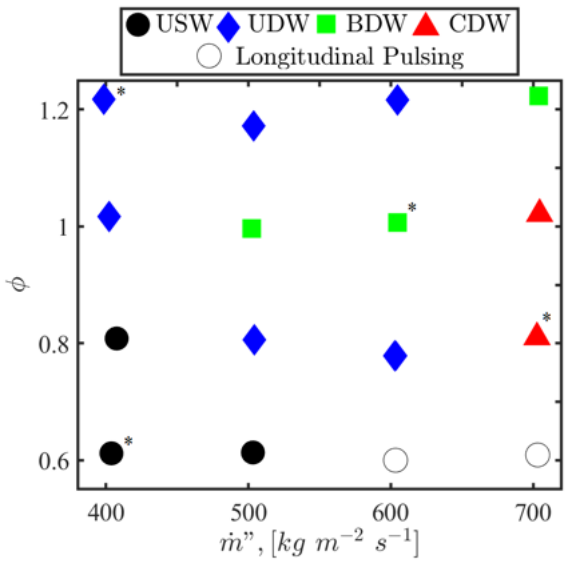

Figure 3.9: Summary of operating conditions considered and identified modes of operation in VAI-W configuration. Examples used in later analysis are identified with an asterisk.

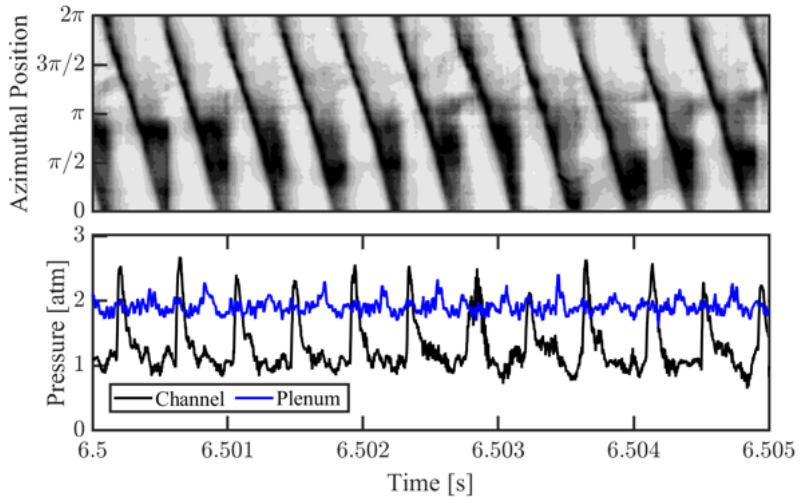

Figure 3.10: Example (top) $x - t$ diagram and (bottom) pressure time-history illustrating steady single-wave operation. Test condition $\dot{m}'' = 400$ kg m^{-2} s^{-1}, $\phi = 0.6$.

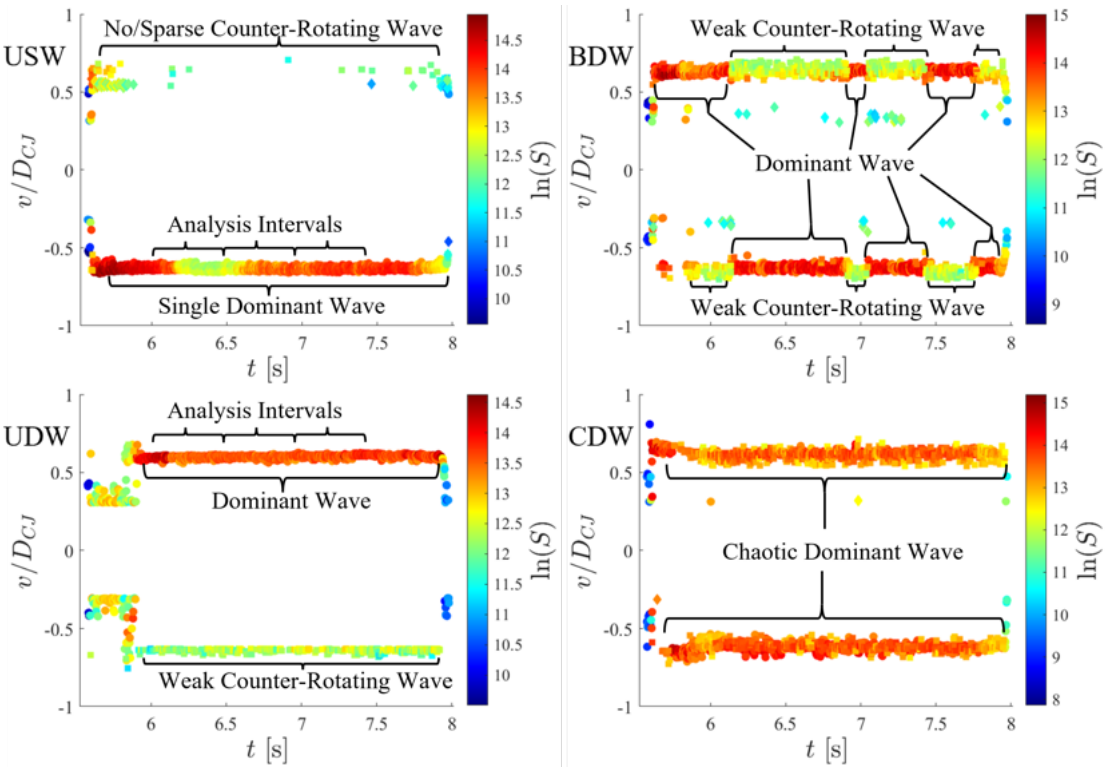

Figure 3.11: Time-history of wave properties evaluated with CWA demonstrating the four modes of rotational operation identified for analysis, starred cases of Figure 3.9: (top, left) USW; (bottom, left) UDW; (top, right) BDW; and (bottom, right) CDW.

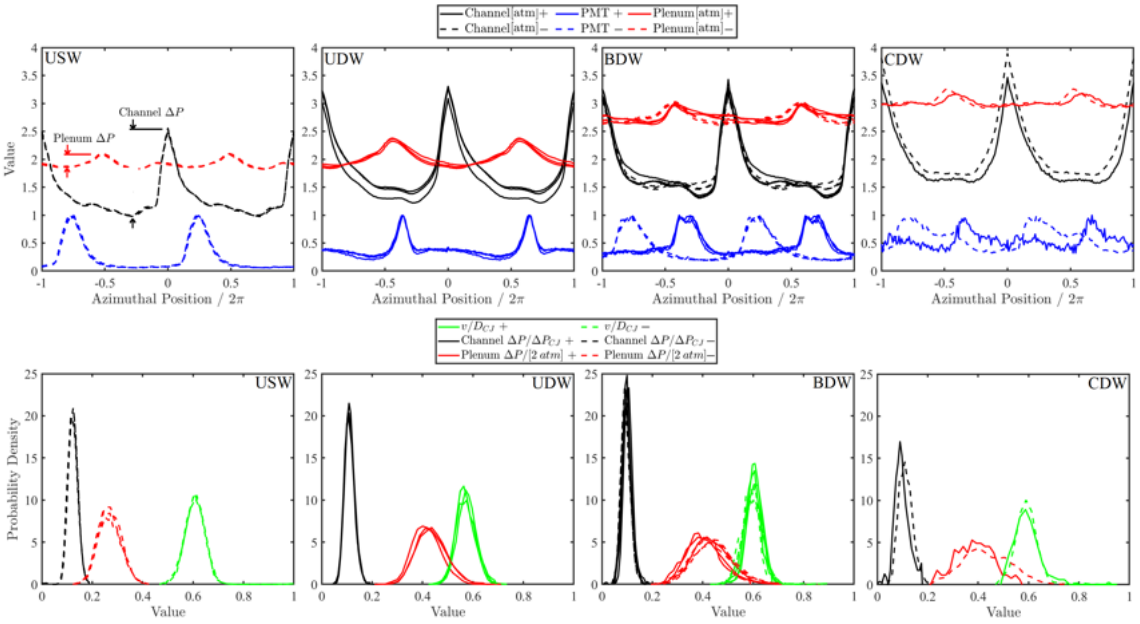

Figure 3.12: Phase-average pressure and PMT profiles (Top) and PDFs of measurable quantities (Bottom) during identified modes of operation. Cases of Figures 3.9 and 3.11 from left-to-right: USW, UDW, BDW, CDW. Solid (dash) lines indicate wave rotating in the clock-wise (counter-clock-wise) direction.

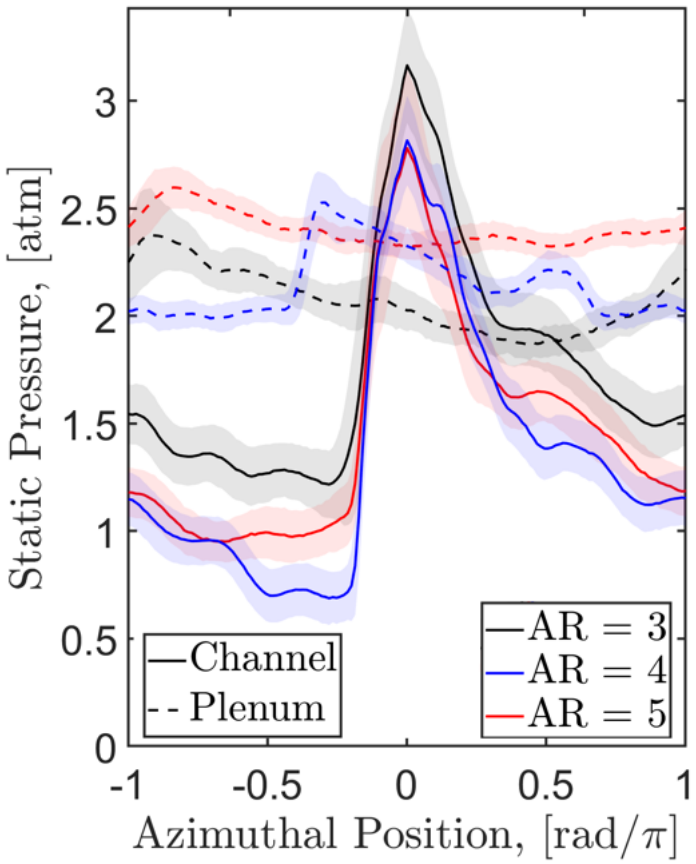

Figure 3.13: Examples of phase-averaged pressure profiles within the channel and plenum. Test conditions: AR = 3, $\dot{m}$ = 430 g/s, ϕ = 0.61; AR = 4, $\dot{m}$ = 405 g/s, ϕ = 0.73; AR = 5, $\dot{m}$ = 380 g/s, ϕ = 0.62. All tests conducted in VAI configuration with no exhaust restriction.

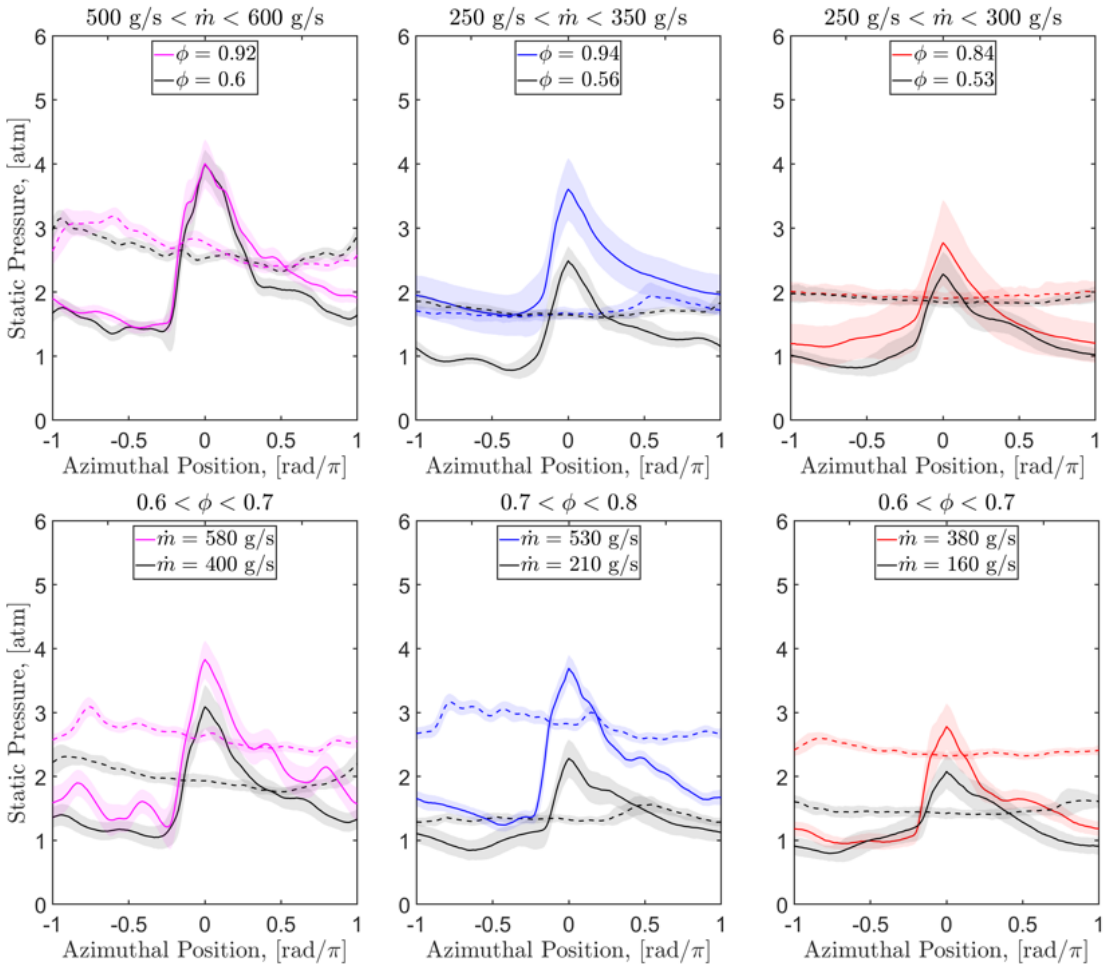

Figure 3.14: Phase-averaged channel and plenum pressure profiles for AR = 3 (left), AR = 4 (middle), and AR = 5 (right) configurations at varying ϕ (top) and $\dot{m}$. All tests conducted in VAI configuration with no exhaust restriction.

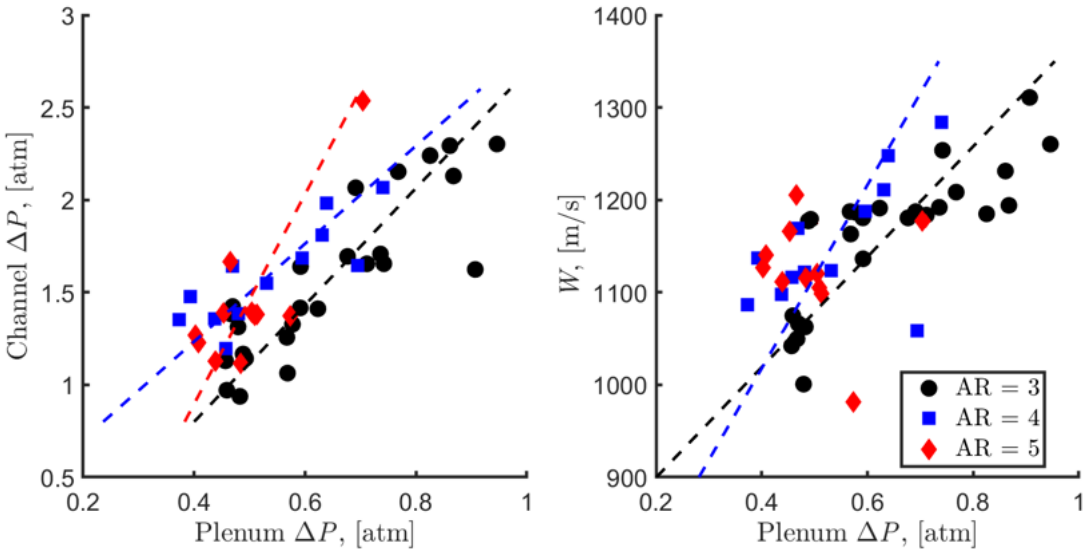

Figure 3.15: Relationship between plenum ΔP and channel ΔP (left) and wave speed W (right) for tests conducted in VAI configuration with no exhaust restriction.

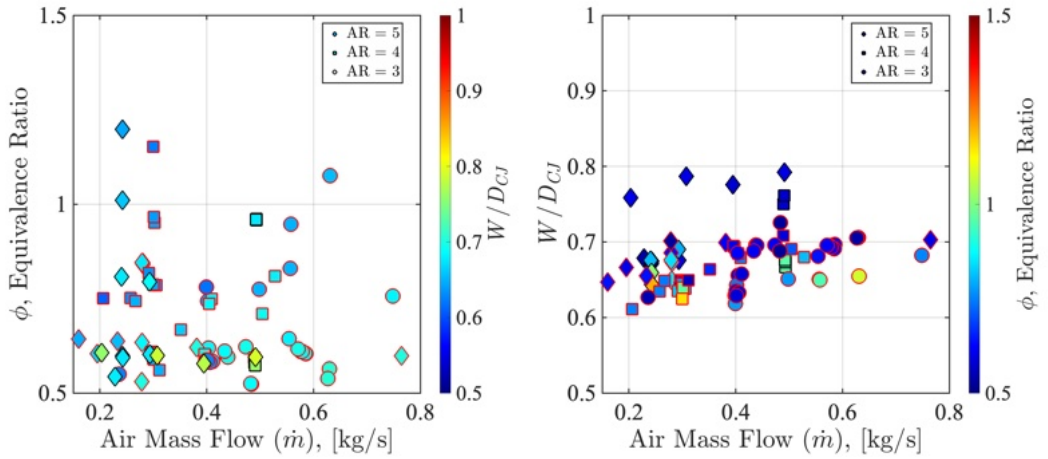

Figure 3.16: Operating map showing all successful air mass flow/equivalence ratio test points (left) and measured wave speed relative to that of the corresponding ideal Chapman-Jouguet detonation (right) in the VAI configuration. Red outlines indicate tests conducted without a nozzle restriction ($A_8/A_{3.1} = 1$), black outlines indicate tests conducted with a 50% nozzle restriction ($A_8/A_{3.2} = 0.5$).

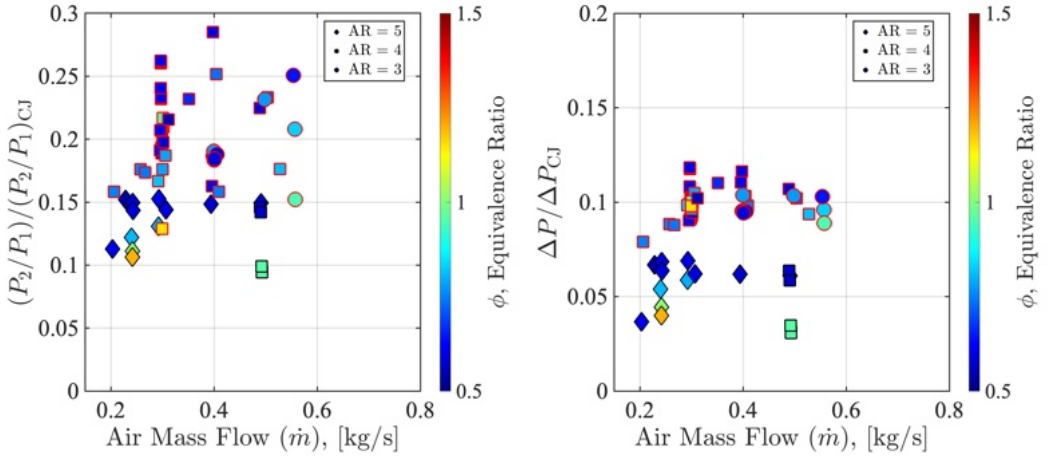

Figure 3.17: Operating map showing pressure ratio (left) and pressure rise ratio (right) relative to those of corresponding ideal Chapman-Jouguet detonations for tests conducted in the VAI configuration. Red outlines indicate tests conducted without a nozzle restriction ($A_8/A_{3.1} = 1$), black outlines indicate tests conducted with a 50% nozzle restriction ($A_8/A_{3.2} = 0.5$).

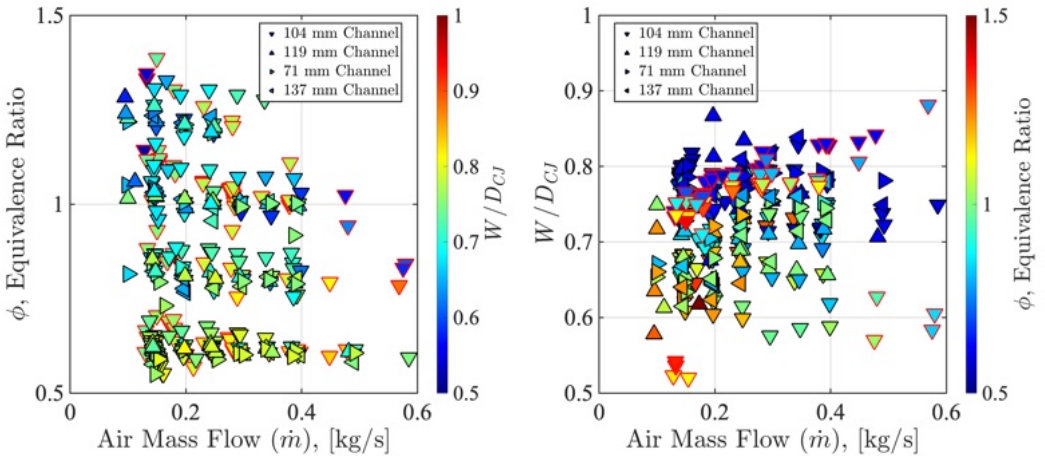

Figure 3.18: Operating map showing all successful air mass flow/equivalence ratio test points (left) and measured wave speed relative to that of the corresponding ideal Chapman-Jouguet detonation (right) in the FAI configuration. Red outlines indicate tests conducted without a nozzle restriction ($A_8/A_{3.1} = 1$), black outlines indicate tests conducted with a 50% nozzle restriction ($A_8/A_{3.2} = 0.5$).

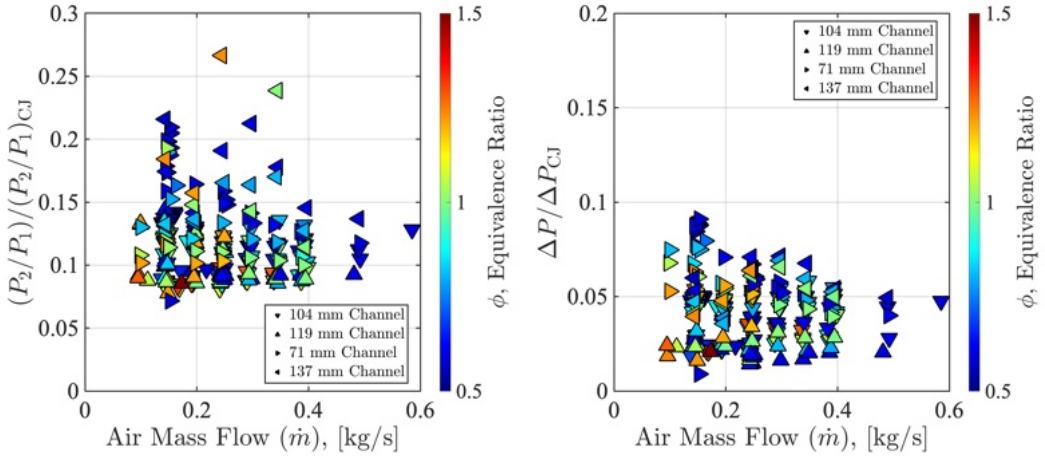

Figure 3.19: Operating map showing pressure ratio (left) and pressure rise ratio (right) relative to those of corresponding ideal Chapman-Jouguet detonations for tests conducted in the FAI configuration. Red outlines indicate tests conducted without a nozzle restriction ($A_8/A_{3.1} = 1$), black outlines indicate tests conducted with a 50% nozzle restriction ($A_8/A_{3.2} = 0.5$).

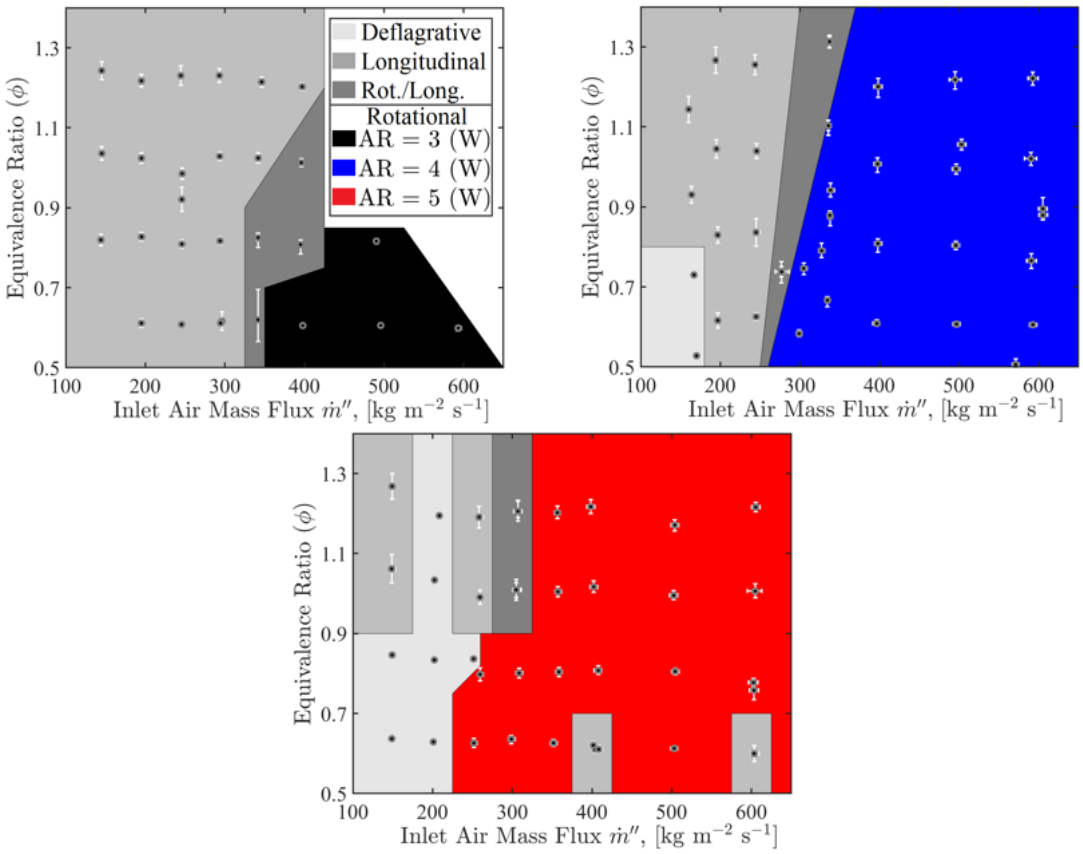

Figure 3.20: Range of conditions tested for VAI-W configuration and regions demonstrating modes of operation. AR = 3 (top left); AR = 4 (top right); AR = 5 (bottom). Error bars indicate 90% of observations/samples during steady operation.

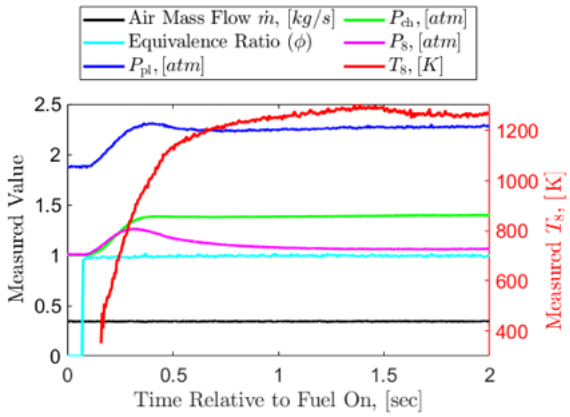

Figure 3.21: Representative sample of data collected for each test case. Test conditions: AR = 5, $\dot{m}'' = 500$ kg m^{-2} s^{-1}, $\phi = 1.0$.

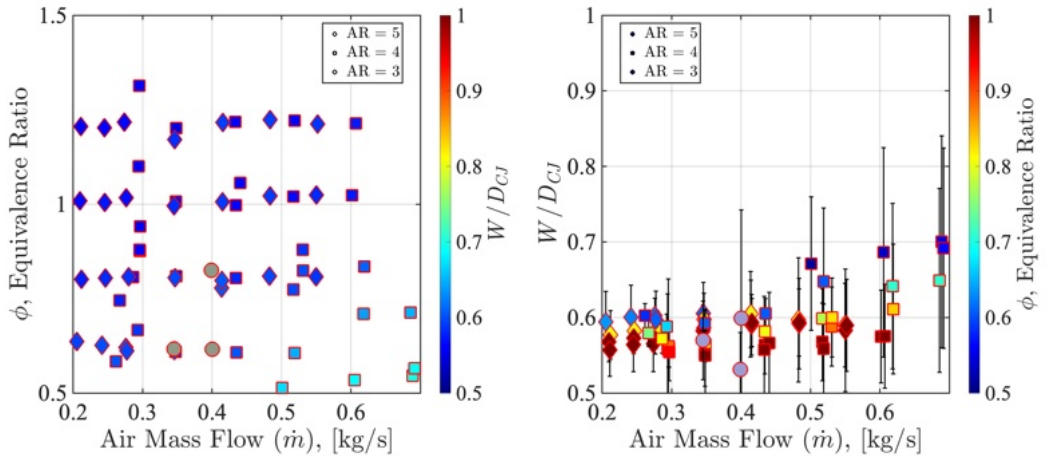

Figure 3.22: Operating map showing all successful air mass flow/equivalence ratio test points (left) and measured wave speed relative to that of the corresponding ideal Chapman-Jouguet detonation (right) in the VAI-W configuration. All tests conducted with a nozzle restriction that corresponds to the same geometric area as that of the VAI configuration with no exhaust nozzle restriction ($A_8/A_{3.2} = 1$ where $A_{3.2}$ is as-defined by Figure 7.8).

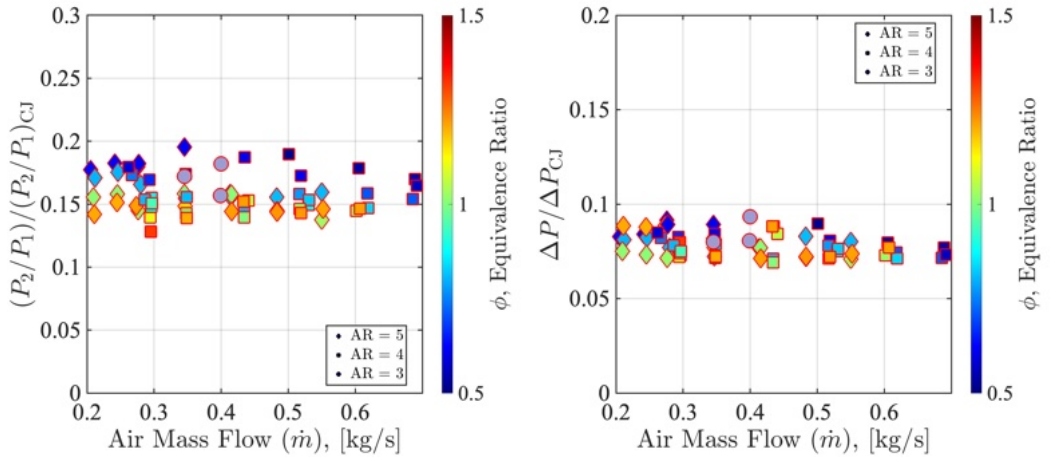

Figure 3.23: Operating map showing pressure ratio (left) and pressure rise ratio (right) relative to those of corresponding ideal Chapman-Jouguet detonations for tests conducted in the VAI-W configuration. All tests conducted with a nozzle restriction that corresponds to the same geometric area as that of the VAI configuration with no exhaust nozzle restriction ($A_8/A_{3.2} = 1$ where $A_{3.2}$ is as-defined by Figure 7.8).

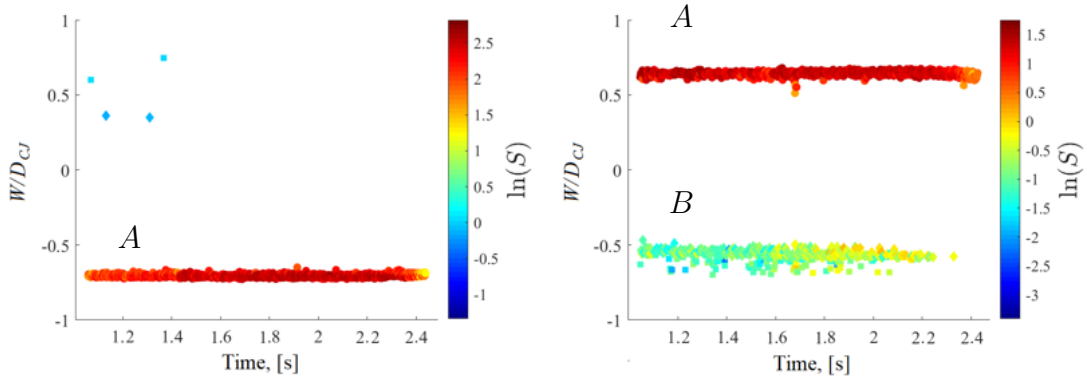

Figure 3.24: Results from Circuit Wave Analysis for two cases. Air mass flow = 380 g/s, $\phi = 0.62$ (left), air mass flow = 160 g/s, $\phi = 0.64$ (right). Labels A and B indicate primary detonation wave and secondary wave, respectively.

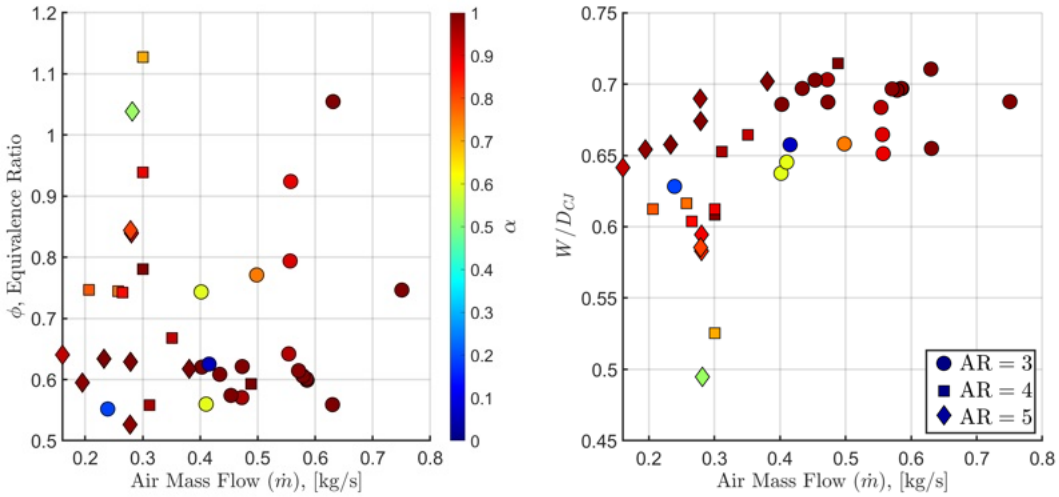

Figure 3.25: Relative wave quality α across all operating conditions (left) and as compared to W/D_{CJ} performance metric (right).

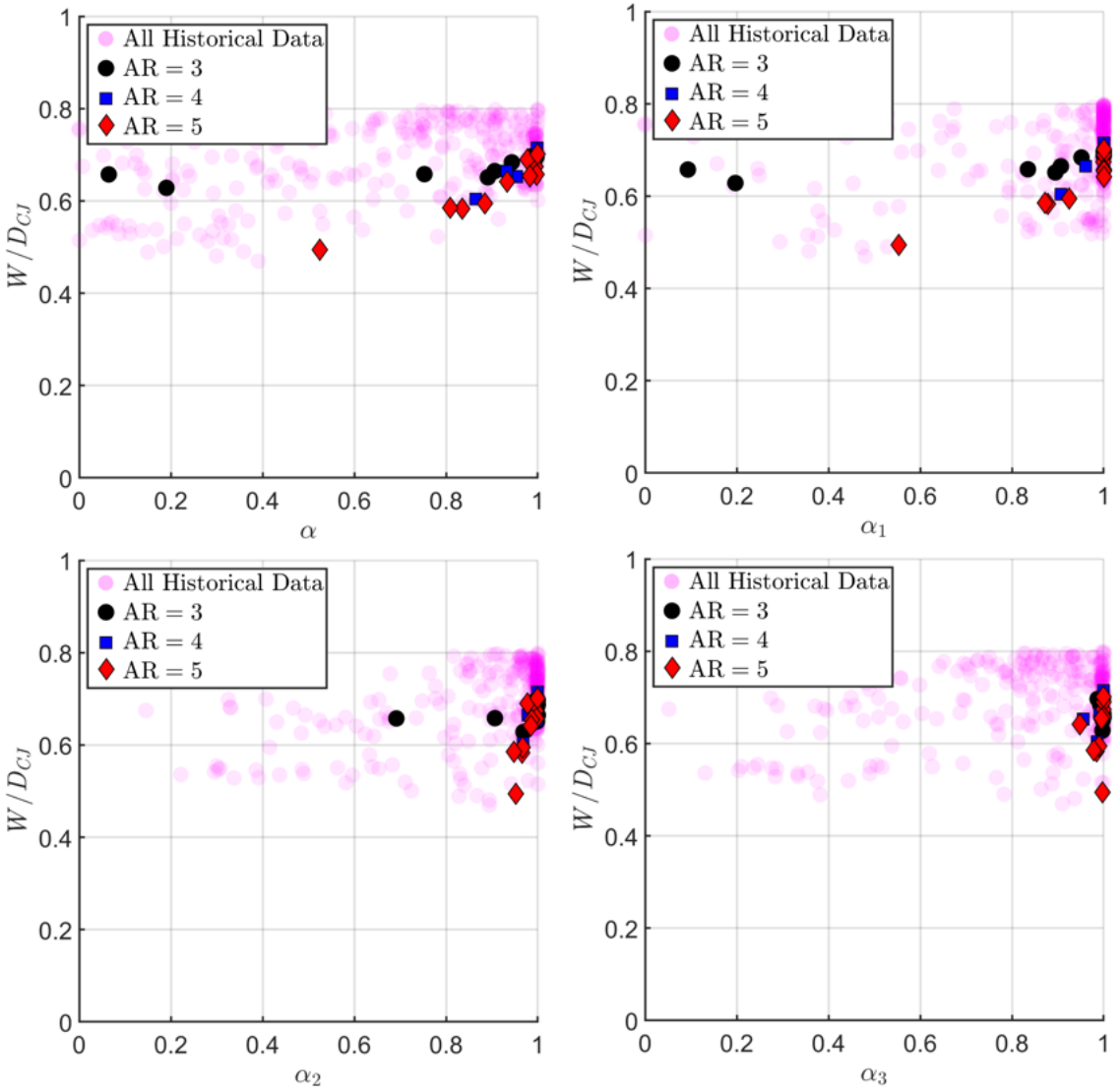

Figure 3.26: Comparison of relative wave quality (α) and individual components (α_1, α_2 and α_3) as a function of wave speed ratio W/D_{CJ} for VAI configuration as compared against historical data from FAI configuration.

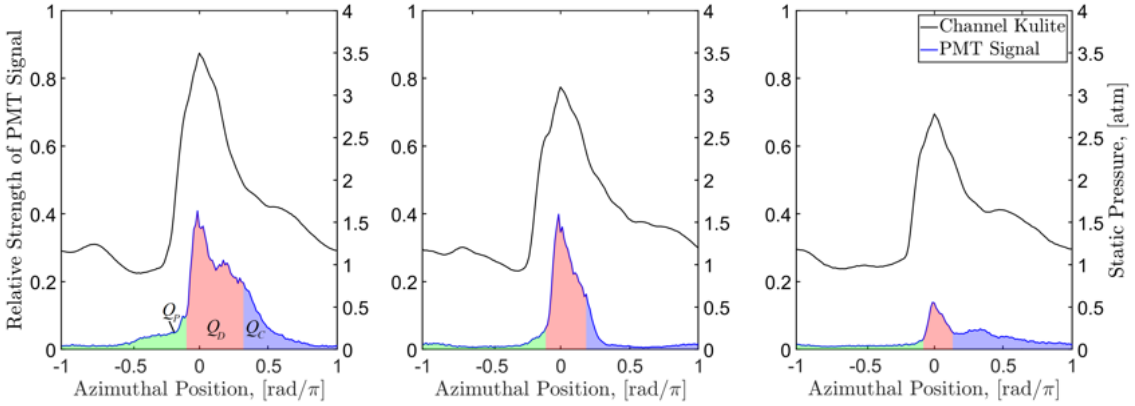

Figure 3.27: Representative 100-cycle phase-average channel pressure and PMT signal profiles for AR = 3 (left), AR = 4 (middle), and AR = 5 (right) in the VAI configuration with no exhaust restriction.

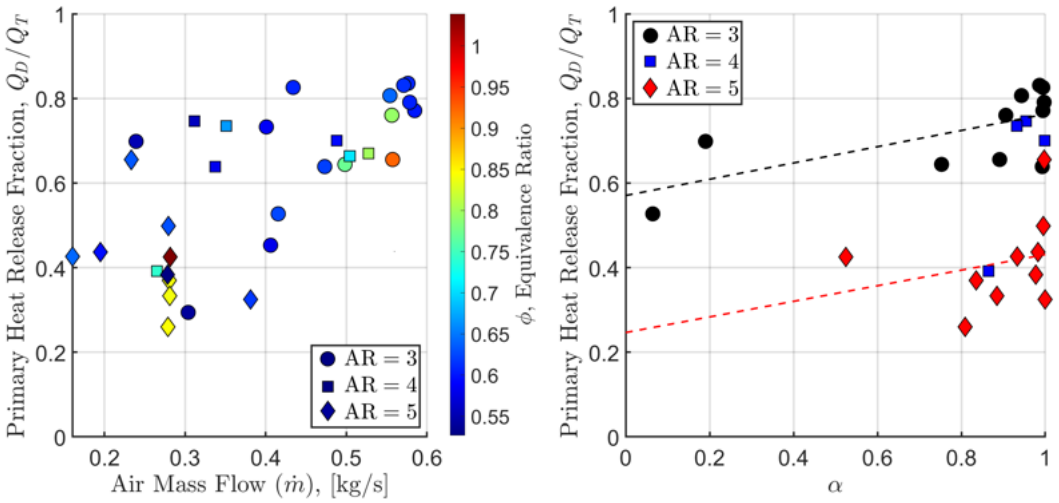

Figure 3.28: Calculated Q_D/Q_T for test cases conducted in the VAI configuration with PMT installed (left) and comparison of Q_D/Q_T with the relative wave quality metric (α) based upon results generated through the CWA methodology (right).

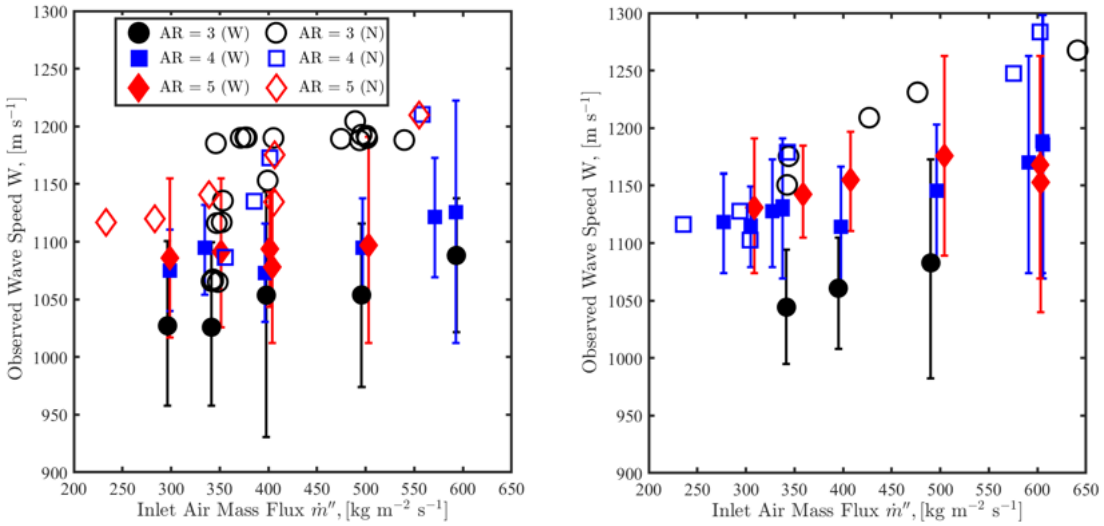

Figure 3.29: Comparison of wave speed between narrow (N) and wide (W) detonation channel operation for test cases conducted at (a) $\phi = 0.6$ and (b) $\phi = 0.8$. Lower wave speeds are observed for the wider channel.

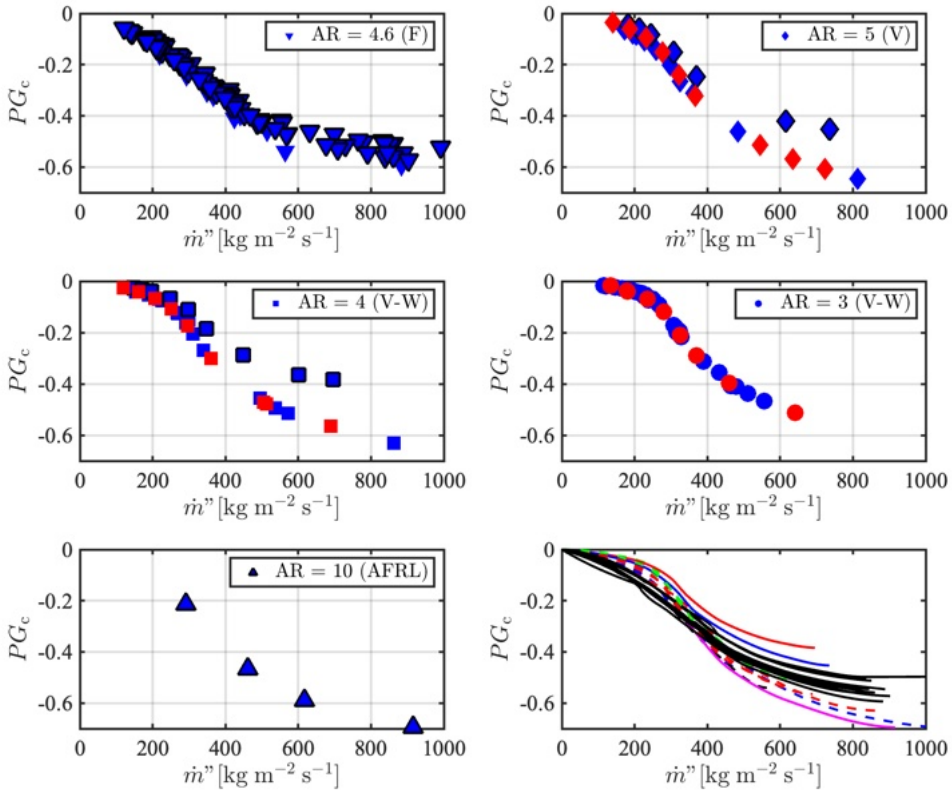

Figure 3.30: Cold flow equivalent Pressure Gain (PG_c) for each RDE configuration. Blue markers indicate 7.6 mm channel, red markers indicate 15.2 mm channel of VAI-W configuration. Outlined markers indicate 50% exhaust restriction installed. Bottom-right plot shows all curves.

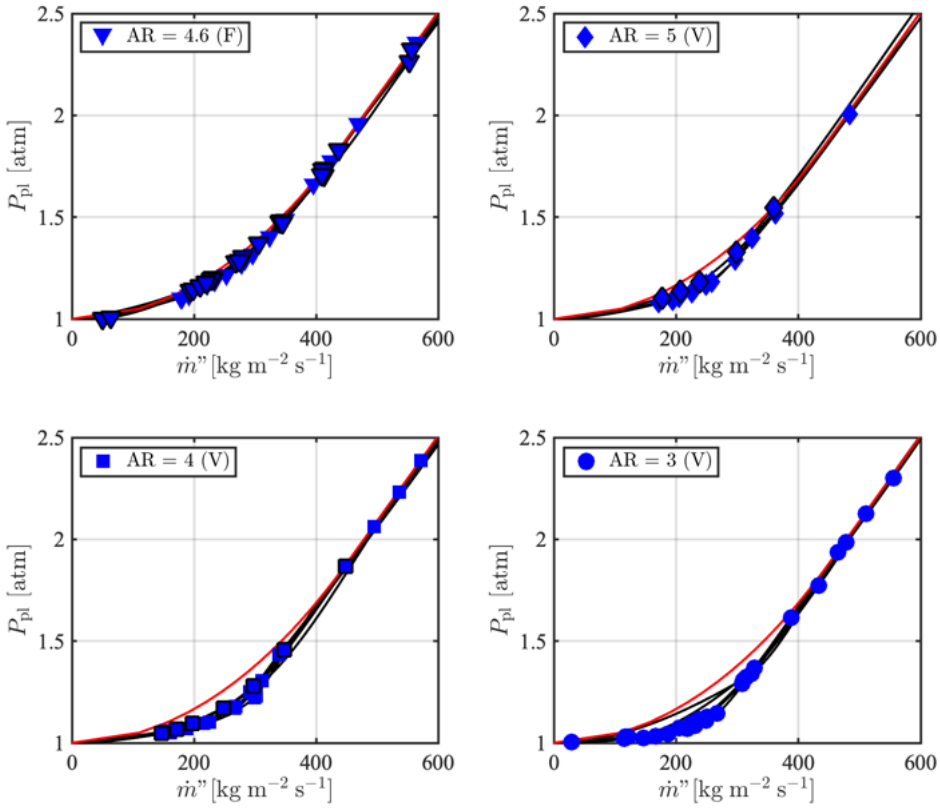

Figure 3.31: Measured plenum pressures during non-reacting flows (markers), curve fits to experimental data (black lines), and theoretical curves based upon choked and partially choked equations (red lines).

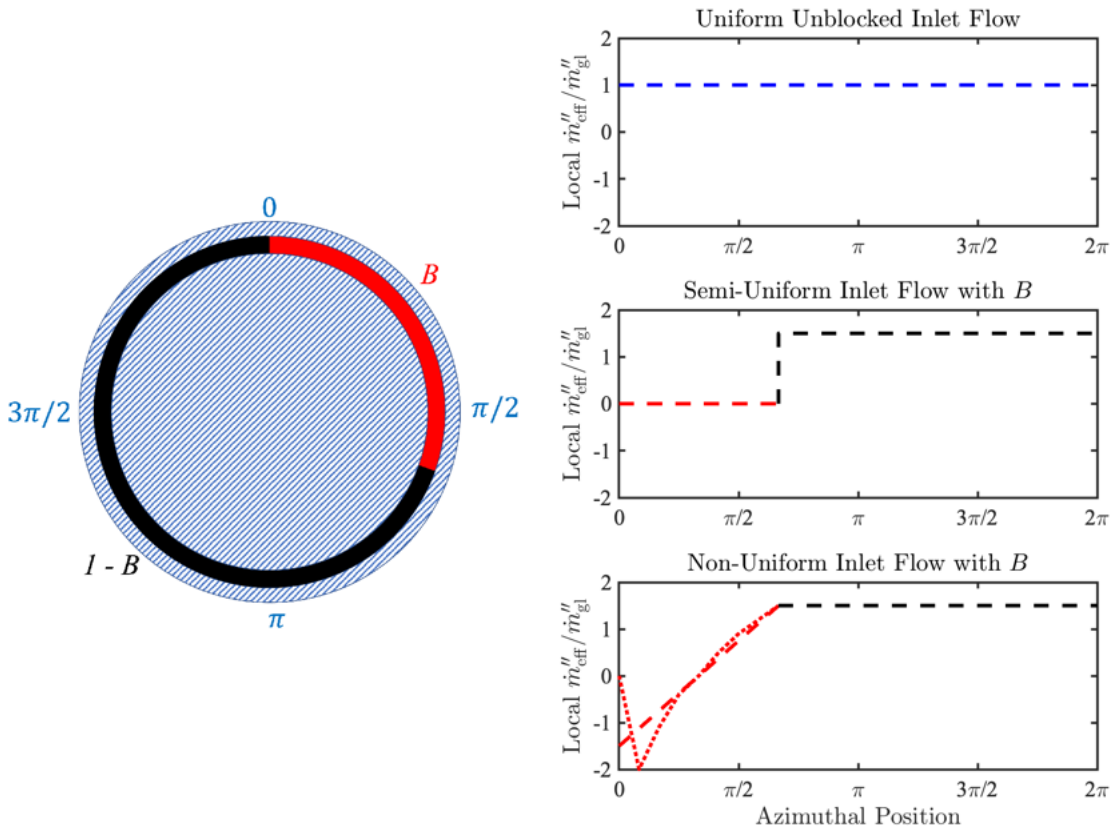

Figure 3.32: Simplified representation of RDE inlet with blocked (red) and unblocked (black) regions shown at left. Three unwrapped air mass flux profiles included for reference at right: uniform unblocked flow (top), semi-uniform flow with blockage (middle), non-uniform flow in blocked region (bottom).

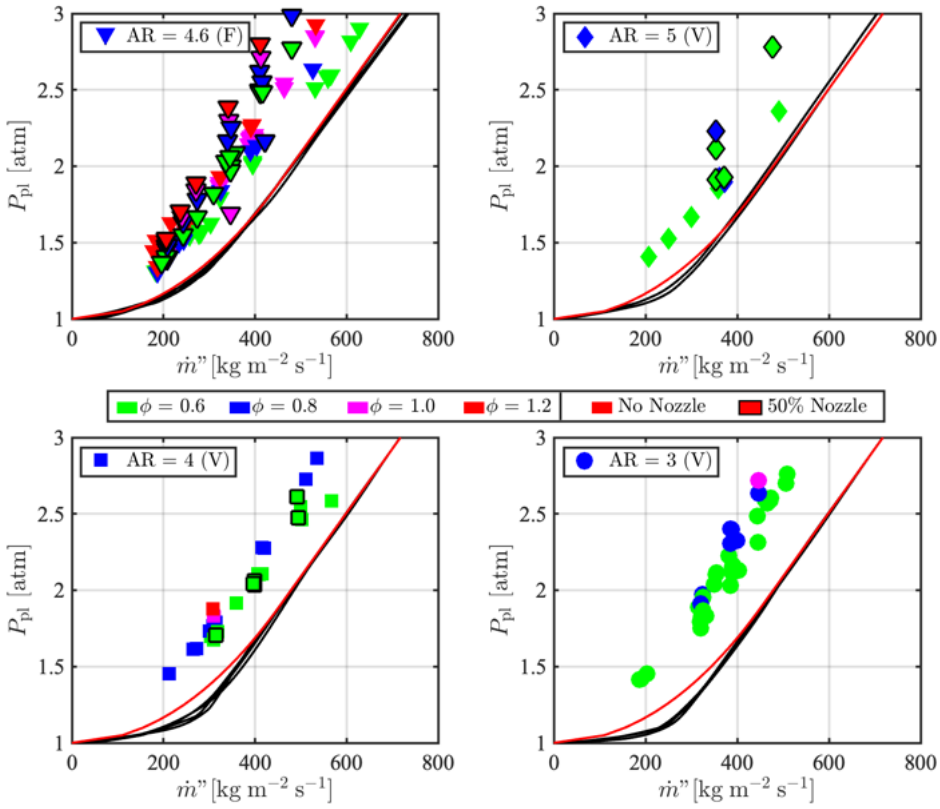

Figure 3.33: Measured plenum pressures during reacting flows (markers) with curve fits to experimental data obtained from non-reacting flows used to determine B (black lines).

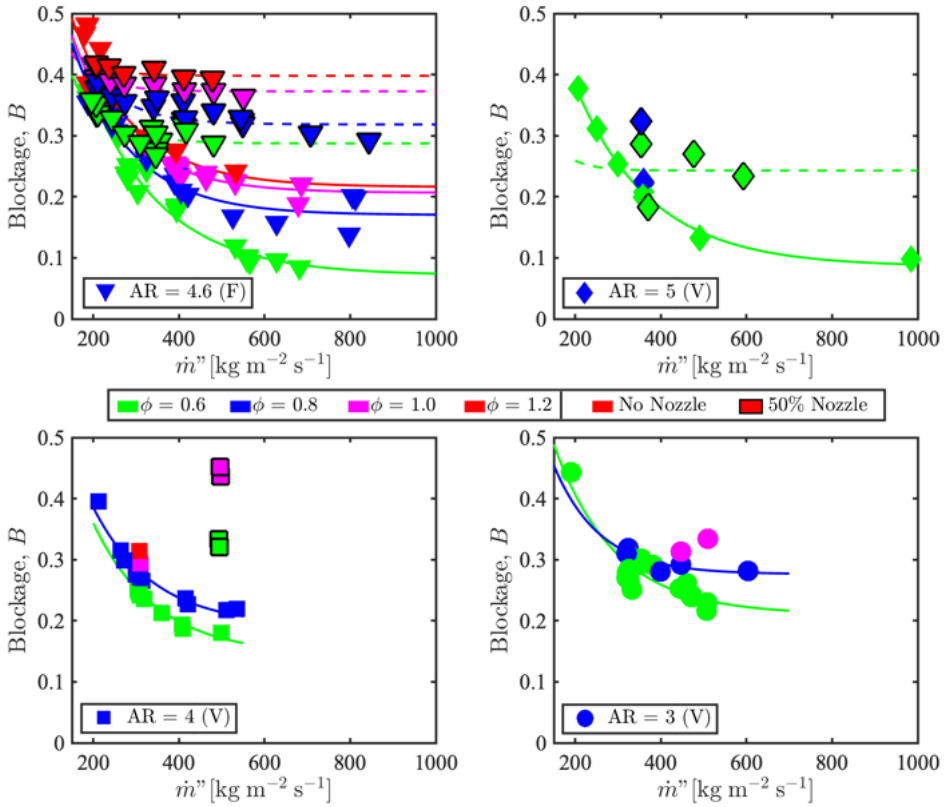

Figure 3.34: Blockage fraction B as a function of inlet air mass flux. Dashed lines indicate fits to configurations with 50% restriction exhaust nozzle, solid lines to configurations with no exhaust restriction.

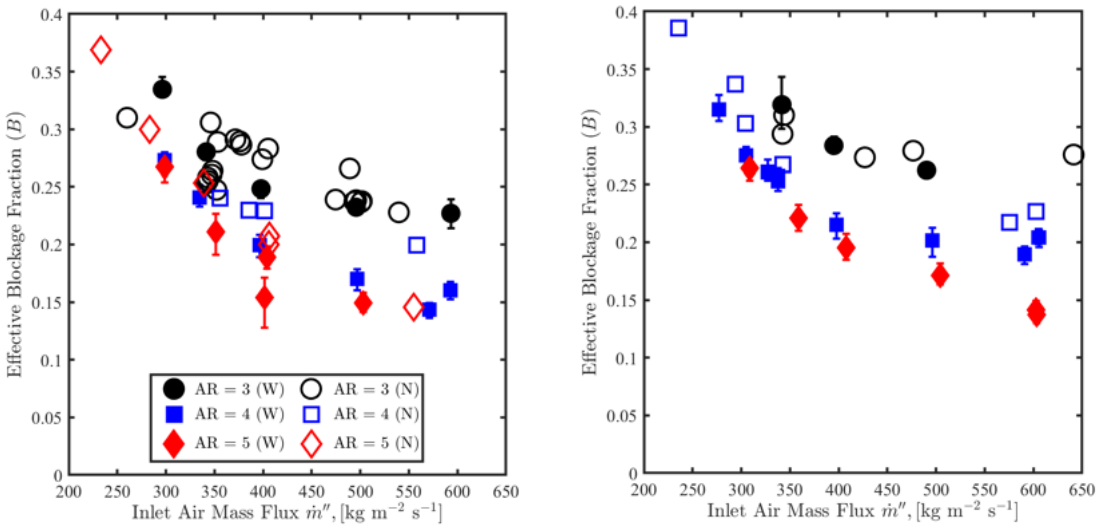

Figure 3.35: Calculated blockage fraction for test cases conducted at (a) $\phi = 0.6$ and (b) $\phi = 0.8$ in the VAI and VAI-W configurations. Similar behavior between wide and narrow configurations with only minor variations observed.

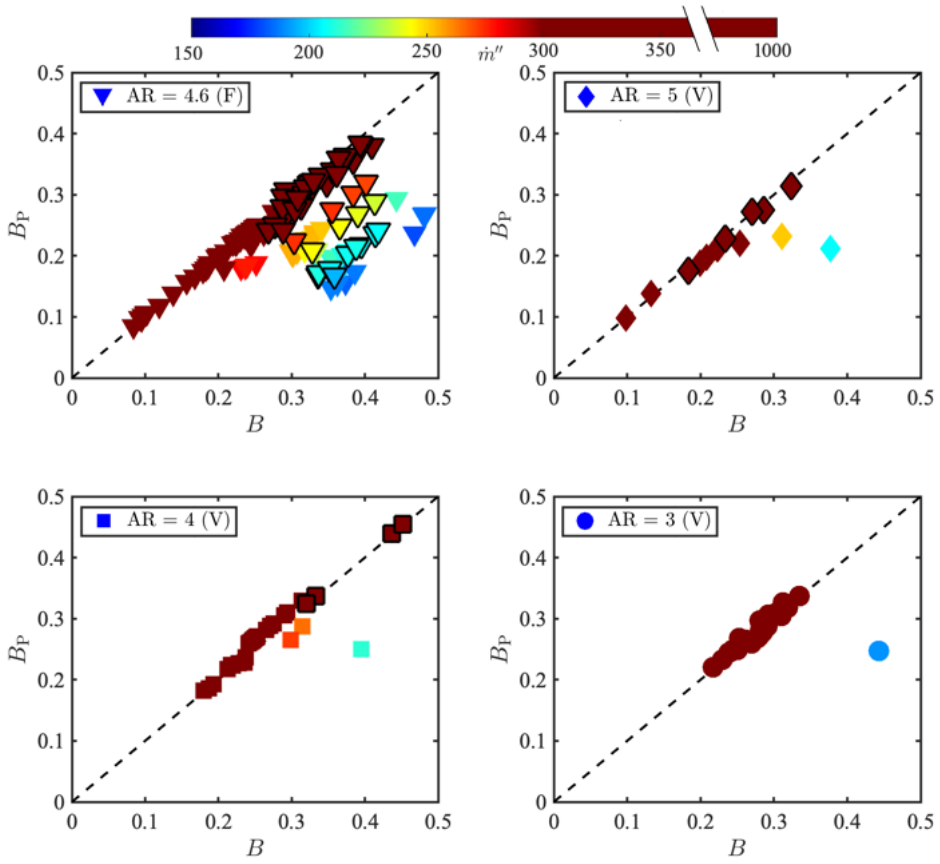

Figure 3.36: Comparison of blockage fraction when controlling by $\dot{m}''$ (x-axis) per Equation (3.9) as defined to be B or P_3 (y-axis) per Equation (3.11) of Deng *et al.* as defined to be B_P [30].

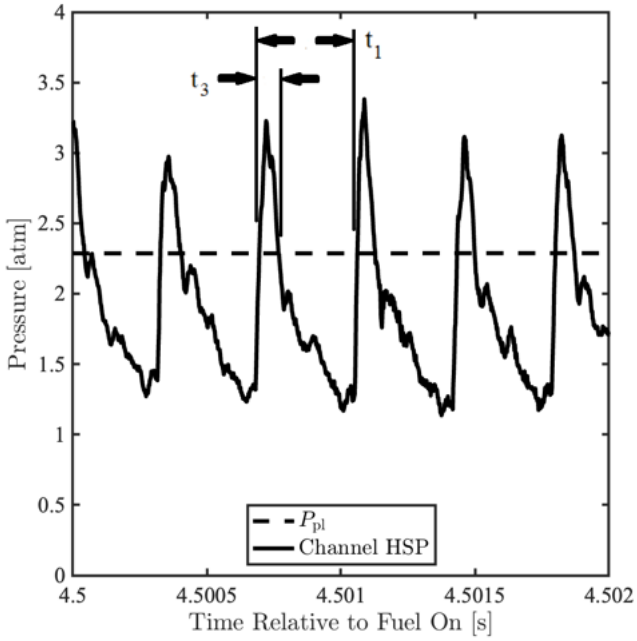

Figure 3.37: Example illustrating the definition of t_1 and t_3. Test conditions: $\dot{m}'' = 470$ kg m^{-2} s^{-1}, $\phi = 0.75$, AR $= 4$, constant area channel.

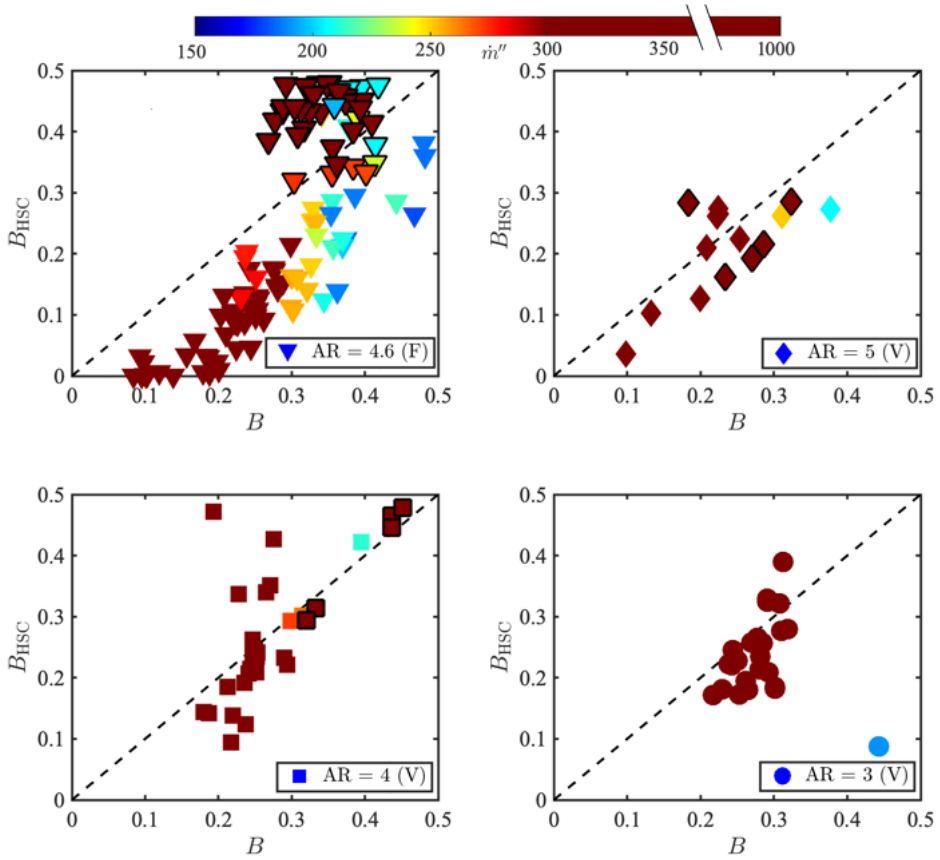

Figure 3.38: Comparison between B and B_{HSC}.

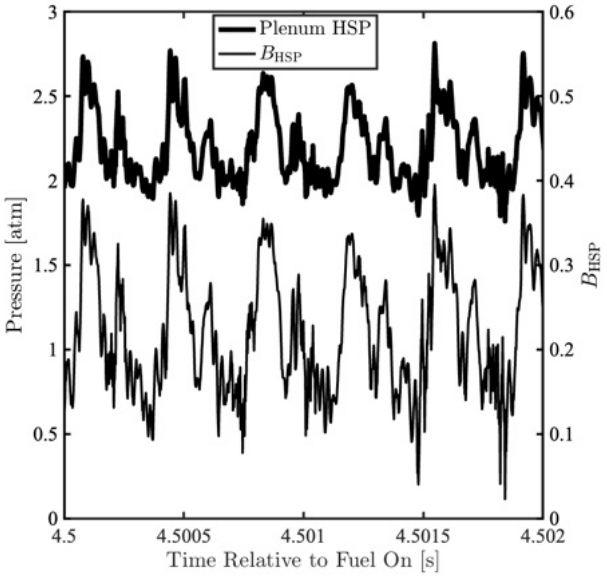

Figure 3.39: Example illustrating variation in B_{HSP}. Test conditions: $\dot{m}'' = 470$ kg m^{-2} s^{-1}, $\phi = 0.75$, Variable inlet with AR = 4, no exhaust restriction.

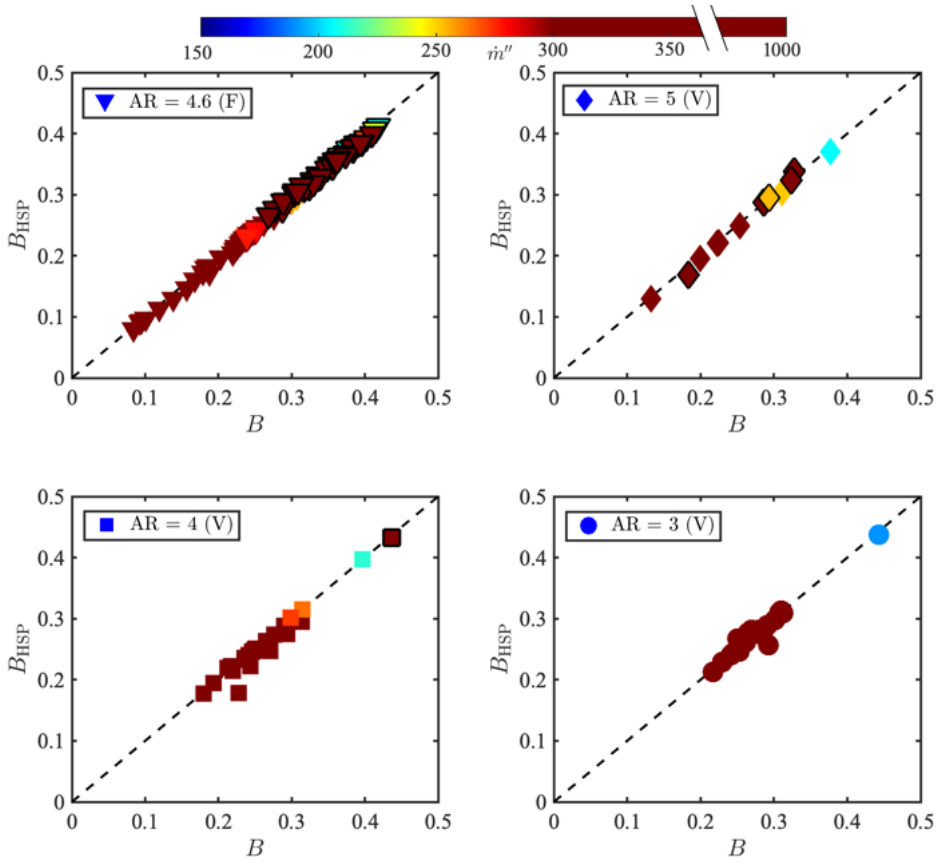

Figure 3.40: Comparison between B and B_{HSP}.

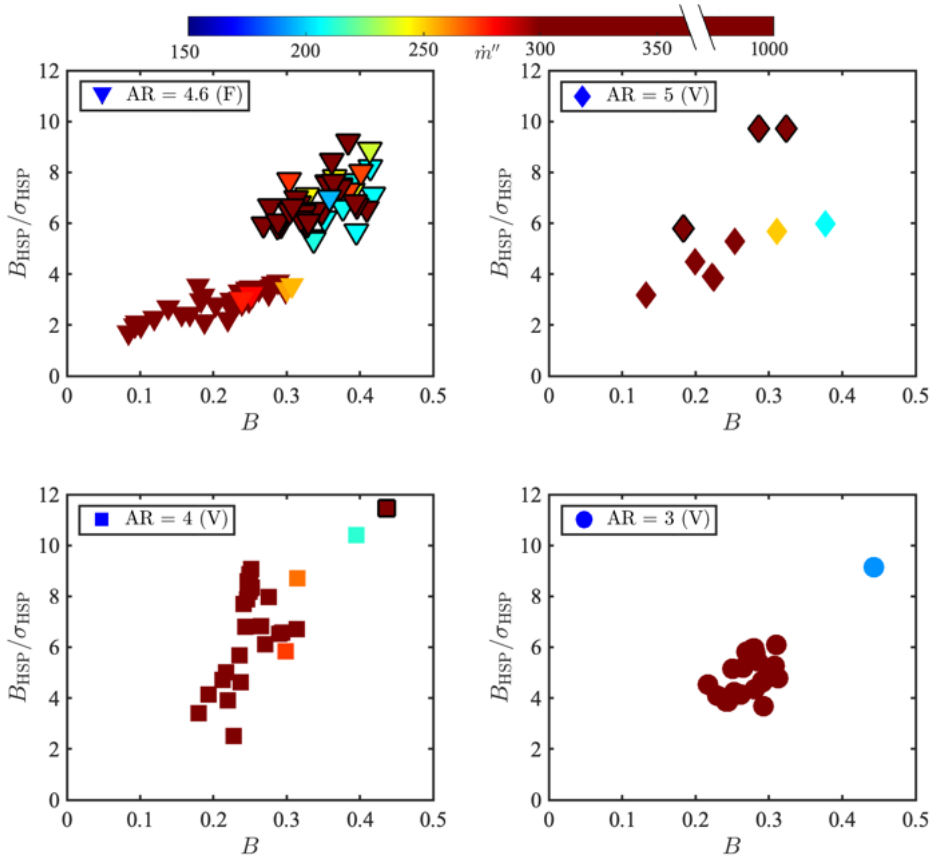

Figure 3.41: Ratio between B_{HSP} and σ_{HSP} as a function of B for all test cases.

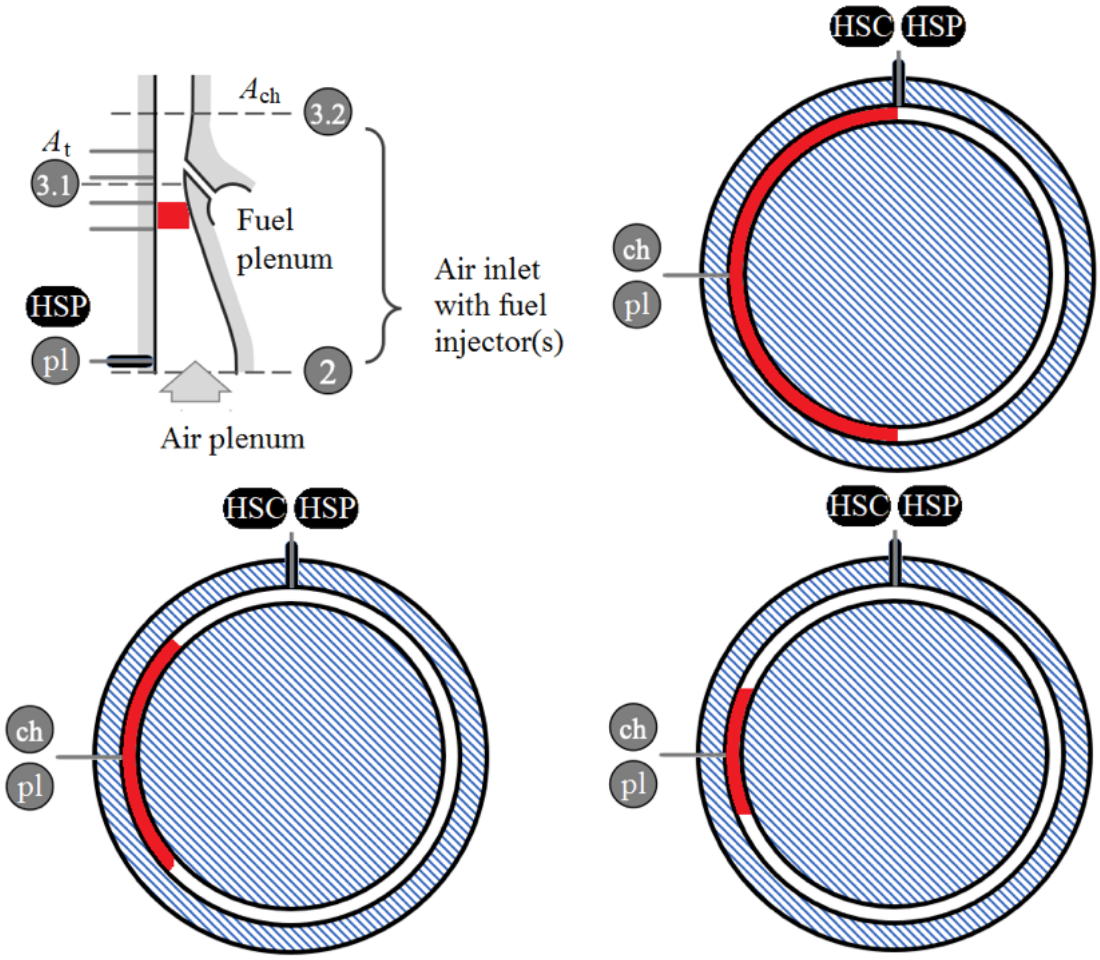

Figure 3.42: Schematic diagram showing the placement of physical inlet blockage, which was placed in-line or diametrically opposite to plenum CTAP.

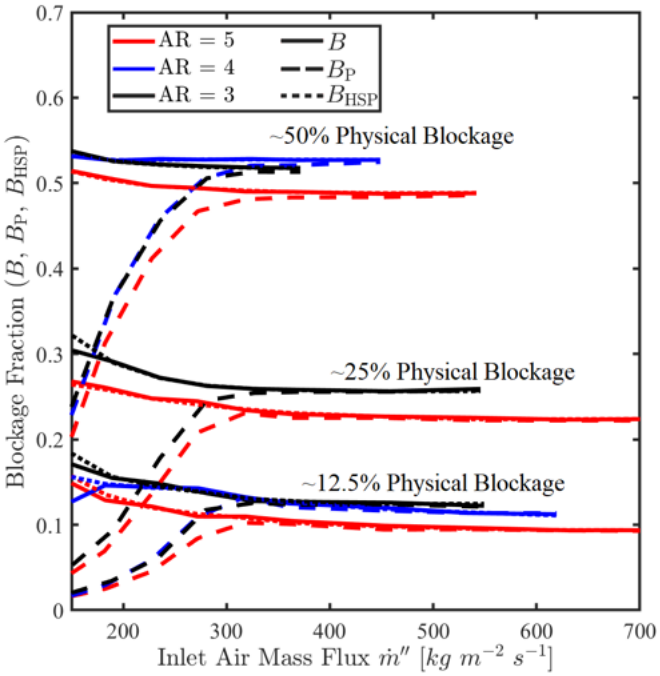

Figure 3.43: Calculated blockage from cold flow tests with physically blocked inlet using the B, B_P, and B_{HSP} methodologies.

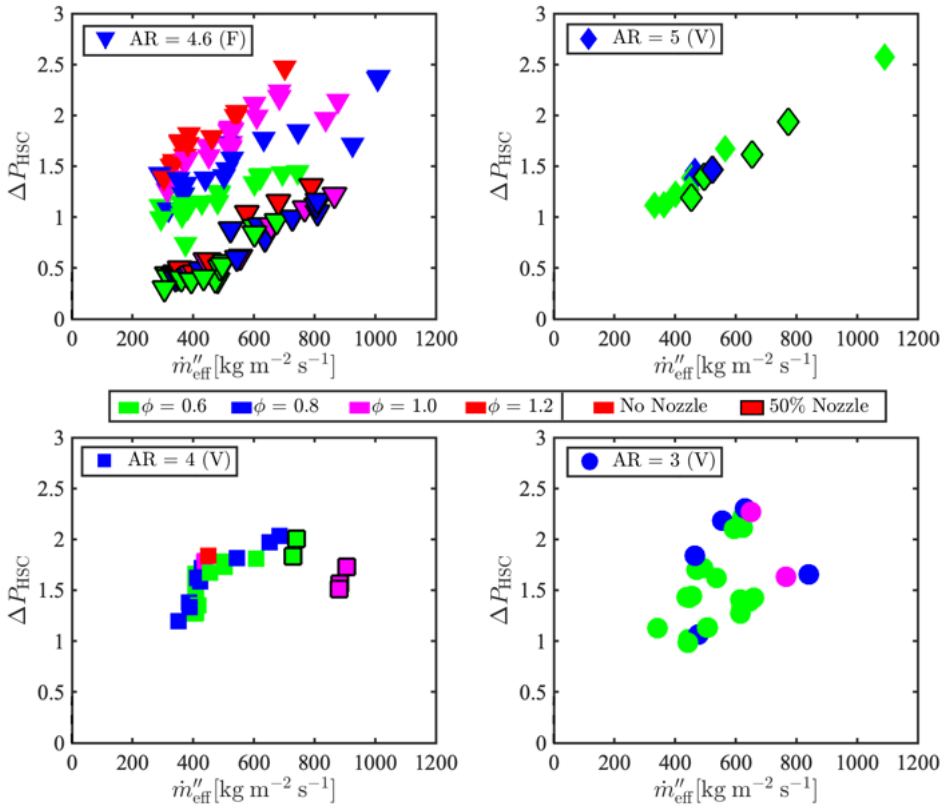

Figure 3.44: Relationship between observed pressure rise, blockage, and inlet air mass flux.

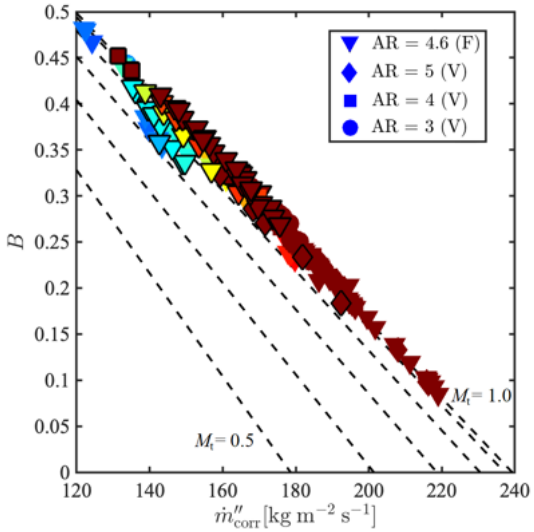

Figure 3.45: B as a function of corrected air mass flux with lines of constant $M_{3.1}$ from 0.5 - 1.0.

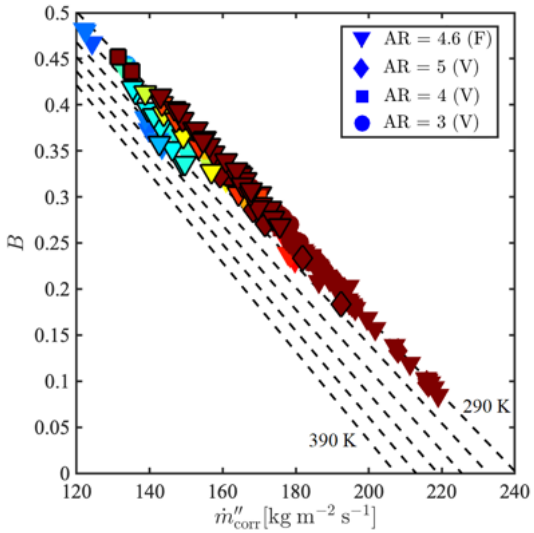

Figure 3.46: B as a function of corrected air mass flux with lines of constant $T_{t,3}$ from 290 - 390 K.

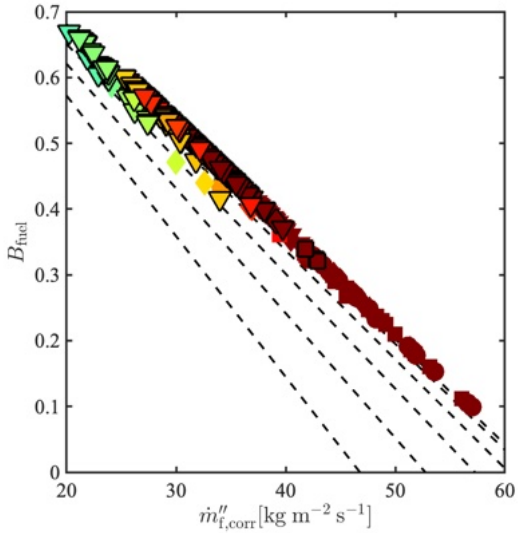

Figure 3.47: B_{fuel} as a function of corrected fuel mass flux with lines of constant M_{f} from 0.5 - 1.0.

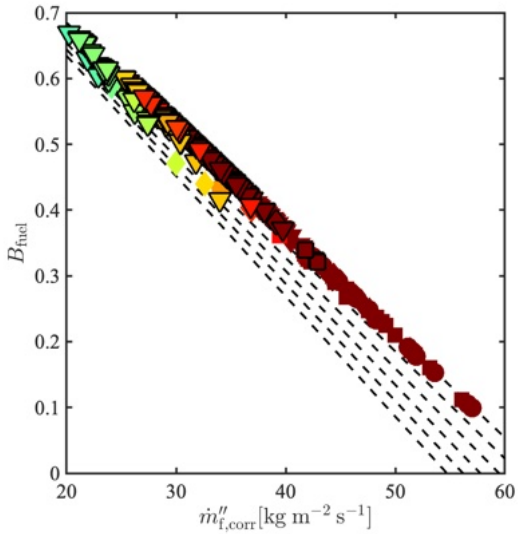

Figure 3.48: B_{fuel} as a function of corrected fuel mass flux with lines of constant T_{f} from 290 - 390 K.

Chapter 4

Analysis of Inlet Dynamics and Flow Field

4.1 Introduction

Several basic characteristics of the flow-field of an operating RDE have previously been outlined through the computations of Nordeen *et al.* [32] and the experimental observations of Andrus *et al.* [33], Tobias *et al.* [34], and Depperschmidt *et al.* [35]. All of these efforts demonstrated the presence of varying degrees of "inflow" to the continuously propagating detonation wave within an RDE, though did not further analyze the impacts of this phenomena. Characterizing and quantifying this phenomena and the associated impacts are objective #3 of this effort and are considered in this section.

Therefore, the final loss mechanism that will examined is losses that result due to flow non-idealities within the fill region of an operating RDE. When looking at canonical representations of the flow field within an RDE, the fill region is generally represented in such a way that would imply it is a relatively benign environment made up of purely or predominantly axial flow. However, through targeted testing with varying degrees of optical access within an operating RDE, it has been demonstrated that this is not the case. A significant amount of "reverse swirl" in the direction counter the wave(s) direction is universally present within the fill region of an operating RDE. This has historically been at best explained away as being insignificant relative to the wave propagation speed or at worst ignored. As will be shown in later sections, a significant inflow to the wave can have significant impacts on the

local pressure gain that can be realized. These impacts result due to the reduction in pre-detonation static pressure and in the reduction of the induced velocity behind the wave.

The flow field of an operating RDE is generally assumed to take the canonical form composed of a triangular fill region, the rotating detonation wave and the expanding flow. In this representation there is no suggestion of significant non-axial components of velocity in the fill region. Although not further explored, the aforementioned computational and experimental efforts have shown the fill region is far more dynamic than might be expected, which has been confirmed through several methodologies that will be further outlined.

4.2 Description and Discussion of Measurement Method

4.2.1 Configurations Considered in the Study

As summarized earlier, a Luminescent Particle Tracking (LPT) methodology was devised to evaluate the flow field of an operating RDE at a variety of conditions at various axial locations. All testing was conducted in the FAI configuration at channel lengths of 71 mm and 119 mm. Both of these configurations were chosen for specific reasons related to the placement of the optical access. Optical access was generated by the use of two different approaches: (1) the port-hole window installed on the outer wall (see Section 2.4.2); or (2) the optically accessible outer body (see Section 2.4.3). The 71 mm channel length enabled the placement of the port-hole window at three discrete axial locations, while the 119 mm channel length enabled the placement of the optically accessible outer body near the RDE inlet.

The FAI configuration with 71 mm or 119 mm channel length was first evaluated with the port-hole window. As noted, the 71 mm channel length was chosen for the preponderance of testing conducted using the LPT methodology as the optically accessible port-hole installed in the outer body was capable of being placed at different axial locations with respect to the fuel/air injection points: near the air/fuel injectors, at the aft end of the channel immediately upstream of the exhaust nozzle, and at the exhaust plane. These locations were identified in Figure 2.10 as the Forward, Aft, and Exhaust locations respectively. By combining measurements at the different locations, a nearly complete representation of the flow field within this configuration

was able to be constructed.

The 119 mm configuration was chosen because this channel length allows for testing in the standard constant area channel geometry while also allowing for the installation of a contoured inner body that generates a detonation channel geometry profile that is similar to that of the VAI RDE configuration. This contoured geometry was suspected to change the degree of interaction between the plenum and channel, because it induces changes in the effective blockage at the inlet through increased burned gas backflow. Although a limited set of LPT measurements were attempted with the OAOB installed, these studies were focused on the use optical chemiluminescence to better visualize and quantify the degree of backflow experienced with the two configurations.

Therefore, in addition to the basic characterization of the flow field throughout the device in the 71 mm channel length configuration, a second evaluation of the flow field near the inlet was conducted with the use of the optically accessible outer body specifically designed for this purpose. This outer body possesses a fused quartz window around the entire annulus, and as outlined in Section 2.4.3, videos were obtained viewing 1/8 of the total circumference Videos were taken directly imaging the base of the RDE channel and RDE air/fuel injector region. All videos were obtained with the FAI RDE configuration, both with (FAI-C) and without the contoured inner channel. Cases that will be further analyzed are of the USW and UDW operating modes outlined in Chapter 3. These modes are chosen for their uni-directional wave propagation nature which allows for appropriate phase-averaging relative to the position of the dominant wave.

This effort was thus a two-pronged approach seeking to characterize the flow field throughout an operating RDE. Although the use of two unique configurations was necessitated by the viewing areas afforded by the two disparate methodologies, when combined the results from both of these approaches allow for an accurate understanding of different aspects of the flow field throughout an operating RDE. This aspect is unique when compared to the previously summarized data available within the literature.

4.2.2 Limitations of Imaging Approach

Regardless of the method of optical access, whether through the small aperture porthole or the wide aperture outer body, the LPT methodology presents several limitations. These include limitations in terms of available viewing areas and in terms of

the approaches themselves. As the port-hole used for the LPT methodology is limited in aperture (a 19 mm diameter circle) and in terms of where it can be placed axially (as shown in Figure 2.10), a true representation of the entirety of the flow field within the RDE cannot be formed directly through this approach. However, by conducting tests at similar conditions with the port-hole placed at differing locations, flow characteristics at various axial locations were observed and quantified for analysis.

The limited aperture of the port-hole window and the sample rate of the camera (70k fps) imposed an upper bound on velocities that were capable of being quantified. The velocities of individual particles were calculated based upon the displacement between successive frames. This approach thus requires that the characteristic feature being tracked (the particle leading edge) must appear within two or more frames, which thus limits the highest possible velocity that can be quantified through this method. Based upon the aperture of the port-hole window (19 mm) and the exposure time (14 μs), the resultant upper bound is approximately 1350 m/s. Velocities exceeding this bound would not be expected as this is of the same order as the observed wave speeds presented in the prior chapter, however, it must be noted as a potential limitation imposed by the small format optical access location.

An additional limitation associated with the LPT methodology is the lack of artificial illumination as would be typical of a conventional particle image velocimetry (PIV) approach. The LPT method is reliant upon the inherent luminescence of the particles as they are heated by the reactions within the channel. This results in the majority of visible particles falling close to the region of peak heat release near the continuously propagating wave(s). This allows for a large sample size in this region but fewer particles in the lower temperature fill region. This lack of planar illumination also precludes locating individual particles in three-dimensional space, and as such particle motions are assumed to be occurring in the azimuthal and axial directions with un-quantifiable radial components of velocity. This is perhaps one of the most significant limitations of the present approach.

Thirdly, the method through which particles were harvested and introduced to the RDE resulted in an unknown distribution of particle sizes and associated masses. This must be noted, as these particles were passively harvested from particles contained in the air supply system. Thus, the particle size distribution cannot be controlled and differs from conventional PIV approaches where particle of desired properties (e.g. material, size, morphology, etc.) are seeded into the flow. Although a representative sample of particles was shown in Figure 2.9, all individual particles used throughout this effort cannot be assured to be of the same size and morphology. As was shown

in Figures 2.11 and 2.12, where two examples of a sequence of frames are given, the particle response time was found to be of the same order as the frame rate of the camera in use (70k fps) , so as such the observed particle directions are believed to be indicative of the true flow direction, while the particle velocities are assumed to only approximate the local flow velocities.

Direct imaging through the optically accessible outer body also has a limited aperture in the axial direction. Additionally, this methodology presented a different challenge than those tests conducted through the PMT port-hole in that the shear volume of visible particles made manual particle tracking of all particles infeasible. Attempts were made to automate this tracking but these methods were found to be non-viable. As such, for these tests the chemiluminescence in specific regions will be used for analysis. The tests in this configuration were conducted with the goal of evaluating the magnitude of burned gas backflow , and as such the particle tracking is of reduced importance.

4.3 Phase-Average Measurement of Inlet Flow Velocity

Analysis has focused on those cases that operate in the Uni-directional Single Wave (USW) and Uni-directional Dominant Wave (UDW) operating modes only. These cases allow for an appropriate phase-averaged representation of the flow field within the RDE to be defined. The RDE configuration in which all LPT testing was conducted did not exhibit operation with any characteristics of the BDW mode, while the CDW mode, which does not have uni-directional waves, made isolating the dominant wave position – which is needed for phase-averaging – impossible. A summary of all tests conducted is shown in Figure 4.1, with the marker colors indicating the axial location of the PMT port-hole through which particle paths were viewed. Two sets of data were taken. One set of data was acquired at a fixed equivalence ratio of $\phi = 0.6$ and increasing mass flow rate; while a second set was acquired at a fixed mass flow rate of 150 $\mathrm{kgs^{-1}m^{-2}}$ and increasing equivalence ratio. These sweeps of holding one variable constant were chosen with the intent that variations in the flow field while varying ϕ and with air mass flow could be isolated.

However, all tests conducted at flow rates exceeding 200 g/s were found to exhibit CDW modes of operation, during which continuous directional changes of the dominant wave were observed. Due to the constant directionality changes observed

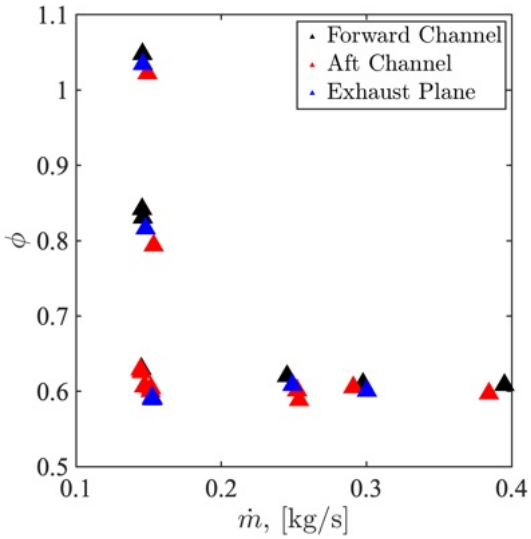

Figure 4.1: Summary of conditions tested using Luminescent Particles. Forward Channel, Aft Channel, and Exhaust Plane axial locations shown previously in Figure 2.10.

when operating in this mode, the analysis to follow will predominantly focus on those cases tested at 150 g/s in which the dominant wave could be clearly identified and appropriate assignment to relative cycle locations could be performed. The higher mass flow cases exhibiting CDW operation will later be considered when analyzing swirl at the exhaust axial position, but the primary focus of the flow field characterization will be on those cases with a clear dominant wave. The $\phi = 1.0$ cases operated with two waves rotating in a uni-directional fashion as with the USW mode, while the lower equivalence ratio cases operated with a uni-directional dominant wave and weaker counter-rotating wave as with the UDW mode. The CWA results for a representative case at each of these nominal run conditions is shown in Figure 4.2. These representative results were obtained while the PMT port-hole was installed at the aft channel location, with similar behaviors observed when tests were conducted with the port-hole installed at the other axial viewing locations.

An example showing the observed particle paths at the various axial locations is shown in Figure 4.3. The lower figure refers to particle paths reconstructed in the forward location of the channel, the middle figure in the aft portion of the channel, and the top figure in the exhaust position. The individual particle paths are shown in the laboratory frame of reference, with the position of first appearance of an individual particle mapped to its azimuthal position relative to the detonation wave at this point. In this representation the wave location (as determined by peak chemiluminescence) is located at $\theta = 0$. The y-axis is located and scaled based upon the total channel length L. The $z = 0$ location is taken to be the axial location of the fuel injectors. As shown previously in Figure 2.10, the maximum axial extent of the viewable area when installed in the Exhaust location is thus $z/L > 1$ due to the viewing area extending beyond the RDE exhaust plane.

The numerous particle tracks of Figure 4.3 represent all observations, which can be distilled into a representative flow field. As outlined in the prior section, the velocity associated with these particle paths was determined in the lab frame of reference based upon the relative displacement of the particle leading edges in sequential frames. These displacements were used to determine the axial and azimuthal components of velocity and the corresponding flow angle. When considering the flow angle, zero degrees corresponds to purely axial flow, while positive and negative signs indicate the azimuthal directionality. In order to generate the representative flow fields that will follow, the representative cycle was segmented into 100 bins of equal azimuthal extent into which the individual realizations were assigned. Mean values and bands

representing 95% of all observations were quantified for the presentations to follow.

The first example of this approach is presented in Figure 4.4, where the phase-average azimuthal components of velocity are given as a function of the relative location within the cycle. Each sub-figure (moving left to right) corresponds to the three axial locations (moving bottom to top) of Figure 4.3. As can be seen in this figure, there is a generally consistent variation of the azimuthal velocity across the cycle. Positive values of azimuthal velocity represents movement in the direction of the wave while negative values represent movement in the direction opposite to the direction the wave travels. As can be seen, approximately 1/4 of the cycle near the inlet and 1/2 of the cycle in the aft channel and exhaust locations exhibits flow in the opposite direction of the wave at nearly the same magnitude of the peak induced velocity in the direction of the wave. This significant negative swirl was identified by Nordeen *et al.* in simulation and notionally identified by Andrus *et al.* but was not quantified in this way. This negative swirl thus indicates that the induced velocity behind the detonation wave is almost immediately lost to the incoming fresh fill which turns into the wave due to the negative pressure gradient following the trailing shock.

This phenomenon is not exclusive to the run conditions outlined above, but it is also observed in the other cases that exhibited a uni-directional operating mode. The azimuthal velocity profiles for the $\dot{m} = 150$ g/s at equivalence ratios of 0.8 and 1.0 are shown in Figures 4.6 and 4.8. As previously outlined, the $\phi = 1.0$ case exhibits operation with two co-rotating waves which can be observed in the data obtained in the aft viewing location (center) as indicated by the presence of two peaks in the velocity profile.

The previous figure show distinct similarities and differences from the $\phi = 0.6$ case. There is significant sparseness in the data obtained near the exhaust for both cases and for data obtained near the base of the RDE channel for the $\phi = 1.0$ case. This indicates that the detonation wave is likely circling downstream of the forward channel axial location and the only luminescent particles that are being tracked are those that are heated by the passing wave and traveling in the same direction as the wave(s) in the positive direction. The inflow is not seen at this location, but it is apparent at the aft channel location.

4.4 Analysis of the Impact of Incoming Azimuthal Velocity on Detonation Properties

The examples presented in the previous section illustrate an inflow to the detonation wave that is of the same magnitude as the observed induced velocity behind the wave. Due to the finite response time of the luminescent particles based upon their finite mass and the temporal resolution imposed by the camera frame-rate, it is assumed that this methodology is unable to resolve the true local velocity of individual particles immediately behind passing detonation shock wave. This limitation is validated based upon the disparate magnitudes of the observed wave speeds as determined through optical chemiluminescence and the peak local velocities as determined through the LPT methodology. An additional validation of this methodology-imposed limitation is provided by Andrus *et al.* [33]. Through manual tracking of local flow features vice the physical particles of the LPT approach, peak velocities immediately behind the wave were commensurate with the propagation velocity. However, this limitation of the LPT approach does not prevent using these results to analyze additional phenomena.

Although this approach cannot be used to directly characterize the induced velocity behind and in the direction of the wave, it was shown that the observed induced velocities are overcome by flow in the direction counter that of the wave prior to the completion of the cycle. As demonstrated by Nordeen *et al.*, this effect is induced by the incoming fresh fill propagating into the trailing oblique shock which results in a pressure gradient that goes from high pressure behind the wave to lower pressure further behind the wave [32]. Based upon the observations of the previous section, this results in a significant inflow to the following wave that is approaching the sonic speed of the reactants within the fresh fill region. As shown by Gamba *et al.*, a portion of the resultant pressure gain of a detonative-based combustion process due to the induced velocity (and associated kinetic energy) behind the detonation wave [36]. As this kinetic energy is found to be lost within a fraction of a cycle to the negative swirl coming into the following wave, this represents a significant loss mechanism that has thus far been identified but only minimally examined.

The inflow component of velocity affects the measurable quantities associated with the flow field in multiple ways. First, the inflow into the wave results in an effective wave propagation speed that is higher than it would appear in the fixed laboratory frame. As a typical C-J wave speed for hydrogen-air mixtures is approximately 1800

m/s, an inflow of 200 m/s would thus imply that the wave is traveling at wave speed ratios (W/D_{CJ}) approximately 10-12% higher than direct optical analysis through a methodology such as CWA or a frequency domain analysis of data from the high-speed pressure transducers would indicate. As experimental measures of wave speeds within operating RDEs typically fall between 65-80% that of the associated C-J wave speed, this phenomenon is thus hypothesized to account for a significant fraction of the wave speed decrement that is observed in nearly all experimental RDE tests [33, 3, 37, 14].

The inflow also has the effect of reducing the induced velocity behind the wave (in the laboratory frame of reference) on a one-for-one basis. As with the shock tube problem and other one-dimensional approximations of a propagating shock wave, it can be shown that the induced velocity behind the shock wave is the difference between the propagation wave speed and the sonic velocity behind the wave. As the wave speed within the laboratory frame of reference is reduced by an amount corresponding to the magnitude of the inflow velocity, the induced velocity behind the wave is similarly reduced. This reduction in induced velocity results in a direct loss of available total pressure and a local under-performance in the gain-producing region of an operating RDE.

A first-order analysis of the post-combustion states that result was conducted to quantify the relative effects of a high-velocity inflow through use of the NASA CEA program [19]. For this analysis sweeps were performed in equivalence ratio with varying degrees of inflow ranging from 0-300 m/s at a starting pressure of 1 atm for hydrogen-air mixtures at ambient temperature. This pressure representative of the pressure within the fill region of the previously presented examples in this section, and the range of equivalence ratios encompass the test conditions of the prior figures. The post-combustion states output by CEA were used to quantify the total pressure behind the wave. The post-detonation static pressure was output directly by CEA, while the dynamic component was calculated based upon the CEA outputs for density, detonation velocity, and sonic velocity in the exhaust products. Idealized results are shown in Figure 4.10.

The effect of increasing inflow is not insignificant, even in these idealized conditions. The peak post-combustion total pressure is observed to decrease from nearly 23 atm with zero inflow to approximately 19 atm with inflow traveling at 300 m/s into the wave. This represents a reduction of approximately 20%, which is of the same order as the negative pressure "gain" that is observed in the FAI configuration at low mass flow run conditions that these sweeps would be representative of. However, these

idealized calculations do not account for the fact that true Chapman-Jouguet static pressure ratios are not observed. This was shown previously in Figure 3.17 for the VAI configuration, and the peak pressure ratios of approximately 0.25 that predicted for a C-J detonation is representative of what's observed across all configurations.

For an additional point of comparison, the post-detonation static pressure output from CEA was modified to thus be 25% of its predicted value, as this represents the upper bound of experimental observations. The same calculations shown in Figure 4.10 using the NASA CEA program were repeated with this enforced static pressure decrement while holding all other flow characteristics constant. This thus represents a detonation where all components except their static pressure ratio are idealized, while the pressure ratio is assumed to match experiment. Although the reduced pressure rise would result in varying flow conditions behind the wave, these conditions are held constant for this first-order approach for trend analysis. Results from this approach are shown in Figure 4.11.

This approach shows a significant decrement to the post-combustion total pressure, which for the corresponding zero inflow examples reduces from a peak of 23 atm for the idealized case to approximately 10 atm for the non-idealized case corresponding to experimentally observed values. In addition to reducing the maximum attainable total pressure behind the detonation wave by greater than 50%, the enforced reduction in static pressure ratio also has the effect of exacerbating the relative performance decrease that results from wave inflow. In this partially-idealized representation of the resultant post-combustion total pressure, it can be seen that an inflow of 300 m/s results in a greater than 30% reduction of available total pressure behind the wave. In the idealized case this reduction was limited to a 20% decrement as compared to the zero inflow condition.

Both the fully idealized and partially idealized cases show that a significant loss in post-combustion total pressure behind the wave of an operating RDE can manifest as a result of wave inflow. This total pressure loss exceeds 30% that of the zero inflow condition in the partially idealized case which is believed to be more representative of reality. This is the first known attempt at quantifying the effect of this phenomena on the decrement in theoretical local gain that results, and shows that this previously identified (but not further analyzed) phenomena is likely to be a significant and thus far unaccounted for driver for RDE under-performance relative to the theoretical.

However, this first-order approach cannot fully isolate these performance decrements from system-level performance. Although the impact on local wave characteristics can be isolated through an analysis such as this, an operating RDE is a coupled

system in which any variations in these local gains will also manifest as variations in other performance measures. As shown in this and other experimental [38, 34, 35] and computational [32] works studying other disparate RDE configurations, this large magnitude inflow appears to be a universally present characteristic of the RDE concept instead of a phenomena induced by a particular design. As such, targeted efforts seeking to experimentally quantify the effect of reducing inflow are unlikely to be possible simply due to the inherent nature of the fill region.

4.5 Evaluation of Exhaust Swirl

As shown in prior figures, significant non-axial components of velocity are present throughout the RDE from near the inlet to the exhaust plane. These non-axial components within the RDE channel were previously discussed, but a key concern for any future use of an RDE will be the residual swirl that remains at the RDE channel exit. This swirl presents three concerns that, depending on application, may be of significant concern to future RDE and/or aerospace vehicle designers.

The first concern is the presence of any swirl independent of direction. If an RDE is to be used directly as a thrust-producing device sans turbomachinery, any non-axial component of velocity that remains at the exhaust plane represents a performance decrement. Though not a direct analog due to the azimuthal vice radial nature, from a thrust performance perspective this is somewhat analogous to cosine losses when analyzing a conventional rocket engine. This concern is thus independent of the local swirl direction and only concerned with the amount of non-axial flow present in the flow field. Kaemming *et al.* [39] surveyed multiple prior computational efforts and demonstrated computationally that this residual swirl can result in an end-to-end pressure gain under-performance by approximately 1%.

The results of the experimental cases tested using the LPT methodology that were outlined in prior sections indicate results of the same order. As shown in the captions of Figures 4.5, 4.7, and 4.9, the total non-axial component of momentum was found to range from 0.3-7.7% in the three cases presented. This was determined by assuming homogeneous gas properties at the RDE exhaust and comparing the ratio of non-axial and axial components of momentum based upon the presented velocity profiles. For the two remaining exhaust plane cases shown in Figure 4.1, the total non-axial components of momentum were found to be 0.7% ($\dot{m} = 250$ g/s, $\phi = 0.6$) and 0.8% ($\dot{m} = 300$ g/s, $\phi = 0.6$). Thus, while the 1% pressure gain under-performance

relative to purely axial flow appears to be valid for higher flow and equivalence ratio test conditions, significant non-axial momentum components can exist at the exhaust plane under lower flow conditions where the station 8 is unlikely to be choked. The work of Kaemming *et al.* which provides this 1% approximation did not provide further geometry or run condition details for comparison [39], but the results found through the LPT method largely agree with this finding, with deviations increasing as air mass flow rates and equivalence ratios are reduced.

The second concern is if there is a dominant directionality of the swirl at the exhaust of the RDE channel. As summarized in the previous paragraphs, when considered independent of direction the swirl can result in a net loss in thrust, but when directionality is considered the net swirl can additionally result in a significant torque that is imparted to the RDE and any vehicle to which it may be coupled. If the swirl component is dominant in one direction (as is the case of Figure 4.9), a significant torque can be imparted to any vehicle that is using an RDE for propulsion.

This phenomena was observed experimentally in the proof of concept flight conducted by Goto *et al.* [40]. In their flight demonstration in which they fired a methane-oxygen RDE at the edge of space, in which only 6 seconds of RDE operation resulted in the vehicle increasing its roll rate by 5.7 deg/s. This angular acceleration of approximately 1 deg/s^2 is not insignificant, as any conventional upper stage rocket engine used in a space launch application is likely to fire for many minutes. These results imply that the resultant spin imparted to the vehicle from an RDE could be on the order of rotations per second, which is a rate that must be later overcome by onboard reaction control systems and/or de-torquers and is well beyond what is seen with conventional rocket engines that typically impart zero spin. Any potential benefits from using an RDE in place of a conventional combustor could be lost to the additional reaction control propellant and/or de-torquers needed (in a rocket-style application) or increased control surface area required (in an air-breathing application) to offset this induced torque.

A third concern would arise if coupling an RDE to turbomachinery. Due to the dynamic nature of RDE operation and the non-homogeneous flow field at the exit plane, any associated turbomachinery would have to be capable of operating at a variety of inlet flow angles. This could include flow entering at varying angles at different azimuthal locations at one time, and at a wide variety of mean angles over time. These mean angles would include a range spanning from positive to negative values relative to the direction of shaft rotation. Limited experimental efforts demonstrating the coupling of an RDE to an off-the-shelf turbomachinery assembly have been

conducted [41], though further understanding of the effects of this non-homogeneous flow field on performance remain to be determined.

The second and third concerns are highlighted but not analyzed in depth, as the system-level impacts will be vehicle/application specific. As noted above, if the overall nozzle swirl is assumed to be approximately 1%, if the bulk of this swirl is unidirectional as with the USW and UDW modes, any coupled vehicle must thus be able to overcome a constant rotational impulse that corresponds to approximately 1% of the overall axial thrust imparted by the RDE. This is not an insignificant contribution, and it is highlighted here as it will be a concern for any future use of an RDE in a propulsive application. The BDW and CDW operating modes outlined in prior sections may actually prove to be beneficial in this respect, as if the dominant wave(s) is/are consistently changing directions the induced torque is likely to effectively cancel itself out.

4.6 Optical Verification of Burned Gas Backflow

An optically accessible outer body was designed to enable direct viewing of the entire circumference of the RDE. Due to the limitations imposed by the axial locations in which the previously summarized port-hole could be installed, this outer body was installed for a test sequence seeking to examine basic flow characteristics near the inlet. The following analysis will focus on observed chemiluminescence within the inlet instead of tracking of the particles that were introduced for these tests. The only deviations from the linear relationship between inlet blockage and corrected air mass flux were observed at very low flow conditions. This was postulated to be due to the presence of burned gas back-flowing into the inlet. The tests conducted with the OAOB sought to verify and characterize this effect. Although chemiluminescence cannot be used to fully quantify the magnitude of any reverse flow, a rise in observed chemiluminescence in this area is indicative of the presence of burned gas, which can only manifest if burned gas is back-flowing.

The area of interest for which analysis will follow was shown previously in Figure 2.12. This notional representation in the figure was determined through the following methodology. Based upon each individual run video, the axial extent of the inlet was manually verified. From this determination, an interrogation area of 3x5 pixels at the axial center of the inlet was defined. The circumferential location was chosen to be the center of frame which represents the point nearest the camera.

As all tests were conducted with the same camera settings and the camera location unchanged, the relative intensity across an average cycle can be compared. The relative intensity within the interrogation area is defined to be S, which is scaled based upon the lowest mean intensity observed when the wave is outside of the interrogation location. Cycle-averaged profiles were generated through the approach used in Figures 3.13 and 3.14.

The results obtained through this methodology for two tests conducted at similar inlet conditions is shown in Figure 4.12. The conditions for these tests were $\dot{m} = 150$ g/s, $\phi = 1.0$. As can be seen, both examples illustrate an elevated relative intensity when the wave passes, which is indicative of the presence of burned gas within the air inlet. The peak relative intensity that occurs at wave passage is magnified in the FAI-C configuration, which indicates that the contoured channel geometry actually induces elevated levels of back-flow. The observed chemiluminescence for both examples indicate the presence of burned gas within the inlet for far greater than 5% of the cycle, which was the posited amount of reverse flow needed to account for the blockage and corrected mass flux deviations at low mass flux conditions.

Although a simplified approach such as this cannot definitively quantify the total amount of reverse flow that is occurring, this method does indicate that burned gas is propagating forward when the RDE is operating. This is in agreement with prior efforts in which the inlet was imaged [22, 28]. As was shown in the previous blockage analysis, a small amount of back-flow (approximately 5% of the bulk forward flow) is sufficient to explain deviations from the linear relationship with corrected mass flux. This preliminary analysis using optical chemiluminescence supports the previous postulation that back-flow is present in an amount that sufficiently alters the local sonic condition at the inlet. This supports the theory that localized choking within the inlet is a necessary but not sufficient condition for RDE operation.

An additional characteristic that can be inferred from the curves of Figure 4.12 is that the presence of a smooth contour beyond the inlet has the unintentional effect of inducing elevated levels of back-flow. Further analysis will be required to completely quantify this effect, but the select examples shown here for similar run conditions indicate that the diodicity of the inlet can alter the amount of back-flow that occurs. This has implications for overall pressure gain, as the elevated levels of back-flow manifest as increased plenum pressures, which thus drive apparent pressure gain down.

4.7 Conclusions

This study presents the first results of the newly developed Luminescent Particle Tracking flow field characterization methodology. This method differs from conventional PIV approaches in that particles are manually harvested iron oxide particles of disparate size and morphology and in that the particles themselves are tracked through the luminescence that results from particle heating. This methodology was used to characterize the flow field within an operating RDE at varying axial locations, through which several characteristics were identified and quantified.

The computational work of Nordeen *et al.* is the first work known to the author in which the presence of non-axial flow into the wave of an operating RDE was identified [32]. Previous efforts using manual tracking of flow features [33] and conventional PIV methods [34, 35] similarly demonstrated significant non-axial components of velocity within an RDE including this inflow. Although all of the above referenced works identified this phenomena, none specifically quantified this behavior nor analyzed the potential effects.

Through the LPT approach, inflow velocities approaching the local speed of sound within the RDE fill region were observed. The observed induced velocity of particles entrained in the flow behind the wave was of similar absolute magnitude, but the flow direction was found to nearly completely reverse prior to the arrival of the next passing of the wave. As the induced velocity behind the wave forms a significant portion of the local gain that may be realized by using a pressure gain device such as an RDE, and the true value of this parameter is decremented by the presence of inflow on a one-for-one basis, this inflow was posited to be a contributing factor to experimental RDE under performance relative to the theoretical.

Through a first-order analysis of an ideal detonation, it was shown that wave inflow on the order of the local sonic velocity in the fill region can reduce the local pressure gain behind the wave by as much as 20%. Including experimental static pressure ratios reduced the theoretical maximum in the zero inflow condition approximately 50%, and the effect of inflow was exacerbated by reducing this a further 30% when included. The detonation wave is the only pressure gain-producing mechanism within the RDE, so any decrements that manifest at the wave will subsequently manifest in the overall system-level performance. This quantification of the effects of flow non-idealities on local gain producing mechanisms and performance impacts serve to satisfy the third and fourth objectives of this work.

However, the resultant local gain cannot be completely isolated from the system-

level performance. Instead, when making a full accounting for the previously analyzed inherent and induced losses present with an RDE, the requisite local gain can be determined and looked at in a comparative manner in seeking to determine if a path to positive pressure gain exists. This compartmentalization of local gain and analysis of associated trends will guide the completion of the final research objective in the next chapter.

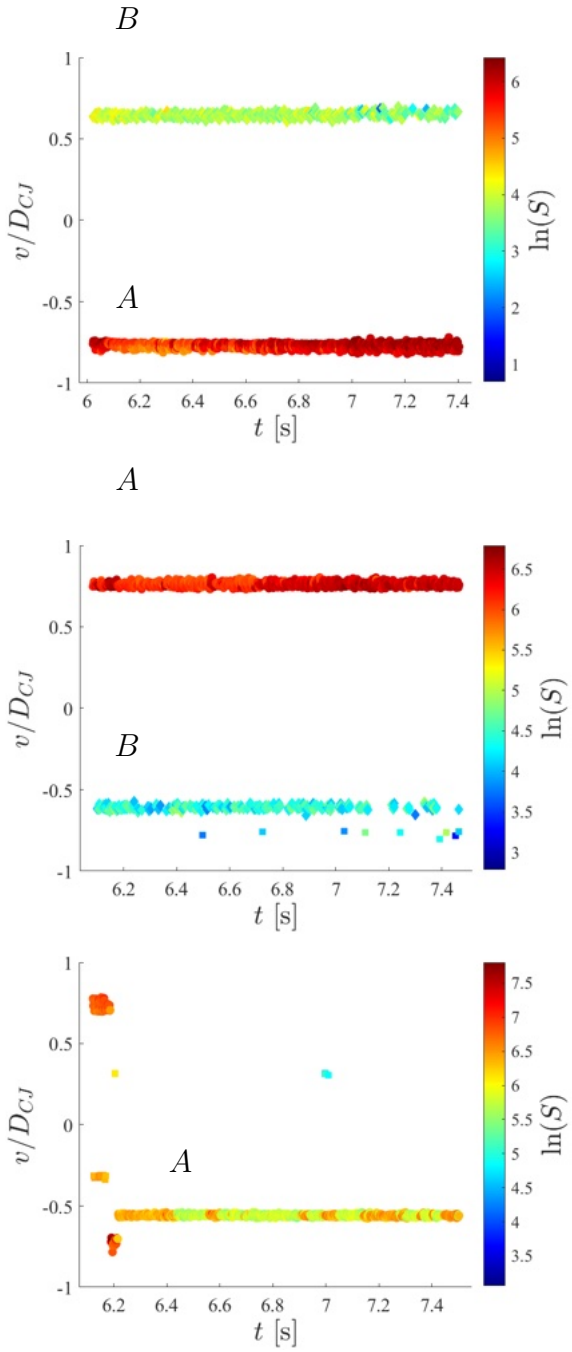

Figure 4.2: CWA results illustrating the uni-directionality of tests conducted at $\dot{m} =$ 150 g/s and a ϕ of 0.6 (top), 0.8 (middle), and 1.0 (bottom). A: primary detonation wave; and B: secondary wave.

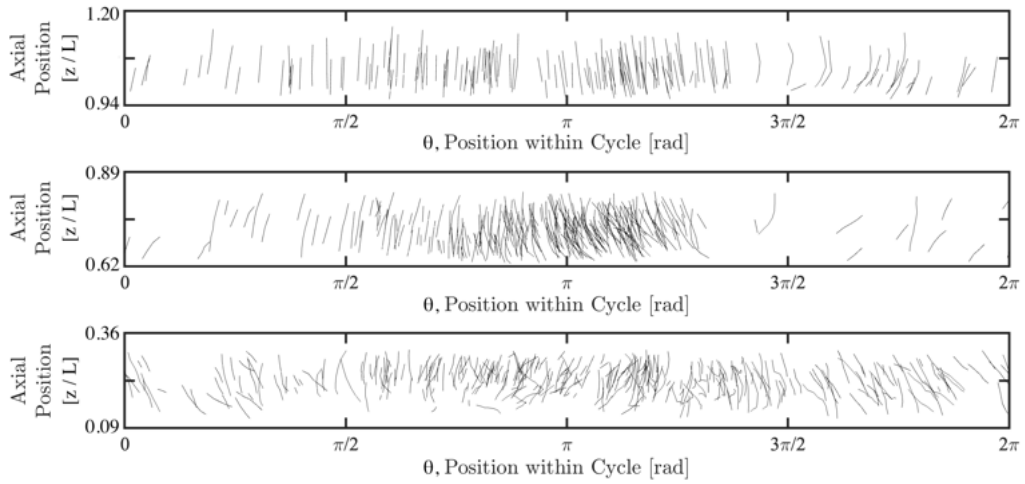

Figure 4.3: Observed particle paths of tests conducted at $\dot{m} = 150$ g/s and a ϕ of 0.6 in the forward channel (bottom), aft channel (middle), and exhaust plane (top) port-hole locations.

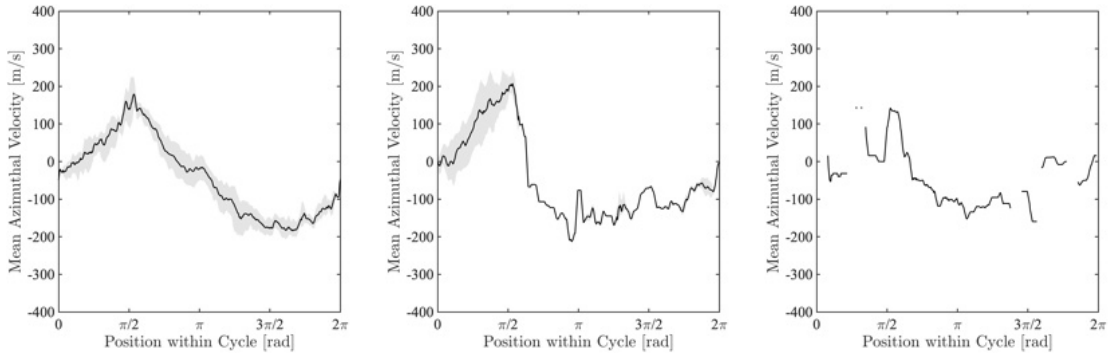

Figure 4.4: Mean azimuthal velocity within RDE when operating at $\dot{m} = 150$ g/s, $\phi = 0.6$. Azimuthal velocity profile as viewed in the forward location (left), aft channel location (right), and at the exhaust plane (right). Bands represent 95% of observations, while lack of observations at particular cycle positions can be observed in sparseness of data at exhaust plane (right).

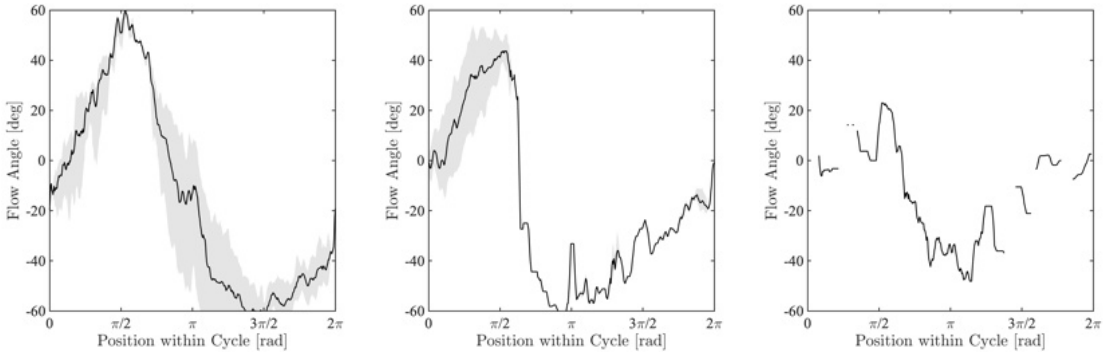

Figure 4.5: Flow angles within RDE when operating at $\dot{m} = 150$ g/s, $\phi = 0.6$. Flow angle profile as viewed in the forward location (left), aft channel location (right), and at the exhaust plane (right). Positive angles represent flow in the direction of the primary wave direction. Bands represent 95% of observations, while lack of observations at particular cycle positions can be observed in sparseness of data at exhaust plane (right). Flow angles indicate 7.7% of total momentum is non-axial at exhaust plane.

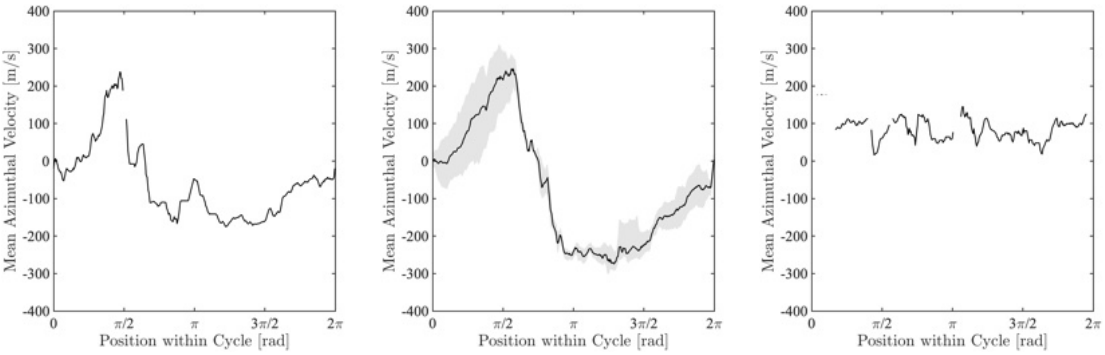

Figure 4.6: Mean azimuthal velocity within RDE when operating at $\dot{m} = 150$ g/s, $\phi = 0.8$. Azimuthal velocity profile as viewed in the forward location (left), aft channel location (right), and at the exhaust plane (right). Bands represent 95% of observations, while lack of observations at particular cycle positions can be observed in sparseness of data at forward channel (left) and exhaust plane locations (right).

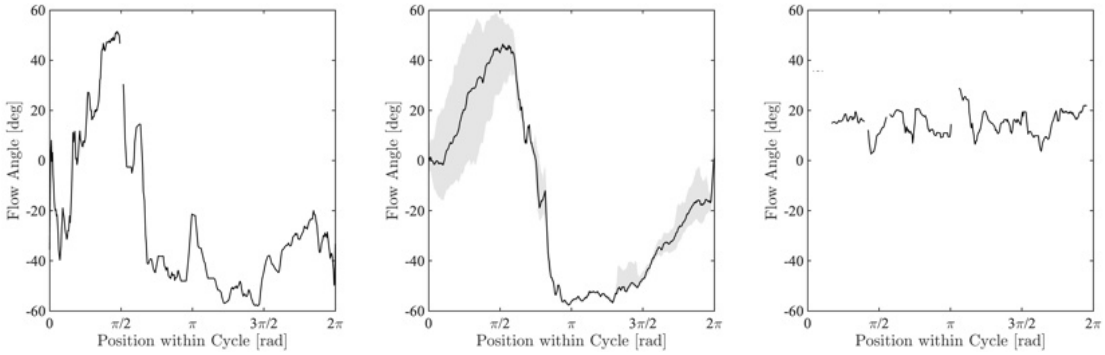

Figure 4.7: Flow angles within RDE when operating at $\dot{m} = 150$ g/s, $\phi = 0.8$. Flow angle profile as viewed in the forward location (left), aft channel location (right), and at the exhaust plane (right). Positive angles represent flow in the direction of the primary wave direction. Bands represent 95% of observations, while lack of observations at particular cycle positions can be observed in sparseness of data at forward channel (left) and exhaust plane locations (right). Flow angles indicate 4.0% of total momentum is non-axial at exhaust plane.

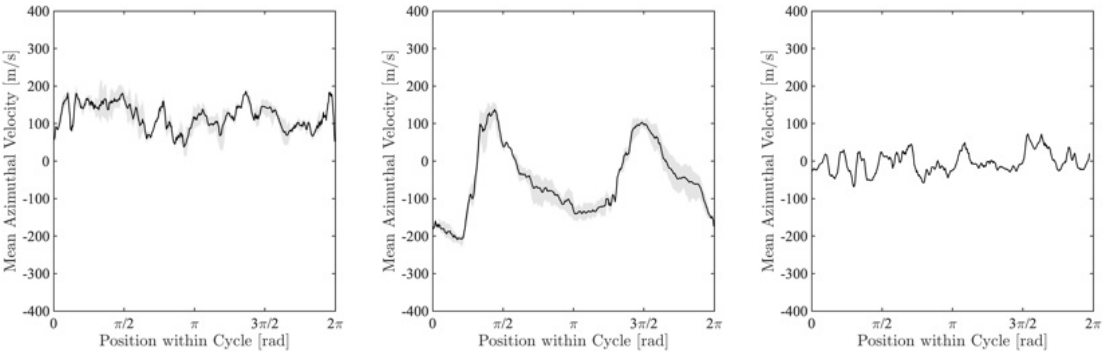

Figure 4.8: Mean azimuthal velocity within RDE when operating at $\dot{m} = 150$ g/s, $\phi = 1.0$. Azimuthal velocity profile as viewed in the forward location (left), aft channel location (right), and at the exhaust plane (right). Bands represent 95% of observations, while lack of observations at particular cycle positions can be observed in sparseness of data at exhaust plane (right).

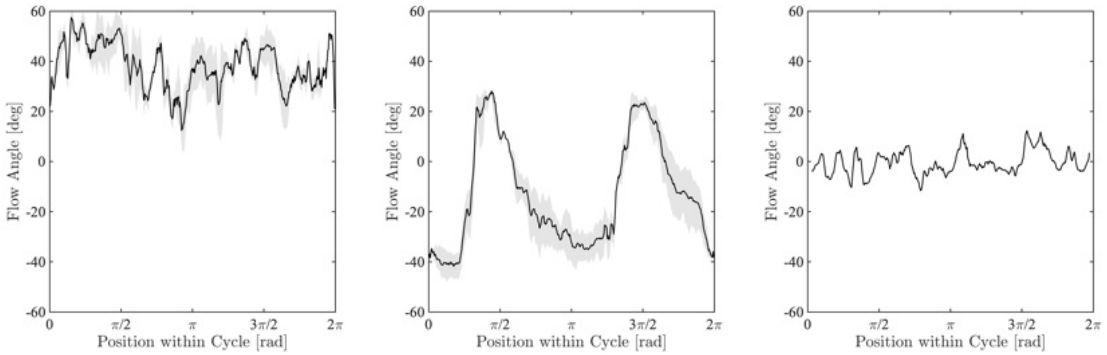

Figure 4.9: Flow angles within RDE when operating at $\dot{m} = 150$ g/s, $\phi = 1.0$. Flow angle profile as viewed in the forward location (left), aft channel location (right), and at the exhaust plane (right). Positive angles represent flow in the direction of the primary wave direction. Bands represent 95% of observations, while lack of observations at particular cycle positions can be observed in sparseness of data at exhaust plane (right). Flow angles indicate 0.3% of total momentum is non-axial at exhaust plane.

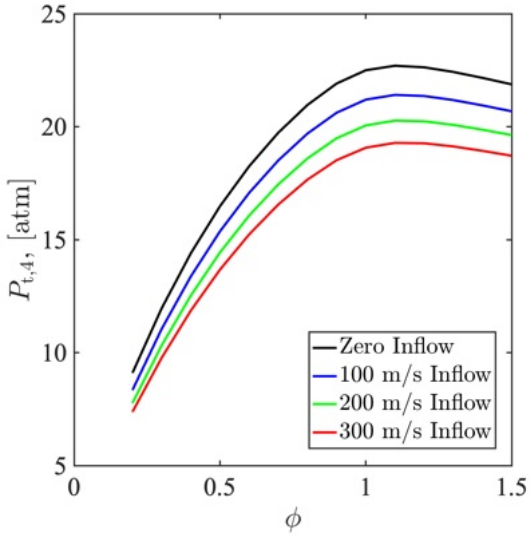

Figure 4.10: Theoretical idealized post-combustion total pressure with varying levels of inflow as predicted by NASA CEA [19].

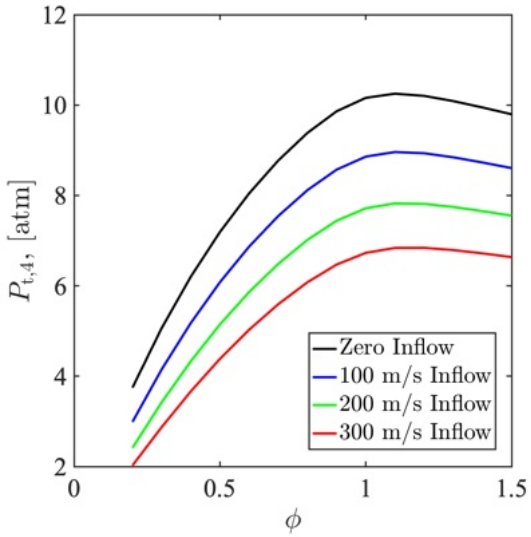

Figure 4.11: Theoretical partially idealized post-combustion total pressure with varying levels of inflow as predicted by NASA CEA [19].

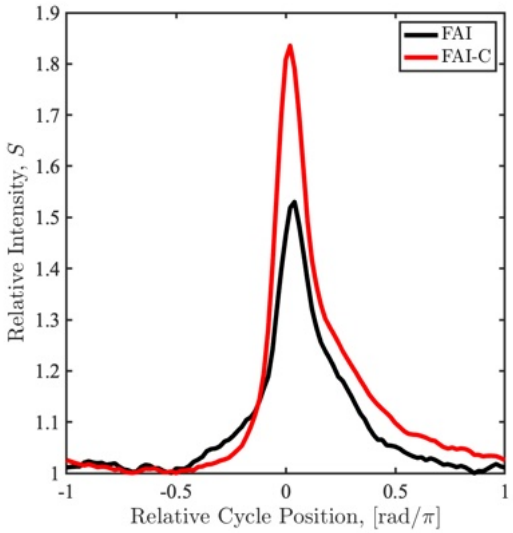

Figure 4.12: Phase-averaged inlet chemiluminescence intensity S for tests conducted in FAI configuration with nominal channel geometry and FAI-C configuration with smooth inner channel contour. Run conditions $\dot{m} = 150$ g/s, $\phi = 1.0$.

Chapter 5

Development of TDLAS Sensor for MHz-rate Measurements of Temperature and Water Vapor Partial Pressure

5.1 Background

5.1.1 Theory of Absorption Spectroscopy

In laser absorption spectroscopy experiments, light with a wavelength that is resonant with the difference in molecular energy levels of a specific transition is directed across a gas. The spectral absorbance $\alpha(\nu)$ of light with optical frequency ν is related to the incident (I_0) and transmitted (I_t) light intensities through Beer-Lambert's Law:

$$\frac{I_\mathrm{t}(\nu)}{I_0(\nu)} = \mathrm{e}^{-\alpha(\nu)} \tag{5.1}$$

where the spectral absorbance is related to the thermodynamic state of the gas according to:

$$\alpha(\nu) = \sum_j \int_0^L S_j(T)\phi_j(\nu - \nu_\mathrm{o}, \Delta\nu_\mathrm{c}, \Delta\nu_\mathrm{d})PX_i\mathrm{d}\ell \tag{5.2}$$

Here, $S_j(T)$ [cm^{-2}/atm] denotes the temperature-dependent line strength of transition j, expressed in pressure-normalized units. P is the gas pressure [atm], X_i is the

mole fraction of the absorbing species, and L [cm] is the path length. The variable ϕ [cm] represents the spectral lineshape profile, which is modeled using a Voigt profile in this work. The Voigt profile results from the convolution of a Lorentzian lineshape with a Gaussian lineshape, and models the effects of collisional broadening and Doppler broadening [42]. $\Delta\nu_\mathrm{d}$ [cm^{-1}] denotes the Doppler full-width at half maximum (FWHM) of the transition, and depends only on temperature and the transition linecenter, given by

$$\Delta\nu_\mathrm{d} = 7.1623 \times 10^{-7} \nu_\mathrm{o} \sqrt{\frac{T}{\overline{M}}}, \tag{5.3}$$

while $\Delta\nu_\mathrm{c}$ [cm^{-1}] is the collisional broadening linewidth (FWHM) of the transition defined as

$$\Delta\nu_\mathrm{c} = P \sum_A X_A \cdot 2\gamma_{B-A}(T) \tag{5.4}$$

and $\gamma_{B-A}(T)$ is the collisional-partner dependent broadening parameter whose temperature dependence is modeled as a power-law according to:

$$2\gamma_{B-A}(T) = 2\gamma_{B-A}(T_0) \left(\frac{T_0}{T}\right)^n \tag{5.5}$$

where T_0 is a reference temperature which in the HITRAN database is 296 K [43].

5.1.2 Quantitative Measurements

The thermodynamic state of the absorbing gas can be inferred from the integrated absorbance (A_j) of two transitions which for uniform properties is given by:

$$A_j = \int_{-\infty}^{\infty} \alpha_j(\nu) \mathrm{d}\nu = S_j(T) P X_i L \tag{5.6}$$

The lineshape profile is normalized to unity and therefore does not contribute to the integral. By taking the ratio of integrated absorbances for two transitions (two-color), the dependence on absorbing species mole fraction, pressure, and path length cancel out but since different transitions have different temperature dependencies, these do not cancel out. Therefore, the two-color ratio of integrated absorbances is only a function of temperature given by:

$$\frac{A_1}{A_2} = \frac{S_1(T)}{S_2(T)} = \frac{S_1(T_0)}{S_2(T_0)} \exp\left[\left(\frac{hc}{k}\right)\left(E_2'' - E_1''\right)\left(\frac{1}{T} - \frac{1}{T_0}\right)\right] \tag{5.7}$$

With temperature known, equation 5.6 can be solved for the absorbing species mole fraction X_i if pressure is known from a sensor or partial pressure if X_i is unknown as shown in equation 5.8.

$$P_i = \frac{A_j}{S_j(T)L} \tag{5.8}$$

If the mixture composition can be estimated and broadening parameters are available, equation 5.4 can be used to infer pressure.

5.1.3 Basics of Scanned-WMS

Scanned-wavelength-modulation spectroscopy (scanned-WMS) is a LAS technique where the wavelength of the laser is rapidly modulated at a frequency f_{mod} while the nominal wavelength is tuned across the absorption feature at a frequency $f_{\text{scan}} << f_{\text{mod}}$. The intensity of the laser is simultaneously modulated but with a phase shift (ψ_1) relative to the wavelength. As the wavelength and intensity are modulated and scanned across the absorption feature, absorption information is encoded into the harmonics of the modulation frequency and side bands centered at $nf_{\text{mod}} \pm if_{\text{scan}}$, with $i = 1, 2, 3, \text{etc.}$ Due to the high modulation frequencies, WMS-nf harmonics are isolated from low-frequency noise and exhibit a high signal-to-noise ratio making WMS suitable for LAS measurements where the absorption signal is weak. Typically side bands outside $i = 2$ can be excluded when extracting the WMS-nf harmonics using digital lock-in amplifiers that further reject noise outside the filters passband [44].

Scanned-WMS can further be made robust to external disturbances by leveraging the dependencies that different harmonics have on absorbance, intensity, and lineshape. For instance, the WMS-1f harmonic signal is primarily dependent on the transmitted light intensity [45], and therefore normalization by the WMS-1f harmonic signal has been used to correct for non-absorbing losses as they are common to all harmonics and cancel each other out making the WMS-2f/1f signal robust against scattering, vibrations, beam steering, and transmission losses at interfaces (windows, lenses, etc.) [46].

To infer gas properties the WMS-2f/1f signal at linecenter is compared to simulated values using the calibration-free WMS model developed by Rieker et al. [47]. Here only a brief introduction is provided and for a detailed review of the model the reader is directed to references [45, 47, 48, 49]. The magnitude of the WMS-2f/1f

signal at linecenter ($S_{2f/1f}(\nu_o)$) in the optically thin limit with uniform properties can be written as:

$$S_{2f/1f}(\nu_o) = \frac{S(T)PX_iL}{i_0 \cdot \pi} \int_{-\pi}^{\pi} \phi(\nu_o + a\cos\theta)\cos(2\theta)\mathrm{d}\theta \tag{5.9}$$

The ratio of the WMS-$2f/1f$ signal at linecenter for two transitions then becomes only a function of temperature, modulation depth (a), and the DC normalized intensity modulation amplitude (i_0). Therefore, the two-color ratio of $S_{2f/1f}(\nu_o)$ signals can be used to infer the temperature of the gas according to:

$$\frac{S_{2f/1f}(\nu_{o,1})}{S_{2f/1f}(\nu_{o,2})} = \frac{i_{0,2}}{i_{0,1}} \frac{S_1(T)}{S_2(T)} \frac{F(\nu_{o,1}, a_1, \phi)}{F(\nu_{o,2}, a_2, \phi)} \tag{5.10}$$

Note that the ratio of integrated absorbances appears explicitly $S_1(T)/S_2(T) = A_1/A_2$. If the gas properties along the path are nonuniform, then by selecting transitions with a linestrength that varies linearly with temperature, it can be shown that the measured temperature is equal to the number density weighted path averaged temperature [50].

Higher-order harmonics can also be used to obtain additional information about the gas properties as different harmonics are sensitive to different aspects of the absorption feature. Though it will not be shown analytically, the WMS-$4f/2f$ signal in the optically thin limit is only a function of the transitions lineshape (ϕ) [48]. At a fixed temperature and therefore $\Delta\nu_d$, the lineshape changes only with the collisional width $\Delta\nu_c$ and so the WMS-$4f/2f$ signal can be used to measure the collisional width of an isolated transition in a bath gas with unknown composition.

5.2 Line selection

Two near-infrared H_2O transitions near 7185.596 cm^{-1} and 6806.03 cm^{-1} are probed using distributed feedback (DFB) laser diodes from NTT Electronics America. These transitions are well characterized and have been used to measure gas properties in various high-temperature and -pressure applications [51, 44, 52, 53, 54, 55]. Spectroscopic parameters for self and nitrogen broadening in addition to linestrengths are taken from [51] and are provided in table 5.1. The wavelength for the lasers near 7185.596 cm^{-1} and 6806.03 cm^{-1} is modulated at 36 MHz and 45 MHz respectively.

Parameter	Line 1	Line 2
ν_o [cm^{-1}]	7185.596	6806.03
$S(296K)$ [cm^{-2}/atm]	1.96E-02	6.40E-07
E'', [cm^{-1}]	1045.1	3291.2
γ_{N_2} [cm^{-1}/atm]	0.045	0.0105
n_{N_2}	0.51	-0.108
γ_{self} [cm^{-1}/atm]	0.198	0.205
n_{self}	0.53	0.86
γ_{H_2} [cm^{-1}/atm]	0.0425	0.0372
n_{H_2}	0.52	0.45
γ_{air} [cm^{-1}/atm]	0.0403	0.0104
n_{air}	0.587	-0.164

Table 5.1: Broadening parameters for H_2O transitions near 715.596 cm^{-1} and 6806.03 cm^{-1} at $T = 296$K.

5.3 Laser characterization

In WMS experiments, knowledge of how the lasers wavelength and intensity vary with time relative to each other is required as the laser characterization is used to simulate WMS signals that are compared to measured signals during post-processing to infer gas properties. When using the calibration-free WMS model, the lasers wavelength and intensity response to sinusoidal modulation is described by equations 5.11 and 5.12.

$$\nu(t) = \nu_o + a\cos(2\pi f_{mod} t) \tag{5.11}$$

$$I_0(t) = I_{DC}[1 + i_0\cos(2\pi f_{mod} t + \psi_1) + i_2\cos(4\pi f_{mod} t + \psi_2)] \tag{5.12}$$

Here, a [cm^{-1}] is the modulation depth, i_0 and i_2 are the first and second-order DC-normalized intensity modulation amplitudes, and ψ_1 and ψ_2 are the relative phase shifts between the wavelength and intensity of the laser. Figure 5.1(a) shows the baseline intensity and etalon signal obtained for laser light modulated at $f_{mod} = 500$ kHz. All five parameters mentioned above can be found by fitting equation 5.11 to the etalon peaks which are each spaced in time by one free spectral range (FSR

[cm^{-1}]) of the etalon [56, 57] and equation 5.12 to the baseline intensity signal. Note that the calibration-free WMS model only accounts for modulation about a nominal wavelength and does not take into account scanning. To account for the effects of scanning, the DC-normalized intensity modulation amplitudes are determined at the transition linecenter using an absorption reference. The values during the up and down portions of the scan will be different due to the phase difference between the wavelength and intensity of the laser but from equation 5.10 by setting $\nu_{o,1} = \nu_{o,2}$ are related through equation 5.13.

$$\frac{S^{up}_{2f/1f}(\nu_o)}{S^{down}_{2f/1f}(\nu_o)} = \frac{i_0^{down}}{i_0^{up}} \tag{5.13}$$

At modulation frequencies much above a few MHz, an etalon is no longer the best way to characterize the modulation depth due to the increasing demand on the sampling rate required to resolve the peaks between scans. Instead, a Fabry-Perot Interferometer (FPI) which scans a certain range of frequencies as the spacing between two confocal spherical mirrors is changed via a piezoelectric transducer is used to analyze the intensity spectrum of the light. The procedure for using an FPI to characterize the lasers modulation depth by fitting to the transmitted intensity spectrum is described in detail by Mathews and Goldenstein [54].

As noted by Mathews and Goldenstein, the fitting procedure to the transmitted intensity spectrum of the FPI is insensitive to the relative phase-shift ψ_1. To determine this parameter, the authors fit to full-spectrum scanned-WMS harmonics obtained at 1 kHz but with the same modulation frequency. For the H_2O transitions probed, this requires a high-temperature static gas cell [58] where the temperature, pressure, and gas composition are known, making ψ_1 the only unknown, provided all other laser parameters are determined. This method may not be practical for industry or other research laboratories not equipped with such a facility.

To address this, we introduce an alternative method that uses only an absorption signal, which can be obtained in any environment and without requiring knowledge of gas properties. This method also avoids dependence on the characterization of other laser parameters. It leverages the fact that the positions of absorption peaks during the up and down portions of a scan are determined entirely by the relative phase shift ψ_1. The only data required to determine ψ_1 using the method presented here is an absorption and baseline intensity signal acquired at the modulation frequency of interest. The general procedure is to first determine φ by fitting equation 5.14

to the baseline intensity signal. Absorbance is then plotted versus wavenumber by generating a vector using equation 5.15 where δ is a free parameter.

$$I_0(t) = c_1 \cos(2\pi f_{\text{mod}} t + \varphi) + c_2 \tag{5.14}$$

$$\nu(t) = \cos(2\pi f_{\text{mod}} t + \delta) \tag{5.15}$$

The two absorption peaks will collapse onto each other once the relative phase-shift $(\varphi - \delta)$ is equal to ψ_1. Figure 5.1(b) illustrates the overlapping of absorbance peaks for data obtained at 500 kHz. To asses the accuracy of this method, ψ_1 was determined for the laser near 7185.596 cm^{-1} at several kHz rate modulation frequencies and compared to the values obtained by using an etalon. The method presented here determined ψ_1 within 1% of the known values which are provided in table 5.2. This method was used to determine ψ_1 for both lasers at the MHz rate modulation frequencies.

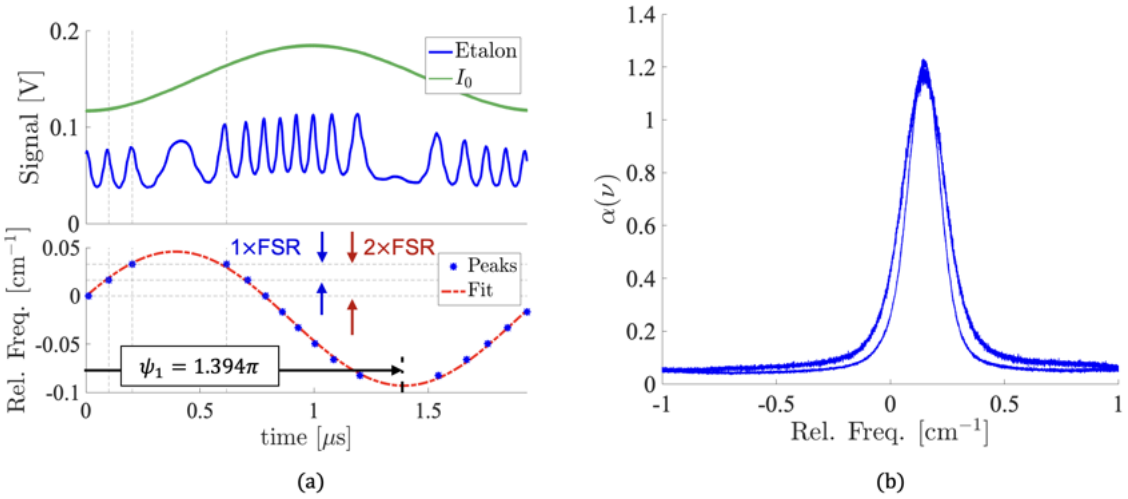

Figure 5.1: (a) Baseline and etalon intensity signals acquired at 500 kHz. (b) Absorbance plotted versus equation 5.15.

f_{mod} [kHz]	Etalon	New Method	% Difference
100	1.274π	1.269π	0.40
200	1.313π	1.302π	0.78
300	1.342π	1.337π	0.37
400	1.369π	1.361π	0.63
500	1.394π	1.400π	-0.38
600	1.418π	1.414π	0.25
750	1.454π	1.452π	0.12
900	1.480π	1.479π	0.12

Table 5.2: Comparison of the relative phase shift ψ_1 as measured by using an etalon signal and the method discussed here with an absorption signal.

5.4 Post-processing

To infer gas properties, background subtracted WMS signals at linecenter are compared to simulated WMS-$2f/1f$ and $-4f/2f$ signals using the calibration-free WMS model. Self broadening parameters in addition to linestrengths are taken from [51] and air broadening parameters are taken from the HITRAN database [43]. A summary of the spectroscopic parameters used is provided in table 5.1.

To perform background subtraction, background intensity signals are acquired in the absence of the absorbing test gas and with the line-of-sight purged from ambient absorption where possible by flowing nitrogen. Background WMS signals are then extracted and vector subtracted from the WMS signals with an absorbing test gas present as described by Rieker et al. [47]. The background subtracted WMS-$2f/1f$ and WMS-$4f/2f$ signals are given by equations 5.16 and 5.17

$$\text{WMS}-2f/1f = \sqrt{\left(\left(\frac{X_{2f}}{R_{1f}}\right)_{\text{raw}} - \left(\frac{X_{2f}}{R_{1f}}\right)_{\text{bg}}\right)^2 + \left(\left(\frac{Y_{2f}}{R_{1f}}\right)_{\text{raw}} - \left(\frac{Y_{2f}}{R_{1f}}\right)_{\text{bg}}\right)^2} \tag{5.16}$$

$$\text{WMS}-4f/2f = \frac{S_{4f}}{S_{2f}} \tag{5.17}$$

where R_{nf} and S_{nf} are the absolute and absorption based magnitudes of the WMS-nf

signal given by equations 5.18 and 5.19.

$$R_{nf} = \sqrt{X_{nf}^2 + Y_{nf}^2} \tag{5.18}$$

$$S_{nf} = \sqrt{((X_{nf})_{\text{raw}} - (X_{nf})_{\text{bg}})^2 + ((Y_{nf})_{\text{raw}} - (Y_{nf})_{\text{bg}})^2}. \tag{5.19}$$

The terms X_{nf} and Y_{nf} are the x- and y-components of the WMS-nf signal and are extracted using a 5th-order Butterworth lowpass filter with a bandwidth of 1.1 MHz following the procedure outline by Sun et al. [59]. Once the background subtracted WMS-$2f/1f$ and WMS-$4f/2f$ signals are extracted, the peak values are determined by using the WMS-$2f$ peaks as a linecenter reference.

Due to using amplified detectors, the frequency dependent gain had to be corrected before inferring gas properties from simulated signals. The WMS-$2f/1f$ and $4f/2f$ peak signals for the laser near 7185.596 cm^{-1} were multiplied by $G_{2f/1f} = 0.95$ and $G_{4f/2f} = 1.85$ and the WMS-$2f/1f$ peak signal for the laser near 6806.03 cm^{-1} was multiplied by $G_{2f/1f} = 1.1$. These gain terms were determined as outlined in [54] but were fine tuned to more closely match the known post-shock static gas properties. Specifically, the $G_{2f/1f}$ value for the laser near 7185.596 cm^{-1} was decreased from 0.985 to 0.95.

Once the background-subtracted WMS signals are extracted and corrected for detector gain, the data can be post-processed using two different methods.

Method 1: This method applies when the gas pressure is known. Look up tables of the WMS-$2f/1f$ signal at linecenter are simulated at the known pressure as a function of species mole fraction and temperature for both transitions. An iterative approach is then employed, where the ratio of WMS-$2f/1f$ signals along with an initial guess for H_2O mole fraction is used to infer a value for temperature. Next, using the WMS-$2f/1f$ signal for the transition at 7185.596 cm^{-1} and the inferred temperature, a value for H_2O mole fraction is determined from the look-up tables and compared to the initial guess. This process is repeated until the inferred values converge. This method is illustrated in the flowchart in figure 5.2 on the left.

Method 2: This method is used when the gas pressure is unknown. In such cases, the WMS-$4f/2f$ signal provides additional information about the collisional width ($\Delta\nu_c$) of each transition. The post-processing procedure involves generating a look-up table for the WMS-$2f/1f$ amplitude at linecenter for each transition, as a function of temperature, collisional width, and H_2O partial pressure. Additionally, for the laser near 7185.596 cm^{-1}, a look-up table for the WMS-$4f/2f$ amplitude at linecenter is

generated as a function of temperature and collisional width. The algorithm begins by using the measured WMS-$4f/2f$ amplitude for the laser near 7185.596 cm^{-1} to estimate $\Delta\nu_{c,1}$ at an initial temperature guess. Since the $4f$ harmonic for the laser near 6806.03 cm^{-1} is outside the detector's bandwidth, $\Delta\nu_{c,2}$ is estimated by scaling $\Delta\nu_{c,1}$ by a factor of 0.75. Next, a look-up table for the two-color ratio of WMS-$2f/1f$ signals is interpolated at the inferred collisional widths. Since the two-color ratio of WMS-$2f/1f$ signals depends only weakly on partial pressure, a constant value is assumed for the purpose of generating the look up table. Temperature is then inferred from the measured WMS-$2f/1f$ ratio and compared to the guessed value. If the two temperature values have not converged, the guessed temperature is updated and the process is repeated. Finally, partial pressure is inferred from the look-up table for the transition near 7185.596 cm^{-1} using the measured WMS-$2f/1f$ signal amplitude, converged temperature, and collisional width. This method is illustrated in the flowchart in figure 5.2 on the right.

Since broadening parameters are available and we know the test gas is a mixture of water vapor and air, we can implement an iterative method to further infer pressure and mole fraction from collisional width and partial pressure. This is done by guessing a value for pressure which is used to compute mole fraction from partial pressure using the relationship $X_{H_2O} = P_{H_2O}/P$. Equation 5.4 is then evaluated for pressure using the inferred collisional width and H_2O mole fraction. This process is iterated until the two pressure values converge. Pressure and H_2O mole fraction inferred by this method are still considered part of method 2.

5.5 Demonstration in shock tube flows

5.5.1 Michigan Hypersonic Expansion Tube (MHExT) Facility

Scanned-wavelength-modulation spectroscopy measurements were acquired in the Michigan Hypersonic Expansion Tube (MHExT) facility, as detailed by Abul-Huda and Gamba [60]. The MHExT features driver, driven, and expansion sections with approximate lengths of 2.29 m, 8 m, and 3 m, respectively, and an inner diameter of about 14 cm. To measure the shock wave's speed and Mach number, two sets of four PCB Piezotronics 113B27 pressure sensors are used — one set in the driven section and one set in the expansion section. Each sensor within a set is evenly spaced by

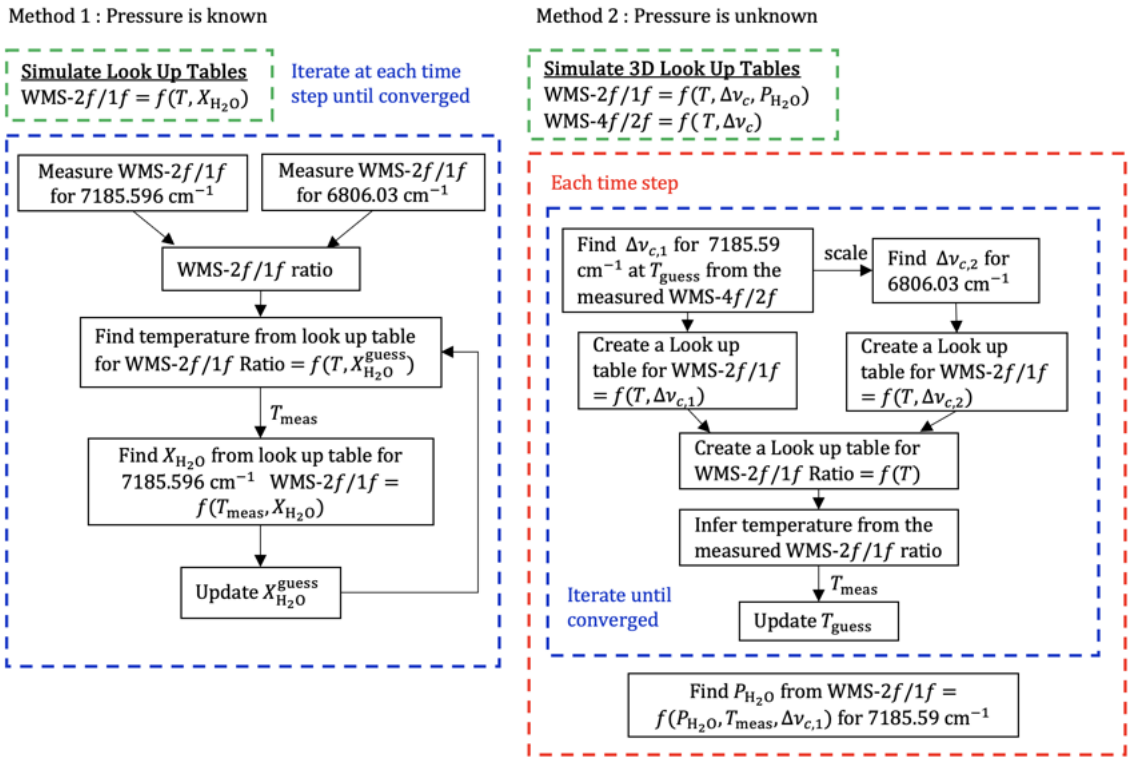

Figure 5.2: Left: Algorithm used to determine temperature and H_2O mole fraction from the WMS-$2f/1f$ signals at a known pressure. Right: Algorithm used to determine temperature and H_2O partial pressure from the WMS-$2f/1f$ and WMS-$4f/2f$ signals.

30.48 cm and sampled at 2 MSa/s.

The LAS sensor is positioned 9.91 m from the driver section and is aligned with the axial location of the first PCB pressure transducer of the set in the expansion section. For the data presented in this manuscript, the driven and expansion sections were not separated by a diaphragm, resulting in an effective driven section length of 11 m. The diaphragm rupture in the driver section was controlled by including a buffer section within the driver section length to allow precise control of the rupture process.

The driver and buffer sections were filled with helium, and the driven section was filled with a mixture of water vapor and air. The mixture was prepared manometri-

cally in a separate heated (30 °C) mixing chamber with a magnetic coupling stirring mechanism. The general procedure was to first vacuum the mixing chamber, fill to the desired H_2O partial pressure, and then fill to the final pressure with air. After allowing some time for mixing, the mixture was transferred into the driven section. This promoted repeatability and uniform mixing.

5.5.2 LAS sensor optics

A schematic of the LAS setup and expansion tube cross-section is shown in figure 5.3. The light from the two DFB NEL laser diodes was combined using a 2x2 50:50 fiber coupler (Thorlabs TW1430R5A2) and collimated to a diameter of 2 mm (Thorlabs F220APC-1310) before being pitched across the expansion tube through 3 mm (0.12 in) thick, 12.7 mm (0.5 in) diameter wedged sapphire windows (Thorlabs WW30530). The light was then collected using an LA1951-C plano-convex lens and focused onto a 150 MHz bandwidth PDA05CF2 amplified detector. To avoid saturation of the detector, it was necessary to add -10dB (FA10T-APC) and -15dB (FA15T-APC) fiber optic attenuators to the path of the laser with transition near 7185.596 cm^{-1} and 6806.03 cm^{-1} respectively before combing with the 2x2 fiber optic coupler. Alignment was controlled using a Thorlabs KC1-S kinematic mount on the pitch optics and a Thorlabs CXY1A XY-translation mount on the catch optics.

Both lasers were sinusoidally scanned over their respective transitions at a rate of 500 kHz producing a measurement rate of 1.0 MHz. The lasers are mounted on laser diode mounts with an external bias-tee connection with an operating range of 10-800 MHz (ILX Lightwave LDM-4984-BTB). Scanning was achieved by connecting the output from a Keysight 33500B series arbitrary waveform generator directly to the laser controller (ILX Lightwave LDC-3908) which controls the nominal temperature and current of the laser diodes. Modulation was applied by connecting the output from a Rigol DG4102 arbitrary waveform generator to the external bias-tee connection. The laser near 7185.596 cm^{-1} was modulated at 35 MHz while the laser near 6806.03 cm^{-1} was modulated at 44 MHz. Both arbitrary waveform generators are time synchronized by connecting the output 10 MHz reference oscillator signal from one to the input of the other. The signal from the photodetector is sampled at 3 GHz by a 12-bit, 2-channel, Econ Express CSE123G2 data acquisition card from GaGe. A summary of the laser controller's set points, and the laser's characterization parameters is provided in table 5.3.

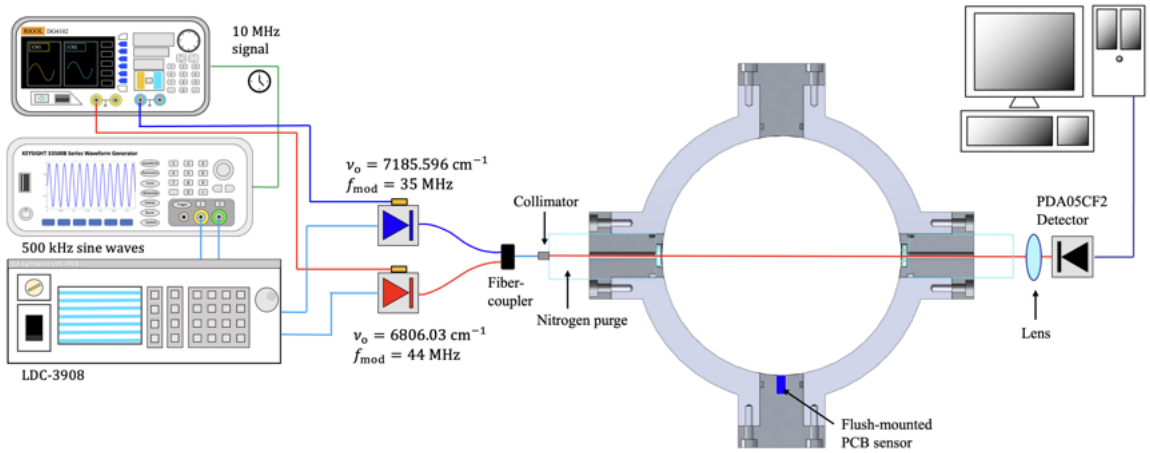

Figure 5.3: Schematic of LAS set up used to acquire static properties behind an incident shock in the MHExT. Pitch and catch optics were built on the plugs using 30 mm cage-mount systems not shown.

Parameter	ν_o = 7185.596 cm^{-1}	ν_o = 6806.03 cm^{-1}
a [cm^{-1}]	0.0901	0.0873
i_0^{up}	0.181	0.211
i_0^{down}	0.275	0.320
i_2	2.24 × 10^{-3}	3.41 × 10^{-3}
ψ_1	1.937π	1.914π
ψ_2	2.47π	2.80π
T_{set} [°C]	23.9	29.43
I_{set} [mA]	99.5	98.67
V_{scan} [V]	0.549	0.510
V_{mod} [V]	4.16	3.0

Table 5.3: Summary of the laser controller set points and laser characterization parameters for scanned - WMS-2f/1f.

5.5.3 Measurements

Scanned-WMS-2f/1f and WMS-4f/2f measurements were collected for three expansion tube operating conditions behind an incident shock at a measurement rate of 1.0

MHz. Table 5.4 summarizes the experimental conditions for the three runs, referred to as runs 1, 2, and 3. The data was post-processed as outlined in section 5.4 using two methods: Method 1, which utilized the known pressure behind the shock wave determined from the incident shock Mach number, and Method 2, which used the WMS-$2f/1f$ and WMS-$4f/2f$ signals to infer temperature and partial pressure.

Figures 5.4 presents time history measurements for run 2 of temperature and H_2O mole fraction inferred from the LAS sensor using Method 1 and for pressure as measured by the PCB sensor. Dashed lines indicate $\pm$ 5% of the expected values determined from normal shock relations and from the mixing chamber fill pressures. The time axis is relative to the arrival of the shock wave. The figure additionally compares the average values of the time history data to the expected values. For all runs, the measured average temperature and H_2O mole fraction values were within 3.5% of the expected values. Error bars represent the 1-σ standard deviation of the time histories.

The data was then post-processed using Method 2 and compared with the average values obtained from Method 1. Figure 5.5(a) displays the WMS-$2f/1f$, -$2f$, and -$4f$ harmonic signals for the laser near 7185.596 cm^{-1}, while figure 5.5(b) shows the time history of temperature and partial pressure inferred using Method 2. Comparison of the time histories for temperature in figures 5.4 and 5.5 reveals that both methods yield essentially the same values. For all runs, temperature and partial pressure inferred by Method 2 where within 5% of the expected values.

Given the availability of broadening parameters, an iterative method was used to determine mole fraction and pressure from the inferred partial pressure and collisional width. Time histories of partial pressure and X_{H_2O} inferred by both post-processing methods for runs 1 and 2 are shown in figure 5.6. We can observe that X_{H_2O} inferred by Method 2 exhibits larger fluctuations compared to the data post-processed using Method 1, even though the partial pressure inferred by both methods shows similar

Run #	P_4 [PSI]	P_1 [Torr]	Ma	P_2 [atm]	T_2 [K]	$P^{MC}_{H_2O}$ [Torr]	P^{MC}_{final} [Torr]	$X^{MC}_{H_2O}$
1	221.9	12.75	4.65	0.419	1499.14	10.1	120	0.084
2	221.2	26.05	4.17	0.687	1265.89	10.6	215.4	0.049
3	223.7	50.05	3.70	1.042	1060.43	15.1	430	0.035

Table 5.4: Summary of fill pressures for the shocktube and mixing chamber (MC), and theoretical post-shock temperature (T_2) and pressure (P_2).

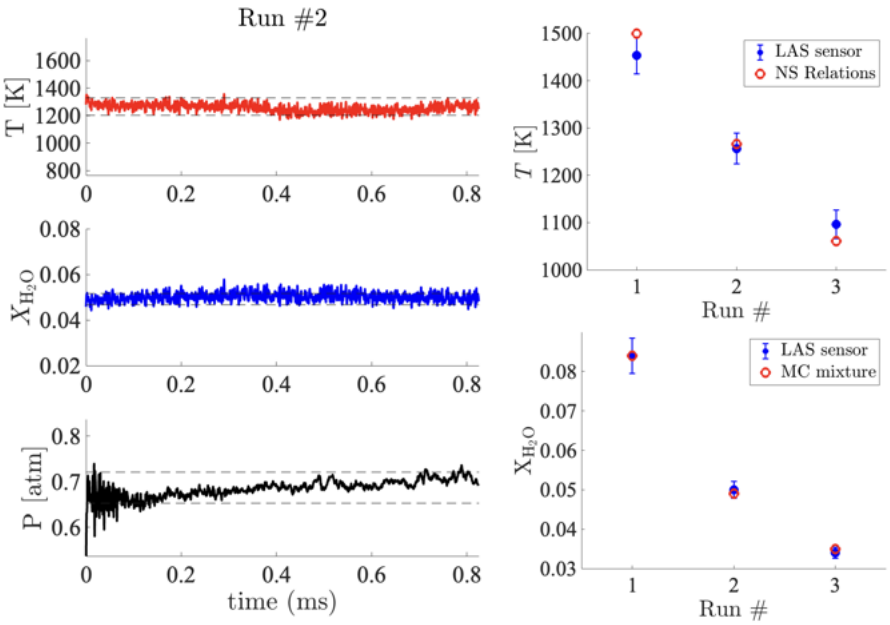

Figure 5.4: Time histories of temperature and H_2O mole fraction inferred for run #2 using post-processing Method 1. On the right, is a comparison of inferred gas properties to the known post-shock temperature and mixing chamber X_{H_2O}. Errorbars represent the 1-σ standard deviation of the time histories.

fluctuation amplitudes. This is primarily because when pressure is underpredicted, mole fraction must increase to maintain the known partial pressure, and vice versa. This shows that while partial pressure can be inferred accurately by both methods, inferring mole fraction from partial pressure and collisional width introduces higher uncertainties than when pressure is known. A summary of the averaged inferred post-incident shock wave gas properties is provided in table 5.5, with $\pm$ values indicating the 1-σ standard deviation.

5.6 Hardware debugging

A key piece of hardware used to obtain MHz-rate scanned-WMS measurements are the laser diode mounts with an external bias-tee connection (ILX Lightwave LDM-4984-BTB). These mounts are initially configured to work with type-1 laser diodes,

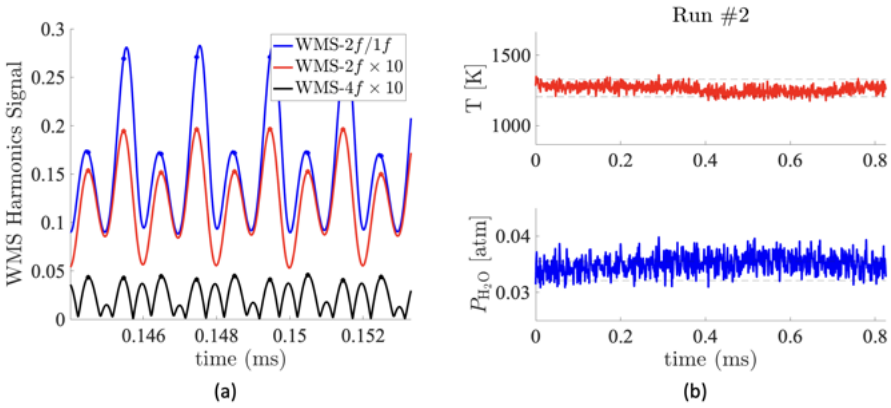

Figure 5.5: (a) Example background subtracted WMS harmonics extracted from run #2. WMS-$2f/1f$ and WMS-$4f$ values are at the WMS-$2f$ peaks location. (b) Inferred temperature and H_2O partial pressure using post-processing method #2.

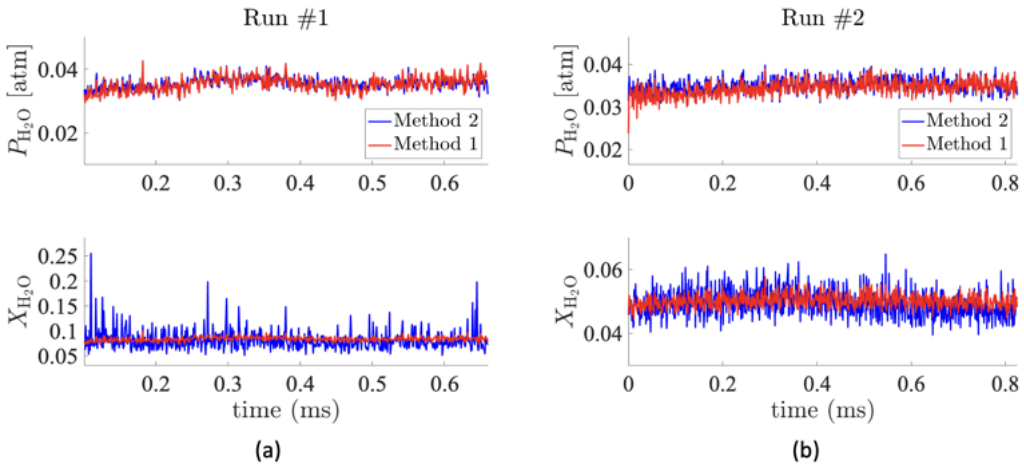

Figure 5.6: Inferred partial pressure and X_{H_2O} for runs #1 and #2 using both post-processing methods. Properties inferred from Method 2 exhibit higher noise characteristics.

which have the laser anode on pin 10 and the cathode on pin 11. However, our laser diodes from NTT Electronics America have the cathode on pin 12 and the anode on pins 11 and 13. This mismatch prevents the application of external modulation via

the bias-tee connection.

Moreover, NTT Electronics America and NewPort Corporation were unable to provide custom wiring solutions for specific laser pin-outs. As a result, the bias-tee LDMs had to be rewired in house to align the bias-tee circuitry with the correct anode and cathode pins. It is important to note that the bias-tee circuitry cannot be modified to accommodate any laser diode pin-out configurations. To the best of our knowledge, the default and custom wiring discussed here are the only possible configurations. Therefore, it is crucial to check the laser pin-out before attempting to use these bias-tee LDMs. The modifications made are outlined below, and the final wiring configuration is summarized in table 5.6.

1. The jumper labeled "B" on the printed circuit board (PCB) had to be unsoldered and the jumper labeled "C" had to be soldered instead.

2. The pin from screw terminal 11 comes cut out of the box to prevent contact with the PCB and needs to be reconnected to the PCB.

3. The inductor-capacitor-resistor (LCR) bridge across pins 10 and 11 needs to be placed across pins 11 and 12 in the same order.

4. The brown wire which would normally be connected to the cathode's screw terminal, is soldered to the LD bias pad.

		T [K]	P [atm]	X_{H_2O}	P_{H_2O} [atm]
Method 1	Run #1	1453.2 ± 39.3	0.421 ± 0.010	0.084 ± 0.0045	0.035 ± 0.0022
	Run #2	1256.6 ± 32.2	0.686 ± 0.020	0.050 ± 0.0021	0.034 ± 0.0018
	Run #3	1096.3 ± 30.1	1.040 ± 0.023	0.034 ± 0.0014	0.036 ± 0.0018
Method 2	Run #1	1450.8 ± 41.6	0.454 ± 0.086	0.082 ± 0.021	0.035 ± 0.0019
	Run #2	1259.6 ± 32.0	0.714 ± 0.069	0.049 ± 0.0042	0.035 ± 0.0017
	Run #3	1107.5 ± 28.6	1.160 ± 0.073	0.033 ± 0.0015	0.038 ± 0.0020

Table 5.5: Summary of the average post- incident shocked wave measured properties from both post-processing methods.

5. The laser anode (pin 11 or 13) was connected to the chassis ground.

In addition to the PCB modifications, we found that the laser controller also affects the laser's stability. For example, scanned-WMS data at kHz rates was successfully obtained using an ILX LDC-3900 laser controller when both modulation and scan waveforms were sent to it. However, when modulation was applied externally through the bias-tee SMA input, the laser's nominal wavelength oscillated because the controller could not stabilize the temperature or current. A similar issue occurred with the ILX LDC-3726 laser diode controller.

To our knowledge, all MHz data published using these bias-tee laser diode mounts have used LDC-3908 laser diode controllers and LDC-3916372 modules with individual modulation ports. In this study, the LDC-3908 was found to effectively control temperature and current without issues. These modifications, including the switch to the LDC-3908 laser controller, resolved all hardware problems encountered while obtaining MHz-rate scanned-WMS data.

However, we did observed differences between older (2017) LDC-3916372 modules and newer (2024) LDC-3916372 modules. The main difference was the newer modules decreased ability to maintain the set current when modulation is applied through the bias-tee, which we compensated for by adjusting the current.

Color	Description	Connected to
Green	Chassis ground	-
Brown	Laser cathode	LD bias pad
Blue	PD cathode	5
Gray	PD anode	4
White	Laser Anode	11
Red	TE+	6
Black	TE-	7
Orange	Therm+	1
Yellow	Therm-	2

Table 5.6: ILX Lightwave LDM-4984-BTB wiring for NTT Electronics America / NEL laser diodes.

Since on NTT Electronics America / NEL laser diodes the anode is connected to ground, it was also necessary to add a jumper from either pins 11 or 13 to the chassis ground.

5.7 Methodology for the measurement of combustion efficiency

5.8 Challenges in measuring combstion efficiency in RDEs

Despite its importance, very few researchers have attempted to measure combustion efficiency [61, 62, 44, 63]. This scarcity is partly due to standard industry gas sampling methods being ineffective for laboratory-scale RDEs, which usually operate for less than 1 second. Additionally, the high heat fluxes associated with these engines, combined with the extreme range of thermodynamic properties over distances of less than 1 mm and time scales of less than 300 µs, make it challenging to measure combustion efficiency based on exhaust flow temperature as recorded by thermocouples. Consequently, more advanced methods are required.

One such method involves using laser absorption spectroscopy (LAS) sensors to obtain high-speed, non-intrusive, *in-situ* measurements of exhaust gas thermodynamic properties. Recently, LAS sensors operating at MHz rates have been demonstrated in rotating detonation rocket engines (RDREs) [54, 64, 65] to measure time-resolved species column densities of CO, CO_2, and H_2O. This work will show that, to infer combustion efficiency, the mole fraction of these species is required. The first reported combustion efficiency measurements using LAS were conducted by Goldenstein et al. [44] for a H_2-air fueled RDE, using average H_2O mole fraction values obtained from a NIR sensor at 50 kHz and a MIR sensor at 10 kHz. A pressure transducer with a 400 kHz bandwidth was used to measure pressure, allowing for the computation of H_2O mole fraction. Peng et al. [63] subsequently extended the MIR sensor to achieve measurements at 20 kHz. Both datasets indicate that combustion efficiency decreases with increasing equivalence ratio, with all reported measurements falling below 60%.

In this work, we present a chemical balance model for H_2-air combustion and derive an equation to infer combustion efficiency based on H_2O mole fraction measurements obtained from LAS sensors. To evaluate the accuracy of combustion efficiency inferred from LAS data, we simulate path-integrated absorption spectra of H_2O transitions near 6806.03 cm^{-1} and 7185.596 cm^{-1} using 3D direct numerical simulation (DNS) data from two RDE geometries operating with H_2-air at an equivalence ratio of 1.0 [66].

LAS measurements typically provide information on temperature, species partial

pressure, and collisional width. However, evaluating combustion efficiency requires measuring species mole fraction, which is dependent on pressure. If pressure is unknown but an accurate spectroscopic database is available, and if the mixture composition can be estimated, then pressure may be inferred from the lineshapes collisional width [67]. In cases where the mixture composition cannot be estimated, as is the case with non-premixed RDEs/RDREs, alternative LAS post-processing methods are needed to infer both pressure and mole fraction. We discuss several such methods.

The first post-processing method is a brute-force approach that utilizes the chemical balance model and known broadening parameters to infer pressure and H_2O mole fraction. This method is detailed further in subsequent sections. The second method uses an iterative approach to simultaneously infer pressure and H_2O mole fraction by assuming a binary mixture of H_2O and N_2. The third method, introduced by Nair et al. [64], infers pressure by estimating gas composition from chemical equilibrium calculations at the exit pressure and CJ-plane entropy $s = s_{CJ}$. This inferred pressure is then used to estimate H_2O mole fraction from partial pressure. The effectiveness of this method is found to be geometry-dependent. The fourth method employs a CTAP measurement at the same axial location as the LAS sensor, thereby avoiding the need for precise broadening parameters. While this method does not allow for direct inference of species or pressure, it provides an average value for H_2O mole fraction. We post-process synthetic LAS data using all four methods and compare the resulting combustion efficiency values to known values from simulations.

5.9 H_2 – Air Combustion Species Model

The mole fractions of H_2 - air combustion product gases at a specified equivalence ratio Φ are uniquely related if we only consider major species that account for >98% of all species present by mole. The chemical reaction can be expressed generally for any combustion efficiency as shown in equation 5.20.

$$\Phi H_2 + \frac{1}{2}\left[O_2 + 3.76N_2\right] \rightarrow \xi H_2O + (\Phi - \xi)H_2 + \frac{1-\xi}{2}O_2 + 1.88N_2 \tag{5.20}$$

This formulation is particularly useful because it allows for expressing the mole fractions of all major species considered as functions of X_{H_2O} and equivalence ratio as shown in equations 5.21 - 5.24.

$$\xi = \frac{X_{H_2O}(\Phi + 2.38)}{1 + X_{H_2O}/2} \tag{5.21}$$

$$X_{H_2} = \frac{\Phi - \xi}{\Phi + (1-\xi)/2 + 1.88} \tag{5.22}$$

$$X_{O_2} = \frac{(1-\xi)/2}{\Phi + (1-\xi)/2 + 1.88} \tag{5.23}$$

$$X_{N_2} = \frac{1.88}{\Phi + (1-\xi)/2 + 1.88} \tag{5.24}$$

From equation 5.20, we can additionally relate combustion efficiency to the moles of H_2O present in the combustion products (ξ). To do this, we start with the combustion efficiency definition based on the fuel mass exiting the RDE which is given in equation 5.25.

$$\eta_c^M = 1 - \frac{\int_{A_{exh.}} \rho u_z Y_{H_2} dA}{\int_{A_{inlet}} \rho u_z Y_{H_2} dA} = 1 - \frac{\dot{m}_{H_2}^{exh.}}{\dot{m}_{H_2}^{inlet}} \tag{5.25}$$

We now express the mass of fuel in terms of moles using the chemical balance given in equation 5.20.

$$\eta_c = 1 - \frac{(\Phi - \xi)\overline{M}_{H_2}}{\Phi \overline{M}_{H_2}} = \frac{\xi}{\Phi} \tag{5.26}$$

A different definition is necessary for fuel rich conditions where part of the fuel introduced cannot form products due to insufficient oxygen. However if we only wish to know the total amount of fuel mass leaving the combustor then the correction can be ignored. Therefore, accounting for both fuel rich and lean conditions, the combustion efficiency can be written as:

$$\eta_c = \begin{cases} \xi/\Phi & \text{if } \Phi \leq 1 \\ \xi & \text{if } \Phi > 1 \end{cases} \tag{5.27}$$

In RDEs, as the detonation wave propagates around the annulus, the air inlet and fuel injectors momentarily stop flowing as the pressure gradient is reversed due to the high-pressure region immediately behind the detonation wave. This coupling between the detonation wave, air inlet, and fuel injector governs mixing and can create localized pockets of rich and lean equivalence ratios depending on their relative

recovery time. Therefore, combustion throughout the annulus occurs at the *local equivalence ratio*, rather than a global equivalence ratio. The equivalence ratio (local or global) at any location can be obtained by solving equations 5.21 and 5.22 to get:

$$\Phi = \frac{2.38(X_{H_2O} + X_{H_2})}{1 - X_{H_2O}/2 - X_{H_2}} \tag{5.28}$$

5.10 Combustion Efficiency Using TDLAS Data

From equation 5.25, it is clear that combustion efficiency is a global performance metric, as it depends on the total fuel mass entering and exiting the combustor. Therefore, to calculate combustion efficiency using equation 5.27, we must first define a global equivalence ratio (Φ^G) and a global H_2O mole fraction ($X^G_{H_2O}$) that represent the flow exiting the combustor. Φ^G is determined from the air and fuel mass flow rates. $X^G_{H_2O}$, which is used to evaluate equation 5.21, is defined by equation 5.29, where N is the number of moles and J is the number of cells at the exhaust plane in the CFD simulations.

$$X^G_{H_2O} = \frac{\sum_{j=1}^{J} N^j_{H_2O}}{\sum_{j=1}^{J} N^j} \tag{5.29}$$

This equation can be rewritten in terms of the total mass flow rate and mass fractions as shown in equation 5.30.

$$X^G_{H_2O} = \frac{\sum_{j=1}^{J} \dot{m}^j Y^j_{H_2O}/\overline{M}_{H_2O}}{\sum_{j=1}^{J} \dot{m}^j/\overline{M}^j_{mix}} \tag{5.30}$$

We now express the mass fraction Y_{H_2O} in terms of the mole fraction X_{H_2O}.

$$X^G_{H_2O} = \frac{\sum_{j}^{J} \dot{m}^j X^j_{H_2O}/\overline{M}^j_{mix}}{\sum_{j}^{J} \dot{m}^j/\overline{M}^j_{mix}} \tag{5.31}$$

Since RDEs produce unsteady and spatially nonuniform flowfields, we do not know the mass flow rate at each measurement location nor do we know the molecular weight. It is then clear that equation 5.31 can only be evaluated using CFD data or from experimental measurements if the exhaust flow is uniform. To arrive at a

result where we can evaluate equation 5.31 with the information we can obtain from LAS data, it is necessary to assume (1) a constant mass flow rate at all measurement locations and (2) a constant mixture molecular weight and therefore a uniform gas constant ($\mathcal{R} = \mathcal{R}_{\text{univ}}/\overline{M}$). The final result is simply that the global H_2O mole fraction for experimental (albeit synthetically generated) data assuming constant mass flow rate and gas constant $\mathcal{R}$ is the average mole fraction for the cycle:

$$\overline{X}_{H_2O} = \frac{1}{J}\sum_{j=1}^{J} X^j_{H_2O} \tag{5.32}$$

Combustion efficiency using LAS data is then given by equation 5.33 where the bar indicates that equation 5.21 has been evaluated with $X_{H_2O} = \overline{X}_{H_2O}$.

$$\overline{\eta}_c = \frac{\overline{\xi}}{\Phi^{\text{G}}} \tag{5.33}$$

Since the LAS data will be processed in four different ways, we will reserve $\overline{\eta}_c$ for LAS data processed from the brute force method, whereas a superscript N_2 will be added to measurements obtained from the iterative method that assumes a binary mixture of H_2O-N_2, a superscript s_{CJ} will be added to measurements inferred from LAS data processed by estimating the exhaust gas composition from equilibrium simulations at constant (s_{CJ}, P), and finally, a superscript CTAP will be added to measurements obtained from LAS data processed using a CTAP measurement. Note that all four of these combustion efficiency values are computed using the same definition but a different LAS post-processing technique that produces a different value for $\overline{X}_{H_2O}$. A summary of the different definitions of combustion efficiency developed here and their description is provided in table 5.7.

One thing to note is that in equation 5.32, J is the number of LAS measurements obtained at the exhaust plane at one instant in time. In LAS experiments however, data is acquired at one measurement location over time. If we assume that the detonation wave is propagating in the annulus steadily at an angular frequency ω_{CJ}, then we can show for any measurement Q_i that $Q_i(t + \Delta t,\theta) = Q_i(t,\theta + \omega_{CJ}\Delta t)$. This assumption is commonly employed in the analysis of RDEs and implies that our measurements of combustion efficiency are not affected by acquiring LAS data at a fixed location over time instead of at many locations at one instant in time.

Symbol	Description
η_c^{M}	This is the fuel mass-based definition computed directly from CFD data using equation 5.25
$\overline{\eta}_c$	This definition is computed using equation 5.33 with $\overline{X}_{\mathrm{H_2O}}$ calculated from LAS data post-processed using the brute force method
$\overline{\eta}_c^{\mathrm{N_2}}$	This definition is computed using equation 5.33 with $\overline{X}_{\mathrm{H_2O}}$ calculated from LAS data post-processed assuming a binary mixture of H_2O-N_2
$\overline{\eta}^{s_{CJ}}$	This definition is computed using equation 5.33 with $\overline{X}_{\mathrm{H_2O}}$ calculated from LAS data post-processed by estimating the equilibrium gas composition at constant (s_{CJ}, P)
$\overline{\eta}_c^{\mathrm{CTAP}}$	This definition is computed using equation 5.33 with $\overline{X}_{\mathrm{H_2O}}$ calculated from LAS data post-processed using a CTAP measurement

Table 5.7: Summary and description of all the combustion efficiency definitions used in this manuscript.

5.11 Post-Processing of TDLAS data

Synthetic absorption spectra were simulated using equation 5.2 with data from high-fidelity 3D-DNS simulations of the UM RDE geometry with an axial air inlet and the AFRL geometry with a radial air inlet [66]. A summary of the simulation conditions is provided in table 5.8. For specific details regarding the numerical simulation approach see [66].

Configuration	Case #	$\dot{m}_{\mathrm{air}}$ [g/s]	$\dot{m}_{\mathrm{fuel}}$ [g/s]	Φ^{G}
UM	1	404.2	11.9	1.01
AFRL	2	320	9.3	1
	3	630	18	1
	4	860	25	1

Table 5.8: Summary of the simulation nominal flow rates and global equivalence ratios for each case.

A least-squares Voigt profile fitting routine was employed in which $\Delta\nu_{\mathrm{c}}$, A_j, and ν_{o} were varied at a fixed temperature. Using the best-fit parameters, temperature is

inferred from the two-color ratio of integrated absorbances and H_2O partial pressure is inferred using equation 5.8.

Since combustion efficiency measurements depend on measuring $\overline{X}_{H_2O}$, we further post-process the data using a brute force method that uses the known collisional width $\Delta\nu_c$ from the best-fit parameters, the inferred partial pressure, and broadening parameters. This method involves residual minimization subject to imposed constraints. For instance, the inferred pressure defines X_{H_2O} through the relationship $X_{H_2O} = P_{H_2O}/P$. If equivalence ratio is further specified, X_{H_2}, X_{N_2}, and X_{O_2} are given by the chemical model. These mole fraction values along with broadening parameters and the inferred temperature can be used to determine the collisional broadening coefficient (γ_{mix}), which when combined with the lineshapes collisional width defines pressure through equation 5.4. Using these constraints, we test pairs of (P, Φ) to search for the minimum residual between the two pressure values.

To reduce the search space further, we use a linear correlation for $P = k\Delta\nu_c$ obtained from simulations to estimate pressure from collisional width alone. Pressure is constrained within 25% of the initial guess and is allowed to vary in increments of 0.05 atm. The increments in equivalence ratio are such that H_2O mole fraction changes by 2%. Combustion efficiency $\overline{\eta}_c$ is then determined as outlined in the previous section.

A simpler and more efficient iterative method is also implemented. In this method of post-processing the data we assume a binary mixture of H_2O and N_2. This is a reasonable assumption to make for H_2-air combustion in which nitrogen and H_2O can account for more than 80% of the mixture by mole at lean and rich equivalence ratios. The same relationships have to be satisfied as in the brute force method but due to the binary mixture assumption, equivalence ratio is now irrelevant. A flowchart representation of the simulation procedure, and LAS post processing procedures described above is shown in figure 5.7.

Other researchers have inferred pressure by estimating the post-detonation gas composition from CANTERA simulations and the Shock & Detonation Toolbox. Specifically, Nair et al. allows the post-detonation gas to equilibrate at constant entropy (s_{CJ}) and pressure (1 atm) and then uses the equilibrium gas composition along with equation 5.4 to infer pressure. We extend this approach to infer species using the relationship $X_{H_2O} = P_{H_2O}/P$.

To eliminate the need for broadening parameters and their associated uncertainty contributions to the inferred combustion efficiency, as well as decrease computational time, $\overline{X}_{H_2O}$ is also estimated from the time history of partial pressure and a CTAP

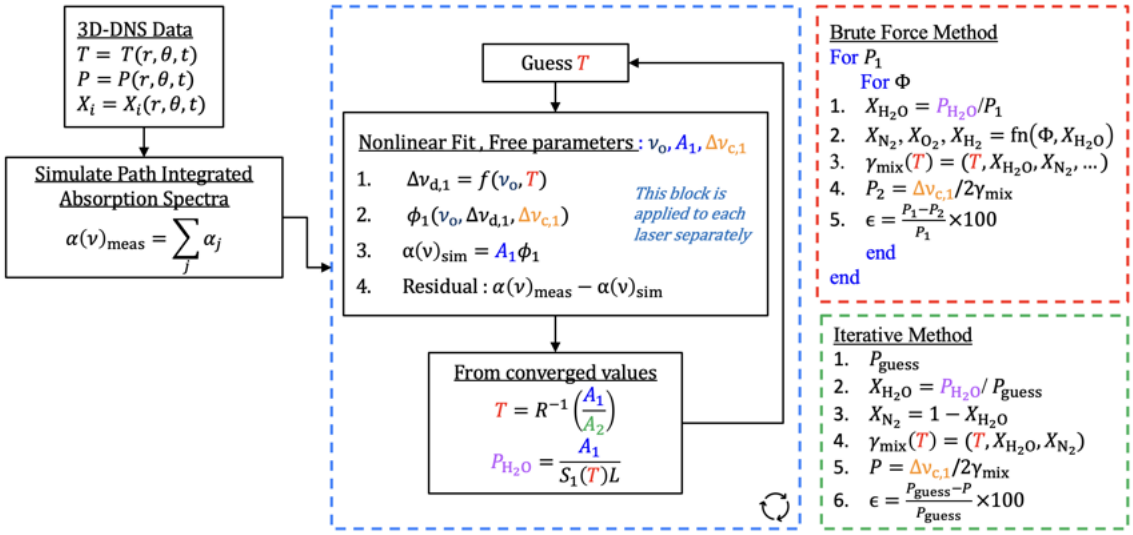

Figure 5.7: Flowchart representation of the absorption spectra simulation procedure and data post-processing procedure for inferring temperature and species partial pressure. The algorithms for the brute force method and iterative method are also shown.

measurement at the same axial location. Mathematically, $\overline{X}_{H_2O} = \overline{P}_{H_2O}/P_{CTAP}$. Here, $\overline{P}_{H_2O}$ is the time averaged partial pressure and the CTAP measurement is taken to be the wall area-averaged pressure. We process the data using the four approaches to draw comparisons.

5.12 Synthetic TDLAS Combustion Efficiency Measurements

Shown in figure 5.8 are the inferred pressure profiles for the axial air inlet (AAI) (case #1) and the radial air inlet (RAI) (case #2) RDE geometries inferred from: (1) the brute force method, (2) the collisional width and equilibrium gas composition at constant (s_{CJ},P), and (3) using the iterative method assuming a binary mixture of H_2O and N_2. For both geometries, the pressure inferred by estimating the gas composition ($P^{s_{CJ}}$) is lower than that from the brute force method (P^{BFM}). If we consider P^{BFM} to be the correct value, by comparing the residual for both geometries we note that

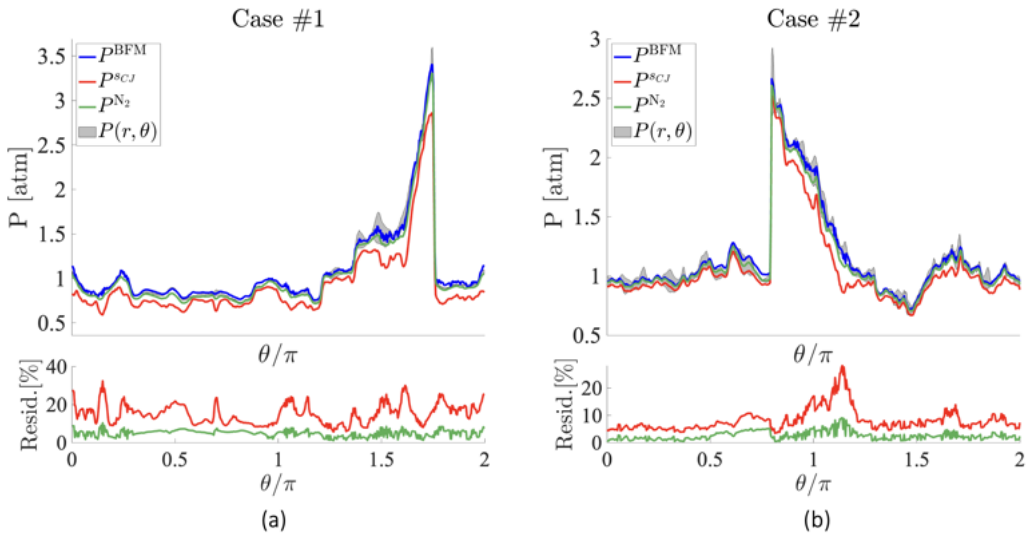

Figure 5.8: Comparison of pressure inferred by the brute force method (P^{BFM}), by estimating the gas composition (P^{sCJ}), and by assuming a binary mixture of H_2O-N_2 (P^{N_2}): (a) case 1, and (b) case 2. $P(r,\theta)$ is the radial and azimuthal variation in pressure at the particular time taken from the original DNS simulation. The residual shown is relative to P^{BFM}.

estimating the equilibrium gas composition gives better results for the RAI geometry. This geometry dependence can be attributed to the mixing properties of each inlet and the degree of fuel/air stratification at the exhaust. The more uniformly mixed reactants produced by the RAI allows the exhaust flow to be better approximated by a single equivalence ratio. Consequently, this method should not be applied to process LAS data from geometries with poor mixing, such as the AAI geometry. Regardless, using P^{sCJ} will overestimate H_2O mole fraction and therefore combustion efficiency. It is worth mentioning that this method was originally used to infer pressure from a cluster of CO lines near 4.98 μm which have collisional broadening coefficients (γ_{mix}) that are less sensitive to gas composition at the operating conditions leading to better results [64, 67]. Therefore, in addition to being geometry dependent, this method is also dependent on the transitions being probed for species detection.

Also shown in figure 5.8 is the pressure trace as determined by the iterative method in which a binary mixture composition of H_2O and N_2 was assumed. This method

produced results comparable to the brute force method with residuals on average less than 5% for the AAI geometry and less than 3% for the RAI geometry. The effectiveness of this method arises from the fact that H_2O and N_2 together account for over 80% of the mixture by mole for equivalence ratios between 0.5 and 1.5. While the exact percentage varies with combustion efficiency, it primarily affects rich equivalence ratios; even with a combustion efficiency of 60%, the combined mole fraction remains above 70%. Therefore, this method is the recommend approach for post-processing LAS data obtained in H_2-air RDEs to infer X_{H_2O} and pressure because of its simpler and faster post-processing technique. While the discussion thus far has focused on pressure, it is important to remember that our primary interested in is X_{H_2O}, which is calculated as P_{H_2O}/P.

Figure 5.9 compares the average combustion efficiency as determined from the different methods discussed previously and summarized in table 5.7. All definitions are generally within the uncertainty of each other except for $\overline{\eta}_c^{s_{CJ}}$ which overpredicts combustion efficiency for all four cases as a direct consequence of the post-processing method underpredicting pressure. Although $\overline{\eta}_c$, $\overline{\eta}_c^{N_2}$, and $\overline{\eta}_c^{CTAP}$ predict essentially the same value, the effects of the uncertainty in the inferred collisional width and broadening parameters are not considered. Including these effects make inferring species and pressure accurately using the brute force method challenging. For this reason, combustion efficiency should be inferred from either the iterative method assuming a binary mixture composition if an accurate spectroscopic database is available, or from the CTAP method. Note that the iterative method also makes use of broadening parameters but it eliminates the uncertainty due to γ_{air}, γ_{H_2}, and Φ. However, the CTAP method is the preferred choice for determining combustion efficiency as it avoids using any broadening parameters. Additionally, Guerrero and Gamba demonstrated that the inferred species mole fraction exhibits a higher standard deviation when derived from the iterative method compared to when the known pressure is utilized to post-process the same data [68]. Therefore, measuring X_{H_2O} should be avoided when possible if pressure is unknown.

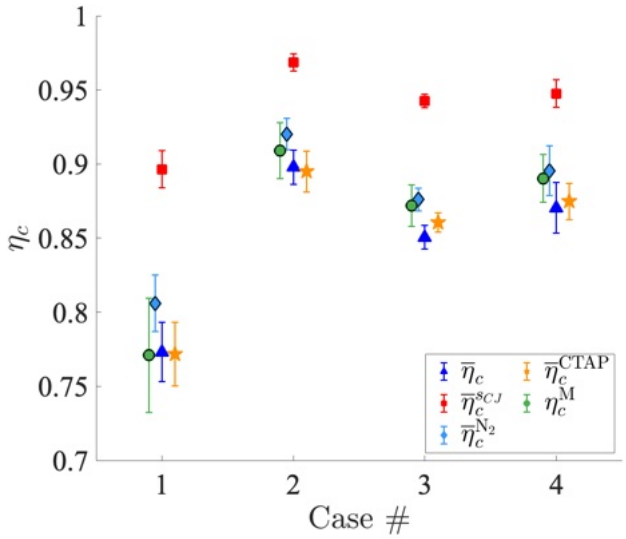

Figure 5.9: Comparison of combustion efficiency inferred from synthetic LAS measurements processed using the brute force method (blue), by estimating the exhaust gas composition (red), using a CTAP measurement (orange), and assuming a binary mixture of H_2O-N_2 (light blue). Combustion efficiency inferred from the CFD data is shown as a reference.

5.13 Demonstration of MHz-rate measurements temperature and combustion efficiency in an RDE

5.14 Introduction

This section presents TDLAS measurements acquired in our nominal 6-inch rotating detonation engine. The sensor design, data post-processing, and validation procedures were previously detailed in section 5, while the methodology for inferring combustion efficiency from TDLAS data was introduced in section 5.7. Here, the sensor is used to obtain measurements in an RDE at the exhaust throat at a measurement rate of 1 MHz. The following subsections describe the RDE configuration, the optical setup, operating conditions, and the resulting measurements.

5.15 Description of RDE

A detailed description of the facility and RDE geometry can be found in [12, 69]. Here a brief overview is provided. Testing was performed on our nominal 154 mm (6 in) outer diameter, axial air inlet RDE with an inlet-to-channel area ratio ($A_{3.1}/A_{3.2}$) of 0.22 and a 50% exit area constriction relative to the channel ($A_8/A_{3.2}$). The channel gap width is 7.6 mm (0.3 in) and the channel length is 110 mm (4.35 in).

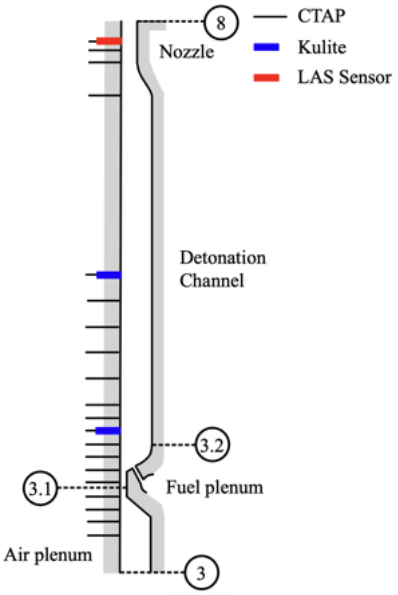

Figure 5.10: Schematic diagram of the instrumentation on the outer body of the RDE used in this study.

Air is supplied from a high-pressure line and is reduced to the required pressure upstream of a sonic nozzle with a throat diameter of 1.4 cm (0.550 in) to control the mass flow rate. An Emerson coriolis flowmeter is located upstream of the sonic nozzle, providing an additional measurement of the air mass flow rate. The two measurements generally agree within 2%. Air is introduced into the RDE air plenum radially via flexible hoses where it is then directed axially into the RDE channel. The fuel mass flow rate is controlled in a similar manner by setting a pressure upstream of a sonic orifice with a known discharge coefficient. Fuel is then introduced into the channel through 120 equally spaced holes, each 0.89 mm (0.035 in) in diameter, positioned at an angle of 30 degrees. Ignition is achieved using a H_2-O_2 predetonator tube which fires a detonation wave tangentially into the RDE channel.

The outer body is instrumented with 16 CTAPs all at the same azimuthal position to measure the axial variation in the average pressure along the length of the channel. Four additional CTAPs are placed near the inlet and throat of the converging exit nozzle to obtain a cycle-averaged exit pressure (p_8). CTAPs 1-16 are at -90° from the LAS sensor, while CTAPs 17-20 are at -45°.

In addition to the CTAP measurements, flush mounted high-speed water-cooled Kulite-EWCTV pressure transducers are placed in the channel to resolve the pressure time trace produced by the detonation wave. These are placed at the same azimuthal location as the LAS sensor. Additional high-speed Kulite-XTL pressure transducers

are placed in the air and fuel plenums. A schematic showing the axial position of all sensor and station numbering is shown in figure 5.10.

High-speed video obtained from a Phantom TMX5010 camera looking upstream of the detonation channel is used to determine the detonation wave speed and operating mode during post-processing [70]. Video is acquired at 50,000 fps with an exposure time of 19 μs and a resolution of 768 x 640 pixels capturing a field of view of approximately 253 mm x 210 mm.

5.16 LAS Sensor Description

The optical assembly was designed for the single-ended technique [63, 71, 49], where the laser beam is reflected off the inner body of the RDE and directed back to the detector. The optical assembly is comprised of off-the-shelf optomechanical components from Thorlabs and is entirely assembled and mounted on a custom cube that secures to the RDE via setscrews. This design allows it to be removed without disassembling or misaligning the optics. The catch optics are further tilted to be concentric with the reflected beam which allows for more effective blocking of stray reflections. A SolidWorks rendering of the sensor design is shown in figure 5.11 and a schematic of the experimental set up is shown in figure 5.12. Part numbers for components purchased from Thorlabs are provided in parenthesis in the description that follows.

The light from the two lasers is fiber-coupled onto a polarization-maintaining single-mode fiber (P3-1310PM-FC-5) using a 2x2 50:50 fiber coupler (TW1430R5A2). This laser light is then collimated to a diameter of 1 mm with a fixed-focus collimator (F110APC-1310) and directed into the RDE by a 5 mm right-angle prism mirror (MRA05-G01) at an angle of 4 degrees. A standard 25.4 mm diameter wedged (30 arcmin) sapphire window (WW31050) is used. The window is supported by o-rings above and below as well as the sides. It is recessed mounted resulting in a path length of approximately 1.3 cm.

The alignment of the optics is managed with a kinematic mount, allowing for tip/tilt adjustments (KC1T). The light reflected out of the RDE passes through an iris to block reflections from the window, a plano-convex lens (LA1131-C) mounted on a translational stage (CXY1A), and is finally collected by a 150 MHz bandwidth amplified biased detector (PDA05CF2). The signal from the photodetector is sampled at 3 GHz using a high-speed digitizer (GaGe Econ Express CSE123G2 data acquisition card). To avoid saturation of the detector, it was necessary to add -10dB

(FA10T-APC) and -15dB (FA15T-APC) fiber optic attenuators to the path of the laser with frequency near 7185.596 cm^{-1} and 6806.03 cm^{-1} respectively before combing with the 2x2 fiber optic coupler. Although not shown in the schematic provided in figure 5.12, the entire optical assembly up to the plano-convex lens is purged from ambient moisture by continuously flowing nitrogen into the volume which is sealed with aluminum tape.

Scanning of the injection current is achieved by connecting the output 500 kHz sine wave signals (phase synchronized) from an arbitrary waveform generator (Keysight 33500B) directly to the laser controller (ILX Lightwave LDC-3908) resulting in a mesurement rate of 1 MHz. The lasers are mounted on laser diode mounts with an external bias-tee connection with an operating range of 10-800 MHz (ILX Lightwave LDM-4984-BTB). Injection current modulation is applied by connecting the output from a second arbitrary waveform generator (Rigol DG4102) to the external bias-tee connection. Both arbitrary waveform generators are time synchronized by connecting the output 10 MHz reference oscillator signal of one of them to the input of the other. Several hardware modifications to the bias-tee LDMs were necessary to achieve the intended functionality and are discussed in Guerrero and Gamba [68].

5.17 RDE Operating Conditions

A summary of the tested RDE conditions and mode of operation is provided in table 5.9. All runs are for hydrogen-air mixtures. The tested conditions are a sweep in $\Phi = [0.6 - 1.5]$ at a fixed air mass flowrate $\dot{m}_{\text{air}} \approx 150[\text{g/s}]$. Followed is a sweep in mass flowrate $\dot{m}_{\text{air}} = 150 - 350[\text{g/s}]$ at a fixed equivalence ratio $\Phi \approx 0.85$. Most runs operated with 2 co-rotating detonation waves or 2 pairs of counter-rotating waves (4 waves total). Normalized wavespeed ratios for runs with $\dot{m}_{\text{air}} < 225[\text{g/s}]$ were around $D/D_{\text{CJ}} \approx 0.5 - 0.6$ while runs with higher air mass flowrates had wavespeed ratios around 0.75. Additionally, from examining run numbers 3433, 3434, and 3443, we can observe a decrease in wave speed with increasing number of waves which is a well known phenomena in the PGC community.

5.18 Measurements

Scanned WMS-$2f/1f$ and $-4f/2f$ signals were acquired at the exit throat of our rotating detonation engine and post-processed as described in Section 5.4. Figure

run	$\dot{m}_{\text{air}}$	Φ	N_{waves}	D/D_{CJ}	$P_{\text{air,pl.}}$ [kPa]	$P_{\text{ch.}}$ [kPa]	P_8 [kPa]
3423	149	0.59	2	0.56	143.9	119.7	99.3
3424	149	0.65	2	0.56	146.0	121.1	99.7
3426	149	0.85	4	0.52	151.2	123.2	98.8
3429	151	1.06	2	0.52	155.0	128.5	99.5
3431	149	1.28	2	0.52	157.2	129.7	99.6
3432	151	1.26	2	0.52	157.0	129.9	99.5
3433	151	1.46	1	0.63	162.1	134.0	100.1
3434	151	1.48	2	0.51	159.4	132.0	99.8
3435	202	0.84	4	0.54	184.2	146.9	100.5
3436	203	0.85	4	0.54	184.8	147.2	101.0
3439	252	0.84	2	0.75	226.9	175.1	106.4
3441	304	0.83	2	0.75	269.2	206.2	113.6
3443	357	0.81	2/3	0.75 / 0.61	314.9	242.0	128.0
3450	255	1.01	2	0.73	235.1	182.4	106.4
3455	202	1.03	4	0.53	191.5	153.1	102.3

Table 5.9: Summary of tested RDE conditions and mode of operation.

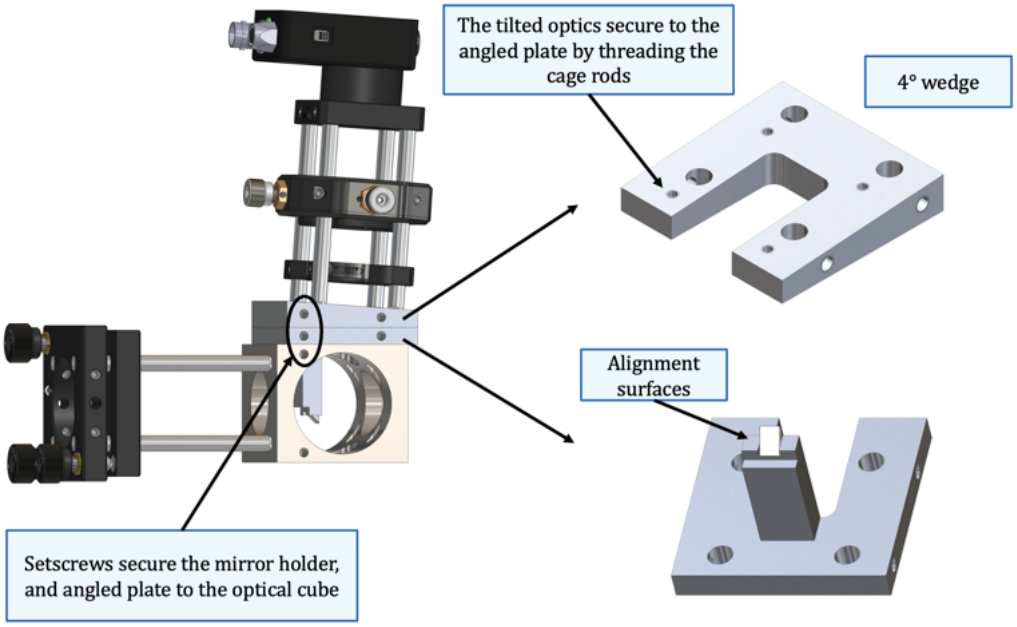

Figure 5.11: SolidWorks rendering of the sensor assembly.

5.13 shows representative WMS-$2f/1f$ and $-4f$ signals on the left, with linecenter peaks marked by circles, and time-series data of these linecenter peaks on the right. For clarity, only the down-scan peaks are displayed.

Figure 5.14 presents time-series measurements of temperature and H_2O partial pressure at a measurement rate of 1 MHz. Due to the short path length and harsh operating conditions, the data exhibit large-amplitude fluctuations. These fluctuations can be attributed to measurement noise but may also reflect actual physical variations caused by sharp gradients in gas properties and spatial non-uniformity. Also shown in Figure 5.14 is the same data after applying a moving average filter with a 10-point window. This filtered data more clearly reveals the detonation wave structure, as indicated by the sharp rises in temperature and partial pressure.

From the time-resolved temperature and P_{H_2O} measurements, time-averaged statistics and combustion efficiency are computed using the methodology described in section 5.7. These values are summarized in table 5.10, and selected results are plotted in figure 5.15 to facilitate comparison. Figure 5.15(a) shows the peak and average tem-

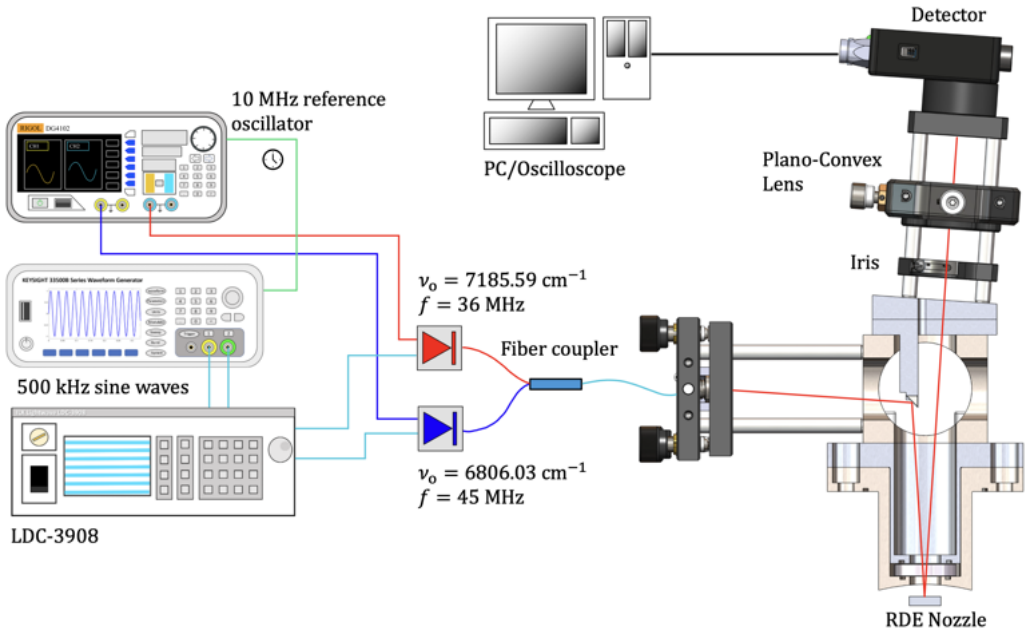

Figure 5.12: Schematic diagram of the tunable diode laser absorption spectroscopy optical assembly for scanned-WMS measurements in the RDE.

peratures—averaged over all steady wave cycles for which data was collected—plotted against equivalence ratio. Both temperature statistics increase with equivalence ratio. Although we might expect a maximum near stoichiometric conditions, the complex flowfield interactions in RDEs can alter the local equivalence ratio at which combustion occurs. Error bars represent the combined uncertainty from sensor accuracy and cycle-to-cycle variation, computed as error^2 = accuracy^2 + (standard deviation)^2.

Figure 5.15(b) plots peak temperature versus combustion efficiency. Despite the measurement uncertainty, at a fixed equivalence ratio, peak temperature increases with combustion efficiency. This is consistent with physical expectations, as combustion efficiency reflects the degree of heat release. Uncertainty in combustion efficiency incorporates contributions from the measured water vapor partial pressure, the global equivalence ratio, and azimuthal variations in the static pressure measurement. Future work will attempt to estimate pressure gain and other performance metrics.

run	T_{avg} [K]	T_{peak} [K]	$T_{\text{peak}}/T_{\text{CJ}}$	η_{c}
3423	1434	1606	0.66	0.62
3424	1446	1642	0.65	0.55
3426	1611	1789	0.63	0.55
3429	1568	1772	0.59	0.50
3431	1638	1854	0.62	0.57
3432	1654	1874	0.63	0.60
3433	1455	1750	0.60	0.55
3434	1574	1793	0.62	0.56
3435	1455	1634	0.58	0.55
3436	1490	1676	0.59	0.53
3439	1588	1722	0.61	0.64
3441	1633	1779	0.63	0.71
3443	1513	1673	0.60	0.59
3450	1631	1777	0.60	0.61
3455	1499	1669	0.56	0.48

Table 5.10: Summary of time-averaged temperature statistics and combustion efficiency.

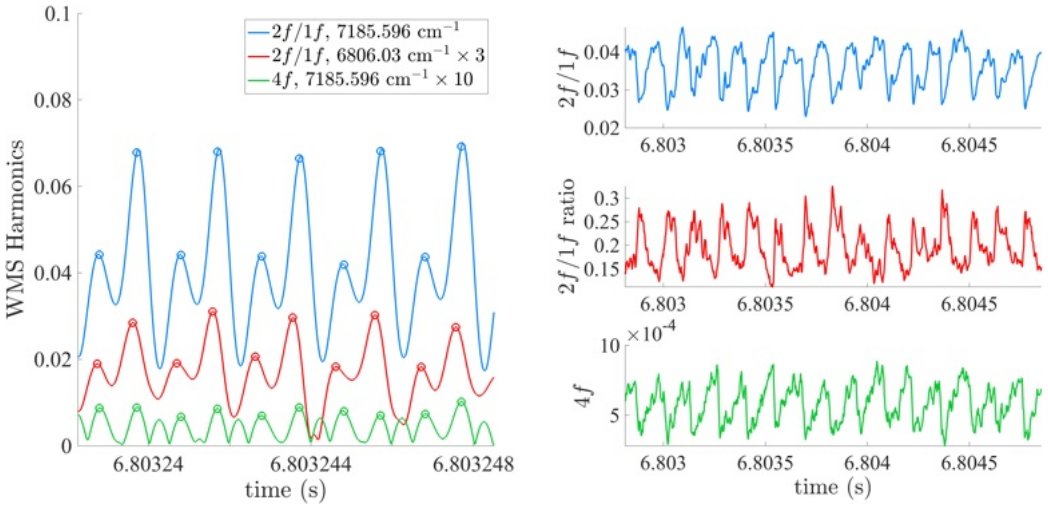

Figure 5.13: Scanned-WMS harmonics extracted from the transmitted intensity signal, uncorrected for the detectors gain. The data was smoothed using a moving average filter of 5 points.

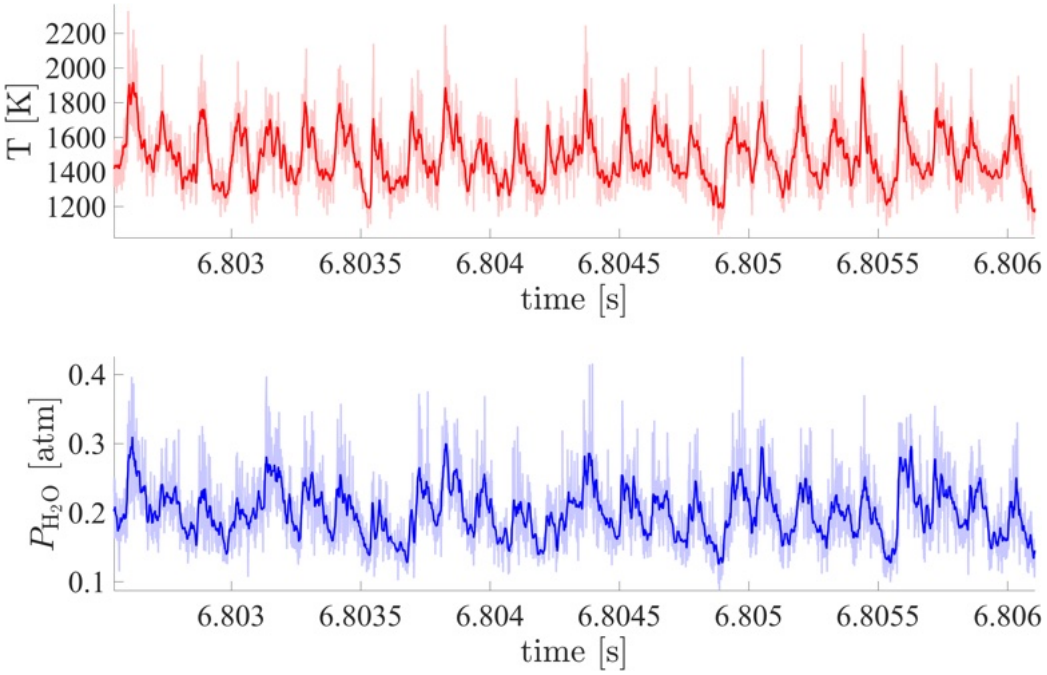

Figure 5.14: Time-resolved temperature and H_2O partial pressure for run 3443. The light-colored time trace is the raw data, and the darker trace is data that has been filtered using a moving average filter of 10 points.

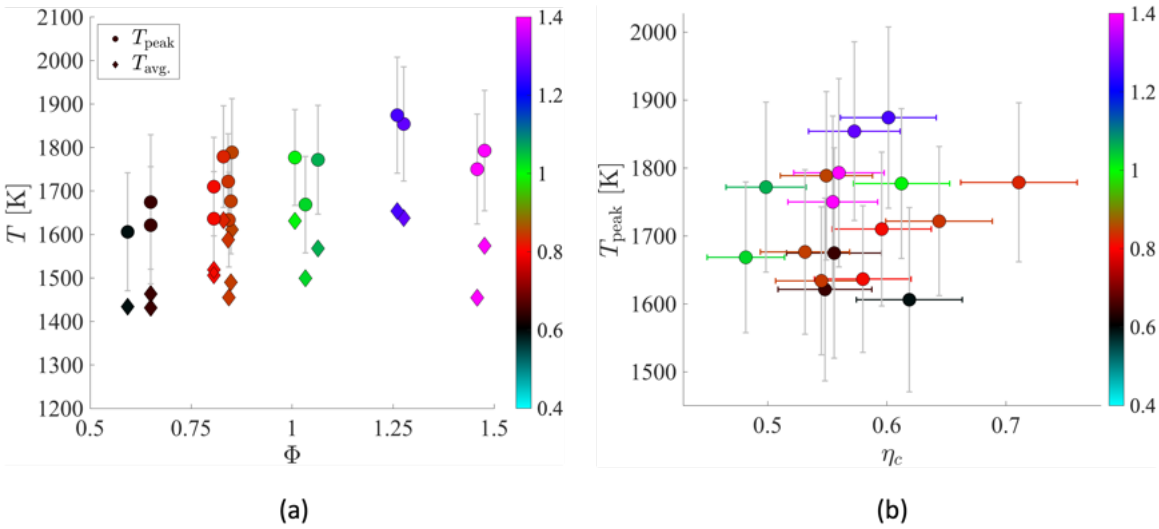

Figure 5.15: (a) Peak and average temperature values averaged over all wave cycles. (b) Average peak temperature values versus combustion efficiency.

Chapter 6

State-to-State Model for RDE Performance Estimation

One must be careful not to associate detonation performance with the system-level performance of a device utilizing detonation combustion. For this reason, the two will be discussed in separate chapters, where this chapter focuses solely on loss mechanisms and performance metrics specifically related to the performance of the detonation wave. Along with discussing the existence of these loss mechanisms, this chapter also provides simple models to examine the effects of each loss on the detonation wave. Finally, the concluding remarks will give opinions on the most impactful loss mechanisms and offer potential remedies.

Before defining detonation performance and associated metric, one should review Table 6.1 for a list of state locations of interest within the detonation wave and the RDE cycle. This chapter will focus primarily on contributions modeling states (3_p)-(3.3), which include the state just ahead of the detonation wave to a state just downstream of the post-detonation expansion.

State	Label	Description
Plenum	3	Plenum condition assuming premixed.
Post-Injector	$3'$	Inlet injection state after inlet pressure drop
Post-Parasitic Combustion	3_p	Pre-detonation state after parasitic combustion
von-Nuemann (VN)	3.1	Post-shock von-Nuemann condition accounting for leaked fuel
Chapman-Jouguet (CJ)	3.2	Post-detonation state accounting for leaked fuel
Post-Expansion	3.3	Post-detonation state after isentropic expansion accounting for detonation work
Post-Commensal	3.4	Post-expansion state after equilibration at a post-expansion pressure accounting for non-commensal fraction and commensal combustion pressure fraction
RDE Exhaust	4	State from which work may be extracted

Table 6.1: Description of States used in Detonation Cycle Analysis

6.1 Description of Detonation Wave Performance and Loss Mechanisms

To characterize the quality of a detonation wave, a few key performance metrics have been defined and used widely in the detonation field. The main two metrics of interest discussed in the literature are the wave speed and the wave pressure ratio, D and PR, respectively. Typically, these measured values are normalized by their ideal CJ value to ascertain how close to ideal is the detonation wave of interest, $\frac{D}{D_{\text{CJ}}}$, and $\frac{PR}{PR_{\text{CJ}}}$. Both of these metrics provide a methodology for comparing measured data to the ideal, one-dimensional CJ detonation properties.

Another metric that will be defined in more detail later is the fraction of fuel consumed in the detonation wave. Think of this term as a marker of combustion efficiency for the detonation wave itself. Ideally, 100% of the input fuel gets processed by the detonation wave; however, literature has shown this is not always the case in the RDE application.[24, 22, 72, 4] This metric will directly affect the prior two

performance metrics negatively, with more details on this exact relationship between the metrics discussed in Section 6.2.1.

This section discusses the known loss mechanisms affecting the performance of detonation waves. These losses include mechanisms that affect detonation waves in general and mechanisms that affect detonation waves due to their application in a system. For example, detonation waves are typically modeled as adiabatic combustion events; however, when using a detonation wave in a combustion device like PDCs/RDEs, the gases transfer some energy to the walls where the detonation resides. While the application causes this effect, it will still be included because of its impact on the performance of the detonation wave.

6.1.1 Incomplete Combustion, Deflagration Losses and Product Re-circulation

Incomplete combustion and deflagration losses within the detonation wave will lead to a decrease in performance, and are lumped together due to the similarity of the two on the performance of the detonation wave. In the same sense, product gas re-circulation, also known as exhaust gas re-circulation (EGR), causes a similar effect to deflagrative pre-burning. In all cases, one should seek to reduce or eliminate all three of these losses to improve detonation performance.

A deflagration loss is defined by combustion occurring outside of the detonation region. This includes deflagration before the detonation wave, termed parasitic combustion, and deflagration occurring after the wave has passed but without contributing to the heat release in the detonation region, termed commensal combustion. The latter occurs when a fraction of the fuel passes through the detonation wave unburnt. Because this unburnt fuel does not necessarily need to combust to degrade the detonation wave performance, another metric that captures this effect is defined as the leaked fuel fraction. Both of these losses reduce the fraction of fuel consumed within the detonation region, and both parasitic and commensal deflagration have been seen experimentally using OH* chemiluminescence by Chacon et al. and Feleo et al.[24, 22, 72, 4]

Chacon et al. imaged a racetrack style RDE, and Figure 6.1 shows a snapshot from a run, where the detonation wave is the brightest feature and is moving from the right to the left. A significant portion of deflagration combustion happens ahead of the detonation, and even large regions of combustion happen after the wave, suggesting that not all of the fuel was consumed by the detonation. These features break the

standard assumptions in the theoretic models, leading to significant reductions in detonation wave performance.

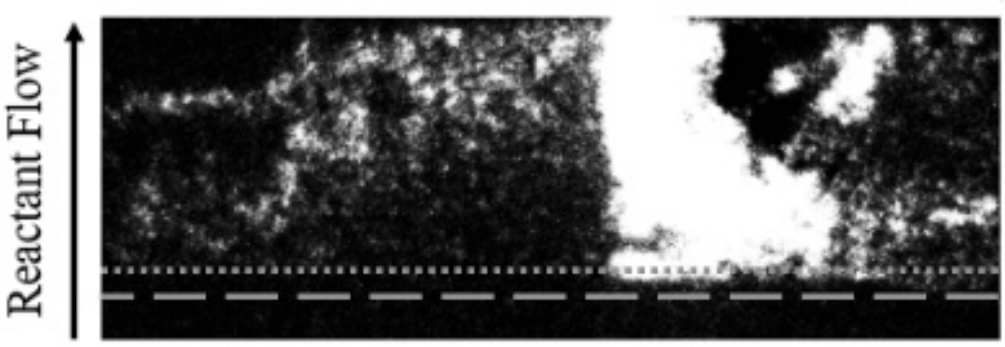

Figure 6.1: Example of pre- and post-detonation deflagrative combustion. Detonation moving right to left, image color altered from [24].

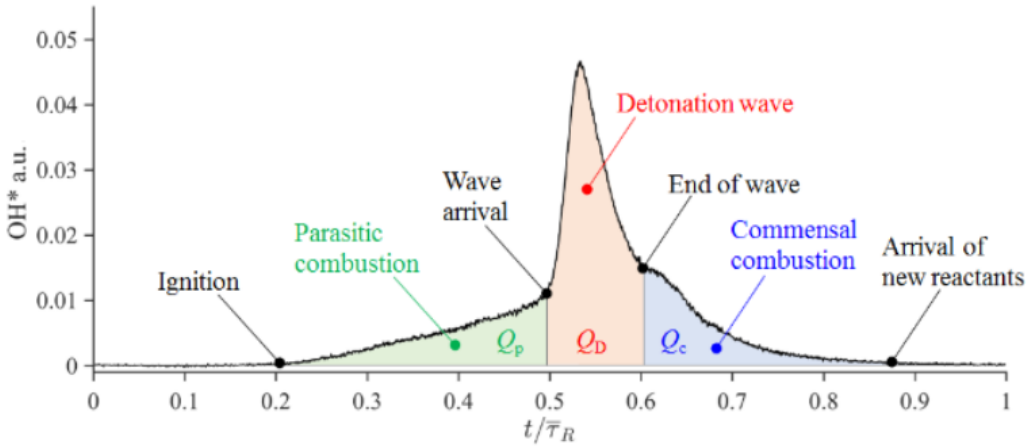

Figure 6.2: Phase Averaged OH* Chemiluminescence Measurement through a Photo-Multiplier Tube. Binned according to location with respect to detonation wave.[72].

When averaging the effects of the deflagration on the wave in a standard cylindrical RDE, Feleo et al. also showed that a significant portion of the heat release during a detonation cycle can occur before and after the detonation wave itself (see Figure 6.2).[72, 4] Initial estimates showed that nearly a quarter of the heat release occurred

before the detonation wave arrived, which increases the speed of sound in this gas and drastically reduces the incoming Mach number of the wave. This would lead to a much lower pressure rise across the detonation and lower propagation speeds of the wave. To make matters worse, nearly a quarter of the heat release occurs behind the detonation wave, suggesting that a large portion of the fuel is not combusted by the wave. This means a large portion of the fuel is along for the ride through the detonation, not contributing to the heat release needed to propagate the wave. With these studies being conducted on different types of RDEs, it also suggests that these effects may be RDE geometry agnostic.

The effects of deflagrative combustion losses on the performance of the detonation wave have been examined in detail by Strakey et al., Burr and Paulson, Barnouin et al., and Raman et al.[73, 74, 75, 76] Strakey et al. examined a variety of losses that reduced RDE performance. These losses included unburnt fuel and parasitic combustion ahead of the detonation wave. Their results provided insight into the effects of these losses on the performance of the detonation wave, showing a reduction in wave speed and detonation pressure ratio.

Burr and Paulson [74] examine the deflagration losses within a modeled RDE cycle, specifically looking at three loss parameters: parasitic combustion, leaked fuel, and commensal combustion post-detonation. This methodology also provided a means to estimate combustion efficiency for the cycle and compare it to RDE performance. They used specific impulse as the performance metric of interest and showed the effects of each loss parameter on the thrust production of the modeled cycle. Their results suggest that parasitic combustion was the most detrimental loss parameter, given that all of the fuel was consumed within the cycle. They also noted the lack of a strong correlation between the modeled specific impulse and the wave speed, suggesting the separation of detonation performance from RDE performance when comparing RDEs to conventional combustion devices.

Barnouin et al. isolated the effects of the deflagration loss terms on the performance of a detonation wave. For consistency with the model used in the research, these deflagration losses will be defined by parasitic deflagration fraction, ξ_{P}, and leaked fuel fraction, ξ_{L}. This effort showed a reduction in the wave speed and pressure ratio with increased loss fractions, where the parasitic combustion ahead of the wave had the most drastic effect. This was due to the combination of the reduction in fuel available for the detonation wave and the increased sound speed in the pre-detonation gases. This led to a much weaker shock wave, in terms of Mach number, resulting in a much lower pressure rise across the shock front.

Raman et al. conducted a review of numerous computational, reduced modeling, and experimental research on the effects of non-ideal processes on the performance of a detonation wave and RDE performance in general. They discuss multiple non-idealities observed in prior research, including product re-circulation and deflagrative combustion within the RDE cycle. With either effect, the performance of the detonation wave (in terms of wave speed and pressure ratio) was reduced. This meta-analysis eventually extended the non-ideal deflagration to RDE performance (thrust in this case). Similarly to the effects on detonation performance, increases in deflagrative combustion reduced the performance of RDE thrust production. Finally, they included an analysis of the impact of deflagration on the operability of the RDE, where, in certain situations, the deflagrative combustion can actually improve the operability of RDEs at the expense of some performance.

Stechmann et al. examined the effects of product re-circulation on the operation of RDEs. [77] Their results looked at the mixing of fuel and oxidizer as the flow paths are modulated by the pressure wave of the previous detonation wave. Along with the study on mixing, Stechmann et al. also focused their efforts on the effects of product re-circulation, specifically examining the auto-ignition times of the mixed reactants relative to the operation times of the RDE. At certain levels of product re-circulation and reactant temperature, they noticed that the auto-ignition time for the reactants dropped below the cycle time of the detonation wave. This leads to the potential for deflagrative combustion occurring in the reactants before the detonation wave arrives.

In a related effort, Fievisohn et al. examined the effect of product re-circulation on the performance of RDEs. They identified timescale thresholds for pockets of auto-ignition of the fresh reactant in a given RDE wave cycle.[78, 79]

Kaemming et al.[26, 39] examined the effects of multiple loss mechanisms, including tracking particle path lines through an ideal detonation wave cycle. A small fraction of particles do not pass through the detonation portion of the wave, therefore reducing the performance of the RDE with respect to ideal conditions. Strakey et al. conducted a computational study that provided insight into multiple loss mechanisms within an RDE.[73] This research showed the adverse effects of pre-detonation wave combustion on the performance of an RDE and examined the portion of unburnt fuel during RDE operation. This prior research led to the development of the Deflagrative Loss Model discussed in Section 6.2.1 of this research.

6.1.2 Lateral Relief

Lateral relief describes another loss mechanism that affects the detonation performance, but only due to the change in boundary conditions relative to the CJ analysis. In certain applications, such as RDEs, the detonation is bounded by a compressible gas layer instead of a solid wall. This allows the high-pressure detonation region to expand laterally into the gas boundary. This has been modeled using an inert boundary on one side of a planar detonation wave, where the consequence of lateral relief is a diminished post-detonation pressure and wave speed relative to the ideal, purely one-dimensional detonation.[80, 81, 82] This has also been studied in the RDE application by Kaemming et al. with similar results.[26]

The following sections will provide additional insight into the effects of lateral relief by modeling the process as simple area change within the detonation region. This will first be analyzed in a framework akin to the CJ analysis, then will be extended to the ZND methodology for further insights. Due to the configuration of RDEs, it is unlikely that this term can ever be eliminated, so it is crucial to understand its impact and how one might mitigate this process without causing any detrimental effects from other known losses.

6.1.2.1 From the CJ Perspective

We start with the one-dimensional conservation equations, like in the CJ theory analysis ; however, now we will not neglect the area terms. Equations 6.1-6.3 are the one-dimensional conservation equations with area change.

$$\rho_1 u_1 A_1 = \rho_2 u_2 A_2 \tag{6.1}$$

$$P_1 A_1 + \rho_1 u_1^2 A_1 = P_2 A_2 + \rho_2 u_2^2 A_2 \tag{6.2}$$

$$h_1 + \frac{u_1^2}{2} = h_2 + \frac{u_2^2}{2} \tag{6.3}$$

In the same manner as the constant area CJ derivation, we solve for the upstream velocity in Equation 6.1:

$$u_1 = \frac{\rho_2 u_2 A_2}{\rho_1 A_1} = \frac{\rho_2 u_2}{\rho_1} AR \tag{6.4}$$

where, $AR = \frac{A_2}{A_1}$ is the area ratio between state 2 and 1. Next, we divide equation 6.2 by A_1 to get it in terms of the area ratio, AR.

$$P_1 + \rho_1 u_1^2 = P_2 AR + \rho_2 u_2^2 AR \tag{6.5}$$

Now we will substitute Equation 6.4 into Equation 6.5 and simplify where possible, resulting in:

$$P_1 + \frac{\rho_2^2 u_2^2}{\rho_1} AR^2 = P_2 AR + \rho_2 u_2^2 AR \tag{6.6}$$

This results in the final equation for the momentum conservation with the mass conservation included in the definition. We similarly substitute Equation 6.4 into the energy equation, Equation 6.3, which results in:

$$h_1 + \frac{\rho_2^2 u_2^2}{2\rho_1^2} AR^2 = h_2 + \frac{u_2^2}{2} \tag{6.7}$$

We are now left with the final two conservation equations, Equation 6.6 and Equation 6.7. Instead of developing a solver for this system of equations, we will iterate on the temperature and density of state 2 with the *fsolve* function provided by the *Scipy* package in *Python*. With a proper initial guess, this solver performs in a similar, if not faster, method as the CEA implementation of the CJ detonation solver.[19]

The steps for this solver are described in Algorithm 1, where an initial guess of the post-detonation pressure and density, $P_{\text{CJ}} = 15P_1$ and $\rho_{\text{CJ}} = 1.5\rho_1$ are used to provide a close approximation. With these initial guesses, an estimated post-detonation enthalpy can be calculated with Equation 6.8. This enthalpy is used within the Gas Object to calculate the equilibrium composition at P_{CJ} and h_{CJ}. After this step, the residuals for the momentum equation and energy equation are calculated with Equation 6.9 and Equation 6.10, respectively. This iteration continues until convergence in the momentum and energy residual are below a certain tolerance. Finally, the state at the CJ plane with area change is returned for further processing.

$$h_{\text{CJ}} = h_1 + 11.25 R_u \frac{T_1}{MW_1} \tag{6.8}$$

$$R_{mom} = P_1 + \frac{\rho_2^2 u_2^2}{\rho_1} AR^2 - P_2 AR - \rho_2 u_2^2 AR \tag{6.9}$$

$$R_{en} = h_1 + \frac{\rho_2^2 u_2^2}{2\rho_1^2} AR^2 - h_2 - \frac{u_2^2}{2} \tag{6.10}$$

Algorithm 1 CJ solver with Area Change

Require: Gas Object at Initial Conditions and Iteration Tolerance, *tol*
  Guess Pressure Ratio of 15 & Density Ratio of 1.5
  Estimate Final Enthalpy ▷ *Equation 6.8*
  while $|R_{mom}| > tol$ & $|R_{en}| > tol$ **do**
    Equilibrate Gas Object at Constant Enthalpy and Pressure
    Calculate Residuals R_{mom} & R_{en} ▷ *Equation 6.9 & Equation 6.10*
  end while
  return Gas Object at CJ Condition at A_2

6.1.2.2 From the ZND Perspective

Figure 6.3 shows an example of a non-zero distance between the shock and the CJ plane. In this example problem, the upper portion of the detonation wave is bound by an inert gas layer. Because of this, an area change can occur between the shock and the CJ plane. Depending on the rate of change of the area within the combustion region, the combustion process can be quenched as the gases expand. At certain area change rates, the CJ condition may not even be reached. This process is sure to occur within an RDE cycle as the downstream portion of the detonation wave is bounded by the post-combustion products, while the upstream portion is bounded by the oxidizer gases.

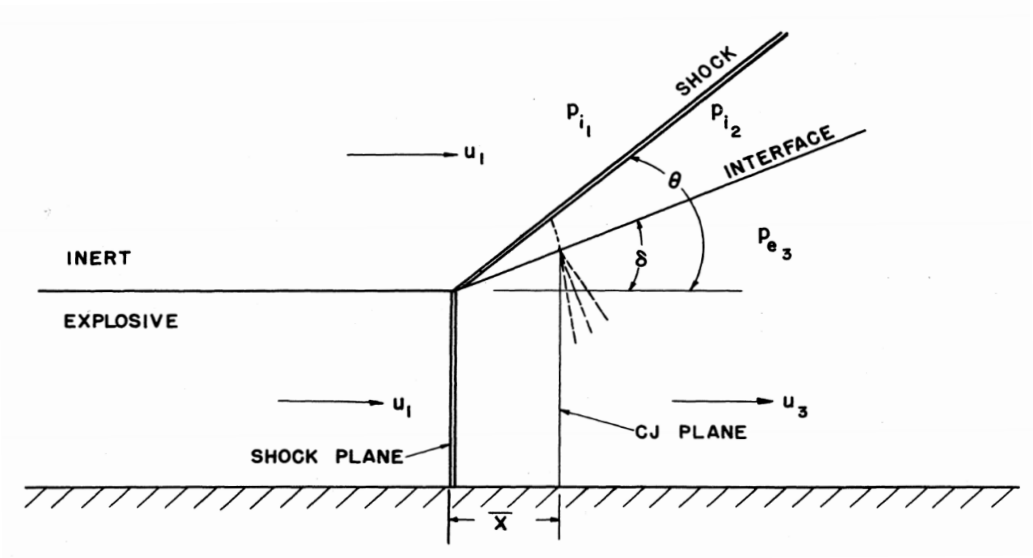

Figure 6.3: Example of Area Change Between Shock Wave and CJ Plane.[81]

The CJ analysis with area change makes one key assumption that may be violated when transitioning to the one-dimensional ZND analysis. This assumption revolves around the fact that the CJ solver assumes equilibrium combustion compositions at the CJ plane. For this reason, we turn our attention to the effects of area change on the detonation as modeled by the ZND method. The following system of equations were adapted from the Shock and Detonation Toolbox provided by CalTech, and are used to solve steady reacting flow with area changes.[83]

$$\frac{d\rho}{dx} = -\frac{\rho}{\eta}\left[\dot{\sigma}' - \frac{M^2}{A}\frac{dA}{dx}\right] \tag{6.11}$$

$$\frac{dP}{dx} = -\frac{\rho U^2}{\eta}\left[\dot{\sigma}' - \frac{1}{A}\frac{dA}{dx}\right] \tag{6.12}$$

$$\frac{dU}{dx} = \frac{U}{\eta}\left[\dot{\sigma}' - \frac{1}{A}\frac{dA}{dx}\right] \tag{6.13}$$

where, $\eta = 1 - M^2$ and $\dot{\sigma}' = \sum_k \sigma_k \frac{dY_k}{dx}$. The latter term is spacial thermicity, which is not in a format that is conducive to solving the ZND profile. The integration process uses *Cantera* to get net species production rates, which are in the time domain,

and calculates the thermicity value as a temporal derivative. We can relate the form specified in the equations above to the standard, time-based species rate and thermicity calculation by applying the chain rule:

$$\frac{d()}{dx} = \frac{d()}{dt}\frac{dt}{dx} = \frac{d()}{dt}\frac{1}{U} \tag{6.14}$$

Applying Equation 6.14 to Equation 6.40, we are left with the familiar definition of the time rate of change in density accoding to:

$$\frac{d\rho}{dt} = -\frac{\rho\dot{\sigma}}{\eta} \tag{6.15}$$

When applying this process to the thermicity calculation, we will apply the chain rule to each species' net production rates:

$$\frac{dY_k}{dx} = \frac{dY_k}{dt}\frac{dt}{dx} = \frac{dY_k}{dt}\frac{1}{U} \tag{6.16}$$

After substitution, the spacial thermicity term can be written as:

$$\dot{\sigma}' = \sum_k \frac{\sigma_k}{U}\frac{dY_k}{dt} = \frac{\dot{\sigma}}{U} \tag{6.17}$$

6.1.3 Heat Transfer

As mentioned earlier in this Chapter, heat transfer within any application based on detonation combustion is sure to exist.[84, 85, 86, 87] The post-detonation state is at elevated temperatures over that of a conventional combustor operating at the same conditions, and in the case of PDCs and RDEs, the boundary condition for the detonation wave is typically a metal wall with no form of boundary layer or film cooling. This allows for incredibly high heat transfer coefficients that heat the walls of the device but also remove energy from the flow. The latter of which is the focus of this section. Both the CJ and ZND analyses assume adiabatic flow; however, we will relax this assumption and examine how removing heat from the detonation wave affects its performance.

6.1.3.1 From the CJ Perspective

From the CJ analysis, we will keep the mass and momentum equations (Equations 6.18 and 6.19) as

$$\dot{m}'' = \rho_1 D = \rho_2 u_2 \tag{6.18}$$

$$P_1 + \rho_1 D^2 = P_2 + \rho_2 u_2^2 \tag{6.19}$$

where D represents the wave speed (in this case, the speed of the reactants moving into the wave). However, we will update the energy equation

$$h_1 + \frac{D^2}{2} + q = h_2 + \frac{u_2^2}{2} \tag{6.20}$$

to account for heat removal from the system. The new form of the energy equation is shown below in Equation 6.21:

$$h_1 + \frac{u_1^2}{2} + q_{out} = h_2 + \frac{u_2^2}{2} \tag{6.21}$$

where q_{out} represents the bulk heat removal rate from the detonation wave as it progresses to the CJ conditions. A slightly modified version of the solver in Algorithm 1 was used to calculate the CJ condition given an initial reactant mixture and a specified heat removed.

6.1.3.2 From the ZND Perspective

Because the ZND analysis includes the integration over a distance (or time) when solving, we get a temperature profile along the combustion wave post-shock. This allows for the specification of a heat transfer coefficient between the detonation product gases and the wall as a function of the gas temperature. With this, we can capture the effects of removing heat from the combustion region on the performance of the detonation wave. More details on this process and the model used to study it are provided in Section 6.2.3

$$\frac{d\rho}{dx} = -\frac{\rho}{\eta}\left[\dot{\sigma}' + \frac{G}{\rho a_f^2}\frac{\bar{q}}{U}\right] \tag{6.22}$$

$$\frac{dP}{dx} = -\frac{\rho U^2}{\eta}\left[\dot{\sigma}' + \frac{G}{\rho a_f^2}\frac{\bar{q}}{U}\right] \tag{6.23}$$

$$\frac{dU}{dx} = \frac{U}{\eta}\left[\dot{\sigma}' + \frac{G}{\rho a_f^2}\frac{\bar{q}}{U}\right] \tag{6.24}$$

where G is the Gruneisen coefficient, and a_f is the frozen speed of sound for the gas, and the heat flux parameter, $\bar{q}$, is the heat transfer rate.

6.1.4 Friction

This section will discuss the frictional forces that may be acting on the detonation wave. Though we will specifically examine friction, any mechanism that results in a loss in momentum through the detonation process will produce similar effects. This is especially true in the first section, which discusses momentum losses, as modeled by friction, from the perspective of the CJ analysis.

6.1.4.1 From the CJ Perspective

Frictional forces require a distance of action, but the CJ model framework uses an infinitesimally thin detonation wave approximation. Hence, we will capture the effect of friction and other momentum loss mechanisms in a single momentum loss variable, F. Equation 6.25 shows an updated momentum conservation equation with the new momentum loss term.

$$P_1 + \frac{\rho_2^2 u_2^2}{\rho_1} AR^2 = P_2 AR + \rho_2 u_2^2 AR - F \tag{6.25}$$

where F represents a total momentum loss from frictional forces and the like. Using this form of the momentum equation changes the residual calculation in the momentum equation but is solved in the same method presented in Algorithm 1.

6.1.4.2 From the ZND Perspective

Using the ZND methodology, friction can be captured directly as we now have the appropriate length scale. Another benefit of the ZND framework is that it includes a time/space dependency. The density rate change rate can now be written as:

$$\frac{d\rho}{dx} = -\frac{\rho}{\eta}\left[\dot{\sigma}'\frac{G}{\rho a_f^2} + (G+1)\bar{\tau}\right] \tag{6.26}$$

The pressure rate of change is now:

$$\frac{dP}{dx} = -\frac{\rho U^2}{\eta}\left[\dot{\sigma}' + \frac{G}{\rho a_f^2}(G + \frac{1}{M^2})\bar{\tau}\right] \tag{6.27}$$

Finally, the velocity rate of change is:

$$\frac{dU}{dx} = \frac{U}{\eta}\left[\dot{\sigma}' + \frac{G}{\rho a_f^2}(G + 1)\bar{\tau}\right] \tag{6.28}$$

where friction, $\bar{\tau}$, is written in terms of coefficient of friction:

$$\bar{\tau} = \frac{4}{D}\tau_w = \frac{2}{t_w}\frac{1}{2}\rho U^2 c_f = \frac{1}{t_w}\rho U^2 c_f \tag{6.29}$$

where c_f is the coefficient of friction. Because friction acts in the lab frame and we are solving the ZND profile in the wave frame, we need to perform a Galilean transform of the velocity term used in Equation 6.29:

$$\bar{\tau} = \frac{1}{t_w}\rho U'^2 c_f \tag{6.30}$$

where $U' = D_{\mathrm{CJ}} - U$, where U is in the wave frame and U' is in the lab frame.

6.2 Description of Detonation Wave Performance Models

The assumptions typically employed in ZND solutions to calculate the fundamental characteristic of a propagating detonation wave assume complete combustion, a one-dimensional flow field of constant cross-sectional area, and adiabatic, inviscid flow. Historical examples have proven that this is not the case in practical detonation-based systems (see Section 6.1). In this section, we will depart from these assumptions and examine the models used to quantify the impacts on the performance of detonation from these effects.

6.2.1 Deflagration Loss Model

The first set of losses will examine the assumption of complete combustion of the fuel provided within the detonation wave. These effects will be captured with a reduced order model termed the Deflagration Loss Model. Section 6.1.1 has provided numerous examples of incomplete combustion within the detonation wave and deflagrative combustion occurring outside of the detonation wave. For modeling purposes, we will reduce these effects into two losses: parasitic deflagrative combustion occurring before the detonation wave and fuel leaking through the detonation wave. These terms were used to define two loss parameters of interest: the parasitic fuel fraction, ξ_P, and the leaked fuel fraction, ξ_L.

The parasitic fuel fraction represents a molar fraction of the initial fuel that is allowed to combust in a deflagrative manner ahead of the detonation wave. Modeling of the parasitic deflagrative combustion assumes a constant-pressure combustion of the specified fuel fraction at the pre-detonation state (temperature, pressure, enthalpy). By using the fuel fraction representation of the loss parameter, we are left with a parameter that varies between zero and one, where one represents a complete deflagration event. We can also relate this parameter in terms of the mole fraction of the fuel consumed parasitically, with respect to the initial moles of the fuel with Equation 6.31:

$$\chi_P = \xi_P \tag{6.31}$$

The definition of the leaked fuel fraction, ξ_L, is slightly more complicated. This fraction represents the fractions of moles of fuel remaining after the parasitic combustion that leak through the detonation wave. It was defined in this manner to also vary between zero and one, where one represents all of the remaining fuel that leaks through the detonation. It can also be referenced to the initial number of moles of fuel with Equation 6.32:

$$\chi_L = \xi_L(1 - \xi_P) \tag{6.32}$$

Finally, we can define the mole fraction of fuel consumed by the detonation wave, again normalized by the initial number of moles of fuel, with Equation 6.33

$$\chi_D = (1 - \xi_P)(1 - \xi_L) \tag{6.33}$$

where:

$$\chi_{\mathrm{P}} + \chi_{\mathrm{D}} + \chi_{\mathrm{L}} = 1 \tag{6.34}$$

Figure 6.4 provides an illustration of the breakdown in the three different processes, including an intermediate state, χ_{NP}, which simply refers to the moles of the fuel that are not consumed by parasitic combustion.

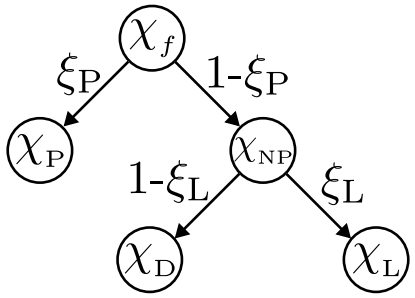

Figure 6.4: Fuel partitioning for the Deflagration Loss Model. χ_{NP} represents an intermediate state of non-parasitic fuel, which is further broken down into detonation and leaked, χ_{D} and χ_{L} respectively.

The goal of this model is to predict the effects of deflagration losses on both the detonation wave. Figure 6.5 shows a schematic of the model. It should be noted that from the perspective of the model, there is no difference in fuel being consumed in parasitic combustion or product gas re-circulation from the previous wave. This means that the parasitic fraction accounts for a combination of the two but cannot distinguish between them. In the same vein, the model is insensitive to what happens to the fuel that leaks through the detonation wave. This means the detonation only cares that the fuel leaked through the detonation, not if/how much was combusted after the wave. Both of these facts make comparison to measured data difficult because the measurements used for comparison are based on imaging of where combustion is seen and cannot account for product gas re-circulation or non-combusted leaked fuel.

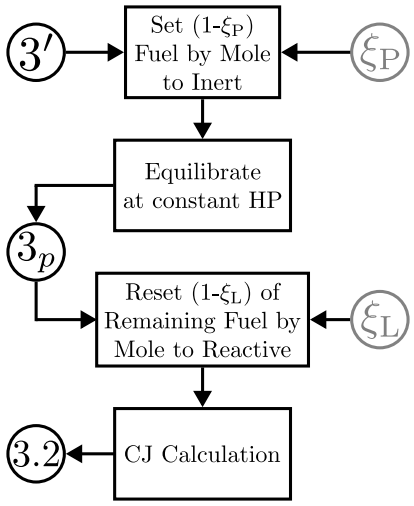

Figure 6.5: Deflagration Loss Model.

A custom implementation of the *Cantera* Solution object, implemented in *Python*, was used to calculate thermodynamic properties at each state, and the CJ solver uses a custom implementation following the methodology provided by Gordon et al.[88, 19] The process for setting the fuel to and from an inert species was done through the addition of non-reactive surrogates of each fuel in question to the reaction mechanism. Each surrogate mimics the thermodynamic properties of its base species without including it in any reaction paths. This allows for a simple method of calculating each step without having to manage multiple gas streams. The pseudo-code of the solution process is shown in Algorithm 2.

Algorithm 2 Deflagration Loss Model

Require: ξ_P, $\xi_L \in [0, 1]$

1: Initialize gas object at pre-detonation initial state: (3′)
2: Set (1-ξ_P) fuel (by mole) to inert
3: Equilibrate at constant pressure/enthalpy, mimicking deflagration burning ahead of the wave: (3_p)
4: Reset (1-ξ_L) of remaining fuel (by mole) to reactive
5: CJ calculation, while accounting for detonative heat release lost by leaked fuel: (3.2)

From this model, two maps of detonation performance metrics of interest were created. Figure 6.6 shows an example of the detonation wave speed, relative to the ideal wave speed, plotted in black against the fraction of parasitic combustion on the x-axis and the fraction of leaked fuel on the y-axis. This map shows a similar drop in the speed of the detonation as either of these parameters are increased. In dashed gray, the pressure ratio across the detonation, relative to the ideal pressure ratio, is plotted against the same deflagration loss fractions. This map shows a much steeper drop-off in pressure ratio as the parasitic combustion increases but is less affected by a similar increase in the leaked fuel fraction. This is due to the fact that the pressure ratio across the detonation scales with the detonation Mach number, relative to the pre-shock state. Parasitic combustion has the effect of decreasing the detonation wave speed while simultaneously increasing the speed of sound of the pre-detonation gases.

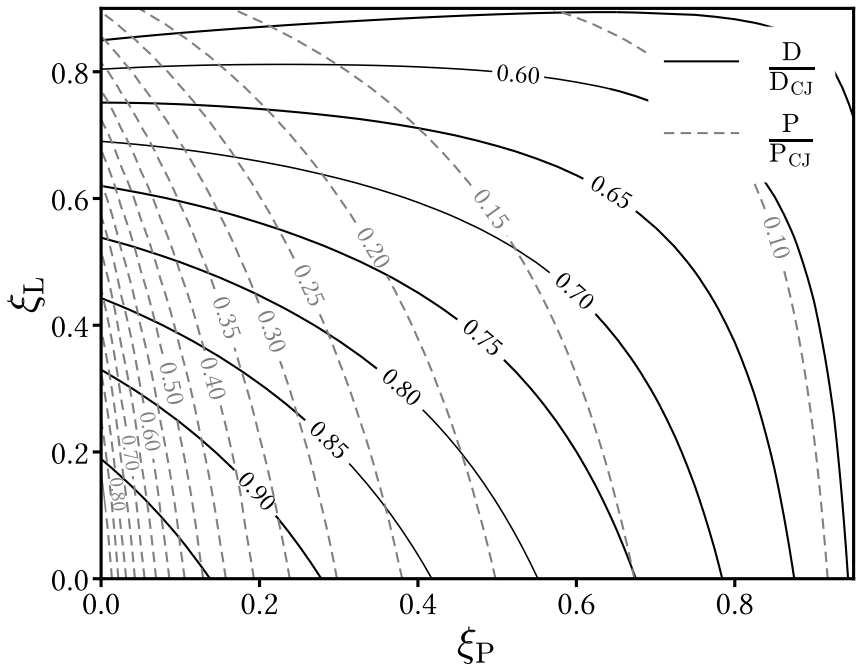

Figure 6.6: Maps of wave speed and pressure ratio relative to ideal values as a function of parasitic combustion fraction and leaked combustion fraction. Hydrogen/air at $\phi = 0.6$.

6.2.2 Non-Ideal CJ Analysis

The next set of potential loss parameters of interest revolves around the core assumptions of the standard CJ analysis. First, we will discuss the role of area change within the detonation region. This phenomenon is likely of no concern in the detonation tube or PDC context, where the walls bound the combustion event; however, this is not the case in RDEs. Because the boundaries of the detonation in a RDE consist of two layers of inert gases rather than solid walls, there exists the potential for area changes to occur within the combustion region due to what is colloquially termed lateral relief. This, in effect, reduces the potential pressure increase across the wave since the detonation wave, in the quasi-one-dimensional sense, due to the expansion occurring as the area increases.

Next, the effects of heat loss to the wall can be accounted for by assuming a known, or specified, heat removal rate, q_{out}. This term provides a simple method for capturing the heat transferred to the cooler walls from the detonation combustion region during operation, and in practice, would vary based on the combustion gas temperature, the wall temperature, and a heat transfer coefficient.

Finally, although likely a small contributor, frictional forces within the detonation region can produce a loss in momentum. This can be studied by specifying a term that accounts for any momentum losses, F, including friction.

The effects of lateral relief, heat transfer, and frictional losses within the detonation region were modeled using Algorithm 3, with the momentum residual modified to account for frictional losses (Equation 6.35) and the energy residual equation modified to account for heat transfer, as shown in Equation 6.36

$$R_{mom} = P_1 + \frac{\rho_2^2 u_2^2}{\rho_1} AR^2 - P_2 AR - \rho_2 u_2^2 AR + F \tag{6.35}$$

$$R_{en} = h_1 + \frac{\rho_2^2 u_2^2}{2\rho_1^2} AR^2 - h_2 - \frac{u_2^2}{2} - q_{out} \tag{6.36}$$

Algorithm 3 Non-Ideal CJ Model

Require: AR, Q, F, Gas Object at Initial Conditions and Iteration Tolerance, tol
  Guess Pressure Ratio of 15 & Density Ratio of 1.5
  Estimate Final Enthalpy ▷ *Equation 6.8*
  while $|R_{mom}| > tol$ & $|R_{en}| > tol$ **do**
    Equilibrate Gas Object at Constant Enthalpy and Pressure
    Calculate Residuals R_{mom} & R_{en} ▷ *Equation 6.35 & Equation 6.36*
  end while
  return Gas Object at CJ Condition at A_2

6.2.3 Non-Ideal ZND Model

The following system of equations were used to solve steady reacting flow with area changes, heat transfer, and friction. They contain all of the losses discussed in Section 6.4 and are written using the temporal thermicity value.

$$\frac{d\rho}{dx} = -\frac{\rho}{\eta}\left[\frac{\dot{\sigma}}{U} + \frac{G}{\rho a_f^2}\left[\frac{\bar{q}}{U} + (G+1)\bar{\tau}\right] - \frac{M^2}{A}\frac{dA}{dx}\right] \tag{6.37}$$

$$\frac{dP}{dx} = -\frac{\rho U^2}{\eta}\left[\frac{\dot{\sigma}}{U} + \frac{G}{\rho a_f^2}\left[\frac{\bar{q}}{U} + (G+\frac{1}{M^2})\bar{\tau}\right] - \frac{1}{A}\frac{dA}{dx}\right] \tag{6.38}$$

$$\frac{dU}{dx} = \frac{U}{\eta}\left[\frac{\dot{\sigma}}{U} + \frac{G}{\rho a_f^2}\left[\frac{\bar{q}}{U} + (G+1)\bar{\tau}\right] - \frac{1}{A}\frac{dA}{dx}\right] \tag{6.39}$$

where, in the instance of an adiabatic, inviscid, constant area solution, these equations reduce back to the rate-change equations used in the standard ZND solution method. For example, Equation 6.37 reduces to known form:

$$\frac{d\rho}{dx} = -\frac{\rho\dot{\sigma}}{\eta U} \tag{6.40}$$

In the solver, the area change rate, $\frac{dA}{dx}$, is specified directly as a function of x and can be calculated ahead of time based on geometric constraints. Likewise, the coefficients, c_h and c_f, are also specified as input parameters to the model. The model integrates over a specified length, l, or until the sonic condition is reached. Algorithm 10 shows the pseudo-code for the non-ideal ZND model.

Algorithm 4 Non-Ideal ZND Solver

Require: $\frac{dA}{dx}, c_f, c_h$, Initial conditions: P_0, T_0, Gas Object, final integration length, l

Calculate CJ wave speed: D_{CJ}
Use wave speed to calculate post-shock state: $\mathbf{Y}_0$ ▷ *Equation 6.41*
while $M_i < 1.0$ & $x_i < l$ **do**
    Set gas object to new state, $\mathbf{Y}_i$
    Calculate re-used terms: $[\frac{1}{\rho_i}, U_i^2, a_i^2, M_i^2, \eta_i]$
    if $c_h \neq 0 \mid c_f \neq 0$ **then**
        Calculate $G_i, \bar{q}_i, \bar{\tau}_i$
    end if
    Calculate net production rates: $\left(\frac{dY_k}{dx}\right)_i$ ▷ *Equation 6.16*
    Calculate spacial thermicity: $\dot{\sigma}'$ ▷ *Equation 6.17*
    Calculate rate changes: $\frac{d\rho}{dx}, \frac{dP}{dx}, \frac{dU}{dx}$: ▷ *Equations 6.37 - 6.39*
    Integrator calculates next state: $\mathbf{Y}_{i+1}$
end while

The state vector for the non-ideal ZND model is shown in Equation 6.41:

$$\mathbf{Y} = [P, \rho, Y_0 \dots Y_k] \tag{6.41}$$

where the states include the pressure, density, and mass fraction of each species. This model framework allows for the study of a detonation wave from the ZND perspective but now accounts for loss mechanisms along the detonation profile.

6.3 Markov Chain Monte Carlo method for Loss Parameter Estimation

This section will discuss the methods used in this research to estimate losses given a set of experimental data. The losses and their required experimental measurements were model-specific; however, the methodology for calculating them relied on Markov Chain Monte Carlo (MCMC). MCMC is a method for estimating the probability density function (PDF) of any unknown distribution, provided one can sample from that distribution. This technique offers a more efficient process for estimating PDFs relative to simple Monte Carlo by relying on a simple "hack" in Bayesian analysis.[89]

Bayes theorem, shown in Equation 6.42, provides a mathematical framework for how one should update their beliefs given a new set of information.

$$\mathcal{P}(\Theta|\mathrm{D}) = \frac{\mathcal{P}(\mathrm{D}|\Theta)\mathcal{P}(\Theta)}{\mathcal{P}(\mathrm{D})} \tag{6.42}$$

where $\Theta = [\theta_0 \dots \theta_i]$ is a set of the parameters of interest, D is the measured data, $\mathcal{P}(\mathrm{D}|\Theta)$ is the likelihood of the measured data based on the given parameter set, $\mathcal{P}(\Theta)$ is the prior distribution, or the prior belief, of the parameters, and $\mathcal{P}(\mathrm{D})$ is the evidence or the probability distribution of all of the data. Typically, the evidence term is difficult, if not impossible, to calculate because one can rarely know the entirety of this distribution.

The genius of MCMC is in the way it evaluates the evidence term algorithmically. To better understand, we first must introduce the process for the Metropolis-Hastings method shown in Algorithm 5.[90, 91]

Algorithm 5 Metropolis-Hastings MCMC

Require: Initial State Vector $\Theta = [\theta_0 \dots \theta_i]$, Some Function $f(\Theta) = \mathcal{P}(\Theta|\mathrm{D})$

1: Initialize at a point in the state space, $\Theta^k = \Theta^0$
2: Propose a new sample in the state space, $\Theta^{k+1} \sim \mathcal{N}(\Theta^k, \mathrm{C})$
3: Evaluate function, f, at Θ^k and Θ^{k+1}
4: Compute acceptance ratio, $a(\Theta^k, \Theta^{k+1}) = min\left(1, \frac{f(\Theta^{k+1})}{f(\Theta^k)}\right)$
5: Draw random sample from a uniform distribution, $u \sim \mathcal{U}[0, 1]$
6: **if** $u \leq a$ **then**
7: Accept new sample, Θ^{k+1}, and move to new location
8: **else**
9: Reject Θ^{k+1} and re-propose new $\Theta^{k+1} \sim \mathcal{N}(\Theta^k, \mathrm{C})$
10: **end if**
11: Increment k
12: Repeat 2-11 for a given number of samples

If we provide the function f as the posterior distribution, we can relate it to Equation 6.42:

$$f(\Theta) = \mathcal{P}(\Theta|D) = \frac{\mathcal{P}(\mathrm{D}|\Theta)\mathcal{P}(\Theta)}{\mathcal{P}(\mathrm{D})} \tag{6.43}$$

MCMC fixes the data between samples; therefore, the evidence term cancels out during the evaluation of the acceptance ratio in step 4 of Algorithm 5. Because of this, we can simplify our function f:

$$f(\Theta) = \mathcal{P}(\Theta|\mathrm{D}) \propto \mathcal{P}(\mathrm{D}|\Theta)\mathcal{P}(\Theta) \tag{6.44}$$

Now, we only require two distributions: the likelihood of the data given the parameters and the prior distribution of the parameters. The likelihood can be any function that relates the "goodness" of fit of the data and parameters. In most cases, as in this research effort, the likelihood function invokes some external model, $\mathrm{M}(\Theta)$, which outputs the same set of data used in the estimation process. To evaluate the goodness-of-fit, it is typical to use a simple multivariate normal distribution. This allows for the form of the likelihood function used throughout the parameter estimation conducted in this research effort, shown in Equation 6.45.

$$\mathcal{P}(\mathrm{D}|\Theta) = \frac{1}{\sqrt{(2\pi)^{\mathrm{N}}|\Sigma|}} \exp\left(-\frac{1}{2}(\mathrm{D} - \mathrm{M}(\Theta))^{\mathrm{T}}\Sigma^{-1}(\mathrm{D} - \mathrm{M}(\Theta))\right) \tag{6.45}$$

, where $\mathrm{M}(\Theta)$ is the model of interest as a function of parameters Θ, D is the experimental measurements, and Σ, is the covariance matrix that takes into account the uncertainty of the measurements. Notably, the data, D, can be of any dimensionality and does not need to be the same size as the parameter set, Θ. The prior, $\mathcal{P}(\Theta)$, can be any distribution, and so long as this distribution contains the optimal parameter within its bounds, the MCMC method will find such a solution.

An example of the Metropolis-Hastings sampling process for a two-dimensional parameter space is shown in Figure 6.7. Figure 6.7 (a) shows the initial proposal process, where the proposal covariance matrix, C, is a bivariate normal of a given variance around the current location. In this step, X^1 was accepted, and the next proposal now emanates from X^1. Figure 6.7 (b) shows an example of rejecting a proposal and re-proposing from the same location, where the move from X^1 to X^2 was rejected, but the move from X^1 to X^3 was accepted. Finally, Figure 6.7 (c) shows the posterior distribution of accepted points after a given number of samples. The resulting points are distributed according to the actual posterior distribution, shown in red. The output samples from the MCMC process can then be used in other Monte Carlo based models, or statistics can be computed from them, such as the expected value and variance of the parameters set.

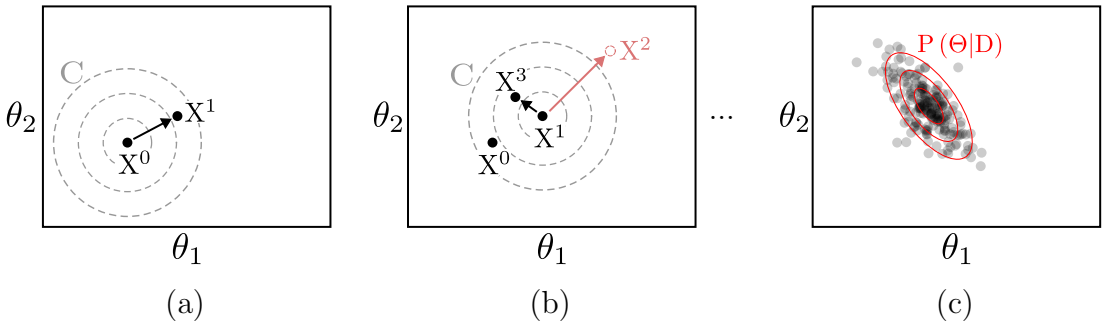

Figure 6.7: Example Markov Chain Monte Carlo Sampling.

With the final set of data points (shown as black dots in Figure 6.7 (c)), one can estimate the shape of the posterior distribution, generate random samples from the final set of points, or estimate the most likely parameter distribution in a learning process. The latter is done throughout this research; however, it is easy to conclude that once the parameter space has been learned sufficiently, one can sample this distribution in other external models.

There is one drawback to the Metropolis-Hastings MCMC algorithm. It starts with a fixed covariance matrix for the proposal distribution. It requires additional tuning to propose new points that are still within the distribution but without getting stuck in a high-probability location. An Adaptive Metropolis algorithm allows for adaptation of the proposal distribution as samples are generated, providing a much more efficient sampling algorithm than the Metropolis-Hastings MCMC method.[92] Delayed Rejection Adaptive Metropolis (DRAM) MCMC extends Adaptive Metropolis MCMC by continually adjusting the proposal covariance matrix based on the current samples in the distribution while also re-proposing a new point using a reduced magnitude covariance matrix if the initial proposal is rejected. The re-proposal process is then repeated until a sample is accepted, with the acceptance ratio calculated based on the recurrent formula provided by Haario et al.[93]. By doing this, the proposal distribution for new points auto-tunes to match the general shape of the distribution it tries to estimate while also delaying the rejection process at each point. This enables more efficient sampling compared to other Monte Carlo methods. The methodology for DRAM is shown in Algorithm 6.

Algorithm 6 Delayed Rejection Adaptive Metropolis MCMC

Require: Initial State Vector $\Theta = [\theta_0 \dots \theta_i]$, Some Function $f(\Theta) = \mathcal{P}(\Theta|\mathrm{D})$

1: Initialize at a point in the state space, $\Theta^k = \Theta^0$, and Proposal Covariance Matrix, $\mathrm{C}^k = \mathrm{C}^0$
2: Propose a new sample in the state space, $\Theta^{k+1} \sim \mathcal{N}(\Theta^k, \mathrm{C}^k)$
3: Evaluate function, f, at Θ^k and Θ^{k+1}
4: Compute acceptance ratio, $a(\Theta^k, \Theta^{k+1}) = min\left(1, \frac{f(\Theta^{k+1})}{f(\Theta^k)}\right)$
5: Draw random sample from a uniform distribution, $u \sim \mathcal{U}[0, 1]$
6: **if** $u \leq a$ **then**
7: Accept new sample, Θ^{k+1}, move to new location, update C^{k+1} based on Haario et al.[93]
8: **else**
9: Reject Θ^{k+1} and re-propose new $\Theta^{k+1} \sim \mathcal{N}(\Theta^k, s\mathrm{C}^k)$, where $s < 1$, go to Step 3
10: **end if**
11: Increment k
12: Repeat 2-11 for a given number of samples

Figure 6.8 shows an example of the DRAM process, where Figure 6.8 (a) shows the initial proposal process in which the proposed point is rejected. Figure 6.8 (b) shows the re-proposal process from a scaled-down covariance matrix. Figure 6.8 (c) shows the update process for the proposal covariance matrix for the next step. The process repeats for a given number of samples, and the resulting posterior distribution will match the results shown in Figure 6.7 (c), without the need for human-in-the-loop tuning, while also being more efficient computationally.

It is essential to recognize that the samples returned from MCMC represent random samples from the posterior distribution but not the exact posterior distribution. This is the trade-off in MCMC and using an exact update to Bayes theorem, which is not always possible analytically. In this project, the *Python* version of the MCMC package call *ParaMonte* was used for the sampling, post-processing, and initial figure generation.[94] This package allows for easy implementation of DRAM MCMC to any model. Also, it can take advantage of multiprocessing speed-ups without the need for a complete change to the analysis code.

Finally, trade-offs exist between using the Monte Carlo method in a given application and other options other than what has been discussed above. For example,

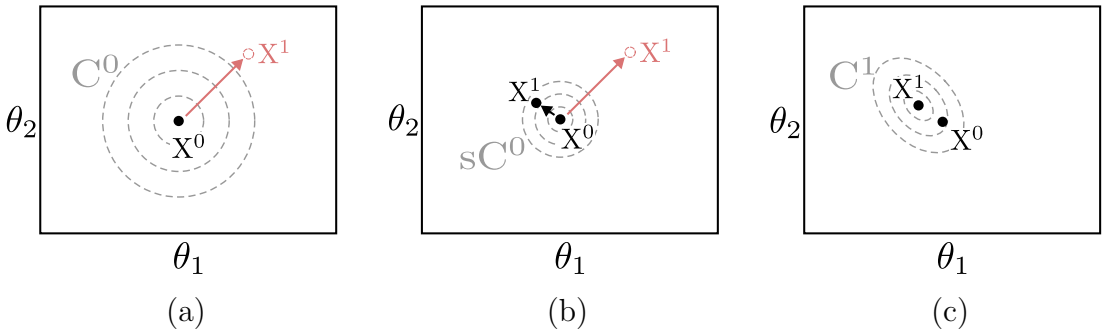

Figure 6.8: Example Delayed Rejection Adaptive Metropolis MCMC Sampling.

the integration of simple functions can be calculated accurately using Monte Carlo sampling with a large enough number of samples. Still, it is much more efficient to use analytical integration if possible. A similar situation arises with MCMC with respect to optimization. Optimization is solving for the best possible answer to the question at hand; however, it returns a single value, and propagating uncertainty and measurement variance through the optimizer is difficult, if not impossible, for certain optimization schemes. MCMC, on the other hand, provides an estimate of the distribution of probable parameter values while also propagating measurement uncertainty and variance through the likelihood function in the Bayesian update. This property of MCMC parameter estimation is particularly well suited for analyzing RDE data sets, as there is typically high cycle-to-cycle variation in measured values.

6.4 Results for Detonation Wave Losses Modeling

The following section provides the results from studying the non-ideal detonation models from Section 6.2. First, an evaluation of the effects of deflagration-based losses will be provided using the Deflagration Loss Model. Next, the non-ideal CJ and ZND models will be examined to study the losses present within the detonation region. This section will conclude with a study combining both of the latter two models, followed by a review of the detonation characteristics as they apply to "weak" detonation waves.

6.4.1 Deflagration Loss Model

The following table provides a list of experimental run conditions and measurements used to evaluate the Deflagration Loss Model. These will be discussed later in this section.

Case	$\dot{m}$, [g/s]	ϕ	U, [m/s]	U/U_{CJ}, [%]	σ_U, [%]	$\frac{P_2}{P_1}$	$\left(\frac{P_2}{P_1}\right)_{CJ}$	σ_P, [%]
654	400	1.1	1564	78.4	3.07	2.3	15.1	6.07
656	130	0.9	1379	71.9	1.05	2.0	13.0	2.73
657	130	1.2	1463	72.1	3.2	1.9	12.5	3.01
658	130	1.4	1520	73.3	7.55	1.9	12.4	3.09
659	160	0.7	1325	74.9	1.19	2.3	17.3	3.4
660	150	0.9	1412	73.1	2.39	2.1	13.8	3.58
661	150	1.1	1469	72.9	4.03	2.1	13.3	3.66
662	150	1.4	1464	70.9	5.99	1.9	12.3	2.95
663	180	0.7	1343	76.0	1.25	2.5	18.9	4.83
664	180	0.9	1451	75.5	1.31	2.2	14.3	3.62
665	180	1.1	1508	75.2	3.76	2.1	13.4	3.76
666	180	1.3	1508	73.3	3.15	2.1	13.7	3.42
667	230	0.6	1387	79.2	1.28	2.1	16.1	5.02
668	230	0.9	1480	77.9	2.62	2.3	15.3	4.69
669	230	1.0	1536	77.6	2.6	2.3	14.8	5.03
670	290	0.6	1403	81.3	1.3	2.2	16.9	6.08
672	280	0.8	1465	77.6	3.02	2.4	16.1	5.34
675	290	1.0	1548	78.3	1.77	2.5	16.0	5.94
677	400	0.6	1399	82.3	1.59	3.4	26.4	8.7
681	400	1.0	1539	78.5	3.83	2.2	14.5	5.5
682	390	1.1	1542	76.9	4.37	2.7	17.4	7.9
686	230	1.3	1562	76.4	1.33	3.0	19.3	8.38

Table 6.2: Summary of experimental operating conditions for select runs used to evaluate the Deflagration Loss Model.

We have already seen how parasitic combustion and leaked fuel affect the performance of a detonation wave in terms of the wave speed and pressure ratio (see Figure 6.6). We will now dive deeper into analyzing these effects on other detonation

performance metrics, defining a representative "gain" of a detonation wave in the process. This "gain" metric examines the change in the available energy at the CJ plane, (3.2), as a function of the two loss parameters, ξ_P, and ξ_L. These results are shown in Figure 6.9, where the "gain" is determined by the energy available at the CJ plane, shown in Equation 6.46.

$$G = h_{t,3.2} - h_{t,3'} \tag{6.46}$$

where the total enthalpy is defined as:

$$h_{t,i} = h_{s,i} + \frac{u_i^2}{2} \tag{6.47}$$

where the velocity, u_i, is referenced in the laboratory frame. In this case, it is assumed $u_{3'} = 0$ and $u_{3.2}$ is the induced velocity at the CJ plane, which is non-zero. The "gain" plotted in Figure 6.9 is normalized by the ideal "gain" calculated at ξ_P, $\xi_L = 0$. All results produced for Figure 6.9 were conducted with a stoichiometric, premixed hydrogen-air detonation operating at an initial pressure of 2 atm and an initial temperature of 300 K. It is clear that both deflagration loss parameters have a significant impact on the available energy at the CJ plane, which comes as no surprise based on the results shown in Figure 6.6.

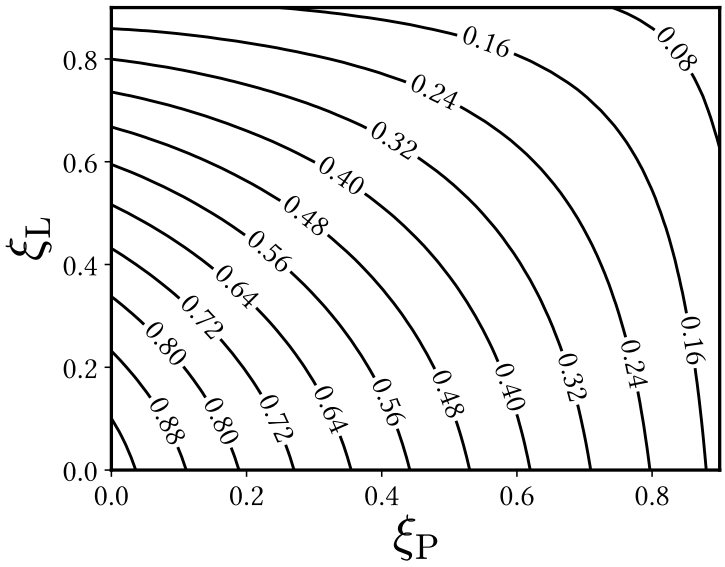

Figure 6.9: Gain, G, at (3.2) versus the deflagration loss parameters. Normalized by the ideal G at ξ_P, $\xi_L = 0$.

The contours of constant "gain" in Figure 6.9 appear to follow the contours of wave speed shown in black in Figure 6.6. Further analysis of the correlation coefficients between the "gain" and both the wave speed and pressure ratio showed a near-perfect correlation between the wave speed and the "gain" as defined in this research, with a correlation coefficient of 0.96. The pressure ratio also had a relatively high correlation coefficient of 0.84. The main driver for the higher correlation in "gain" with the wave speed stems from the fact that higher wave speed inevitably produces a higher induced velocity at the CJ plane, $u_{3.2}$.

These results point to the need for reductions in the deflagration loss parameters if one wishes to improve the performance of the detonation wave, with a particular focus on improving the wave speed. However, the question remains whether the "gain" metric defined in Equation 6.46 is also critical to the performance of the RDE. More discussion on this front will be included in the next chapter, but now we will focus solely on the detonation wave performance.

Figure 6.10 shows a normalized "gain" at the CJ plane as a function of the fraction of fuel consumed in the detonation wave, χ_D, defined by Equation 6.33. The solid lines represent constant leaked fraction, ξ_L, which ranges from $[0, 0.9]$ in steps of

0.15, where the right most solid line represents $\xi_L = 0.0$ and the left most solid line represents $\xi_L = 0.9$. The dashed lines represent a constant parasitic fraction, ξ_P, with the same range and steps where the top dashed line represents $\xi_P = 0.0$ and the bottom dashed line represents $\xi_P = 0.9$. From this plot, it is clear that there is a high correlation between the "gain" and the fraction of fuel consumed in the detonation wave, where the correlation coefficient was calculated to be 0.99. As the detonation fraction approaches 0, so does the "gain" metric, which means that the model is approaching the ideal deflagration device with the same initial conditions.

An interesting takeaway from Figure 6.10 is the fact that at a high detonation fraction, in the range of 0.8, the "gain" can vary between approximately 0.7 and 0.9 of the ideal detonation "gain". This means that it is of increased importance where the heat addition is distributed. For example, parasitic combustion appears to be much worse than leaked fuel of the same magnitude for both the "gain" and the detonation pressure ratio. This result means that despite consuming a large fraction of fuel in the detonation if the rest of the fuel was consumed in a parasitic manner, the performance of the wave is worse than if that fuel had simply leaked through without contributing to the detonation heat release, a similar result as the detonation pressure ratio.

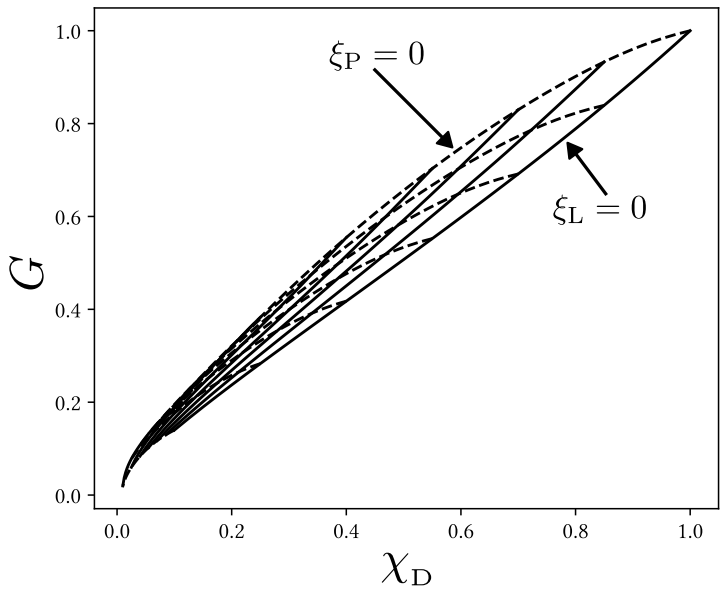

Figure 6.10: Gain, G, versus detonation fraction, χ_D. Solid lines of constant leaked fraction, ξ_L, and dashed lines of constant parasitic fraction, ξ_P. Line separated by loss parameter increments of $0.15 \in [0, 0.9]$.

To better capture the sensitivity of the "gain" metric across the detonation wave to each loss parameter in the Deflagration Loss model, a global sensitivity analysis was conducted using the Sobol Indices method.[95] Table 6.3 shows the total and first-order sensitivities, along with their associated 95% confidence interval. To generate these results, 6144 sets of loss parameters were drawn according to the Sobol methodology, and the secondary effects were neglected as the null value was contained within all 95% confidence intervals. As expected from the examination of Figure 6.6, the "gain" metric is most influenced by the parasitic fraction. This is likely due to the pre-heating of the pre-detonation reactants, which essentially reduces the Mach number, and therefore strength, of the detonation wave. The leaked fraction is also detrimental to the "gain"; however, it was slightly less impactful, echoing the sentiment that the parasitic combustion appears to be most impactful on detonation performance.

Sobol Index	ξ_P	ϵ_{ξ_P}	ξ_L	ϵ_{ξ_L}
S_T	0.64	0.06	0.44	0.05
S_1	0.56	0.07	0.36	0.06

Table 6.3: Sobol's Sensitivity Indices for the loss parameters in the Deflagration Loss Model.

Using the deflagration loss model and the experimental dataset shown in Table 6.2, the deflagration loss parameters were estimated for each case, and the following results of these values were compared to other measurements of interest. The loss parameters were estimated using the measured wave speed and pressure ratio (from high-speed pressure transducers within the RDE channel) and the MCMC framework discussed in Section 6.3. With the parasitic and leaked fuel fractions, the detonation fraction, χ_D, can be calculated with Equation 6.33. Figure 6.11 shows a visualization of the correlation between the estimated detonation performance and the bulk flow conditions within an experimental RDE.

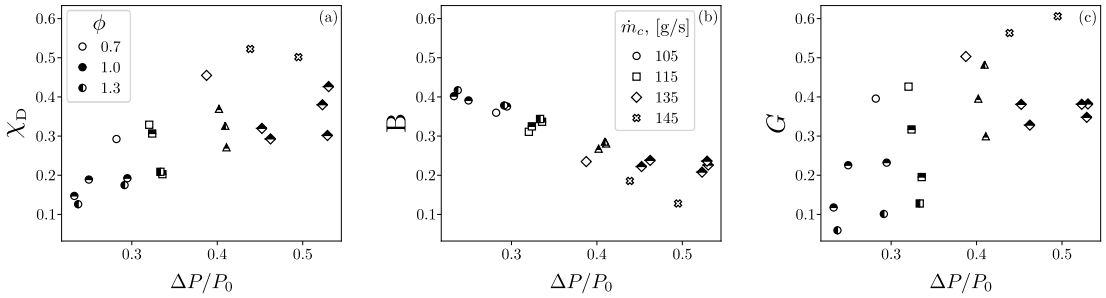

Figure 6.11: Estimated detonation fraction (a) and estimated "gain" at the CJ plane (b) versus inlet pressure drop normalized by plenum total pressure.

Figure 6.11 (a) shows the estimated detonation fraction as a function of the inlet pressure drop normalized by the plenum total pressure. This subplot is binned into three different equivalence ratio bands of lean, stoichiometric, and rich (shown by the marker fill style), as well as binning the corrected mass flow rate by marker shape, where the corrected mass flow rate is normalized by the total pressure and temperature of the plenum, Equation 6.48. At a given equivalence ratio, the detonation fraction appears to correlate directly with the inlet pressure drop, which is also a function of the corrected mass flow rate. At a certain mass flow rate/inlet pressure

drop, this trend levels off. This is especially evident in the lean and stoichiometric conditions, unfilled and filled marker styles, respectively.

$$\dot{m}_c = \dot{m} \frac{\sqrt{\frac{T_t}{T_{ref}}}}{\frac{P_t}{P_{ref}}} \tag{6.48}$$

Figure 6.11 (b) shows the calculated blockage fraction, B, as defined by Feleo et al., versus the inlet pressure drop.[96] As the inlet pressure drop increases, the inlet blockage decreases, indicating a "stiffer" inlet results in a much lower blockage fraction. This intuitively makes sense based on the argument that a higher inlet pressure drop would better resist the blockage caused by the detonation wave. The blockage fraction itself is not a great indicator of performance, so a comparison with the "gain" across the detonation wave is required. One note on the blockage fraction is that a lower inlet blockage (stiffer inlet) results in a decrease in the parasitic combustion fraction. This indicates that a trade-off must be made between the inlet pressure drop and the parasitic combustion fraction to maximize performance across the cycle.

Figure 6.11 (c) shows the "gain" as a function of the normalized inlet pressure drop, where the gain is normalized by the ideal gain with no deflagration losses. This plot shows that the "gain" increases with increased inlet pressure drop and under leaner conditions. At a given mass flow rate, a leaner condition results in less pressure drop across the inlet due to the lower blockage from the fuel injection. This subplot raises the issue that in an experimental setting, the "gain" across the detonation wave is also inversely correlated with the inlet pressure drop. This result will be discussed again with the full State to State model in a later section, but in general, it is concerning, as the performance of the device is highly correlated with inlet pressure losses.[39]

To reduce inlet pressure losses, a lower corrected mass flow is required. However, based on experimental data, a lower corrected mass flow results in a higher blockage fraction and could even lead to inlet backflow. Based on these results, there appears to be an inverse correlation between the detonation performance and the inlet pressure drop. It should be noted that these performance estimates are focused strictly on the performance of the detonation wave; a more robust model is required to estimate the RDE performance.

The final aspect of this analysis includes a short discussion of detonation-based combustion as a lower entropy combustion method over deflagration. We will start

with the knowledge that in the Deflagration Loss Model, the fuel is distributed to certain reaction bins, which means that the heat release is distributed in a certain way to produce a final CJ state, (3.2). A direct connection can be drawn to the work in RAM jet combustors, where tailoring the heat release distribution can result in an optimal performing device. We will examine a similar concept with the deflagration loss model by calculating the detonation work, and the entropy production at the CJ state, (3.2), normalized by the entropy produced in an ideal deflagration combustor at the same initial conditions. These results are shown in Figure 6.12, where the heat release distribution is shown with contours of constant parasitic fraction in dashed lines and constant leaked fraction in solid lines.

$$q_{in} = \mathrm{LHV}_f Y_f \tag{6.49}$$

From this plot, we can glean two key takeaways: the entropy production decreases as a function of the leaked fuel fraction and the trade-off between entropy production and detonation work. First, the reason for the decreasing entropy production with increased leaked fuel fraction is solely due to the fact that the deflagration loss model does not provide a combustion path for leaked fuel, as it stops at the CJ plane. In this vein, the entropy production is minimized by not burning any of the fuel; therefore, it is argued that the entropy production across the detonation, on its own, may not be a valid performance metric for characterizing RDE performance.

Moving to the second observation, at a given leaked fuel fraction, a reduction in entropy production (due to lower parasitic fraction) comes at the cost of a higher detonation work term; therefore, a reduction in available energy for work extraction. The issue arises that a higher performing detonation, in terms of wave speed and detonation fuel fraction, requires a higher detonation work to be sustained.

Another result of this analysis is the discussion surrounding performance evaluations in RDEs, where one can work to improve the detonation wave performance (wave speed, detonation fraction, pressure ratio, etc.); however, the benefits of RDE devices are only realized based on the work extraction that occurs downstream of the detonation wave and other cycle performance metrics like inlet pressure drop. This leads to the need for a RDE performance modeling framework based on the full RDE cycle, such as the State to State model discussed in Algorithm 9 in Section 6.7.1, to evaluate the actual benefits of RDEs and where shortcomings may be corrected to improve performance.

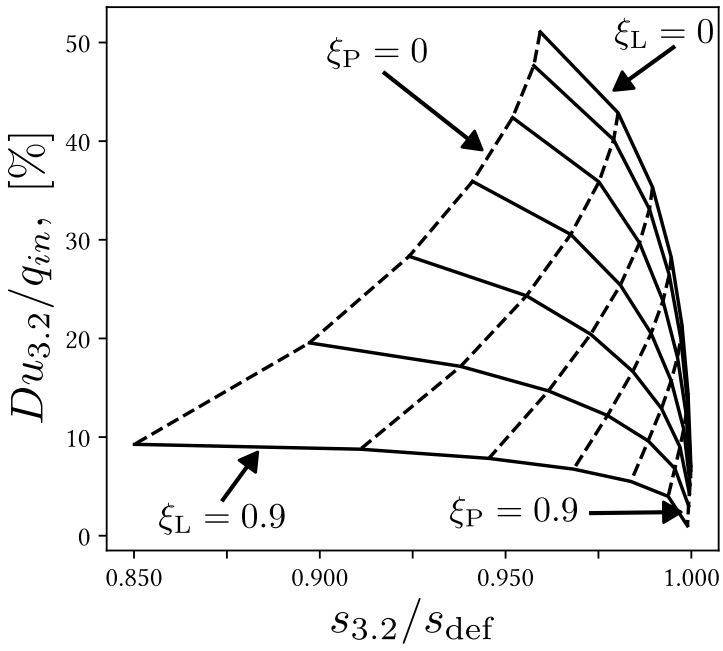

Figure 6.12: Detonation work required (normalized by heat addition) versus entropy creation as a function of heat release partitioning. Entropy normalized by ideal deflagration at the same initial conditions. Dashes lines of constant parasitic fraction, ξ_P, and solid lines of constant leaked fraction, ξ_L.

6.4.1.1 MCMC Results

The methods outlined in Section 6.3 were applied to the set of runs given in Table 6.2. For each run, the average value of wave speed and pressure ratio, along with their associated measurement variance, were used to learn the deflagration loss fractions by the MCMC sampling process. Table 6.4 shows the final results of the MCMC sampler, where the two listed deflagration fractions are the expected value (mean) from the posterior distribution. Finally, the effective sample size is shown as an indicator of sampler efficiency.

Run Number	ξ_P	ξ_L	ESS	Run Number	ξ_P	ξ_L	ESS
654	0.48	0.18	23074	667	0.50	0.09	45244
656	0.65	0.46	20974	668	0.52	0.23	21483
657	0.68	0.54	27805	669	0.54	0.41	33182
658	0.72	0.55	27847	670	0.45	0.05	15181
659	0.55	0.35	36750	672	0.53	0.32	17999
660	0.63	0.48	36086	675	0.52	0.39	32004
662	0.67	0.47	41768	677	0.34	0.24	30767
663	0.53	0.30	14062	681	0.50	0.24	28232
664	0.58	0.27	20924	682	0.48	0.42	28090
665	0.61	0.48	44535	686	0.32	0.52	25508
666	0.64	0.42	32459				

Table 6.4: MCMC Sampling Results for the Deflagration Loss Model.

Figure 6.13 shows an example of the posterior distribution of a selected run, with the marginal distributions for each parameter on the upper and right plots and a kernel density estimate of the posterior distribution piloted on the model parameter map in the center. The posterior seems to trace out a path along a constant wave speed line but spanning a wide range of pressure ratios. This is indicative of the measurement uncertainty and variance in both of these measurements. As the model is less certain of the pressure ratio, or more cycle-to-cycle variation occurs in the pressure ratio measurement, the posterior is also less certain in the parameters it samples. This is a key example of error propagation through MCMC parameter estimation and the usefulness of MCMC in general.

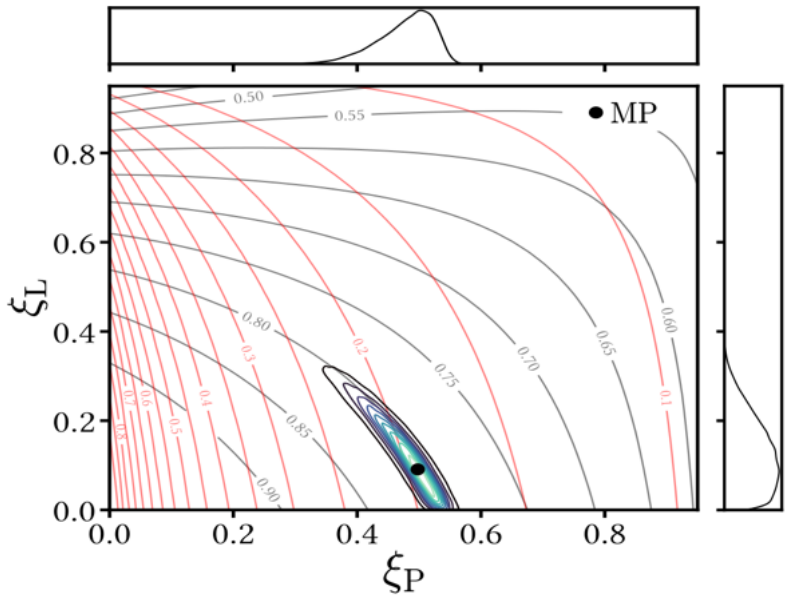

Figure 6.13: Posterior Distribution of the Deflagration Loss Parameters for Run 667.

Another important factor in the uncertainty in the value for ξ_L is the fact that the model does not allow for all combinations of measured values. In this example, the measured values of wave speed and pressure ratio are 1414 m/s and 2.1335, respectively, while the maximum a-posteriori, MAP, of the two quantities are 1412 m/s and 2.489. The map does not include the experimental measurement combination within its bounds, so the MCMC sampler finds the closest representation allowed for by the model. In this specific case, the measured pressure ratio was much lower than the minimum pressure ratio on the map, given the measured wave speed, suggesting other potential loss terms are missing from this model. With these concerns acknowledged, a comparison to experimental data was conducted to determine the validity of the model.

6.4.1.2 Comparison to Measured Deflagration

Experimentally, it is difficult to quantify the heat release distribution (in both space and time) over the cycle, but the OH* chemiluminescence emission can be used as a marker for the locations and, to an extent, the magnitude of the heat release. This approach was outlined by Feleo et al. [72], who conducted OH* emission measure-

ments at a single fixed point in the RDE as a function of time using a photo-multiplier tube (PMT) and suitable collection optics and filters (see Figure 6.2 for an example). To relate the PMT data for each run to the deflagration loss fractions, the following methodology was used under the assumption that the PMT captures all of the heat release processes and that the fuel is completely consumed within this measurement window. The PMT data in Figure 6.2 were broken down into three regions: parasitic combustion section, detonation section, and commensal combustion section. The area under the curves for each region in Figure 6.2 was used to determine the percentage and total heat release in these regions. The relationships between components of the PMT data and the deflagration loss parameters are shown below.

First, the total area under the OH* distribution in Figure 6.2 is set as the total heat release, inherently assuming 100% combustion efficiency. Thus:

$$Q_T = Q_P + Q_D + Q_C \tag{6.50}$$

Each term is normalized by the total heat release to obtain the fraction of heat release in each region:

$$\%Q_P + \%Q_D + \%Q_C = 1 \tag{6.51}$$

The parasitic and leaked combustion parameters from the deflagration loss model are related to the measured quantities by the following equations:

$$\xi_P = \frac{Q_P}{Q_T} = \%Q_P \tag{6.52}$$

$$\xi_L = \frac{Q_C}{Q_T - Q_P} = \frac{\%Q_C}{1 - \%Q_P} \tag{6.53}$$

With these relationships developed, a comparison was made between the estimated deflagration loss fraction from the MCMC application and the measured PMT values from Feleo et al. converted into the deflagration loss fractions. Figure 6.14 compares the results for all the experimental cases listed in Table 6.2. In nearly all cases, parasitic combustion estimated with the deflagration loss model was much higher than the PMT data suggests, while the estimates for leaked fuel were only slightly lower than measured, in general. Inputting all PMT points into the deflagration loss model predicts higher wave speeds and pressure ratios than measured values, indicative of the difference between what the PMT is measuring and the actual deflagration losses.

From these initial results, it is clear that the deflagration loss model and the PMT data do not result in the same parameters. This could be mostly due to the

fact that the PMT methodology may not properly capture EGR, while the parasitic combustion fraction accounts for both EGR and combustion of fresh reactants. The trend of the PMT data falling towards the lower end of the parasitic combustion parameter is indicative of this phenomenon. Another area where this comparison may be lacking is dependent on the location of the measurements from PMT data. The PMT will only measure the OH* emission where there is combustion, so the sensor may miss certain regions of combustion depending on its axial location. The assumption for this analysis was that the PMT was located in the fill region and captured the full cycle combustion, which allowed for the conversion of the measured heat release distribution to the deflagration loss model parameters. This is most certainly not the case, as the combustion processes may occur both ahead of and aft of the axial location of the PMT sensor within the RDE.

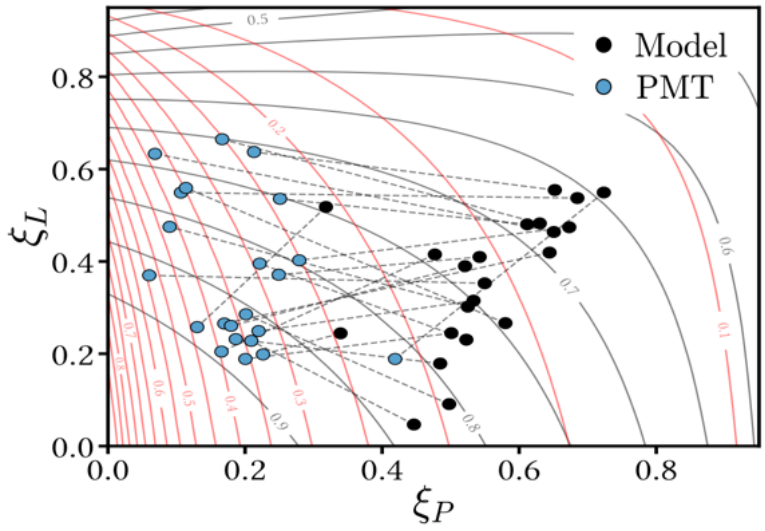

Figure 6.14: Comparison of deflagration loss model parameters to PMT measurement. Wave speed is shown as black contours, and the pressure ratio is shown as red contours.

To try to account for these issues, the simplest next step was to add a term that was separate from the commensal combustion fraction that accounts for leaked fuel that is not consumed within the PMT measurement location. This would be leaked fuel, which the PMT model does not account for but is captured in the detonation

model. This is described as follows:

$$Q_T = Q_P + Q_D + Q_C + Q_L \tag{6.54}$$

where the Q_L term is heat (fuel) that leaked through the detonation but was not combusted within the measurement window of the PMT. These terms are re-normalized to percentages with the following equation:

$$\%Q_P + \%Q_D + \%Q_C + \%Q_L = 1 \tag{6.55}$$

Equations 6.56-6.58 (below) shows the updated conversion from the measured heat release distribution from the PMT data to the model parameters, but now including the purely leaked fuel term. An increase in the purely leaked fuel will lead to an increase in the model leaked fuel parameter, ξ_L, and a slight decrease in the parasitic combustion parameter, ξ_P. The additional purely leaked parameter also acts as a proxy for combustion efficiency, as shown by Equation 6.58. In this analysis, it is not possible to validate the updated model with the PMT data and the purely leaked parameter because the heat release profiles are calculated assuming complete combustion. Additional measurements would be needed to estimate the combustion efficiency of the RDE.

$$\xi_P = \frac{Q_P}{Q_T} = \frac{Q_P}{Q_P + Q_D + Q_C + Q_L} \tag{6.56}$$

$$\xi_L = \frac{Q_C + Q_L}{Q_T - Q_C} = \frac{Q_C + Q_L}{Q_D + Q_C + Q_L} \tag{6.57}$$

$$\eta_c = \frac{Q_T - Q_L}{Q_T} = \frac{Q_P + Q_D + Q_C}{Q_T} = 1 - \frac{Q_L}{Q_T} \tag{6.58}$$

In the same manner, an example re-circulation fraction, ξ_R parameter, can be introduced in an attempt to account for product gas re-circulation that would not be captured by the PMT. This results in a simple addition to the parasitic fraction calculated from the PMT data.

Figure 6.15 shows an example of the effects of the 10% purely leaked parameter for the PMT relations, as well as having $\xi_R = 0.2$. Including the purely leaked fraction makes a slight trade between the parasitic fraction and the leaked parameter, where there is a much more drastic increase in the leaked fraction relative to the slight decrease in the parasitic fraction. The plot also shows an example of adding a re-circulation fraction that simply acts as a linear shift in the parasitic fraction. This is

because the amount of flow re-circulation will change the calculated ξ_P for the PMT data but does not count towards the measured heat release profile.

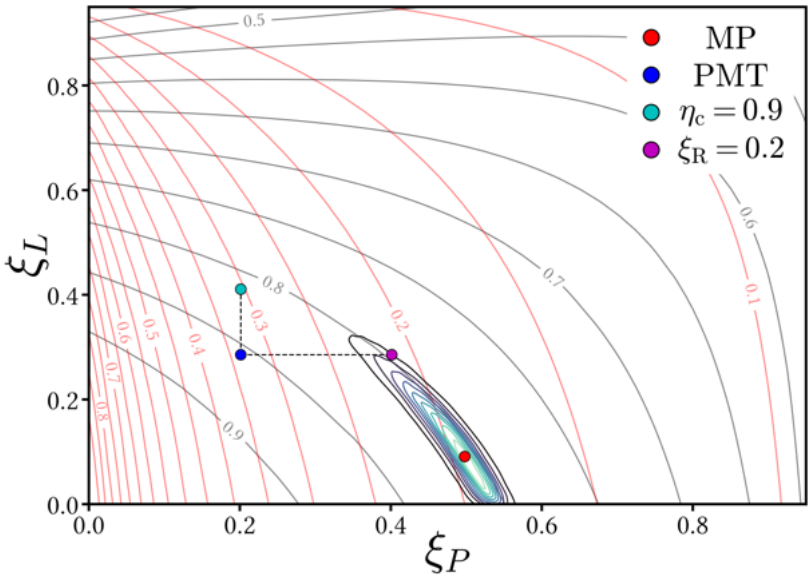

Figure 6.15: Example effects of additional loss parameters.

The search for additional parameters to gain a better model fit to the PMT measurements was not exhaustive, as the model and the PMT data represent two different outputs. Despite the discrepancy between the measured values, this model and its results were critical to inform the modeling choices for the state-based RDE cycle model.

6.4.2 Non-Ideal CJ and ZND Models

This section includes the results from both the non-ideal CJ model and the non-ideal ZND model. Because these two models produce similar results in most cases, it makes sense to study their outputs simultaneously. Each loss parameter will be examined on its own and in concert with other losses to determine the individual and compounding effects on detonation performance.

6.4.2.1 Lateral Relief

First, the lateral relief study will be examined by varying the area ratio from 1.0 to 2.0. Figure 6.16 shows the results of this process, where the calculated wave speed, normalized by ideal, is shown in the left subplot as a function of the area ratio for a hydrogen-air detonation at standard temperature and pressure. These results show a modest decrease in wave speed over the change in area ratios. However, when examining the change in the detonation pressure ratio, we see a much more drastic impact. These results are shown in the right subplot and predict a halving of the pressure ratio across the detonation when the CJ area is twice that of the initial area.

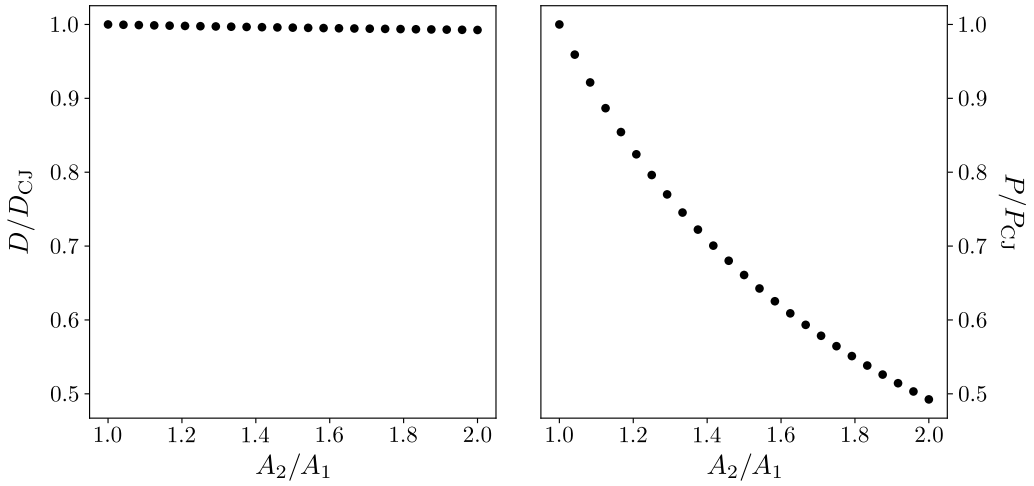

Figure 6.16: Normalized Wave speed and Detonation Pressure Ratio versus Area Ratio using the CJ Solver.

Although the non-ideal CJ framework provides a method to capture the effects of area changes across the detonation wave, it assumes complete equilibrium between the two states. This assumption can easily be tested for validity through the use of the full time marching solution using a modified, non-ideal ZND analysis framework. Figure 6.17 shows the results as a constant area variation rate was specified between 0 and 0.001 m^2/m. It contains the pressure (a), Mach number (b), and laboratory frame velocity (c) profiles for each simulation.

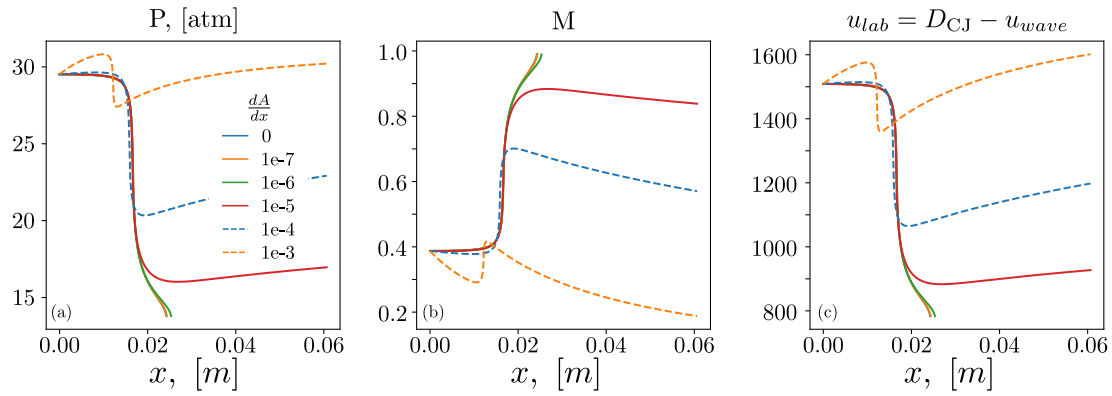

Figure 6.17: ZND profiles as a function of the area change rate for a stoichiometric detonation. Static pressure (a), Mach number (b), and laboratory frame velocity (c).

For small increases in area, $\frac{dA}{dx} \leq$ 1e-6, there is minimal change in these profiles. However, as the area change rate increases, we now notice that the Mach number never reaches $M = 1$, which is the definition of the CJ detonation. Also, as the area change rate increases, we notice an increase in pressure through the induction zone. This is due to the expansion in the area slowing the flow and returning some of the kinetic energy to potential energy (pressure).

Because the ZND solver requires a wave speed as the input condition to calculate the shock strength and post-shock state, we need to vary this parameter from the ideal CJ wave speed that is typically used. This was done for the results shown in Figure 6.18, where ΔU represents a decrease in wave speed from ideal. This sweep in initial velocities was conducted at an area change rate of 1e-5. The figure includes subplots of the pressure, temperature, density, Mach number, thermicity, and laboratory frame velocity across the profiles.

Figure 6.18 shows that as the wave speed is decreased, the maximum Mach number profile slowly increases as well, up to the point where the Mach number reaches the sonic condition. As the velocity decrement increases, the profile continues to reach the sonic condition; however, at a much later value, due to the decrease in the pressure and temperature jump across a weaker shock. This also comes with an increased induction length. In addition, the thermicity profile appears to be clipped before returning to the zero value associated with complete combustion, an aspect that will be reviewed in a later section.

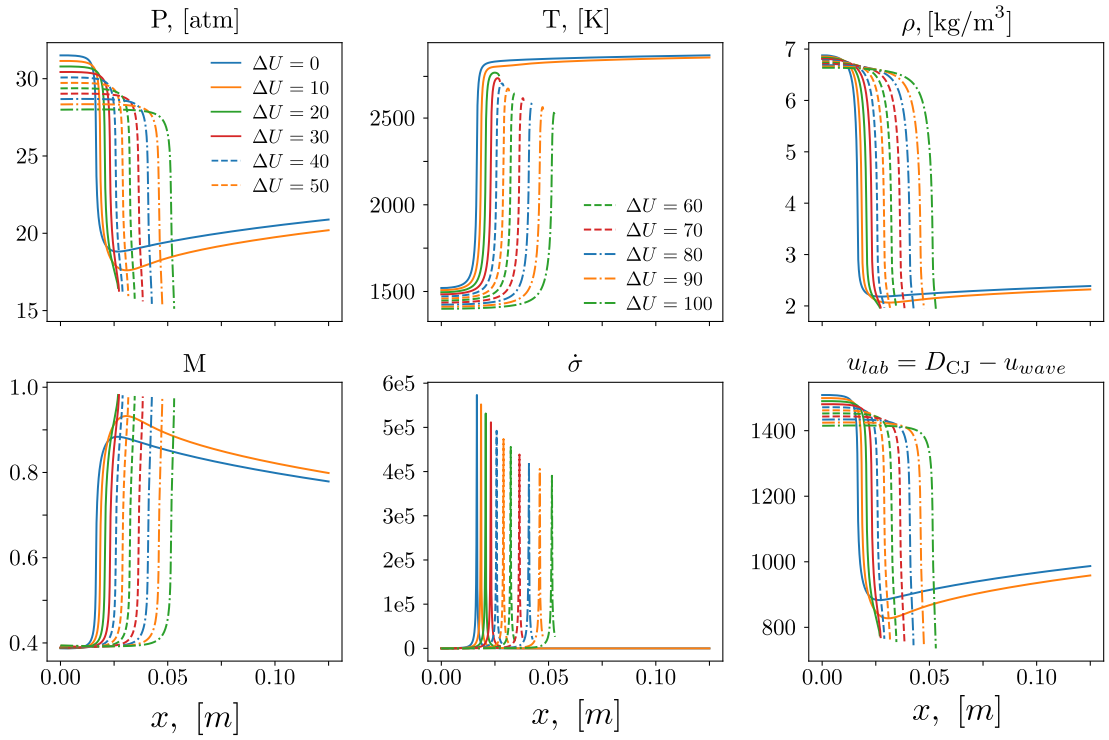

Figure 6.18: ZND profiles at an area change rate, $\frac{dA}{dx}$ = 1e-5, as a function of the velocity decrement for a stoichiometric detonation.

The question now is, what is the correct velocity decrement value? If probed using the non-ideal CJ solver from earlier in this section, the wave speed at a larger area change rate will not produce a significant enough reduction to allow for the CJ condition to be met using the ZND solver. More detail on this subject will be included at the end of this section; however, it led to the development of an iteration methodology used to determine the maximum wave speed that allows the ZND solver to reach the CJ condition, shown in Algorithm 7.

Now that we have defined the algorithm used to find the maximum wave speed, we will examine some of the results. Figure 6.19 shows the Mach number versus distance on the left subplot and the thermicity versus distance on the right subplot. The initial starting point of $\Delta U = 0$ is shown in the red line, the intermediate velocity decrements are shown in the light black lines, and the final velocity, which satisfies the CJ condition, is shown in blue. The final velocity decrement of 88.6 $[m/s]$ was

calculated as the minimum velocity decrement to achieve the CJ condition. The final area change calculated across the ZND structure with this method was 1.039, which would result in an estimated wave speed decrement of less than 1 m/s. This indicates that the assumption of complete equilibrium in the CJ solver may not account for the finite rate effects present in the ZND methodology.

Algorithm 7 ZND with Area Change Solver

Require: $\frac{dA}{dx}$

Initialize solver at ideal CJ wave speed: $U_0 = D_{\text{CJ}}$
while $M_i \neq 1.0$ **do**
    Integrate ZND profile
    if $M_i < M_{i-1}$ **then**
        Break (No convergence possible at $\frac{dA}{dx}$)
    end if
    Decrease initial velocity: U_{i+1}
end while

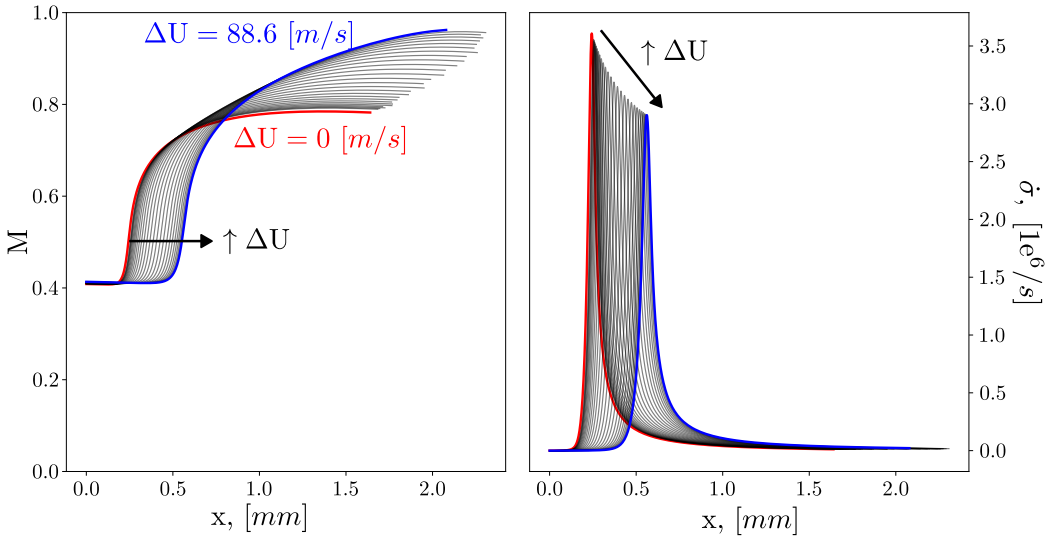

Figure 6.19: ZND profiles during the solution of the ZND iteration method. The red line assumes the ideal CJ wave speed without area change, the blue line represents the first wave speed that allows for the sonic condition for the given area expansion rate, and the black line shows each intermediate step. $\frac{dA}{dx} = 6e^{-4}$.

One interesting takeaway from this plot is the fact that the induction length based on the maximum thermicity has increased with the velocity decrement, at the same time the peak thermicity value has also decreased. Both of these results can be attributed to the lower temperature and pressure ratios provided by the weaker shock.

Comparison of ZND Iteration Method and CJ Solver with Area Change

Now we have a method for solving for the wave speed of a detonation with area expansion in the reaction zone through the use of a ZND solver. The next step is to compare these results with the CJ solver and the area expansion discussed earlier in this section. Figure 6.20 shows the wave speed as a function of the area ratio between the shock and the CJ plane for the CJ solver (orange) and the ZND solver using the wave speed maximization optimizer (blue). It is clear from these results that the CJ solver predicts minimal changes in wave speed as the area ratio is varied to a roughly 3.5% increase in area. The ZND solver, on the other hand, predicts a much steeper drop-off in wave speed, even at these lower area ratios. Note that the wave speed calculated for the ZND solver with no area change is about 5 m/s higher than that of the CJ solver.

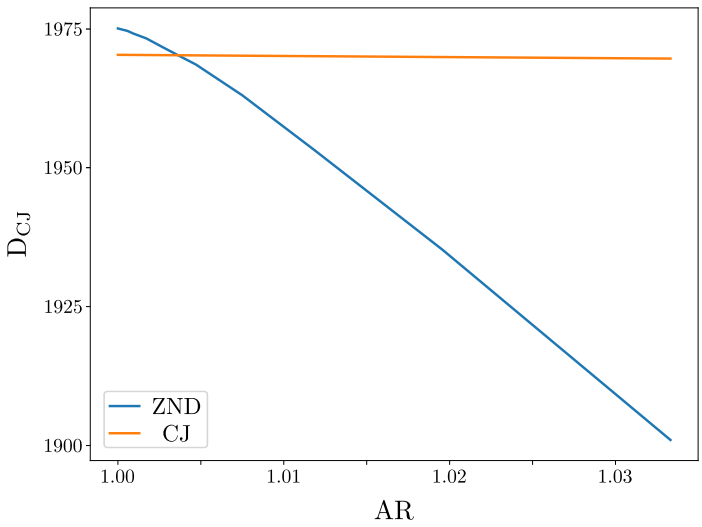

Figure 6.20: Comparison of ZND and CJ solver with area ratio.

This change is likely due to the use of finite-rate chemistry in the solver, as opposed to the equilibrium assumption used in the CJ calculation. Previous testing has shown that even for an ideal case, the final state of the ZND solver can have up to 3.6% difference in thermodynamic properties compared to the CJ solver. Table 6.5 shows the percent difference between the CJ state calculated from the CJ and ZND solvers using an ideal stoichiometric detonation in air for three different fuels and two different reaction mechanisms.

Fuel	Mech	P	T	ρ	h
H_2	GRI3.0	3.42	0.71	2.86	2.64
CH_4	GRI3.0	3.44	0.72	2.86	3.42
C_2H_6	GRI3.0	3.6	0.76	2.99	3.22
H_2	San Diego	-0.16	-0.02	-0.14	-0.12
CH_4	San Diego	-2.04	-0.25	-1.77	-1.98
C_2H_6	San Diego	-2.56	-0.3	-2.23	-2.23

Table 6.5: Table of thermodynamic property percent differences between the CJ solver and the ZND solver's final state.

This change in properties is shown in Table 6.5, was likely due to the larger changes in the concentrations of the major species between the two solvers, where some of the

major species had percentage differences up to 94%. Table 6.6 shows the results for a hydrogen-air detonation using the GRI3.0 mechanism as a reference.

Species	X_{CJ}	X_{ZND}	% Difference
$N2$	0.632	0.635	0.47
$H2O$	0.295	0.293	0.68
$H2$	0.0314	0.0309	1.59
OH	0.0178	0.0201	12.9
$O2$	0.00782	0.0105	34.3
NO	0.00773	0.000465	94.0
H	0.00599	0.00677	13.0
O	0.00210	0.00272	29.5

Table 6.6: Table of major species for an ideal hydrogen-air detonation using the GRI3.0 mechanism.

From these results, we can see the drastic difference between the equilibrium assumption in the CJ solver and the result that finite-rate chemistry predicts. Although these results are likely specific to the reaction mechanism of choice, it is clear that the two do not produce the exact same CJ state. Notably, the reaction mechanisms in question are not directly calibrated for detonation combustion, which may prove to be a major factor in the previously discussed discrepancies.

6.4.2.2 Heat Transfer in the Detonation Region

Next, we examine the effects of heat transfer within the detonation region. This will initially focus on the modified CJ solver and then move to the ZND implementation. **CJ Solver** Figure 6.21 shows plots of the normalized wave speed and detonation pressure ratio as a function of the heat removed from the detonation normalized by the ideal detonation heat release. These results were determined using Algorithm 1. The left subplot shows the wave speed, normalized by the ideal wave speed with no heat transfer, and the right subplot shows the pressure ratio across the detonation wave, normalized by the same ideal pressure ratio. A significant heat transfer value, on the order of 30% of the heat available in the fuel, can be removed with only a 10% reduction in the wave speed; however, this would produce a nearly 20% reduction in the pressure ratio across the wave. This result is similar to the parasitic combustion results in Section 6.4.1, where the wave speed was moderately affected, but the

pressure ratio dropped significantly.

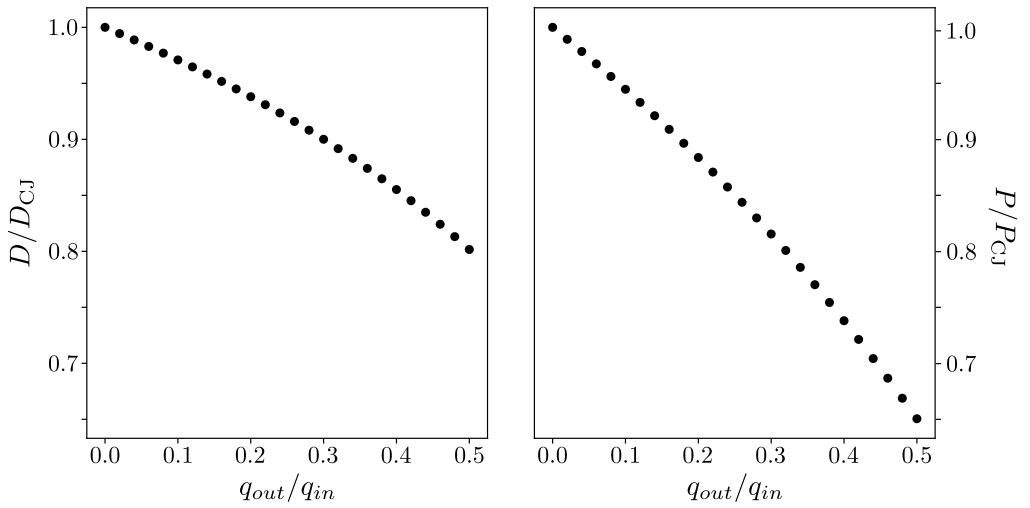

Figure 6.21: Normalized Wavespeed (left) and Detonation Pressure Ratio (right) versus Normalized Heat Transfer.

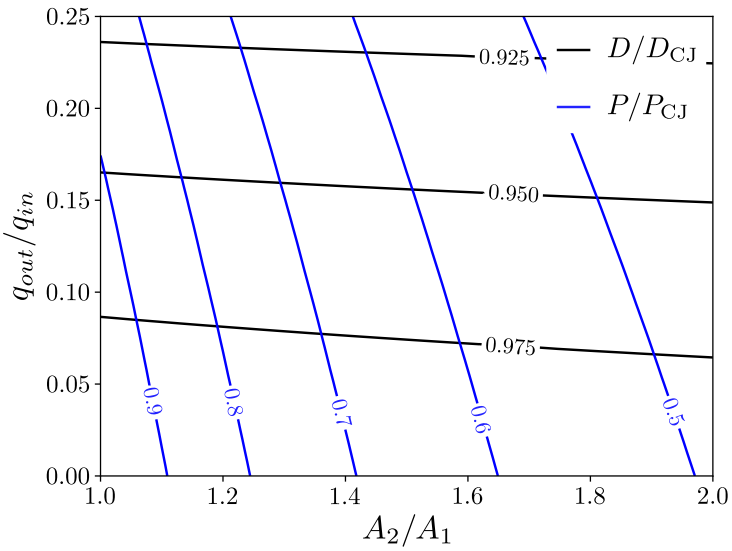

Figure 6.22: Contour Plots of Normalized Wavespeed (black) and Detonation Pressure Ratio (blue) versus Area Change and Normalized Heat Transfer.

If we pull in the CJ analysis results with area change from Section 6.4.2.1, we can study the effects of both area change and heat transfer within the detonation region. Figure 6.22 shows these results as contour plots of the normalized wave speed in black and the normalized pressure ratio in blue. In this example, the removed heat was studied only up to 25% of the heat content in the fuel. In Figure 6.22, we can see that the changes in the area ratio produce less impact on the detonation wave speed compared to the heat transfer but a higher impact on the pressure ratio. Together, these loss mechanisms, even at low magnitudes, can produce significant losses in wave speed and pressure ratio compared to the expected performance of an ideal detonation wave.

ZND Solver Much like the results for the area change, when integrating the ZND profile with heat transfer, there exists a parameter space where the CJ condition will not be met. Because of this, the velocity decrement minimizer in Algorithm 7 was used to calculate the reduction in wave speed from the ideal that allows for the CJ condition to be met. This algorithm was modified to accept the heat transfer coefficient as an input rather than the area change rate. Unlike the results with only area change, the heat transfer coefficient was more troublesome to achieve convergence. Figure 6.23 shows an example sweep of the calculated velocity decrement from ideal required to

attain the CJ condition. It is clear that the solver methodology does not produce a smooth and consistent result expected from the CJ analysis of heat transfer, and any coefficient above 0.05 could not converge within the velocity decrement bounds of [0, 1000] [m/s]. Therefore, the remaining analysis is best viewed from a qualitative perspective.

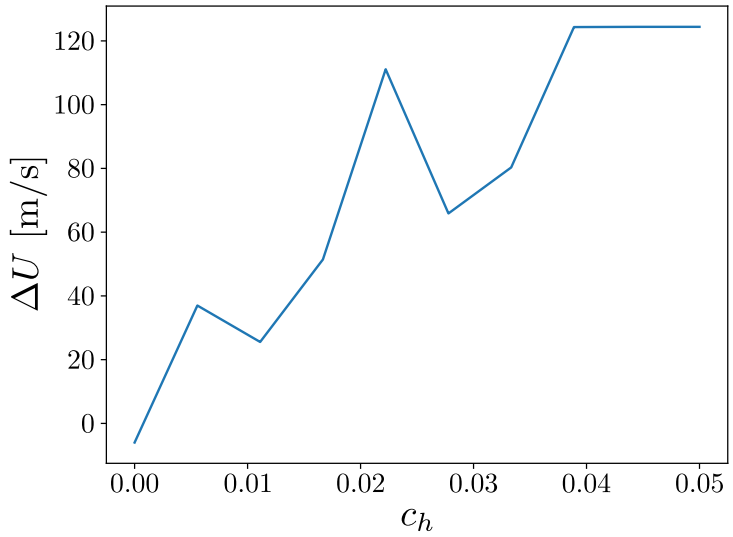

Figure 6.23: Velocity Decrement from Ideal CJ Wave speed versus Heat Transfer Coefficient.

Figure 6.24 shows the normalized wave speed and pressure ratio as a function of the heat transfer coefficient. In general, the wave speed and pressure ratio decrease at a similar rate with heat transfer. This differs slightly from the above results of the CJ analysis, where Figure 6.21 shows that the pressure ratio decreases faster. This is likely due to the difficulty in achieving a converged ZND result and the fact that the ZND model does not assume complete equilibrium at the CJ plane.

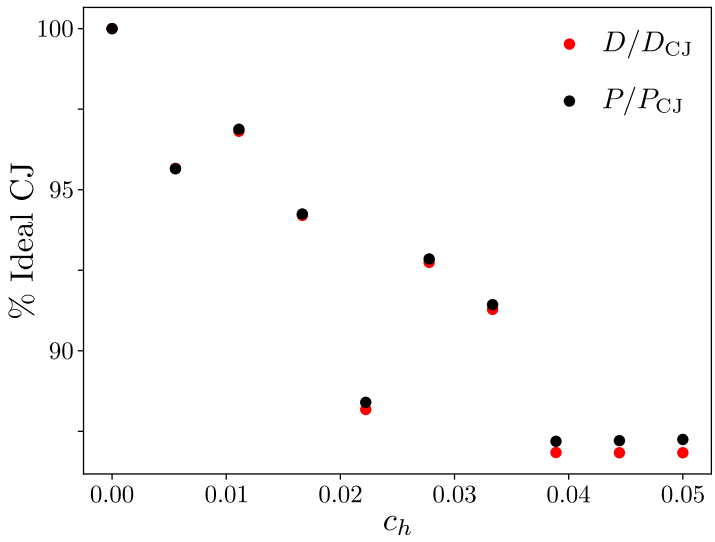

Figure 6.24: Wavespeed and Pressure Ratio from ZND model as a function of the heat transfer coefficient.

The previous results show how heat transfer within the detonation region can negatively affect the performance of the detonation wave. Like the other loss parameters, heat transfer from the detonation wave to the boundary will reduce both the wave speed and the pressure ratio across the detonation wave. In this case, heat transfer will almost equally decrease both metrics, something that is often seen experimentally (see Table 6.2).

6.4.2.3 Friction in the Detonation Region

This section discusses the results from the momentum loss sweep, which accounts for friction within the detonation region. For the CJ analysis, the total momentum loss term varied, while the ZND analysis varied the friction coefficient.

CJ Solver Figure 6.25 shows the normalized wave speed and pressure ratio across the detonation wave as a function of the momentum loss term, F. This plot shows a steady acceleration in the loss in both metrics as the momentum loss term increases. Both metrics decrease at roughly the same rate with the momentum losses.

Figure 6.26 shows the result for the CJ solver with a momentum loss combined with area change (left) and heat transfer (right). From these plots, we can see which

terms are most detrimental across their specified parameter sweep. The left subplot shows that the momentum loss solely determines the wave speed (see Figure 6.16), while both the momentum losses and the area change provide a similar decrease in the pressure ratio.

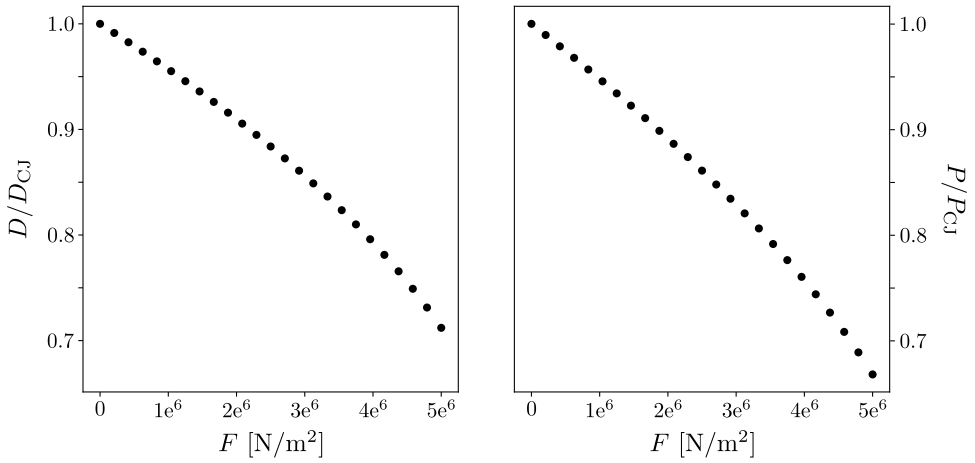

Figure 6.25: Normalized detonation performance as a function of the total frictional momentum loss. Wave speed (left) and pressure ratio (right).

Finally, the right subplot shows the relationship between the normalized performance metrics as a function of the momentum loss and heat transfer. This plot shows that across the parameter space, the heat transfer provides slightly less of a change in both performance metrics. Note that while the area ratio and heat transfer losses can be easily related to a given input metric, the momentum loss term bounds were arbitrarily set. With a more customized momentum loss term with physical bounds, these results could change to indicate that the momentum loss is not more detrimental to the detonation performance.

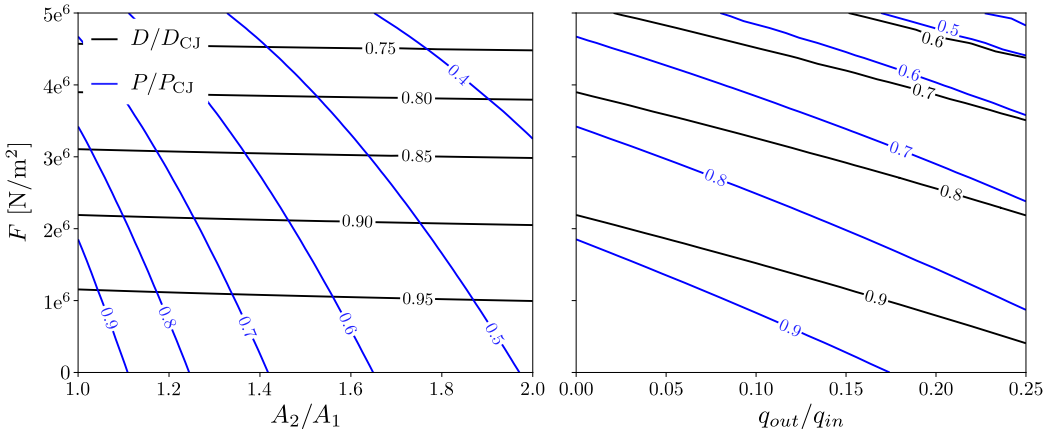

Figure 6.26: Contours of normalized detonation performance as a function of total frictional momentum losses, area change, and heat transfer. Wave speed (black) and pressure ratio (blue).

ZND with Friction Finally, we examine the ZND solve with a friction coefficient specified to capture the momentum losses through the detonation wave. This solver used the same velocity decrementing scheme presented in Algorithm 7, and in general, produced similar results to the CJ solver (see Figure 6.25).

Figure 6.27 shows the thermicity across the detonation wave as a function of the friction coefficient. From this plot, we can see that as the friction increases, the thermicity profile does not return to the post-combustion value seen in the case with no skin friction. This is because the sonic condition is achieved before the reaction can complete.

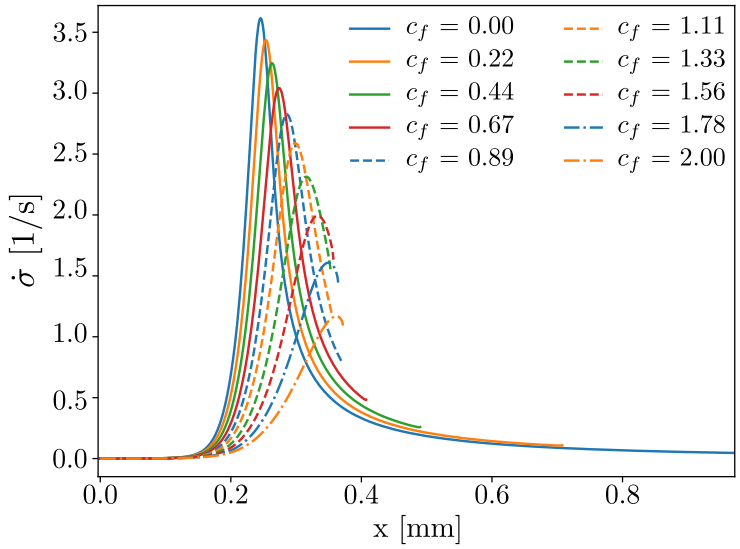

Figure 6.27: Thermicity profiles from ZND solver with friction as a function of the coefficient of friction.

To confirm that the CJ plane was reached before the fuel was completely consumed, the CJ chemical composition was analyzed. Figure 6.28 shows the mole fraction of hydrogen remaining at the CJ plane as a function of an increasing friction coefficient. This clearly shows that at a high enough value of friction, the combustion process is halted due to reaching the CJ plane prematurely, and the trend approaches the limit of the initial mole fraction of the reactants. This result does bring questions as to the validity of the velocity decrement algorithm used to solve these ZND profiles. A potential update to the methodology may result in solutions where the majority of the fuel is consumed regardless of the friction coefficient.

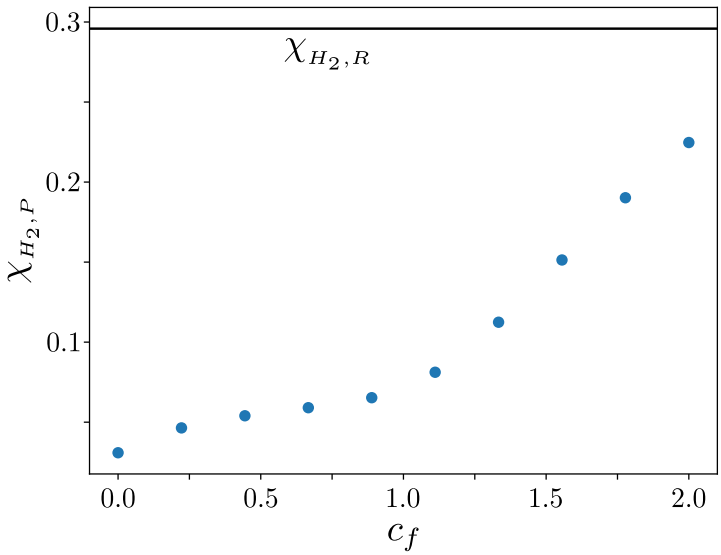

Figure 6.28: Final fuel content at the end of the ZND profile as a function of friction coefficient.

If the ZND solution indeed shows a valid trend, this would indicate a limiting frictional loss that still allows for a detonation wave by definition. This would also be another process by which the fuel may leak through the detonation wave. Regardless of the cause, if the CJ plane is reached before complete combustion, there will be a fraction of fuel that cannot contribute to the heat release within the detonation. Section 6.4.4 will provide some additional discussion on this front.

6.4.2.4 Non-Ideal CJ Model without Deflagration Losses

With each loss metric discussed, the next step was to evaluate the combination of all three losses. Algorithm 3 allows for the study of all three of the aforementioned loss mechanisms, and the high arching results of evaluating this model are discussed in this section. Because of the issue with convergence seen in some of the non-ideal ZND sweeps, this section will focus solely on the CJ model. Figure 6.29 shows the Sobol Indices for the CJ model with the three loss mechanisms discussed in this section. Each index is binned by the performance metric of interest: wave speed, pressure ratio, and the "gain" metric from Equation 6.46, moving from left to right. This plot shows how sensitive each performance metric is to each loss metric, where a

higher sensitivity index indicates which loss metric produces the most change to the performance metric of interest. In this case, we can also deduce the directional change associated with the Sobol indices, as we know that all parameters have a detrimental effect.

The wave speed shows almost zero sensitivity to the area change, which was also evident from the results in Section 6.4.2.1, and is moderately sensitive to heat transfer. By a small margin, the wave speed was most sensitive to the momentum removal from the frictional forces. The detonation pressure ratio is almost entirely determined by the area ratio, showing little dependence on the other two loss mechanisms. Finally, the gain metric, as defined by Equation 6.46, is predominately determined by the heat losses, with a moderate sensitivity to the momentum losses. This result makes sense as we have defined a gain metric based on energy gained across the detonation wave. As one removes energy through heat transfer in this example, there should be a direct reduction in gain across the wave. While momentum losses inevitably affect the energy gain metric, it is not the same extent.

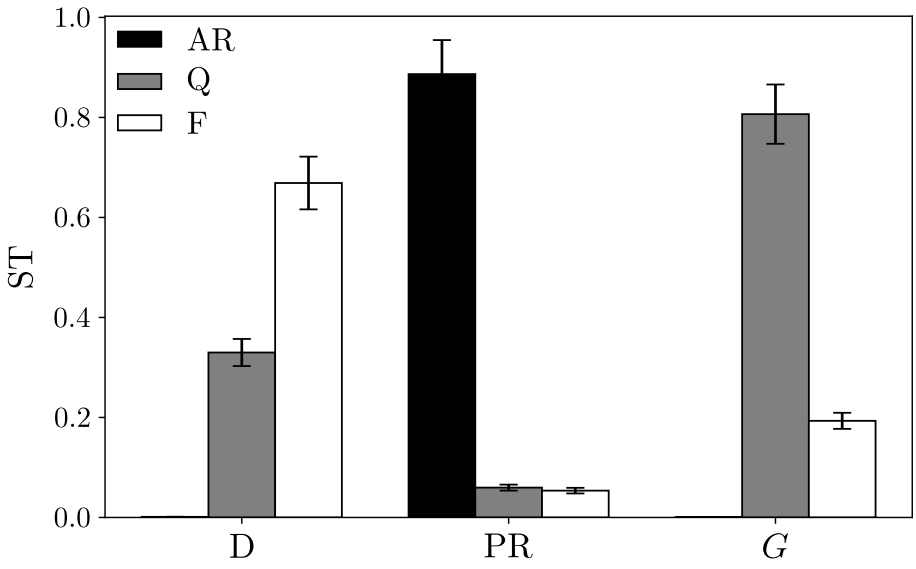

Figure 6.29: Sobol Indices for the Non-Ideal CJ Model.

Essentially, all loss mechanisms affect detonation performance to different degrees, where each is a key contributor to a given performance metric. This means that depending on which performance metric is of interest or which makes sense for a

given application, optimization would be weighted to a different loss mechanism. The troubling result from this analysis is the fact that the detonation pressure ratio is particularly sensitive to the change in area. Because of the boundary conditions associated with the RDE, this would likely be a difficult metric to reduce. With the detonation pressure ratio decreasing, it will become more difficult to achieve an overall cycle pressure gain, something that will be discussed throughout this work. For a given detonation wave, the amount of lateral relief is completely dependent on the geometry of the RDE and bulk flow conditions. We will discuss the effect in more detail in the next chapter, but the inlet performance of the RDE is critical to overall performance. This is defined as the ratio of the channel static pressure to the total plenum pressure, and higher-performing systems typically fall in the direction of a less "stiff" inlet. A less stiff inlet with a channel pressure near the plenum pressure will be more susceptible to detonation wave perturbations, allowing a higher level of lateral relief in the detonation region.

In addition, for a practical detonation-based system, heat transfer from the detonation wave to the walls of the device would be incredibly difficult. As this is the leading factor for changes in the gain metric, it becomes difficult to image a system that achieves an energy "gain" solely across the detonation wave that is near the theoretical values provided by the standard CJ analysis. This also raises questions as to the viability of the detonation energy gain metric as a useful performance metric for any system-level application of detonation combustion.

6.4.3 Non-Ideal CJ Loss Model with Deflagration Losses

With the individual loss mechanisms affected detonation performance discussed in the previous sections, a non-ideal CJ model with deflagration losses was constructed. Algorithm 8 provides the pseudo-code for the solver, which includes five loss metrics specific to the detonation wave.

Algorithm 8 Non-Ideal Deflagration Loss Model

Require: ξ_P, ξ_L, AR, Q, F, Gas objects
  Set $(1 - \xi_P)$ of fuel to inert
  Equilibrate at constant enthalpy and pressure
  if $\xi_L \neq 0$ **then**
    Set $(1 - \xi_L)$ remaining fuel to inert
  end if
  Run non-ideal CJ model ▷ *Algorithm 3*
  return Pre-Detonation State, Post-Detonation State, D_{CJ}, u_{ind}

Figure 6.30 shows the resulting Sobol Indices for the Non-Ideal Deflagration Loss Model. With the inclusion of the deflagration losses, the secondary effect changes how the area ratio, heat transfer, and momentum losses affect each performance metric. Now, the decrement in wave speed is most sensitive to the parasitic combustion fraction, with moderate sensitivity to all other loss metrics aside from the area ratio. The detonation pressure ratio is now nearly entirely determined by the parasitic combustion fraction, with a small sensitivity to the area ratio. This result echoes the variations in the pressure ratio with small changes in the parasitic combustion fraction seen in Figure 6.6. Finally, the energy gain metric is now predominately a function of the parasitic combustion fraction and the heat loss metric.

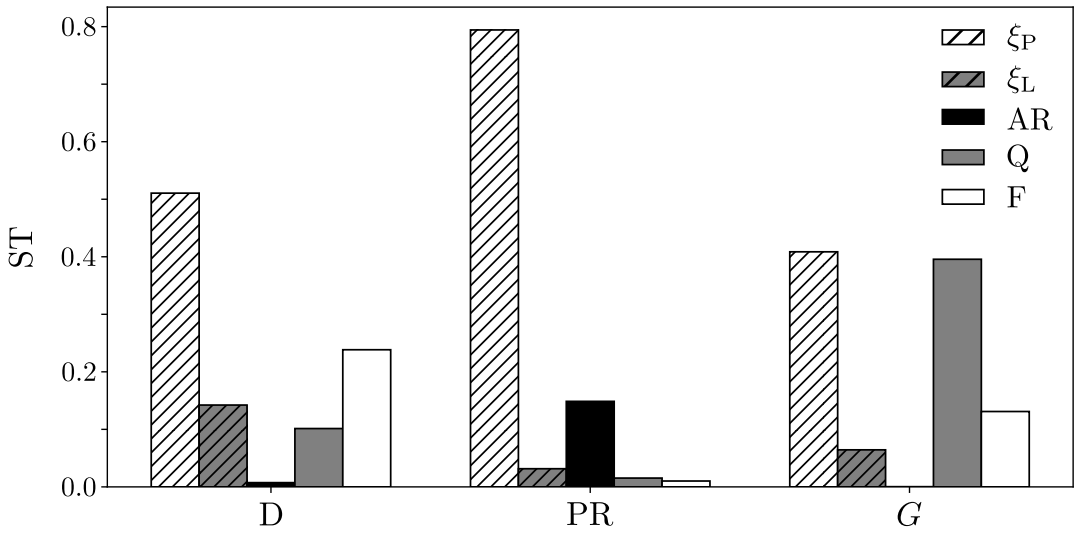

Figure 6.30: Sobol Indices for the Non-Ideal CJ Model with Deflagration Losses.

Across the board, the parasitic combustion fraction had the largest impact on the detonation performance metrics. This result was partially expected from the analysis done in Section 6.4.1, but the magnitude of the parasitic combustion effects was much higher than initial expectations. As a reminder, this term captures the effects of both pre-detonation deflagrative burning and product gas re-circulation. As one can imagine, there is a direct link between the stiffness of the RDE inlet and the propensity for product gas re-circulation and parasitic combustion. As the inlet becomes less stiff, the detonation wave is more impactful on the inlet flow, resulting in additional inlet blockage and a higher likelihood for the effects captured with the parasitic combustion fraction. See Figure 6.11 in Section 6.4.1 for an example of this relationship.

6.4.3.1 Parameter Estimation

Using the updated deflagration loss model with other non-idealities from Algorithm 8, another MCMC study was conducted to attempt to gather a better estimation of the parasitic and leaked fuel fraction. Recall from Section 6.4.1 that the base deflagration loss model over-predicted the measured PMT values by a significant margin. We have already discussed the issues with the PMT measurements not capturing the full effects

of the deflagration loss parameters; however, it is also true that the base deflagration loss model can only attribute degradation in detonation performance to parasitic combustion and leaked fuel. With the addition of the non-ideal detonation effects, the model has other mechanisms for binning the different losses.

The MCMC sampler was conducted in a manner similar to that discussed in Section 6.4.1.1; however, only 1000 accepted samples were requested due to the extended evaluation time with this version of the model. Table 6.7 shows the results of the MCMC sampling, showing the mean values for each parameter.

Run	ξ_P	ξ_L	AR	Q/Q_{in}	F/1000
654.0	0.3	0.24	1.52	0.04	16.37
656.0	0.42	0.41	1.49	0.01	14.57
657.0	0.38	0.27	1.35	0.0	0.0
658.0	0.35	0.26	1.56	0.02	18.15
659.0	0.31	0.5	1.44	0.02	25.95
660.0	0.36	0.37	1.49	0.02	23.03
662.0	0.37	0.3	1.53	0.04	14.9
663.0	0.34	0.44	1.46	0.03	24.49
664.0	0.4	0.34	1.47	0.02	13.46
665.0	0.33	0.3	1.55	0.01	19.6
666.0	0.34	0.3	1.52	0.01	18.26
667.0	0.42	0.41	1.46	0.04	9.88
668.0	0.34	0.31	1.52	0.04	17.14
669.0	0.35	0.28	1.54	0.01	13.07
670.0	0.41	0.39	1.5	0.01	15.88
672.0	0.36	0.35	1.49	0.02	16.09
675.0	0.3	0.25	1.52	0.04	16.76
677.0	0.31	0.42	1.44	0.04	22.87
681.0	0.3	0.25	1.54	0.04	19.16
682.0	0.34	0.27	1.48	0.05	5.46
686.0	0.27	0.32	1.5	0.01	16.37

Table 6.7: Deflagration Loss Model with Non-Ideal Effects

As expected, the additional loss mechanisms allow for convergence to deflagration loss fractions that were lower than those determined from the base deflagration loss

model (see Table 6.4). With these results, Figure 6.31 shows the comparison of the estimated deflagration loss fractions. It shows the base model results in black, the PMT measurement values in blue, and the non-ideal deflagration loss model results in red. Across the board, the next loss mechanisms allow the model to better predict the values that the PMT is measuring. Now, the estimated deflagration losses fall much closer to their measured PMT value and are much lower in magnitude relative to the base model predictions. These new values are also much more in line with the expected deflagration loss parameters.

In general, the new model predicts larger changes in area ratio and momentum losses than it does in heat losses. Nearly every test point predicted the area ratio across the detonation falls around the 1.5 value, suggesting a large amount of lateral relief is expected for these test cases. This is also particularly interesting as the geometry of the RDE was held constant across the data set; however, the bulk flow conditions did vary. With this model change, the updated model also allows for a prediction as to the magnitude of the lateral relief, given the experimental measurements, showing the value of the MCMC sampling methodology.

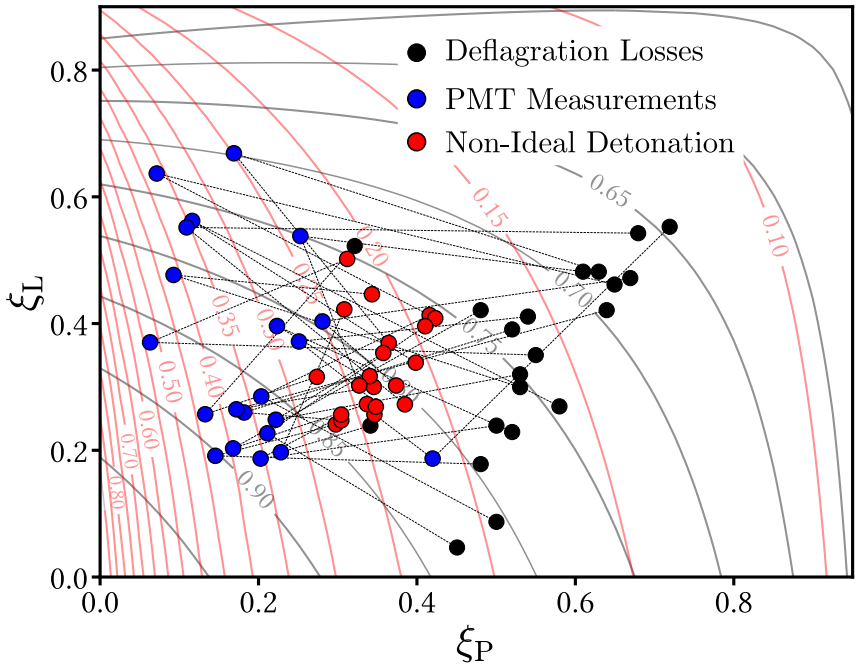

Figure 6.31: Deflagration Loss Parameter Estimation with Non-Ideal Loss Mechanisms. Compared to the Base Model and PMT Measurements.

6.4.4 Additional Thoughts on Weak Detonations

During the evaluation of the ZND solver with no ideal effects, there were parameter sets that caused the CJ plane to be reached before the full heat release could occur. An example is shown in Figure 6.27, where the thermicity profile never returns down to a non-reactive value. When inspecting the remaining fuel fraction in Figure 6.28, a large fraction of the fuel was still remaining, confirming the suspicions from the thermicity profiles. The same result was also observed for the variation in area across the ZND profile. To better resolve these findings, the following will examine this phenomenon in more detail.

We will first define a term that captures the heat release achieved at the CJ plane as the loss parameters were swept. To do this, we will define the reactant enthalpy, h_1, and the fuel mass fraction of the reactants, Y_f, which is hydrogen for this example. We can then determine the ground state enthalpy for the products at the CJ plane, $h_2|_{(P_{std},T_{std},X)}$. From this, we can calculate the heat released during the reaction with

the following:

$$HR = \frac{h_1 - h_2|_{(P_{std}, T_{std}, X)}}{Y_f} \tag{6.59}$$

Figure 6.32 shows the results of this comparison, where the ZND solver was initialized as a stoichiometric hydrogen-air detonation with no losses discussed in the previous sections; however, the initial wave speed was manually decreased from the ideal CJ wave speed. This was done to simulate any method by which the detonation wave would not be at the CJ wave speed. This plot shows the velocity decrement sweep in blue, an equivalence ratio sweep in orange, and a leaked fuel sweep in magenta. The sweep of the equivalence ratio involved decreasing the equivalence from 1.0 to 0.2, calculating the ideal CJ wave speed at the equivalence ratio. This was done to compare the amount of fuel contributing to the detonation propagation.

The sweep in the leaked fuel fraction was done by calculating the non-ideal wave speed using Algorithm 2 without any parasitic combustion fraction. After the wave speed was calculated to initialize the ZND solver, the leaked fuel was kept as an inert species for the remainder of the ZND marching scheme. For clarity's sake, one can think of the velocity-decrementing sweep in blue as having the wave speed as an input, while the heat release is the output. For the equivalence ratio and the leaked fuel sweep, the heat release is now the input, and the wave speed becomes the output. In addition, the heat release plotted on the y-axis is normalized by the ideal heat release.

It is clear that all of the profiles are a near-match, showing a decrease in one parameter corresponds to a decrease in the other. One key takeaway from this figure is that manually decreasing the wave speed (blue) provides the same output as specifying a leaked fuel fraction (magenta). That is, the decrement in wave speed captures the same physical effects as the leaked fuel fraction. The question remains as to the causal chain for these effects. On the one hand, the logic holds that if fuel is not combusted within the detonation region, then the performance will decrease. This can be calculated directly from the conservation equations by noting that the energy released would decrease. However, this result could suggest that any external process that reduces the wave speed (area change, friction, etc.) will result in a decrease in the maximum amount of fuel that can be consumed within the detonation wave.

It is likely that both of these aspects are at play, and if the model framework allows for it, the contributions of each can be dissected. For this research, however, this topic remains a question for future efforts.

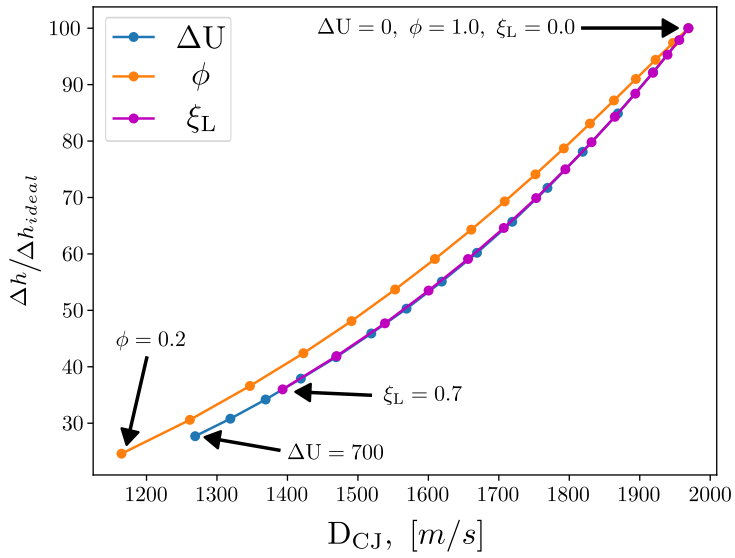

Figure 6.32: Heat release versus ideal as a function of velocity decrement and equivalence ratio.

The final area of interest that arose from the prior results is the discussion around a weak detonation wave. For reference, if a wave speed is seen near the product gas speed of sound, do we have a detonation wave of a simple deflagrative combustion wave? We have seen many non-ideal mechanisms that adversely affect the performance of the detonation wave, and the combination of all of the above could result in an exceptionally low wave speed. So, to determine whether or not a detonation is achieved in a practical device, we can revisit some of the characteristics of detonation waves.

By definition, the CJ plane is sonic with respect to the wave, and as the velocity of the wave decreases, it means that less fuel is required to burn before thermal choking begins. Here is the interesting takeaway: these velocity-decremented ZND solutions still meet the definitions for a CJ detonation, but at a reduced fuel consumption. We can prove this concept by examining the $P - \nu$ diagram for the velocity-decremented ZND profiles shown in Figure 6.33. The solid black line represents the shock Hugoniot for the initial conditions, assuming an average ratio of specific heats across the shock. Each ZND profile's Rayleigh line is plotted as a solid line, where the color in each sub-figure represents the velocity decrement in $[m/s]$. Along with the Rayleigh line, a new Rankine-Hugoniot (RH) line is plotted as a dashed line. These RH lines were

constructed using the heat release value calculated with Equation 6.59 and the average ratio of specific heats through the ZND profile.

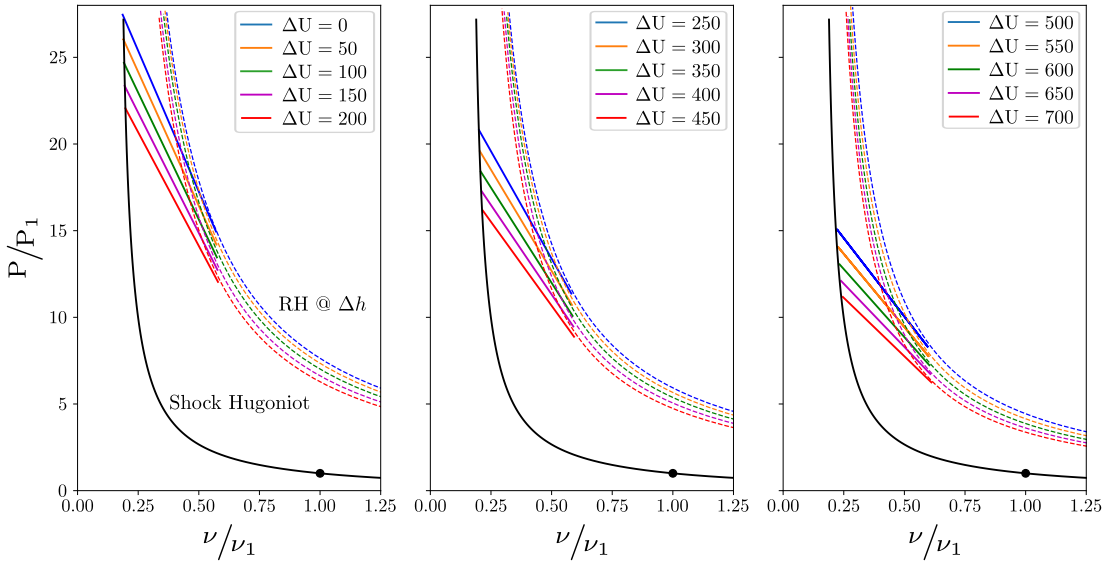

Figure 6.33: $P - \nu$ Diagrams at Different Velocity Decrement Values.

The first takeaway is that each ZND solution follows along the same shock Hugoniot but at different pressure and density ratios based on the speed of the shock. This comes as no surprise, but it is good to check for consistency in the solver. Next, and more importantly, each Rayleigh line is tangent to the associated RH line at the calculated heat release. This is another definition of a detonation wave, a shock coupled with heat release, resulting in thermal choking behind the wave at the CJ plane. Now, we have demonstrated, alongside the results from the Deflagration Loss Model, that a detonation wave moving at a reduced speed still meets all criteria for a CJ detonation; however, now it is at a lower heat release value or with a differing initial condition due to parasitic combustion. These results suggest that wave speed and pressure ratio alone and/or normalized by ideal are not adequate classification metrics for a detonation wave. We have shown in multiple models that all of the criteria for a detonation wave are met depending on the loss mechanism, but the performance decreases from what the ideal CJ analysis predicts.

6.5 Description of RDE Performance Metrics

In previous sections, the loss mechanism specific to the detonation wave, regardless of whether they were the result of the RDE flowpath characteristic, and how the performance of the detonation wave is affected, were discussed. Performance decreases within the detonation wave itself and may or may not be perfectly correlated with the performance of the RDE system. It is important to note that the performance metrics for the detonation wave are not the same as those used to describe RDE performance; therefore, this section will give an overview of the performance metric of interest used in this analysis.

The first metric is the pressure gain, as defined by Kaemming and Paxson.[97] This quantity seeks to capture the cycle-averaged total pressure ratio between the exit plane of the RDE and the RDE inlet and is used as a marker to determine the additional thrust or work extraction available as a result of the detonation-based combustion cycle. On this front, thrust and specific impulse are also terms that are used to describe the performance of direct thrust-producing applications.

$$PG = \frac{P_{t,8}}{P_{t,3}} - 1 \tag{6.60}$$

where station 8 is at the RDE exit plane and station 3 is in the RDE oxidizer plenum.

Whether air-breathing or rocket style, RDE thrust (or specific impulse) provides a metric that is both measurable and specific to the application. It *can* also provide a metric for which other combustion-based cycles may be compared to RDEs. A great example of this is in rocket-style RDE, where thrust and specific impulse are both critical measurements for the final application and can be related to standard rocket motors. The specific impulse also directly relates to the next performance metric, combustion efficiency.

Although not a metric that would demonstrate a performance gain, it is a metric that measures how well the RDE is using the energy provided within the fuel of choice. It can be a comparison point when combined with other performance metrics, such as thrust, to project the performance of RDEs, given a more complete combustion process. In most cases, this metric is also specific to the RDE in question rather than an application, as poor combustion efficiency would be corrected before the RDE was ever used in that application.

Specific to air-breathing applications, inlet pressure losses are a critical metric in determining the performance of a system using a RDE. We have already touched on

the fact that the performance of the detonation wave has an inverse correlation to this term (see Section 6.4), and because it is related to pressure gain, the inlet pressure drop is nearly perfectly correlated. Although the effects of the inlet pressure losses will be captured in other performance metrics, it is important to try to distinguish them from other losses. This will provide insights on how to mitigate inlet losses while not increasing the impact of other loss mechanisms.

Finally, we examine the potential for entropy production in the RDE combustion process. From the CJ analysis and the results in Section 6.4.1, combusting fuel in a detonative manner will reduce the entropy produced versus deflagration under the same initial conditions. The key aspect is the reduction of the combustion entropy. Within the rest of the RDE cycle, other forms of entropy production exist that could potentially outweigh any reduction from the combustion process. It should be noted that entropy production is difficult, if not impossible, to measure directly, so this metric is more suited to modeling the RDE cycle.

6.6 Description of RDE Loss Mechanisms

The following sections provide a detailed description of each loss mechanism studied in this research effort. Additional historical information on each mechanism will also be provided.

6.6.1 Inlet Blockage

Inlet blockage is a phenomenon specific to RDE devices, especially air-breathing RDEs, as the oxidizer plenum is exposed directly to the combustion chamber. Due to the local pressure rise in the detonation region, there exists the potential for back-flowing product gases and a large fraction of the inlet being blocked to forward flow.[98, 99, 100, 101, 102, 103, 104, 96] The effect is especially evident in RDEs operating with large inlet to channel area ratios, operating with low channel static pressure to plenum total pressure ratios, or operating at low plenum pressures relative to the expected post-detonation pressure. For the first two cases, convention would say the inlets are high performing due to the lower inlet pressure losses.[39] The detonation wave provides a continually propagating region of high-pressure post-combustion gases that blocks the inlet, which potentially limits the effective performance that these devices can achieve.[104] As we will discover throughout this

chapter, inlet blockage and detonation performance are inversely correlated, which means that there is no method, outside of a valved inlet, to reduce inlet blockage and improve detonation performance. The remainder of this section will discuss historical examples of inlet-related studies, specifically focusing on the blockage and backflow aspects.

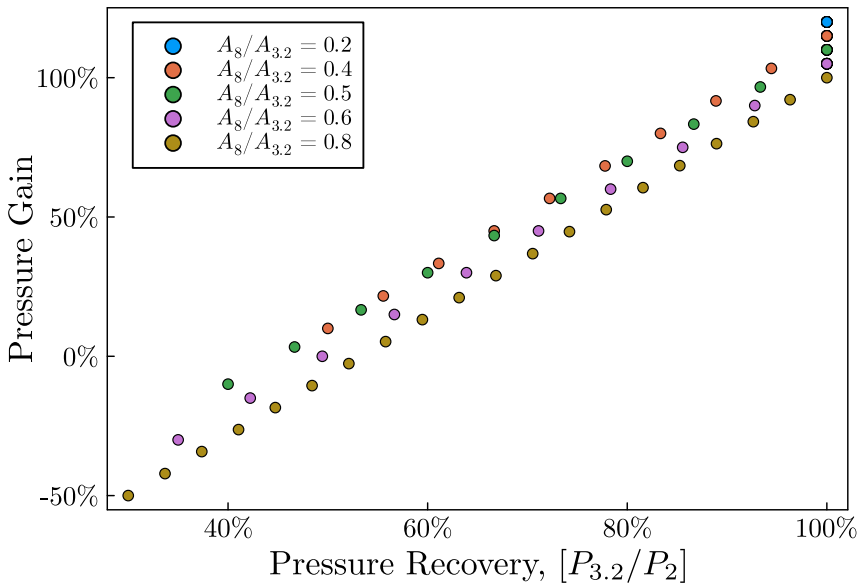

Figure 6.34: Scaling of Pressure Gain through a modeled RDE with respect to inlet pressure recovery. Data taken from Kaemming et al. [39].

The reason for inlet blockage being a critical loss metric comes from the work of Kaemming et al. who examined the effects of different loss mechanisms on the predicted pressure gain of a modeled RDE operating in a ramjet configuration.[39] Their results showed a highly linear correlation between the pressure recovery through the inlet of the RDE and the predicted pressure gain. Figure 6.34 shows a scatter plot of their data at five different nozzle to channel area ratios, $A_8/A_{3.2}$. Although the magnitudes of the pressure gain varied with the nozzle area ratio, the scaling with respect to the pressure recovery was similar between all geometries, suggesting that if one seeks to improve the potential for pressure gain, the inlet pressure recovery is a key metric to address.

Through the use of a reduced order model, Bedick et al. examined the inlet

dynamics associated with the blockage caused by the detonation wave. Their model determined that the inlet blockage based on the amount of time pressure behind the detonation wave was above the driving plenum pressure.[102] Therefore, their form of inlet blockage can be formulated according to the following definition of *blockage ratio* BR:

$$\mathrm{BR} = n_{\mathrm{waves}} \frac{t_{\mathrm{int}}}{\tau_{\mathrm{wave}}} \tag{6.61}$$

where t_{int} is the time in which the channel pressure is higher than the plenum pressure, τ_{wave} is the rotational time of the wave, and n_{waves} is the number of waves. Based on this metric, Bedick et al. also defined the effective area of the inlet based on the calculated blockage ratio according to

$$A_{\mathrm{eff}} = A_{\mathrm{min}}(1 - \mathrm{BR})$$

This methodology assumes a constant plenum pressure ahead of the inlet, which can then be used to compare with a measured pressure ratio in the channel. Deng et al. used this definition of blockage ratio, but also provided another formulation of blockage ratio.[30] Their version of blockage ratio was defined by assuming the injector is sonic when flowing in the forward direction, along with constant gas properties, and that the pressure rise in the plenum from cold flow to hot flow due to the detonation wave can be related to an area change. At a fixed mass flow rate, which is typically the case for experimental RDE testing, the sonic mass flow rate is simply a function of the pressure and area where $P_{0,Cold}A_{Cold} = P_{0,Hot}A_{Hot}$. With these assumptions, Deng et al. defines their plenum pressure-based blockage ratio as

$$BR_{sonic} = 1 - \frac{A_{Hot}}{A_{Cold}} = 1 - \frac{P_{0,Cold}}{P_{0,Hot}} \tag{6.62}$$

Feleo et al. [96] defined an inlet blockage parameter using a different approach. They refer to *inlet block fraction*, B, as a measure of the ratio between the mass flux through the device during fueled operation, relative to the corresponding mass flux under un-fueled operation (i.e., non-combustion operation) at the same inlet plenum pressure observed during fueled operation. By expressing this quantity in terms of a mass flux evaluated at the actual inlet throat (the geometric area of the inlet, A_{g}), the inlet blockage fraction can thus be defined as

$$B = 1 - \frac{\dot{m}''_{\mathrm{Hot}}}{\dot{m}''_{\mathrm{Cold}|P_{\mathrm{t},3}}} \tag{6.63}$$

This essentially quantifies the change in the inlet conditions caused by the presence of the detonation wave and represents the change in the effective flow area (A_{eff}) through the RDE inlet. A blockage fraction value of zero would indicate that the effective area has not changed (i.e., $A_{\text{eff}} = A_{\text{g}}$), while a value of one means that the inlet is impenetrable (i.e., $A_{\text{eff}} = 0$). During operation, the blockage fraction is observed to vary with the operating conditions and geometry over a wide range of possible values ($0 \leq B \leq 1$) [96].

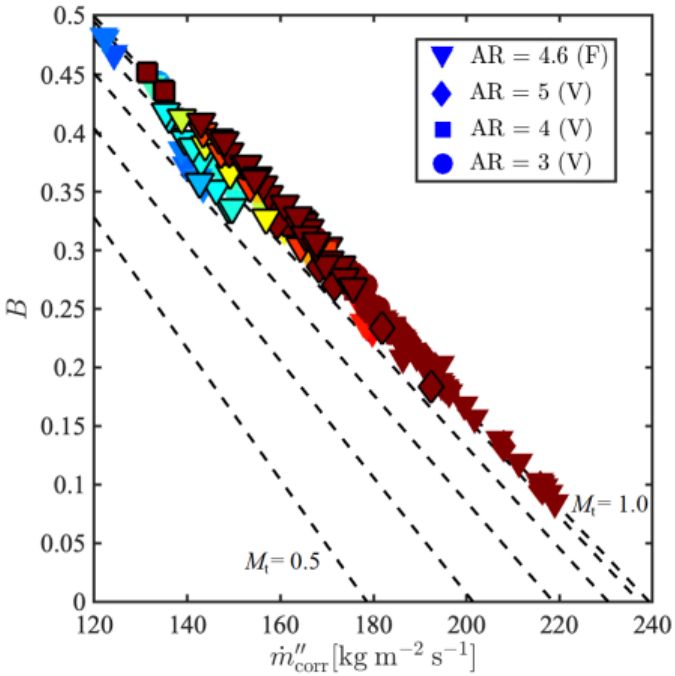

Figure 6.35: Blockage fraction as a function of corrected inlet mass flux. Figure adapted from [96].

Independently of the exact definition of inlet blockage, the concept is a useful metric to quantify the coupling between the detonation wave in the RDE channel and the plenum conditions upstream, where higher values of blockage reflect a plenum that is more significantly affected by the detonation wave. Figure 6.35 shows the blockage calculated for a set of operating conditions and inlet-to-channel area ratios

(AR) as a function of the corrected mass flux through the unblocked portion of the inlet. It is important to note that the inlet air temperature and composition were assumed to be standard day temperatures and pure air, which could break down if there is significant backflow into the plenum at high blockage values. This figure also plots lines of constant Mach number (M_t) through the unblocked portion of the inlet throat (i.e., through the effective area $A_{eff} = (1 - B)A_g$). The results indicate a non-zero value of blockage fraction when operating in a detonative mode (independently of the exact characteristics of one or multiple competing detonation and secondary waves), and these values nearly completely collapse along the $M_t = 1$ inlet (throat) condition. This suggests that the Mach number in the unblocked portion of the RDE inlet is, under most conditions, sonic during operation. An exception could be at higher levels of blockage, where the trend deviates, but the inlet throat Mach number remains larger than about 0.7. Larger magnitudes of inlet blockage would likely be correlated with a higher likelihood of backflow into the air plenum, changing the air temperature and/or composition.

Another important finding associated with the unblocked region of the inlet being choked is the potential for a larger plenum to channel static pressure ratios, $P_0/P_{s,ch}$, across the inlet. This increase pressure ratio is unfortunately directly at odds with the results from Kaemming et al.[39], where the higher performing RDE configuration, in terms of pressure gain, was achieved at a higher inlet pressure recovery (lower plenum to static pressure ratio). A sonic inlet, even for a fraction of the cycle, can produce a low pressure recovery in the RDE channel and at some conditions, it will produce super-sonic inflow for part or all of the inflowing region ahead of the detonation wave.

Schwer and Kailasanath saw similar results of inlet choking through the flowing region in a two-dimensional computational study of a RDE with a non-ideal inlet.[100] Their research compared the results of two non-ideal inlet models with the normally used ideal inlet, where an ideal inlet allows for no backflow into the plenum. The results were shown for all three models on an inlet consisting of fifty injection ports, with an effective area ratio between the channel flow area and the injectors of 0.2. One interesting finding of their results was the Mach number profile through the inlet injectors across the cycle, where the injectors ahead of the detonation wave are all sonic through their minimum area, resulting in under-expanded jets in the fill region of the RDE. Much like the results from Feleo et al., the Mach number profile through unblocked injectors appear to be sonic, or approaching sonic as the wave passes further away from the injector.

The Schwer and Kailasanath work also show the pressure perturbations from the

detonation wave propagated back upstream into the air plenum for the non-ideal inlet cases. This is also shown in experimental measurements through the use of high-speed pressure measurements. Research conducted on the UM RDE on axial type air inlets of various geometries showed pressure perturbation from the detonation wave propagate back upstream into the plenum, despite operating a higher inlet mass fluxes that would choke the inlet.[103] This result suggests that the inlet must be un-choked during a portion of the cycle for any pressure perturbation to propagate back into the plenum. Based on this data-set, there appears to be a correlation between a detonation operation and the inlet being, on average, un-choked. Even if the forward flowing portion of the inlet is choked, if there is any blockage, the average inlet Mach number across the whole cycle will be less than one by definition.

From an average inlet flow perspective, the pressure recovery can be increased by operating the inlet at a lower corrected mass flux, essentially lowering the Mach number through the inlet. However, from the perspective of a RDE, a less restrictive inlet can result in higher blockage [96] or higher inlet backflow, as shown in a numerical study conducted by Paxson and Miki.[104] Their research computationally examined the inlet backflow, and the resulting performance changes, in both a quasi-two-dimensional and three-dimensional RDE. They define an inlet diodicity metric to which the performance characteristics were compared. The inlet diodicity term, Equation 6.64, quantifies the amount of backflow into the plenum caused by the detonation wave. By allowing backflow in their simulation, they saw reductions in the potential for pressure gain, where the limiting condition they explored reduced performance to that of an ideal constant pressure combustor. These results echoed the results of Kaemming et al.[39] in that plenum dynamics are a large contributor to the overall reduction in RDE performance, at least from a modeling standpoint. One key trade-off of particular interest to this study is the relationship between the stiffness of the air inlet on an air-breathing RDE and the propensity for reverse flow through said inlet during detonation operation, which has consequences on operability and realized performance [104]. Here inlet stiffness is defined as the static to total pressure ratio between the RDE channel and the plenum, respectively.

$$\delta = 1 - \frac{A_{\text{i,back}}}{A_{\text{i,forward}}} \tag{6.64}$$

where, $A_{\text{i,back}}$ is the effective backward-flowing area and $A_{\text{i,forward}}$ is the effective forward-flowing area of the inlet. This term allowed for the exploration of inlets with asymmetric forward and backward flow characteristics, where an ideal inlet

would be a perfect diode, $\delta = 1$, which allows no flow from the channel back into the plenum. As expected, the higher the diodicity of the inlet, the lower the percentage of backflow and the higher the pressure gain. The issue that now arises is that the pressure gain is dependent on the pressure recovery through the inlet, while simultaneously depending on the backflow through the inlet. A low backflow inlet might feature restrictive areas, high corrected fluxes, and/or restrictive geometric features that negatively affect forward-flowing characteristics. In any of these cases, the pressure gain now becomes a trade-off between backflow and pressure recovery, two terms that are inversely correlated.

The results from previous studies suggest that the pressure gain in the RDE operation is highly dependent on the flow characteristic of the inlet. On the one hand, the inlet should be operated in a less restrictive configuration to improve pressure recovery. On the other hand, this is likely to increase the responsiveness of the plenum to the detonation wave, also increasing the probability of inlet backflow and blockage.

6.6.2 Incomplete Combustion, Deflagration Losses and Product Gas Re-Circulation

The majority of the discussion on deflagration losses and product re-circulation effects was provided in Section 6.1.1. These effects directly impact the performance of the detonation wave, but are a factor caused by the RDE configuration. Like discussed in the previous section, the plenum of the RDE is directly exposed to the combustion channel. This, in concert with the high pressure, post-detonation gases, allows for backflow and mixing of product gases with the fresh incoming reactants. This elevates the temperature within the reactant mixture, elevating the potential for pre-detonation ignition. Product gas re-circulation, even without pre-ignition, will increase the speed of sound ahead of the detonation wave, resulting in reduced detonation performance. This reduction in performance will likely trickle downstream and reduce the overall cycle performance.

Even without product re-circulation from the backflow products, the fill region will be in contact with post-combustion gases for a large fraction of the cycle time. Kaemming et al. showed that this layer can also produce a mixing of the two streams and modeled any pre-ignition in this region based on a laminar flame speed argument.[26] Regardless of the cause of the product gas re-circulation and pre-ignition, these likely reduce the overall cycle performance and within an RDE cycle would be extremely

difficult to eliminate completely.

One other key benefit proposed for RDE is the high energy density, due to the larger mass flux operation versus a deflagrative device.This theoretically allows the RDE to consume the same amount of fuel at a much more compact size, which is a great benefit for rocket-style RDEs. However, in an air-breathing configuration, the compact design can raise additional concerns. Aside from cooling the combustor walls with the higher heat loads, the compactness of the device can also affect the combustion efficiency. We have seen that there exists the potential for leaked fuel through the detonation wave in Chapter 6, now we shift our focus to what happens to this fuel after leaking through the detonation wave. With this high flux through the RDE channel, it is likely that some of this leaked fuel will exit the RDE channel before combusting, reducing the combustion efficiency and reducing the compactness benefit.

6.6.3 Non-Zero Azimuthal Velocity

The following section discusses the presence of non-zero azimuthal velocity within the RDE flowpath. This includes both in the inlet region ahead of the detonation wave and at the exit plane of the RDE. Due to the boundary conditions present in RDE flowpaths, this non-zero azimuthal velocity profile is likely self-exited by the detonation wave, and produces different losses depending on the location and magnitude of the azimuthal velocity. In the inlet region, this will primarily affect the detonation wave and inlet performance, whereas at the exit plane it will reduce the thrust of the device. Each scenario will be examined in more detail in the following sections, along with examples of these phenomena in experimental and computational settings.

To introduce the concept of non-zero azimuthal velocity throughout the RDE flowpath, Figure 6.36 shows a computational result of the laboratory frame particle paths within an RDE device. This figure provides an example of both the non-zero azimuthal velocity in the inlet region, as well as the larger variations in azimuthal velocity at the exit plane. Another relevant aspect of Figure 6.36 is that depending on where the exit plane is defined, the magnitude and variance in the azimuthal velocity will also change drastically.

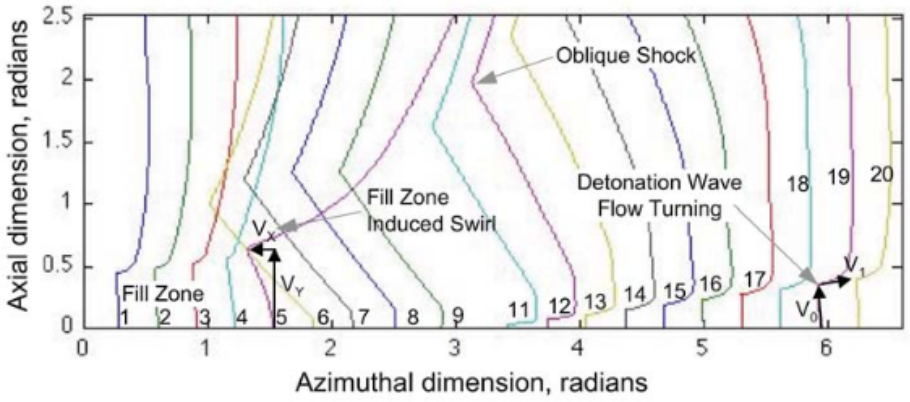

Figure 6.36: Example of Laboratory Frame Particle Paths within a RDE Flowpath.[32]

Figure 6.37 extends this example to a set of RDE simulations with additional hardware after the RDE exit plane. Moving from bottom to top shows the RDE alone (c), the RDE with an inner- and outer-body extension (b), and the RDE with the extension and a converging-diverging nozzle. This figure shows the development of the azimuthal velocity (swirl) as a function of the RDE length, which varies in magnitude and variance over the length of each configuration. Finally, Figure 6.37 (a) provide some insights on the required post RDE flow conditioning required to remove the larger perturbations in swirl generated by the detonation wave.

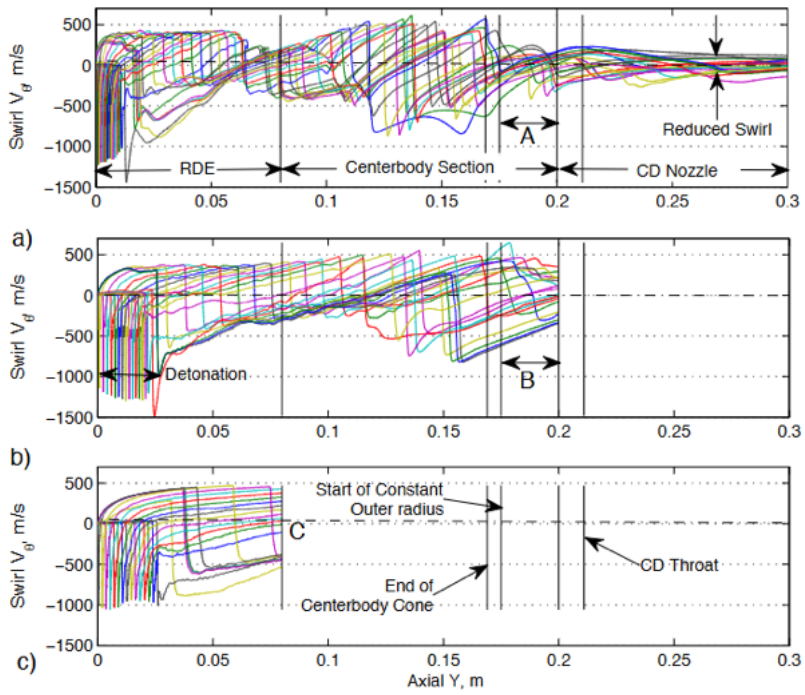

Figure 6.37: Azimuthal Velocity Components of Various Particles within RDE geometries. Standard RDE configuration (a), RDE with Extension (b), and RDE with Extension and Converging-Diverging Nozzle.[105]

6.6.3.1 Inlet Plane and Pre-Detonation

This section examines the fluid velocity profiles in the inlet region of the RDE, just ahead of the detonation wave. Typically, the inlet region fill velocity is thought to be purely axial with no azimuthal component. Several prior computational and experimental results have shown that this might not be the case.[106, 32, 33, 107] In 2-D computational study on RDEs, Nordeen et al. examined the paths of multiple particles as they propagate through the wave. These particles paths were initialized at various azimuthal locations around the RDE channel, allowing for the capture of the state diagram of the particles through a single cycle of the RDE (see Figure 6.36).[106, 32] For the present section, the most relevant finding from Nordeen et al. was the path-lines in the fill region of the RDE. Just after the wave passes, the particle paths of the fresh reactants are perfectly axial, which was shown as the y-

direction in the study. This is the typical assumption of the inflow velocity of the fill region and depending on boundary conditions specified in the CFD simulation, and this may be enforced by any inlet sub-model. However, further downstream of the initial fill region, and hence a further distance from the previous passing wave, the particle paths begin to turn towards the incoming wave with the highest degree of turning (up to 20° off the axial direction) directly ahead of the detonation wave. These results indicated that the assumption of purely axial inflow in the fill region of a RDE may need to be revisited.

On the experimental side, Andrus et al. studied a pre-mixed, hydrogen-air RDE operated at a stoichiometric condition and 0.38 kg/s.[33] Their research was primarily to study the effects of pre-mixed RDEs; however, the high speed video imaging captured luminescent particles during the run. These particles were not intentionally placed in the RDE, so there were only five particles that could be analyzed. Their analysis showed that the particles had a non-zero azimuthal velocity profile throughout the cycle, and specifically had azimuthal velocities ahead of the wave between 100-200 m/s in the direction opposite of the wave propagation. These results echoed what was seen in Nordeen et al. but in an experimental setting on a completely different geometry with higher azimuthal velocity magnitudes.

In recent years, other experimental particle imaging velocimetry (PIV) experiments have been conducted to include exhaust plane measurements conducted by Depperschmidt et al. and channel PIV measurements directly ahead of a nozzle section in Tobias et al.[35, 34] None of these studies examined velocities in the fill region of the RDE; however, they provide information on the velocity profile downstream of the combustion process, which has other effects on performance and is the subject of further investigation. These research efforts confirm the complex flow field in the RDE cycle with a non-zero azimuthal velocity profile throughout the locations examined. Another experimental PIV study in RDEs was conducted by Dunn et al. on a stoichiometric hydrogen-air RDE.[108] This research only presented a single time step of the PIV measurement and compared the results with the CFD particle paths. Due to the lack of available data in this study, no conclusions could be drawn about the flow field before the detonation wave.

Initial experimental particle tracking measurements were conducted at the University of Michigan, on the Pintle style injector configuration discussed by Duvall et al.[12] Though not classic PIV, these measurements were made with high speed imaging of luminescent particles that appeared within the flow field at the inlet region of each test. These particles appeared in the same manner as discussed in [33], but in

a much larger number. Three cases were carried out at a mass flow rate of 150 g/s and equivalence ratios of [0.6, 0.8, 1.0]. Figure 6.38 shows an example of the particle paths captured during the steady segment of the leanest run, denoting the somewhat arbitrary regions of interest in relation to the wave's location in the cycle. The particle paths showed non-zero azimuthal velocity varying throughout the cycle, with a significant negative azimuthal velocity profile just ahead of the detonation wave. This indicated that there exist the potential for non-axial flow in the inlet region due to the complexities of the detonation process within the RDE cycle.

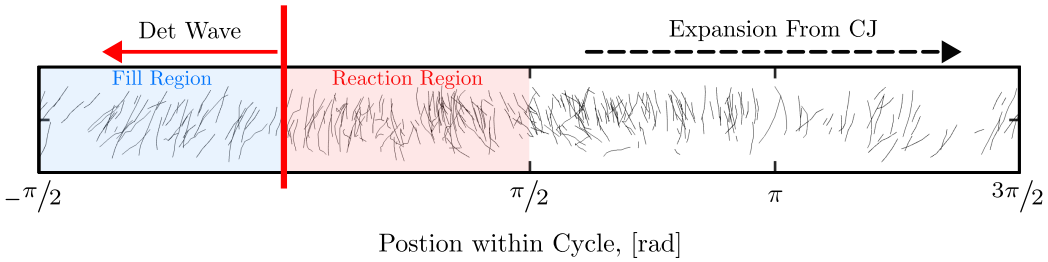

Figure 6.38: Inlet measurement of luminescent particles through RDE cycle.

From the data shown in Figure 6.38, it was determined that the azimuthal velocity profile ahead of the wave was roughly -158±26m/s, moving towards the next incoming detonation wave. Similar results were seen for the case operating at an equivalence ratio of 0.8, with a slightly lower magnitude of -82 ± 40m/s. Unfortunately, the stoichiometric case exhibited strong, counter-propagating secondary waves, so the particle paths were highly non-uniform depending on the location of the secondary wave. These results are preliminary and additional testing is required to determine the validity of these measurements. However, this data represents a third instance, on a third unique geometry, with a significant non-zero azimuthal velocity flowing into the wave.

To better illustrate the non-zero azimuthal profile, the particle paths were binned by azimuthal location and then averaged. Figure 6.39 shows the results of this process for the paths from Figure 6.38. The detonation wave is propagating from the right to left in this figure and shown with the solid red line. The same three region of interest from Figure 6.38 are also shown to give context about the location, and implications, of the velocity profile of each region. First, the fill region is highlighted with light blue. In this region the velocity is negative, meaning moving in the opposite direction of the wave, with an average magnitude between 100-200 m/s. Next, the

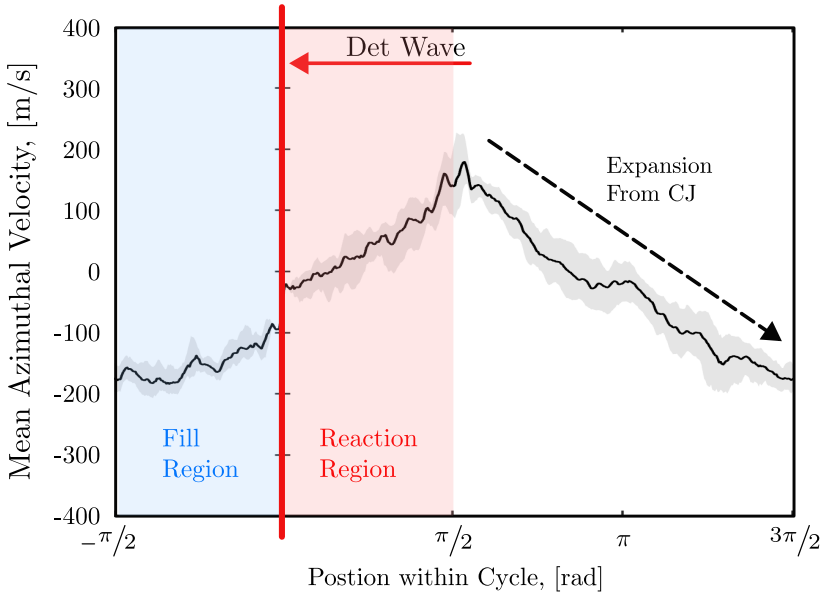

Figure 6.39: Azimuthal velocity profile for an experimental RDE run. Hydrogen-Air operating at 150 g/s air mass flow rate and $\phi = 0.6$.

reaction region, red shaded, is shown directly after the detonation wave. In this region the velocity profile increases to a peak value nearly a quarter of the lap behind the leading edge of the detonation wave. It would be expected that the post-detonation azimuthal velocity was in the direction of the wave; however, in an ideal detonation the peak induced velocity would be located directly behind the leading shock at the Von-Nuemann condition, (3.1). The reason for the slowly increasing velocity profile is likely due to the size of the particles. Although an exact size of these particles was not known, they were likely too large to react to the sudden change in induced velocity post shock. For this reason, the induction region is labeled up to the peak velocity, even though this boundary may be somewhat arbitrary. Finally, the velocity profile reverts course, accelerating against the direction of wave propagation in the final region, without highlighting. This is attributed to the expansion process the must proceed the detonation wave as the process from the CJ plane, (3.2), to the post-detonation expansion state, (3.3). This process has been discussed previously, and can also be seen clearly in the results from Watanabe et al. who show the laboratory frame velocity profile experimentally measured in a radial style RDE.[109]

6.6.3.2 Moving Shock Wave with Non-Zero Incoming Velocity

To assist with the analysis of the inlet plane non-zero azimuthal velocity profile, some prior knowledge about moving shock waves with incoming velocity profiles is required in order to understand the process of adapting this analysis to a detonation wave. A detailed explanation of the effects of non-zero incoming velocity on a moving shock wave of fixed strength is given by Anderson, but a summary of the analysis is provided below.[110] Figure 6.40 (a) shows an example of a standard moving shock wave, moving from right to left in the laboratory frame of reference (subscript l). In this example the medium through which the wave is propagating, (1), is initially at rest, $u_1 = 0$, which allows for the simple transform into the wave reference frame (subscript w). As the wave passes through the medium, the shock induces a velocity, $u_{\mathrm{i,l}}$, which pulls the post-shock fluid, (2), in the direction of the wave propagation (in the laboratory frame). In this analysis, W_* just references the wave's speed, while u_* is the velocity of the gas at each state.

The analysis was then extended to examine the effects of an incoming velocity profile ahead of the shock wave, shown in Figure 6.40 (b). For this example, the strength of the wave is fixed, which is shown as a constant wave velocity in the wave frame of reference, W_{w}. A non-zero incoming velocity, u_1, reduces the velocity of the

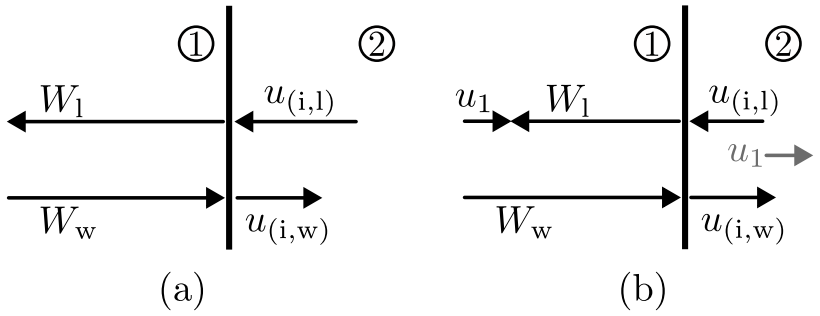

Figure 6.40: Fixed strength shock wave moving from right to left into quiescent flow (a) and flow with a non-zero incoming velocity (b). Pre-shock state is given by ① and post-shock state is given by ②

shock wave in the laboratory frame, W_l, subsequently reducing the induced velocity in the laboratory frame, $u_{i,l}$. As explained by Anderson, because the shock is fixed strength (fixed incoming velocity in the wave frame, W_w) the non-zero initial velocity, u_1, is simply subtracted from the wave speed in the wave frame, W_w, producing the wave speed observed in the laboratory frame, W_l

When assuming the same static pressure ahead of both waves, and a shock of fixed strength, the static pressure behind the shock wave with incoming flow is also constant between the two cases. However, the state at the induced velocity of (b) is now less than that of (a), meaning a lower total pressure or total enthalpy. This represents a decrease in the usable work in the post shock state of (b). Viewed from an energy perspective, the post-shock state in (a) has a higher total enthalpy compared to the post-shock state in (b). A similar analysis can be applied to a detonation wave of fixed strength, which will be discussed in the Methodology section. In should be noted that because the static pressure (and temperature) ahead of the wave is assumed constant between cases but case (b) has a non-zero initial velocity, case (b) also has a higher upstream total pressure, or total enthalpy when frame from an energy perspective. This means the change in total pressure, or total enthalpy, *across* a wave of fixed strength is reduced more than the simple reduction in the total pressure, or total enthalpy, at the post-shock state.

6.6.3.3 Nozzle Plane Velocity Distribution

It was briefly discussed in Section 6.6.3.1, but like the inlet plane, the exit plane of the RDE is not at a constant axial velocity across the cycle. The non-zero azimuthal velocity effectively reduces the energy available for thrust production in the axial direction.[97] Experimental PIV studies have shown a large fraction of non-zero azimuthal velocity across the exit plane profile.[35, 34, 111] Not only does this effect make direct integration with turbomachinery problematic, it also results in a loss of thrust performance as the azimuthal velocity magnitude increases. These effects can also be seen in computational studies, in which particle tracking was conducted.[106, 32, 105, 112]

Figure 6.41 shows experimental results using PIV at the exit plane of a RDE.[34] The left subplot shows the distribution of the azimuthal velocity measurements, while the right subplots shows the axial distribution. From these, measurements, and the computation results shown in Figure 6.36, we can conclude that the exit plane azimuthal velocity profile of the RDE has highly variant probability densities. The swirl must be imparted by some exchange in momentum within the flow field, and an associate transfer in kinetic energy. Because this velocity is not acting in the direction of the thrust production, it acts as a direct loss in thrust performance of the RDE. Higher variations in the azimuthal velocity profile would incur a larger penalty in thrust, which would be depended on the location of the detonation wave relative to the exit plane (see Figure 6.37). Upon review of the previous historical data, it also appears that the azimuthal velocity profile is self excited by the detonation wave, the general RDE flowpath, or a combination of the two.

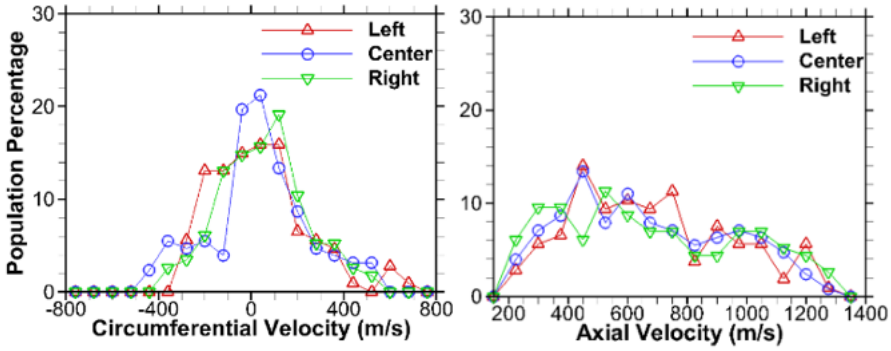

Figure 6.41: Experimental Exit Plane PIV Results.[34]

6.6.4 Post-Detonation Expansion, Heat Transfer and Friction in RDE Flowpath

This section focuses on the post-detonation heat transfer and friction effects within the RDE flowpath. Section 6.1.3 and Section 6.1.4 discussed how this effects the performance of the detonation wave, but now we shift focus to these effect the post-detonation gases. After the detonation wave (marked by the CJ plane), there is still substantial expansion within the cycle caused by the difference in the detonation area with respect to the remaining area of the RDE flowpath (see Section 6.6.3 from above). Figure 6.42 shows a simple example of the relationship between the area of the detonation products at the CJ plane defined by continuity (blue) and some post expansion area downstream of the detonation wave (cyan). This example is shown in the wave frame of reference, and is indicative of the how the boundary conditions of the RDE allow, or enforce, a large post-detonation expansion within the RDE channel. For this example, it is assumed that the mass flow rate going into the device also goes through the detonation area, as well as the example post-expansion areas shown. Depending on the configuration of the RDE, the mass flow rate, and the wave speed of the detonation, these area ratios can be well above 10, resulting in expansion to atmospheric pressures, or below, within the RDE channel.

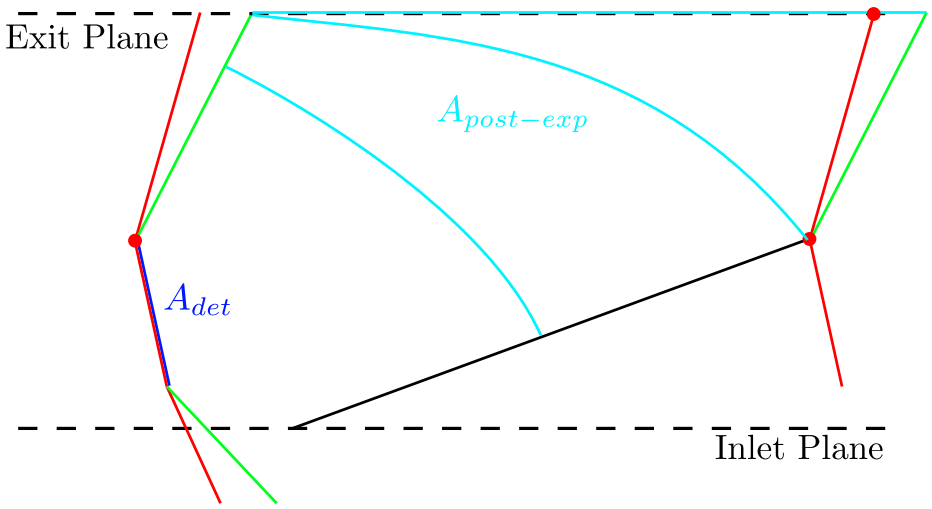

Figure 6.42: Example of the Change in Area from the CJ Plane to a Post-Expansion Location

Typically, this process is modeled as an isentropic expansion, either through a simple model or through the method of characteristic formation of choice.[113, 114, 74, 112] (Section 6.7.1) In reality, there will still be heat transfer and frictional forces effecting the post-detonation gases that require accounting. These effects can significantly reduce the gas temperature and the total pressure of the product gas exiting the RDE, resulting in a decrease in cycle performance. We can model these effects using a one-dimensional flow integrator that includes these loss mechanisms, referred to as a generalized one-dimensional flow solver, and developed by Hodges.[115] With this modeling methodology, we can include the area expansion, heat transfer, and friction as the post-detonation gases expand toward the RDE exit plane.

6.7 Modeling of RDE Losses

Now that the RDE loss mechanisms and physical processes have been described, the next step is to develop reduced order models that all for the study of each mechanism with regard to the performance of RDEs. These models include a state-based RDE cycle model with additional losses, a detailed model of the cause and effects of non-zero azimuthal swirl within the RDE flowpath, and finally, a model used to capture the effects of inlet blockage and its coupling with the performance of the detonation wave.

6.7.1 State to State Cycle Model

As discussed in Section 6.4.1, the deflagration loss model only captures the performance impacts related to the detonation wave, so the following model, termed State to State model, was developed to determine the effects of these loss parameters on the RDE performance through a simple RDE cycle model. Along with the tracking of additional states through the detonation cycle, the State to State model also includes additional loss parameters that describe the distribution of the heat release across all processes occurring within the RDE cycle, along with RDE specific losses. The first loss parameter included is an inlet pressure loss fraction, $\xi_{\Delta P}$, which calculates a pressure drop across the inlet during operation. This value is defined $\in [0, 1]$, where the zero value represents no inlet losses ($P_{3'} = P_3$), and the value of one represents an inlet loss resulting in a channel pressure equal to the ambient ($P_{3'} = P_{amb}$). Having an inlet pressure fraction of one is not realizable in any real device, but the bound-

aries were set to normalize this loss parameter in a manor consistent with the other losses. It should be noted that this loss term captures a combination of the pressure losses through a non-ideal inlet, as well as the conversion of pressure to velocity through the fill region ahead of the detonation wave. This term can be related to the pre-detonation static channel pressure, $P_{3'}$, through the following relationship:

$$P_{3'} = (P_{amb} - P_3)\xi_{\Delta P} + P_3 \tag{6.65}$$

The next new parameter is the non-commensal combustion fraction, ξ_{NC}. This parameter captures the fraction of leaked fuel, post-expansion, that is not consumed before exiting the RDE. It also is bounded $\in [0, 1]$ like the parasitic and leaked fractions, where a higher value means that less of the leaked fuel burns post-expansion. By definition, if there is no leaked fuel, $\xi_{\text{L}} = 0.0$, then this term becomes irrelevant to the model.

The final new parameter is the commensal combustion pressure fraction, ξ_{NC}. This term captures the average pressure at which the commensal combustion occurs. The parameter is also bounded $\in [0, 1]$, where a lower value indicates a higher combustion pressure. At $\xi_{\text{CP}} = 0.0$, the commensal combustion occurs at the calculated post-expansion pressure, $P_{3.3}$, while $\xi_{\text{CP}} = 1.0$ means that the commensal combustion occurs at the specified ambient conditions, P_{amb}. This term is useful in capturing the average channel pressure downstream of the detonation region, which is often much lower than any ideal pressure calculated through the detonation solver. The relationship between this parameter and the commensal combustion pressure is given below:

$$P_{3.4} = (P_{amb} - P_{3.3})\xi_{\text{CP}} + P_{amb} \tag{6.66}$$

The inclusion of these two parameters follows the methodology of the deflagration loss model, where all parameters are bounded $\in [0, 1]$ and a lower value of a given parameter corresponds to a higher performance of detonation/RDE. Including the new loss parameters, specifically the non-commensal fraction, the partitioning of fuel is shown in Figure 6.43, with equations shown below:

$$\chi_0 = \chi_{\text{P}} + \chi_{\text{D}} + \chi_{\text{C}} + \chi_{\text{NC}} = 1 \tag{6.67}$$

where the leaked mole fraction from Equations 6.32 is further partitioned into a commensal mole fraction, χ_{C}, and the non-commensal mole fraction, χ_{NC}. The parasitic and detonation mole fractions remain the same as in Equation 6.31 and Equation

6.33, where the commensal and non-commensal mole fractions are given in Equation 6.68 and Equation 6.69, respectively.

$$\chi_{\mathrm{C}} = \xi_{\mathrm{L}}(1-\xi_{\mathrm{P}})(1-\xi_{\mathrm{NC}}) \tag{6.68}$$

$$\chi_{\mathrm{NC}} = \xi_{\mathrm{L}}\xi_{\mathrm{NC}}(1-\xi_{\mathrm{P}}) \tag{6.69}$$

With this model formulation, a total combustion efficiency is also defined, shown with the substitution of Equation 6.69:

$$\eta_c = \frac{1-\chi_{NC}}{\chi_0} = 1-\xi_{\mathrm{L}}\xi_{\mathrm{NC}}(1-\xi_{\mathrm{P}}) \tag{6.70}$$

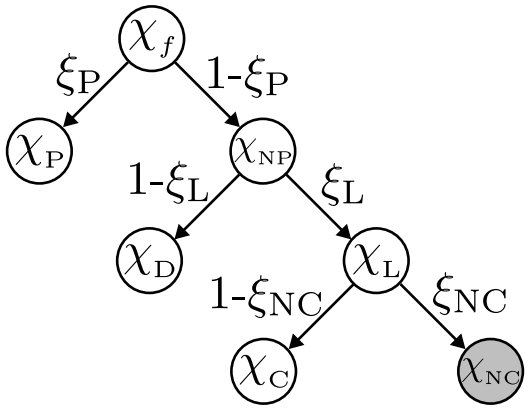

Figure 6.43: Fuel partitioning for State to State Model. Fuel fraction not consumed within cycle shown with gray background.

From this derivation, the combustion efficiency is always 100% if any of the following are true: all of the fuel is consumed parasitically, there is no leaked fuel, or there is no non-commensal fuel. The State to State model captures both the effects of the new loss parameters associated with bulk flow quantities (inlet losses and RDE channel pressures) as well as properly accounting for detonation-specific process from the Deflagration Loss Model. This model also applies the detonation work correction in calculating the post-expansion state, (3.3).

Algorithm 9 State to State Model

Require: $\xi_{\Delta P}$, ξ_{P}, ξ_{L}, ξ_{CP}, $\xi_{\mathrm{NC}} \in [0, 1]$
Initial reactant mixture at plenum conditions: ③
Apply inlet pressure drop from $\xi_{\Delta P}$(Equation 6.65): ③′
Run Deflagration Loss Model assuming initial azimuthal velocity pre-detonation is zero ($u_{3_p} = 0$) with ξ_{P} and ξ_{L}: ③.2
Isentropic expansion to match detonation work, assuming post-expansion azimuthal velocity is zero ($u_{3.3} = u_{3.4} = 0$): ③.3
Reset (1-ξ_{NC}) moles of fuel to reactive
Set commensal combustion pressure based on ξ_{CP}(Equation 6.66)
Equilibrate remaining reactive fuel at constant commensal pressure/enthalpy: ③.4
if No Additional Losses **then**
    ③.4 = ④
else
    Calculate additional losses: ④
end if
Calculate I_{SP} expanding ④ to P_{amb}

With the additional states and loss mechanisms included in the State to State model, it was used to examine the performance of both the detonation wave and a modeled RDE cycle. Algorithm 9 shows the steps used to calculate the states in the modeled cycle, as well as the specific thrust output used as one of the performance metrics of interest. Figure 6.44 shows a visual representation of these steps, where additional losses can be applied between ③.4 and ④. For example, a non-zero azimuthal velocity profile can be applied to the exit plane, which effectively reduces the axial velocity component that produces thrust (see Section 6.6.3.3), or an accounting for the oblique shock effects could also be applied here. For the results shown in this chapter, it is assumed that no other losses occur, so ④ is the same as ③.4. This produces the best-case thrust estimate, which will later be compared to the best case thrust achievable in an ideal deflagration device.

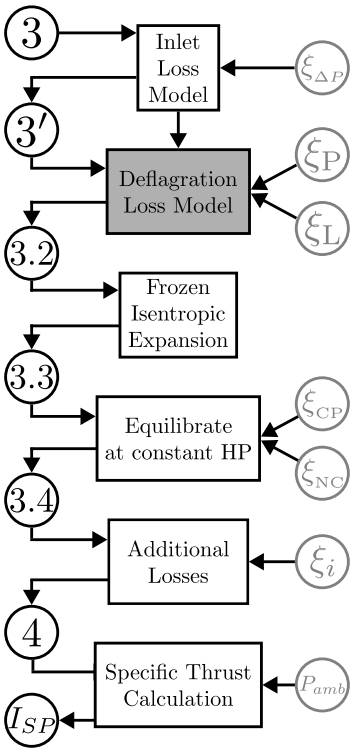

Figure 6.44: State to State Model Diagram.

The specific impulse will be calculated from the change in enthalpy between ④ and the ambient exhaust condition. This assumes isentropic expansion from ④ to an ambient pressure specified in the model, where all of the results in this analysis assume the exhaust pressure to be one atmosphere. Through the calculation of ④ in the State to State model, and Equation 6.71, a specific impulse can be predicted for the model. In the case of this research, the calculated specific thrust will always be normalized by the specific thrust of an ideal deflagration device with the same initial conditions. For this simple thrust model, it is assumed that all expansion from ④ occurs in the axial direction, and the nozzle geometry allows for perfect expansion. This provides the maximum estimated thrust performance of the RDE cycle.

$$I_{sp} = \frac{1}{g_0}\sqrt{2\left(h_4 - h|_{P_{amb},s_4}\right)} \tag{6.71}$$

If the gain of the detonation-based cycle is determined by pressure, PG in Equa-

tion 6.60, then the components of the pressure gain can be broken down into their contributing processes included in the State to State model. First, we will define pressure ratio terms that account for the process included in the State to State model. The inlet pressure ratio term, Equation 6.72, relates the static pressure in the channel, pre-detonation, to the total plenum pressure term in Equation 6.60. This term captures viscous losses, mixing losses, total-to-static pressure conversion into velocity, and other additional processes which modulate the pre-detonation pressure.

$$PR_{inlet} = \frac{P_{3'}}{P_{t,3}} \tag{6.72}$$

Equation 6.73 relates the pre-detonation static pressure to the post-detonation static pressure at the CJ plane, (3.2). This term captures all of the effects included in the Deflagration Loss Model.

$$PR_{w} = \frac{P_{3.2}}{P_{3'}} \tag{6.73}$$

Equation 6.74 is the static pressure ratio of the expansion process from the CJ plane to the post-expansion state, (3.3). The need for this term was discussed previously; however, it is important to note that this pressure ratio scales proportionally to the detonation work term, $Du_{3.2}$.

$$PR_{exp} = \frac{P_{3.3}}{P_{3.2}} \tag{6.74}$$

Finally, Equation 6.75 captures any addition process from the post-expansion state to the final total pressure at the exit of the RDE.

$$PR_{i} = \frac{P_{t,8}}{P_{3.3}} \tag{6.75}$$

substituting these pressure ratios into Equation 6.60 yields:

$$PG \propto PR_{inlet} PR_{w} PR_{exp} PR_{i} - 1 \tag{6.76}$$

This relationship allows us to examine, in a rudimentary manner, the effects of the inlet losses, deflagration losses, post-detonation expansion requirements, and any additional loss on pressure gain across the device. It should be noted that both the inlet pressure ratio and the expansion pressure ratio are less than unity, $PR_{inlet} < 1.0$ and $PR_{exp} < 1.0$. Assuming no additional losses in the system, this means that to

achieve a pressure gain across the device, the pressure losses across the inlet and the expansion process must be overcome by the gain across the detonation wave.

Unfortunately, increasing the gain across the detonation (from an energy or pressure perspective) has a negative consequence elsewhere. For example, an improved detonation pressure ratio will have a more severe effect on the RDE inlet flow field, potentially further reducing the inlet pressure ratio term. It would also increase the detonation work requirement as the post-detonation expansion process is proportional to the detonation wave speed.

6.7.2 Non-Zero Azimuthal Velocity Model

The following sections discuss the model implementations used to study the effects of non-zero azimuthal velocity within the RDE flowpath. The first model examines the effect in the inlet region, just ahead of the detonation wave using the conservation of angular momentum to establish a causal link between the phenomena and the detonation wave, and also predicts the magnitude of pre-detonation azimuthal velocity. Finally, a simple nozzle model will be shown that examines the change in thrust given an exit plane velocity profile with varying azimuthal components.

6.7.2.1 Inlet Plane and Pre-Detonation

Analyzing the possibility of non-zero velocity within a RDE fill region required the development of an RDE inlet model that quantifies and predicts the potential azimuthal velocity magnitude. This model and the methods used to determine its implication on RDE performing will be discussed below, but first, the methods for analyzing moving shock waves, Section 6.6.3.2, will be applied to a detonation wave to determine the differences in the pre- and post-detonation state as a non-zero incoming velocity is introduced. This model will be used to examine the ideal detonation wave, but also includes the deflagration loss model, which is discussed in Section 6.4.1, with additional losses and processes.

Section 6.6.3.2 discussed an example problem of a moving shock wave, of fixed strength, into a medium with and without an incoming velocity. This section will expand this analysis to an ideal detonation wave. Figure 6.45 shows an example of the typical ideal detonation process (a), along side an example of a detonation wave propagating into a non-zero incoming velocity, (b). The two states this initial analysis will focus on is the upstream, labeled ③ and the CJ condition, ③.2.

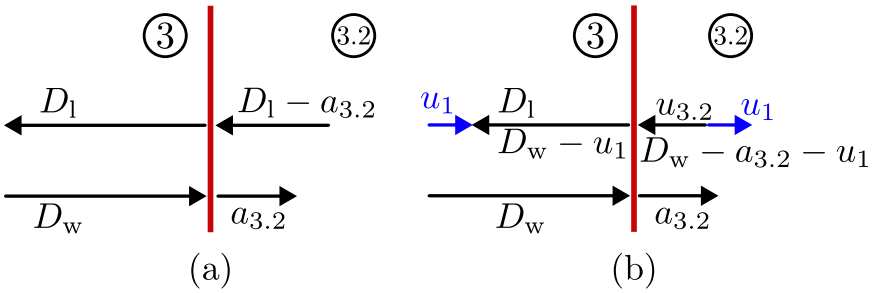

Figure 6.45: Effects of non-zero incoming velocity on an ideal detonation wave.

Much like the analysis for a moving shock wave, the effects of a non-zero incoming velocity on a detonation of fixed strength follow a similar process. Here, the detonation wave speed in the wave frame of reference, D_w, is constant between cases (a) and (b). This means that the wave speed observed in the laboratory, D_l, is reduced by the magnitude of the incoming velocity, u_1. The CJ state, (3.2), in an ideal case, (a), has an induced velocity that is simply the wave speed in the laboratory frame, D_l, minus the speed of sound at (3.2), $a_{3.2}$ shown in Equation 6.77.

$$u_{3.2} = D_l - a_{3.2} \tag{6.77}$$

When accounting for a non-zero incoming velocity, case (b), both the laboratory wave speed, D_l, and the induced velocity, $u_{3.2}$, are reduced by the magnitude of the incoming velocity, u_1. This means that the speed of the wave, measured in the laboratory frame is lower, while also producing a lower induced velocity at the CJ state, (3.2). This reduction in the induced velocity at (3.2) in case (b) is a direct reduction in the potential gain through the detonation process. Now that the initial impact on detonation performance has been described, the remainder of this section will focus on the model implementation.

The model uses a control volume analysis of the RDE flowpath, beginning far upstream in the plenum region and concluding with an exit plane drawn at the midpoint of the detonation wave height. This analysis relies on the conservation of angular momentum at the exit plane to examine the processes near the inlet region of the RDE. The control volume in question is shown in Figure 6.46. The exit plane region can be broken down into 4 distinct regions:

- ZND Region for a fixed "strength" detonation

- Isentropic Expansion Region
- Constant Pressure Product Region
- Constant Pressure Fill Region

The ZND region refers to a fixed "strength" detonation wave as an input parameter. This is meant to mimic the analysis shown in Figure 6.45, where a non-zero incoming azimuthal velocity changes the wave speed in the laboratory frame, but the wave speed ("strength") is fixed in the wave frame. The regions are separated in a non-dimensional space that is normalized the distance by the flowpath circumference:

$$\bar{x} = \frac{x}{\pi \mathrm{OD}} \tag{6.78}$$

where x represents the distance along the annulus flow path in physical space and $\bar{x} \in [0, 1]$ represents that distance normalized by the total annulus flowpath distance based on the outer diameter of the RDE in question. The following non-dimensional locations of interest are then defined as: $\bar{x}_{\mathrm{ZND}}$, representing the end of the ZND reaction zone, $\bar{x}_{\mathrm{Exp}}$, representing the end of an expansion region, and $\bar{x}_{\mathrm{Fill}}$, representing the end of the constant pressure products zone and beginning of the constant pressure inlet fill region. These regions, shown in Figure 6.46, are not scaled, with an exaggeration in size to show the breakdown more clearly.

To define these regions, a blockage fraction is required. In the case of the current model, this blockage fraction, $\mathrm{B_P}$ will be defined as the region behind the detonation shock front that has a higher pressure than the plenum, P_0. For this model, the blockage fraction is a measured value based on phase-averaged high-speed pressure transducers located in the detonation region and provides a similar measurement of inlet blockage to that described in Shepard et al. and Feleo et al.[3, 96]

Next, it is assumed that the fill region of the inlet recovers in a way such that a linear boundary forms between the post-expansion product and the fresh reactant fill. This assumption allows for the geometric determination of the length scales associated with the post-expansion products and the fill region, where:

$$\bar{x}_{\mathrm{Fill}} = 1 - \frac{1 - \mathrm{B_P}}{2} \tag{6.79}$$

where $\mathrm{B_P}$ determines the length between the shock front and the part of the Expansion region at which the pressure equals the plenum pressure, P_0. It should be noted that

the expansion region extends slightly past the B_P line in Figure 6.46. This is due to the fact that the expansion in the RDE channel continues until the static channel pressure, P_{ch}, is reached. This means that the use of the blockage fraction does not directly define the end of the expansion region; therefore, an additional derivation is required to determine this length.

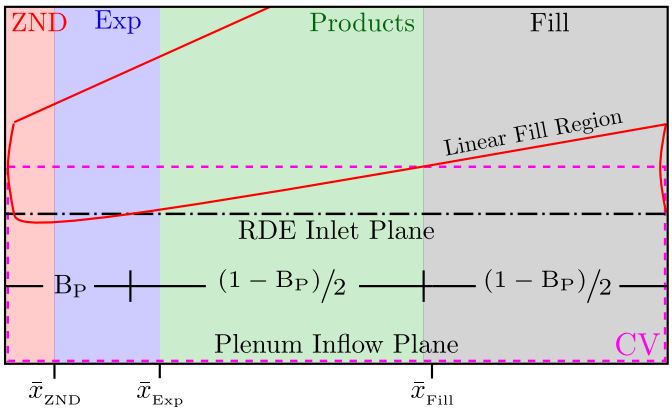

Figure 6.46: Example RDE flow field used in this model with inlet flow area shown with a dashed-dotted line. Unrolled representation of the RDE flow field process regions broken down by color based on the region of interest at the control volume exit, along with non-dimensional length scales. Control volume of interest shown by dashed, magenta lines.

The expansion process is modeled with a simple exponential decay from the CJ pressure to the channel static pressure. It is determined based on the blockage, B_P, as the characteristic length, along with the CJ pressure determined by the ZND solution end-point, P_{CJ}, and the measured plenum pressure, P_0. The modeling of the expansion as an exponential decay is similar to the method used by Kaemming et al. in their cycle model, except they use a time constant of the decay that is fit on a simulation of a 6" nominal OD RDE.[26] The goal with this model is to be able to examine any arbitrary RDE geometry in a reduced manor, which requires fitting a decay constant based on the flow conditions and RDE geometry, both assumed to be known inputs to the model. The exponential pressure decay rate is defined as:

$$\frac{dP}{dt} = -kP, \;\; P(t) = P_0 e^{-kt}$$

where the decay constant, k, governs the expansion process. Moving into non-dimensional space coordinates and substituting the known initial pressure leaves:

$$P(\bar{x}) = P_{\mathrm{CJ}} e^{-k\bar{x}} \tag{6.80}$$

where the above implementation provides the pressure as a function of non-dimensional space. Next, this equation is rearranged to solve for the decay constant, k, as a function of known quantities. First, the correct non-dimensional length must be calculated based on the non-dimensional distance between end of the ZND region and the blockage fraction, $\mathrm{B_P}$:

$$\bar{x}_{\mathrm{Exp}|P_0} = \mathrm{B_P} - \bar{x}_{\mathrm{ZND}} \tag{6.81}$$

where $\bar{x}_{\mathrm{ZND}}$ is the non-dimensional length of the ZND region and $\bar{x}_{\mathrm{Exp}|P_0}$ is the length of the expansion region up to the point of equality with the plenum pressure, P_0. With this information, the decay constant, in non-dimensional space, is simply:

$$k = \frac{-\ln(\frac{P_0}{P_{\mathrm{CJ}}})}{\bar{x}_{\mathrm{Exp}|P_0}} \tag{6.82}$$

where all values on the right hand side are measured quantities or outputs from the ZND solution. As one might have deduced, this treatment could mean that the expansion rate, which is a function of the blockage fraction, can be different for the same RDE geometry operating under different flow conditions. To date, no known methods exist for determining the exact blockage fraction a-priori, so the model must rely on experimental measurements or parametric sweeps of inputs.

Next, we give the derivation of the system of equations required to model the expansion process. The expansion modeling is conducted in the non-dimensional space defined above. First, the driver of the expansion process is the pressure change moving from the CJ plane to the static pressure within the channel. The pressure profile governing the expansion is modeled as an exponential decay process:

$$\frac{dP}{d\bar{x}} = -kP_i \tag{6.83}$$

where k is determined by Equation 6.82 and P_i is the pressure at the current step. The velocity change rate in an isentropic expansion is governed by the following:

$$\frac{d|\mathbf{u}|}{d\bar{x}} = \sqrt{-2\frac{dh}{d\bar{x}}} \tag{6.84}$$

where $\frac{d|\mathbf{u}|}{d\bar{x}}$ represents the change in the magnitude of the velocity vector, given a change in enthalpy, $\frac{dh}{d\bar{x}}$. However, a simplification can be made based on the definition of the change in enthalpy in an isentropic expansion being a function of the density and pressure change rate:

$$\frac{dh}{d\bar{x}} = \frac{1}{\rho_i}\frac{dP}{d\bar{x}} \tag{6.85}$$

where the density, ρ_i, at the given step is determined through the use of a *Cantera* gas object using the GRI3.0 mechanism.[88, 116] Finally, this is reduced to the following equation used to calculate the velocity magnitude rate of change:

$$\frac{d|\mathbf{u}|}{d\bar{x}} = \sqrt{\frac{-2}{\rho_i}\frac{dP}{d\bar{x}}} = \sqrt{\frac{2kP}{\rho_i}} \tag{6.86}$$

Using 6.86 in the integration process results in changes in velocity based on the non-dimensional space; however, the analysis requires a dimensional velocity along the control volume exit. Equation 6.86 can be used to find the dimensional velocity profile through the use of the chain rule:

$$\frac{d|\mathbf{u}|}{dx} = \frac{d|\mathbf{u}|}{d\bar{x}}\frac{d\bar{x}}{dx} \tag{6.87}$$

where $\frac{d\bar{x}}{dx} = \frac{1}{\pi OD}$ based on Equation 6.78. This substitution results in:

$$\frac{d|\mathbf{u}|}{dx} = \sqrt{\frac{-2}{\rho_i}\frac{dP}{d\bar{x}}}\frac{1}{\pi OD} = \sqrt{\frac{2kP}{\rho_i}}\frac{1}{\pi OD} \tag{6.88}$$

An expansion angle is also included in the model since the expansion to static pressure within the RDE flowpath is not purely azimuthal. For reference, u represents the azimuthal velocity component, while v represents the axial velocity component. This angle, α, along with the associate vector components are shown in Figure 6.47, and can either be estimated based on the RDE geometry and wave fill height, or included in the parameter estimation process. It is assumed that this expansion flow angle is constant during the expansion process and is native only to the control volume exit plane of the expansion region. Included in this assumption is that the expansion process occurring in the combustion region of the ZND solution contributes to purely azimuthal-velocity changes, i.e. no change in axial velocity. The equations for each velocity component's rate of change in the expansion region are given below:

$$\frac{du}{dx} = \cos(\alpha)\frac{d|\mathbf{u}|}{dx} \tag{6.89}$$

$$\frac{dv}{dx} = \sin(\alpha)\frac{d|\mathbf{u}|}{dx} \tag{6.90}$$

As will be discussed later, this model will assume that the axial velocity profile along the control volume exit plane is relatively constant. The axial velocity profile will still be calculated to provide an estimated thrust; however, in the case of the control volume modeling, a non-zero expansion angle is included to reduce the contribution of the expansion process to the azimuthal direction. This methodology attempts to capture expansion effects in the azimuthal direction, knowing that the expansion will not be fully azimuthal.

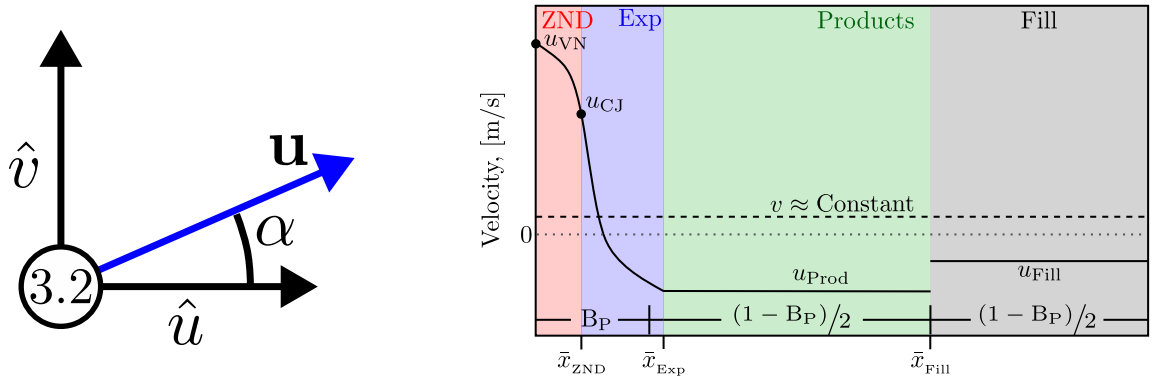

Figure 6.48: Velocity component profiles (in laboratory frame) at the control volume exit. A positive azimuthal velocity, u, is defined by the direction of wave propagation, i.e. a negative velocity means the flow is moving towards the incoming detonation wave.

To solve the for the expansion profiles, Equations 6.83, 6.88, 6.89 and 6.90 are then integrated until the channel static pressure, P_{ch} is reached. Figure 6.48 shows an example case of the velocity profiles calculated along the exit plane of the proposed control volume, showing the azimuthal velocity, u, as solid lines, and the axial velocity, v, shown with dashed lines. Of particular interest is the azimuthal velocity profile, which shows a negative velocity component in the Expansion, post-expansion Product, and Fill regions. The discussion of where the negative azimuthal fill velocity

comes from will be discussed later in this section. The changes in azimuthal velocity in the ZND region are assumed constant based on fixing the "strength" of the detonation wave; however, the azimuthal velocity profile in the Expansion region will be governed by the expansion angle, α, where higher expansion angles will result in lower changes in azimuthal velocity.

The proposed inlet model has defined a control volume such that the inlet to the control volume is located far enough upstream from the detonation wave that we can assume that there is no inlet angular momentum. There are no next torques on the RDE device or other external forces; therefore the exit angular momentum must be zero as well. Because the flow field at the exit of the control volume is much more complex than the inlet, a derivation of the conservation of angular momentum in a control volume must be conducted beginning from first principles. Below shows this derivation of the process, starting from the same derivation discussed by Shepherd and Karahara[114], but then deviating with a few key assumptions that result in the version used in this model. Conservation of angular momentum in a control volume is defined as:

$$M = \frac{\partial}{\partial t}\int_{\Omega} \mathbf{r} \times \rho \mathbf{u} \mathrm{d}V + \int_{\partial\Omega} (\mathbf{r} \times \rho \mathbf{u})\mathbf{n} \cdot \mathbf{u} \mathrm{d}S$$

The net angular momentum, referred to as swirl, in the plenum region, well upstream of the RDE, is assumed to be zero in the RDE control volume inlet; therefore, it is required that the exit plane net swirl is also zero. The domain is periodic, so averaging over the cycle allows for the following reduction:

$$0 = \frac{1}{\mathrm{T}}\int_{0}^{\mathrm{T}} \int_{\delta\Omega} (\mathbf{r} \times \rho \mathbf{u})\mathbf{n} \cdot \mathrm{d}S \mathrm{d}t$$

Transforming into the steady, wave reference frame:

$$0 = \int_{\mathrm{A}} r\rho uv dS$$

where r is the radial distance and each velocity component is broken out, u is the azimuthal velocity, and v is the axial velocity. Assuming no variation in the radial direction and a fixed area plane, the conservation of angular momentum can further reduce to:

$$0 = \frac{1}{2\pi}\int_{0}^{2\pi} \rho(\theta', z)u(\theta', z)v(\theta', z)\mathrm{d}\theta'$$

Because the analysis is conducted at the same axial height, the dependence on the axial location can be removed, leaving:

$$0 = \int_0^{2\pi} \rho(\theta')u(\theta')v(\theta')d\theta'$$

Next, the equations are transformed from the physical space θ' to the non-dimensional distance, $\bar{x}$, defined in Equation 6.78. Leaving the following equation of swirl conservation in the azimuthal direction in terms of the non-dimensional distance.

$$\int_0^1 \rho(\bar{x})u(\bar{x})v(\bar{x})d\bar{x} = 0$$

Due to the complexity of the axial flow across the control volume exit, it will be assumed that the fluctuations in the axial velocity along this profile are negligible. This argument has partial support when examining the particle path profile in certain CFD solutions along a plane drawn at the mid-point of the detonation wave.[117, 118, 119] In these computational studies, the axial velocity component appears to be relatively constant, and drawing tangent lines to the particle paths at the mid-point of the detonation resulted in an average estimated flow angle (in the wave frame) of 10.4° with a standard deviation of only ±1.69°. The discussion from the previous section mentions the calculation of the axial velocity change through the expansions; however, this modeled axial velocity would be along a particle path that intersects the detonation wave directly at the mid-point, which cannot be used as a surrogate for other particle paths because of the complexities with the back-flowing region of the RDE. This means that the velocity profile along the exit plane of the proposed control volume is the result of particle paths passing through diffident axial locations of the detonation wave. For example, the velocity profiles closer to the Fill region will have propagated through the lower portion of the detonation wave and likely achieved a relatively high axial velocity backwards through the inlet. A more complex inlet model is required to accurately capture this effect. With the assumption of constant axial velocity along the exit plane, the conservation of angular momentum reduces to:

$$\int_0^1 \rho(\bar{x})u(\bar{x})d\bar{x} = 0 \tag{6.91}$$

where the azimuthal velocity profile is calculated based on the model assumptions discussed previously. Using the four regions shown in Figure 6.46, the integral can be

separated, leaving the following:

$$\int_0^{\bar{x}_{ZND}} \rho(\bar{x})u(\bar{x})d\bar{x} + \int_{\bar{x}_{ZND}}^{\bar{x}_{Exp}} \rho(\bar{x})u(\bar{x})d\bar{x} + \int_{\bar{x}_{Exp}}^{\bar{x}_{Fill}} \rho(\bar{x})u(\bar{x})d\bar{x} + \int_{\bar{x}_{Fill}}^{1} \rho(\bar{x})u(\bar{x})d\bar{x} = 0$$

The ZND region and the Exp region are integrated across their respective profiles using a Simpson's Rule integrator in the model, while the other two regions can be reduced down to simple algebraic expressions by assuming uniform composition, pressure and velocity in each region. For the post-expansion Product region, this reduces down to:

$$\int_{\bar{x}_{Exp}}^{\bar{x}_{Fill}} \rho(\bar{x})u(\bar{x})d\bar{x} = \rho_{_{Prod}} u_{_{Prod}} (\bar{x}_{Fill} - \bar{x}_{Exp})$$

And for the reactant Fill region:

$$\int_{\bar{x}_{Fill}}^{1} \rho(\bar{x})u(\bar{x})d\bar{x} = \rho_{_{Fill}} u_{_{Fill}} (1 - \bar{x}_{Fill})$$

In this case, $\rho_{_{Fill}}$ is the density of the pre-detonation reactants and $u_{_{Fill}}$ is the azimuthal velocity of the Fill region, and must be calculated in order to conserve swirl at the exit plane of the control volume. This equation is shown below:

$$u_{_{Fill}} = \frac{-\left(\int\limits_{ZND} \rho u d\bar{x} + \int\limits_{Exp} \rho u d\bar{x} + \rho_{_{Prod}} u_{_{Prod}} (\bar{x}_{Fill} - \bar{x}_{Exp})\right)}{\rho_{_{Fill}} (1 - \bar{x}_{Fill})}$$

With this result, the azimuthal velocity in the fill region required to maintain a net swirl condition of zero can be calculated. The model is then iterated using the calculated $u_{_{Fill}}$ as an input, where the non-zero incoming fill velocity must be propagated back through the model, adjusting the laboratory frame wave speed, and therefore the azimuthal velocity profile across the control volume exit plane. Refer to Figure 6.45 for an example of what happens when the "strength" of the detonation wave is fixed, but now a non-zero incoming flow is introduced.

Now that the model has been properly introduced, a quick example of the model outputs was examined for an ideal hydrogen-air detonation operating at an equivalence ratio of 0.6. Figure 6.49 shows the pressure (a), azimuthal velocity in the

laboratory frame (b), and the swirl profile (c), where a positive velocity is defined as moving in the same direction as the detonation wave. The most interesting features highlighted on these graphs are the azimuthal velocity, u, and the swirl term, $\rho u v$, which contains the constant axial velocity component, v, only to maintain the proper units. Figure 6.49 (b) shows that the initial azimuthal velocity starts in the same direction as the wave propagation, due to the high induced velocity behind the shock wave. The ZND process then brings the flow to the CJ condition, effective slowing the particle in the lab frame. Examining the expansion process, the velocity at the end of the expansion process is relatively large in the direction opposite to the wave propagation direction. This is due to the fact that the boundary condition in the RDE is not a zero-velocity wall, but a static pressure boundary, allowing for expansion past the zero-velocity point that would exist in a detonation tube.[120] After iteration over the calculated azimuthal fill velocity, the model predicted a negative azimuthal velocity in the fill region, with a magnitude of -41 m/s.

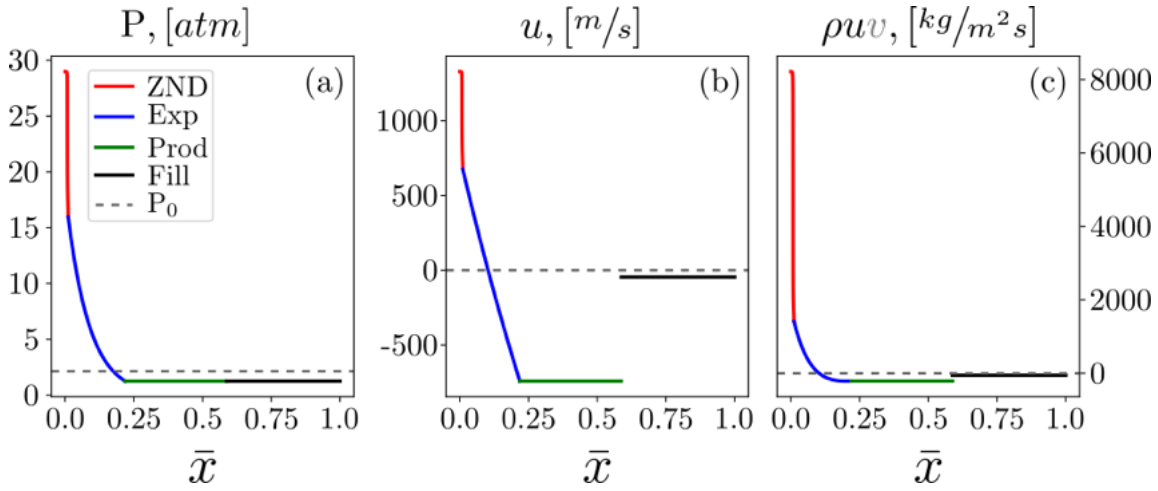

Figure 6.49: Example of the modeled profiles at the control volume exit for an ideal, hydrogen air detonation-based on an experimental run. $P_0 = 2.14$, $P_{ch} = 1.256$, and $\phi = 0.6$. Pressure profile (a), azimuthal velocity profile (b), and swirl profile (c).

From closer examination of Figure 6.49 (c), it is clear that the detonation wave produces a high positive swirl value due to the high density and high induced velocity throughout the ZND region. Despite the shorter length of the ZND region, it still has a large positive contribution to the net swirl. The expansion process also has a

significant contribution to the swirl in the positive direction, but because the expansion wave both decreases in azimuthal velocity and density, the magnitude in slightly lower than the ZND swirl contribution. This is up to the point at which the azimuthal velocity changes direction and the expansion region begins contributing negatively to the total swirl. However, this is at an even lower density relative to the beginning of the expansion region, netting an overall positive swirl contribution through the expansion process for this example. Post-expansion, the products are assumed to have a constant azimuthal velocity and density and to contribute negatively to the total swirl. The total swirl contributions from the ZND, Expansion and Product region leave a positive net swirl component, requiring the fill region to counter the remain positive swirl value. The increased density over the constant-pressure product region means that the azimuthal velocity magnitude is lower than the Product region azimuthal velocity; however, this still results in a negative velocity in the laboratory frame, which differs significantly from the assumptions typically used in RDE modeling of the inlet region. This treatment of the azimuthal velocity profile produces profiles similar to those shown in Figure 6.39 outside of the ZND region, which is likely caused by the larger than optimal particle sizes in the experimental setting not being able to fully resolve the high velocity gradients in this region.

The previous example looked at a sample problem with an ideal detonation, and the following describes the final implementation of the model, along with how each process is accounted for including the Deflagration Loss fraction from Section 6.1.1 The final model takes as inputs the deflagration loss parameters, ξ_{P} $and \xi_{\mathrm{L}}$, and the expansion region angle, α. The model iterates over the Fill region azimuthal velocity until converged, and uses the final solution to determine the laboratory wave speed, detonation pressure ratio, and induced azimuthal fill velocity. The goal of this analysis is to capture the effects of non-zero azimuthal fill velocity and deflagration combustion on the potential performance of a given RDE.

The modeling process starts with a gas mixture of the appropriate reactants at the total pressure, P_0, and the total temperature, T_0 in advance of the detonation wave, along with the outer diameter of the RDE for conversion to non-dimensional space, and the blockage fraction, $\mathrm{B_P}$. The channel static pressure, P_{ch}, is also assumed to be a known/measured value and is representative of the static pressure in the Fill region. It is assumed that these states are known from measurements and specified flow conditions, and a constant state vector is defined, $\mathbf{X_0}$:

$$\mathbf{X_0} = [\mathrm{OD}, \mathrm{fuel}, \phi, P_0, T_0, P_{ch}, \mathrm{B_P}] \tag{6.92}$$

where these values are RDE and flow dependent. This state vector will be used for both exercising the model and in a parameter estimation effort.

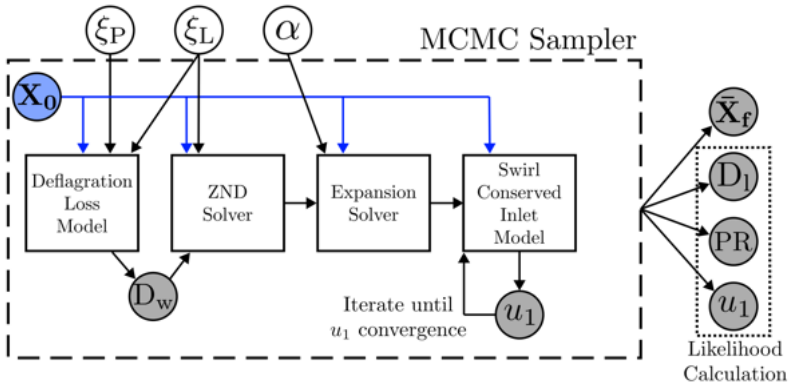

Figure 6.50: Diagram of the model used in the MCMC sampling process.

Figure 6.50 shows a model diagram, specifically highlighting the steps used in the parameter estimation process. With the initial state vector, $\mathbf{X_0}$, and the deflagration loss parameters, the deflagration loss model calculates a detonation wave speed in the wave frame, D_w. This wave speed, along with the initial state vector, are then used as inputs for the ZND solver. The ZND solver outputs a point-wise solution along the detonation processes starting from the shock wave and ending at the CJ plane. The final state of the ZND solution, along with the calculated, normalized distances, are passed to the Expansion solver. This solver also accounts for the constant expansion angle, α, input. Next, the state profiles from the ZND and Expansion solver are passed to the angular momentum conservation equations to calculate an azimuthal fill velocity. This last step is then iterated to account for the non-zero azimuthal fill velocity until convergence. Finally, the model produces a set of outputs that includes: a state vector along the control volume exit, $\bar{\mathbf{X}}_\mathbf{f}$, the laboratory wave speed, D_l, the CJ pressure ratio, PR and the calculated inlet azimuthal velocity, u_1. For clarity, these steps are shown in detail in Algorithm 10.

Algorithm 10 Non-Zero Swirl Model

Require: ξ_P, $\xi_L \in [0, 1]$ and $\alpha \in [0°, 90°]$

With $\mathbf{X_0}$, ξ_P, and ξ_L: Calculate wave speed in wave frame, D_w, with Deflagration Loss Model.

With $\mathbf{X_0}$, ξ_L, and D_w: Calculate ZND profile with Non-Ideal ZND Solver.

With $\mathbf{X_0}$, α, and ZND profile: Calculate expansion profile with Expansion Solver.

With $\mathbf{X_0}$ and expansion profile: Calculate initial guess of azimuthal fill velocity, u_1, with Swirl Conserved Inlet Model

while $u_{1,in} \neq u_{1,out}$ **do**

Iterate over Swirl Conserved Inlet Model with previous $u_{1,out}$ serving as new $u_{1,in}$

end while

Output state profile along control volume exit, $\bar{\mathbf{X}}_\mathbf{f}$, laboratory wave speed, D_l, detonation pressure ratio, PR, and converged induced azimuthal fill velocity, u_1.

In the case of the Markov Chain Monte Carlo (MCMC) sampling process, the model fixes the initial state vector, $\mathbf{X_0}$, while sampling over the deflagration loss parameters and the expansion angle [ξ_P, ξ_L, α]. The wave speed, pressure ratio, and azimuthal fill velocity [D_l, PR, u_1] are then used to evaluate the likelihood of the input parameters given the experimentally measured values of each output. This process seeks to learn the parameters that best fit the measurements, while also accounting for the error and uncertainty of each measurement. This parameter estimation process builds on the approach described in Section 6.3, which provided a detailed description of the sampling process.

6.7.2.2 Exit Plane

Assuming an isentropic flow with an ideal gas, the change in velocity based on a change in pressure can be calculated from Equation 6.93. We can use this as the baseline velocity achievable from a given post-detonation state. In the following example, we can simply assume that we get a velocity magnitude of 1250 m/s from the modeled expansion process. Following the examples from Section 6.6.3.3, we will specify a distribution in the azimuthal velocity component by drawing flow angles from a normal distribution of mean zero and a range of variances. Figure 6.51 shows a visual representation of the flow angle, which is defined off the axial direction and

varies $\in [-90, 90]$ degrees. With these flow angles, the individual components of the velocity vector are calculated with Equation 6.94.

$$V = \sqrt{h_4 - h_(P, s_4)} \tag{6.93}$$

$$u = V\cos(\theta),\ \ v = V\sin(\theta) \tag{6.94}$$

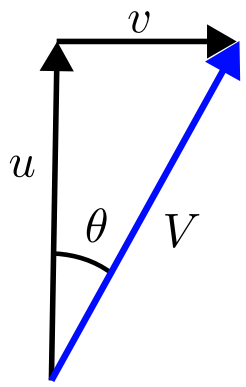

Figure 6.51: Flow Angle Diagram, with Angle Definition.

$$\theta \sim \mathcal{N}[0, \sigma_\theta] \tag{6.95}$$

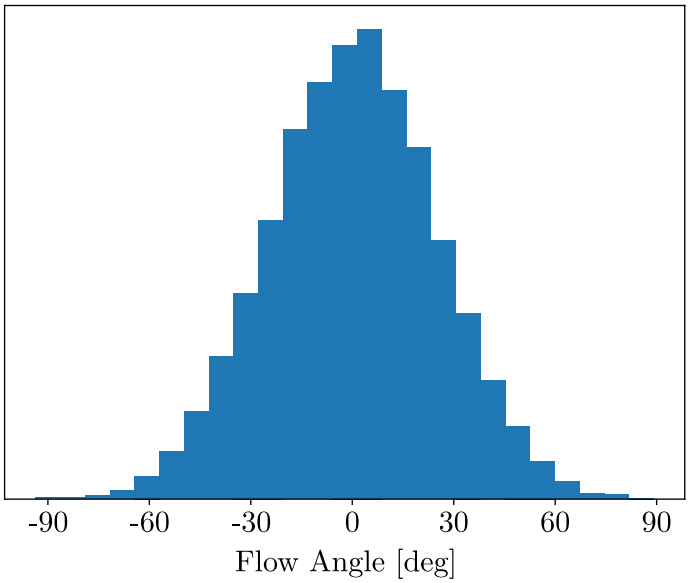

Figure 6.52: Histogram of Flow Angles using a 20 Degrees Standard Deviation.

Figure 6.52 shows an example of the flow angle distributions given an angle variation of 20 degrees. From this distribution, an axial velocity profile can be generated, allowing for the calculation of the expected value of the axial velocity, which corresponds to the specific thrust of the device. Finally, this value can be compared to the total velocity magnitude, V, to measure the degradation in the mean axial velocity as a function of the expansion angle distribution.

6.7.3 Blockage and Effective Area Ratio Inlet Model

The following will describe and develop the effective area ratio parameter used, in concert with the blockage fraction, B, from Feleo et al., to evaluate the impacts of the passing detonation wave on the RDE inlet. First, we assume isentropic flow between the RDE plenum and the inlet throat, along with assuming no changes in the gas composition between the cold and hot flow conditions. We start with the definition of the steady, uniform mass flow rate through an area (taken to be the geometric area of the inlet), which can be expressed as:

$$\dot{m} = c_{\mathrm{d}} \frac{A_{\mathrm{g}} P_0}{\sqrt{T_0}} \sqrt{\frac{\gamma}{R}} M_{\mathrm{g}} \left(1 + \frac{\gamma - 1}{2} M_{\mathrm{g}}^2\right)^{-\frac{(\gamma+1)}{2(\gamma-1)}} \tag{6.96}$$

This form of the mass flow function has a dependency on the total pressure and temperature, which change between fueled and un-fueled operation of the RDE. We can then introduce the corrected mass flow rate defined as:

$$\dot{m}_{\mathrm{c}} = \dot{m}\frac{\sqrt{\Theta}}{\Delta} \tag{6.97}$$

with

$$\Theta = \frac{T}{T_{\mathrm{ref}}}$$

and

$$\Delta = \frac{P}{P_{\mathrm{ref}}}$$

where P_{ref} and T_{ref} correspond to standard day conditions of 1 atm and 298.15 K, respectively. When cast in this form, the change in plenum total conditions can be properly accounted; thus,

$$\dot{m}_{\mathrm{c}} = A_{\mathrm{g}}c_{\mathrm{d}}\frac{P_0}{\Delta}\sqrt{\frac{\Theta}{T_0}}\sqrt{\frac{\gamma}{R}}M_{\mathrm{t}}\left(1+\frac{\gamma-1}{2}M_{\mathrm{t}}^2\right)^{-\frac{(\gamma+1)}{2(\gamma-1)}} \tag{6.98}$$

The effective flow area is defined by:

$$A_{\mathrm{e}} = A_{\mathrm{g}}c_{\mathrm{d}} \tag{6.99}$$

with c_{d} defined as the discharge coefficient through the inlet. Substituting into the effective area definition and assuming a fixed (frozen) gas composition, the corrected mass flow rate becomes a function of effective area and Mach number at the inlet throat only; i.e.,

$$\dot{m}_{\mathrm{c}} = A_{\mathrm{e}}\frac{P_{\mathrm{ref}}}{\sqrt{T_{\mathrm{ref}}}}\sqrt{\frac{\gamma}{R}}M_{\mathrm{t}}\left(1+\frac{\gamma-1}{2}M_{\mathrm{t}}^2\right)^{-\frac{(\gamma+1)}{2(\gamma-1)}} \tag{6.100}$$

The ratio of the corrected mass flow rates for fueled and un-fueled operation can then be taken to remove like terms and get a ratio of the effective areas between the two modes of operation:

$$\frac{\dot{m}_{\mathrm{c,H}}}{\dot{m}_{\mathrm{c,C}}} = \frac{A_{\mathrm{e,H}}}{A_{\mathrm{e,C}}}\frac{M_{\mathrm{t,H}}}{M_{\mathrm{t,C}}}\left(\frac{1+\frac{\gamma-1}{2}M_{\mathrm{t,H}}^2}{1+\frac{\gamma-1}{2}M_{\mathrm{t,C}}^2}\right)^{-\frac{(\gamma+1)}{2(\gamma-1)}} \tag{6.101}$$

where the subscript H refers to the conditions during operation and C represents the cold-flow conditions. The quantity of interest is the effective area ratio, α, is defined as:

$$\alpha = \frac{A_{\mathrm{e,H}}}{A_{\mathrm{e,C}}} \tag{6.102}$$

which represents the change in the effective area ratio as the RDE operates.

After substituting Equation 6.102 into Equation 6.101 and solving for α we are left with:

$$\alpha = \frac{\dot{m}_{\mathrm{c,H}}}{\dot{m}_{\mathrm{c,C}}} \frac{M_{\mathrm{t,C}}}{M_{\mathrm{t,H}}} \left(\frac{1 + \frac{\gamma-1}{2} M_{\mathrm{t,C}}^2}{1 + \frac{\gamma-1}{2} M_{\mathrm{t,H}}^2} \right)^{-\frac{(\gamma+1)}{2(\gamma-1)}} \tag{6.103}$$

Equation 6.103 now allows us to calculate the effective area change in terms of corrected mass flow and Mach number for the cold flow and hot flow. By assuming isentropic flow from the plenum to the inlet throat, the Mach number can be calculated from the pressure ratio between the plenum total and throat static, with the caveat that the Mach number at the throat can be at most sonic. This was accomplished with the isentropic flow equation evaluated between the plenum and the inlet throat:

$$M_{\mathrm{t}} = \sqrt{\frac{2}{\gamma - 1} \left[\left(\frac{P_0}{P_{\mathrm{t}}} \right)^{\frac{\gamma-1}{\gamma}} - 1 \right]} \tag{6.104}$$

Given a measure of the plenum-to-inlet throat pressure ratio, P_0/P_{t}, the Mach number at the throat can be evaluated for each condition, leaving the effective area ratio as a function of the corrected mass flow rate and the pressure ratio only. In order to calculate this quantity only the nominal mass flow rate, the total plenum pressure and temperature, and the static pressure at the inlet throat are needed. This methodology allows for the calculation of effective area changes without the need for cold-flow calibration data, which is required for the method presented by Feleo et al. [96].

Equation 6.104 is written in a steady and uniform flow form; however, the detonation wave creates a non-uniform flow field in the inlet plane. Though we can assume a quasi-steady process by time averaging over many laps, we are still left with a non-uniform profile across the inlet flow area. So we will need to provide an averaging method to calculate the Hot flow Mach number, specifically the Hot flow inlet static pressure. In the experimental setting, this is done using the phase-averaged high-speed pressure measurements, which effectively provides the static pressure across the inlet flow area. The area averaged inlet static pressure can then be defined as:

$$P_{\mathrm{t}} \equiv \bar{P}^{A}_{inj} = \frac{1}{A_{inj}} \int P(A) dA \tag{6.105}$$

Equation 6.104 still assumes that the gas properties remain constant from cold to hot flow (constant γ) and the total temperature of the plenum also remains constant. These assumptions almost certainty break down as the inlet blockage increases because of the higher potential and magnitude of the product gas backflow.

Finally, the relationship between the effective area ratio and the blockage fraction from Feleo et al. [96] is shown below:

$$1 - \alpha = \frac{A_{\mathrm{e,C}} - A_{\mathrm{e,H}}}{A_{\mathrm{e,C}}} \tag{6.106}$$

This formulation is arranged in a form that determines the percent change in the effective area from the cold flow to the hot flow conditions.

In practice, the blockage fraction defined by Feleo et al. uses the measured mass flow rate instead of a mass flux based on the geometric inlet area:

$$B = 1 - \frac{\dot{m}''_{Hot}}{\dot{m}''_{Cold|P_{0,Hot}}} = 1 - \frac{\dot{m}_{Hot}}{\dot{m}_{Cold|P_{0,Hot}}} \tag{6.107}$$

where $\dot{m}_{Hot}$ is calculated at the metering orifice and $\dot{m}_{Cold|P_{0,Hot}}$ is calculated by curve fit on a calibration dataset.

Under the same assumption of an isentropic inlet used in the derivation of the effective area ratio, the mass flow rate equation (Equation 6.96) can be substituted into the blockage fraction. After simplifying, this yields:

$$B = 1 - \frac{A_{e,H}}{A_{e,C}} \left(\frac{M_H (1 + \frac{\gamma-1}{2} M_H^2)}{M_C (1 + \frac{\gamma-1}{2} M_C^2)} \right)^{\frac{-(\gamma+1)}{2(\gamma-1)}} \tag{6.108}$$

In this sense, the blockage fraction does not reduce to a simple area ratio, unless under certain inlet Mach number conditions. It is a relationship of the area ratio caused by the blockage and a change in some inlet average Mach number.

6.7.3.1 Uncertainty Quantification for Blockage Fraction and Effective Area Ratio

For the uncertainty analysis of the two blockage fraction definitions, a Monte Carlo based uncertainty propagation was conducted for the effective area ratio, while stan-

dard uncertainty propagation technique were used to examine the blockage fraction. The following assumes uncorrelated uncertainties in the measurement and only examines the bias (systematic error) of the sensors and not the random uncertainty, which can simply be assumed as a constant between the two methods, given the same data set.

The effective area ratio can be reduced to the following dependencies for error analysis. Each term is assumed to be a time-averaged quantity, using the stable portion of the run as a single averaged point. Written in terms of the random variables in the definition of the effective area ratio:

$$\alpha \propto \frac{P_{0,C}}{P_{0,H}} \sqrt{\frac{T_{0,H}}{T_{0,C}}} \left(\frac{P_{0,C} P_H}{P_C P_{0,H}} \right)^{\frac{-(\gamma+1)}{2\gamma}} \frac{\psi(P_{0,C}, P_C)}{\psi(P_{0,H}, P_H)} \tag{6.109}$$

where:

$$\psi(P_{0,i}, P_i) \equiv \sqrt{\left(\frac{P_{0,i}}{P_i} \right)^{\frac{\gamma-1}{\gamma}} - 1}$$

therefore the uncertainty in the effective area ratio can be related as:

$$\sigma_\alpha^2 = \sum_{i=0}^{N} \left(\frac{d\alpha}{dx_i} \sigma_{x_i} \right)^2 \tag{6.110}$$

where i represents the random variables in Equation 6.109.

Rather than taking a complex partial derivative through Equation 6.109, a simple Monte Carlo uncertainty propagation was carried out using 20,000 samples, where each input variable was assumed to be normally distributed around a measured mean value with the standard deviation based on the systemic uncertainty of the sensor (see Table 6.8).

It should be noted that this discussion of the uncertainty in the measurement of the effective area ratio does not account for any discrepancy in the location of the static pressure measurement at the geometric throat. The methodology will therefore assume that the static pressure measurement is exactly at the geometric throat. Because of this fact, the uncertainty quantities of the effective area ratio that are calculated with this method are a best-case scenario.

The uncertainty analysis of the blockage fraction requires a more detailed analysis than the effective area ratio due to the need to calculate a cold-flow equivalent mass flow rate, given the measured plenum total pressure during the hot-flow portion of the

run. This calculation is broken down into two techniques depending on the measured plenum pressure, one for an un-choked inlet and one for a choked inlet for the cold-flow equivalence mass flow rate.

In the un-choked region of the cold flow equivalent mass flow rate calculation: if the plenum pressure is at a calibration point, the uncertainty in the mass flow rate should remain the same as the measured uncertainty. If the plenum pressure is not at a calibration point, then a linear interpolation is conducted to estimate the cold-flow equivalent mass flow rate, along with the uncertainty. The cold-flow equivalent mass flow rate is estimated by the following:

$$\dot{\bar{m}}_C = \dot{\bar{m}}_0 + (\dot{\bar{m}}_1 - \dot{\bar{m}}_0)\,\frac{\bar{P}_{0,H} - \bar{P}_{0,0}}{\bar{P}_{0,1} - \bar{P}_{0,0}} \tag{6.111}$$

where $\dot{\bar{m}}_C$ is the estimated mass flow rate given the measured hot flow plenum pressure, $P_{0,H}$. Subscripts 0 and 1 refer to the calibrations points directly below and above the measured hot flow plenum pressure.

Because the interpolation process is linear, the standard, correlated uncertainty propagation can be applied:

$$\begin{aligned}\sigma^2_{\dot{m}_C} = &(\frac{d\dot{m}_C}{d\dot{m}_0}\sigma_{\dot{m}_0})^2 + (\frac{d\dot{m}_C}{d\dot{m}_1}\sigma_{\dot{m}_1})^2 + \\ &(\frac{d\dot{m}_C}{dP_{0,0}}\sigma_{P_{0,0}})^2 + (\frac{d\dot{m}_C}{dP_{0,1}}\sigma_{P_{0,1}})^2\end{aligned} \tag{6.112}$$

It should be noted that this formulation of the error propagation ignores the fact that the mass flow rate is not linear with plenum pressure while the inlet is un-choked. So, this only represents the propagation of the uncertainty from the systematic measurement uncertainty. Also, because of the assumption that the individual sensor uncertainties are independent, the mass flow rate and the plenum pressure uncertainties are also assumed to be uncorrelated. This assumption is valid since the uncertainty in the mass flow rate is only correlated with the orifice pressure measurement, which is independent from the uncertainty in the plenum pressure measurement.

For the choked cold-flow equivalent, a choked flow line is generated based on the calibration points that are certain to be choked. This yields an estimated slope, intercept, and flow area, based on the data and its associated uncertainty. Hot-flow pressures within the choked region are then propagated through the choked flow line:

$$\dot{m}_{choked} = m_{fit} P_{0,choked} + b_{fit} \tag{6.113}$$

where m and b are the slope and intercept of the curve fit. The uncertainty of the choked cold flow equivalent mass flow is given by:

$$\sigma_{\dot{m}} = \sqrt{(P_0\sigma_m)^2 + (m\sigma_{P_0})^2 + \sigma_b^2} \tag{6.114}$$

Figure 6.53 shows an example of the calibration process and the uncertainty propagation. The points in black represent the calibration points, while the red and blue points are the estimated values outside of the calibration dataset, un-choked and choked, respectively.

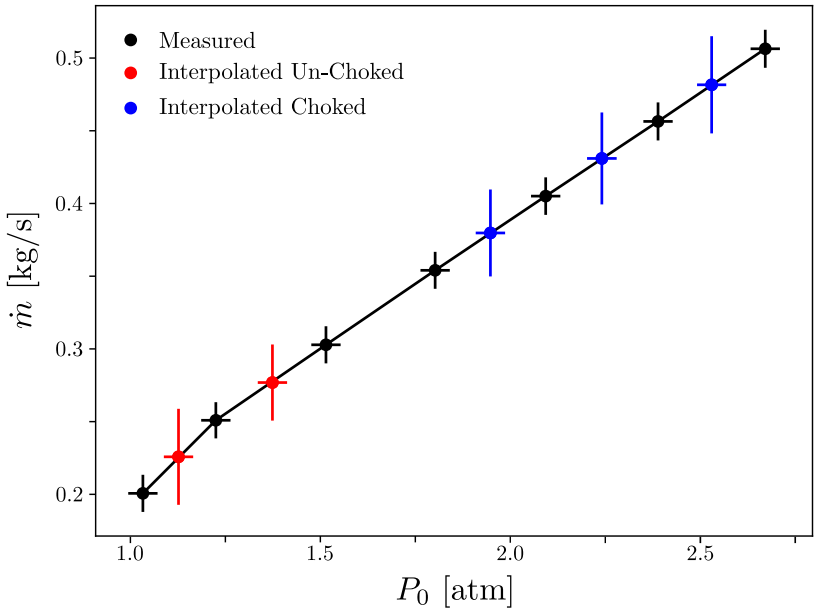

Figure 6.53: Curve Fit Errors for Cold Flow Interpolation.

Now the uncertainty in the blockage fraction, based on the systematic error, is given by:

$$\sigma_B = \sqrt{\left(\frac{\sigma_{\dot{m}_H}}{\dot{m}_C}\right)^2 + \left(\frac{\dot{m}_H}{\dot{m}_C^2}\sigma_{\dot{m}_C}\right)^2} \tag{6.115}$$

where $\sigma_{\dot{m}_C}$ is determined by either Equation 6.112 if the cold flow equivalent is un-choked, Equation 6.114 if the cold flow equivalent is choked, or the nominal mass flow uncertainty if at a calibration point.

Table 6.8 shows the published instrument uncertainty for the measurement locations of interest used in the calculation of the blockage fraction and the effective area ratio.

Measurement	Full Scale	Sensor Uncertainty
$P_{0,orifice}$	500 [psi]	0.25% FS
$P_{0,plenum}$	200 [psi]	0.25% FS
P_s	30 [psi]	0.25% FS
T	1260 [°C]	max(0.75%, 2.2 [°C])

Table 6.8: Summary of Measurement Uncertainty

Using the uncertainty analysis discussed above, with sensor errors in Table 6.8, Figure 6.54 shows the uncertainty of the measured value on a set of runs with varying mass flow rate. This figure shows that at low corrected mass flow rates, the effective area ratio has a much larger uncertainty; however, outside of the low flow rate condition, the effective area ratio provides a more accurate measurement methodology.

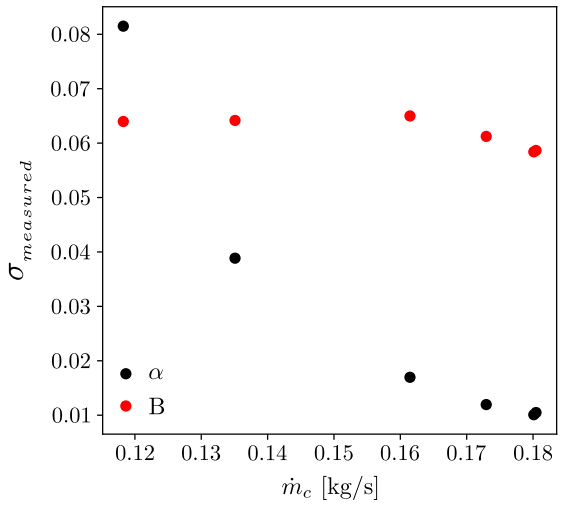

Figure 6.54: Experimental Measurement Standard Deviations for Blockage Fraction and Effective Area Ratio versus Mass Flow Rate.

Finally, a study was performed to examine the difference in the measured blockage fraction and effective area ratio across a much larger set of experimental data. Figure

6.55 shows the effective area ratio plotted against the blockage fraction (a) and the inlet pressure recovery (b). This plot shows that, when accounting for measurement error, the blockage fraction and effective area ratio are essentially measuring the same value. This means that we can use one in place of the other, depending on which value is more readily calculable. Figure 6.55 (b) shows that pressure recovery scales well with the effective area ratio, where the highest effective areas correspond to a stiffer inlet. As a refresher, the inlet stiffness is defined as the ratio between the channel static pressure and the total pressure of the plenum. As with the large majority of analysis on the injector, the inlet blockage, regardless of definition, is correlated directly with the stiffness of the inlet.

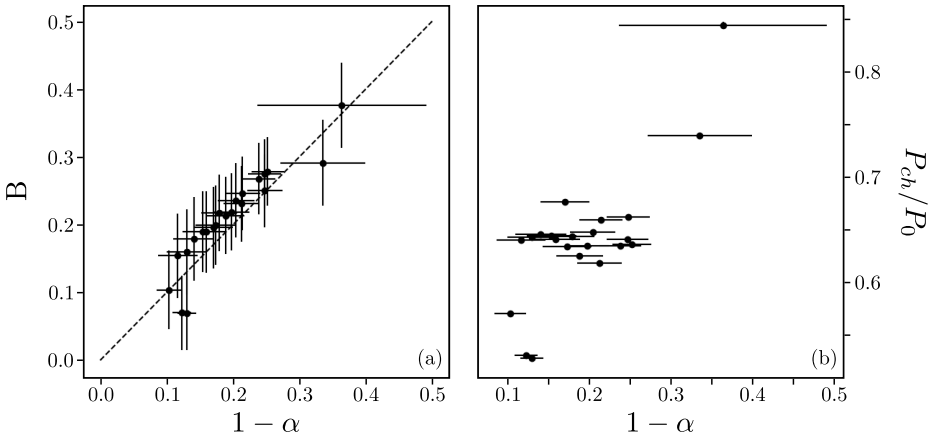

Figure 6.55: Blockage Fraction versus one minus the Effective Area Ratio (left). Injector Pressure Losses versus one minus the Effective Area Ratio (right).

6.7.3.2 Dynamic Inlet Model

With the knowledge of the two blockage measurement methods, a simple dynamic inlet model was used to provide additional insight as to what these blockage fractions are actually measuring. The model itself generates an arbitrary pressure profile across the inlet in a manor similar to the analysis in Bedick et al. Initially, an arbitrary pressure profile was used, assuming air as both the driving plenum gas and as the gas within the RDE channel. The pressure profile is generated assuming a isentropic, exponential decay from a peak pressure down to a given channel pressure. This expansion process provides the channel pressure against which the inlet is driving. In

cases where the channel pressure profile is greater than the plenum pressure, the inlet allows for backwards flow, otherwise the inlet is flowing in the forward directions. Parametric pressure profile were generated by specifying a range of the following values: plenum total pressure, peak pressure (simulating the detonation wave), channel static pressure, and a location where the pressure profile equals the plenum pressure, BR. With the arbitrary pressure profiles, the blockage fraction, B, and the effective area ratio, α, can be calculated and compared to the specified blockage ratio BR.

Figure 6.56 shows an example of the pressure profile (subplot (a)) and the associated Mach number profile determined from the pressure profile. The vertical, dashed black line represents the location where the pressure profile equals the plenum pressure, BR, while the dashed blue line represents the point at which all backward-flowing gases have been replenished through the plenum. This location is another blockage metric that captures when the inlet begins to fill the fresh reactants and will be denoted as BR_{fill}. The details of the determination of the Mach profile will be given later in this section, but Figure 6.56 (b) shows an example of the profile, where the Mach number is correlated with the mass flow rate through the inlet.

$$\mathrm{BR}_{fill} = \frac{x_{fill}}{\pi OD} \tag{6.116}$$

Figure 6.56 also shows the different flow regions, as shown by the shading of the Mach profile plot. These regions show where backflow is present, where the backward flow is re-filling, and finally, where the forward flow begins. This highlights the differences in the blockage ratio, BR, and the location were fill resumes, BR_{fill}

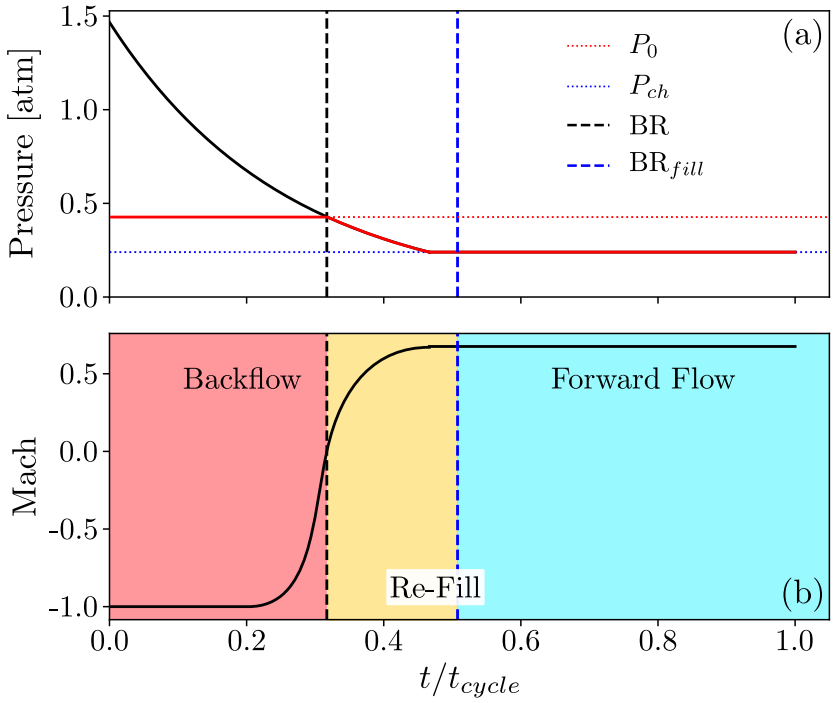

Figure 6.56: Example of the randomly generated air profile.

The process for generating the Mach number profile from the modeled pressure profile starts with a set of initial states for the air profile generation:

$$\mathbf{X}_0 = [A_{inj}, P_0, P_{peak}, P_{ch}, \mathrm{BR}]$$

This set was used to generate a profile of across the injector and does not provide any predictive characteristic. As mentioned earlier the pressure decay was modeled as an isentropic exponential decay process, where the equation for the pressure as a function of a non-dimensional space is given by:

$$P(\bar{x}) = P_{peak} exp(-k\bar{x}) \tag{6.117}$$

where $\bar{x}$ is a non-dimensional distance, $\frac{x}{\pi OD}$, such that it aligns with the definition of the blockage fraction.

This equation can then be rearranged solve for the decay constant, k. given a specified blockage ratio, plenum pressure, and peak pressure, where the initial pressure of the expansion process is the peak pressure, P_{peak}.

$$k = \frac{-\ln(\frac{P_0}{P_{peak}})}{\mathrm{BR}} \tag{6.118}$$

Using the newly determined decay constant, the expansion process is modeled out to the point at which the pressure profile reaches the specified channel pressure. Upon reaching this pressure, the remaining flow area is assumed to be a region of constant static pressure flowing in the forward direction. An example of the pressure profile is seen in Figure 6.56 (a)

The next step is to relate the pressure profile to a mass flux profile through the inlet as a function of the non-dimensional distance $\bar{x}$. Using the pressure ratio profile, and assuming a isentropic inlet (with a constant c_d in both directions) the Mach number profile can be determined using the following equation:

$$M_i = \sqrt{\frac{2}{\gamma+1}\left[\left(\frac{P_{0,i}}{P_{s,i}}\right)^{\frac{\gamma-1}{\gamma}}\right]} \tag{6.119}$$

where the Mach number for each differential area is based on the total driving pressure, injector static pressure, and the ratio of specific heats at each point along the profile. In the backward flowing portion of the inlet, the driving ($P_{0,i}$) pressure is assumed to be that of the pressure profile, while the static pressure ($P_{s,i}$) is assumed to be the specified plenum pressure. The opposite is true for the forward flowing region, where the static pressure is assumed to be that of the pressure profile. An example Mach profile is shown in Figure 6.56 (b). A mass flux profile can then be generated using the Mach profile and the mass flow function:

$$\dot{m}_i'' = P_{0,i}\sqrt{\frac{\gamma}{RT_0}}M_i\left(1+\frac{\gamma-1}{2}M_i^2\right)^{\frac{-(\gamma+1)}{2(\gamma-1)}} \tag{6.120}$$

where the total temperature and gas properties are assumed to be constant and that of air.

To solve for the mass flow rate across the inlet, numerical integration was conducted on the mass flux profile:

$$\dot{m} = \int \dot{m}'' dA \tag{6.121}$$

yielding the nominal mass flow rate through the inlet, given the set of initial conditions.

In addition, the area averaged pressure (Equation 6.105) and the Mach number based on this quantity will be calculated, along with an area averaged Mach number. It should be noted that the area-averaged Mach number and the Mach number based on the area-averaged pressure are not measuring the same quantity but are useful when analyzing the effective area ratio, α, as this is defined as equivalent to the area average pressure. The area average Mach number is given by:

$$\bar{M} = \frac{1}{A} \int M(A) dA \tag{6.122}$$

while the Mach number based on the area averaged pressure, Equation 6.105, is given by:

$$\bar{M}|_{\bar{P}^A} = \sqrt{\frac{2}{\gamma - 1} \left[\left(\frac{P_0}{\bar{P}^A} \right)^{\frac{\gamma-1}{\gamma}} - 1 \right]} \tag{6.123}$$

where it is important to note that this is the Mach number that is used in the calculation of the effective area ratio.

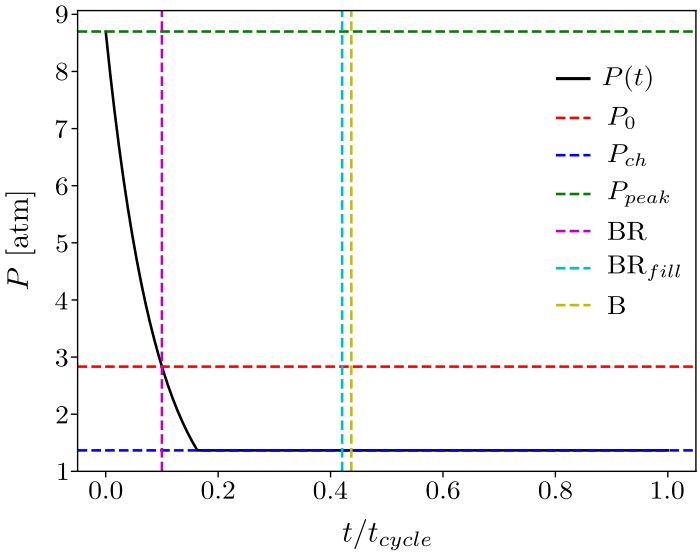

Figure 6.57: Example of Dynamic Inlet Model Pressure Profile

6.7.3.3 Extension to Detonations

A simple extension of the dynamic inlet model can be made to account for real detonation effects. In this case, the input parameters change to include the fuel and equivalence ratio, and rely on the detonation calculation to get the peak pressure instead of directly specifying it. There are two options for the detonation solver, using the CJ pressure ratio or calculating the full ZND profile. The former uses the exact processes discussed in the previous section, where the CJ pressure is substituted in as the peak pressure, while the latter models the expansion starting from the CJ plane, accounting for the induction zone length. In either method, the expansion process is modeled as an exponential, isentropic expansion, but now using the post-detonation gas properties. To this end, the calculations of the Mach and mass flux profiles used the product gas composition in the backwards flowing portion of the inlet, while the forward flowing portion still used the properties of air. By modeling the detonation, there is now a high correlation of the peak pressure to the channel pressure, which is used as the pre-detonation state. The goal with this is to more accurately capture the effects of the detonation wave on the injector of the RDE.

6.8 Results for RDE Losses Modeling

The following sections will discuss the results from the RDE loss models discussed in the previous section. This will begin with an in depth review of the State to State model with included loss mechanisms. Next, the non-zero velocity models will be evaluated, both at the inlet plane and the exit plane. Finally, we finish on a discussion of inlet blockage and it's relationship to RDE performance.

6.8.1 State to State Cycle Model

The follow results were constructed using the State to State model, shown in Figure 6.44 and Algorithm 9. The input conditions for the model were stoichiometric, hydrogen-air, operating at a premixed inlet condition of 2 atm and 300 K. It is assumed that the exhaust pressure is that of standard day sea level, 1 atm. The loss parameters varied between $[0, 0.9]$ except for the pressure drop fraction which was varied between $[0, 0.5]$. For reference, based on these specific initial conditions a $\xi_{\Delta P} = 0.5$ value results in an inlet pressure drop of 0.5 atm.

Figure 6.58 shows an example of a T-s diagram for the State to State model, incrementally adding loss parameters. Figure 6.58 (a) represents the ideal detonation, which accounts for the loss in available energy due to the post-detonation expansion process. Along with the ideal detonation, an ideal deflagration is shown with a dashed line, starting from the same initial conditions, which is also the case when $\xi_P = 1.0$. From this subplot, it is clear that the ideal detonation results in a final state with less entropy production, at a similar final combustion temperature; therefore, at a higher isobar. A dotted black line is also drawn around the final state of the ideal deflagration cycle (un-filled marker). This is a constant specific impulse line, where the final states above the line result in a high specific impulse compared to the ideal deflagration when isentropically expanding to the same final pressure. In Figure 6.58 (a), it is clear that the ideal detonation should produce thrust more efficiently than the ideal deflagration due to the significant reduction in entropy production between the two cycles at a similar total heat release. This version can be thought of as the "standard" model of RDE and other pressure gain cycles, where the expectation is a higher post-combustion pressure than the equivalent deflagration-based cycle.

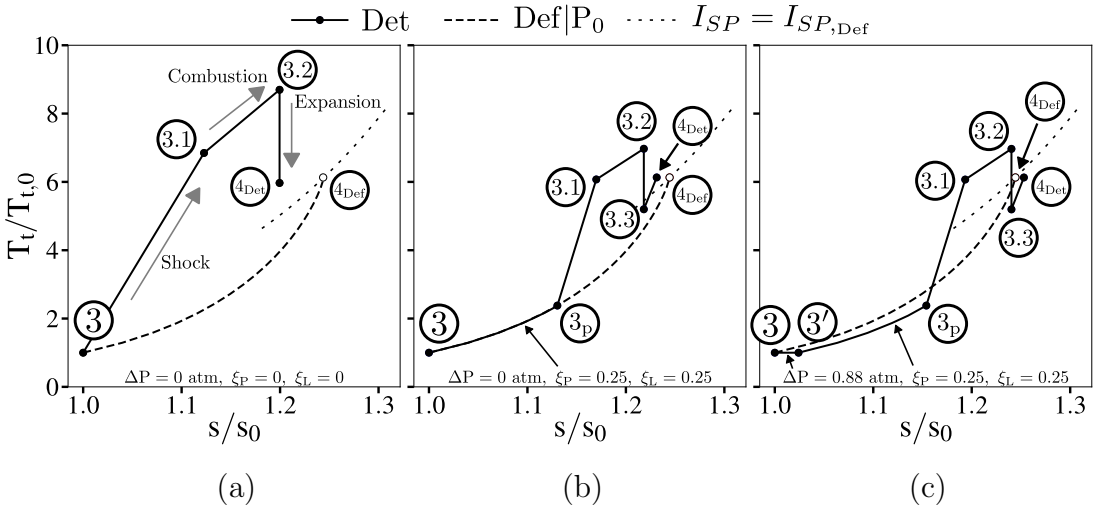

Figure 6.58: T-s Diagram State to State Model with ξ_{NC}, ξ_{CP}= 0.0.

As loss parameters are added, specifically the deflagration loss parameters, ξ_{P} and ξ_{L}, the detonation cycle begins to approach the same end state as the ideal deflagration. Figure 6.58 (b) shows an example of this with relatively moderate values of the deflagration loss parameters, ξ_{P}, $\xi_{\mathrm{L}} = 0.25$. The distinction between the post-expansion state, (3.3), and the equilibrium exhaust state, (3.4) equals (4), is clearly shown. Because it is assumed that the fuel is fully consumed at (4), the resulting final state for the detonation in Figure 6.58 (b) still falls above the line of constant specific impulse. In this example, the entropy production of the non-ideal detonation is approaching that of the ideal deflagration device due to the larger entropy production caused by the parasitic combustion occurring before the wave. This results in a decrease in the post-detonation pressure, based on the final state isobar.

Finally, Figure 6.58 (c) shows the T-s diagram for a detonation with the same deflagration loss parameters as Figure 6.58 (b), but now with an inlet pressure loss of $\Delta P = 0.88$ atm. This value was obtained from an experimental case with similar total conditions of the plenum and corresponds to a pressure drop fraction of $\xi_{\Delta P} = 0.74$. Because of the high inlet pressure loss, the parasitic combustion is occurring at a much lower static pressure, resulting in a further increase in the entropy production due to the parasitic combustion. With this combination of parameters, even assuming complete combustion at the post-expansion pressure (ξ_{NC}, $\xi_{\mathrm{CP}} = 0.0$), the non-ideal

detonation cycle results in a final state that is less efficient from an entropy production point of view, as well as producing less thrust than the ideal deflagration. These results show that there exist combinations of loss parameters that would result in a RDE producing much less thrust than expected, even if the combustion efficiency is 100%.

Figure 6.59 is shown below to clarify the treatment process of the post-expansion state. As was discussed in the Model Description section, the state model includes a non-commensal fuel fraction, ξ_{NC}, and a commensal pressure fraction, ξ_{CP}. The gray box outlines the potential final state, ④, based on these two parameters. The non-commensal fraction determines the amount of heat released from ③.③ to ④, where a higher non-commensal fraction means less heat release, resulting in a final state, ④, much closer to the post-expansion state, ③.③. The commensal pressure fraction, ξ_{CP}, determined the pressure at which commensal combustion occurs, where lower values correspond to combustion pressures near the post-expansion pressure at ③.③ and higher values are combustion pressures near the ambient condition, P_{amb}.

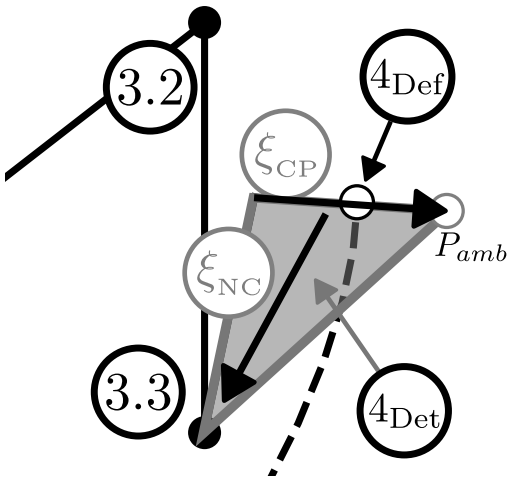

Figure 6.59: Post-expansion Treatment for the State to State Model.

When accounting for the detonation work, $Du_{3.2}$, the energy "gain" equation is now referenced to the equilibrated post-expansion state, ④. This is shown below:

$$G_4 = h_{t,4} - h_{t,3'} \tag{6.124}$$

With this definition, the gain reduces to zero for all combinations of loss parameters. This is solely due to the decrease in energy available from the detonation work term. Because of this result, it appears that defining a RDE "gain" based on the energy available is an improper definition. To combat this, the analysis shifts focus to the thrust production, or specific impulse in the case of this section, because a better definition of "gain" is available in a detonation-based cycle.

First, the "gain" in the specific impulse over an ideal deflagration device is defined in Equation 6.125. Where $I_{SP,Def,ideal}$ is calculated assuming complete combustion at the total conditions of the plenum, and also assumes no losses through an inlet of the arbitrary deflagrative combustion. The calculated $I_{SP,Det}$ from the model is then normalized by the ideal deflagration specific impulse to provide a "gain" in thrust efficiency from the RDE.

$$I_{SP,norm} = \frac{I_{SP,Det}}{I_{SP,Def,ideal}} \tag{6.125}$$

An example of the specific thrust gain is shown in Figure 6.60, where the two loss parameters of interest, ξ_{P} and ξ_{L}, are compared at two different inlet pressure drops. For this figure, the other loss parameters are set to zero, which allows for the comparison of these results with the deflagration loss model in Figure 6.6 at the case of zero pressure drop, shown in solid lines. At the zero inlet pressure drop condition, all combinations of deflagration loss parameters resulted in a normalized specific impulse greater than 1.0. This means that the modeled cycle would result in a more efficient thrust production, relative to an ideal deflagration at the same plenum conditions. When accounting for losses in the deflagration device, these values of normalized specific thrust would improve, indicating a potential performance benefit.

At an inlet pressure drop fraction of $\xi_{\Delta P} = 0.5$, the resultant lines of constant normalized specific impulse shift toward the bottom left of the figure. This results in cases where the modeled specific impulse is less than that of the ideal deflagration device at the same initial conditions. The combination of the inlet pressure losses with the parasitic fraction is particularly harmful due to the larger fraction of fuel being consumed at a lower static pressure, a result echoed in Figure 6.58.

Compared to the results in the base deflagration loss model results shown in Figure 6.6, it appears that the contours of normalized specific impulse from Figure 6.60 follow closely to the contours of detonation pressure ratio shown by the dashed gray lines in Figure 6.6. This result may suggest that the detonation pressure ratio is a better indicator of the RDE performance than the wave speed, regardless of the inlet pressure losses included in Figure 6.60. A deeper discussion on the pressure

ratio effect on the RDE performance will be included later in this section, but first we will examine the RDE performance as a function of the wave speed and detonation fraction, χ_{D}.

Figure 6.61 shows the normalized specific thrust as a function of the normalized wave speed, $\frac{D}{D_{\mathrm{CJ}}}$, in subplot (a) and the detonation fraction, χ_{D}, in subplot (b). These plots are shown with a non-commensal fraction, $\xi_{\mathrm{NC}} = 0$, which by default enforces the commensal combustion pressure to also be zero. Two inlet pressure drops are shown on the subplots, where the black lines denote zero pressure drop, and the gray lines represent a pressure drop fraction of $\xi_{\Delta P} = 0.5$. Like Figure 6.10, lines of constant parasitic fraction, ξ_{P}, are shown in a solid style, and the lines of constant leaked fraction, ξ_{L}, are shown in a dashed style.

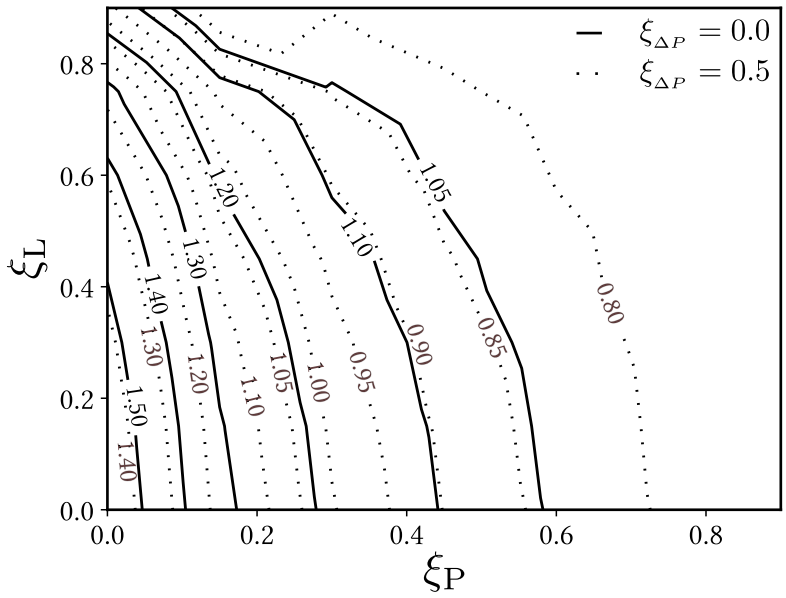

Figure 6.60: Specific impulse gain of RDE versus an ideal deflagration device as a function of the parasitic combustion fraction, ξ_{P}, and the leaked fuel fraction, ξ_{L}, at two inlet pressure drop fractions, $\xi_{\Delta P}$= 0 in solid and $\xi_{\Delta P}$= 0.5 in dotted styles. Assuming complete combustion of leaked fuel and the post-expansion pressure $P_{3.3}$. (ξ_{NC}, ξ_{CP}= 0.0)

Figure 6.61 (a) examines the normalized specific impulse as a function of the wave speed, relative to the ideal CJ speed. This figure shows the effects of the deflagration

loss parameters on both the detonation wave and the RDE performance. The wave speed follows similar contours with increases in either loss parameter. The most interesting aspect of this plot is the low correlation between wave speed and the prediction of specific impulse. Looking at the contours with no pressure drop (black lines), at a wave speed of 80% of the CJ speed, the normalized specific impulse can vary widely between 105-150% of the ideal deflagration. This result suggests that wave speed, and detonation performance in general, may not be the best marker for successful RDE performance. Although these values indicate an improved performance of the ideal deflagration cycle, as additional losses are accounted for, the performance starts to dip below the deflagration specific impulse. For example, Figure 6.61 (a) also shows the contours of the deflagration loss parameters, but now at an inlet pressure drop fraction of $\xi_{\Delta P} = 0.5$. With added inlet losses, the contour shifts downward, resulting in combinations of deflagration loss parameters with worse thrust performance relative to the ideal deflagration cycle. This result ignores the non-commensal fraction, ξ_{NC}, and the commensal pressure fraction, ξ_{CP}, so with these losses included the expected performance would decrease further.

Figure 6.61 (b) shows the same contours of deflagration loss parameters and the inlet pressure drop as Figure 6.61 (a), but now plots the detonation fraction on the horizontal axis. With zero inlet pressure drop (black lines), the performance converges to the deflagration cycle as the detonation fraction, χ_{D}, approaches zero. This result was expected based on the model methodology, especially when other losses are neglected. Similarly to Figure 6.61 (a), a moderately high detonation fraction does not necessarily indicate improved RDE performance. For example, at a detonation fraction of 80%, the normalized specific thrust can vary between 130-155% of the ideal deflagration cycle. Though this band is slightly tighter than the wave speed variation, it also provides evidence that the performance of the detonation wave is not solely linked to the the performance of the RDE cycle.

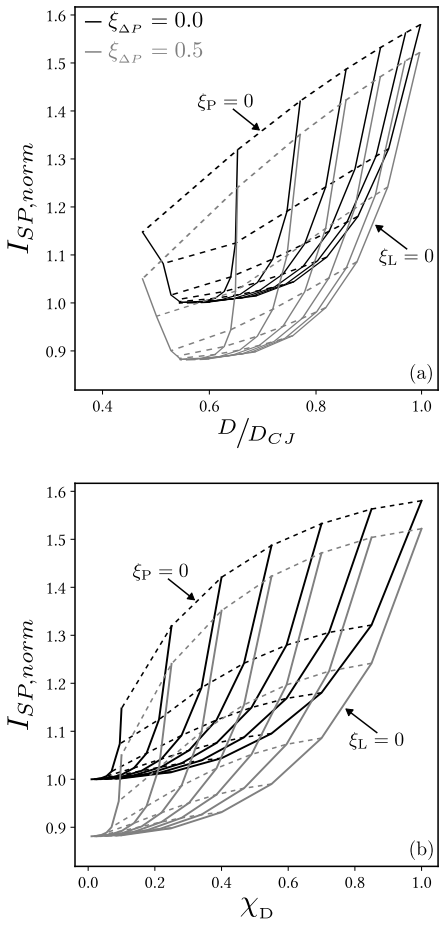

Figure 6.61: Normalized specific impulse versus normalized wave speed and detonation fraction. Lines separated by deflagration loss parameter increments of $0.15 \in [0, 0.9]$. Assuming ξ_{NC}, ξ_{CP}= 0.0.

The previous analysis of the State to State model focused only on three of the five loss parameters. Now, the examination of the non-commensal fraction, ξ_{NC}, and the commensal combustion pressure fraction, ξ_{CP}, is carried out on a manner similar to that shown in Figure 6.61. Figure 6.62 shows the contours of the two deflagration loss parameters, ξ_P and ξ_L, but now plotting the normalized specific impulse on the left axes and the estimated combustion efficiency, defined by Equation 6.70, on the bottom axes. Each subplot shows a different combination of loss parameters and their

effects on the combustion efficiency and specific impulse of the modeled cycle. Figure 6.62 (a) fixed the inlet pressure drop and commensal combustion pressure fractions to zero and shows two different magnitudes of the non-commensal fraction. Because $\xi_{\text{NC}} = 0$ means the combustion efficiency is 100% (see Equation 6.70), the figure uses the next step in the non-commensal fraction, $\xi_{\text{NC}} = 0.15$, as the starting point, this is shown with the black contours. The right most solid line represents the zero leaked fraction case, which also indicated a 100% combustion efficiency (see again Equation 6.70). Along this line, as the parasitic combustion fraction increase (moving from top to bottom) the combustion efficiency remains at 100%; however, the normalized specific impulse decreases. This is yet another example of the difficulties in relating the performance of the detonation wave to the performance of the cycle.

Next, the non-commensal fraction was increased to the maximum value used in the parametric sweep, $\xi_{\text{NC}} = 0.9$, shown by the gray contours. This increase in non-commensal fraction drastically reduces the estimated combustion efficiency. At this value of non-commensal fraction, high values of parasitic fraction or leaked fraction results in an estimated specific thrust less than that of the ideal deflagration cycle. The geometry of the RDE, specifically the length, will likely have an impact on the non-commensal fraction, and hence the combustion efficiency of the RDE. One of the promises of RDEs is the compact geometry; however, if the fuel is not able to be consumed before exiting the device, then the performance increases may not even achieve the same performance of a deflagration based combustor design with similar initial conditions. The exploration of these trade-offs is left for a future effort.

Figure 6.62 (b) takes the $\xi_{\text{NC}} = 0.9$ contour from Figure 6.62 (a), now shown in black, and applies the inlet pressure drop fraction of $\xi_{\Delta P} = 0.5$ to the model (shown in gray). This subplot also fixed the commensal combustion pressure fraction at zero. The addition of the inlet pressure drop did not change the combustion efficiency, as one would expect; however, it does reduce the specific impulse performance in a manner similar to the results shown in Figure 6.61. This once again echoes the fact that the performance of the RDE is also heavily dependent on the geometry, and specifically the inlet losses.[39, 104]

Finally, the same contour of $\xi_{\text{NC}} = 0.9$ from Figure 6.62 (a) is shown in Figure 6.62 (c) in black, but now the commensal combustion pressure fraction is increased from 0 to 0.9. This subplot also fixed the inlet pressure drop fraction to zero. Recall that the fraction in the commensal combustion pressure indicates the average pressure at which commensal combustion occurs, ranging from the post-expansion pressure, $P_{3.4}$, at $\xi_{\text{CP}} = 0$ to the ambient pressure, $\xi_{\text{CP}} = 1$. As the commensal combustion pressure

decreases (gray contours), performance decreases dramatically, mainly due to the fact that the thrust production occurs through an isentropic expansion from ④, and the lower the initial pressure at ④, the less expansion can occur. Regardless of the available energy at ④ if the exit pressure is too low, it is likely that the detonation cycle would not perform as well as the ideal deflagration, even without other loss parameters.

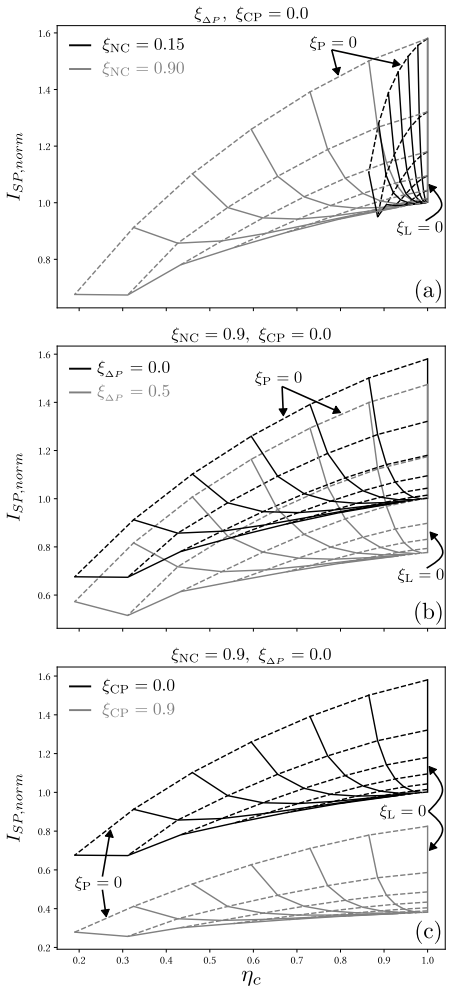

Figure 6.62: Normalized specific impulse versus combustion efficiency, η_c, with effects of each loss parameter isolated. Changes in non-commensal fraction, ξ_{NC}, at a fixed $\xi_{\Delta P}$, $\xi_{\mathrm{CP}} = 0$ (a). Changes in inlet pressure drop fraction, $\xi_{\Delta P}$, at a fixed $\xi_{\mathrm{NC}} = 0.9$, $\xi_{\mathrm{CP}} = 0$ (b). Changes in commensal pressure fraction, ξ_{CP}, at a fixed $\xi_{\Delta P} = 0$, $\xi_{\mathrm{NC}} = 0.9$ (c).

Figure 6.63 shows an example of the detrimental effects of the commensal combustion pressure fraction. This is shown by the normalized specific impulse versus the commensal combustion pressure, $P_{3.4}$, which also indicates P_4 based on the assump-

tion of no additional losses occurring after the equilibration process. As the commensal combustion pressure decreases, so does the specific impulse. Despite having no additional losses, at a commensal combustion fraction high enough, the performance of the RDE cycle are predicted to be similar to that of the ideal deflagration. It should be noted that in the current implementation of the model reducing the commensal combustion pressure does not effect the velocity profile through the channel. This means that the commensal combustion pressure fraction acts as a pressure loss term. In reality, the static pressure change for which this parameters is trying to capture would lead to a change in the velocity profile. However, not all the velocity changes that occur from the post-expansion state, (3.3), to the equilibrated post-commensal state, (3.4), are in the axial direction. In a RDE, there exist azimuthal velocity profiles with non-insignificant magnitudes.[121, 109] In this version of the State to State model, the commensal combustion fraction can be thought of as treating the expansion from (3.3) to (3.4) (due to the change in static pressure) as a purely azimuthal expansion process; therefore, it does not contribute to the axial velocity component, and hence the specific impulse. An improved model with proper treatment of the expansion process from (3.3) to (3.4) is left for future efforts.

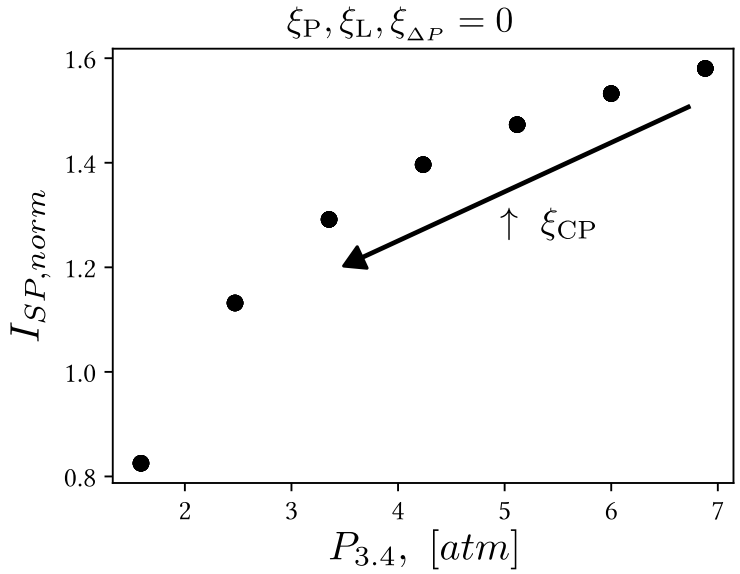

Figure 6.63: Normalized specific impulse versus commensal combustion pressure, $P_{3.4}$.

Figure 6.64 shows the normalized detonation work versus the modeled specific impulse, normalized by the ideal deflagration specific impulse. This plot shows fixed contours of ξ_{P} and ξ_{L}, while maintaining zero losses elsewhere. Much like Figure 6.12, this plot shows that as the performance of the RDE improves with lower loss fractions, so does the amount of energy required to maintain the wave frame of reference.

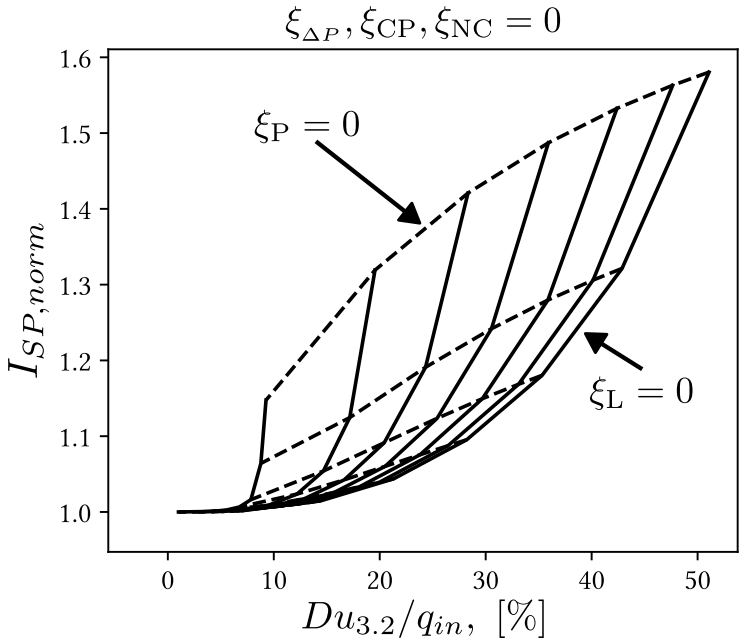

Figure 6.64: Normalized specific impulse versus normalized detonation work as a function of ξ_{P} and ξ_{L}. $\xi_{\Delta P}$, ξ_{CP}, $\xi_{\mathrm{NC}} = 0$.

In a final examination of the State to State model, the Sobol sensitivity indices were calculated for the five input loss parameters, with respect to the output specific impulse. These results are shown in Table 6.9 below. From the sensitivity parameters, it is evident that the most impactful parameter on specific impulse production is the commensal combustion pressure. This term, which acts as an average post-detonation combustion pressure, effectively reduces the pressure from which the gases can expand to product thrust. In reducing this post-detonation pressure, the thrust is decreased regardless of the energy input (combustion efficiency).

The next two most sensitive parameters are the parasitic combustion fraction and the inlet pressure drop fraction. Both of these parameters had a similar impact on

the thrust production from the cycle, where the inlet pressure drop fraction acts as a direct decrease on the pressure throughout the cycle. The inlet pressure drop has been seen to correlate directly with thrust production in RDEs, so this result comes as no surprise.[39, 122] The parasitic combustion fraction, similarly to the Deflagration Loss model, has a much more detrimental impact on thrust production than the leaked fuel fraction, where in the full cycle model the difference between the two are much more stark. This is due to the State to State model capturing what happened to the leaked fuel, post-detonation, where the Deflagration Loss model does not.

Parameter	S_T	ϵ_{S_T}	S_1	ϵ_{S_1}
$\xi_{\Delta P}$	0.25	0.02	0.25	0.04
ξ_P	0.29	0.03	0.22	0.06
ξ_L	0.12	0.02	0.06	0.03
ξ_{CP}	0.42	0.04	0.4	0.06
ξ_{NC}	0.01	0.00	0.00	0.01

Table 6.9: Sobol's Sensitivity Indices for the loss parameters in the State to State Model.

In general, the most important aspects for improved RDE performance appear to be increasing channel static pressure, reducing inlet pressure losses (through geometric or flow means) and reduce the parasitic combustion (provide the fuel is fully consumed elsewhere). One note of interest is the fact that the parasitic combustion fraction is the only loss mechanisms of the three that affects the performance of the wave. The other two are cycle specific losses that are less effected by the detonation wave performance, which provides another reason for framing RDE performance according to the desired use case, rather than to wave speed or detonation stability. For example, if detonation performance, in terms of wave speed, is improved with a much more restrictive inlet, then the cycle performance may decrease despite the improvement in the detonation wave.

6.8.2 Non-Zero Azimuthal Velocity Model

The following section discusses the results from the non-zero azimuthal velocity models described in Section 6.6.3. This will initially focus on the inlet region, but then move to performance impacts due to exit plane swirl.

6.8.2.1 Inlet Plane and Pre-Detonation

The following section will discuss the impacts of a non-zero incoming velocity on the potential performance of a detonation wave. First, an ideal detonation will be analyzed, similar to the example in Figure 6.45, to examine the best-case scenario. Then the same analysis will be applied to non-ideal detonation, accounting for parasitic deflagration and leaked fuel. Finally, analysis of the full non-zero swirl model from Algorithm 10 is applied across a parametric sweep of the loss parameters to determine the relationship between the expected performance of the RDE as a function of each parameter.

First, we examine the performance of an ideal detonation wave, defined from the pre-detonation state to the CJ plane, as a function of an arbitrarily specified azimuthal fill velocity. A stoichiometric, hydrogen-air detonation was used for this analysis with standard day initial temperature and pressure. Following the process discussed in the Section 6.6.3.1, Figure 6.65 shows the effects of a non-zero incoming velocity of the state ahead of the wave, and the CJ state, (3.2), behind the wave. This figure shows a change in the properties at the CJ plane as a function of incoming velocity, normalized by the zero incoming velocity cases, subscript i. First, the wave speed in the laboratory frame, D_l, is reduced in magnitude directly by the incoming velocity magnitude because the detonation wave speed is fixed in the wave reference frame. Similarly, the laboratory frame induced velocity, $u_{3.2}$, is also reduced directly by the incoming velocity magnitude.

The pressure ratio and temperature ratios were then compared. Equation 6.126 shows an example of the definition of these ratios, specifically the pressure ratio. These terms compare the laboratory frame total quantity ratio across the wave with the ideal case with no incoming velocity, subscript i. The total pressure and temperature ahead of the wave are assumed to be constant as the velocity is increased, allowing for the cancellation of the pre-detonation total quantities and also reducing the static quantities of the pre-detonation state. Increasing the incoming velocity reduces both static quantities in the CJ plane while also reducing the induced velocity, resulting in a decreased total quantity in the CJ plane relative to the case of zero incoming velocity.

$$\frac{PR}{PR_i} = \frac{\frac{P_{0,3.2}}{P_{0,3}}}{\left(\frac{P_{0,3.2}}{P_{0,3}}\right)_i} = \frac{P_{0,3.2}}{(P_{0,3.2})_i} \tag{6.126}$$

Figure 6.65 shows a slight drop-off in the total temperature achieved at the CJ condition, with respect to ideal. However, there is a much steeper drop-off in the total pressure. Without accounting for any other losses, a slight increase in the incoming flow velocity can have significant reductions in the total pressure gain through the detonation cycle. For example, the incoming velocity profile shown in Figure 6.39 would result in an approximately 25% decrease in the theoretical pressure gain of the cycle, just due to the incoming velocity alone.

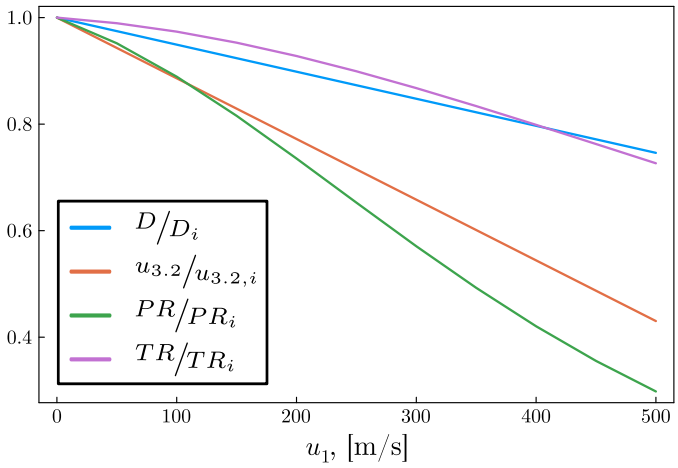

Figure 6.65: Decrement in ideal detonation properties at the Chapman-Jouguet plane with increasing incoming velocity. Hydrogen-air detonation at standard temperature and pressure, and $\phi = 1.0$.

With the effect of incoming velocity on the post-detonation state of an ideal detonation covered in the previous section, the focus is shifted to non-ideal detonation effects. First, the effects of parasitic deflagration on the same four parameters shown in Figure 6.65 are reproduced, along with a sweep at multiple values of parasitic fraction, ξ_P. These results are shown in Figure 6.66 where the condition of $\xi_P = 0.0$ has the same values as in Figure 6.65. The value through which the normalization is performed is the ideal detonation with no losses and no incoming azimuthal velocity. This analysis was also conducted using a stoichiometric hydrogen-air detonation at a standard day initial temperature and pressure. Similarly to the results from Figure 6.6, parasitic combustion reduces the wave speed by a slight margin, but has a much more drastic effect on the pressure ratio compared to ideal. A small initial fraction

of parasitic combustion (ξ_P= 0.1), even without incoming velocity, can reduce the total pressure ratio by 50%. As the parasitic fraction increases, the effects from the incoming velocity are diminished; however, the combination of parasitic combustion and incoming velocity can reduce the total pressure ratio by nearly 80% for small values of each ($\xi_P > 0.2$ & $u_1 \geq 100$ m/s). The effects on the total temperature ratio are similar to the cases of the total pressure ratio with increased parasitic combustion. This is due to the higher pre-detonation temperature because of the deflagration combustion.

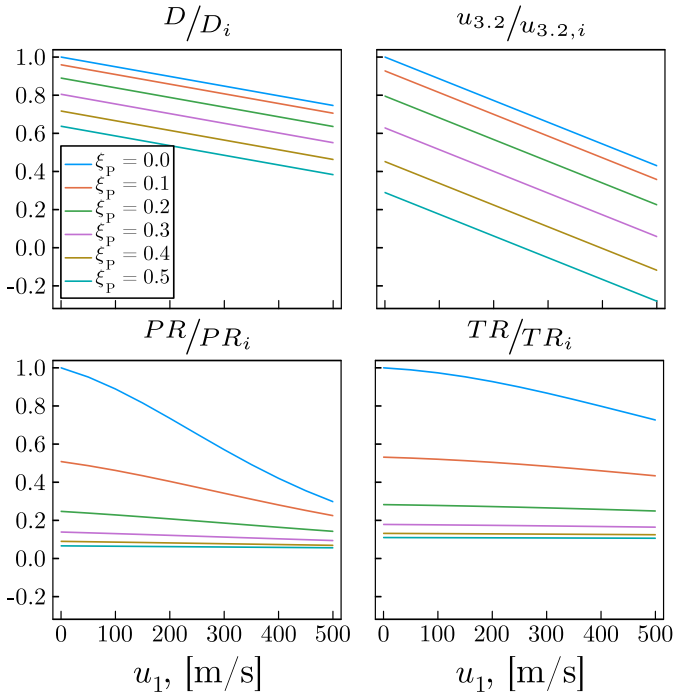

Figure 6.66: Decrement in ideal detonation properties at the CJ plane with increasing incoming velocity for a non-ideal detonation with parasitic combustion. Stoichiometric hydrogen-air detonation at standard temperature and pressure, and $\xi_L = 0$.

Next, the effects of leaked fuel fraction were examined along with changes in the incoming velocity. Figure 6.67 shows the changes in the four parameters of interest, with each trace representing an increase in leaked fuel fraction, ξ_L. From these results, it is clear that on its own, leaked fuel does not have the same drastic effects on

performance compared to parasitic combustion; however, the combination of leaked fuel and incoming velocity still have a significant effect on the performance. Even at moderate leaked fuel fractions and azimuthal velocities, the wave speed remains above 80% of the ideal CJ speed; however, the total pressure ratio is reduced by a much larger percentage. For example, a leaked fuel fraction of $\xi_P = 0.3$ and an azimuthal velocity of $u_1 = 250$ m/s resulted in a wave speed 80% of the CJ speed, but the total pressure ratio was only 55% of the ideal pressure ratio. This is a significant reduction in the "gain" across the detonation, despite what would be considered a relatively high wave speed.

Using the axial velocity solution from the expansion process, Equation 6.90, a specific thrust value can be calculated with respect to the input loss parameters using the model from Algorithm 10. The following analysis will parametrically examine the effects of each parameter on the expected performance of the detonation wave and the RDE. For reference, detonation performance included the laboratory wave speed, the total pressure at the CJ plane and the induced velocity at the CJ plane. Both of the last two terms directly effect the gain across the detonation.[36] The RDE performance metric of interest is the modeled specific thrust, which will be assumed to be the axial velocity, v, predicted at the end of the expansion region, and can be related to thrust by, $F = \dot{m}v$. The following results were constructed using same the geometry from Section 6.6.3, using a stoichiometric hydrogen-air reactant composition. Table 6.10 shows the measured values that were used as the geometric and flow property inputs for exercising the model. With this data, a parametric study was conducted for each loss parameter, with the deflagration loss parameters varying between [0.0-0.5], and the expansion angle varying between [0-90°].

$\dot{m}, [g/s]$	ϕ	$P_0, [atm]$	$P_{ch}, [atm]$	PR_i	$D_{\mathrm{CJ},i}, [m/s]$	$u_{3.2,i}, [m/s]$	$\mathrm{B_P}$
301	1.02	2.34	1.33	21.89	1986.3	882.6	0.27

Table 6.10: Run 106 Initial Conditions

Figure 6.68 shows contour plots of the effects of the deflagration loss parameters on the laboratory wave speed, total pressure at the CJ plane, and the induced velocity at the CJ plane, all relative to the ideal case with no losses. Also, the specific thrust, or axial velocity post-expansion, is shown as a marker of the thrust performance of the RDE given each loss parameter. The contours in Figure 6.68 are shown for a fixed expansion angle, $\alpha = 45°$. In general, both loss parameters reduce the wave speed and induced velocities in a similar manor; however, the parasitic combustion

appears to effect the pressure ratio and axial velocity to a greater degree. Specifically, a 10% parasitic deflagration loss results in a 50% reduction in the total pressure ratio, resulting in a significant loss in the "gain" across the wave. Closer examination of the induced velocity at the CJ plane shows negative values at high leaked fuel fraction and no parasitic deflagration. This is caused because the calculated induced azimuthal inlet fill velocity was greater than the induced velocity of the detonation wave at the CJ plane. Therefore, the laboratory frame induced velocity at the CJ plane is moving opposite of the wave direction.

Next, Figure 6.69 shows the same RDE performance predictions, now plotted against the parasitic deflagration fraction and the expansion angle, fixing the leaked fraction, $\xi_L = 0.0$. Because the expansion angle dictates the predicted azimuthal fill velocity, it has negative impacts on the detonation wave performance (wave speed, CJ total pressure, and CJ induced velocity) despite not directly affecting the detonation wave as modeled. Compared to Figure 6.68, it appears that the expansion angle has a similar effect on the detonation wave performance as the leaked fraction, ξ_L. The main difference is the predicted specific thrust values associated with the RDE performance. As expected, a higher expansion angle results in a higher specific thrust, due to the larger contribution to the axial direction in the expansion process from the CJ plane. The predicted maximum velocity, approximately 2800 m/s, assumed purely axial expansion from the CJ plane, with no other loss parameters. It is unlikely that this value could be achieved based on the azimuthal expansion process required discussed. For reference, with the same initial conditions, an ideal deflagration results in a specific thrust value of approximately 1200 m/s, when expanded to the same standard day atmospheric conditions. When comparing the modeled specific thrust to the results from the ideal deflagration, there exists a minimum expansion angle required to produce the same thrust, even without other losses. This is shown by the transition from the light blue contour to the gray, where at a given parasitic fraction any value of the expansion angle below the gray contour would produce less thrust than the ideal deflagration. As the parasitic fraction increases, this minimum expansion angle also increases.

Finally, Figure 6.70 shows the results for the leaked fuel fraction, ξ_L, and the expansion angle, α, with the parasitic fraction fixed, $\xi_P = 0.0$. The results echo the fact that the expansion angle and leaked fuel fraction have a similar impact on the detonation wave performance at lower leaked fuel fractions. At higher fractions, the leaked fuel becomes more dominant in terms of reducing performance. For the specific thrust, the effects of the leaked fuel have an impact similar to that of the parasitic

combustion fraction from Figure 6.69. This is due to the assumption of the model of a frozen chemistry expansion process in the expansion region. With this assumption, any leaked fuel is not combusted before exiting the RDE; therefore, the total heat release is reduced. Figure 6.69 was created with no leaked fuel fraction, so despite the fact that the parasitic deflagration reduces detonation performance more than leaked fuel, the parasitic deflagration does at least consume all of the fuel. A more detailed expansion model is required to better estimate the specific thrust with the leaked fuel fraction, allowing the leaked fuel to combust along the expansion process, which almost certainly occurs within the RDE in an experimental setting.[24, 22, 72, 4]

Using the experimental data discussed in Section 6.6.3, parameter estimation was conducted to predict deflagration losses and the expansion angle in the manor shown in Figure 6.50. Table 6.11 shows the initial conditions for each case, together with the measured values and their uncertainties. MCMC sampling was conducted using the Delayed Rejection Adaptive Metropolis (DRAM) implementation through the use of the *Paramonte* sampling package.[94] The sampling requested 2500 accepted points, initialized at a random location for each case. The input parameters for the model were treated as uniformly distributed with the following bounds: deflagration loss parameters $\xi_P, \xi_L \in [0, 1]$ and expansion angle $\alpha \in [0°, 90°]$.

Run	$\dot{m}, [g/s]$	$P_0, [atm]$	$P_{ch}, [atm]$	ϕ	$u_1, [m/s]$	$D_l, [m/s]$	PR
2848	148	1.43	1.17	0.56	-158 ± 26	1193 ± 220	1.62 ± 0.15
2849	148	1.47	1.21	0.80	-82 ± 40	1253 ± 150	1.78 ± 0.23

Table 6.11: Table of run conditions for cases with particle tracking.

After sampling the request amount of points, the *Paramonte* program systematically reduces the samples to remove auto-correlation between the points. The result of this process leaves a set of independent, identically distributed samples that follow the posterior distribution of the probability of the input parameters based on the given data. Table 6.12 shows the results of the sampling process, including the number of i.i.d samples for each case. Also included are the most probable input parameters, the model outputs for the most probable input parameters, and the percent error in the predicted outputs relative to the measured values. Initial inspection of these results shows that the most probable point for each case resulted in a large discrepancy between the model output and the measured values. For example, the error in the pressure ratio, PR, for each case was large, with the modeled output predicting a much higher pressure ratio. Table 6.12 also shows the same two cases,

but now the pressure ratio was not included in the sampling process. The discussion of the pressure ratio mismatch will be discussed later, but first, the focus will shift to the posterior distributions of these cases.

Run	Samples	ξ_{P}	ξ_{L}	α	$D_{\mathrm{l},pred}$	PR_{pred}	$u_{1,pred}$	$e_{D_{\mathrm{l}}}$	e_{PR}	e_{u_1}
2848	2497	0.58	0.01	64.6	1182	2.48	-156	0.9	53.1	1.3
2848*	2500	0.47	0.16	65.4	1194	-	-158	0.1	-	≈ 0
2849	2498	0.54	0.45	5.3	1254	2.09	-82	0.1	17.4	≈ 0
2849*	2499	0.46	0.52	26.9	1253	-	-82	≈ 0	-	≈ 0

Table 6.12: Sampling Most Probable Values and Errors Relative to Measured Quantities. * represents cases not matching pressure ratio, PR.

Figure 6.71 shows the sampling results for Run 2848, with the pressure ratio term included in the fitting process. Figure 6.71 (a) plots the posterior distributions of the input parameters, conditioned on the data, with the most probable value highlighted with a black point. This point is also summarized in Table 6.12. Due to the low measured wave speed and pressure ratio, the sampling process produces a posterior distribution with high parasitic combustion. These results are in line with the results from Section 6.4.1, where the pressure ratio is drastically reduced with even low fractions of parasitic deflagration ahead of the wave. Closer examination of the predicted expansion angle shows a large magnitude (relative to the azimuthal direction), indicating a smaller azimuthal expansion profile, which means that the majority of the expansion process is predicted to be in the axial direction. This large expansion angle is good in terms of the thrust prediction from this model.

Examining the post-predictive distributions of the samples in Figure 6.71 (b), it is clear that the predicted pressure ratio is significantly higher than the measured pressure ratio. It is unclear at the moment if the measured pressure ratio is accurately captured, as the location of the sensor, relative to the wave, is not known for this experimental run. The opposite holds for the laboratory frame wave speed and the induced azimuthal fill velocity. Both of these distribution match closely with the measured values, indicating that the model fit the data well for these two terms.

As mentioned in this section, the pressure ratio predicted by the most probable input parameters for both cases deviated significantly from the measured value. Note that the pressure ratio measurement assumed that the high-speed probe is measuring directly in the detonation wave. With the validity of this assumption now in question, a second effort was conducted sampling the same two cases, but now ignoring the

pressure ratio term as an output value in the fitting process. Now, the sampler fits the input parameters based on the wave speed, D_1, and the measured azimuthal velocity of the inlet, u_1, only. An example of these results are shown below in Figure 6.72 for run 2848.

Figure 6.72 (a) shows the posterior distributions of the loss parameters, where the distributions are highly biased compared to those shown in Figure 6.71 (a). Of particular interest are the posterior distributions of the deflagration loss parameters, where the most probable point for the conditional distributions are significantly different from the marginal distribution for each parameter. For example, the parasitic loss parameter, ξ_P, has a marginal distribution with a most probable point near 0.2, while the conditional distribution predicts a value of 0.47 as the most probable value. This result is likely due to the high probability density of the expansion angle, α, around the value of 65°.

In general, the sampling process without the pressure ratio term matched the measured laboratory wave speed and induced azimuthal velocity. This resulted in similar loss parameters, which can be seen in Table 6.12. Despite removing the pressure ratio from the fitting process, the sample results in Figure 6.72 (b) predict a nearly identical pressure ratio as in the case where the pressure ratio was included. It is suspected that these results indicate that the measured pressure ratio may be lower than the actual pressure ratio. More data is required to confirm the suspicion; however, with improved measurements of the pressure ratio across the wave, these results predict a pressure ratio that one might hope to measure based on the current implementation of the model. It should be noted that it is unlikely that the model is capturing all of the necessary processes to predict an accurate pressure ratio, but it does provide more evidence that the pressure ratio measurement may not be as accurate as one would hope. An accurate measurement of the pressure ratio is required to capture the "gain" across the detonation wave, and these results indicate that this value might be higher than what was measured, indicating that performance may not be as bad as the initial measurement would predict, at least according to the model methodology.

Using the results from the sampling process, Table 6.12, an estimated specific thrust can be calculated based on the most probable loss parameters. Table 6.13 shows the results of the predicted axial thrust, v_{pred}, compared to the specific thrust of an ideal deflagration, v_{defl}, starting at the same plenum conditions and expanding to standard day pressure. Run 2848, with and without the pressure ratio fitting, predicted higher specific thrust than an ideal deflagration. However, run 2849 had a

much worse performance than the ideal deflagration for both sampling cases. This was a result of the smaller expansion angle predicted for Run 2849, combined with the higher deflagration loss parameters.

Run	$v_{pred}, [m/s]$	$v_{defl}, [m/s]$	% Defl.
2848	677	668	1.3
2848*	748	668	12.1
2849	100	781	-87.3
2849*	328	781	-58.0

Table 6.13: Specific thrust results for Runs 2848 and 2849 based on most probable loss parameters from Table 6.12. *Represents fitting process without pressure ratio.

6.8.2.2 Exit Plane

This section will provide a brief discussion of the effects of the non-zero azimuthal velocity on the RDE performance, In this case, thrust will be used as a metric, which can also be normalized by the mass flow rate to give a specific thrust metric. The follow analysis examines the how a variation in the flow direction can change the thrust production due to a fraction of the flow not being aligned with the thrust producing direction.

We will assume that a post-combustion state can provide the enthalpy required to expand to a velocity of 1250 m/s. This perfectly expanded gas will then be subjected to a flow direction distribution of differing variance. See Figure 6.51 for an example of the flow direction distribution. Figure 6.73 shows the results from subjecting the ideally expanded flow to a flow angle distribution with a standard deviation of $\pm$ 20 degrees. The subplot (a) shows the axial velocity distribution, where subplot (b) shows the azimuthal velocity distribution which matches the normal distribution form provided by the flow angle distribution. This figure shows how a variation in the flow angle can reduce the expected axial velocity component, resulting in a direct loss in thrust performance.

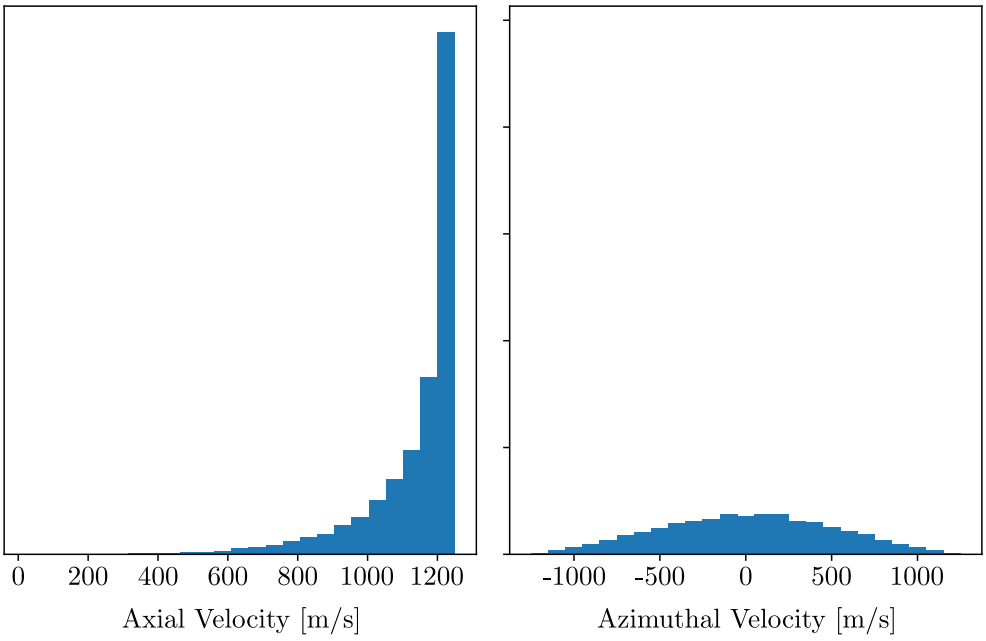

Figure 6.73: u and v Velocity Distributions with a 20 Degree Flow Angle Standard Deviation.

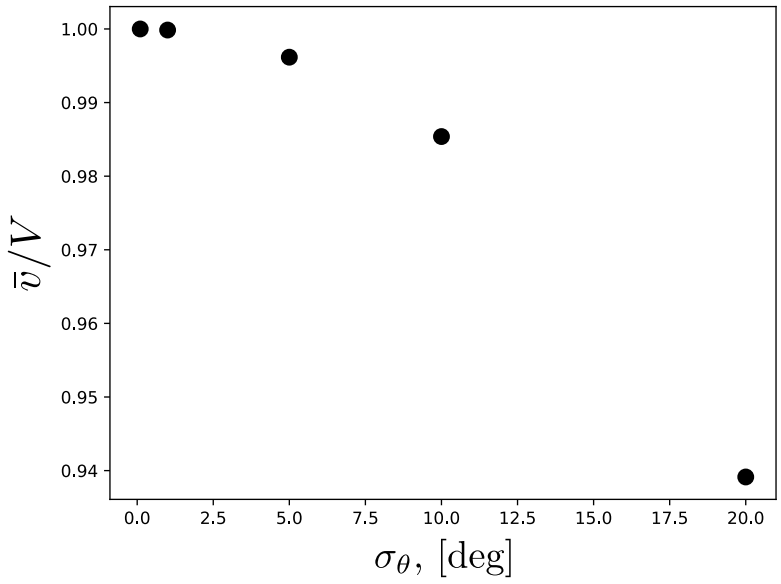

Figure 6.74: Normalized Axial Velocity versus Flow Angle Standard Deviation.

To extend this analysis, Figure 6.74 shows the average axial velocity, normalized by the ideal expansion velocity, V, as a function of the standard deviation in the flow angle. As expected, as the variance in the flow angle increases, so does the loss in the mean axial velocity. At the highest variance, the thrust losses are approaching 10% of the thrust from the perfectly axially expanded flow. Although this loss is not large in magnitude, the variance in the flow profile is something inherent to the operation of a RDE. This means that depending on the variation in the nozzle exit flow, a noticeable percentage of the expected performance is lost to azimuthal velocity, regardless of any other loss mechanism.

6.8.3 Blockage and Dynamic Inlet Model

The following section discusses the results from the parametric study of the dynamic inlet model. This section focuses only on an example conducted using air as both the forward and reverse-flowing gas; however, these results can be extended to the detonation model. We have already discussed that the effective area ratio, α, provides a similar measurement as the blockage fraction, BR, so we will only include the

blockage fraction in the following analysis, but understand the similarity between the two.

First, Figure 6.75 shows the entirety of the test points, plotting the fill-based blockage ratio, BR_{fill} as a function of the mass-based blockage fraction, B. The points are colored by the specified value of the blockage ratio defined by Bedick et al. BR.[102] From this figure, we can see that across nearly all cases, the fill-based blockage and the blockage fraction capture the same value. This result is likely due to this implementation of the inlet model, which predicts choked reverse, or forward, flow for the majority of the cycle.

Figure 6.76 shows a typical example of the inlet Mach profile from the dynamic inlet model, where the inlet profile is choked for nearly all of the injector area. Figure 6.77 shows a zoomed in view of the Mach profile, showing that there is a transition region of sub-critical flow. However, this region is so small relative to the full profile that its contributions to the overall mass flow rate are negligible.

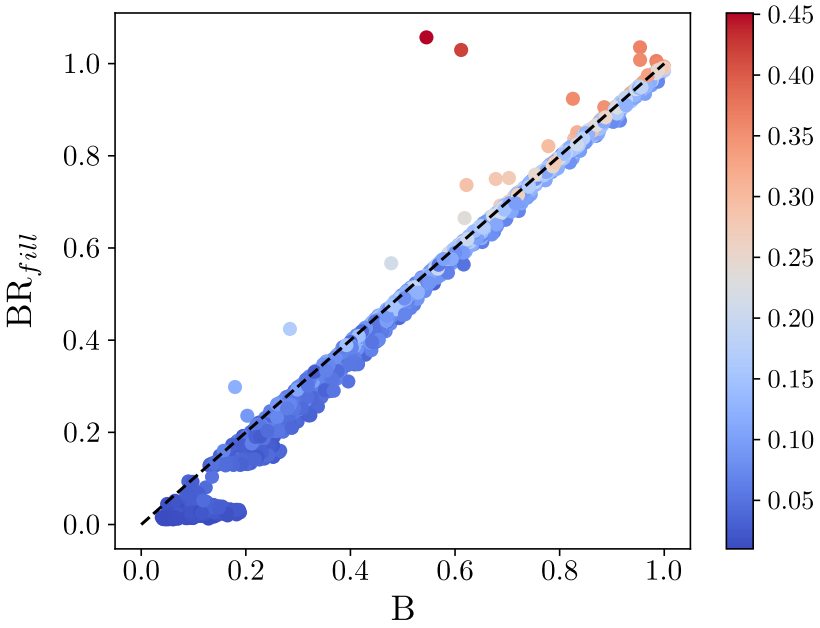

Figure 6.75: Blockage Fraction versus Fill Based Blockage: Air Examples

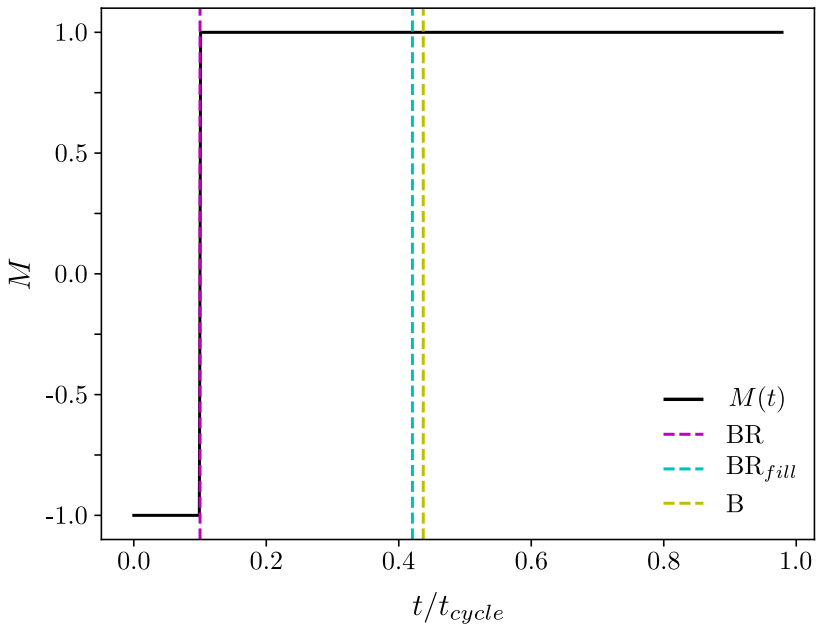

Figure 6.76: Mach Profile Typical of Dynamic Inlet Model: Full Profile

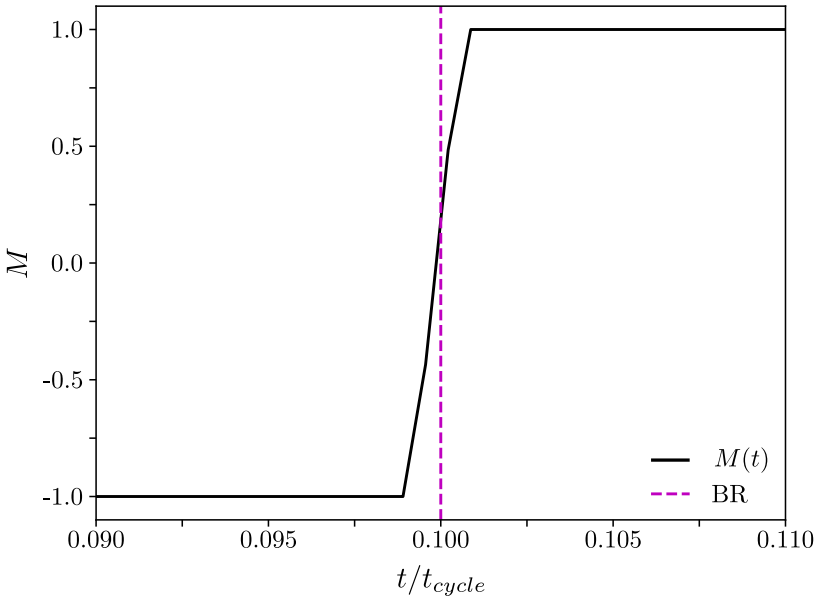

Figure 6.77: Mach Profile Typical of Dynamic Inlet Model: Zoomed on Un-choked Region

This result is interesting because it matches the blockage fraction, B, so well. As discussed by Feleo et al., the blockage fraction does not determine the inlet flow profile, so any arbitrary profile can match a given blockage value.[96] From these results, it appears that assuming a choked forward flowing region is not a poor assumption given the propensity for this result across the dynamic inlet model and the nearly identical values in the blockage fraction and fill-based blockage.

Finally, another situation of interest was discovered using the dynamic inlet model. This is best shown in Figure 6.78, where the maximum pressure is high relative to the plenum pressure (15x the channel pressure in this example), but the blockage ratio, BR, is low (5% in this example). Using the Bedick et al. definition of inlet blockage would describe the inlet as mostly forward flowing; however, this is not the case when examining the blockage fraction or the fill-based blockage. These terms show that over 30% of the inlet is blocked to the forward flow.

This example is representative of a RDE operating at a low mass flow rate condition, where the plenum and channel pressures are nearly matched. At this condition, with an ideal detonation, the detonation pressure ratio is over 13 times higher than the plenum pressure. At this condition, a significant amount of backflow is achieved

despite the small area of back-flowing gases. This backflow must be re-introduced through the injector, but the plenum-to-channel pressure ratio is low, leading to an extended delay in the re-fill process, eventually resulting in a large fraction of the inlet being blocked to forward flow. This re-injection process is important to capture with any RDE inlet model, and the dynamic inlet model discussed in this study provides this and matches well with other definitions of blockage.

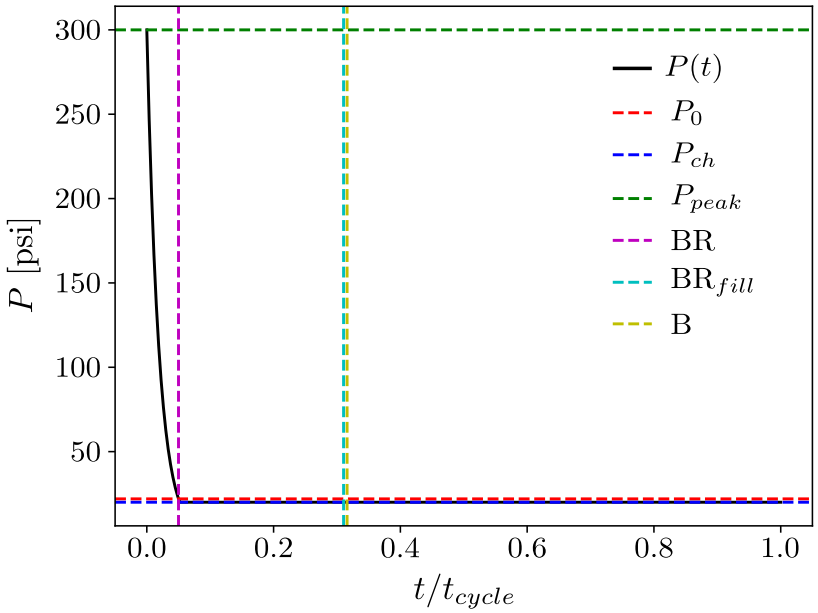

Figure 6.78: Example of High Backflow at Low Blockage Ratio

Inlet blockage is an extremely important metric when studying the operation and performance of the RDE device. The local pressure gain across the detonation wave provides a high-pressure region that directly affects the RDE injector. Depending on the overall bulk flow conditions, this high pressure zone leads to inlet blockage and significant backflow of post-detonation product gases. It is important to robustly model the inlet of the RDE and close coupling with the detonation wave in order to model the RDE more accurately as a whole system.

This study was dedicated to the study of loss mechanisms specific to detonation waves and then they were translated to losses to the RDE performance. We introduced these mechanisms, along with some definitions of detonation performance. These loss metrics included deflagration combustion based losses, specifically focusing on para-

sitic combustion occurring before the wave and fuel that leaks through the detonation before contributing to the detonation heat release. These results show a decrease in performance as each loss metric was increased, where the parasitic combustion had the more significant impact.

Next, a study was conducted to examine other non-ideal effects impacting the detonation wave directly. These included area changes between the pre-detonation state and the CJ plane, which simulate lateral relief of the wave, momentum losses through effects like friction, and heat transfer out of the detonation wave to a given boundary conditions. In general, each metric produced a decrease in the detonation wave performance; however, the area ratio did not produce a significant change in the wave speed using a non-ideal CJ solution technique. Further examination of a non-ideal ZND solver showed that the area change would indeed produce a change in the wave speed but is only captured using the ZND solver with finite-rate chemistry.

The non-ideal CJ solver was then used in concert with the deflagration loss model to show the overall sensitivity of the detonation performance to each loss metric. Across the board, it appears that the parasitic combustion fraction produced the largest impacts on the performance of the detonation wave, while other loss metrics provided moderate impacts across different performance metrics.

This study provided a discussion on the classification of a weak detonation wave versus a similarly performing deflagrative combustion wave. With certain combinations of losses, the detonation wave will produce a performance output similar to that in a deflagration wave, but it will still exhibit the defining characteristics of a detonation. This result makes the determination of detonation combustion more difficult. Across this chapter, the performance of a non-ideal detonation wave was studied; however, additional modeling and analysis are required to determine if the loss in detonation performance has an impact on the performance of a device relying on detonation combustion. The results of these loss mechanisms at the detonation wave will inevitably affect the system-level performance and associated loss mechanisms.

This study also examined different loss mechanisms and processes specific to the RDE device. This was done through the study of multiple models, either dedicated to a certain aspect of RDE operation, or as a state-based cycle model. The state-to-state model presented in this work allowed for the variation in detonation performance, with the inclusion of losses seen within RDE devices. From this simple model, we could observe the scaling for a specific impulse metric as different losses are included. From this model, we have seen that the specific impulse for a RDE can provide an improvement over a conventional deflagration-based system, even with losses within

the detonation wave. However, when we include RDE processes, specifically the inlet pressure ratio, we find that the RDE may be short of an equivalent deflagrative system.

One particular combination of losses that is detrimental to the performance of RDEs is inlet pressure loss combined with parasitic combustion. As the fluid moves through the RDE inlet, the static channel to the plenum total pressure must drop by some fraction. This means that the pre-detonation state is occurring at a static pressure lower than that being supplied by the plenum. As the stiffness of the inlet increases, so does the inlet pressure drop. When parasitic burning occurs at this reduced pressure, it provides a compounding effect that increases overall entropy production, leading to a reduction in performance.

We have also found that the stiffness of the inlet is correlated with the parasitic combustion fraction. This is because as the inlet becomes less stiff, i.e., lower pressure drop, the detonation wave provides an increased impact on the inlet. This allows for increased inlet blockage and the potential for backward-flowing product gases. These product gases increase the temperature, and hence the speed of sound, of the pre-detonation state at best. This would result in a lower Mach number for the shock wave that leads to the detonation, reducing the overall detonation performance in terms of wave speed and pressure rate. At worst, the backward-flowing products will increase the likelihood of parasitic combustion ahead of the wave, resulting in reductions in performance.

The issue becomes the trade-space between inlet losses and detonation performance. A high-performance detonation wave, especially in terms of pressure ratio, will undoubtedly have a more significant impact on the inlet. Inlet stiffness could be increased through a reduction in inlet flow area; however, this will result in inlet losses that also reduce performance. Because of this coupling between the detonation and the inlet, a situation may arise where one would seek to reduce the performance of the detonation in order to preserve the performance of the inlet. As both experiment and modeling have shown, the inlet performance provides a nearly linear scaling factor on the pressure gain performance of the RDE.

Inlet and detonation performance trade-offs are not the only issues discovered in this section. We must also consider the effects of the non-zero azimuthal velocity profile that the detonation wave necessarily excites. Essentially, the detonation wave, being an unsteady phenomenon, progressing circumferentially around the RDE channel induces a wide variation in the azimuthal velocity profile across the RDE. This directly reduces the RDE's ability to convert the fuel gain across the detonation wave

into device-level performance, such as thrust.

Finally, to maintain the detonation progression, some fraction of the energy gained across the detonation wave is lost to the system. This is inherent to detonation waves and, along with the RDE geometric configuration, the cause of the non-zero azimuthal velocity perturbations. This term also scales with the detonation performance, where the higher the wave speed, the larger the detonation work requirement. This raised the question as to the usefulness of a detonation-based system, and the detonation itself is producing the adverse effects on the inlet and with the non-zero azimuthal velocity, while also requiring an energy return path proportional to its performance just to sustain itself.

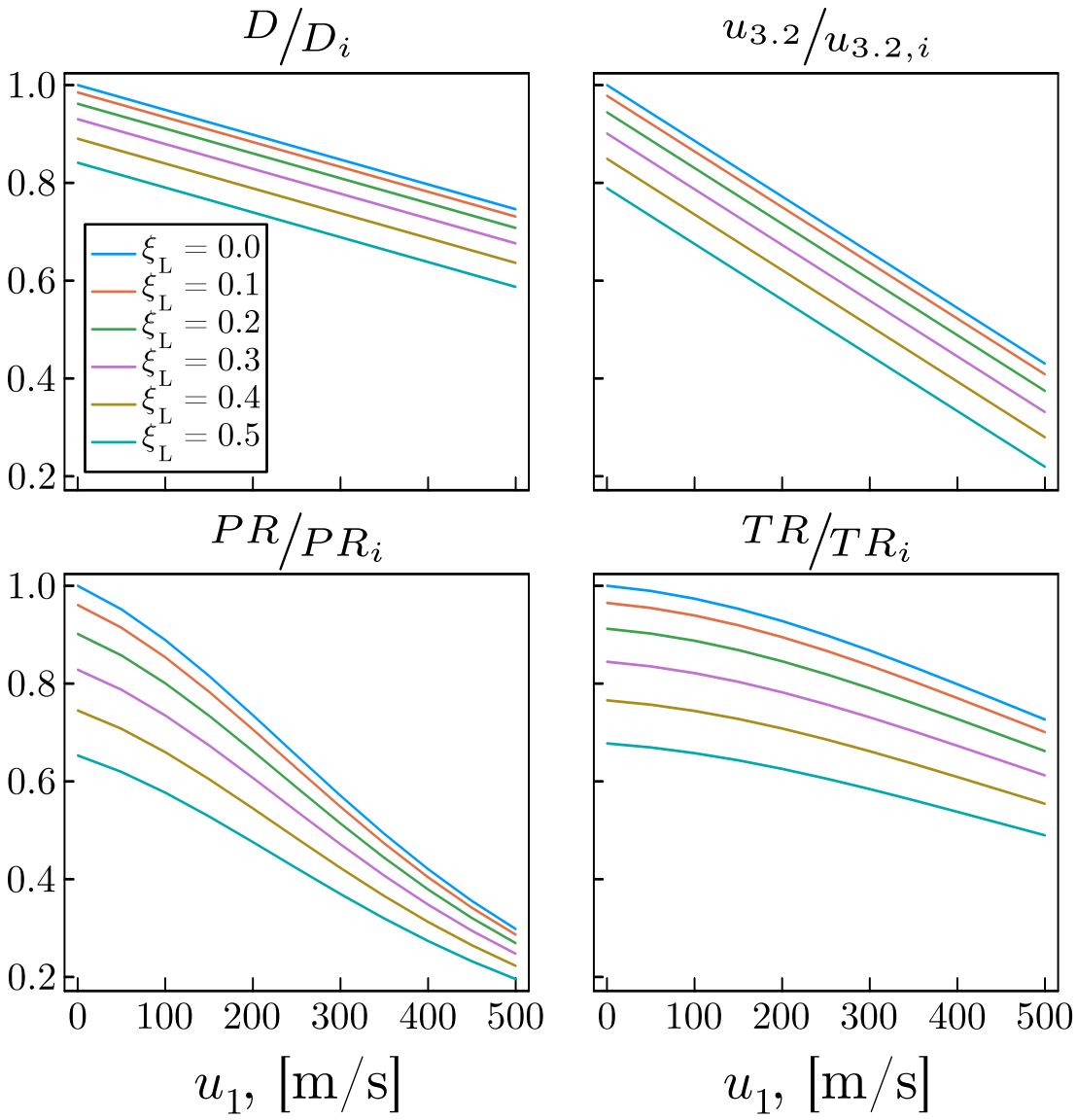

Figure 6.67: Decrement in ideal detonation properties at the CJ plane with increasing incoming velocity for a non-ideal detonation with leaked fuel. Stoichiometric hydrogen-air detonation at standard temperature and pressure, and $\xi_P = 0$.

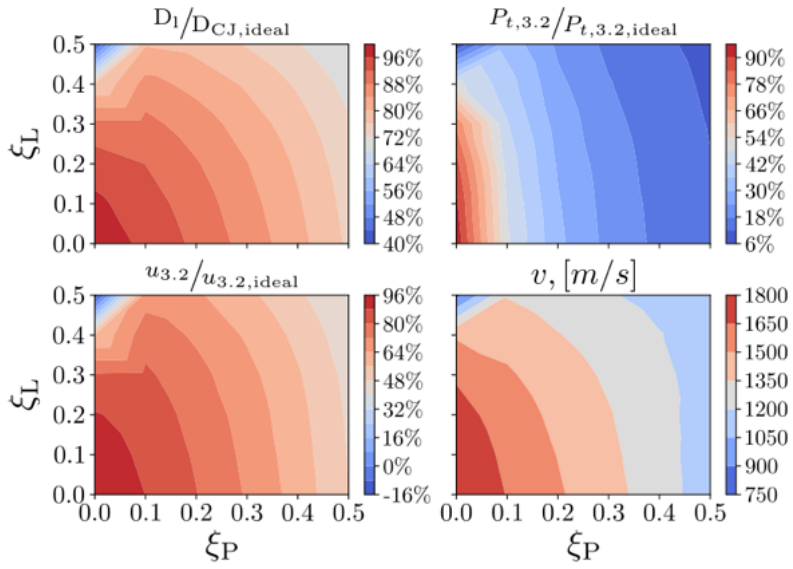

Figure 6.68: Modeled performance contours versus deflagration loss parameters. Fixed expansion angle, $\alpha = 45°$

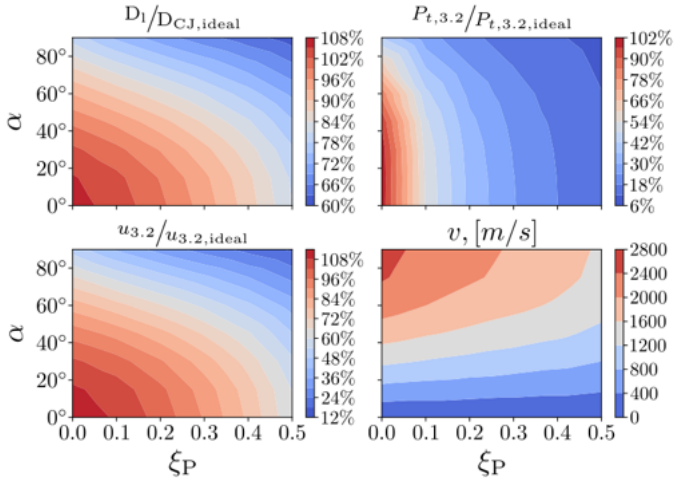

Figure 6.69: Modeled performance contours versus parasitic deflagration fraction and expansion angle. Fixed leaked fuel fraction, $\xi_L = 0.0$

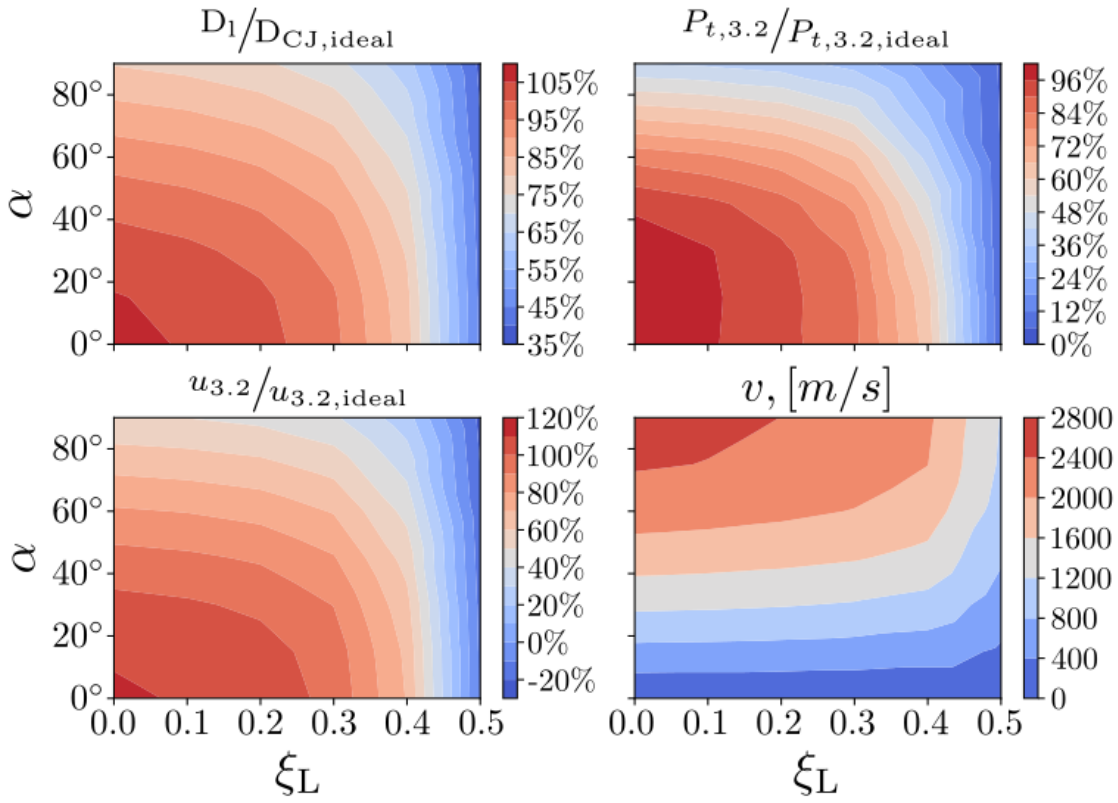

Figure 6.70: Modeled performance contours versus leaked fuel fraction and expansion angle. Fixed parasitic deflagration fraction, $\xi_P = 0.0$

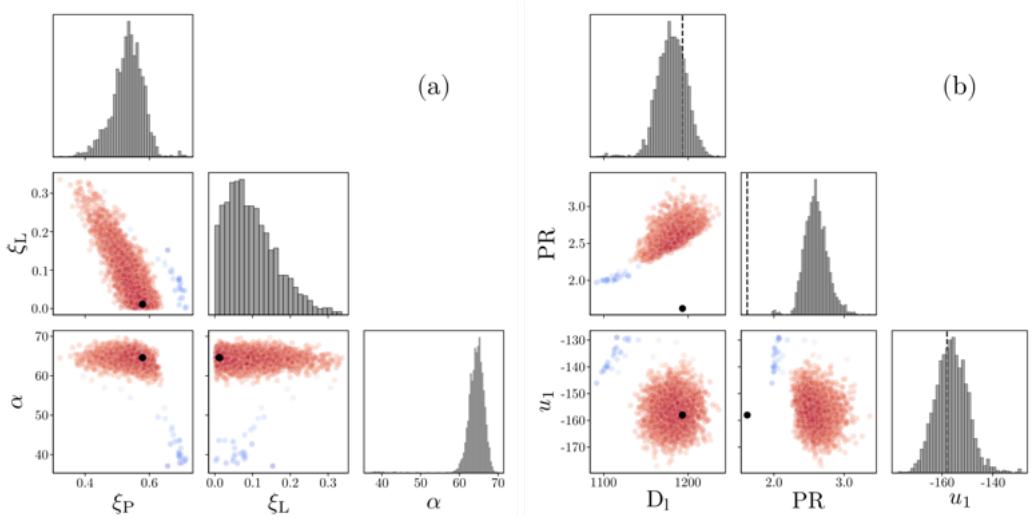

Figure 6.71: Run 2848 Sampler Results. Posterior distribution of loss parameters (a), post-predictive distribution of model outputs (b).

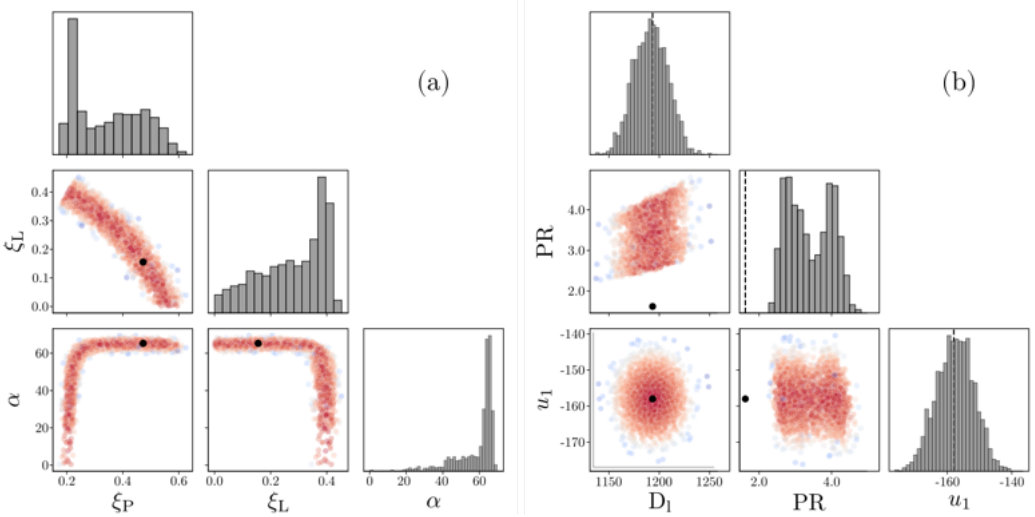

Figure 6.72: Run 2848 Sampler Results ignoring the pressure ratio measurement. Posterior distribution of loss parameters (a), post-predictive distribution of model outputs (b).

Chapter 7

RDE Simulations for Emission Prediction

7.1 Motivation

With stricter emissions regulations being adopted for engines in all such applications, especially power generation, emissions behavior should be addressed in RDEs if they are to become viable alternatives to conventional gas turbine engines. The type and intensity of emissions produced depend on the type of fuel and oxidizer used. Although RDEs have been studied in multiple fuel-oxidizer configurations, including methane-oxygen [123, 124] and ethylene-air [125, 126], a significant amount of work has been done with hydrogen-air configurations [127, 101, 128, 129]. The pursuit of using hydrogen as a fuel stems from its abundance in the environment, its storage capabilities, and its ability to produce 2.75 times more energy than hydrocarbon fuels [130]. Additionally, the use of pure hydrogen over hydrocarbon fuels eliminates the production of carbon emissions. However, if hydrogen is used with air as an oxidizer, as is the case in power generation and air-breathing propulsion applications, the oxidation of nitrogen occurs during the combustion process, and emissions of nitrogen oxides are produced, which are commonly referred to as NO_x. Despite the extensive research performed on NO_x emissions in gas turbine engines [131, 132, 133], a far lesser amount of research has focused on NO_x emissions in RDEs. Given the stark differences between gas turbines and RDEs in multiple regards, further study of NO_x emissions behavior in RDEs may prove beneficial for RDE development.

The flow structure within an RDE is significantly different from that in a conven-

tional engine, as shock waves and supersonic flow are present within the combustor. The presence of such waves generates large fluctuations in temperature and pressure, which could in turn impact net emissions given the sensitivity of NO_x to temperature. Previous numerical work [134] found that even though such conditions exist in RDEs and could possibly contribute to higher emissions, NO_x levels were not significantly high, and residence times at high temperatures remained short. However, this study used a 2-D idealized RDE setup and did not take into account non-idealities such as local equivalence ratio variability and parasitic combustion commonly seen in practical RDEs [135, 136, 137]. These non-idealities, which are incurred from necessarily separating injection of fuel and oxidizer to avoid flashback of detonations into the manifolds [138, 139], highlight the influence the injection process has in determining RDE flow structure and operation [140]. Therefore, NO_x emissions analysis should be performed in practical RDE systems if the consideration of non-idealities and the non-premixed flow structure is desired.

More recent work has focused on NO_x emissions in practical RDE systems from both experimental and numerical perspectives. Experiments from [62] provided an initial step for looking at NO_x emissions under a range of equivalence ratios at constant air mass flow rate, showing that measured NO_x emissions remained low across all conditions. This finding is supportive of the hypothesis from [141] that NO_x emissions should generally be lower in RDEs, as compared to conventional engines, due to the shorter residence times at high temperatures. Even though this work has provided some initial conclusions regarding NO_x behavior in RDEs, it does not provide detailed flow structures within practical RDEs along with resulting NO_x formation patterns that are only obtainable through the use of high-fidelity simulations.

The results presented in this section seek to remedy the issue of scarcity in NO_x emissions research for RDEs by providing a comprehensive view of the flowfield in practical RDE systems, as well as how the modification of operating parameters ultimately affect this flowfield and resulting NO_x formation. Understanding emissions behavior in RDEs can prove useful for specific applications, such as power generation where RDEs can potentially replace conventional lean-premixed swirl combustors, but it also provides greater insight into the entire flowfield within an RDE through the inherent link between NO_x and temperature. Given that adiabatic flame temperature, a fundamental parameter in the definition of efficiency and thermodynamic behavior in a combustion process, has been shown to be directly correlated to NO_x emissions across a range of equivalence ratios [142], and that NO_x production in general is highly sensitive to local temperature, the observed behavior of NO_x emissions in

RDEs can reveal significant information about the spatial and temporal variations in thermochemical composition causing such behavior. As such, NO_x formation can be viewed as not only just a marker of emissions levels in RDEs for compliance with engine regulations, but also as a marker for RDE system behavior in general. Thus, the goal of the work presented in this section is to build upon previous simulations of practical RDEs with the simulation of NO_x chemistry in RDEs, which will ultimately provide a more firm understanding of NO_x formation itself along with RDE flow behavior on the whole.

7.2 Capturing NO_x Chemistry in Simulations

7.2.1 Review of NO_x Formation Mechanisms

To first inform the decision on selecting a simple yet accurate NO_x chemistry mechanism for RDE simulations, the basic components of NO_x formation must be explored. Three main mechanisms through which NO_x is produced during combustion are thermal NO_x, prompt NO_x, and fuel NO_x.

Thermal NO_x is arguably the most important type as it's the most prominent source of overall NO_x production. This type of NO_x formation stems from the inherent oxidation of nitrogen in air and is also referred to as the Zeldovich mechanism [143]. It is directly proportional to temperature, meaning that higher temperatures produce higher amounts of thermal NO_x. In pure hydrogen-air combustion, which is the focus of this work for RDEs, this thermal mechanism becomes dominant due to increased combustion temperatures as compared to other fuel types [144]. The strong temperature dependence is also corroborated by the nitrogen oxidation reactions having a high activation energy [145]. Since RDEs involve moving zones of high pressure and temperature (detonation waves) theory would suggest that thermal NO_x would be the most prevalent near these waves and the least prevalent in other regions of low pressure and temperature.

Prompt NO_x has a minor role in the overall formation of NO_x, with its percentage of total NO_x produced being less than 5% [146]. This type of NO_x production arises from reactions of airborne nitrogen with hydrocarbon fragments [147]. Considering its small effect on overall NO_x production as well as the absence of hydrocarbon fragments in pure hydrogen-air combustion simulations, prompt NO_x can be neglected as an important path for NO_x formation.

Fuel NO_x is the final main mechanism of NO_x formation, but this can also be neglected in the current work as it pertains to formation of NO_x through nitrogen contained within certain fuel sources such as heavy oils or coal [147]. Since pure hydrogen obviously contains no nitrogen in it, fuel NO_x is non-existent in the present study on hydrogen-air combustion in RDEs.

7.2.2 NO_x Mechanism Selection Process

Reasoning for choosing a specific NO_x chemistry mechanism is now described based on previously described NO_x formation pathways. A common chemistry mechanism used for hydrogen-air RDE simulations within the Advanced Propulsion Concepts Laboratory (APCL) is the H_2-O_2 mechanism from [148]. This mechanism constitutes 9 species and 19 reactions, making it an adequately lean mechanism to use in RDE simulations while still maintaining proper accuracy in replicating hydrogen fuel combustion. This mechanism has also been validated within APCL for use in RDEs [140]. Since the present goal is to select a hydrogen-air mechanism that accounts for NO_x production while still maintaining simplicity, in a similar fashion to the mechanism from [148], some key factors concerning the methods through which NO_x is formed must be considered.

First and foremost, the main pathway through which NO_x production is to originate was selected to be thermal NO_x with prompt NO_x and fuel NO_x neglected. The rationale for such a decision is based on the large impact that thermal NO_x has on the overall production of NO_x over the other two types. In addition, the highly dependent nature of NO_x formation on temperature makes thermal NO_x an even more crucial pathway to consider in RDEs where high pressure, high temperature detonation waves are present. Also, as was previously stated, the absence of hydrocarbon fragments and fuel-bound nitrogen in pure hydrogen combustion render prompt and fuel NO_x non-existent.

As [145] suggests there are two more main paths, in addition to thermal NO_x, through which NO_x can be formed in pure hydrogen-air combustion in particular. These two paths are the N_2O path and the NNH path. According to [147], however, the "greenhouse" gas N_2O has a negligent effect on overall NO_x production when high temperatures are present during the combustion process. Additionally, the NNH route has proved to be "a very minor route to NO in most combustion systems" [149].

The consideration of all these pathways to NO_x formation ultimately led to the selection of the Jachimowski mechanism [150] for use in this work. This 13 species, 33

reaction mechanism is for H_2-Air combustion with an extended Zeldovich mechanism added for thermal NO_x production considerations. It was specifically constructed for scramjet combustor applications and has been validated against experimental ignition delay and burning velocity data. The fact that this mechanism was designed for high Mach flows increases confidence in using it in RDE simulations where shock waves are present. Furthermore, the simplicity of the mechanism in only adding 4 species and 14 reactions more than the mechanism from [148] that is commonly used for H_2-Air combustion in RDEs within APCL makes it the optimal size for large-scale RDE simulations including NO_x formation while still maintaining computational speed.

After initial validation and testing with this mechanism it was found that it performed as expected, with only a few minor species profile issues present. A small modification to the mechanism from Wilson and MacCormack was adopted and tests were performed again with much better results in certain cases. This modified mechanism was ultimately the one used for the present work. A more detailed explanation of this testing and validation is provided in the subsequent sections of this section.

7.3 Verification of OpenFOAM Solver for Ignition Delay Calculations

To validate the chosen NO_x mechanism for use in 3-D RDE simulations, a suite of tests were performed to confirm metrics such as ignition delay, species evolution, NO_x levels, and wave speed in simplified configurations. The first major step in this process involved the validation of ignition delay times, since ignition delay largely determines the entire combustion process of a fuel mixture [152]. To ensure this validation process could be completed properly, the UMReactingFlow OpenFOAM solver first had to be verified for accuracy purposes. The verification process was necessary to confirm that the UMReactingFlow solver was accurately providing ignition delay times before this metric could be used to validate the NO_x mechanism in particular.

The GRI 1.2 [153] and GRI 2.11 [154] mechanisms were used to verify ignition delay curves for H_2-O_2 and CH_4-O_2 mixtures, respectively. Details of the mixtures and test conditions are shown in Tab. 7.1. The ignition delay data for the H_2-O_2 mixture, modeled by the GRI 1.2 mechanism, is shown in Fig. 7.1. The plots show excellent qualitative agreement between the OpenFOAM solver, the GRI test data, and corresponding experimental data from [155] for both initial pressures tested. When viewing the corresponding quantitative data from Tab. 7.1, it is seen that the

results show good agreement here as well, with root mean squared (RMS) errors less than 4% for the 1 atm case and less than 8% for the 2 atm case.

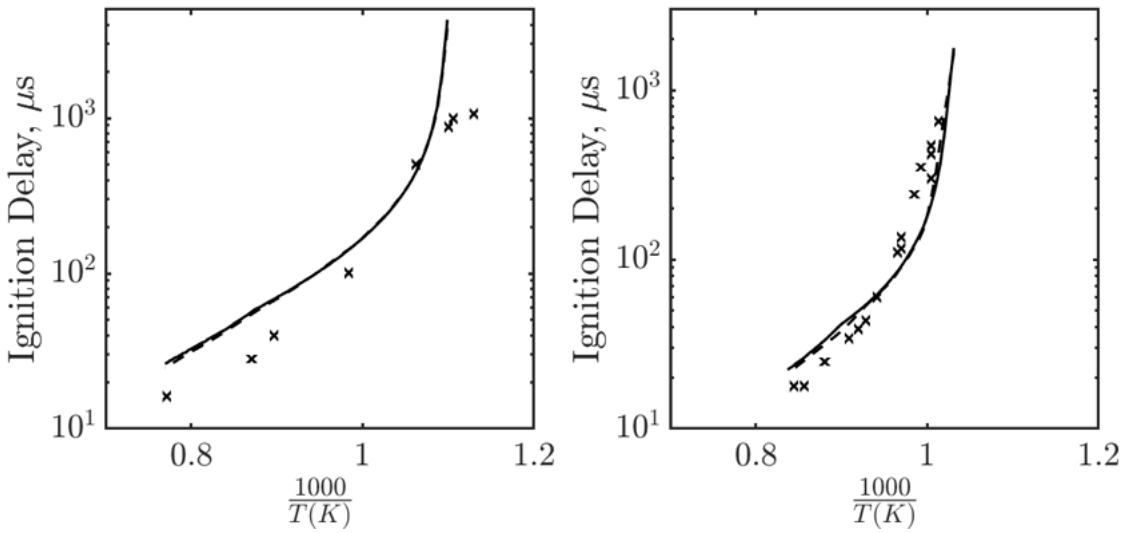

Figure 7.1: Ignition delay curves using GRI 1.2 and H_2-O_2 conditions defined in Tab. 7.1, at p = 1 atm (left) and p = 2 atm (right). OpenFOAM data is defined by solid lines, GRI data by dashed lines, and experimental data from [155] by (x).

In addition to the GRI 1.2 test, a CH_4-O_2 mixture was also tested using the GRI 2.11 mechanism, and ignition delay results are plotted in Fig. 7.2. In a similar manner to the H_2-O_2 mixture, the results here are in excellent agreement both qualitatively and quantitatively. Ignition delay values trend correctly along with GRI test data for a range of temperatures, and match relatively well with the experimental data from [156]. RMS errors are less than 8% for the 10.95 atm case tested, as shown in Tab. 7.1.

Overall, results showed good agreement between all cases and mechanisms tested, thus confirming the accuracy at which ignition delay times were being reported by the UMReactingFlow OpenFOAM solver. These results allowed for the continuation of validation procedures for the selected NO_x mechanism wherein ignition delay is used as a key metric for comparison.

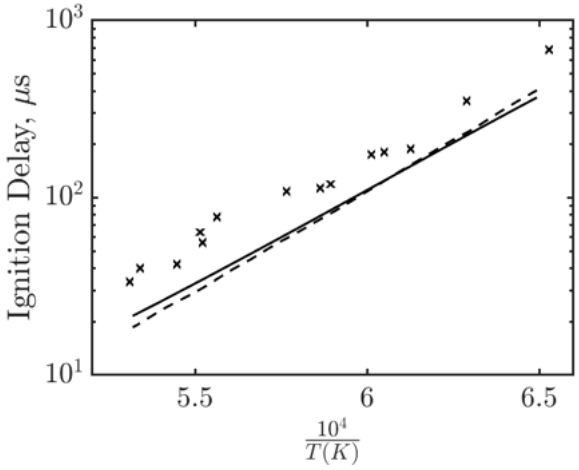

Figure 7.2: Ignition delay curves using GRI 2.11 and CH_4-O_2 conditions defined in Tab. 7.1, at p = 10.95 atm. OpenFOAM data is defined by solid lines, GRI data by dashed lines, and experimental data from [156] by (x).

Mechanism	Mixture	Initial Pressure (atm)	Mean % Error	RMS % Error
GRI 1.2	Stoichiometric H_2-Air	1	2.64	3.43
		2	5.65	7.56
GRI 2.11	3.5% CH_4 7% O_2 89.5% Ar	10.95	6.51	7.91

Table 7.1: Mechanism and mixture conditions from which the OpenFOAM solver is verified against using ignition delay curves, along with percentage errors in ignition delay between OpenFOAM and reference GRI data.

7.4 Validation of NO_x Chemical Mechanism

7.4.1 O-D Studies

For validation of the Jachimowski NO_x mechanism, three prior studies were used to compare ignition delay times against for H_2-O_2 mixtures. These studies, namely [157], [158], and [159], essentially used the Jachimowski mechanism for their own validation procedures of chemistry mechanisms. Each of these studies used a different method for calculating ignition delay time, which was taken into account when running the validation tests. Fureby did not provide the details of the method, whereas Gerlinger et al. used the maximum rate of temperature change method, and Kumar et al.

used the half consumption of hydrogen method. As such, the same methods used by Gerlinger et al. and Kumar et al. were employed in the corresponding validation cases to allow for direct comparisons. In addition, the maximum rate of pressure change method was used for comparisons to Fureby to be consistent with previous experimental results from [155].

Figure 7.3 shows the initial ignition delay validation results for the Jachimowski mechanism. From the data it can be seen that the results from [157] and [159] show excellent agreement across the entire curve of ignition delay. This finding is corroborated by the quantitative data shown in Tab. 7.2, which shows RMS percentage errors less than 19% overall between the mechanism running in the UMReactingFlow solver versus the other datasets. Greater deviation is seen in for the datasets from [158], but this is due to the fact that [158] uses a slightly modified version of the original Jachimowski mechanism from [150]. The fact that a modification was made to the original Jachimowski mechanism, which is described in [151], brought into question the validity of the original mechanism despite the good agreement seen in the initial results.

To further investigate the discrepancy between the original and modified Jachimowski mechanisms, species profiles were calculated in a 0-D reactor configuration similar to the one used for the ignition delay studies. Figure 7.4 shows species profile information for a range of cases with various mixture compositions, as taken from [160], along with data directly from [160] for comparison. These plots clearly show a mismatch in the H_2O and OH species profiles between the original mechanism and the reference data. Through testing it was determined that thermodynamic data was not playing a role in this anomaly, so the mismatch between profiles had to stem from either the reactions used within the mechanism itself or the rate coefficients of the reactions. When comparing the data from [160] to that which was produced with the modified Jachimowski mechanism from [151], much better agreement was seen in the initial profiles for the H_2O and OH species. This "modification" to the original mechanism simply removed one reaction, modified one reaction, and changed two rate coefficients (one of them being from the single modified reaction), all while keeping the same number of species and the majority of the formation pathways intact. In fact, all changes came from the H_2-O_2 subset of the mechanism, whereas no NO_x reactions were modified, and the single removed reaction, which pertained to OH radical production, was not present in the H_2-O_2 mechanism from [148] that is used elsewhere in this report. [161] provides further information regarding the justification of these changes made by [151]. As shown by Fig. 7.4, the slight modifications to

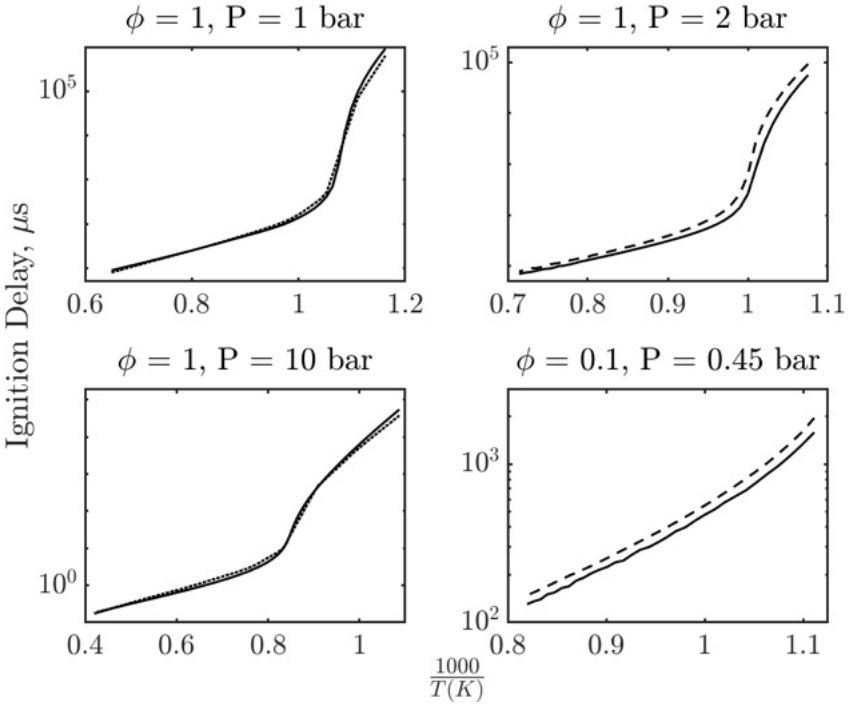

Figure 7.3: Ignition delay curves using multiple initial conditions with an H_2-O_2 mixture and the original Jachimowski mechanism from [150]. OpenFOAM data using the original mechanism is defined by solid lines, data from [157] (top left) and [159] (bottom left) using the original mechanism by dotted lines, and data from [158] using the modified mechanism by dashed lines.

the mechanism fix the species profile mismatches, and this translates to lowering the RMS error against NO species data from [160], bringing it from 53% to 43%.

In light of this finding in fixing species profile mismatches, the modified Jachimowski mechanism of [151] was tested for the range of ignition delay studies previously shown in Fig. 7.3. The ignition delay results with the modified Jachimowski mechanism are shown in Fig. 7.5, with the new iteration of the Jachimowski mechanism performing similarly to the original, as expected. When viewing the quantitative differences between the mechanism and the reference data, as shown in Tab. 7.2, the expected similarity to results from [158] are apparent, as the comparisons are for the same modified mechanism now. Greater deviation is now seen between data from

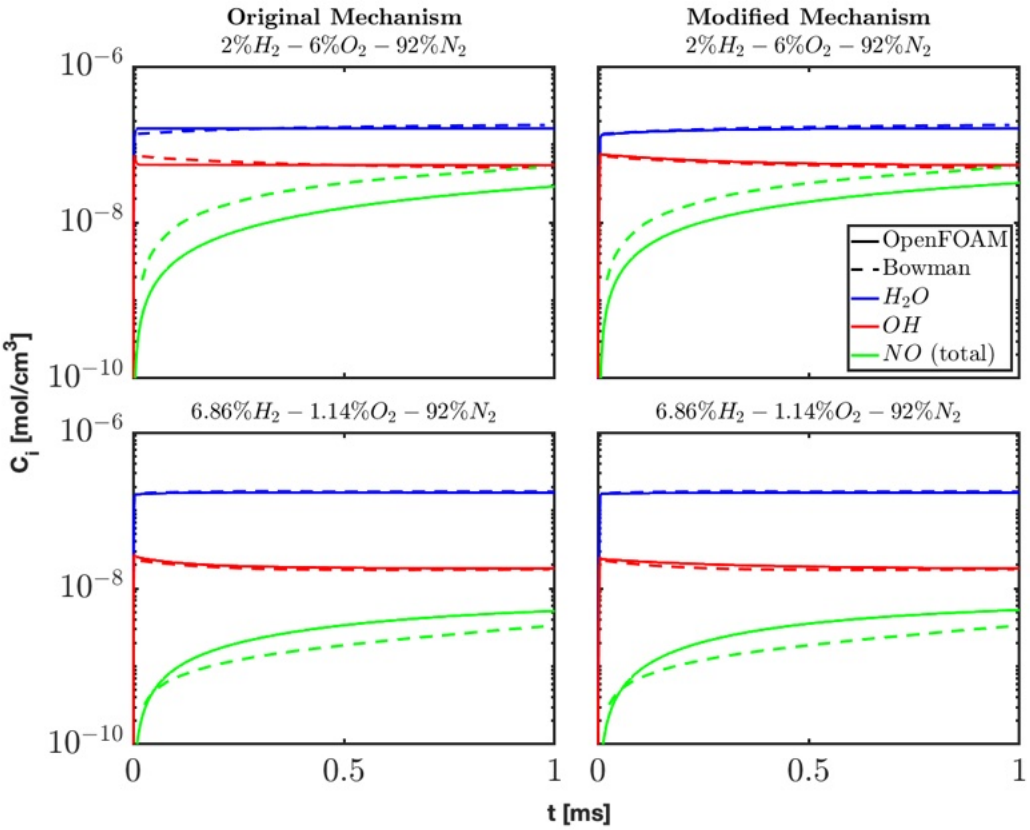

Figure 7.4: Select species profiles through time for several cases using both the original Jachimowski mechanism from [150] (left) and the modified Jachimowski mechanism from [151] (right).

[157] and [159], but this is also expected since data from these sources originates from the original Jachimowski mechanism, not the modified one. If parallels are drawn between the comparisons of same mechanisms, namely the modified mechanism compared to [158] and the original mechanism compared to [157] and [159], the RMS errors between modified mechanisms are much lower (1-3%) than those for the original mechanisms (16-19%). This signifies much stronger agreement between the modified mechanisms, allowing for greater confidence in the correctness of such mechanism. Overall, the ignition delay results show excellent agreement across a range of conditions as compared to recent literature utilizing the same mechanism, thus

providing strong evidence for validation of the mechanism.

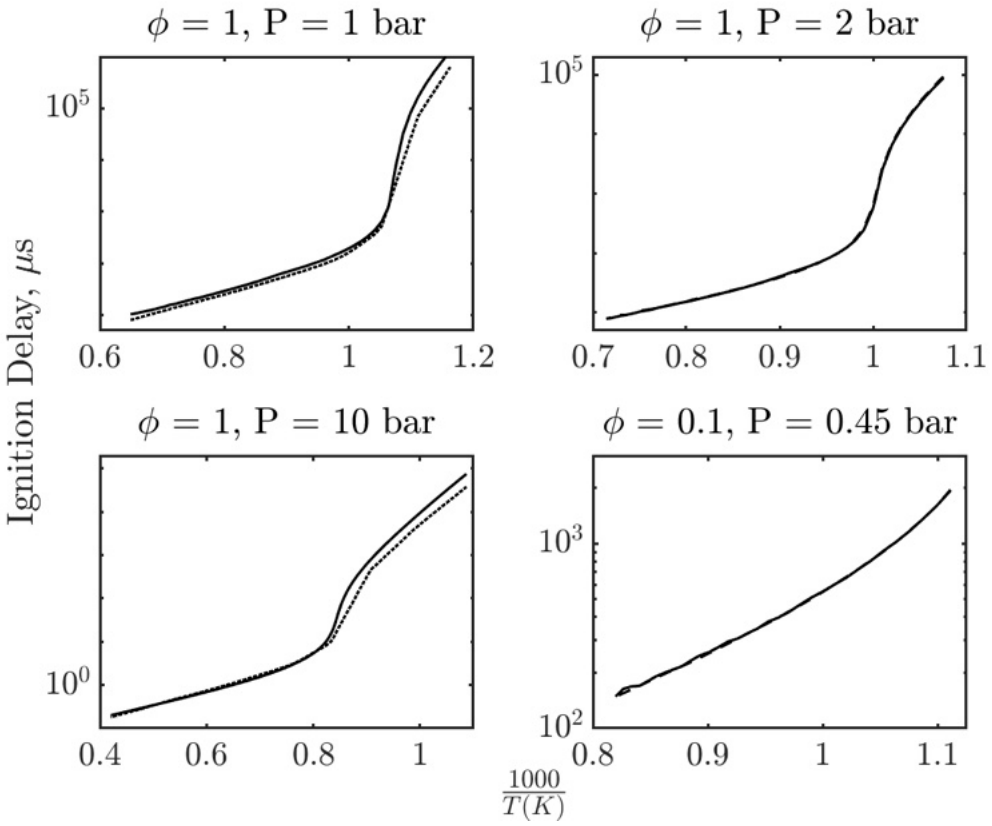

Figure 7.5: Ignition delay curves using multiple initial conditions with an H_2-O_2 mixture and the modified Jachimowski mechanism from [151]. OpenFOAM data using the modified mechanism is defined by sold lines, data from [157] (top left) and [159] (bottom left) using the original mechanism by dotted lines, and data from [158] using the modified mechanism by dashed lines.

7.4.2 1-D Studies

NO_x concentrations from the modified Jachimowski mechanism (13 species, 32 reactions) were also examined in the 1-D detonation tube case against a similar skeletal

			Original Mechanism [150]			Modified Mechanism [151]		
Comparison	Pressure [bar]	ϕ	Mean % Error	Max % Error	RMS % Error	Mean % Error	Max % Error	RMS % Error
Fureby	1	1	11.29	59.63	19.15	25.30	110.28	57.72
Gerlinger et al.	2	1	30.48	107.54	29.14	2.38	9.45	3.14
	0.45	0.1	14.39	20.85	13.54	1.02	5.40	1.58
Kumar et al.	10	1	13.37	36.59	16.18	18.11	101.06	50.50

Table 7.2: Percentage errors from ignition delay curves between OpenFOAM and reference data, for both the original Jachimowski mechanism from [150] and the modified Jachimowski mechanism from [151].

mechanism used by [134] (12 species, 27 reactions) as well as detailed NO_x mechanisms from [162] (19 species, 64 reactions) and [163] (31 species, 210 reactions). The profiles of NO mole fraction from these mechanisms at multiple time instances in the simulations are shown in Fig. 7.6. As expected, the detailed mechanisms produce more NO, mainly due to the addition of more NO formation pathways not present in the skeletal mechanisms, such as the NNH route. Nevertheless, the percentage differences of peak NO values between the Jachimowski mechanism and [162] are around 54-63% and between the Jachimowski mechanism and [163] are around 46-53%, which is reasonable given the large difference in the complexity of chemistry used. When comparing the Jachimowski mechanism to another similar skeletal mechanism from [134], the results are in better agreement, with percentage differences between 12-18%. These results further confirm the appropriateness of using the Jachimowski mechanism in simulations containing detonative combustion.

7.4.3 2-D Studies

Lastly, before fully moving to 3-D RDE simulations, the Jachimowski NO_x mechanism was tested in a 2-D idealized RDE configuration. The configuration consisted of a 2-D rectangular channel with a periodic boundary condition in which a detonation wave propagated. An injection boundary condition identical to the one detailed by Schwer and Kailasanath was used, wherein the injection flux was determined based on a critical pressure for choked flow and the effect of a passing detonation wave. The simulations used hydrogen-air chemistry at stoichiometric conditions and a domain temperature and pressure of 300 K and 1 atm, respectively. Simulations were initialized with H_2-O_2-NO_x chemistry, using both the original [150] and modified [151] Jachimowski mechanisms, from a quasi-steady state previously achieved by [164] with H_2-O_2 chemistry from the mechanism of [148]. Simulations ran for roughly 4

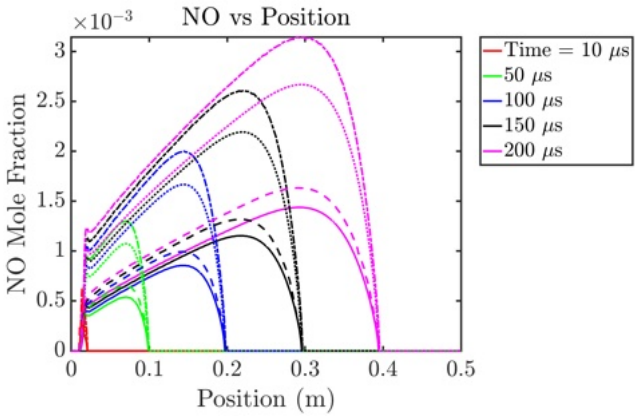

Figure 7.6: NO mole fraction vs position in 1-D detonation tube at several time instances for the following mechanisms: [151] (solid), [134] (dashed), [162] (chain), and [163] (dotted).

wave cycles of 0.26 ms and were compared to results from the H_2-O_2 simulation using the mechanism from [148].

Figure 7.7 shows the pressure differences from the H_2-O_2 mechanism [148] for both the original [150] and modified [151] H_2-O_2-NO_x mechanisms. The results show a relatively small difference in pressures after a single wave cycle, but this difference is exacerbated for the original Jachimowski mechanism with increasing wave cycles. This pronounced difference in pressure signifies a marked difference in the speed of the propagating detonation wave throughout the wave cycle, which is inherently tied to the chemical reactions occurring at the wave front that are defined by the chemical mechanism used. As such, it can be surmised from Fig. 7.7 that the wave speeds are in much closer alignment between the modified Jachimowski mechanism from [151] and the H_2-O_2 mechanism from [148] than between the original Jachimowski mechanism [150] and the one from [148]. To further confirm this, the wave speeds are calculated for each cycle across all 3 chemical mechanisms, and the differences to the mechanism of [148] are calculated as well. This data is shown in Tab. 7.3. To obtain wave speeds, the distances traveled by the maximum pressure point (signifying the wave front) along a horizontal line 2.51 cm from the inlet plane were calculated after each wave cycle, and the speed of the wave was deduced from the distance and time measurements. The results show excellent agreement between the modified mechanism H_2-O_2-NO_x and the H_2-O_2, with average wave speeds within 1 m/s of

each other across 4 wave cycles. This result amounts to a 6x decrease in wave speed differences when going from the original NO_x mechanism to the modified one, thus highlighting the significance of modifying the species and reaction parameters based on the species profile results previously shown in Fig. 7.4. Overall, the excellent agreement in pressure profiles and wave speeds between the modified NO_x mechanism and the H_2-O_2 mechanism from [148] further confirms the validation of the modified NO_x mechanism for use in 3-D RDE simulations.

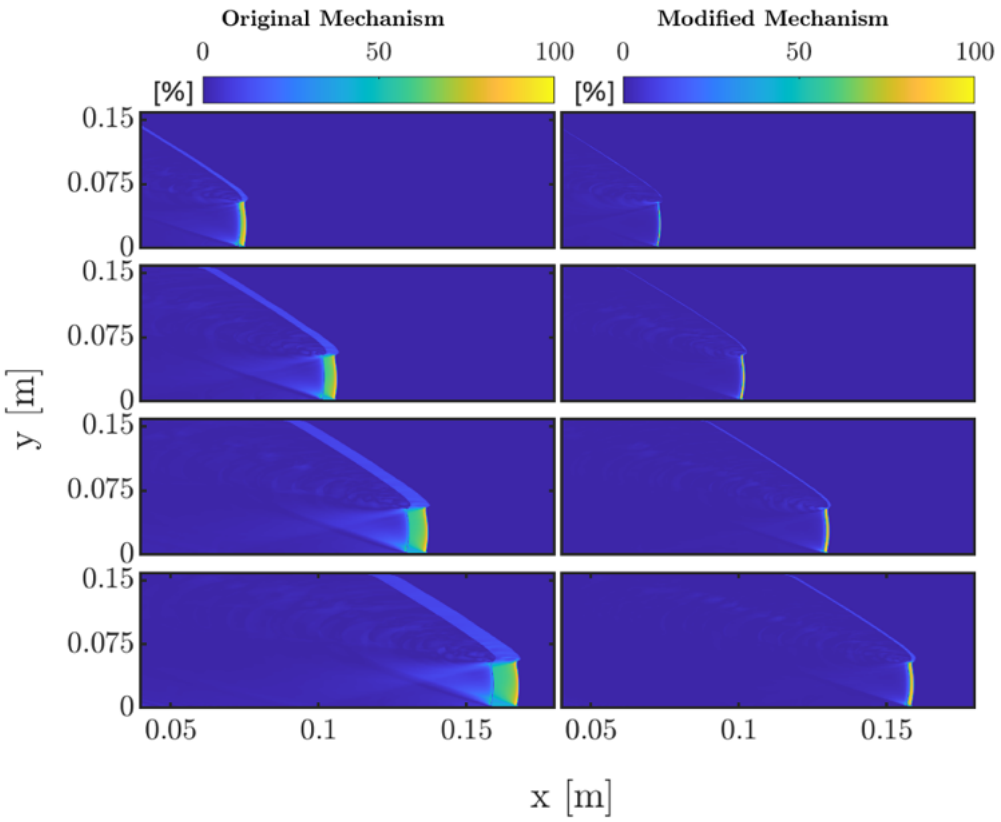

Figure 7.7: Pressure percentage difference between H_2-O_2 mechanism [148] and: (left) original H_2-O_2-NO_x mechanism [150]; (right) modified H_2-O_2-NO_x mechanism [151]. Differences are shown after each of 4 consecutive wave cycles (from top to bottom).

Wave Cycle	Wave Velocity [m/s]			% Difference to Mueller et al.	
	Mueller et al.	Jachimowski	Wilson and MacCormack	Jachimowski	Wilson and MacCormack
1	1946.92	1954.62	1945.38	0.395	0.079
2	1950.00	1959.23	1949.23	0.473	0.039
3	1950.77	1959.23	1949.23	0.434	0.079
4	1950.77	1958.46	1949.23	0.394	0.079
Average	1949.62	1957.88	1948.27	0.424	0.069

Table 7.3: Wave speed measurements and differences in wave speeds for multiple chemical mechanisms across multiple wave cycles in a 2-D RDE. Wave speed was calculated using distance traveled by the maximum pressure point along a horizontal line 2.51 cm from the inlet plane after each wave cycle.

7.5 NO_x Formation in 3-D RDEs

Given the extensive validation of the modified Jachimowski mechanism from [151] shown in the previous section, this mechanism was ultimately used in 3-D RDE simulations to study NO_x behavior in such systems.

High-fidelity numerical simulations of full-scale RDE systems are employed with the use of the UMReactingFlow solver, wherein the governing equations for conservation of mass, momentum, and energy in addition to species conservation with chemical reactions are solved, and the ideal gas equation of state closes the system of equations. The solver uses MPI-based decomposition to allow for parallel operation and it ran on roughly 4000 to 5000 cores to obtain the 3-D RDE results in the following subsections.

The cross-sectional views of the three-dimensional RDE configurations used are shown in Fig. 7.8. A continuous air injection inlet along with 120 uniformly spaced fuel injectors are used in both the Air Force Research Laboratory (AFRL) [165] and the University of Michigan (UM) [166, 136, 167] geometries, with the major difference between geometries being the air inlet designs used. The UM design injects air axially into the combustor with an Axial Air Inlet (AAI), whereas the AFRL design injects air radially with a Radial Air Inlet (RAI). These two geometries have previously been shown to produce different flow behaviors and detonation structures even for nominally similar operating mass flow rates [168, 164, 167]. Specifically for the AFRL RAI design, a 0.3 inch combustor annular gap and a 0.069 inch air injector gap are used in this work. Additional dimensions for each design are noted in Fig. 7.8. Hydrogen-air combustion is modeled in the RDEs, with Tab. 7.4 detailing the various fuel and oxidizer mass flow rates and global equivalence ratios used for each

case. In addition, cases 2, 3, and 4 in particular corresponding to cases 2.2.2.1, 3.2.2.1 and 4.2.2.1, in [165], respectively.

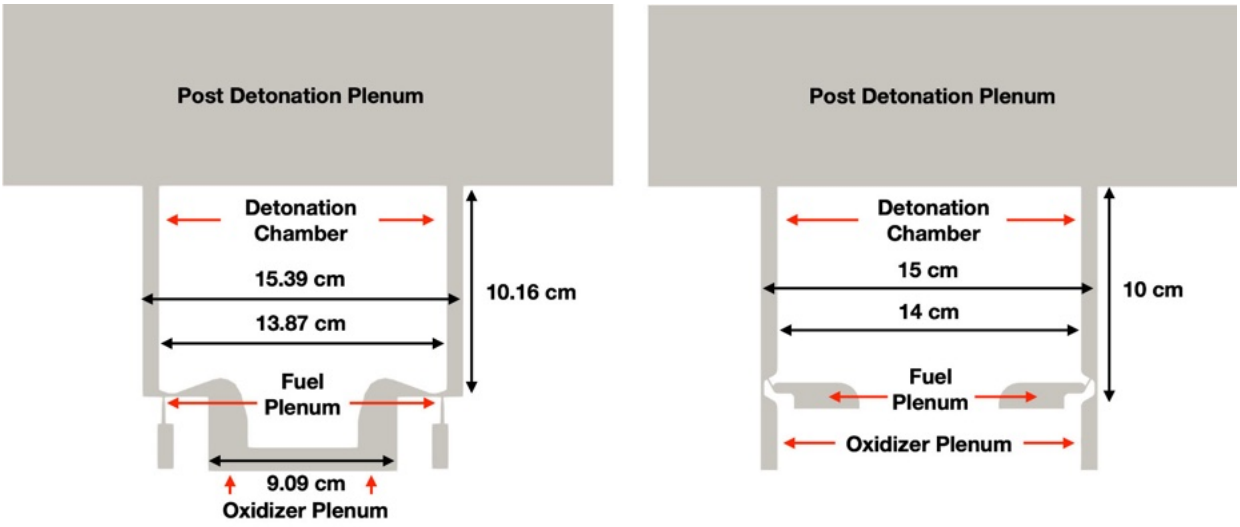

Figure 7.8: Cross-section schematics for AFRL RAI configuration (Left) and UM AAI configuration (Right).

Configuration	Case	$\dot{m}_{air}$ [g/s]	$\dot{m}_{fuel}$ [g/s]	ϕ
UM AAI	1	404.2	11.9	1.01
AFRL RAI	2	320	9.3	1.0
	3	630	18.0	1.0
	4	860	25.0	1.0

Table 7.4: 3-D RDE Case Configurations.

Adiabatic, no-slip walls are used for the boundary conditions of each case. Additionally, a constant mass flow rate boundary condition is prescribed at the fuel and oxidizer inlet planes, upstream in a truncated plenum region, with these conditions detailed in Tab. 7.4. Both RDE configurations are represented by unstructured meshes, with the UM AAI and AFRL RAI meshes containing roughly 25×10^6 and 48×10^6 control volumes in their entire domains, respectively. The UM AAI mesh has a resolution of 10^{-4} m in the injector region and 2×10^{-4} m up to 0.04 m in the

detonation chamber, whereas the AFRL RAI mesh has a resolution of 2×10^{-4} m in the detonation chamber. These grid resolutions are identical to the ones used by Sato, Sato et al., who found that all appropriate physics involved in such RDE configurations are sufficiently resolved while comparing reasonably well to experimental data. Similar resolution has been used in other studies as well [169, 170, 73].

The simulations were first initialized with H_2-O_2 chemistry defined by the mechanism from [148], and after statistical stationarity was achieved the chemistry was switched to H_2-O_2-NO_x chemistry defined by the mechanism from [151]. The simulations were then run for roughly 10 wave cycles, or 2.48 ms, with the NO_x chemistry to allow for sufficient time for NO_x to develop within the system. The results provided in the remainder of this section show both instantaneous and temporally averaged data from this 2.48 ms time period from multiple viewpoints within the RDE, namely the mid-channel, the exit plane, and radial injector cuts alike.

7.5.1 Instantaneous Data

Figure 7.9 shows instantaneous mid-channel snapshots of pressure, temperature, and NO_x for all cases studied after 2.48 ms of simulation time. These snapshots show that both geometry and mass flow rate have a significant impact on resulting NO_x levels and formation patterns. When viewing results for different geometries first, it is seen that the RAI design produces long, coherent trails of NO_x azimuthally behind the detonation waves, with the most intense levels usually seen near the detonation fronts where high temperatures are present. This behavior is expected since the NO_x chemistry mechanism used for these simulations only accounts for thermal NO_x production, making NO_x formation primarily sensitive to high temperature. In contrast to the RAI geometry, the AAI geometry produces more incoherent patterns of NO_x. This observation is supported by the non-uniformity seen in the temperature plot for the AAI geometry, specifically in the refill region, with evidence of PC present due to prominent temperature striations there. The presence of PC is consistent with previous experimental and computational studies of the AAI geometry [171, 129], and this works to weaken detonation waves and reduce peak pressure and peak heat release experienced across them. The combination of PC, reduced peak pressure and peak heat release, and weaker waves in the AAI RDE is realized in the significant reduction in fuel efficiency (η), shown for all cases in Fig. 7.10, as compared to the RAI RDE, with average exit plane fuel efficiency values of 71.72% and 90.31% seen in AAI case 1 and RAI case 2, respectively. However, the reduction in heat release and

the fuel burned in the AAI case is ultimately reflected in lower overall NO_x emissions. As such, conclusions from Fig. 7.9 alone suggest that while PC leads to weaker waves and less efficient combustion, it also inversely correlates with NO_x production given the incoherence and lower average heat release it induces.

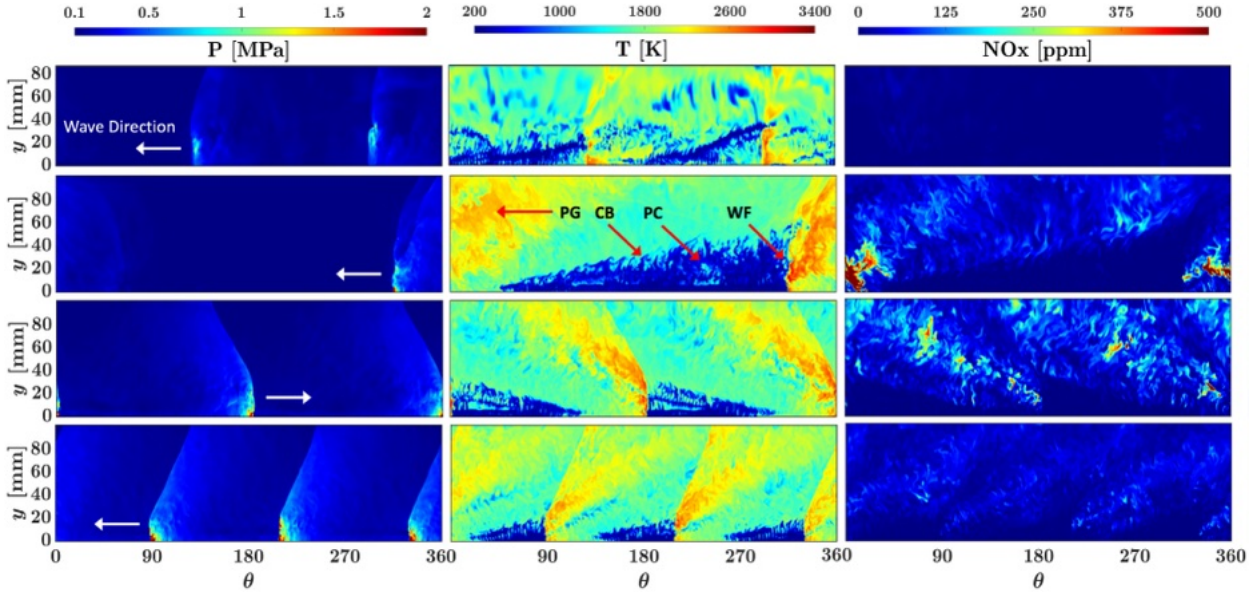

Figure 7.9: Instantaneous pressure, temperature, and NO_x at mid-channel for all cases studied at 2.48 ms. Case 1 (top) to Case 4 (bottom).

Figure 7.9 shows the effect mass flow rate has on flow structure and emissions behavior in the RAI geometry. As mass flow rate increases, the RDE generally begins to operate with an increased amount of detonation waves in the combustor. The refill regions behind these waves ultimately adjust to these changes by reducing in azimuthal length and axial height. Injector recovery is also faster behind the detonation waves as a result of higher plenum pressures. As noted in previous studies using an AAI geometry [167], this helps to produce more steady fuel/oxidizer injection, thus increasing detonation strength and reducing PC. From Fig. 7.9 these trends seen with increasing mass flow rate are clear between cases 2 and 3, with average temperature and NO_x increasing as increased detonation strength would imply. However, case 4 shows differing behavior, with an even further increase in mass flow rate yet a reduction in NO_x produced. It should be noted though that Fig. 7.9 shows case 4 at

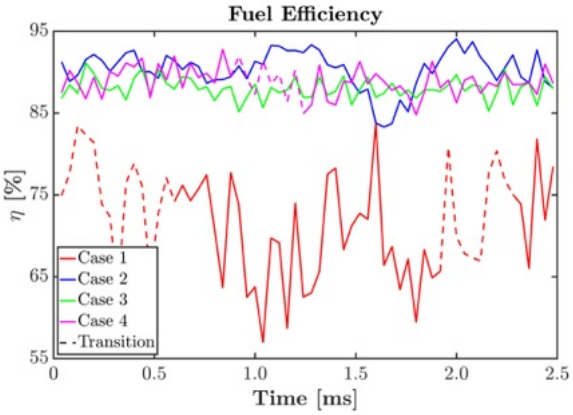

Figure 7.10: Fuel efficiency values (η) from injection to exit over time for all cases. Dashed lines represent transitory periods between wave modes, specifically between 1 and 2 waves for case 1 and between 2 and 3 waves for case 4.

an instant when the RDE operates with 3 waves after transitioning from 2 waves at the same mass flow rate condition. As such, the role this wave splitting process has on case 4 (as well as case 1 which splits from 1 to 2 waves) remains important in understanding the relationship between mass flow rate, detonation strength, and NO_x emissions, which will be discussed further in Sec. 7.5.2. Nevertheless, qualitative trends are observed among all 3 RAI cases, wherein detonation waves become thinner and tighter with increasing mass flow rate, leading to thinner, tighter trails of NO_x production in the post-detonation regions.

When viewing instantaneous radial cuts of cases 1 and 2, as shown in Fig. 7.11, the effect PC has on NO_x emissions in RDEs becomes apparent. These snapshots, which are taken from an azimuthal location in the refill region behind the detonation waves, show recirculation of gases in both geometries, which can ultimately lead to parasitic combustion in the refill region. However, the interesting observation here is that recirculation in the AAI geometry is more prominent near the injection plane, resulting in greater heat release and more NO_x production in this area. Within the RAI geometry heat release is delayed further axially into the detonation chamber, resulting in the axial delay of NO_x production. These results clearly show the effect that injector design has on recirculation and consequently PC and NO_x production, with the AAI injector design more distinctly promoting radial recirculation within the detonation chamber. This behavior is also reported in previous experimental and computational

studies with this AAI geometry [136, 167]. Although this behavior largely explains the processes through which most NO_x is formed within the AAI geometry, this geometry still inherently produces less NO_x overall than the RAI geometry. Weaker overall detonation waves from the prominent PC in the AAI geometry, as already discussed, is most likely contributing to such reductions in NO_x emissions, but this relationship is discussed in further detail in Sec. 7.5.2.

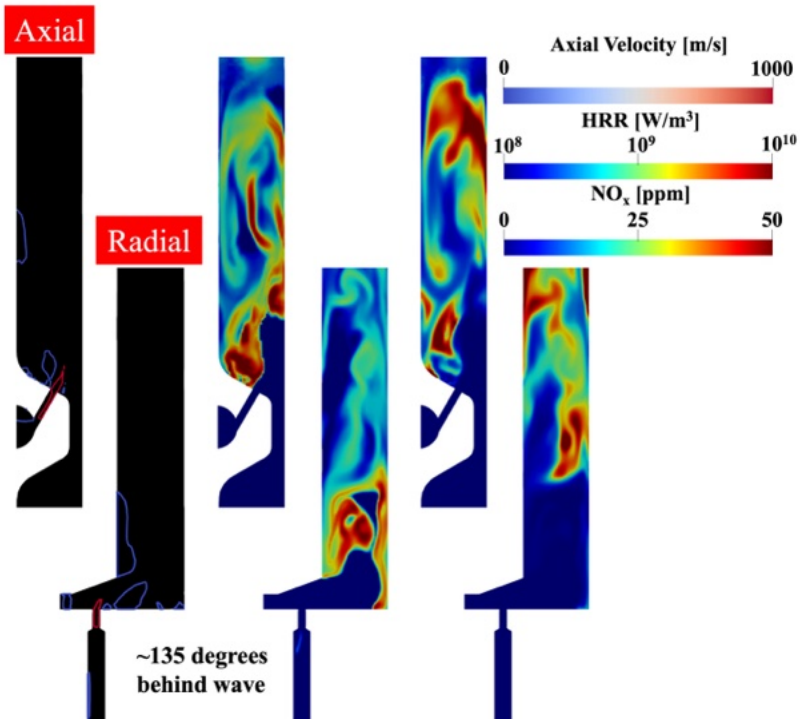

Figure 7.11: Instantaneous axial velocity, heat release rate, and NO_x (left to right) at radial injector cut for case 1 (top) and case 2 (bottom). Blue and red contours on axial velocity plots signify values of 0 m/s and 1,000 m/s respectively.

7.5.2 Temporally Averaged Data

Before the temporally averaged data is discussed, a brief explanation of the temporal averaging process is described. The mid-channel data, shown in Figs. 7.13 and 7.14, is obtained by shifting waves on top of each other with respect to azimuthal location

and then temporally averaging the result. This wave shifting process is detailed in Fig. 7.12. The waves are shifted by marking locations of maximum pressure at an axial location of 3 mm above the bottom of the detonation chamber. Once these locations are marked, the plots of certain parameters (such as temperature in Fig. 7.12) can be shifted to the position of the wave in the first frame. The aggregated waves can then be averaged to obtain a wave profile detailing the average detonation structure through time. In the instances where multiple waves occur within the RDE system, the amount to shift the waves on top of one another is obtained by averaging the distances each individual wave moved through every timestep. In addition to their role in temporal averaging, the marked pressure locations are also used for calculating distances between waves through every timestep. This allows for the calculation of wave speeds for all waves in the system in each case, and metrics from these calculations are shown in Tab. 7.5, including maximum pressure, temperature, heat release rate, and NO_x, along with the minimum, maximum, average and standard deviation (σ) of wave speed (W). The temporally averaged radial cuts, shown in Figs. 7.15 and 7.16, are averaged in a similar manner to the mid-channel data, except no wave shifting is implemented before temporally averaging.

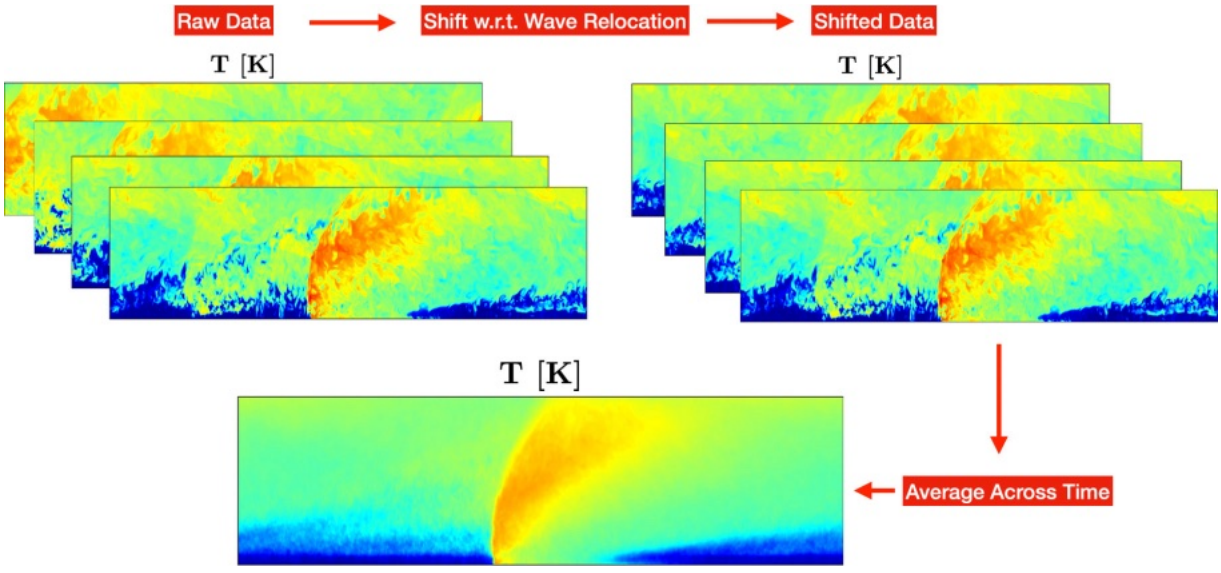

Figure 7.12: Depiction of wave shifting process used to generate temporally averaged mid-channel plots of flow properties with temperature used as an example.

Mid-channel temporally averaged properties of all cases, shown in Fig. 7.13, show mostly similar trends to the ones seen in the instantaneous plots in Fig. 7.9. NO_x emissions are much higher in the RAI cases as opposed to the single AAI case. The disorganization in NO_x production seen in the AAI case is now absent, with a clear trail of NO_x stemming from behind the detonation wave. Additionally, it is seen again that as additional waves spawn with increasing mass flow rate, the waves themselves begin to tighten and by consequence produce tighter trails of NO_x in the post-detonation region. The intensity of NO_x emissions is similar between cases 2 and 3, as similar maximum temperatures and pressures are noted in these cases. As for cases 1 and 4, temperatures, pressures, and NO_x emissions are lower than in cases 2 and 3. It is noted though that the temporally averaged results for case 1 and 4 in Fig. 7.13 are before the systems transitioned from 1 to 2 waves and 2 to 3 waves respectively, with data before and after the transition shown in Fig. 7.14 for these cases.

When combining the qualitative behavior seen in Fig. 7.13 with the corresponding mid-channel properties tabulated in Tab. 7.5, a clear trend between detonation strength and NO_x production begins to form. Table 7.5 shows that as mass flow rate increases from case 2 to case 3 the strength of the detonation waves, as signified by maximum pressure, increases accordingly. When this occurs, peak temperature and NO_x increase as well. However, this trend does not appear to be linear when the other cases are taken into account. The trend that detonation strength follows likens to the one observed in [167] where strength and wave speed follow a staggered pattern based on mass flow rate. More specifically, as mass flow rate increases, the wave speed and strength of waves increases linearly until a certain point when the waves ultimately split. Once the waves split, a noticeable dip in wave strength and wave speed is seen. As mass flow rate continues to increase, though, wave speed and strength continue to increase linearly again. Although fewer mass flow rate conditions are tested in this study than in [167], which limits the correlations that can be made between detonation strength and mass flow rate, the trend noticed by [167] still holds based on the available data. When air mass flow rate increases from 320 g/s to 630 g/s and the number of waves changes from 1 to 2 waves (from case 2 to 3), maximum pressure and average wave speed increase by 17.2% and 2.9%, respectively. Considering that this change is not too dramatic compared to the dramatic increase in mass flow rate (96.9%), it can be surmised that in the region of mass flow rates between these two conditions the properties noted above experience a marked decrease when the wave ultimately splits into two and slowly increase above the values seen at the lower mass flow rate condition before the split as mass flow rate continues to

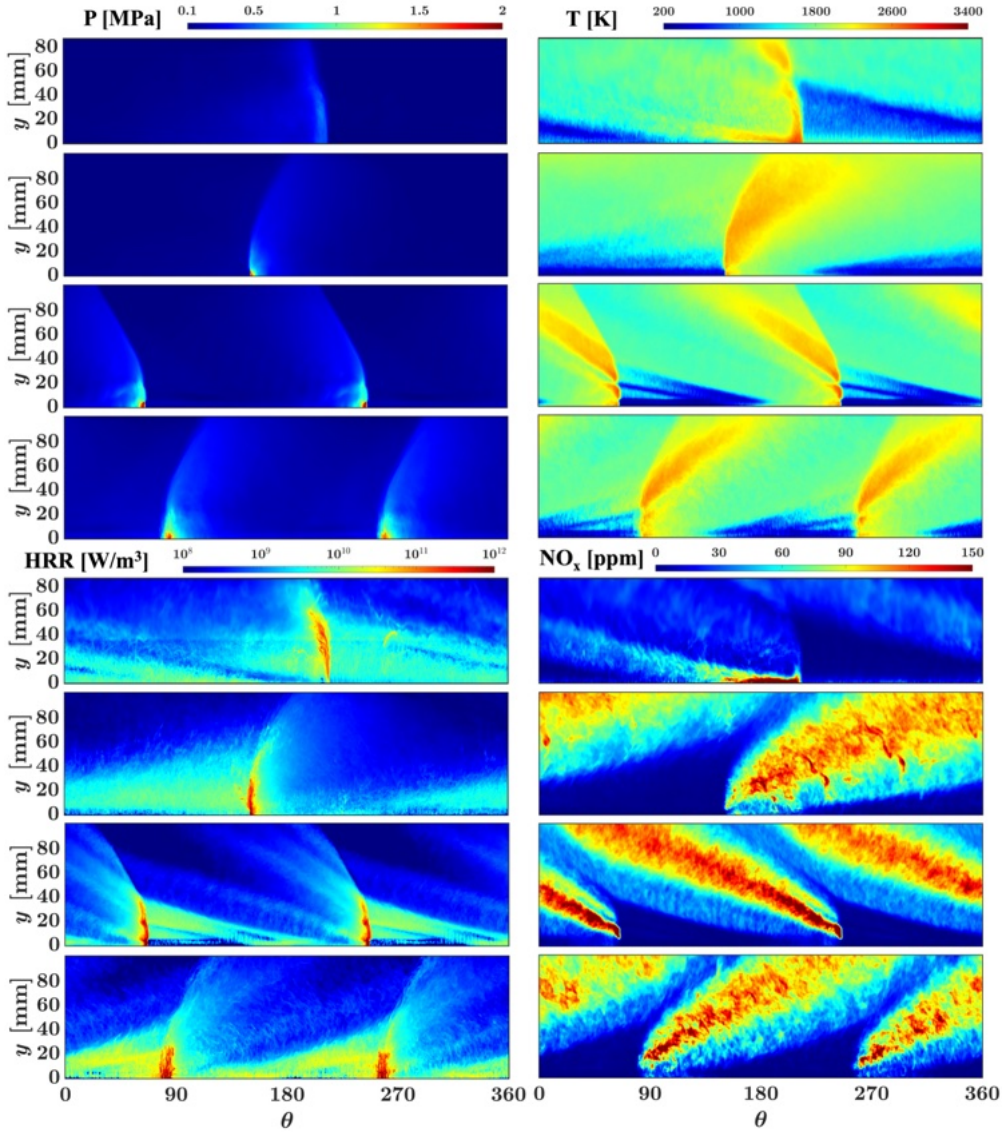

Figure 7.13: Temporally averaged pressure, temperature, heat release rate, and NO_x for all cases. Case 1 (top) to case 4 (bottom). In cases where wave transitions occurred temporal averages are shown only before the transition process.

increase. During this increase temperature and NO_x levels rise as well. Then, as the

air mass flow rate continues to increase another 36.5% from case 3 to 4, maximum pressure and average wave speed actually decrease by 14.8% and 3.4% respectively, signifying the beginning of unsteadiness leading to another wave transition. Here, average wave speed and maximum NO_x already start to suffer in case 4 as counter-propagating waves shed off the main ones, and the system ultimately transitions to 3 waves, leading to another marked decrease in all properties and thus a decrease in wave strength and NO_x emissions. This marked decrease is also seen in the AAI geometry when the system transitions from 1 to 2 waves, reducing detonation strength and NO_x emissions in the process. As such, the behaviors noted between all cases confirms a significant correlation between detonation strength and the NO_x emissions levels produced accordingly.

Case #	# of Waves	Time in Mode [ms]	P_{max} [MPa]	T_{max} [K]	HRR_{max} [TW/m^3]	NO_{xmax} [ppm]	W_{min} [m/s]	W_{max} [m/s]	W_{avg} [m/s]	σ_W [m/s]
1	1	1.32	0.603	2793.23	0.969	289.95	1208.14	2059.59	1803.32	168.60
1	2	0.20	0.437	2330.98	0.600	33.09	920.49	1737.42	1332.40	226.50
2	1	2.48	1.818	2526.48	6.203	163.26	1160.53	2068.27	1800.03	203.59
3	2	2.48	2.130	2781.60	5.491	236.00	1803.99	1895.91	1852.40	21.77
4	2	0.88	1.856	2660.36	5.112	224.58	1516.73	1987.83	1791.95	85.46
4	3	1.24	1.720	2376.73	3.943	100.43	1562.69	1826.97	1702.55	52.97

Table 7.5: Flow properties at mid-channel for all cases.

Figure 7.14 shows mid-channel data in cases 1 and 4 before and after their transitions between wave modes. It is clear from these plots that detonation strength reduces significantly after the wave splitting process as was previously noted and can be seen in the data from Tab. 7.5. The standard deviation in wave speed for case 4 before and after the transition reveals the system's propensity for wave splitting to achieve steadier operation, with a higher variation in wave speed seen before the split as opposed to afterward. This is not the case for case 1 though, but it should be noted that as the deviation in wave speed increases here after the wave splitting process occurs, the averaging span for this case after transitioning is significantly shorter than that of case 4 in the same condition.

Another interesting effect of the transitions is the notable change in the detonation structure of the waves. First, after an additional wave is added to the systems the heights of the detonation waves shrink in both cases. This behavior is consistent with previous studies [164, 165] and is a result of the refill region height reducing due to the reduced time between two waves passing over an injector. When additional waves are present at the same mass flow rate condition, the fresh mixture does not

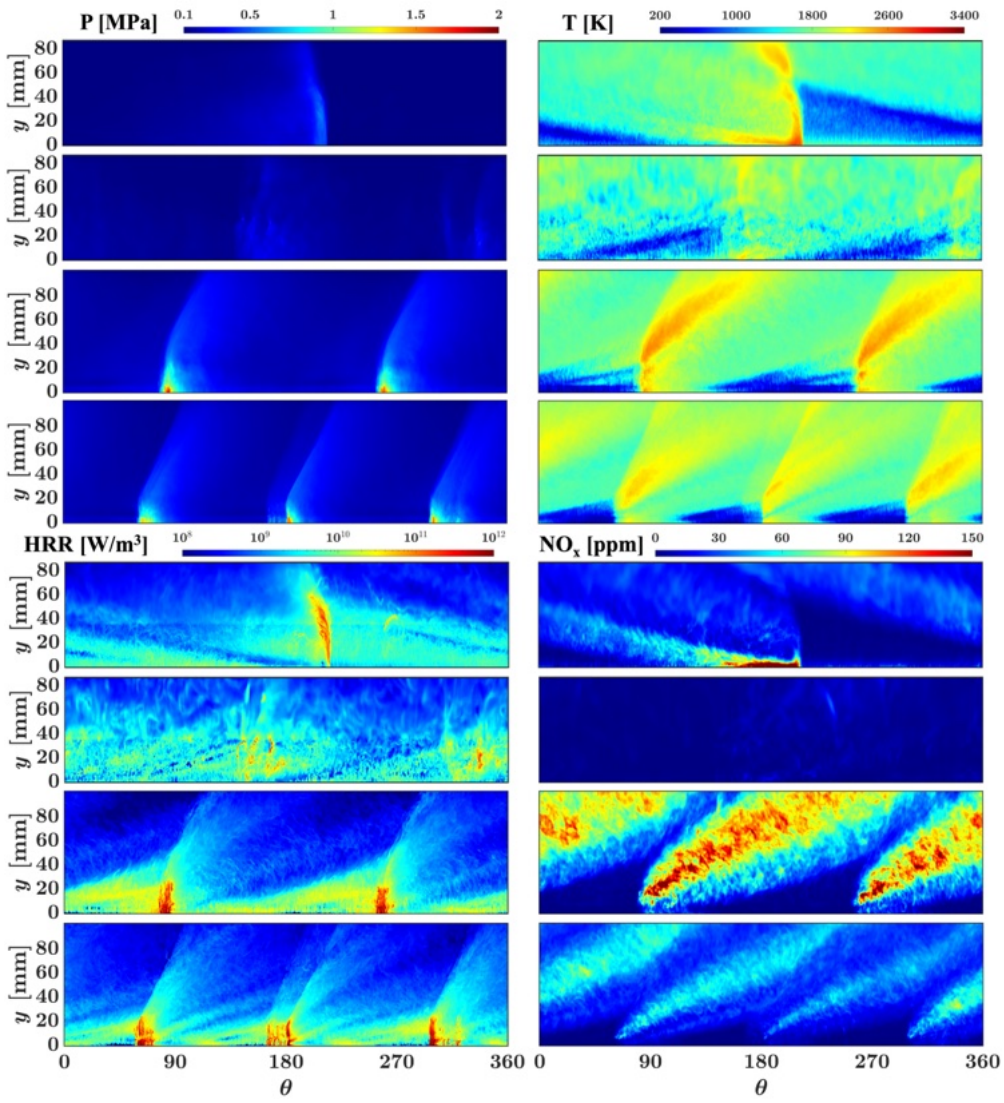

Figure 7.14: Temporally averaged pressure, temperature, heat release rate, and NO_x for Case 1 and Case 4 that experienced wave transitions. From top to bottom: Case 1 before transition, case 1 after transition, case 4 before transition, case 4 after transition.

penetrate as much axially into the chamber. Since detonation height ties directly to

refill height [164], the detonation height reduces. Additionally, it can be said that this extra wave effectively reduces the azimuthal residence time between waves since another wave is present in the system with mass flow rate remaining constant. This notion is corroborated by [134], who showed that operating an RDE in a multi-wave mode as opposed to a single-wave mode reduced the length scale between waves and consequently reduced residence time in the high temperature region, resulting in significantly lower NO_x emissions. Second, the weakening of the waves lowers the peak pressures experienced across them. This has the effect of increasing the induction length across the wave, leading to slower, less intense heat release spread out across the wave and ultimately less compact and efficient combustion. This behavior leads to lower average temperatures inside the newly formed waves and less NO_x produced in the system as a result. As such, both wave structure and wave strength are clearly affected by the wave splitting process and since these parameters are directly tied to NO_x emissions levels, NO_x is consequently affected with more waves at the same mass flow rate condition generating less NO_x overall.

The trends seen in the mid-channel temporal averages from Fig. 7.13 are also seen in the radial temporal averages shown in Fig. 7.15. NO_x levels are much lower in the AAI RDE than in the RAI RDE, which is a direct result of the lower average temperatures seen in the AAI RDE. Also, the location of most NO_x production in the AAI RDE is near the injector plane due to the presence of increased recirculation here based on the axial air injection design. This process traps hot product gases near the inner wall close to the fuel injectors, promoting PC and in turn NO_x formation here. Regarding the average temperatures in all plots, it is seen that a threshold temperature of around 1700 K must be met before significant NO_x formation occurs. The injector design, presence of PC, and lengthened lower temperature structure in the axial direction in the AAI RDE all work together to reduce heat release in the detonation chamber, reducing the maximum temperature reached near the exit of the combustor as compared to the RAI RDE. As such, no significant NO_x production occurs near the exit of the combustor in the AAI RDE, with the majority of NO_x forming near the injector plane as a result of PC.

In the RAI RDE cases, more uniformity is seen in the radial temperature profiles at lower axial positions in the combustor, with increasing radial uniformity seen with increasing mass flow rate and decreasing detonation height. This behavior, a clear result from better combustion efficiency and detonation strength with the RAI design, allows for temperatures to reach the 1700 K threshold temperature in rather short axial distances into the combustor, causing more significant NO_x to be

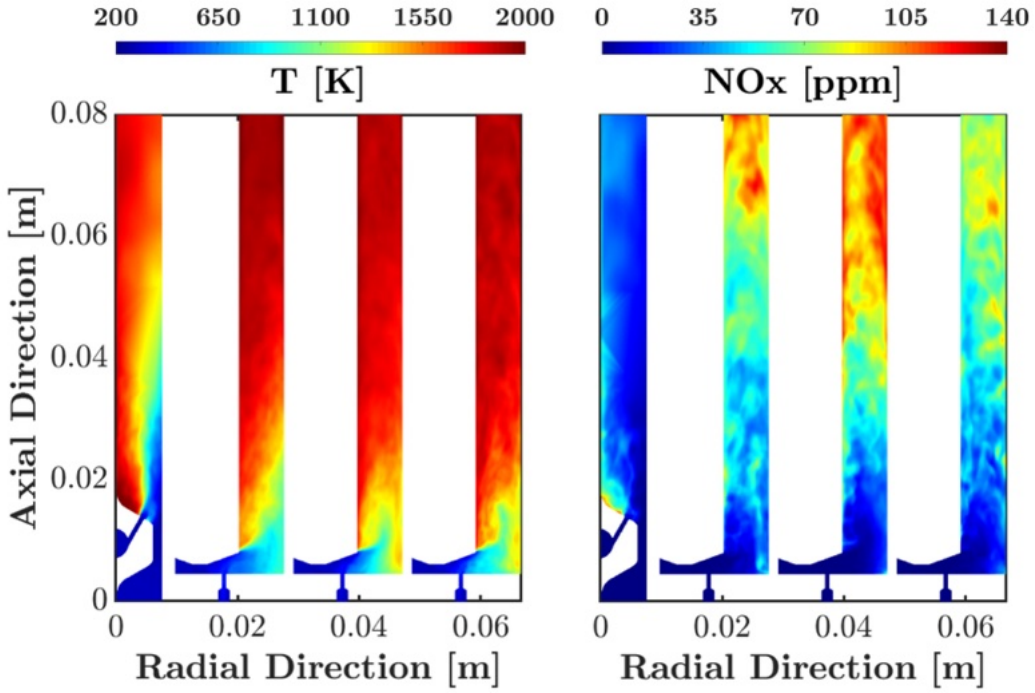

Figure 7.15: Temporally averaged temperature and NO_x at radial injector cut for all cases. Case 1 (left) to case 4 (right). In cases where wave transitions occurred temporal averages are shown only before the transition process.

produced here as a result. The impingement of the cool temperature stream into the detonation chamber from the refill region is seen in each case, with case 3 showing the most well-formed, centered region of all cases in terms of radial location within the detonation chamber. This well-formed, centered refill region structure in case 3, which is indicative of the detonation wave structure as well, is most likely why the NO_x produced in this case is more radially uniform than in all other cases, and is a direct result of the detonation strength seen in this case as previously noted. At lower mass flow rates, the detonation waves favor the outer wall, as they are not strong enough to significantly affect injector flow. As mass flow rate increases, the detonation waves strengthen, leading to higher peak pressures that affect injector recovery to a greater extent, a trend also seen in [167, 164]. This response by the stronger detonation waves shifts the radial location of the refill region and consequently the radial location of the waves. As such, greater radial uniformity is seen in the stronger detonation wave

cases, leading to greater radial uniformity in resulting NO_x emissions.

As for the radial temporal averages in cases 1 and 4 before and after their wave mode transitions, which are shown in Fig. 7.16, the results remain consistent with mid-channel findings. In case 1, the AAI RDE, greater variability is seen in the temperature profile before the system splits from 1 to 2 waves, but wave strength remains stronger in the single wave mode, which alludes to the fact that higher NO_x levels are observed before the split. Interestingly, the greatest NO_x production maintains itself near the inner wall and injection plane both before and after wave splitting, indicating that the primary mechanism of NO_x formation in the AAI RDE is indifferent to wave number and is more of a direct consequence of injector design and the PC this promotes. As for the RAI RDE in case 4, system behavior before wave splitting likens to that of case 3, as 2 waves are present in both cases, strong detonations are observed, and higher amounts of radially uniform NO_x are observed. The changing temperature structure after the split along with the mid-channel statistics from Tab. 7.5 support the claim that detonation strength directly affects NO_x production, as lower peak pressures and resulting heat release values are noted upon splitting to 3 waves. The wave splitting processes in case 4 negatively impact fuel efficiency, shown in Fig. 7.10, as average exit plane fuel efficiency values are 89.55% and 88.30% before and after the split. This minimal decrease in efficiency is most likely because the waves in this system are already relatively strong compared to the ones in the AAI system and the system is more efficient in general, leading to minute changes in efficiency levels between wave modes. Interestingly, in case 1 the average fuel efficiency actually increases from 69.33% to 74.52%. However, the caveat here is that this system is only in a mode with 2 waves for 0.2 ms, less than a full cycle, and so the exit plane values most likely haven't adjusted to the new mode of operation in the range of times averaged. As such, the average fuel efficiency obtained for case 1 after wave splitting should be disregarded. Nevertheless, the radial distributions for both cases before and after wave splitting show a marked reduction in NO_x, thus further supporting the link between detonation strength and NO_x emissions levels.

7.5.3 Emissions Levels

As is previously evident from temporally averaged mid-channel and radial data, it is seen that the RAI RDE produces significantly more NO_x than the AAI RDE, even at nominally similar mass flow rate conditions. Additionally, as mass flow rate increases in the RAI RDE, the flow properties of the system appear to behave in a

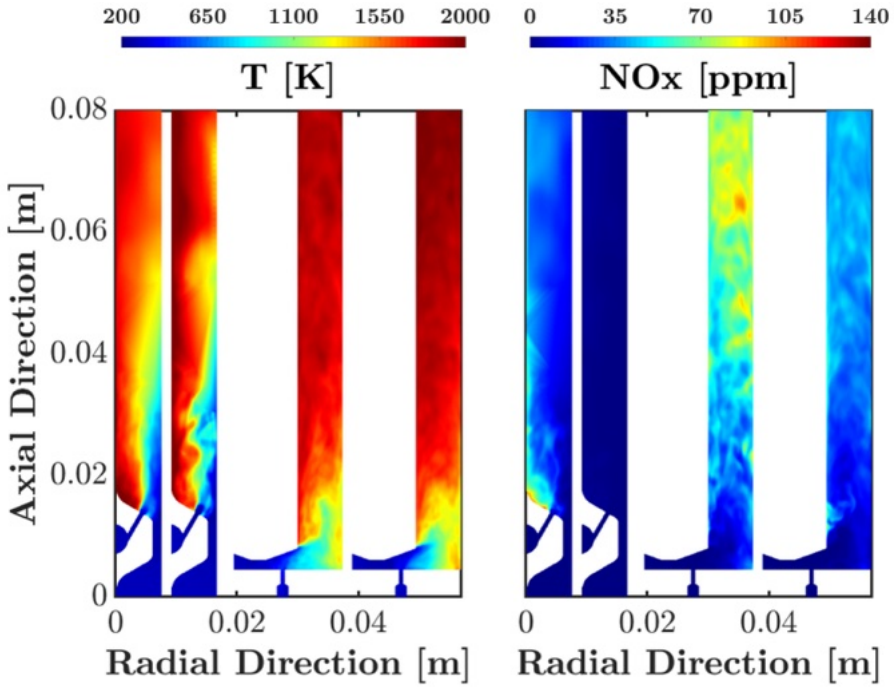

Figure 7.16: Temporally averaged temperature and NO_x at radial injector cut for case 1 and case 4 that experienced wave transitions. From left to right: Case 1 before transition, case 1 after transition, case 4 before transition, case 4 after transition.

staggered manner, with detonation strength increasing to a point and then markedly decreasing after the system reaches an unstable point and wave splitting occurs. To further understand how these behaviors affect NO_x at the exit of the combustor, an important metric of interest for power generation applications, average NO_x levels at the exit plane are plotted in time for each case in Fig. 7.17.

From the average NO_x values at the exit plane it is seen that NO_x levels in the AAI RDE stay below those in the RAI RDE cases at most times throughout the simulation, even before the wave splitting process. This again is a result of the detonation strength seen in the AAI case, where the weaker overall pressures observed lead to an increase in induction length and a delay and reduction in overall combustion. Additionally, the nature of the injector design in the AAI RDE promotes PC within the system and PC is more prominent in this configuration than in the RAI RDE as a result, leading to inherent losses in this system that manifest themselves in

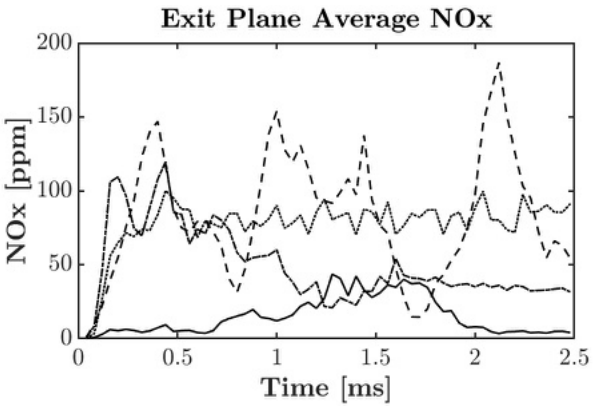

Figure 7.17: Spatially averaged NO_x at combustor exit plane over time for case 1 (solid), case 2 (dashed), case 3 (dotted), and case 4 (chain).

the weaker observed detonations. Overall, the average exit plane emissions for each case corroborate previous conclusions on detonation strength and system stability noted beforehand. This feature indicates that NO_x generation occurs predominantly in the region near the detonation wave, and the time-scales are relatively short for further production downstream.

Regarding the connection between exit plane NO_x levels and system stability in specific, it is observed in most cases that steady NO_x levels appear at the exit when the systems remain relatively stable. However, in certain cases where wave transitions occur, significant changes in NO_x emissions are observed, indicating the strong sensitivity of NO_x as a marker for system stability. In addition, specific instabilities in wave propagation, as seen in case 2 where only 1 wave is present in the system, can be noted from exit plane NO_x levels where highly oscillatory behavior occurs. These instabilities arise from the increased PC seen in both RDE geometries at lower mass flow rates and are evidenced by the high variability in wave speeds for these cases, as shown in Tab. 7.5. Since case 2 in specific is the only case to stay within the single-wave mode for the entire simulation, the wave in this system experiences these instabilities the most frequently within the context of the RAI RDE cases. As a result, the pre-burning of fresh mixture, detonation weakening, and combustion delay from increased induction length spawned from PC in this case are reflected in the local spikes and dips in exit plane NO_x emissions. In the higher mass flow rate cases, where less PC is observed and is also observed in previous studies [167, 164], steadier

behavior is seen in exit plane NO_x emissions over time. As such, exit plane NO_x emissions levels have shown to be a reliable marker for determining system stability within the detonation chamber, specifically with regard to instabilities arising from the presence of PC.

In terms of fuel conversion efficiency at the exit plane, a relationship forms between efficiency and NO_x levels when comparing the AAI and RAI cases at nominally similar mass flow rate conditions. In particular, Fig. 7.17 shows lower NO_x levels in AAI case 1, and the average exit plane fuel efficiency for this case is 71.72%. This fuel efficiency is the fraction of mass flow rate of fuel burned in the combustor divided by the total fuel mass flow rate entering the combustor. The mass flow rate of fuel burned is the difference between fuel mass flow rate entering the combustor and fuel mass flow rate exiting the combustor at the exit plane. Fuel efficiency values through time are shown for all cases in Fig. 7.10. For RAI case 2, significantly higher levels of NO_x are in the system, and the fuel efficiency is 90.31%. These numbers support the claim that weaker waves and a greater presence of PC in the AAI RDE help reduce fuel efficiency yet ultimately reduce NO_x emissions as well. However, the relationship between efficiency and NO_x levels breaks down when looking solely at the RAI cases for different mass flow rate conditions. Average fuel efficiency values of 90.31%, 87.98%, and 88.88% are seen for cases 2, 3, and 4, respectively, with average NO_x levels progressively decreasing from case 2 to case 4. This behavior suggests a more nuanced relationship between the efficiency and NO_x emissions in these cases, supported by the more nuanced differences in these cases where combustor geometry does not change. Nevertheless, the relationship holds between the AAI and RAI cases at nominally similar mass flow rate conditions as previously mentioned. When wave splitting occurs in RAI case 4, the trend continues to hold, as average fuel efficiency decreases from 89.55% to 88.30%. This decreasing efficiency behavior through wave splitting processes is consistent with a decrease in wave strength and resulting NO_x emissions, thus supporting the relationship between such parameters as already evident between AAI case 1 and RAI case 2. Interestingly, though, the trend reverses with AAI case 1 through wave splitting, as the average fuel efficiency increases from 69.33% to 74.52%. It should be noted though that this system spends less than a full cycle with 2 waves present (0.2 ms), and the system would need at least 1 full cycle to propagate the effects of the new wave mode to the exit plane. Additionally, the short amount of time available to average over amplifies the uncertainty in the measurement. As such, this anomaly should be disregarded in this discussion, and relationship between fuel efficiency, wave strength, and NO_x should hold. Therefore,

although no general trend can be inferred between fuel efficiency and NO_x emissions for all 4 cases studied, a correlation between decreasing efficiency and decreasing NO_x emissions is evident when specifically comparing overall data between AAI case 1 and RAI case 2 and data for RAI case 4 before and after wave splitting processes.

When the data shown in Fig. 7.17 is temporally averaged it is revealed that average NO_x levels through the full simulation time in the AAI RDE are 15.0 ppm, which is over 5.5 times less than the RAI RDE NO_x levels (83.4 ppm) at the nominally similar mass flow rate condition in case 2. Additionally, the AAI RDE exit plane emissions levels are still roughly 3.3 times lower than the levels seen in case 4 (49.6 ppm) which has the lowest NO_x levels of all RAI RDE cases. This data, combined with the premise from [140] that the injection process has a large impact on flow structure, residence time, and detonation strength, strongly suggests that injector design significantly affects resulting NO_x emissions. However, despite the stark differences in RDE injector design and accompanying emissions, the average exit emissions levels in all cases are relatively low compared to data in [134]. The simulations in [134] were of 2-D idealized RDE systems though, so they do not take into account the non-idealities of practical 3-D RDEs with discrete injection that affect NO_x production. Nevertheless, RDE exit plane emissions levels in this study remain under 100 ppm on average, with local spikes not exceeding 200 ppm for RAI case 2. Since average NO_x exhaust levels in a stationary gas turbine amount to 22-240 ppm [172], the NO_x emissions levels found in this study are very similar to those in traditional gas turbines relying on pure deflagrative combustion. [134] specifically strays away from comparing RDE NO_x emissions to those in more traditional engines, as a direct comparison between vastly different engine designs and functions is difficult. Although a direct comparison still cannot be made between RDE and gas turbine emissions, and the corresponding exit plane emissions comparisons should be taken lightly, this study differs from [134] in that it explores more practical, 3-D, non-ideal RDE systems with multiple operating conditions. In addition, all cases are run at stoichiometric conditions to ensure an ideal burning scenario and ultimately an upper limit for NO_x emissions production. As such, less uncertainty remains in the correlations made in this study than in those expressed by [134], although further analysis may still be necessary to determine more nuance patterns of emissions evolution in specific RDE configurations.

7.6 Summary

Emissions are an important factor to consider when designing an RDE, yet little research has been done on the subject to date. The unique detonative flow characteristics of RDEs harbor uncertainty in how emissions should develop in these systems as compared to how they develop under traditional deflagrative combustion seen in gas turbine engines. Additionally, the non-idealities arising in practical 3-D RDEs should be assessed to determine their effects on flow structure and consequently emissions levels. This section studied the behaviors seen in practical RDEs under different geometric and operating conditions to understand how these ultimately affected resulting NO_x emissions patterns.

Before simulating NO_x emissions within full 3-D RDE systems, however, NO_x formation mechanisms were reviewed and an appropriate chemical mechanism was selected to represent NO_x reactions in the simulations, which was the modified Jachimowski mechanism from [151]. The selected mechanism was then validated across a range of 0-D, 1-D, and 2-D tests designed to test the suitability of such mechanism for use in simulating detonation-containing flows. Ignition delay values, NO_x emissions levels and species profiles, and detonation wave speeds were all found to be in excellent agreement with reference simulations and experiments, thus confirming the decision to use the modified Jachimowski mechanism in simulations of practical 3-D RDEs.

The 3-D RDE simulations involving NO_x chemistry were run for nearly ten wave cycles to allow enough time for NO_x to fully form within the systems. Instantaneous and temporally averaged data were then analyzed at mid-channel, radial, and exit plane locations to determine the effects differing detonation structures have on NO_x emissions patterns. Results showed a large discrepancy in NO_x levels between the AAI and RAI RDEs even at nominally similar mass flow rate conditions. The increased presence of parasitic combustion in the AAI RDE effectively reduced detonative combustion efficiency, leading to overall weaker detonation waves. This ultimately broadened the induction zone in this system, leading to delayed combustion and lower peak levels of heat release and thereby reduced overall NO_x emissions. It was noted that the parasitic combustion in the AAI RDE, induced by its injector design's propensity for recirculating hot product gases into the refill region, did lead to NO_x formation but the levels produced were significantly smaller than those seen in the RAI RDE in the direct wake of the detonation waves.

Furthermore, a strong correlation was found between detonation strength and NO_x

emissions, with greater peak pressure leading to greater NO_x formation. As mass flow rate was increased in the RAI RDE, detonation waves generally increased in strength in a staggered linear manner. In specific, wave speed and strength increased to a point of instability in the system until wave splitting occurred, wherein a marked reduction in wave speed and strength was noticed. Waves appeared to intensify linearly again with increasing mass flow rate. The effect of wave splitting was determined to greatly reduce NO_x emissions by way of the large reduction in wave strength. As such, all cases in this study, whether they experienced entirely steady operation or wave splitting processes, showed evidence that increasing detonation wave strength directly increases NO_x formation.

Another finding from the study was the greater radial uniformity seen in detonation structure and therefore NO_x emissions when mass flow rate increased. This highlighted the effect stronger detonations and injector stiffness have on resulting flow characteristics of fresh mixture into the detonation chamber. The lower mass flow rate cases showed increased axial impingement of fresh cool mixture into the chamber, resulting in greater detonation heights and delayed combustion and NO_x formation in the axial direction. Additionally, the location of this increased axial impingement near the outer wall shifted radial dominance of the detonation waves to the outer wall in these cases.

In terms of emissions levels at the exit plane of the combustor, results supported previous findings from mid-channel and radial data. It was noted that exit plane NO_x levels can be seen as a marker for system stability in RDEs given their sensitivity to wave instabilities and wave splitting processes. Finally, it was determined that despite the unique flow characteristics RDEs bring about over pure deflagrative combustion, average NO_x levels at the combustor exit remain similar to exhaust levels seen in stationary gas turbines from literature. This finding suggests the strong capability for RDEs to provide much more efficient combustion and work extraction than gas turbines without suffering from significantly higher emissions. However, as already noted in this section, care should be taken when designing an RDE for maximum efficiency, as the tradeoff for increasing efficiency and detonation strength is an increase in emissions levels.

Overall, this section provided a comprehensive view of the mannerisms of NO_x formation within practical RDEs, highlighting the various connections observed between NO_x and other important flow parameters, and how those connections relate to system-wide flow behavior and structure.

Chapter 8

Lagrangian Analysis in RDE Simulations

8.1 Lagrangian Analysis

8.1.1 Motivation

The goal of this section is to introduce Lagrangian analysis for use in numerical simulations of RDEs. Lagrangian analysis provides a unique method for describing fluid flow within a CFD simulation as compared to the Eulerian approach, as it uses the concept of a control mass as opposed to control volumes to follow a fluid element through the entirety of the flow domain. If used correctly within the context of RDE simulations, this type of data can provide important information regarding how fluid elements interact with detonation waves, as well as how pre-detonation conditions within the combustor affect post-detonation fluid behavior. Trajectories of fluid elements can be tracked with such an analysis, as well as residence time in the system. Lagrangian analysis provides a wide range of capabilities for analyzing RDE flow structures, and its presentation in this section seeks to highlight these capabilities and provide basis for further Lagrangian analysis of RDEs as seen in Sec. 8.2.

8.1.2 Lagrangian Analysis vs Eulerian Analysis

Lagrangian analysis can be a very useful tool in CFD to extract supplemental information to what is already collected from an Eulerian perspective, as the frame of

reference is changed to move with the fluid. In convential CFD, or in the Eulerian frame of reference, control volume analysis is employed wherein each cell in a mesh is a fixed control volume that allows for flow to enter and exit its domain. Fluxes of properties are calculated along boundaries between cells at each timestep, and flow parameters are updated accordingly in each cell. As such, the Eulerian cells track the fluid in time through a fixed space. This approach is inherently limited by the mesh resolution of the Eulerian cells, as the detail provided by such an approach only retains the fidelity of the minimum cell size, since properties are constant within a cell and no further division of properties is made within the cells themselves.

The Lagrangian frame of reference differs significantly from the Eulerian one, as it centers around a control mass instead of a control volume. This means that a Lagrangian particle, composed of a fixed mass, is tracked through the system in time and in space, as opposed to being in a fixed space as an Eulerian cell. As such, the Lagrangian perspective provides different information about the flowfield, as it shows a particular trajectory of the tracked particle through space and time. An example of Lagrangian particle trajectories inside a 3-D RDE is shown in Fig. 8.1, where the trajectories are colored by temperature. The trajectory information can be useful in determining flow behavior based on processes occurring within the domain, as the trajectory shows where exactly the fluid element of interest traversed. The additional spatial information also allows for residence time to be determined. Although the Lagrangian approach provides uniquely new information to be extracted from the flowfield in a CFD simulation, it comes with downsides as well. For one, in a strictly Lagrangian simulation, information regarding the entire flow domain is lost, as only particle trajectories are obtained and so the amount of data available for extraction is limited by the number of particles injected into the domain. It is obviously possible to increase the number of injected particles to properly saturate the domain, but this may come at a significant cost depending on the nature of the domain and the type of flow being modeled, in a similar way that Eulerian mesh size impacts simulation cost and performance. Secondly, the Lagrangian particles are still limited by the minimum timestep used in the simulation, which in turn relates to particle movement and the resulting spatial resolution achieved in the particle trajectories. As such, despite the unique benefits Lagrangian analysis garners over traditional Eulerian CFD, it is ultimately limited in the same manner that Eulerian simulations are by spatial and temporal resolution.

One interesting solution to obtain both the full flowfield information of the domain of interest and the individual trajectories of fluid elements is to couple the Eulerian

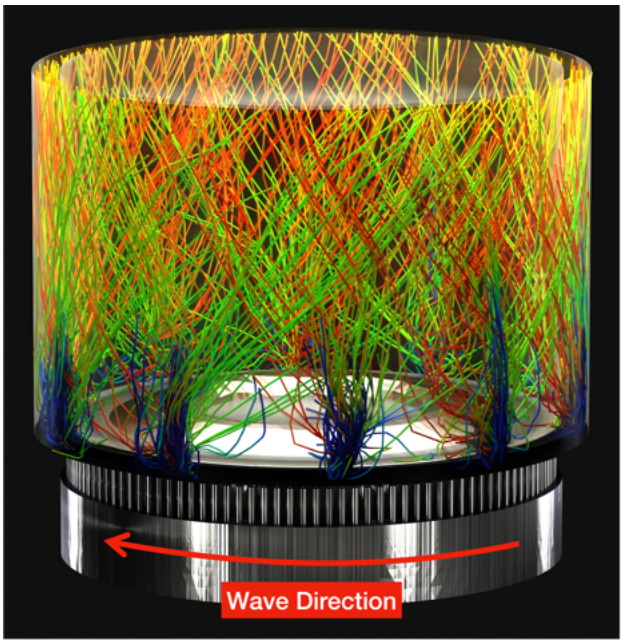

Figure 8.1: Particle trajectories throughout the detonation chamber in the AFRL RDE at every 12th injector, colored by temperature.

and Lagrangian methods together. This solution takes advantage of the benefits of both methods, allowing for macroscopic flow features to be analyzed with Eulerian information and detailed fluid trajectories to be analyzed with Lagrangian information. In coupling these two methods, the downsides to each one are not diminished, however, but they are combined in the sense that there is one limiting spatial and temporal resolution for the combined methodology. If this parameter is controlled properly in an Eulerian-Lagrangian simulation, then significant information can be gained from such a simulation that details both macroscopic flow features and microscopic flow trajectories. The Lagrangian analysis shown throughout this section involves the Eulerian-Lagrangian method, which will be described further in this section. Before the method is explained further, however, it is useful to understand how Lagrangian analysis has been used in previous research, which is discussed in the following two sections.

8.1.3 Lagrangian Uses in Experiments

To understand the benefits of using Lagrangian analysis, an examination of its use in recent research is performed. Experimentally, a method called PIV (particle image velocimetry) has been used to extract flow field parameters such as velocity magnitude so as to produce images showing flow structure along certain planes within an RDE. PIV is a non-intrusive, high accuracy, and high resolution method for obtaining detailed flow information, which has been used by several recent studies for RDEs in particular [108, 173, 174, 175]. One plot from [175], shown in Fig. 8.2, depicts velocity vectors at various axial locations downstream of an RDE throat nozzle with an attached aerospike. Such a plot provides detailed information about the uniformity of the flow in specific locations and response of the flow to geometric features. PIV measurements may also be used to understand periodicity of cycles in an RDE, as well as the stability of the system on the whole, as exemplified by work from [176]. Here, the changes in axial and azimuthal velocity components at the exit plane of the combustor are used to signify the location and propagation of detonation waves within the combustor. The wealth of experimental RDE research that effectively uses PIV measurements for a range of analysis applications speaks to the benefit that Lagrangian analysis can provide for understanding flow features within an RDE system.

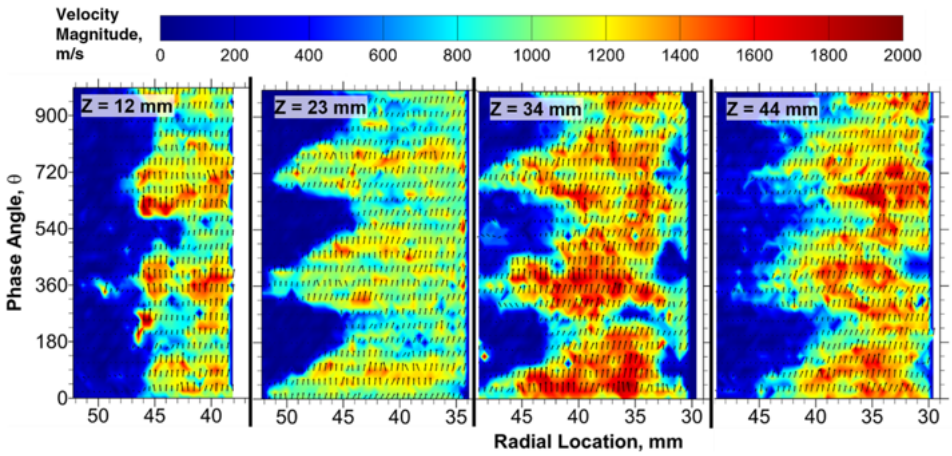

Figure 8.2: Velocity vectors and magnitude at different axial locations downstream of an RDE nozzle throat with an aerospike, from [175].

8.1.4 Lagrangian Uses with Numerical Approaches

On the numerical side of combustion research, Lagrangian analysis has been implemented in various ways to provide more robust spatiotemporal information within flowfields. A typical approach to utilizing Lagrangian analysis, which is the approach used in this section, is to couple Lagrangian analysis with Eulerian CFD, thus creating a combined Eulerian-Lagrangian description of the flow. The Lagrangian particles used in such an approach may represent the same phase as the fluid in the Eulerian component of the flow, thereby rendering the particles as simple trackers moving throughout the flowfield. This allows for the particles to track the trajectories of fluid elements moving through the system along with specific properties of the fluid such as temperature and pressure. The tracking method, termed Lagrangian Particle Tracking (LPT), can be accomplished in two different manners, namely through an offline or online approach. In the offline approach, particles are simulated in post-processing, which requires large disk space requirements, but provides flexibility in modifying the solution algorithm for better accuracy in trajectory integration, and allows for higher-order temporal interpolation given sufficient data [177]. Hamlington et al. have used an offline approach to model the thermochemical trajectories of particles in high-speed turbulent premixed flows. Contrary to the offline approach, the online approach calculates particle trajectories during runtime of the simulation, thus reducing storage requirements for the entire Eulerian flowfield for all timesteps. Several recent studies have implemented this approach for use in analyzing both compressible, turbulent, reacting flows [178, 179] and detonations alike [180]. In addition to the offline and online tracking methods used when particles represent the underlying fluid within the Eulerian frame, Lagrangian analysis may be used to represent separate phases of the fluid altogether. This technique is useful for modeling liquid-fueled detonations [181] and liquid-fueled RDEs [182, 183], wherein the fuel is in the liquid phase and is dispersed into the gas phase within the combustor, and the two phases fully react with one another through models such as evaporation models or drag models. A 3-D view of a temperature and heat release rate within an RDE using the two-phase Lagrangian approach, from [182], is shown in Fig. 8.3. Overall, numerical work has shown to use Lagrangian analysis in multiple beneficial ways to provide more robust models for combustion and better interpretation of processes occurring when fluid undergoes detonative combustion.

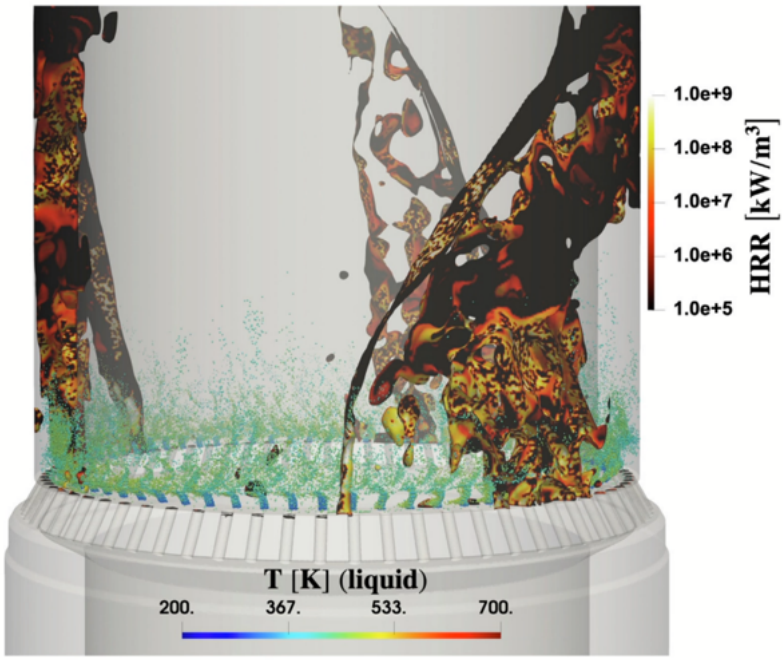

Figure 8.3: 3-D view of three rotating detonation waves in an full-scale RDE system, from [182]. Liquid droplets are colored by temperature and detonation wave fronts are colored by heat release rate.

8.1.5 Governing Equations for Lagrangian Particle Tracking

For the current work Lagrangian analysis is coupled to an Eulerian CFD framework in a one-way setup, wherein the Lagrangian particles rely on information from the underlying Eulerian flowfield to advance in time, but this information is not reciprocated back to the Eulerian cells and thus does not affect them. This type of Lagrangian analysis is known as LPT, as particles are simply tracked from point A to point B within the flow domain of the Eulerian simulation without actively affecting the flow, meaning that the particles are nothing more than massless tracers of flow behavior through the system. A more formal way of describing this is through the Stokes number, which is written as:

$$Stk = \frac{t_0 u_0}{l_0} \tag{8.1}$$

where t_0 is the relaxation time of the particle, u_0 is the fluid velocity, and l_0 is the characteristic length scale of the flow. The Stokes number basically represents how responsive particles are to surrounding flow. The response time of the particle, t_0, is dependant on the density and size of the particle itself. If this varies, as it would in a fully two-way coupled system wherein particles represent fluid droplets or the like, then the Stokes number varies and the particles may become more affected or less affected by the surrounding fluid. However, in the case of LPT, which is used here, particles are massless, so t_0 and the Stokes number are exactly 0. This means that the particles are instantaneously affected by the surrounding flow, and they are also imaginary tracer particles since they carry no mass. Thus, these particles rely on information from the Eulerian flowfield to move through the system, yet provide no information back to the underlying flow and are mainly used for calculating flow trajectories through space and time.

To track particles through time during the simulation with the LPT method, the particle position through time must be connected to the underlying Eulerian flow velocity, a relationship which is written as:

$$\frac{d\mathbf{r}}{dt} = \mathbf{U}_c, \tag{8.2}$$

where $\mathbf{r}$ represents the particle position vector, $\mathbf{U}_c$ is the carrier (Eulerian) velocity vector, and Δt is the simulation timestep. So for each change in timestep (Δt) the particle position is updated based on its current position at time t and the addition of the position change incurred from the underlying carrier velocity to the new time $t + \Delta t$. This update in the position vector of a particle is written as:

$$\mathbf{r}_{t+\Delta t} = \mathbf{r}_t + \mathbf{U}_c \Delta t, \tag{8.3}$$

where the t subscript is the current time and $t + \Delta t$ is the new time after completion of a single timestep Δt. Equations 8.2 and 8.3 fully define how the particles move in the LPT simulations described here, and no additional models are used (i.e. evaporation, drag, etc.) since the particles are simply massless tracer particles. The following section describes the implementation of this procedure into the UMReactingFlow solver for use in high-fidelity simulations of RDEs.

8.1.6 Application to UMReactingFlow Solver and Lagrangian Setup

The implementation of the LPT methodology to the UMReactingFlow solver involves one main modification to existing capabilities of the solver, which is simply to use the Eulerian-Lagrangian framework already built into the UMReactingFlow solver while disabling all models that incorporate mass and heat transfer between the Eulerian and Lagrangian phases. The UMReactingFlow solver has previously been built upon an Eulerian-Lagrangian framework for use in high fidelity simulations of detonation-containing two-phase flows (usually using liquid fuels). As such, previous studies using this solver have shown both canonical results of colliding jets impacted by a detonation wave [184] and applied results of a liquid-fueled RDE with comparisons to experiments [182]. The simulations presented here simply extend the capabilities of this established Eulerian-Lagrangian framework by allowing for massless, perfectly elastic particles to be tracked throughout the system, with implementation based on the governing equations provided in the previous section. This implementation is solely focused on particle movement as a function of the underlying Eulerian velocity, as seen in Eq. 8.2, where particle velocity is directly equal to Eulerian flow velocity. No additional drag model, evaporation model, or the like is used in this implementation, and so the implementation is considered a one-way coupling, as Lagrangian movement is informed by Eulerian flow properties, and no Lagrangian information is returned to be used by the Eulerian phase. At each time step during the simulation, the particles are advanced, and their position updated based on Eq. 8.3. The particles also store the history of gas phase properties that they encounter as they move from injection location to the exit. These properties are taken directly from the underlying Eulerian cells with no interpolation method used, so the recorded data is directly tied to the resolution of the Eulerian mesh.

For the particular simulations presented here, a structured injection scheme is used for the particle injection procedure. Within the solver code, parameters have been written to allow for easy modification of injection locations based on spatial coordinates and dimensions defined in input files. The code was customized to allow for distinct injection schemes within both fuel and oxidizer injectors. Figure 8.4 shows an example of the injection locations used for both fuel and oxidizer particles in the present simulations. It can be seen that the fuel particles are injected at the midpoints of the fuel injectors themselves, and they are positioned along the exit plane of the fuel injectors. A single particle is injected at each fuel injector midpoint, leading to a total

of 120 fuel particles injected per injection step. The oxidizer particles are injected in an axial line within the oxidizer throat, and are spaced equidistant from one another along this line within the axial bounds of the throat. The axial line forms a radially-facing ring when rotated around the combustor axis, and the radius of this ring is set to 0.063 m, essentially at the radial midpoint of the oxidizer throat. The axial line of particles consists of 5 particles per injection location around the circumference of the ring, and this axial line is repeated for every 1° around the circumference of the ring. This creates a total of 1,800 oxidizer particles injected within the oxidizer throat at each injection interval, which combined with the fuel particles yields a total of 1,920 particles injected per injection interval. The injection interval (Δt_{inj} in Fig. 8.4) is set to 1/20th of a wave cycle, and properties of particles are recorded at an interval of 1/48th of a wave cycle. For the present Eulerian-Lagrangian simulations, 4 wave cycles are simulated with injection occurring throughout the entirety of the simulations, with a single wave cycle time of roughly 0.24 ms and a total simulation time of 0.96 ms. Given the injection interval and the simulation time, it is seen that a total of 153,600 particles are injected in each simulation. These data recording and injection interval metrics were employed to ensure adequate statistical analysis within the confines of data size limitations. All Eulerian-Lagrangian simulations used throughout this report, including within this section as well as Sec. 8.2, utilize these same metrics. The simulations performed in particular are cases 2 through 4 for the AFRL RAI RDE, as first described in Sec. 7.5, and they are continued from the quasi-steady state H_2-Air-NO_x solutions shown in Sec. 7. General validation of these simulations is provided in the following section before additional analysis relating to NO_x formation is performed in Sec. 8.2.

8.1.7 Validation of LPT Method in RDE Simulations

In an effort to ensure that the LPT method previously described in this section retains accuracy and robustness for use in simulations of full-scale RDEs, an initial validation procedure is performed. The validation mainly consists of comparing Eulerian and Lagrangian properties from the simulations (cases 2 through 4 with the AFRL RDE) to ensure Lagrangian particles are properly representing the flow. As already stated in the previous section, validation of the UMReactingFlow solver has already been performed for high-fidelity simulations of detonation-containing flows using the Eulerian-Lagrangian framework to model two separate phases [184, 182]. As such, the validation presented here is mainly an additional validation of the Eulerian-

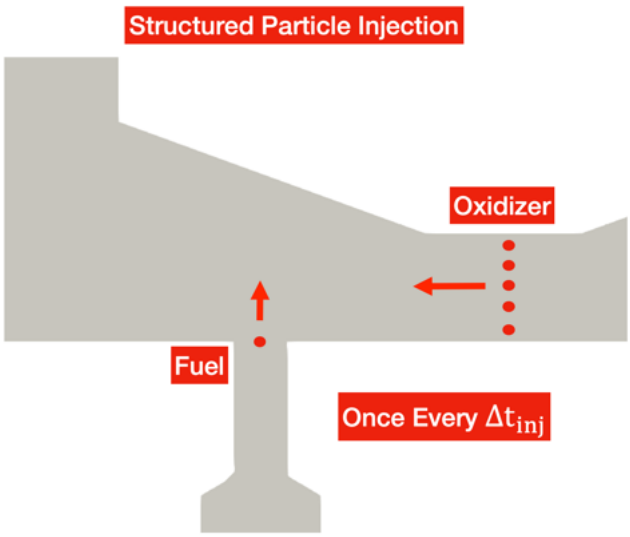

Figure 8.4: Example of structured injection of Lagrangian particles at specific locations within the fuel and oxidizer throats in the AFRL RAI RDE.

Lagrangian capabilities of the UMReactingFlow solver for LPT in particular. Since LPT is defined by massless particle tracking and the particle movement is therefore solely defined by the Eulerian carrier velocity, the present validation will mainly focus on velocity measurements between the Eulerian and Lagrangian descriptions. Additional comparisons are made between the fluid property of pressure to understand how the detonation wave is tracked between both descriptions.

As a starting point for analysis, the Lagrangian data is compared to Eulerian field information for equivalent variables. Figures 8.5 and 8.6 show data collected from both the Lagrangian and Eulerian methods within the RDE chamber, for case 2 and for all cases, respectively. The Eulerian data is obtained from fixed probes at the mid-channel of the detonation chamber. These probes are placed every 0.5 degrees azimuthally and are set at an axial location of 3 mm above the chamber bottom. Conversely, the Lagrangian particles record information as they move through the combustor, so different particles may be at different axial locations within the combustor at a specific time recording. A visual depiction of the location of the Eulerian probes versus the Lagrangian particles, along with a sample unwrapped pressure plot obtained from each dataset, is shown in Fig. 8.7. The key difference between the fixed probes and the moving particles leads to differences in the data collected, which is

explained further in this section.

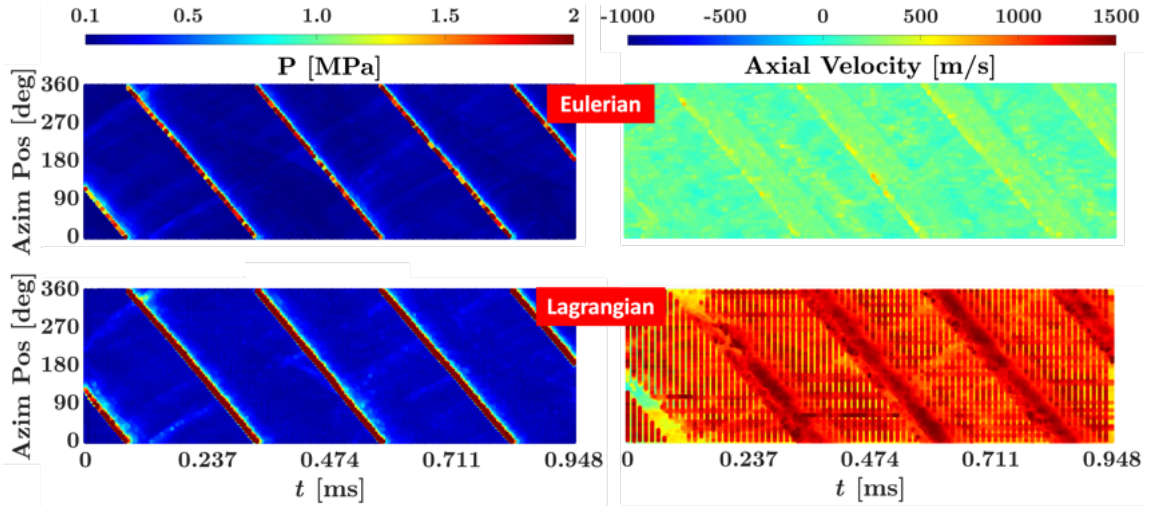

Figure 8.5: Pressure (left) and axial velocity (right) for case 2 within the RDE chamber through azimuthal position and time, recorded with Eulerian probes fixed azimuthally around the mid-channel of the annulus (top) and moving Lagrangian particles (bottom).

When viewing the pressure plots of Figs 8.5 and 8.6, the Eulerian and Lagrangian descriptions of the flow appear similar to one another from a macroscopic perspective. The wave front is captured properly in both descriptions, and similar pressure peaks are observed at this front. Additionally, weaker reflected and secondary waves can be observed in both descriptions across all cases. However, one noticeable difference is the greater uniformity in peak pressure seen at the wave front of the Lagrangian description. The Eulerian probes cannot reproduce this uniformity, as they are fixed to single axial locations within the mid-channel of the combustor. In contrast, the use of Lagrangian particles that move throughout all locations within the combustor assists in better defining the peak pressure at the wave front, as the various positions of the particles can map the irregular 3-D wave front present in such an RDE, especially if the wave front is shifted off from the locations of fixed probes, and due to the finite sampling rate of the Eulerian data.

Another interesting observation from Figs. 8.5 and 8.6 is that the lower pressures observed behind the wave front are generally higher from the Lagrangian perspective than from the Eulerian one. This is because the particles are moving through the

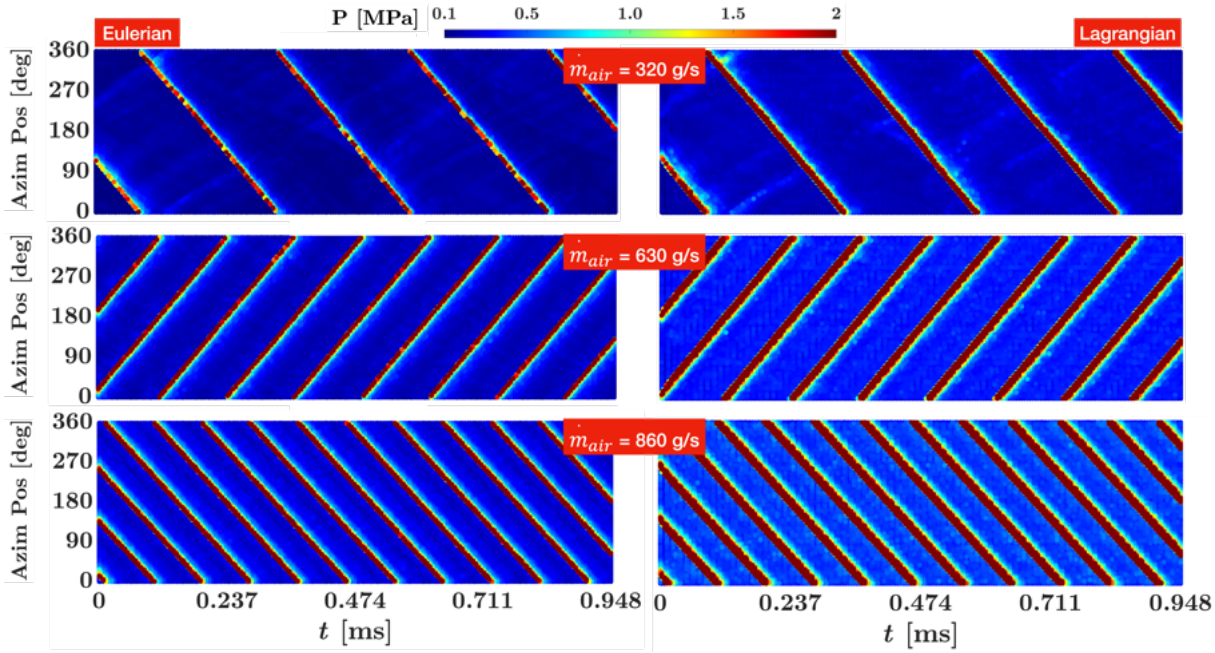

Figure 8.6: Pressure within the RDE chamber through azimuthal position and time for all AFRL RDE cases, using the Eulerian probes (left) and the Lagrangian particles (right).

system, so if they encounter a detonation wave they will be affected by the wave and the fluid properties they record will change accordingly. As such, after exiting a detonation wave, the particles will record higher pressures than ambient before ultimately expanding axially toward the chamber exit. Nevertheless, some particles do remain near the chamber bottom after contact with a wave, but these particles are a minority within the system.

Although only minor differences are seen in the pressure plots of Figs. 8.5 and 8.6, more prominent ones are seen in the axial velocity plots for case 2 in Fig. 8.5. Both descriptions of axial velocity capture the wave front properly, but the Lagrangian axial velocities are generally much higher than the Eulerian ones. This result links to the previous mention that the particles are actively moving through the system. This movement with respect to recording properties within the chamber allows for the post-detonation velocity of fluid elements coming into contact with detonation waves to be revealed by the Lagrangian plot, which is not possible with fixed probes. The

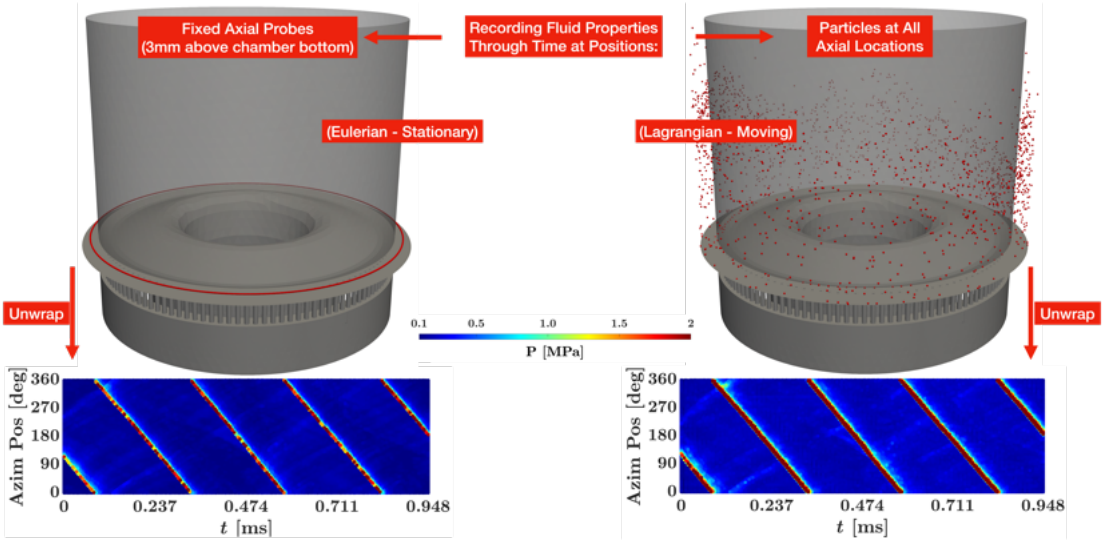

Figure 8.7: Depiction of how both the Eulerian probes (left) and Lagrangian particles (right) are used to generate position-time diagrams of pressure.

general increasing axial position of particles as they move through the chamber and collide with detonation waves, along with the expansion of fluid in the post-detonation region within the chamber, allows for the moving particles to record higher axial velocities throughout the entirety of the post-detonation region. However, it should still be noted that the Lagrangian plot is not indicative of all fluid behavior within the system, as some particles remain that record lower axial velocities throughout their life-cycles, but these values are plotted over in the plot shown. Nevertheless, the Eulerian plot is also not indicative of all fluid behavior within the system, as its restriction to one fixed axial location hinders it from providing information elsewhere downstream in the chamber.

In a similar vein to previously shown results in Fig. 8.5 for case 2 specifically, average pressure and axial velocity versus axial position at the mid-channel of the combustor is shown in Fig. 8.8 from both the Lagrangian and Eulerian perspectives. The Eulerian averages are again taken from mid-channel data, but this data now comes from all mid-channel cells throughout the length of the combustor rather than fixed probes at the base of the chamber. The Lagrangian data comes from the particles themselves at all times and at locations within the same mid-channel envelope as the Eulerian data, specifically within an 800 micron width annular envelope at

the center of the detonation chamber. The Lagrangian data taken from this envelope is binned into axial locations with a resolution of 200 microns to obtain averages at each axial location. Reasonable agreement is observed in both pressure and axial velocity between the two descriptions, which is to be expected given that the Lagrangian particles record information based on the Eulerian cell they reside in at the time of recording. For locations near the base of the detonation chamber, the values of pressure and axial velocity are almost identical between descriptions. The main difference seen in this data, however, is the slight discrepancy between the Eulerian and Lagrangian pressures as axial location increases. This data is representing fluid that has most likely been in contact with a detonation wave after significantly advancing through the detonation chamber. With this notion, it can be surmised that the individual Lagrangian particles composing the average pressure profile in Fig. 8.8 may represent fluid that is at different stages of maturity within the detonation chamber after contact with a detonation wave, which may provide evidence for why a difference is seen in the Lagrangian pressure profile as compared to the Eulerian one. Additionally, the Lagrangian description is limited by the particle number, injection frequency, and injection recording interval, which can all factor into the completeness of the average pressure profile presented. As such, minor differences in pressure between the two descriptions seem reasonably acceptable for the present validation study, especially given that the axial velocity measurements remain extremely similar throughout the axial extent of the detonation chamber.

To further confirm the accuracy of particle movement defined by the Eulerian flowfield in the present simulations, a comparison is made between the Eulerian and Lagrangian descriptions of both axial and azimuthal velocity components for all cases, which are plotted in Figs. 8.9 and 8.10, respectively. Both figures show excellent agreement between the axial and azimuthal velocity components across all axial locations within the detonation chamber, with only minor discrepancies seen in all cases between 10 and 25 mm into the chamber. As already observed for case 2 specifically, this location corresponds to the detonation wave region, and so the discrepancies observed are a result of the detonation wave itself having some effect on the recorded properties. Despite these discrepancies, the Lagrangian profiles respond almost exactly as the Eulerian profiles do with increasing axial location, be it through the gradual increase in axial velocity or the oscillatory behavior observed in azimuthal velocity induced by the detonation wave, and the profiles generally match from a qualitative standpoint. Additionally, the RMS errors of the profiles as a whole, which are tabulated in Tab. 8.1, are relatively low for all cases, with axial velocity errors

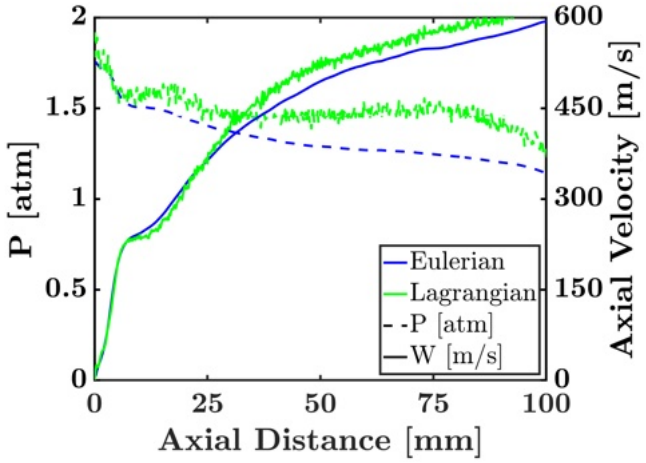

Figure 8.8: Average pressure and axial velocity versus axial position within the combustor for Eulerian and Lagrangian data of case 2. Eulerian data comes from mid-channel averages and Lagrangian data comes from averages of particles within the same mid-channel envelope as the Eulerian data. An axial distance of 0 mm denotes the chamber bottom.

within 11.33% and azimuthal velocity erorrs within 6.19%. Also, the Eulerian profiles mostly fall within the 99% confidence intervals of the Lagrangian profiles, which are marked at multiple axial distances in Figs 8.9 and 8.10. This is significant because it provides 99% confidence that the mean flow behavior is being tracked properly with the Lagrangian method and a given amount of particles that satisfies the Central Limit Theorem. If particle count was further increased, though, it would naturally follow that the Lagrangian mean would converge with the Eulerian one and the confidence interval would narrow accordingly. However, reasonable agreement is already seen with the current particle count based on the Lagrangian confidence intervals, which thereby provides assurance in the use of the Lagrangian recording methodology in this context. Overall, this data shows that for several different simulations with various flow rates and detonation waves present, the velocity profiles match reasonably well between the Eulerian and Lagrangian descriptions. Since the velocity of the Eulerian flowfield is directly connected to the Lagrangian particle movement, the similarity in this quantity across descriptions provides confidence that the Eulerian-Lagrangian simulations are working as intended, and the Lagrangian particles are

accurately recording flow information as they are tracked throughout the RDE.

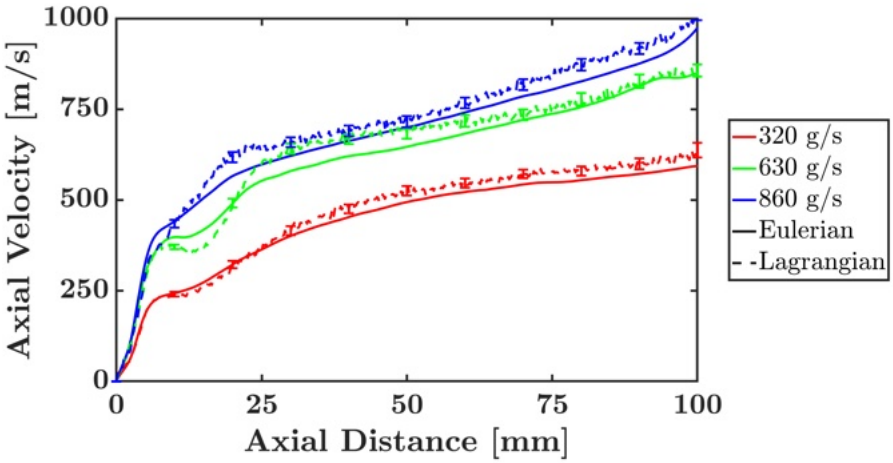

Figure 8.9: Average axial velocity versus axial position within the combustor for Eulerian and Lagrangian data of all AFRL RDE cases. Eulerian data comes from mid-channel averages and Lagrangian data comes from averages of particles within the same mid-channel envelope as the Eulerian data. An axial distance of 0 mm denotes the chamber bottom. The error bars in the Lagrangian data represent the 99% confidence interval about the mean.

Case	$\dot{m}_{oxi}$ [g/s]	RMS % Errors (L vs E)	
		Axial Velocity [m/s]	Azim. Velocity [m/s]
2	320	11.25	6.19
3	630	11.33	6.17
4	860	9.99	5.01

Table 8.1: RMS percentage errors between (L)agrangian and (E)ulerian data for axial and azimuthal velocity components throughout the axial extent of the mid-channel of the combustor. Data shown is for all AFRL RDE cases.

To provide additional confirmation that the Lagrangian particles properly represent the Eulerian flowfield through the chamber, a sensitivity analysis was performed on the axial binning resolution used to obtain axial velocity profiles through axial position. In the sensitivity analysis, multiple binning resolutions between 50 and

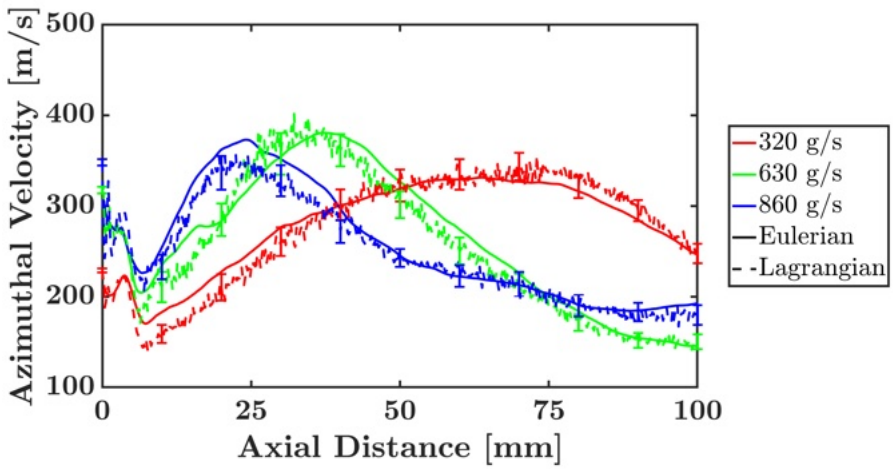

Figure 8.10: Average azimuthal velocity versus axial position within the combustor for Eulerian and Lagrangian data of all AFRL RDE cases. Eulerian data comes from mid-channel averages and Lagrangian data comes from averages of particles within the same mid-channel envelope as the Eulerian data. An axial distance of 0 mm denotes the chamber bottom. The error bars in the Lagrangian data represent the 99% confidence interval about the mean.

1600 μm were used to obtain axial velocity profiles from Lagrangian particles, and the RMS percentage errors were computed against the Eulerian data which had a nominal resolution of 200 μm. Based on the methodology of the Eulerian-Lagrangian method previously presented in this section, along with the previous results showing good agreement between Eulerian and Lagrangian data using similar resolutions through the chamber, it is expected from this analysis that the RMS errors between Eulerian and Lagrangian data will decrease to a limiting value when the resolutions between both datasets converge. Figure 8.11 shows the trend in RMS percentage error with varying axial binning resolution in the Lagrangian data for all cases.

From Fig. 8.11, the expected behavior is seen in the general trend of RMS percentage error for all cases. As the axial binning resolution is decreased towards the resolution used in the Eulerian simulation, the RMS percentage errors decrease accordingly. Once the Eulerian resolution of 200 μm is reached, the errors begin to level off around 10%. As noted previously, this value of roughly 10% is considered good agreement given the particle recording time and particle count used. The value

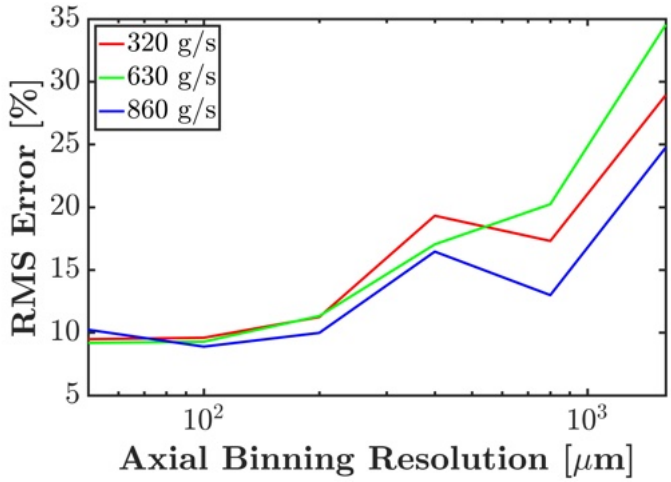

Figure 8.11: RMS percentage errors between Lagrangian and Eulerian data for axial velocity components throughout the axial extent of the mid-channel of the combustor, plotted as a function of axial bin resolution in the Lagrangian data. All errors in Lagrangian data are relative to the Eulerian data at a fixed axial resolution of 200μm. Data shown is for all AFRL RDE cases.

at which the leveling behavior occurs with decreasing bin size may be reduced with increasing particle count, although this was not directly tested. Nevertheless, the trend seen wherein RMS error decreases with decreasing bin size provides confidence in the accuracy of the Lagrangian data at representing the Eulerian flowfield for a similar resolution. With decreasing resolution in the Lagrangian data beyond the Eulerian resolution (200 μm), the RMS error continues to decrease slightly, then begins to increase again at 50 μm. This behavior shows the expected limiting behavior of error between Eulerian and Lagrangian data when resolution converges, and it also shows the negative effect of increasing RMS error that a significant decrease in bin size has on the average axial velocity recorded by the Lagrangian particles. As resolution is decreased too much beyond the Eulerian resolution, not enough particle data may be present to provide an accurate representation of the axial velocity, and the RMS error suffers accordingly. Even so, the limiting behavior observed as resolutions converge between the Eulerian and Lagrangian descriptions, along with the generally good agreement seen between the descriptions at similar resolutions, suggests that the Eulerian-Lagrangian flow solver is working properly, and the Lagrangian particles

adequately represent flow behavior throughout the RDE for all AFRL RDE cases.

8.1.8 Summary

This section introduced the concept of Lagrangian analysis in CFD so that it may ultimately be applied to the RDE simulations viewed in this report, particularly in Sec. 8.2. The Lagrangian formulation was contrasted to the Eulerian formulation, with specific note taken between the ideas of control masses and control volumes. The use of Lagrangian techniques in both experiments and simulations was shown so as to emphasize the benefits of data acquisition it brings in the goal to better define the processes fluid elements undergo within RDE systems. The specific form of Lagrangian analysis selected for use here was defined, which was namely online Lagrangian Particle Tracking (LPT), and its theoretical formulation and application to the UMReactingFlow solver was described. Application to the UMReactingFlow solver included mention of particle injection frequency, fluid property recording frequency, and the specific location and structured nature of injections. Lastly, a validation procedure was performed for the proposed Eulerian-Lagrangian method, with specific attention given to pressure and velocity. Pressure plots constructed from both Eulerian probes and Lagrangian particles showed similar behavior in representing the detonation wave front through position and time, with minor differences attributed to the inherent movement of particles with the Lagrangian method. For velocity, both the axial and azimuthal velocity components were compared through axial position between Eulerian and Lagrangian data, and reasonable agreement was seen in resulting RMS percentage errors. Additionally, limiting behavior in the RMS percentage errors was observed with converging resolutions between Lagrangian and Eulerian data. The introduction of the LPT method and its validation in this section provide confidence in the application of the method in simulations of practical RDEs as is performed in Sec. 8.2.

8.2 NO_x Emissions using Lagrangian Analysis in RDEs

8.2.1 Motivation

The goal of this section is to provide further analysis for the Lagrangian simulations detailed in Sec. 8.1 by providing an application for which such analysis will prove beneficial to knowledge of RDE flow behavior. This application pertains to NO_x formation within an RDE, and this section explores how fluid properties obtained from Lagrangian particle tracks can provide insight into RDE flow mechanisms that directly affect NO_x production. Residence times obtained from Lagrangian trajectories are compared between mass flow rate conditions and linked to NO_x behavior within an RDE system. Additionally, the unique spatial information provided by the Lagrangian description is leveraged to determine mechanisms for post-detonation NO_x production based on pre-detonation conditions of particles, such as pre-detonation temperature. This collective analysis provides evidence for not only how NO_x formation occurs within an RDE system, but also for how the system behaves as a whole and how fluid properties are connected and are affected by changes in operating parameters. Thus, this section seeks to advance the general knowledge of flow behavior in an RDE through the use of Lagrangian trajectory information, with specific application to NO_x emissions. As previously alluded to in Sec. 7, little research has been done on NO_x formation in RDEs, and none of the work that has been done has used either high-fidelity simulations of a practical RDE system or an extensive Eulerian-Lagrangian description of the flow. Thus, great benefit can be obtained from the work presented in this section in terms of the understanding of NO_x production in general and how it connects to specific flow behaviors within the RDE system.

8.2.2 Simulation Setup

The simulations used in this section follow the same specifications for LPT as described in Sec. 8.1, and are continued simulations of the H_2-Air-NO_x simulations presented in Sec. 7. The cases simulated are cases 2 through 4 with the AFRL RAI RDE, as first described in Sec. 7.5, with stoichometric hydrogen-air at several mass flow rate conditions. The present simulations are run for 4 wave cycles of roughly 0.24 ms, leading to a total simulation time of 0.96 ms. Roughly 150,000 particles are injected throughout the simulation, with all major fluid properties recorded by

each particle as it traverses through the domain. For additional details regarding the specific metrics used for injection, such as injection location, injection frequency, recording frequency, and the like, please refer to Sec. 8.1.

8.2.3 General Particle Behavior

Figure 8.12 shows the 3-D trajectories of the first-injected particles through the full simulation at every location around the RDE annulus for case 2. In relation to these trajectories the detonation wave is rotating clockwise around the annulus. As such, the moment when particles interact with the detonation wave can be observed, as the particles take on an induced velocity from the wave, causing their trajectories to change to include an azimuthal component. This behavior is similar to the induced swirl seen in [185]. It is also observed from Fig. 8.12 that particle temperature is proportional to axial height within the combustor, which is expected given that most particles will be processed by a detonation wave within the first few centimeters axially into the chamber and in turn heat up. However, the interesting observation is that NO_x is not directly proportional to axial height, as some particles exhibit low NO_x near the exit of the combustor whereas others exhibit high NO_x. This nuanced behavior is partially due to the pre-detonation temperatures of particles before encountering a detonation wave, which can have a significant effect on the resulting wave that is formed and corresponding emissions. These effects are discussed in the next section.

8.2.3.1 Residence Time vs Mass Flow Rate

Since the residence time of fluid elements within the combustor will have a direct affect on temperature and therefore NO_x production, it is imperative to look at the connection between such parameters. However, to properly view this connection in the context of the present simulations in which mass flow rate is varied, it is important to first view the connection between residence time and mass flow rate. Although this connection may seem trivial, as higher mass flow rates should inherently reduce residence time in the combustor, it is still important to highlight the connection, as it reveals the relationship between pressure and velocity within the RDE. As seen in Fig. 8.13, which shows the spatiotemporal averages of pressure and axial velocity along the mid-channel of the RDE for all cases, higher pressures are observed with increasing mass flow rate, which leads to greater capacity for expansion behind the detonation

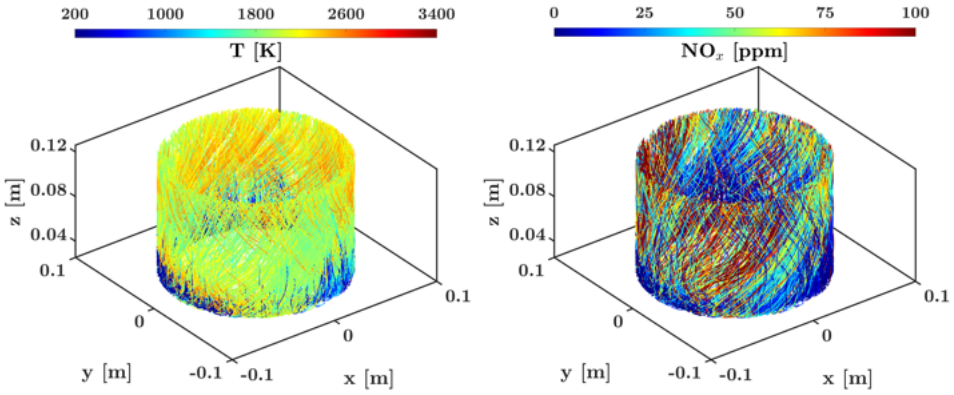

Figure 8.12: 3-D trajectories of the first-injected particles through 0.96 ms, originating from every location around the RDE annulus for case 2, colored by temperature (left) and NO_x (right). The detonation wave is rotating clockwise from this perspective.

waves. This results in greater axial velocity components of the flow with increasing axial distance inside the detonation chamber, as also shown in Fig. 8.13. The presence of stronger shocks accounts for the higher average pressures observed with increasing mass flow rate, as also observed by [167], which thus leads to greater axial expansion and faster exit flow rates. To see the effect this has on residence time, mid-channel averages of axial velocity are plotted for all cases in Fig. 8.14, with average post-detonation particle pathlines superimposed on the wave fronts and limited by wave cycle. This figure shows a clear distinction between behavior at different mass flow rates, with particles showing a more axially-dominant path in the post-detonation regime as mass flow rate is increased. This result, along with the greater peak axial velocities observed in the underlying mid-channel averages, suggests that the particles in the higher mass flow rate cases are controlled more by the axial component of velocity than the azimuthal component, and as such are transported to the combustor exit faster, thereby reducing overall residence time. If the residence times for the average post-detonation particle pathlines shown in Fig. 8.14 are extrapolated to the exit plane, the resulting overall residence times are calculated as 0.302 ms, 0.179 ms, and 0.188 ms for cases 2, 3, and 4, respectively. As such, it is confirmed from both the Eulerian and Lagrangian data that with increasing mass flow rate, the axial velocity component directly increases due to greater expansion from higher pressure conditions, and as a result particle residence time decreases. Although this result is expected and may seem trivial, it provides greater understanding for the connected

mechanisms in the RDE system that determine overall flow behavior.

On a separate note regarding Fig. 8.13, the 95% confidence intervals are plotted in a few key locations in addition to the mean profiles. These intervals provide an interesting perspective from which to view the mean profiles, as they are constructed from the standard deviations in the properties in temporal space after they are already averaged spatially throughout the mid-channel of the annulus. This means that the plotted confidence intervals give the notion of how much error could persist in the mean profile values through time. The determination to construct confidence intervals in this manner that disregards the uncertainty along the spatial dimension was made because it is already known that significant variation will persist throughout space in the mid-channel, as there are distinctly different flow regions present, such as the refill region and the detonation wave itself, that considerably alter the flow. As such, a more fitting confidence interval to calculate in this case is one which only considers the variation in the spatially-averaged mid-channel properties through time, as this will provide a notion of the uncertainty of the mean axial profiles in time. The fact that both the pressure and axial velocity profiles exhibit relatively narrow 95% confidence interval bands across all cases suggests that the spatially-averaged mid-channel behavior remains rather steady through time. This is an important observation, as it proves the existence of steady behavior overall in the coupled processes within the RDE through time, despite the presence of more granular, chaotic processes when viewing the RDE in terms of uncoupled flow structures at separate time instances. This measurement also sheds some light on the perspective from which to view specific uncertainties in such systems, and how changing this perspective can provide valuable insight into overall behavior.

8.2.3.2 Residence Time vs NO_x

Given the correlation between residence time and mass flow rate described previously, the correlation between residence time and NO_x can now be viewed using the Lagrangian data. Figure 8.15 shows scatter plots of NO_x and residence time of all particles as a function of pressure and temperature for all cases. From this figure it is immediately apparent that the residence time decreases as mass flow rate increases, as already suggested in the previous subsection, and NO_x decreases accordingly. In addition, the highest amounts of NO_x are seen at generally lower pressures and higher residence times, and significant NO_x production generally only occurs after a threshold temperature of roughly 1800 K is reached. Significant NO_x levels at low pressures,

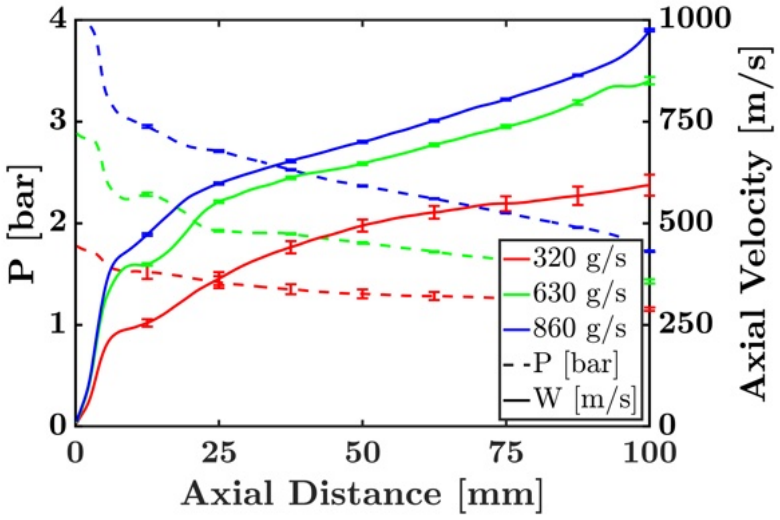

Figure 8.13: Spatiotemporally averaged pressure and axial velocity along the combustor mid-channel. The error bars represent the 95% confidence interval about the mean as averaged through time only. As such, the confidence intervals are built from standard deviations in the spatially-averaged mid-channel parameters upon averaging through time.

high temperatures, and high residence times is indicative of deflagrative burning occurring within the detonation chamber. This behavior can be exacerbated by the presence of weaker, less efficient waves, which has already been observed for lower mass flow rate cases in Sec. 7. This therefore explains the increased amount of high NO_x levels in the low pressure, high temperature regions of lower mass flow rate cases. As for the increase in NO_x levels after a specific temperature is reached, this is also expected since the NO_x mechanism used in the present simulations is based on thermal NO_x production, which inherently has a specific activation temperature at which significant NO_x formation commences.

If the same Lagrangian data is viewed within the context of particle properties as they cross over the exit plane of the combustor, a similar correlation is observed wherein residence time is proportional to both average exit plane NO_x and average exit plane temperature, as seen in Tab. 8.2. Additionally, the average residence times at the exit plane ultimately decrease with increasing mass flow rate, as was already surmised from previous mid-channel results, and the residence time values are very

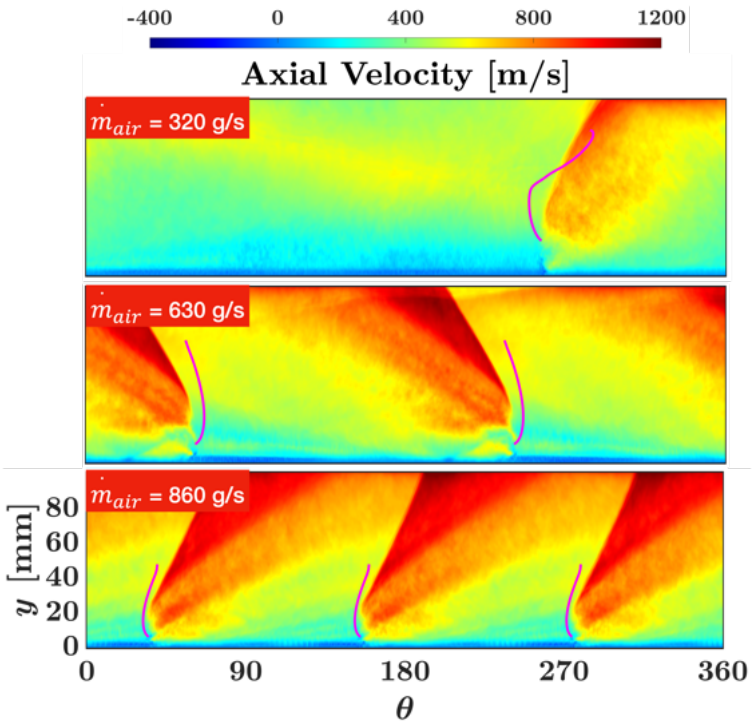

Figure 8.14: Wave shifted temporal averages of axial velocity at the mid-channel for all AFRL cases. The pink lines at the wave fronts represent average particle pathlines after hitting a wave, limited by time between waves.

similar to the extrapolated ones from the post-detonation particle pathlines detailed in the previous subsection. Another interesting observation from Tab. 8.2 is that the amount of particles that actually reach the exit plane increases with increasing mass flow rate. If more particles reach the exit in the same time frame, they must inherently be traveling faster, which is why residence times are lower. This also helps prevent inefficient deflagration from occurring within the detonation chamber, as average temperatures realized at the exit are reduced, which also leads to a reduction in NO_x seen at the exit plane. All of this data points to a strong connection being present between residence time and NO_x production, but to further confirm this relationship it would be useful to understand particle behavior in relation to the detonation waves themselves. The analysis of particles interacting with detonation waves under various flow conditions, along with the consequences of these interactions in relation to NO_x

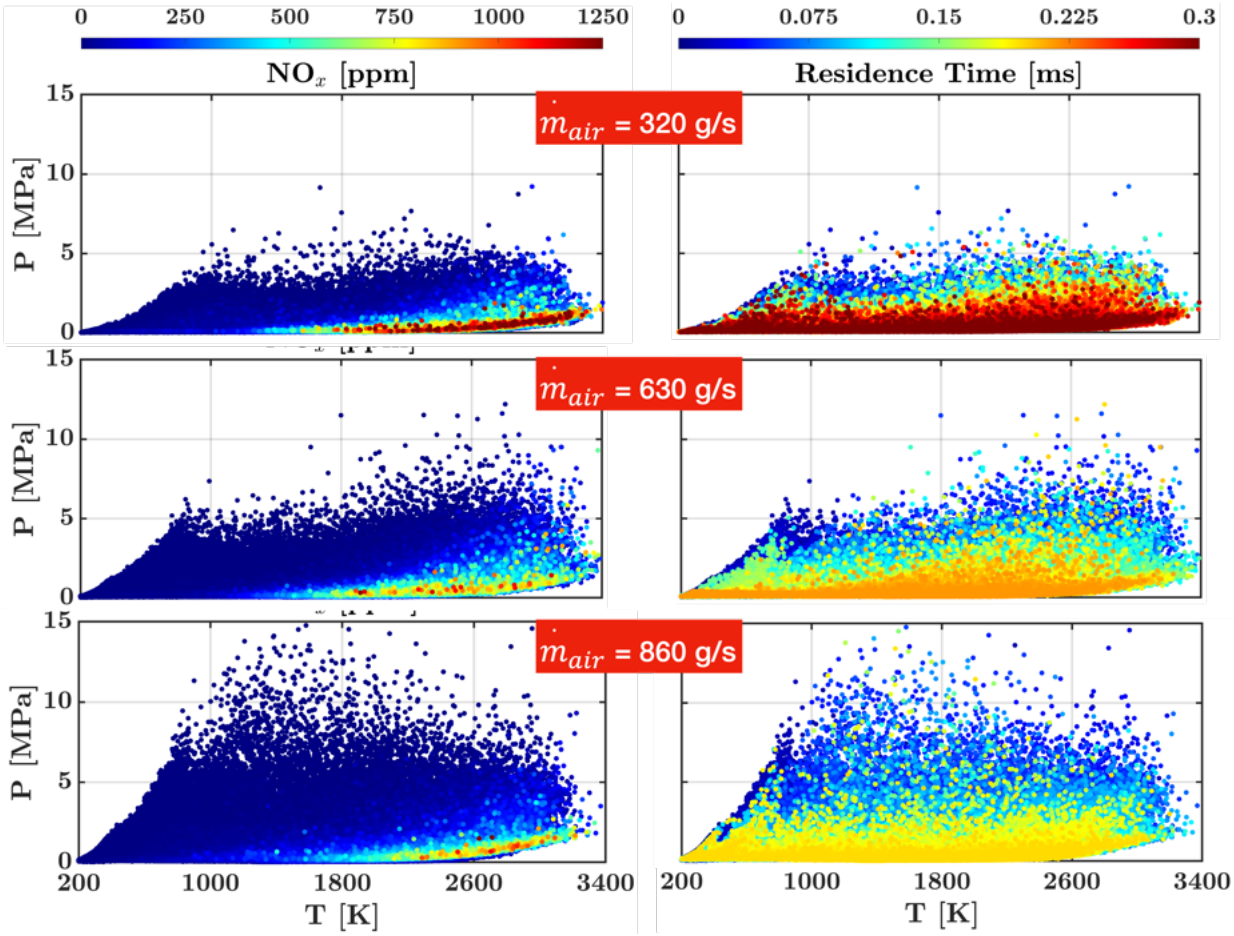

Figure 8.15: Scatter plot showing all particle recordings of pressure and temperature, colored by both NO_x (left) and residence time (right), for each case with the AFRL geometry. The residence times plotted are limited by the average residence time to reach the exit plane of the combustor.

production, is presented in the following section.

Case	$\dot{m}_{oxi}$ [g/s]	# of Waves	Residence Time [ms]	NO_x [ppm]	T [K]	P [kPa]	Particles Reaching Exit [%]
2	320	1	0.305	68	2028	121	66
3	630	2	0.218	62	1865	139	75
4	860	3	0.198	34	1841	143	78

Table 8.2: Average properties observed by particles at the exit plane of the combustor for each case with the AFRL geometry. Residence times are calculated from particle injection to reaching the exit plane of the combustor.

8.2.4 Interactions Between Particles and Detonation Waves

8.2.4.1 Conditioning on Pre-Detonation Temperature

To understand how detonation waves process reactants and affect fluid elements within an RDE system, it is useful to examine the fluid properties of particles after first encountering a detonation wave. Particle tracks are first separated by initial pre-detonation conditions immediately before their first collision with a detonation wave, namely three temperature conditions which are $T < 500$ K, $500\ K \leq T \leq 1000$ K, and $T > 1000$ K. The separated particle tracks are then averaged at each time interval after they collide with the detonation wave, a process that is depicted in Fig. 8.16. This is done for all particle tracks for each pre-detonation temperature condition to obtain average NO_x, temperature, pressure, axial velocity, and heat release curves as shown in Figs. 8.18, 8.19, and 8.20.

Before looking specifically at post-detonation behavior for all three temperature conditions, the particle tracks can be viewed in physical space in a similar manner to Fig. 8.12. A random selection of 500 particle tracks in each temperature condition is plotted throughout the detonation chamber for case 2 in Fig. 8.17. The tracks are colored by temperature, and the magenta lines at fixed axial locations represent the average axial position of all particles in each temperature condition upon first colliding with the detonation wave. One observation from these plots is that for all conditions, significant temperature rise is seen in the particles only after the particles reach the detonation wave. Before this point, close to the chamber bottom, particles remain at temperatures well below 1000 K. Despite the increased axial extent at which low temperature particles persist in the combustor with increasing pre-detonation temperature condition, several tracks are seen in these conditions in which temperature

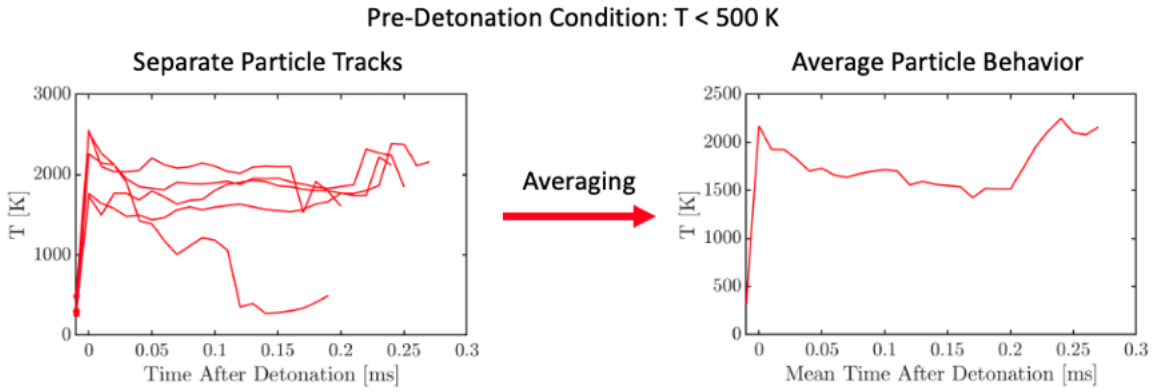

Figure 8.16: Averaging process used for particle properties at specific pre-detonation conditions. This example shows averaging temperature over 5 particle tracks with pre-detonation conditions of T $<$ 500 K, which are the first plotted points denoted by $*$ in the separate track plot (left).

rises closer to the chamber bottom, indicating the occurrence of parasitic combustion before detonation. In fact, it is because of this additional axial space and corresponding residence time before wave contact that particles in these conditions are allowed to increase in pre-detonation temperature, in contrast to particles that are subjected to the detonation wave in much shorter residence times. This correlation between residence time and pre-detonation temperature will be discussed further in a later section.

Another interesting observation from Fig. 8.17 is that a greater number of particles exhibit high temperatures (above 1800 K) for a significant axial extent above the average axial position of wave contact with increasing pre-detonation temperature. This is because the average pressure at wave contact is higher for higher pre-detonation temperatures, so when wave contact occurs, the relative spike in pressure across the wave front will be reduced with increasing average pressure. This ultimately reduces the impact the detonation wave has on affecting post-detonation expansion, thereby increasing the time for expansion to occur and the fluid to cool accordingly. As such, if pre-detonation temperature is high, then the inherently higher post-detonation temperature will remain higher for a greater period of time. This observation is crucial to understanding how NO_x emissions should ultimately behave in the post-detonation region in an RDE, and it is shown in Fig. 8.18, which provides basis for the next topic

of discussion.

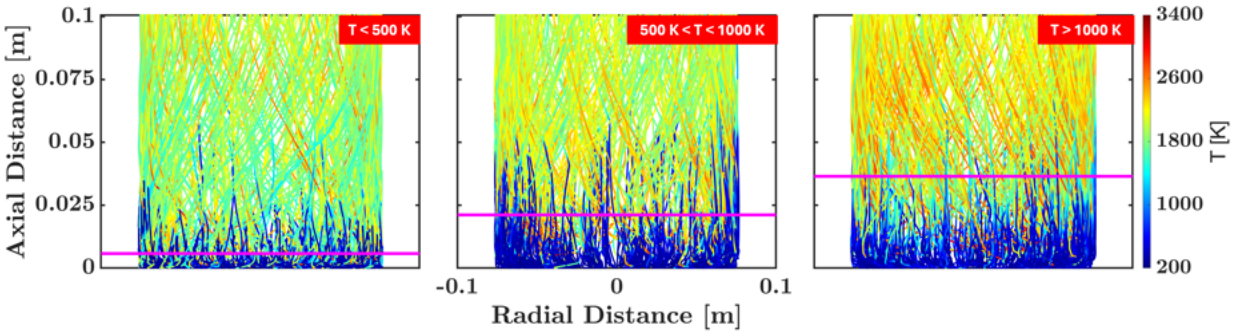

Figure 8.17: Trajectories of 500 randomly selected particles for each temperature condition for case 2, colored by temperature. Magenta lines at fixed locations represent the average axial position at which particles first collide with a detonation wave.

Figure 8.18 shows average NO_x and temperature values of tracked particles through time for all cases after first colliding with a detonation wave. Data is separated based on the initial temperature of the particles immediately before being affected by the detonation wave. Post-detonation particle behavior is shown through time that is normalized by the average wave cycle time, τ, which is also shown in Tab. 8.3 for each case. The data in Fig. 8.18 shows that for all ranges of initial temperatures before the detonation wave, an initial spike in temperature is seen after the detonation wave, followed by a corresponding spike in NO_x formation. However, significant NO_x formation is only seen after a certain threshold temperature of roughly 1800 K is reached. This temperature threshold is expected, as 1800 K is roughly the temperature at which the thermal mechanism of NO_x production, which is the main focus of the chemistry mechanism used, becomes significant [131], allowing for a chain of reactions to occur between atomic nitrogen and combustion radicals to form NO_x. When temperatures decrease below this threshold, NO_x levels decrease accordingly. This observation indicates that the process of generating significant levels of NO_x is insensitive to the initial temperature and is mainly predicated on if the threshold temperature for nitrogen oxidation is reached.

Despite the insensitivity of the initial temperature to the process of generating significant NO_x production, the initial temperature does affect the overall spike in NO_x production and peak value behind the detonation wave. For the initial temperature ranges $T < 500$ K, $500\ K \leq T \leq 1000$ K, and $T > 1000$ K the average increases

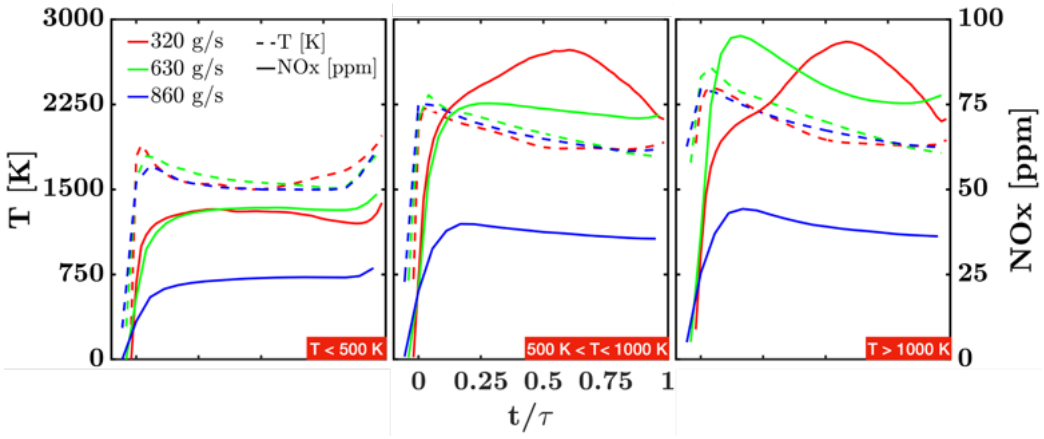

Figure 8.18: Average NO_x and temperature of particles through normalized time after first collision with detonation wave for all AFRL RDE cases, grouped by pre-detonation temperature. The first data point shows pre-detonation properties immediately before collision with a detonation wave. Time 0 represents the moment the particles interact with the detonation wave. Time 1 represents 1 azimuthal wave cycle between waves in the system.

in temperature across the detonation wave between all cases were 465%, 208%, and 30%, respectively. The corresponding average increases in NO_x across the detonation wave between all cases were 16,721%, 2,839%, and 417%, respectively. This shows a clear trend that for each case as the initial temperature increases, the detonation wave becomes weaker and the temperature spike across the wave decreases, leading to a smaller spike in NO_x produced. Additionally, higher levels of NO_x are already present in the particles with higher initial temperatures, with average NO_x values at initial temperatures above 1000 K roughly 63 times higher than those with temperatures below 500 K for all cases. This is most likely because these particles were injected into post-detonation regions where temperatures were already elevated and NO_x had already formed. As such, when these particles first experience a detonation wave the threshold temperature is met again and they produce more NO_x in addition to the NO_x already present. Interestingly, though, a limit on peak NO_x production is present in this system, as evident in Fig. 8.18, as the peak NO_x values are first seen to increase with an increase in initial temperature above 500 K and then stabilize after a further increase past 1000 K. One explanation for this is that the rate limit is reached for either combustion radical production or nitrogen oxidation beyond this

temperature, and so NO_x production slows as a result. However, the post-detonation temperature remains high for longer durations for all initial temperatures above 500 K, which keeps the fluid above the threshold temperature for NO_x production and allows for steady NO_x levels at high values.

Figure 8.19 shows a similar plot to that of Fig. 8.18 but with average NO_x and pressure plotted for all cases instead of average NO_x and temperature. In these plots the data is still separated by the same pre-detonation temperature conditions as before. From this data, a significantly larger increase in pressure is observed across the detonation wave for initial temperatures below 500 K as compared to initial temperatures above 500 K. This is because a detonation wave is stronger in a colder temperature medium as a result of increased reactivity at colder temperatures and reduced heat transfer losses, thus allowing for more energy to directly translate to the wave and cause a larger increase in both temperature and pressure across the wave. As such, the percentage increase of NO_x is proportionally smaller across the wave for increasing initial temperature, as mentioned before, and the corresponding average percentage increases of pressure between all cases are smaller as well, with the $T < 500$ K, $500\ K \leq T \leq 1000$ K, and $T > 1000$ K conditions yielding pressure increases of 648%, 261%, and 28% across the wave, respectively. This reduction in pressure difference across the wave with increasing initial temperature corroborates that the detonation waves are weaker with increasing temperature, thereby reducing their possible heat release and thus the amount of NO_x that can be formed from their resulting product gases. Although less NO_x is formed relatively across the wave with increasing initial temperature, the absolute NO_x formation is still greater with increasing temperature due to the increased residence time above the threshold temperature in the post-detonation regime.

In addition to the increasing pre-detonation temperature corresponding to smaller pressure increases, weaker waves, and less NO_x production relatively across the wave, the effect of mass flow rate is seen in Fig. 8.19, with generally higher peak pressures seen as mass flow rate increases. This again is most likely due to an overall colder medium in the higher mass flow rate cases, lending to the formation of stronger shocks and higher peak pressures. This is confirmed in the distributions of particles in each pre-detonation condition, wherein for case 2, 52.61% of the particles held an initial pre-detonation temperature of $T < 500$ K, 8.79% of the particles held a temperature of $500\ K \leq T \leq 1000$ K, and 38.60% of particles held a temperature of $T > 1000$ K. When increasing mass flow rate to cases 3 and 4, the percentage of particles in the $500\ K \leq T \leq 1000$ K condition remain relatively unchanged, with percentages of 9.83%

and 9.21% for cases 3 and 4, respectively. However, a dramatic shift is seen between the low temperature condition and high temperature condition with increasing flow rate, as the percentages for the T $<$ 500 K condition change to 75.69% and 79.11% and the percentages for the T $>$ 1000 K condition change to 14.48% and 11.69%, both for cases 3 and 4, respectively. As such, these particle distributions corroborate the claim that less high-temperature particles are present when mass flow rate is increased, resulting in a colder overall medium for stronger shocks to form in. These stronger shocks can of course yield a greater increase in relative NO_x across the wave, but this does not have as significant of an effect on absolute NO_x in the system as does pre-detonation temperature as previously shown. As a result, since high-temperature pre-detonation conditions have been shown to lead to higher post-detonation absolute NO_x emissions, a clear correlation can be made wherein NO_x production is inversely correlated to mass flow rate. Residence time remains a key factor in understanding this correlation, which will be discussed later in this work.

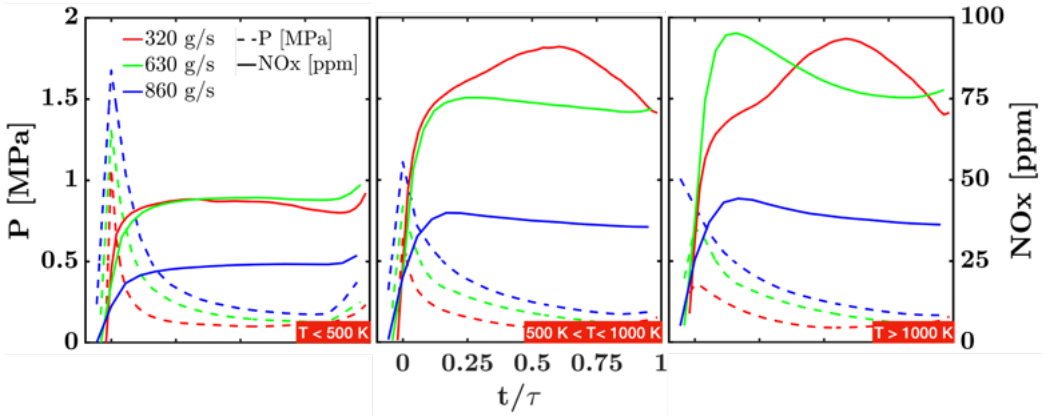

Figure 8.19: Average NO_x and pressure of particles through normalized time after first collision with detonation wave for all AFRL RDE cases, grouped by pre-detonation temperature. The first data point shows pre-detonation properties immediately before collision with a detonation wave. Time 0 represents the moment the particles interact with the detonation wave. Time 1 represents 1 azimuthal wave cycle between waves in the system.

Another observation from Fig. 8.19 is that the high pressures of particles with initial temperatures below 500 K are expanded much more quickly back to ambient conditions than the pressures seen in the higher temperature particles. This is

because of the direct correlation between expansion velocity and the pressure difference between the high-pressure region behind the wave front and ambient conditions. Through this correlation, a stronger detonation wave generates a higher pressure differential and thus increases expansion velocity, causing more rapid expansion behind the wave. In turn, a faster response is observed in fluid temperature, since a fluid that is expanding faster will cool down faster as well. This response is reflected in Fig. 8.18, with the initial decrease of temperature behind the detonation wave beginning more abruptly after the detonation for the stronger wave condition ($T < 500$ K) than for the weaker wave conditions. As a direct consequence of this behavior, along with the fact that pre-detonation temperature is already higher for the weaker wave conditions, the residence time at high temperatures is shorter for the stronger wave condition, resulting in a faster response in NO_x levels being reduced. However, it should still be noted that the larger pressure and temperature differentials brought about by the stronger detonation waves still increase the differential in NO_x produced by the waves, albeit for shorter residence times behind the waves. If particles are subjected to multiple waves, however, they will be subjected to longer residence times at higher temperatures and will produce more NO_x. Although not shown in Figs. 8.18 and 8.19, which only focus on post-detonation properties during a single wave cycle, secondary spikes in temperature and pressure can be observed in cases where multiple waves are present, resulting in sustained high temperatures and in turn sustained high levels of NO_x behind the initial wave.

Figure 8.20 shows yet another similar plot to that of Fig. 8.18 but with average axial velocity and heat release rate plotted for all cases. The trends in heat release rate closely follow the trends seen in pressure, as pre-detonation heat release increases with increasing pre-detonation temperature, which leads to greater absolute NO_x formation. This seems like a trivial result, but it is worth noting to strengthen the connection between temperature and heat release in the sense that an increased pre-detonation temperature promotes combustion before contact with a detonation wave, or parasitic combustion, which is then signified by greater heat release from such a process. Absolute heat release may not show a clear trend across all temperature conditions, but relative heat release across the wave weakens with increasing pre-detonation temperature, as reactants are already burned before wave contact, thus limiting the detonative burning that can occur and weakening the waves. Heat release also shows similar behavior to pressure with increasing mass flow rate, as greater flow rates exhibit both greater heat release and pressure, although the heat release values across all mass flow rates are not significantly different overall.

When viewing the axial velocity plots of Fig. 8.20, it is observed that the post-detonation values generally increase with increasing pre-detonation temperature and pressure. This is because the fluid is already at a higher initial axial velocity before wave contact in the higher temperature cases, which arises from the parasitic combustion experienced by the fluid, followed by expansion processes occurring in the pre-detonation regime. The higher initial axial velocity ultimately allows the expansion process behind the wave to elevate the axial velocity of the fluid to a greater absolute value in the post-detonation regime. Absolute axial velocity values are especially linked to pressure values, as in the case of increasing mass flow rate in the system, the spike in pressure across the detonation wave increases, and the axial velocity realized in the post-detonation regime rises as well. These greater magnitudes of axial velocity behind the wave are indicative of greater expansion and reduced fluid temperatures, which provides more support for why NO_x emissions are generally lower at higher mass flow rates. Relative changes in axial velocity remain similar across all temperature conditions, with the average difference between peak velocity immediately after wave contact and pre-detonation velocity ranging from 300 to 400 m/s. This may indicate that, although wave strength is indeed changing as a result of temperature conditions before wave contact, as evidenced by post-detonation pressure and heat release, it doesn't directly affect the resulting change in fluid velocity. From this data it appears that the more direct contributor to post-detonation axial velocity magnitude is the pre-detonation velocity itself, which is directly affected by temperature and pressure changes stemming from loss mechanisms in the pre-detonation regime.

8.2.4.2 Conditioning on Pre-Detonation Mixture Fraction

To further understand the post-detonation behavior of particles in the RDE, a pre-detonation mixture fraction (Z) condition is used in place of temperature. The three conditions by which the data is separated are $Z < 0.33$, $0.33 \leq Z \leq 0.67$, and $0.67 < Z$. Average post-detonation temperature and NO_x are plotted for each of these conditions in Fig. 8.21. The data shows expected behavior, as the lowest mixture fraction condition (relating to the most oxidizer in the mixture) produces the greatest amount of NO_x behind the detonation wave. Additionally, for all pre-detonation conditions, the greatest NO_x levels are seen in the lower mass flow rate cases. This behavior indicates that greater mixedness of fuel into the oxidizer stream in general produces more NO_x, and that greater mixedness is present in the lower mass flow rate

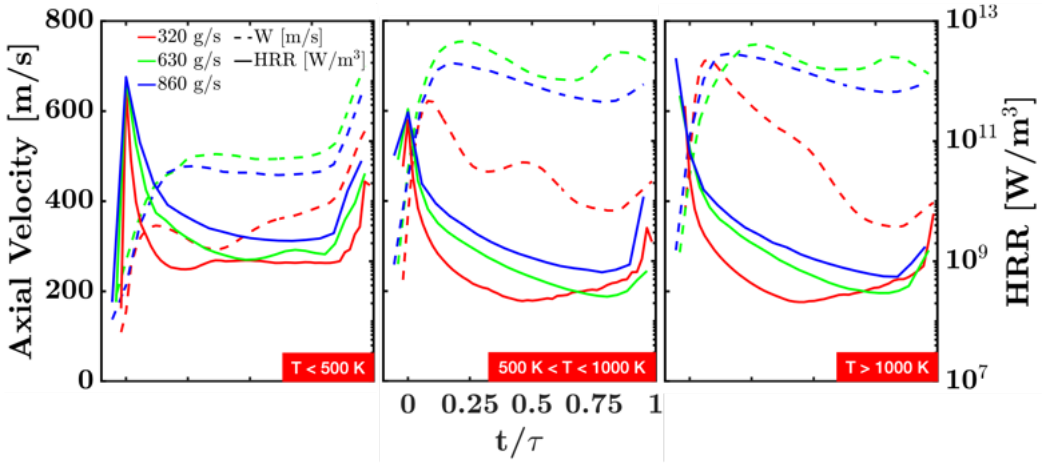

Figure 8.20: Average axial velocity and heat release rate of particles through normalized time after first collision with detonation wave for all AFRL RDE cases, grouped by pre-detonation temperature. The first data point shows pre-detonation properties immediately before collision with a detonation wave. Time 0 represents the moment the particles interact with the detonation wave. Time 1 represents 1 azimuthal wave cycle between waves in the system.

cases where greater NO_x is seen as a result. However, this increased mixing seen in the lower mass flow rate case can potentially be allowing pre-burning in the overall mixture before it can be processed by the detonation wave. This behavior is confirmed by the increased pre-detonation temperatures seen as mass flow rate decreases in the system, and it explains why both the waves are weaker and the NO_x emissions are greater as a result.

In terms of the percentages of particles in each mixture fraction condition, it is seen that the percentage of high mixture fraction particles ($Z > 0.67$) immediately before detonation increase by 85.3% from case 2 to case 3 and by 38.5% from case 3 to case 4, which is indicative of less overall mixing of the fuel into the oxidizer in the system. However, as evidenced in Tab. 8.3, which details the normalized residence times of particles in specific pre-detonation temperature and mixture fraction conditions, the absolute timescales of mixing for the $Z < 0.33$ condition before detonation scale according to the wave cycle time, τ, which decreases rather linearly with increasing mass flow rate and wave number. This means that for the particles that do sufficiently mix in each case, the mixing occurs at a rate that is correlated to the

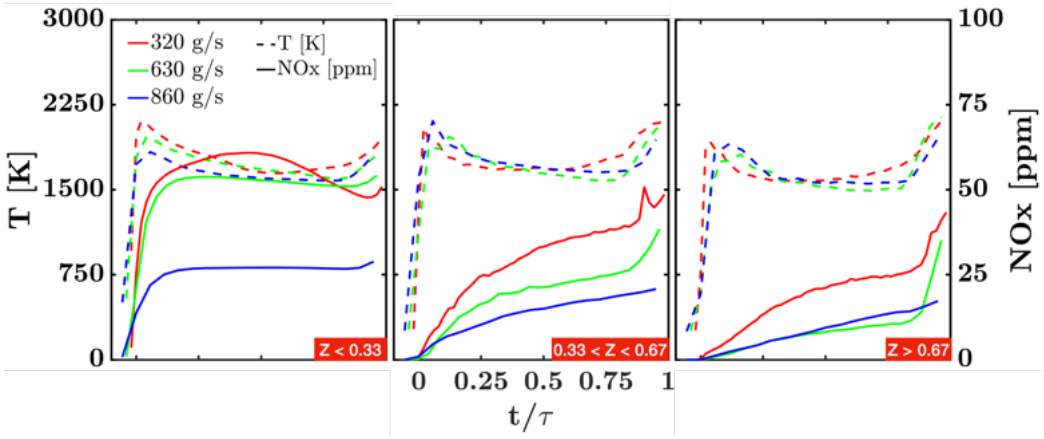

Figure 8.21: Average NO_x and temperature of particles through normalized time after first collision with detonation wave for all AFRL RDE cases, grouped by pre-detonation mixture fraction. The first data point shows pre-detonation properties immediately before collision with a detonation wave. Time 0 represents the moment the particles interact with the detonation wave. Time 1 represents 1 azimuthal wave cycle between waves in the system.

mass flow rate, so higher mass flow rate cases allow for particles to reach lower mixture fraction states more quickly. This faster mixing process in the higher mass flow rate cases may leave the pre-detonation mixture less mixed overall from a percentage perspective, but it allows for faster overall mixing that promotes uniformity in the fuel-air mixture processed by the detonation wave due to the faster injection recovery time with increasing mass flow rate [137]. As such, greater mixture uniformity in the pre-detonation regime can help mitigate parasitic combustion before mixture processing by the detonation wave, which is reflected in the reduction of high pre-detonation temperature particles at increasing mass flow rates. This ultimately reduces the residence time for which particles remain at high-temperatures, which again supports the conclusion that increasing flow rate in an RDE reduces the exposure of fluid to high temperature conditions in the system, which in turn reduces NO_x emissions.

Case	# of Waves	τ [ms]	T < 500 K $[t/\tau]$	500 K < T < 1000 K $[t/\tau]$	T > 1000 K $[t/\tau]$	Z < 0.33 $[t/\tau]$	0.33 < Z < 0.67 $[t/\tau]$	Z > 0.67 $[t/\tau]$
2	1	0.249	0.29	0.52	0.70	0.47	0.09	0.06
3	2	0.124	0.38	0.69	0.78	0.47	0.10	0.07
3	3	0.089	0.39	0.73	0.76	0.47	0.20	0.11

Table 8.3: Residence times of particles from injection up to reaching pre-detonation temperature and mixture fraction conditions immediately before contact with detonation waves, normalized by average wave cycle times (τ).

8.2.4.3 Connection Between Mass Flow Rate, Residence Time, and NO_x Emissions

When observing the residence times of particles in more detail, the connection between mass flow rate, residence time, and NO_x formation becomes more apparent. Tab. 8.3 shows the normalized residence times of particles in specific pre-detonation temperature and mixture fraction conditions, along with the average cycle time between waves in the system. From this data it is apparent that the normalized residence times for both mixture fraction (as already explained above) and temperature conditions remain insensitive to changes in mass flow rate. This suggests that all particles are moving faster in the system, as the absolute residence times decrease with decreasing cycle time. This can be noted in the temperature and pressure profiles shown in Figs. 8.18, 8.19, and 8.21, as the normalized profiles between all mass flow rate cases remain in line with one another through time, especially upon first contact with the detonation waves. Overall residence times confirm this notion of faster overall fluid movement with increasing flow rate, as the average residence times from injection to crossing the exit plane of the combustor are 0.305 ms, 0.218 ms, and 0.198 ms for cases 2, 3, and 4, respectively. This data, coupled with the fact that the percentage of particles in high-temperature pre-detonation conditions decreases with increasing mass flow rate, supports the conclusion that a reduction in residence time directly reduces NO_x emissions levels. Additionally, the conclusions relating to pre-burning, mixing, and pre-detonation temperature affecting NO_x production further align with the relationship between mass flow rate, residence time, and NO_x production. As such, it can be gleaned from the LPT description of RDE NO_x emissions that as mass flow rate is increased in the system, residence time is reduced, therefore limiting

the amount of fluid that can be exposed to high-temperature conditions for extended periods. These high-temperature conditions correspond to the greatest amounts of NO_x production in the post-detonation regime, so their limiting as mass flow rate increases ultimately reduces overall NO_x in the RDE as a result.

8.2.5 Summary

This section extended the analysis of NO_x formation in RDEs, first presented in Sec. 7, by applying the LPT method described in Sec. 8.1 to the AFRL RDE cases. The simulations were started from the final states achieved in Sec. 7 and were run for roughly four additional wave cycles. Initial analysis involved a description of general particle behavior within the system for the various flow rate conditions, with specific relationships between residence time, mass flow rate, and NO_x emissions outlined.

Regarding interactions between particles and detonation waves, particle properties immediately before being processed by detonation waves, along with particle properties after the detonation wave passed, were analyzed to determine the effect pre-detonation properties have on resulting NO_x emissions. It was found that lower initial temperatures correlated to stronger detonation waves and thus larger pressure, heat release, and temperature differentials across the waves. This led to larger increases in relative NO_x produced across the detonation waves. Additionally, it was found that the most significant NO_x formation occurred when the particle temperature held above a threshold temperature of 1800 K, which was in line with previous literature on the mechanism of thermal NO_x production. For all ranges of pre-detonation temperatures the threshold temperature was reached and significant NO_x was produced behind the detonation wave, but the stronger detonation wave condition ($T < 500$ K) showed more rapid expansion directly behind the wave, which helped to cool the post-detonation gases more quickly and reduce the residence time of particles above the threshold temperature. Nevertheless, the stronger detonation wave conditions produced the largest relative increases in NO_x across the wave, indicating that detonation strength was directly correlated to NO_x production in a practical RDE system.

In terms of absolute NO_x emissions levels in the post-detonation regime, it was shown that higher-temperature pre-detonation conditions generated the most NO_x emissions. Additionally, the amount of high-temperature particles in the pre-detonation regime significantly reduced with increasing mass flow rate, which is most likely why overall NO_x emissions decreased with increasing mass flow rate. It was found that the

normalized residence times of particles in the pre-detonation regime were insensitive to mass flow rate, suggesting that all particles were faster in the system as mass flow rate was increased. This trend also held for the overall residence times of particles within the combustor, and it corroborated the claim that increasing mass flow rate directly decreases residence time, which in turn decreases overall NO_x emissions in the RDE.

Furthermore, post-detonation behavior was examined under several mixture fraction pre-detonation conditons in place of temperature pre-detonation conditions. The results showed that higher mixture fraction particles ($Z > 0.67$) increased with increasing mass flow rate, suggesting less overall mixing down to the $Z < 0.33$ condition from a percentage perspective. However, the normalized residence times for different mixture fraction conditions in the pre-detonation regime again showed insensitivity to mass flow rate, signifying faster overall mixing with increased mass flow rate, thus mitigating pre-burning and high-temperatures in the pre-detonation regime and thereby helping to reduce NO_x emissions with increasing mass flow rate. The reduced mixing timescales with increasing mass flow rate also supported the general connection seen between mass flow rate, residence time, and NO_x emissions within this particular RDE system.

The conclusions from this section ultimately strengthened some of the previous links observed in Sec. 7, such as the link between temperature and NO_x formation, and extended them to show how pr-detonation properties significantly affect post-detonation emissions characteristics. The application of the LPT method allowed for pre-detonation, post-detonation, and overall residence time behavior to be captured and related to NO_x emissions, thereby increasing the amount of valuable data that can possibly be extracted from high-fidelity simulations of RDEs for the purpose of defining emissions behavior.

Bibliography

[1] Chacon, F., and Gamba, M., "Study of Parasitic Combustion in an Optically Accessible Continuous Wave Rotating Detonation Engine," *AIAA Scitech 2019 Forum*, 2019. https://doi.org/10.2514/6.2019-0473.

[2] Chacon, F., and Gamba, M., "Technique for the Quantification of Temporally Resolved Wave Properties from Two-Dimensional Periodic Data: Circuit Wave Analysis," *to be Submitted to AIAA Journal*, 2019.

[3] Shepard, J., Feleo, A., and Gamba, M., "Effects of Inlet Area Ratio on Operability of an Axial Air Inlet Rotating Detonation Combustor," *AIAA Propulsion and Energy 2021 Forum*, Paper No. AIAA 2021-3676, 2021. https://doi.org/10.2514/6.2021-3676.

[4] Feleo, A., Chacon, F., and Gamba, M., "Effects of Heat Release Distribution on Detonation Properties in a H2/Air Rotating Detonation Combustor from OH* Chemiluminesence," *AIAA Propulsion and Energy 2019 Forum*, Paper No. AIAA-2019-4045, 2019. https://doi.org/10.2514/6.2019-4045.

[5] Feleo, A., White, L. W., and Gamba, M., "Effects of CO2 Diluent on Rotating Detonation Combustor Operation," *AIAA Scitech 2021 Forum*, Paper. No AIAA-2021-0901, 2021. https://doi.org/10.2514/6.2021-0901, URL https://arc.aiaa.org/doi/abs/10.2514/6.2021-0901.

[6] Chacon, F., "Non-Ideal Phenomena in Rotating Detonation Combustors," Ph.D. thesis, University of Michigan, 2020.

[7] Chacon, F., Feleo, A. D., and Gamba, M., "Secondary waves dynamics and their impact on detonation structure in rotating detonation combustors,"

Shock Waves, Vol. 31, No. 7, 2021, pp. 675–702. https://doi.org/10.1007/s00193-021-01034-6.

[8] Abdulmohsin, R., *Gas dynamics and heat transfer in a packed pebble-bed reactor for the 4th generation nuclear energy*, Missouri University of Science and Technology, 2013.

[9] Feleo, A. D., and Gamba, M., "Evaluation of Uncertainties of Pressure Gain Measurements in Rotating Detonation Combustor," *AIAA Journal*, Vol. 62, No. 1, 2024, pp. 108–126.

[10] Feleo, A., Chacon, F., and Gamba, M., "Uncertainties in Thrust and EAP Measurements of a Rotating Detonation Combustor with Axial Air Inlet," *AIAA Propulsion and Energy 2020 Forum*, Paper No. AIAA-2020-3856, 2020. https://doi.org/10.2514/6.2020-3856, URL https://doi.org/10.2514/6.2020-3856.

[11] Chacon, F., Feleo, A., and Gamba, M., "Impact of Inlet Area Ratio on the Operation of an Axial Air Inlet Configuration Rotating Detonation Combustor," *AIAA Propulsion and Energy 2019 Forum*, Paper No. AIAA 2019-4450, 2019. https://doi.org/10.2514/6.2019-4450.

[12] Duvall, J., Chacon, F., Harvey, C., and Gamba, M., "Study of the Effects of Various Injection Geometries on the Operation of a Rotating Detonation Engine," *2018 AIAA Aerospace Sciences Meeting*, Paper No. AIAA-2018-0631, 2018. https://doi.org/10.2514/6.2018-0631, URL https://doi.org/10.2514/6.2018-0631.

[13] Rankin, B. A., Richardson, D. R., Caswell, A. W., Naples, A., Hoke, J., and Schauer, F., "Imaging of OH* Chemiluminescence in an Optically Accessible Nonpremixed Rotating Detonation Engine," *53rd AIAA Aerospace Sciences Meeting*, Paper No. AIAA-2015-1604, 2015. https://doi.org/10.2514/6.2015-1604.

[14] Rankin, B. A., Fotia, M. L., Paxson, D. E., Hoke, J. L., and Schauer, F. R., "Experimental and numerical evaluation of pressure gain combustion in a rotating detonation engine," *53rd AIAA Aerospace Sciences Meeting*, 2015. https://doi.org/10.2514/6.2015-0877, URL http://arc.aiaa.org.

[15] Sbalzarini, I. F., and Koumoutsakos, P., "Feature point tracking and trajectory analysis for video imaging in cell biology," *Journal of structural biology*, Vol. 151, No. 2, 2005, pp. 182–195.

[16] Schneider, C. A., Rasband, W. S., and Eliceiri, K. W., "NIH Image to ImageJ: 25 years of image analysis," *Nature methods*, Vol. 9, No. 7, 2012, pp. 671–675.

[17] Farrance, I., and Frenkel, R., "Uncertainty of measurement: a review of the rules for calculating uncertainty components through functional relationships," *The Clinical Biochemist Reviews*, Vol. 33, No. 2, 2012, p. 49.

[18] Alam, M., Setoguchi, T., Matsuo, S., and Kim, H., "Nozzle geometry variations on the discharge coefficient," *Propulsion and Power Research*, Vol. 5, No. 1, 2016, pp. 22–33.

[19] Gordon, S., and McBride, B. J., "Computer program for calculation of complex chemical equilibrium compositions and applications. Part 1: Analysis," *NASA RP 1311*, 1994.

[20] Anand, V., St. George, A., Driscoll, R., and Gutmark, E., "Analysis of Air Inlet and Fuel Plenum Behavior in a Rotating Detonation Combustor," *Experimental Thermal and Fluid Science*, Vol. 70, 2016, pp. 408–416. https://doi.org/https://doi.org/10.1016/j.expthermflusci.2015.10.007.

[21] Shepard, J., Feleo, A., and Gamba, M., "The Effect of Facility Induced Back-pressure on Rotating Detonation Combustor Operation," *AIAA Scitech 2022 Forum*, Paper No. AIAA 2022-0517, 2022. https://doi.org/10.2514/6.2022-0517.

[22] Chacon, F., and Gamba, M., "OH PLIF Visualization of an Optically Accessible Rotating Detonation Combustor," *AIAA Propulsion and Energy 2019 Forum*, Paper No. AIAA-2019-4217, 2019. https://doi.org/10.2514/6.2019-4217.

[23] Chacon, F., and Gamba, M., "Effect of Secondary Waves on Rotating Detonation Combustor Properties," *Proceedings of the 27th International Colloquium on the Dynamics of Explosions and Reactive Systems*, 2019.

[24] Chacon, F., and Gamba, M., "Study of parasitic combustion in an optically accessible continuous wave rotating detonation engine," *AIAA Scitech 2019 Forum*, Paper No. 2019-0473, 2019. https://doi.org/10.2514/6.2019-0473.

[25] Shank, J., "Development and Testing of a Rotating Detonation Engine Run on Hydrogen and Air," Ph.D. thesis, Air Force Institute of Technology, 2012.

[26] Kaemming, T., Fotia, M. L., Hoke, J., and Schauer, F., "Thermodynamic Modeling of a Rotating Detonation Engine Through a Reduced-Order Approach," *Journal of Propulsion and Power*, Vol. 33, No. 5, 2017, pp. 1170–1178. https://doi.org/10.2514/1.b36237, URL https://doi.org/10.2514/1.b36237.

[27] Schwer, D., and Kailasanath, K., "Feedback into Mixture Plenums in Rotating Detonation Engines," *50th AIAA Aerospace Sciences Meeting including the New Horizons Forum and Aerospace Exposition*, 2012. https://doi.org/10.2514/6.2012-617.

[28] Matsuoka, K., Tanaka, M., Noda, T., Kawasaki, A., and Kasahara, J., "Experimental investigation on a rotating detonation cycle with burned gas backflow," *Combustion and Flame*, Vol. 225, 2021, pp. 13–19. https://doi.org/10.1016/j.combustflame.2020.10.048.

[29] Mikoshiba, K., Sardeshmukh, S. V., and Heister, S. D., "On the response of annular injectors to rotating detonation waves," *Shock Waves*, 2019. https://doi.org/10.1007/s00193-019-00900-8, URL https://doi.org/10.1007/s00193-019-00900-8.

[30] Deng, L., Ma, H., Xu, C., Zhou, C., and Liu, X., "Investigation on the propagation process of rotating detonation wave," *Acta Astronautica*, Vol. 139, 2017, pp. 278–287. https://doi.org/https://doi.org/10.1016/j.actaastro.2017.07.024.

[31] Kurzke, J., "Correlations hidden in compressor maps," *Turbo Expo: Power for Land, Sea, and Air*, Vol. 54617, 2011, pp. 161–170. https://doi.org/10.1115/GT2011-45519.

[32] Nordeen, C. A., Schwer, D., Schauer, F., Hoke, J., Barber, T., and Cetegen, B., "Thermodynamic model of a rotating detonation engine," *Combustion, Explosion, and Shock Waves*, Vol. 50, No. 5, 2014, pp. 568–577.

[33] Andrus, I., Polanka, M., King, P., Schauer, F., and Hoke, J., "Experimentation of Premixed Rotating Detonation Engine Using Variable Slot Feed Plenum," *Journal of Propulsion and Power*, Vol. 33, No. 6, 2017, pp. 1448–1458. https://doi.org/10.2514/1.B36261.

[34] Tobias, J., Miller, R., and Agrawal, A. K., "Flow Measurements Inside a Rotating Detonation Combustor," *AIAA Propulsion and Energy 2020 Forum*, 2020, p. 3869.

[35] Depperschmidt, D., Miller, R., Tobias, J., Uddi, M., Agrawal, A. K., and Stout, J. B., "Time-Resolved PIV Diagnostics to Measure Flow Field Exiting Methane-Fueled Rotating Detonation Combustor," *AIAA Scitech 2019 Forum*, Paper No. AIAA-2019-1514, 2019. https://doi.org/10.2514/6.2019-1514, URL https://doi.org/10.2514/6.2019-1514.

[36] Gamba, M., Feleo, A., Shepard, J., and Chacon, F., "State-to-State Model for Rotating Detonation Combustors," *Proceedings of the 28th International Colloquium on the Dynamics of Explosions and Reactive Systems*, 2022.

[37] Feleo, A., Shepard, J., and Gamba, M., "Elevated Inlet Temperature Effects on the Operation of a Rotating Detonation Combustor," *AIAA Scitech 2021 Forum*, Paper No. AIAA-2021-3673, 2021.

[38] Andrus, I. Q., King, P., Fotia, M., Schauer, F., and Hoke, J., "Experimental Analogue of a Pre-Mixed Rotating Detonation Engine In Plane Flow," *53rd AIAA Aerospace Sciences Meeting*, Paper No. AIAA-2015-1105, 2015. https://doi.org/10.2514/6.2015-1105, URL http://dx.doi.org/10.2514/6.2015-1105.

[39] Kaemming, T. A., Fotia, M. L., Hoke, J. L., and Schumacker, S. A., "Quantification of the loss mechanisms of a ram rotating detonation engine," *AIAA Scitech 2020 Forum*, Paper No. AIAA-2020-0927, 2020. https://doi.org/10.2514/6.2020-0927.

[40] Goto, K., Matsuoka, K., Matsuyama, K., Kawasaki, A., Watanabe, H., Itouyama, N., Ishihara, K., Buyakofu, V., Noda, T., Kasahara, J., Matsuo, A., Funaki, I., Nakata, D., Uchiumi, M., Habu, H., Takeuchi, S., Arakawa, S., Masuda, J., Maehara, K., Nakao, T., and Yamada, K., "Space Flight Demonstration of Rotating Detonation Engine Using Sounding Rocket S-520-31," *Journal of Spacecraft and Rockets*, 2022, p. 273–285. https://doi.org/10.2514/1.a35401.

[41] Naples, A., Knisely, A., Hoke, J., and Schauer, F., "Infinite line pressure probe and flush transducer measurements in a rotating detonation engine channel," *AIAA Scitech 2019 Forum*, Paper No. AIAA-2019-2022, 2019. https://doi.org/10.2514/6.2019-2022.

[42] Schreier, F., "Optimized implementations of rational approximations for the Voigt and complex error function," *Journal of Quantitative Spectroscopy and Radiative Transfer*, Vol. 112, No. 6, 2011, pp. 1010–1025.

[43] Gordon, I. E., Rothman, L. S., Hargreaves, R., Hashemi, R., Karlovets, E. V., Skinner, F., Conway, E. K., Hill, C., Kochanov, R. V., Tan, Y., et al., "The HITRAN2020 molecular spectroscopic database," *Journal of quantitative spectroscopy and radiative transfer*, Vol. 277, 2022, p. 107949.

[44] Goldenstein, C. S., Almodóvar, C. A., Jeffries, J. B., Hanson, R. K., and Brophy, C. M., "High-bandwidth scanned-wavelength-modulation spectroscopy sensors for temperature and H2O in a rotating detonation engine," *Measurement Science and Technology*, Vol. 25, No. 10, 2014, p. 105104.

[45] Rieker, G., Li, H., Liu, X., Jeffries, J., Hanson, R., Allen, M., Wehe, S., Mulhall, P., and Kindle, H., "A diode laser sensor for rapid, sensitive measurements of gas temperature and water vapour concentration at high temperatures and pressures," *Measurement Science and Technology*, Vol. 18, No. 5, 2007, p. 1195.

[46] Rieker, G. B., *Wavelength-modulation spectroscopy for measurements of gas temperature and concentration in harsh environments*, Stanford university, 2009.

[47] Rieker, G. B., Jeffries, J. B., and Hanson, R. K., "Calibration-free wavelength-modulation spectroscopy for measurements of gas temperature and concentration in harsh environments," *Applied optics*, Vol. 48, No. 29, 2009, pp. 5546–5560.

[48] Sun, K., *Utilization of multiple harmonics of wavelength modulation absorption spectroscopy for practical gas sensing*, Stanford University, 2013.

[49] Mathews, G. C., Blaisdell, M. G., Lemcherfi, A. I., Slabaugh, C. D., and Goldenstein, C. S., "High-bandwidth absorption-spectroscopy measurements of temperature, pressure, CO, and H2O in the annulus of a rotating detonation rocket engine," *Applied Physics B*, Vol. 127, No. 12, 2021, pp. 1–23.

[50] Goldenstein, C. S., Schultz, I. A., Jeffries, J. B., and Hanson, R. K., "Two-color absorption spectroscopy strategy for measuring the column density and path average temperature of the absorbing species in nonuniform gases," *Applied optics*, Vol. 52, No. 33, 2013, pp. 7950–7962.

[51] Goldenstein, C., Spearrin, R., Schultz, I., Jeffries, J., and Hanson, R., "Wavelength-modulation spectroscopy near 1.4 μm for measurements of H2O and temperature in high-pressure and-temperature gases," *Measurement Science and Technology*, Vol. 25, No. 5, 2014, p. 055101.

[52] Goldenstein, C. S., Spearrin, R. M., Jeffries, J. B., and Hanson, R. K., "Infrared laser absorption sensors for multiple performance parameters in a detonation combustor," *Proceedings of the Combustion Institute*, Vol. 35, No. 3, 2015, pp. 3739–3747.

[53] Schultz, I. A., Goldenstein, C. S., Jeffries, J. B., Hanson, R. K., Rockwell, R. D., and Goyne, C. P., "Spatially resolved water measurements in a scramjet combustor using diode laser absorption," *Journal of Propulsion and Power*, Vol. 30, No. 6, 2014, pp. 1551–1558.

[54] Mathews, G., and Goldenstein, C., "Near-GHz scanned-wavelength-modulation spectroscopy for MHz thermometry and H2O measurements in aluminized fireballs of energetic materials," *Applied Physics B*, Vol. 126, No. 11, 2020, pp. 1–17.

[55] Schwartz, C. J., Stiborek, J. W., Butler, A., Chen, D., Guildenbecher, D. R., Welliver, M., Glumac, N., and Goldenstein, C., "Near-MHz temperature and H2O measurements in post-detonation fireballs of 25 g hemispherical explosives using scanned-wavelength-modulation spectroscopy," *Applied Optics*, 2023.

[56] Li, H., Rieker, G. B., Liu, X., Jeffries, J. B., and Hanson, R. K., "Extension of wavelength-modulation spectroscopy to large modulation depth for diode laser absorption measurements in high-pressure gases," *Applied optics*, Vol. 45, No. 5, 2006, pp. 1052–1061.

[57] Li, Z., Wang, Z., Mével, R., Wang, W., and Chao, X., "A utility for characterising laser diode wavelength-to-time response for wavelength modulation spectroscopy application," *Applied Physics B*, Vol. 129, No. 1, 2023, p. 5.

[58] Schwarm, K. K., Dinh, H. Q., Goldenstein, C. S., Pineda, D. I., and Spearrin, R. M., "High-pressure and high-temperature gas cell for absorption spectroscopy studies at wavelengths up to 8 μm," *Journal of Quantitative Spectroscopy and Radiative Transfer*, Vol. 227, 2019, pp. 145–151.

[59] Sun, K., Chao, X., Sur, R., Goldenstein, C., Jeffries, J., and Hanson, R., "Analysis of calibration-free wavelength-scanned wavelength modulation spectroscopy for practical gas sensing using tunable diode lasers," *Measurement Science and Technology*, Vol. 24, No. 12, 2013, p. 125203.

[60] Abul-Huda, Y. M., and Gamba, M., "Design and Characterization of the Michigan Hypersonic Expansion Tube Facility (MHExT)," *53rd AIAA Aerospace Sciences Meeting*, Paper No. AIAA-2015-1785, 2015. https://doi.org/10.2514/6.2015-1785, URL http://dx.doi.org/10.2514/6.2015-1785.

[61] Xu, S., Song, F., Wu, Y., Zhou, J., Cheng, P., Yang, X., and Chen, X., "Experimental investigation on combustion efficiency of a partially premixed kerosene-air rotating detonation combustor," *Fuel*, Vol. 329, 2022, p. 125418. https://doi.org/10.1016/j.fuel.2022.125418.

[62] Ferguson, D. H., O'Meara, B., Roy, A., and Johnson, K., "Experimental measurements of NOx emissions in a Rotating Detonation Engine," *AIAA Scitech 2020 Forum*, Paper No. AIAA-2020-0204, 2020. https://doi.org/10.2514/6.2020-0204, URL https://doi.org/10.2514/6.2020-0204.

[63] Peng, W. Y., Cassady, S. J., Strand, C. L., Goldenstein, C. S., Spearrin, R. M., Brophy, C. M., Jeffries, J. B., and Hanson, R. K., "Single-ended mid-infrared laser-absorption sensor for time-resolved measurements of water concentration and temperature within the annulus of a rotating detonation engine," *Proceedings of the Combustion Institute*, Vol. 37, No. 2, 2019, pp. 1435–1443.

[64] Nair, A. P., Lee, D. D., Pineda, D. I., Kriesel, J., Hargus, W. A., Bennewitz, J. W., Danczyk, S. A., and Spearrin, R. M., "MHz laser absorption spectroscopy via diplexed RF modulation for pressure, temperature, and species in rotating detonation rocket flows," *Applied Physics B*, Vol. 126, No. 8, 2020, pp. 1–20.

[65] Kuenning, N., Nair, A. P., Keller, A. R., Minesi, N., Spearrin, R. M., Ozen, E., Kriesel, J., Bigler, B. R., Bennewitz, J. W., Burr, J. R., et al., "Simultaneous in-chamber MHz sensing of CO, H2O, temperature, and pressure via mid-infrared laser absorption in a rotating detonation rocket engine," *AIAA SCITECH 2023 Forum*, 2023, p. 2062.

[66] Beck, C. V., and Raman, V., "NOx Formation Processes in Rotating Detonation Engines," *Frontiers in Aerospace Engineering*, Vol. 3, 2024. https://doi.org/10.3389/fpace.2024.1335906.

[67] Nair, A. P., Minesi, N. Q., Kuenning, N. M., Keller, A. R., and Spearrin, R. M., "Optical pressure sensing at MHz rates via collisional line broadening of carbon monoxide: uncertainty quantification in reacting flows," *Applied Physics B*, Vol. 129, No. 4, 2023, p. 51.

[68] Guerrero, J. I., and Gamba, M., "Post-Incident Shock Wave Measurements of Gas Properties at 1 MHz Using Scanned-Wavelength-Modulation Spectroscopy," *AIAA SCITECH 2025 Forum*, 2025, p. 0862.

[69] Chacon, F., Duvall, J., and Gamba, M., "Evaluation of Pressure Rise and Oscillation in a Rotating Detonation Engine," *2018 AIAA Aerospace Sciences Meeting*, Paper No. AIAA-2018-0405, 2018. https://doi.org/10.2514/6.2018-0405, URL https://doi.org/10.2514/6.2018-0405.

[70] Chacon, F., and Gamba, M., "Detonation Wave Dynamics in a Rotating Detonation Engine," *AIAA Scitech 2019 Forum*, Paper No. AIAA-2019-0198, 2019. https://doi.org/10.2514/6.2019-0198, URL https://doi.org/10.2514/6.2019-0198.

[71] Cassady, S. J., Peng, W. Y., Strand, C. L., Dausen, D. F., Codoni, J. R., Brophy, C. M., and Hanson, R. K., "Time-resolved, single-ended laser absorption thermometry and H2O, CO2, and CO speciation in a H2/C2H4-fueled rotating detonation engine," *Proceedings of the Combustion Institute*, Vol. 38, No. 1, 2021, pp. 1719–1727.

[72] Feleo, A., France, J., White, L. W., and Gamba, M., "Evaluation of OH Emission for Determining Operation of a Rotating Detonation Engine," *AIAA Scitech 2019 Forum*, Paper No. AIAA-2019-2252, 2019. https://doi.org/10.2514/6.2019-2252, URL https://doi.org/10.2514/6.2019-2252.

[73] Strakey, P., Ferguson, D., Sisler, A., and Nix, A., "Computationally Quantifying Loss Mechanisms in a Rotating Detonation Engine," *54th AIAA Aerospace Sciences Meeting*, American Institute of Aeronautics and Astronautics Inc, AIAA, 2016. https://doi.org/10.2514/6.2016-0900, URL https://arc.aiaa.org/doi/abs/10.2514/6.2016-0900.

[74] Burr, J. R., and Paulson, E., "Thermodynamic Performance Results for Rotating Detonation Rocket Engine with Distributed Heat Addition using Cantera," *AIAA Propulsion and Energy 2021 Forum*, Paper No. AIAA-2021-3682, 2021. https://doi.org/10.2514/6.2021-3682.

[75] Barnouin, P., Bach, E., Gutmark, E. J., Paschereit, C. O., and Bohon, M., "Low-Order Model for Detonation Velocity Suppression in Rotating Detonation Combustors," *AIAA SCITECH 2023 Forum*, American Institute of Aeronautics and Astronautics Inc, AIAA, ???? https://doi.org/10.2514/6.2023-1291, URL https://arc.aiaa.org/doi/abs/10.2514/6.2023-1291.

[76] Raman, V., Prakash, S., and Gamba, M., "Nonidealities in Rotating Detonation Engines," *Annual Review of Fluid Mechanics*, Vol. 55, No. 1, 2023, pp. 639–674. https://doi.org/10.1146/annurev-fluid-120720-032612.

[77] Stechmann, D. P., Sardeshmukh, S., Heister, S. D., and Mikoshiba, K., "Role of ignition delay in rotating detonation engine performance and operability," *Journal of Propulsion and Power*, Vol. 35, No. 1, 2019, pp. 125–140.

[78] Fievisohn, R. T., Hoke, J. L., and Holley, A., "Thermodynamic and operability implications of product recirculation in rotating detonation engines," *AIAA Propulsion and Energy Forum and Exposition, 2019*, 2019. https://doi.org/10.2514/6.2019-4449, URL http://arc.aiaa.org.

[79] Fievisohn, R. T., Hoke, J., and Schumaker, S. A., "Product Recirculation and Incipient Autoignition in a Rotating Detonation Engine," *AIAA Scitech 2020 Forum*, Paper No. AIAA-2020-2286, 2020. https://doi.org/10.2514/6.2020-2286, URL https://doi.org/10.2514/6.2020-2286.

[80] Sommers, W. P., "The Interaction of a Detonation Wave with an Inert Boundary," Ph.D. thesis, University of Michigan, 1961.

[81] Dabora, E. K., "The Influence of a Compressible Boundary on the Propagation of Gaseous Detonations," *Technical Report*, 1963.

[82] Sichel, M., "A Hydrodynamic Theory for the Interaction of a Gaseous Detonation with a Compressible Boundary," *2nd Aerospace Sciences Meeting*, 1965. https://doi.org/10.2514/6.1965-39, URL https://arc.aiaa.org/doi/abs/10.2514/6.1965-39.

[83] Browne, S. T., Ziegler, J. L., Bitter, N. P., Schmidt, B. E., Lawson, J., and Shepherd, J. E., "SDToolbox: Numerical Solution Methods for Shock and Detonation Jump Conditions," *GALCIT Report FM2018.001*, 2023.

[84] Roy, A., Strakey, P., Sidwell, T., and Ferguson, D. H., *Unsteady Heat Transfer Analysis to Predict Combustor Wall Temperature in Rotating Detonation Engine*, ???? https://doi.org/10.2514/6.2015-4191, URL https://arc.aiaa.org/doi/abs/10.2514/6.2015-4191.

[85] Theuerkauf, S. W., Schauer, F., Anthony, R. J., Paxson, D. E., Stevens, C. A., and Hoke, J., "Comparison of Simulated and Measured Instantaneous Heat Flux in a Rotating Detonation Engine," *54th AIAA Aerospace Sciences Meeting*, Paper No. AIAA-2016-1200, 2016. https://doi.org/10.2514/6.2016-1200.

[86] Stevens, C. A., Fotia, M., Hoke, J., and Schauer, F., *Quasi Steady Heat Transfer Measuments in an RDE*, ???? https://doi.org/10.2514/6.2018-1884, URL https://arc.aiaa.org/doi/abs/10.2514/6.2018-1884.

[87] Sridhara, S. R., Sandri, U., Nassini, P. C., Polanka, M. D., Bohon, M., and Andreini, A., *Quantification of Heat Loads for Rotating Detonation Combustors with Gas Turbine Conditions*, ???? https://doi.org/10.2514/6.2024-2433, URL https://arc.aiaa.org/doi/abs/10.2514/6.2024-2433.

[88] Goodwin, D. G., Speth, R. L., Moffat, H. K., and Weber, B. W., "Cantera: An Object-oriented Software Toolkit for Chemical Kinetics, Thermodynamics, and Transport Processes," https://www.cantera.org, 2021. https://doi.org/10.5281/ZENODO.4527812.

[89] Dellaportas, P., and Roberts, G. O., *An Introduction to MCMC*, Springer New York, New York, NY, 2003, pp. 1–41. https://doi.org/10.1007/978-0-387-21811-3_1, URL https://doi.org/10.1007/978-0-387-21811-3_1.

[90] Metropolis, N., Rosenbluth, A., Rosenbluth, M., Teller, A., and Teller, E., "Equations of State Calculations by Fast Computing Machines," *Journal of Chemical Physics*, , No. 6, 1953, pp. 1087–1091.

[91] Hastings, W., "Monte Carlo Sampling Methods using Markov Chains and their Applications," *Biometrika*, , No. 1, 1970, pp. 97–109. URL https://doi.org/10.1093/biomet/57.1.97.

[92] Haario, H., Saksman, E., and Tamminen, J., "An adaptive Metropolis algorithm," *Bernoulli*, Vol. 7, No. 2, 2001, pp. 223–242. https://doi.org/10.2307/3318737.

[93] Haario, H., Laine, M., Mira, A., and Saksman, E., "DRAM: Efficient adaptive MCMC," *Statistics and Computing*, 2006, pp. 339–354. URL https://doi.org/10.1007/s11222-006-9438-0.

[94] Shahmoradi, A., Bagheri, F., and Osborne, J. A., "Fast fully-reproducible serial/parallel Monte Carlo and MCMC simulations and visualizations via ParaMonte::Python library," *arXiv e-prints*, 2020, arXiv:2010.00724.

[95] Sobol, I., "Global sensitivity indices for nonlinear mathematical models and their Monte Carlo estimates," *Mathematics and Computers in Simulation*, Vol. 55, No. 1, 2001, pp. 271–280. https://doi.org/https://doi.org/10.1016/S0378-4754(00)00270-6, URL https://www.sciencedirect.com/science/article/pii/S0378475400002706, the Second IMACS Seminar on Monte Carlo Methods.

[96] Feleo, A., Shepard, J., and Gamba, M., "Evaluation of Reaction-Induced Effective Inlet Blockage of Rotating Detonation Combustors," , 2024. In preparation.

[97] Kaemming, T. A., and Paxson, D. E., "Determining the Pressure Gain of Pressure Gain Combustion," *2018 Joint Propulsion Conference*, Paper No. AIAA-2018-4567, 2018. https://doi.org/10.2514/6.2018-4567.

[98] Bykovskii, F. A., Zhdan, S. A., and Vedernikov, E. F., "Continuous Spin Detonations," *Journal of Propulsion and Power*, Vol. 22, No. 6, 2006, pp. 1204–1216. https://doi.org/10.2514/1.17656, URL http://dx.doi.org/10.2514/1.17656.

[99] Nordeen, C., Schwer, D., Schauer, F., Hoke, J., Cetegen, B., and Barber, T., "Thermodynamic Modeling of a Rotating Detonation Engine," *49th AIAA Aerospace Sciences Meeting including the New Horizons Forum and Aerospace Exposition*, Paper No. AIAA-2011-803, 2011. https://doi.org/10.2514/6.2011-803, URL https://doi.org/10.2514/6.2011-803.

[100] Schwer, D., and Kailasanath, K., "Effect of Inlet on Fill Region and Performance of Rotating Detonation Engines," *47th AIAA/ASME/SAE/ASEE Joint Propulsion Conference & Exhibit*, 2011. https://doi.org/10.2514/6.2011-6044, URL https://arc.aiaa.org/doi/abs/10.2514/6.2011-6044.

[101] Naples, A., Hoke, J., Karnesky, J., and Schauer, F., "Flowfield characterization of a rotating detonation engine," *51st AIAA Aerospace Sciences Meeting including the New Horizons Forum and Aerospace Exposition 2013*, Paper No. AIAA-2013-278, 2013. https://doi.org/10.2514/6.2013-278.

[102] Bedick, C., Ferguson, D. H., and Strakey, P., "Validation and Application of a Reduced-Order Rotating Detonation Engine Inlet and Fill Zone Model," *AIAA Scitech 2021 Forum*, Paper No. AIAA-2021-0193, 2021. https://doi.org/10.2514/6.2021-0193, URL https://doi.org/10.2514/6.2021-0193.

[103] Feleo, A., Shepard, J., and Gamba, M., "Prediction of Detonation-Induced Disturbances Propagating Upstream into Inlets of Rotating Detonation Combustors," *AIAA Propulsion and Energy 2021 Forum*, Paper No. AIAA-2021-3687, 2021. https://doi.org/10.2514/6.2021-3687.

[104] Paxson, D. E., and Miki, K., "Computational Assessment of Inlet Backflow Effects on Rotating Detonation Engine Performance and Operability," *AIAA SCITECH 2022 Forum*, Paper No. AIAA-2022-1263, 2022. https://doi.org/10.2514/6.2022-1263.

[105] Nordeen, C. A., Schwer, D., Corrigan, A. T., and Cetegen, B., "Radial Effects on Rotating Detonation Engine Swirl," *51st AIAA/SAE/ASEE Joint Propulsion Conference*, Paper No. AIAA-2015-3781, 2015. https://doi.org/10.2514/6.2015-3781.

[106] Nordeen, C., Schwer, D., Schauer, F., Hoke, J., Barber, T., and Cetegen, B., "Energy Transfer in a Rotating Detonation Engine," *47th AIAA/ASME/SAE/ASEE Joint Propulsion Conference & Exhibit*, 2011, p. 6045.

[107] Shepard, J., Joshua, "Experimental Characterization of Rotating Detonation Engine Loss Mechanisms," Ph.D. thesis, University of Michigan, 2023.

[108] Dunn, I. B., Sosa, J., Salvadori, M., Ahmed, K. A., and Menon, S., "Flowfield Velocity Measurements of a Rotating Detonation Engine," *AIAA Scitech 2020 Forum*, Paper No. AIAA-2020-1176, 2020. https://doi.org/10.2514/6.2020-1176, URL https://doi.org/10.2514/6.2020-1176.

[109] Watanabe, T., Jourdaine, N. H., Tsuboi, N., Kojima, T., and Hayashi, K. A., *Three-dimensional Numerical Simulation of Disk Rotating Detonation Engine; Unsteady Flow Structure*, ???? https://doi.org/10.2514/6.2019-1498, URL https://arc.aiaa.org/doi/abs/10.2514/6.2019-1498.

[110] Anderson, J. D., *Modern compressible flow: with historical perspective*, McGraw-Hill New York, 1990.

[111] Huang, X., Chang, P.-H., Teo, Z. W., Li, J.-M., Teo, C. J., and Khoo, B. C., "Particle Image Velocimetry Measurements of Unsteady Exhaust from a Linearized Continuous Detonation Combustor," *AIAA SCITECH 2023 Forum*, American Institute of Aeronautics and Astronautics, 2023. https://doi.org/10.2514/6.2023-1106, URL https://arc.aiaa.org/doi/abs/10.2514/6.2023-1106.

[112] Grunenwald, J. A., Braun, J., and Paniagua, G., *Analysis of the Physics of Rotating Detonation with a Method of Characteristics Model*, ???? https://doi.org/10.2514/6.2024-2037, URL https://arc.aiaa.org/doi/abs/10.2514/6.2024-2037.

[113] Fievisohn, R. T., and Yu, K. H., "Steady-State Analysis of Rotating Detonation Engine Flowfields with the Method of Characteristics," *Journal of Propulsion and Power*, Vol. 33, No. 1, 2017, pp. 89–99. https://doi.org/10.2514/1.b36103, URL https://doi.org/10.2514/1.b36103.

[114] Shepherd, J. E., and Kasahara, J., "Analytical Models for the Thrust of a Rotating Detonation Engine," *Technical Report FM2017.001*, 2017.

[115] Hodges, B. K., "Generalized One-Dimensional Compressible Flow Techniques," *Internation Journal of Applied Engineering*, Vol. 7, No. 1, 1991, pp. 56–63.

[116] Smith, G. P., Golden, D. M., Frenklach, M., Moriarty, N. W., Eiteneer, B., Goldenberg, M., Bowman, C. T., Hanson, R. K., Song, S., Jr., W. C. G., Lissianski, V. V., and Win, Z., "GRI-Mech 3.0," , 2023. URL https://www.me.berkeley.edu/gri_mech/.

[117] Schwer, D., and Kailasanath, K., "Numerical Investigation of Rotating Detonation Engines," *46th AIAA/ASME/SAE/ASEE Joint Propulsion Conference & Exhibit*, 2010. https://doi.org/10.2514/6.2010-6880, URL https://arc.aiaa.org/doi/abs/10.2514/6.2010-6880.

[118] Schwer, D. A., and Kailasanath, K., *Physics of Heat-Release in Rotating Detonation Engines*, ???? https://doi.org/10.2514/6.2015-1602, URL https://arc.aiaa.org/doi/abs/10.2514/6.2015-1602.

[119] Lau-Chapdelaine, S. S.-M., Radulescu, M. I., and Hong, Z., *Quasi-Two-Dimensional Simulation of a Rotating Detonation Engine Combustor and Injector*, ???? https://doi.org/10.2514/6.2020-3878, URL https://arc.aiaa.org/doi/abs/10.2514/6.2020-3878.

[120] Taylor, G. I., "The Dynamics of the Combustion Products Behind Plane and Spherical Detonation Fronts in Explosives," *Proceedings of the Royal Society of London. Series A. Mathematical and Physical Sciences*, Vol. 200, No. 1061, 1950, pp. 235–247. https://doi.org/10.1098/rspa.1950.0014, URL https://royalsocietypublishing.org/doi/abs/10.1098/rspa.1950.0014.

[121] Huff, R., and Gamba, M., "Effects of Non-Idealities on Gain in a Detonation Cycle," *Proceedings of the 29th International Colloquium on the Dynamics of Explosions and Reactive Systems*, Vol. 29, No. 236, 2023. URL http://www.icders.org/ICDERS2023/abstracts/ICDERS2023-236.pdf.

[122] Feleo, A. D., and Gamba, M., "Evaluation of Uncertainties of Pressure Gain Measurements in Rotating Detonation Combustor," *AIAA Journal*, 2023, p. 1–19. https://doi.org/10.2514/1.j063205.

[123] Prakash, S., Raman, V., Lietz, C. F., Hargus Jr, W. A., and Schumaker, S. A., "Numerical Simulation of a Methane-Oxygen Rotating Detonation Rocket Engine," *Proceedings of the Combustion Institute*, Vol. 38, No. 3, 2021, pp. 3777–3786.

[124] Lietz, C., Ross, M., Desai, Y., and Hargus, W. A., "Numerical Investigation of Operational Performance in a Methane-Oxygen Rotating Detonation Rocket Engine," *AIAA Scitech 2020 Forum*, 2020, p. 0687.

[125] Wilhite, J., Driscoll, R. B., St. George, A. C., Anand, V., and Gutmark, E. J., "Investigation of a Rotating Detonation Engine using Ethylene-Air Mixtures," *54th AIAA Aerospace Sciences Meeting*, 2016, p. 1650.

[126] Sato, T., and Raman, V., "Detonation Structure in Ethylene/Air-Based Non-premixed Rotating Detonation Engine," *Journal of Propulsion and Power*, Vol. 36, No. 5, 2020, pp. 752–762.

[127] Rankin, B. A., Fotia, M., Paxson, D. E., Hoke, J., and Schauer, F., "Experimental and Numerical Evaluation of Pressure Gain Combustion in a Rotating Detonation Engine," *53rd AIAA Aerospace Sciences Meeting*, 2015, p. 0877.

[128] Kindracki, J., Wolański, P., and Gut, Z., "Experimental research on the rotating detonation in gaseous fuels–oxygen mixtures," *Shock Waves*, Vol. 21, No. 2, 2011, pp. 75–84. https://doi.org/10.1007/s00193-011-0298-y, URL http://dx.doi.org/10.1007/s00193-011-0298-y.

[129] Sato, T., Chacon, F., White, L., Raman, V., and Gamba, M., "Mixing and Detonation Structure in a Rotating Detonation Engine with an Axial Air Inlet," *Proceedings of the Combustion Institute*, Vol. 38, No. 3, 2021, pp. 3769–3776.

[130] Petrescu, R. V. V., Machin, A., Fontanez, K., Arango, J. C., Marquez, F. M., and Petrescu, F. I. T., "Hydrogen for Aircraft Power and Propulsion," *International Journal of Hydrogen Energy*, Vol. 45, No. 41, 2020, pp. 20740–20764.

[131] Correa, S. M., "A Review of NO_x Formation Under Gas-Turbine Combustion Conditions," *Combustion Science and Technology*, Vol. 87, No. 1-6, 1993, pp. 329–362. https://doi.org/10.1080/00102209208947221.

[132] Lieuwen, T. C., and Yang, V., *Gas Turbine Emissions*, Vol. 38, Cambridge University Press, 2013.

[133] Pavri, R., and Moore, G. D., "Gas Turbine Emissions and Control," *Atlanta: GE Energy Services*, Vol. 1, 2001, pp. 1–20.

[134] Schwer, D. A., and Kailasanath, K., "Characterizing NO_x Emissions for Air-Breathing Rotating Detonation Engines," *52nd AIAA/SAE/ASEE Joint Propulsion Conference, 2016*, 2016, p. 4779.

[135] Raman, V., Prakash, S., and Gamba, M., "Nonidealities in Rotating Detonation Engines," *Annual Review of Fluid Mechanics*, Vol. 55, No. 1, 2023, p. 639–674. https://doi.org/10.1146/annurev-fluid-120720-032612, URL http://dx.doi.org/10.1146/annurev-fluid-120720-032612.

[136] Chacon, F., and Gamba, M., "Study of Parasitic Combustion in an Optically Accessible Continuous Wave Rotating Detonation Engine," *AIAA Scitech 2019 Forum*, 2019, p. 0473.

[137] Sato, T., Beck, C. V., and Raman, V., "Numerical and boundary condition effects on the prediction of detonation engine behavior using detailed numerical simulations," *Frontiers in Aerospace Engineering*, Vol. 2, 2023, p. 1123249. https://doi.org/10.3389/fpace.2023.1123249.

[138] Anand, V., and Gutmark, E., "Rotating Detonation Combustors and Their Similarities to Rocket Instabilities," , 2019. https://doi.org/10.1016/j.pecs.2019.04.001.

[139] Wolański, P., "Detonative Propulsion," *Proceedings of the Combustion Institute*, Vol. 34, No. 1, 2013. https://doi.org/10.1016/j.proci.2012.10.005.

[140] Prakash, S., Fiévet, R., Raman, V., Burr, J., and Yu, K. H., "Analysis of the Detonation Wave Structure in a Linearized Rotating Detonation Engine," *AIAA Journal*, Vol. 58, No. 12, 2020, pp. 5063–5077. https://doi.org/10.2514/1.j058156, URL https://doi.org/10.2514/1.j058156.

[141] Frolov, S. M., Basevich, V. Y., Aksenov, V. S., Gusev, P. A., Ivanov, V. S., Medvedev, S. N., Smetanyuk, V. A., Avdeev, K. A., and Frolov, F. S., "Formation of nitrogen oxides in detonation waves," *Russian Journal of Physical Chemistry B*, Vol. 5, No. 4, 2011, pp. 661–663. https://doi.org/10.1134/s1990793111040166, URL https://doi.org/10.1134/s1990793111040166.

[142] Nabi, M. N., "Theoretical Investigation of Engine Thermal Efficiency, Adiabatic Flame Temperature, NO_x Emission and Combustion-Related Parameters for Different Oxygenated Fuels," *Applied Thermal Engineering*, Vol. 30, No. 8-9, 2010, pp. 839–844.

[143] Zel'dovich, Y. B., "The Oxidation of Nitrogen in Combustion and Explosions," *J. Acta Physicochimica*, Vol. 21, 1946, p. 577.

[144] Li, J., Huang, H., Kobayashi, N., He, Z., and Nagai, Y., "Study on Using Hydrogen and Ammonia as Fuels: Combustion Characteristics and NO_x Formation," *International Journal of Energy Research*, Vol. 38, No. 9, 2014, pp. 1214–1223. https://doi.org/10.1002/er.3141.

[145] Skottene, M., and Rian, K. E., "A Study of NO_x Formation in Hydrogen Flames," *International Journal of Hydrogen Energy*, Vol. 32, No. 15 SPEC. ISS., 2007, pp. 3572–3585. https://doi.org/10.1016/j.ijhydene.2007.02.038.

[146] Liviu-Constantin, S., and Daniela-Elena, M., "Simplified Mechanism Used to Estimate the NO_x Emission of Diesel Engine," *Proceedings of the 2nd International Conference on Manufacturing Engineering, Quality and Production Systems*, 2010, pp. 61–64.

[147] Williams, A., and Clarke, A., "The Principles Behind Controlling NO_x Emissions," *Energy & Environment*, Vol. 3, No. 3, 1992, pp. 280–295.

[148] Mueller, M. A., Kim, T. J., Yetter, R. A., and Dryer, F. L., "Flow Reactor Studies and Kinetic Modeling of the H2/O2 Reaction," *International Journal of Chemical Kinetics*, Vol. 31, No. 2, 1999, pp. 113–125. https://doi.org/10.1002/(SICI)1097-4601(1999)31:2⟨113::AID-KIN5⟩3.0.CO;2-0.

[149] Haworth, N. L., Mackie, J. C., and Bacskay, G. B., "An Ab Initio Quantum Chemical and Kinetic Study of the NNH + O Reaction Potential Energy Surface: How Important Is This Route to NO in Combustion?" *Journal of Physical Chemistry A*, Vol. 107, No. 35, 2003, pp. 6792–6803. https://doi.org/10.1021/jp034421p.

[150] Jachimowski, C. J., "Analytical Study of the Hydrogen-Air Reaction Mechanism with Application to Scramjet Combustion," *NASA Technical Paper*, Vol. 2791, 1988.

[151] Wilson, G. J., and MacCormack, R. W., "Modeling Supersonic Combustion Using a Fully Implicit Numerical Method," *AIAA Journal*, Vol. 30, No. 4, 1992, pp. 1008–1015. https://doi.org/10.2514/3.11021.

[152] Petrukhin, N. V., Grishin, N. N., and Sergeev, S. M., "Ignition Delay Time - an Important Fuel Property," *Chemistry and Technology of Fuels and Oils*, Vol. 51, No. 6, 2016, pp. 581–584. https://doi.org/10.1007/s10553-016-0642-0.

[153] "GRI-Mech 1.2," , 1994. URL https://combustion.berkeley.edu/gri-mech/.

[154] "GRI-Mech 2.11," , 1995. URL https://combustion.berkeley.edu/gri-mech/.

[155] Slack, M., and Grillo, A., "Investigation of hydrogen-air ignition sensitized by nitric oxide and by nitrogen dioxide. Final report," Tech. rep., Grumman Aerospace Corp., Bethpage, NY (USA), 1977.

[156] Lifshitz, A., Scheller, K., Burcat, A., and Skinner, G. B., "Shock-Tube Investigation of Ignition in Methane-Oxygen-Argon Mixtures," *Combustion and Flame*, Vol. 16, No. 3, 1971, pp. 311–321.

[157] Fureby, C., "Large Eddy Simulations of the LAPCAT-II and the SSFE Combustor Configurations," *AIAA Scitech 2020 Forum*, Vol. 1 Part F, Orlando, Florida, 2020, pp. 1–13.

[158] Gerlinger, P., Nold, K., and Aigner, M., "Influence of Reaction Mechanisms, Grid Spacing, and Inflow Conditions on the Numerical Simulation of Lifted Supersonic Flames," *International Journal for Numerical Methods in Fluids*, Vol. 62, No. 12, 2010, pp. 1357–1380. https://doi.org/10.1002/fld.2076.

[159] Kumar, P. P., Kim, K. S., Oh, S., and Choi, J. Y., "Numerical Comparison of Hydrogen-Air Reaction Mechanisms for Unsteady Shock-Induced Combustion Applications," *Journal of Mechanical Science and Technology*, Vol. 29, No. 3, 2015, pp. 893–898. https://doi.org/10.1007/s12206-015-0202-2.

[160] Bowman, C. T., "Investigation Of Nitric Oxide Formation Kinetics In Combustion Processes: The Hydrogen-Oxygen-Nitrogen Reaction," *Combustion Science and Technology*, Vol. 3, No. 1, 1971. https://doi.org/10.1080/00102207108952269.

[161] Clutter, J. K., "Computation of High-Speed Reacting Flows," Ph.D. thesis, University of Florida, 1997.

[162] UCSD, "Chemical-Kinetic Mechanisms for Combustion Applications, San Diego Mechanism Web Page," , 2018. URL http://combustion.ucsd.edu.

[163] Glarborg, P., Miller, J. A., Ruscic, B., and Klippenstein, S. J., "Modeling Nitrogen Chemistry in Combustion," *Progress in Energy and Combustion Science*, Vol. 67, 2018, pp. 31–68.

[164] Sato, T., "High-Fidelity Simulations of Rotating Detonation Engines," Ph.D. thesis, University of Michigan, 2020.

[165] Rankin, B. A., Fotia, M. L., Naples, A. G., Stevens, C. A., Hoke, J. L., Kaemming, T. A., Theuerkauf, S. W., and Schauer, F. R., "Overview of Performance, Application, and Analysis of Rotating Detonation Engine Technologies," *Journal of Propulsion and Power*, Vol. 33, No. 1, 2017, pp. 131–143. https://doi.org/10.2514/1.B36303, URL http://arc.aiaa.org/doi/10.2514/1.B36303.

[166] Chacon, F., and Gamba, M., "Development of an Optically Accessible Continuous Wave Rotating Detonation Engine," *2018 Joint Propulsion Conference*, 2018.

[167] Sato, T., Chacon, F., Gamba, M., and Raman, V., "Mass Flow Rate Effect on a Rotating Detonation Combustor with an Axial Air Injection," *Shock Waves*, Vol. 31, No. 7, 2021, pp. 741–751. https://doi.org/10.1007/s00193-020-00984-7.

[168] *Detailed Chemical Kinetics Based Simulation of Detonation-Containing Flows*, Turbo Expo, Vol. Volume 4A: Combustion, Fuels, and Emissions, ASME, 2018. https://doi.org/10.1115/GT2018-75878.

[169] Pal, P., Kumar, G., Drennan, S. A., Rankin, B. A., and Som, S., "Multidimensional Numerical Modeling of Combustion Dynamics in a Non-premixed Rotating Detonation Engine with Adaptive Mesh Refinement," *Journal of Energy Resources Technology*, Vol. 143, No. 11, 2021.

[170] Prakash, S., and Raman, V., "The Effects of Mixture Preburning on Detonation Wave Propagation," *Proceedings of the Combustion Institute*, Vol. 38, 2021.

[171] Chacon, F., and Gamba, M., "Detonation Wave Dynamics in a Rotating Detonation Engine," *AIAA Scitech 2019 Forum*, 2019, p. 0198.

[172] Layi, R., "Exergy and Environmental Considerations in Gas Turbine Technology and Applications," *Gas Turbines*, 2010, p. 29. https://doi.org/10.5772/10206.

[173] Walters, I. V., Gejji, R. M., Heister, S. D., and Slabaugh, C. D., "Flow and Performance Analysis of a Natural Gas-Air Rotating Detonation Engine with High-Speed Velocimetry," *Combustion and Flame*, Vol. 232, 2021, p. 111549.

[174] Fugger, C. A., Cho, K. Y., Hoke, J. L., Gomez-Gomez, M., Meyer, T., Schumaker, S. A., and Caswell, A. W., "Detonation dynamics visualization from

megahertz imaging," *AIAA Scitech 2020 Forum*, Vol. 1 PartF, 2020, pp. 1–13. https://doi.org/10.2514/6.2020-0441, URL http://arc.aiaa.org.

[175] Tobias, J. R., and Agrawal, A. K., "Flow Development in Radial Plane of Rotating Detonation Engine Integrated with Aerospike," *Journal of Propulsion and Power*, Vol. 39, No. 3, 2023, pp. 318–330.

[176] Journell, C. L., Gejji, R. M., Walters, I. V., Lemcherfi, A. I., Slabaugh, C. D., and Stout, J. B., "High-Speed Diagnostics in a Natural Gas–Air Rotating Detonation Engine," *Journal of Propulsion and Power*, Vol. 36, No. 4, 2020, pp. 498–507.

[177] Hamlington, P. E., Darragh, R., Briner, C. A., Towery, C. A., Taylor, B. D., and Poludnenko, A. Y., "Lagrangian Analysis of High-Speed Turbulent Premixed Reacting Flows: Thermochemical Trajectories in Hydrogen–Air Flames," *Combustion and Flame*, Vol. 186, 2017, pp. 193–207.

[178] Kozak, Y., Dammati, S. S., Bravo, L. G., Hamlington, P. E., and Poludnenko, A., "Novel Lagrangian-Particle Tracking Method for Highly Compressible, Turbulent, Reacting Flows," *AIAA SciTech 2019 Forum*, 2019, p. 1642.

[179] Kozak, Y., Dammati, S. S., Bravo, L. G., Hamlington, P. E., and Poludnenko, A. Y., "WENO Interpolation for Lagrangian Particles in Highly Compressible Flow Regimes," *Journal of Computational Physics*, Vol. 402, 2020, p. 109054.

[180] Nordeen, C. A., and Schwer, D. A., "Quasi-Steady-State Analysis of a High Resolution Detonation Simulation," *AIAA SciTech 2019 Forum*, 2019, p. 1745.

[181] Schwer, D. A., "Multi-Dimensional Simulations of Liquid-Fueled JP10/Oxygen Detonations," *AIAA Propulsion and Energy 2019 Forum*, 2019, p. 4042.

[182] Prakash, S., Bielawski, R., Raman, V., Ahmed, K., and Bennewitz, J., "Three-Dimensional Numerical Simulations of a Liquid RP-2/O2 Based Rotating Detonation Engine," *Combustion and Flame*, Vol. 259, 2024, p. 113097.

[183] Meng, Q., Zhao, M., Zheng, H., and Zhang, H., "Eulerian-Lagrangian Modelling of Rotating Detonative Combustion in Partially Pre-Vaporized n-Heptane Sprays with Hydrogen Addition," *Fuel*, Vol. 290, 2021, p. 119808.

[184] Bielawski, R., Prakash, S., and Raman, V., "High-fidelity Simulations of Liquid-gas Colliding Jets Impacted by a Detonation Wave," *28th International Colloquium on the Dynamics of Explosions and Reactive Systems*, 2022.

[185] Nordeen, C. A., Schwer, D., Schauer, F., Hoke, J., Barber, T., and Cetegen, B., "Thermodynamic Model of a Rotating Detonation Engine," *Combustion, Explosion, and Shock Waves*, Vol. 50, 2014, pp. 568–577.